PROCEEDINGS OF

ICADD-7

Seventh International Conference on the Analysis of Discontinuous Deformation

December 10-12, 2005
Honolulu, Hawaii

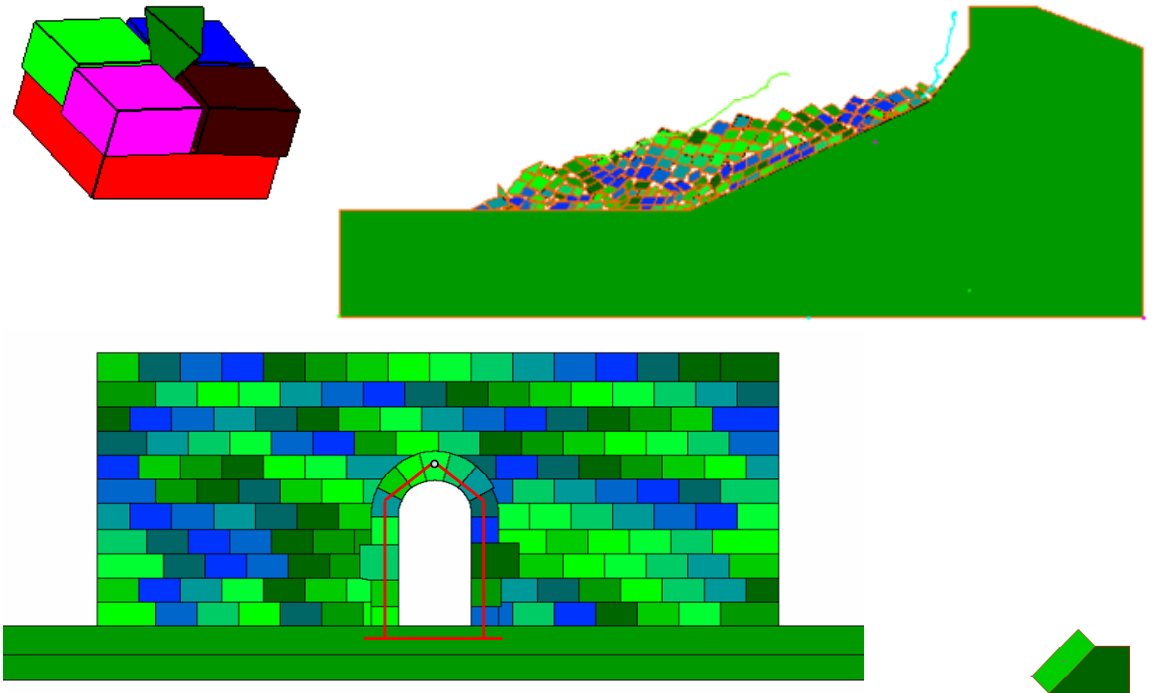

Proceedings Compiled & Edited by

Mary M. MacLaughlin,
Montana Tech of The University of Montana
Nicholas Sitar,
University of California at Berkeley

ICADD-7 International Organizing Committee:

John Tinucci, Agapito Associates, Inc., *Conference Chair*
Mary MacLaughlin, Montana Tech, *Technical Program Chair*
Nicholas Sitar, UC-Berkeley, *Conference and Technical Program Co-Chair*
Gen-hua Shi, DDA Company
David Doolin, UC-Berkeley
Yosef Hatzor, Ben Gurion University
Friedrich Scheele, University of Capetown
Ali Mortazavi, Amirkabir University of Technology (Tehran, Iran)
Richard McNearny, Montana Tech

The Organizing Committee would like to express appreciation to the American Rock Mechanics Association and DDA Company for supporting ICADD-7.

The figures shown on the front cover may be found in the following papers:

Analysis and improvement of scheme to detect contacts in 3D blocky systems by Wang et al.
Earthquake response analysis of a rock-fall by discontinuous deformation analysis by Sasaki et al.
Dynamic back analysis of structural failures in archeological sites to obtain paleo-seismic parameters using DDA by Kamai and Hatzor
DDA Benchmark Testing at UCT – A Summary by Scheele and Bates

The figure on the back cover may be found in:

Producing Joint Polygons, Cutting Rock Blocks and Finding Removable Blocks for General Free Surfaces Using 3-D DDA by Shi

Papers originating in Iran were published as submitted, and were not reviewed or modified.

Copies of the Proceedings may be available by contacting ARMA or Prof. Mary MacLaughlin, Montana Tech, Butte, Montana 59701 USA (email: mmaclaughlin@mtech.edu)

The Conference was held December 10-12, 2005, on the campus of the University of Hawaii, in Honolulu, Hawaii.

Table of Contents

Manifold, Keyblock, and Other Methods of Analysis:

Preface

The theme of this 7th International Conference on Analysis of Discontinuous Deformation, *Stability Analyses using Discontinuous Methods,* goes to the heart of the class of problems that provide some of the greatest challenges in the analysis of rock masses, namely the kinematics of deformations along discontinuities. These problems arise in the analyses of cuts and excavations, tunnels and underground openings, and natural slopes and require the ability to analyze and identify both the potential for failure and the failure mechanism.

In this context the introduction of the Discontinuous Deformation Analysis in Dr. Shi's dissertation in 1988 opened new possibilities for rapid and cost-effective visualization and analysis of the deformation of discontinuous media. It was a pleasure and privilege for me to have been a witness to this beginning. Since its introduction, DDA has evolved from the original 2-D formulation to a sophisticated 3-D analysis technique and, as the papers in these proceedings attest, it has been adapted for use in a wide range of very challenging applications. More importantly, the method has proved useful both as an advanced research tool as well as a practical engineering analysis tool, and its use has spread throughout the international rock mechanics community.

This conference would not have been possible without the efforts of Dr. Mary MacLaughlin, Dr. John Tinucci and Dr. Gen-hua Shi, who worked tirelessly on planning and organizing of the conference in this beautiful venue. We are also very grateful to the sponsors: Geolabs, Inc., The University of Hawaii, and the American Rock Mechanics Association. Finally, we would like to thank the authors of the papers for their contributions and participation.

Nicholas Sitar
Conference and Technical Program Co-Chair
UC Berkeley
November 2005

(This page intentionally left blank.)

Producing Joint Polygons, Cutting Rock Blocks and Finding Removable Blocks for General Free Surfaces Using 3-D DDA

Gen-hua Shi
DDA Company, Belmont, California, USA

ABSTRACT: This paper contributes to the field of knowledge on joint rock mass behavior by demonstrating the relationship between joint spacing and length in forming blocks. Based on the joint length and joint spacing, this paper describes a process of statistically generating finite joint polygons in 3-d space. The joint polygons then cut different types of rock block systems. If the ratio of joint length divided by joint spacing is less than 10, the rock mass is likely connected and stable. If this joint length ratio is greater than 10, the rock is likely to be blocky and removable blocks should be found.

The paper also presents an algorithm for finding all removable blocks along any given moving direction. The rock mass boundary can be any excavated and natural free surfaces. The algorithm works for both joint sets and for any joint system where each joint has its own direction. This is an application of polygon cutting code DC of 3-d DDA.

1. THREE DIMENSIONAL JOINTS

The geometric information of joints is represented by geological map or joint map. Joint maps are joint trace maps. The joint trace maps are the cross-section of the three dimensional joint polygons or joint discs. In order to form three dimensional block systems, three dimensional joint systems are needed.

1.1. Joint Polygons

In order to simulate the joint polygons for each joint set, the average joint polygon 'length' is needed. In most cases, however, the average joint length can be represented by the joint trace length since there is very little information which can be offered about the extension of the joints beyond the rock surface back into the rock mass. The mathematical relation of the joint trace length and joint polygon length is studied here in this paper.

The real shapes of three dimensional joints are complex polygons. Mathematically speaking any complex shape can be represented by polygons. The joint polygons may be complex and variable. However, very limited information can be given about the joint polygon shapes from joint trace maps. The joint polygons are often to be simplified as discs with different diameters, different locations and different directions. This is a popular choice.

1.2. Representation of Joint Polygons

Assume the horizontal tectonic force is the main factor of forming the rock fractures. In this paper, the joint polygons are simplified as squares where the edges are parallel to joint dip direction and joint strike direction respectively.

However, using the joint squares to compute blocks, the joint squares are divided to triangles. The actual input joint shapes of this block computation code DC of 3-d DDA are triangle combinations or general polygons. Therefore the joint squares can be change to general joint

polygons if more joint shape information can be obtain in the future. The block computation code still works without any modification.

1.3. Joint Trace Length and Joint Disc Diameter

The simplest representation of a joint in 3-d space is a disc. Denote the average joint trace length of a joint set as L_{tr}. Denote the joint disc diameter as D. The edge length of the circumscribed square of joint disc is D. The average length L_{tr} of joint traces is equal to the area of the joint disc divided by edge length of circumscribed square D. (See Figure 1)

$$L_{tr} = \pi\left(D/2\right)^2 / D = \left(\pi/4\right)D$$

$$D = \left(4/\pi\right)L_{tr} = 1.2732L_{tr}$$

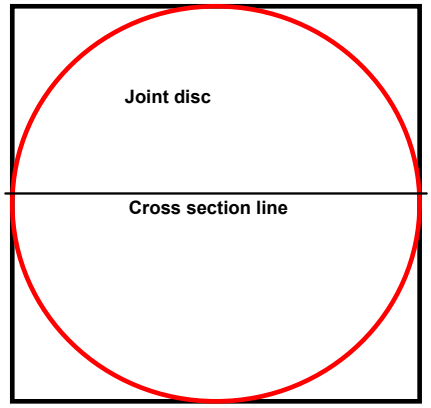

Fig. 1. Joint disc and cross section line

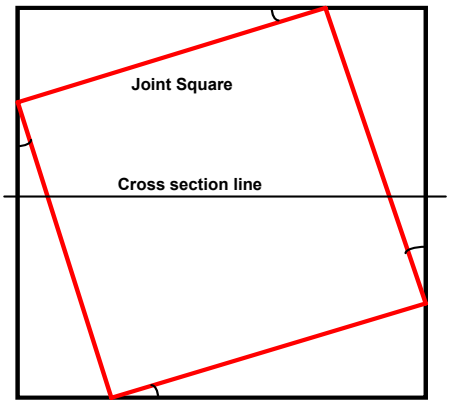

Fig. 2. Joint square and cross section line

1.4. Joint Trace Length and Square Edge Length of Joints

Another simplest representation of a joint in 3-d space is a square. Denote the average joint trace length of a joint set as L_{tr}. Denote the edge length of joint squares as E. Denote the angle of section line and the square edge as α.

The circumscribed square of the joint square with edge E will contain the joint square. All of four nodes of the joint square are in the four edges of the circumscribed square. The circumscribed square with two edges parallel to the section line has edge length C: (See Figure 2)

$$C = \left(\sin\alpha + \cos\alpha\right)E$$

The average length L_{tr} of joint traces equal to the joint square area divided by the edge length of the circumscribed square C:

$$L_{tr} = E^2 / C = E^2 / \left(\left(\sin\alpha + \cos\alpha\right)E\right)$$

$$L_{tr} = E / \left(\sin\alpha + \cos\alpha\right)$$

$$E = \left(\sin\alpha + \cos\alpha\right)L_{tr}$$

Compute average square edge length E_{av} over the angle α

$$E_{av} = \left(\int_0^{\pi/2} E d\alpha \right) / (\pi / 2)$$

$$E_{av} = \left(\int_0^{\pi/2} (\sin\alpha + \cos\alpha) L_{tr} d\alpha \right) / (\pi / 2)$$

$$E_{av} = (4/\pi) L_{tr} = 1.2732 L_{tr}$$

It is seems a wonderful coincident that the formulae for disc diameter *D* and square edge E_{av} are exactly the same. Theoretically, the edge length E_{av} of joint squares is 1.2732 times of the average joint trace length. Again, the joint trace is the intersection line segment of a joint square with the section plane. Therefore, the three dimensional joint polygon is longer than its joint traces.

1.5. Joint Trace Spacing and Joint Plane Spacing

Joint plane spacing is measured along the joint plane normal direction. Joint plane spacing is the distance of two parallel joint planes. In any section plane, the joint trace spacing is generally larger than the joint plane spacing. The joint trace spacing is different in different section plane directions. The joint spacing should be the joint plane spacing in the direction perpendicular to the joint plane. Therefore, the joint spacing is independent of the directions of the section plane.
Denote the joint plane spacing as S_{3d}

Denote the joint trace spacing as S_{tr}

Denote the angle between the upward normal vectors of joint plane and section plane as β

The mathematical relation of S_{3d} and S_{tr} is:

$$S_{3d} = S_{tr} \sin\beta$$

2. PRODUCING JOINT SQUARES BY PERTURBATION

2.1. Define the Boundary of the Space where Joint Squares Are Produced

In this paper, square shape joint polygons are produced based upon the average joint spacing and average edge length of joint 'squares'. Using a simple statistical approach, the joint squares are produced for each joint set. The joint squares become the joint polygons after the trimming by the boundary faces. Figure 5 shows an example of simulated 3-d joint polygons representing a single set of joints.

Several boundary planes are chosen to delimit the space where the joint squares are produced. The boundary planes form a three dimensional convex target block. This convex target block is the space filled by joint squares. Actually, the space where the joint squares are produced is larger than the target block defined by the boundary planes. Therefore some joint squares which are only partly inside of the target block can still be produced.

2.2. Parallel Joint Plane Groups with Distance Equal to the Joint Spacing

The first step of statistically producing joint squares is to produce an equally distanced parallel plane group for each joint set as shown in Figure 3. The planes are confined in the boundary of the target block. Each plane in the same group has the same dip angle and dip direction angle of the corresponding joint set. The distance between the planes of the same group is exactly the joint spacing of the corresponding joint set. The meaning of forming parallel plane groups is to divide the space as zones based on joint set direction and joint spacing of the joint set.

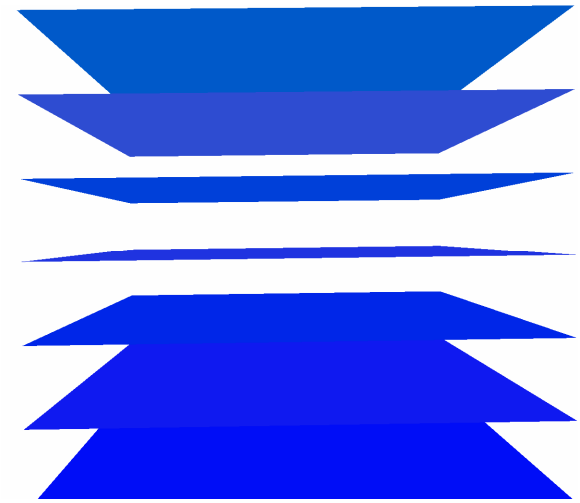

Fig. 3. Parallel joint planes with distance equal to the joint spacing

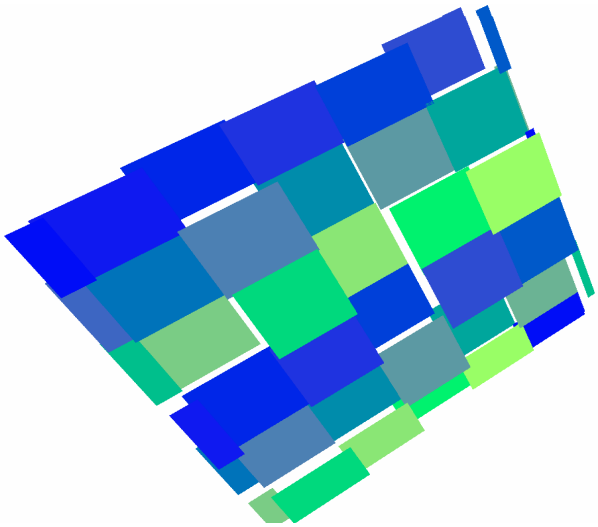

Fig. 4. Perturbation of joint squares in each joint plane

2.3. Dividing Each Joint Plane to Squares

Each joint plane is divided into equally sized squares. The edges of the squares are parallel to the strike direction and the dip direction of their joint set. The strike direction of a joint set is the direction of the intersection line between the joint plane and horizontal plane. The dip direction is on the joint plane and perpendicular to the strike direction.

The edge length of joint squares is the joint length E_{av} which is 1.2732 times of the joint trace length in according to the theory. This procedure is to produce one layer joint squares in each zone. The boundary to boundary distance of the joint squares in the joint plane is equal to the joint bridge. Here the joint bridge can be both positive and negative. For negative bridge, the joint squares are overlapped.

2.4. Perturbation of Joint Squares in Each Joint Plane

Firstly the joint square edge is perturbed statistically. After the perturbation, the joint squares are still plane squares and the edge directions are remain the same. Only the edge length is changed in some degree.

Secondly, the joint squares in a joint plane are moved randomly in the normal direction of the joint plane. This is the perturbation of the joint square spacing. This procedure is the perturbation of joint sizes, joint bridges and joint spacing. This is the simulation of the three dimensional joints by joint squares. (See Figure 4)

2.5. Trimming Joint Squares by Boundary Planes to Fit in the Target Block

The joint squares which are inside the target block are kept. If a joint square is in the target block side of all boundary planes, this joint square is inside the target block. If a joint square is in the other side of the target block from any one boundary plane, this joint square is completely in the outside of the target block.

If a joint square is partly inside of the target block and partly outside of the target block, this joint square is a boundary joint square. For a boundary square, there are one or more boundary planes which intersect the boundary joint square. The boundary joint squares have to be trimmed by

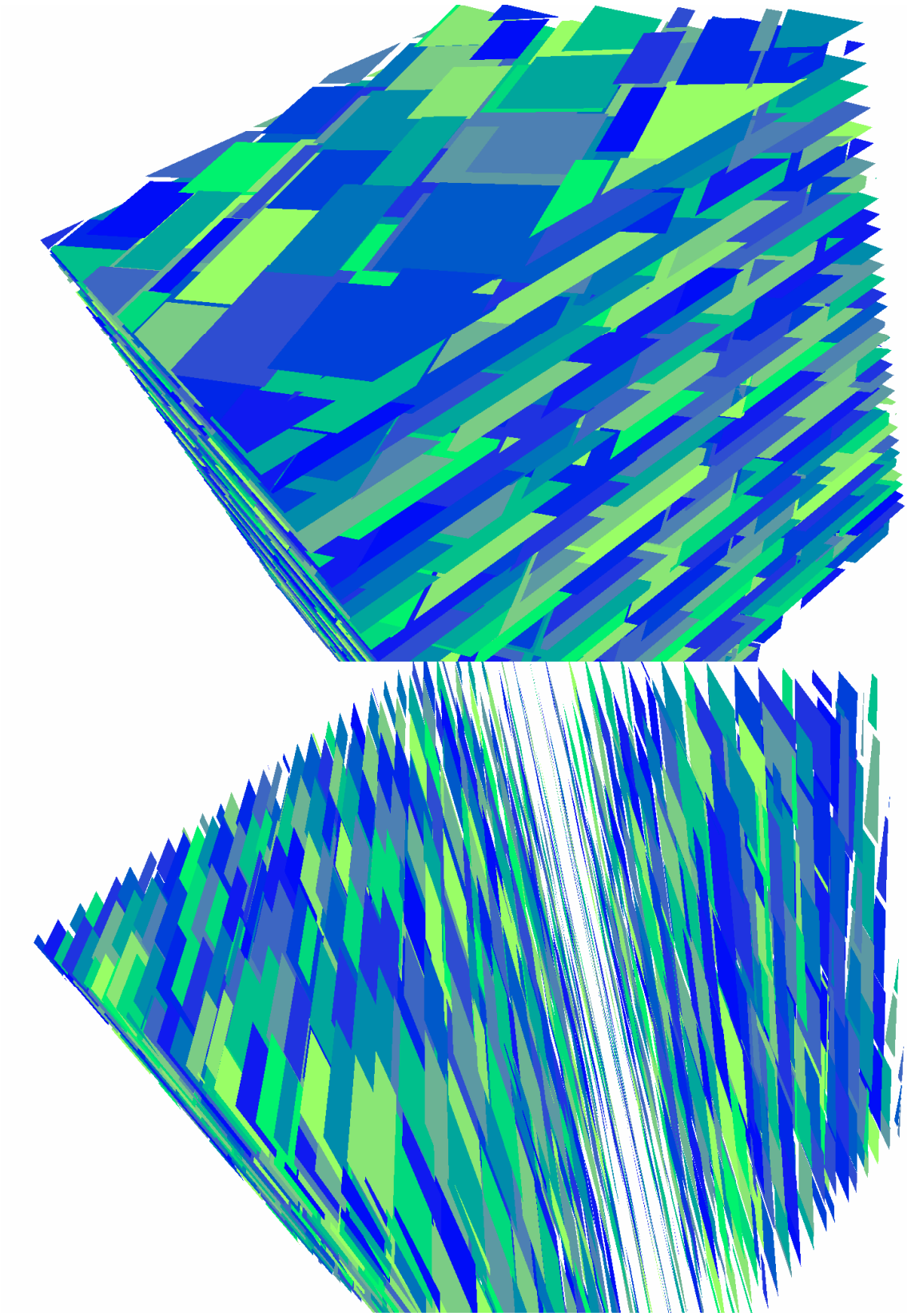

Fig. 5. Statistically produced joint polygons of a joint set

those boundary planes which intersect this joint square. Therefore, after the trimming by boundary planes, a joint square is not a square any more, it is a generally shaped convex polygon. This three-dimensional joint producing code is used to produce general convex joint polygons which can have any number of edges. Figure 5 shows the statistically produced joint polygons of a joint set.

3. CUTTING 3-D BLOCKS FROM JOINT POLYGONS

3.1. What Kind of Three-Dimensional Blocks the Joint Polygons Can Possibly to Produce

To determine the joint blocks, all joint sets must be simulated or the individual joint polygons must be input. The produced joint polygons of all joint sets, all input joint polygon and all boundary faces are the input data for the three dimensional DDA cutting program DC. The cutting program DC computes 3-d blocks. Figure 9 and Figure 11 show a portion of the three dimensional blocks.

If the individual joints are all much longer compare with the dimension of the target block, all intersected blocks are convex block. In this case, the blocks are simple and the computation, the algorithm and the related theory are all simple.

However, if the joint polygons are shorter than the diameter of the target block, the joint polygons are terminated in the middle of the target block. In the later case, the computation, the algorithm and the related theory could be substantially complex. Also, the produced blocks could be complex in the following ways:

- The blocks can be concave
- The polygon faces of the blocks can be concave
- The number of polygon faces of one block can be unusually large
- Inside a block there can have other smaller blocks which are sub-blocks
- Inside a block, the sub-block can contain its own sub-block
- The blocks can have through holes such as a ring
- Inside a block, the sub-blocks and holes can be connected in points or edges
- As block faces, a polygon can contain another polygons which are sub-polygons
- Inside a polygon, a sub-polygons can contain its own sub-polygons

3.2. The Theory and Algorithms of the polygon Cutting Code

Since the blocks can be as complex as mentioned in the previous section, the theory and the algorithm have to consider and to cover all of these complicated cases. Furthermore, the polygons can be statistically produced and can be in high degree of randomness. Therefore, the computer code has to be general.

It seems that the task of forming blocks from polygons is a purely geometric task. This task completely belongs to the category of computational geometry. However, in order for this computer code to solve every possible case, the algorithms and the theory of this program have to be based strictly on Algebraic Topology. Many topological principles are adapted in this program DC: orientation, finite covers, convex body, close chain, boundary chain and relation matrices. The main structure of DC is the following:

(i) Build 0-2 relation matrix in 3-d space to find nodes: 0-d are the intersection points, 2-d are the cutting polygons
(ii) Build 0-2 relation matrix in each plane to find nodes in this plane: 0-d are the intersection points, 2-d are the cutting polygons
(iii) Build 1-0 relation matrix in each intersection line to find divided edges: 1-d are the intersection line of cutting polygons, 0-d are the intersection points of cutting polygons on the intersection line
(iv) Build 0-1 relation matrix in each plane to find its formed polygon: 0-d are the intersection points, 1-d are the formed edges on the given plane
(v) Build 1-2 relation matrix to find the maximum close chain (boundary chain in this case): 1-d are the formed edges, 2-d are the formed polygons in 3-d space
(vi) Build 1-2 relation matrix of the maximum 3-d blocks to find the formed blocks: 1-d are the formed edges, 2-d are the formed polygons in 3-d space

The code DC performs the numerical computation. The code DC operates under the limited accuracy the computer can offer. Especially, in some ill-conditioned combinations, more difficulties occur.
It is not necessary to involve advanced mathematics here. After practice of the code DC, it would be much easier to understand the mathematics behind.

3.3. The Differences from the Other Three-Dimensional Block Producing Methods

Generally speaking, there are two ways to form three-dimensional blocks: block integration and block differentiation. The method of block integration is to put simple blocks together to construct the desired shape. The simple blocks are basically made by given nodes. The short coming of the block integration method is the possibility of having gap or penetrations between blocks.

The block differentiation method is a block cutting method. Most block cutting codes produce convex blocks. It is assumed that the joint polygons are long enough to cut through the target block.

DC in itself is a block cutting code. DC uses polygons to cut blocks. These polygons can be of any length. The input polygons of DC can terminate in the middle of the target block. The produced blocks can be of any shape: convex, concave or blocks with bubble and holes.

DC can also perform block integration. With all faces of simple blocks as input, DC can compute the integrated block. Also DC can find the penetration or gap and sub-blocks of the input simple blocks. Therefore DC code is also a trouble-free block integration code.

3.4. The Self-Checking of the Three-Dimensional Block Cutting Code

Self-checking of the block cutting code DC is important for both programmer and user. Also the three-dimensional graphic can directly see the polygons and the produced blocks. If there are only few polygons, the results of DC code can be checked intuitively. The major checks of DC code are:

Two-dimensional topological check: for any formed polygon P_i double boundary operation is zero.

$$\partial\partial P_i = 0$$

Three-dimensional topological check: for any formed block B_i double boundary operation is zero and the sum of all block boundaries are the boundary of the target block T .

$$\partial\partial B_i = 0$$

$$\sum_i \partial B_i = \partial T$$

Bock volume summation check: the summation of the block volumes $V(B_i)$ should equal to the volume $V(T)$ of the target block.

$$\sum_i V(B_i) = V(T)$$

The volume checking is a convincing examination. For example, if the target block is simply a cube and the six square faces of the cube are also the cutting polygons, the summation of the block volumes should equal to the cube volume.

3.5. Restrictions of the Three-Dimensional Block Cutting Code on the Input Polygons

Actually, the DC code input three-dimensional generally shaped triangles. Triangles in the same plane can be overlapped. Therefore the entered objects of code DC are the overlapped triangles which can be more complex than any convex or concave polygons. There is one restriction for the current version DC. The union set of overlapped triangles can not have inner holes. Hopefully this restriction will be removed from the later version soon.

4. JOINTED LENGTH RATIO

4.1. Definition of Joint Length Ratio

Denote the average joint plane spacing of all joint sets as S_{3d} . Denote the average joint trace length of all joint sets as L_{tr} . Given S_{3d} , as the average joint trace length L_{tr} is longer, more blocks are formed. The joint length ratio R_{ls} is defined as:

$$R_{ls} = L_{tr} / S_{3d}$$

The joint length ratio R_{ls} will be the most important factor for forming blocks. The total volume and the number of the joint blocks will be the most important factor of the rock global stability.

4.2. Joint Sets Information

The following are examples of joint set data for producing joint polygons by statistics.

Table 1. Joint set angle data

Joint set	Dip angle	Dip direction
1	84°	221°
2	83°	299°
3	9°	59°

Table 2. Joint spacing and joint trace length data

Joint set	Spacing S_{3d}	Length L_{tr}	Bridge
1	0.60 m	2.54m	0.10m
2	1.92m	2.71m	0.10m
3	0.59m	3.23m	0.10m

4.3. Joint Length Ratio and Global Rock Stability

In the next two sections, four cases with different edge lengths of joint squares are studied. Here E_{av} is the edge length of the produced joint square. Table 3 shows the results of the computation of the following two sections.

Table 3. Joint set angle data

Case	Square Edge Length	Length Ratio R_{ls}	Volume of inner blocks
1	$E_{av} = 1.3L_{tr}$	4.82	2.54%
2	$E_{av} = 2.0L_{tr}$	7.84	12.24%
3	$E_{av} = 3.0L_{tr}$	11.11	44.54%
4	$E_{av} = 4.0L_{tr}$	14.83	65.06%

When $R_{ls} < 10$, the majority of the rock mass is connected, only local stability or key block need to be examined.

When $R_{ls} > 10$, the majority of the rock mass is blocky. The global stability of rock masses must be examined.

These results provide valuable guidelines for the type of analysis required for excavations.

5. JOINTED AND CONNECTED ROCK MASSES

5.1. Jointed Rock Masses with Less Than 5% Volume of Inner Blocks

In case the joint length is small and the joint spacing is large, few inner blocks are produced. This means the whole rock mass is basically block-free. In a case where the volume of all inner blocks is less than 5%, more than 95% of the rock volume is connected. Therefore, global stability of the rock mass is ensured.

Since the few individual blocks are surrounded by the connected rock mass, the blocks are unlikely to make any movement. Therefore, the rock mass stability is about the same as the cases without inner blocks.

In this section, polygon producing and block volume statistics of the joint system with 1.3 times joint trace length are examined. Here, the joint spacing is still the original value.

The space for producing joint polygons and computing blocks is the target block. Here the target block is a three-dimensional cube with dimensions:
20m × 20m × 20m
As the checking sum, the volume summation of all blocks is 8,000.0000000000 cubic meters. It indicates that the whole computation is accurate.

The average joint length ratio in this simulation is $R_{ls} = 4.82$

The total inner block volume is 2.54 % of the total rock volume.

Figure 6 shows the connected main boundary block with 4354 and 4098 polygons respectively. The surfaces of the main block are mainly the cubic boundary surfaces.

Figure 7 shows one fifth of the individual blocks excluding the connected boundary main block

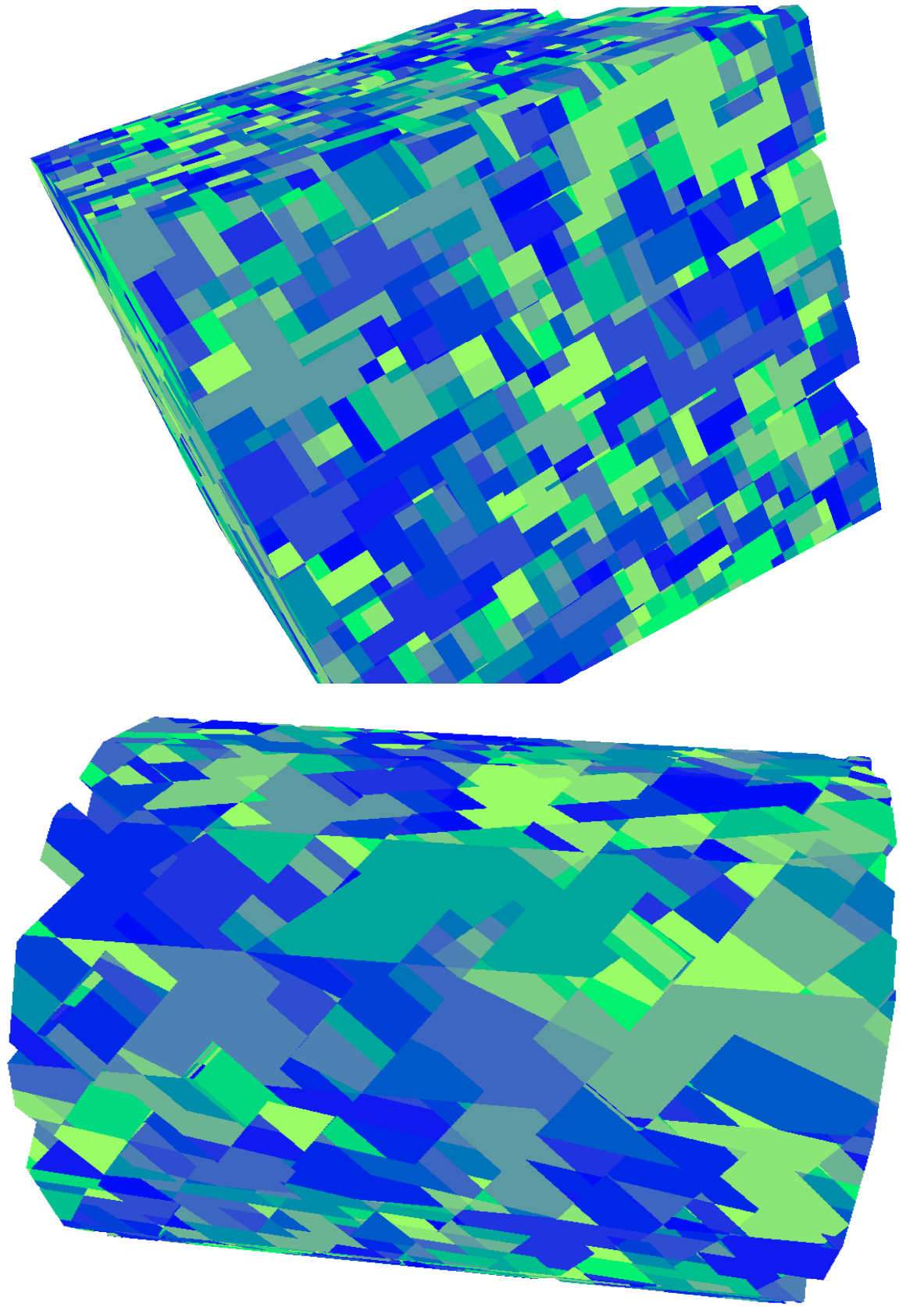

Fig. 6. The single connected main boundary block with 4354 and 4098 polygons

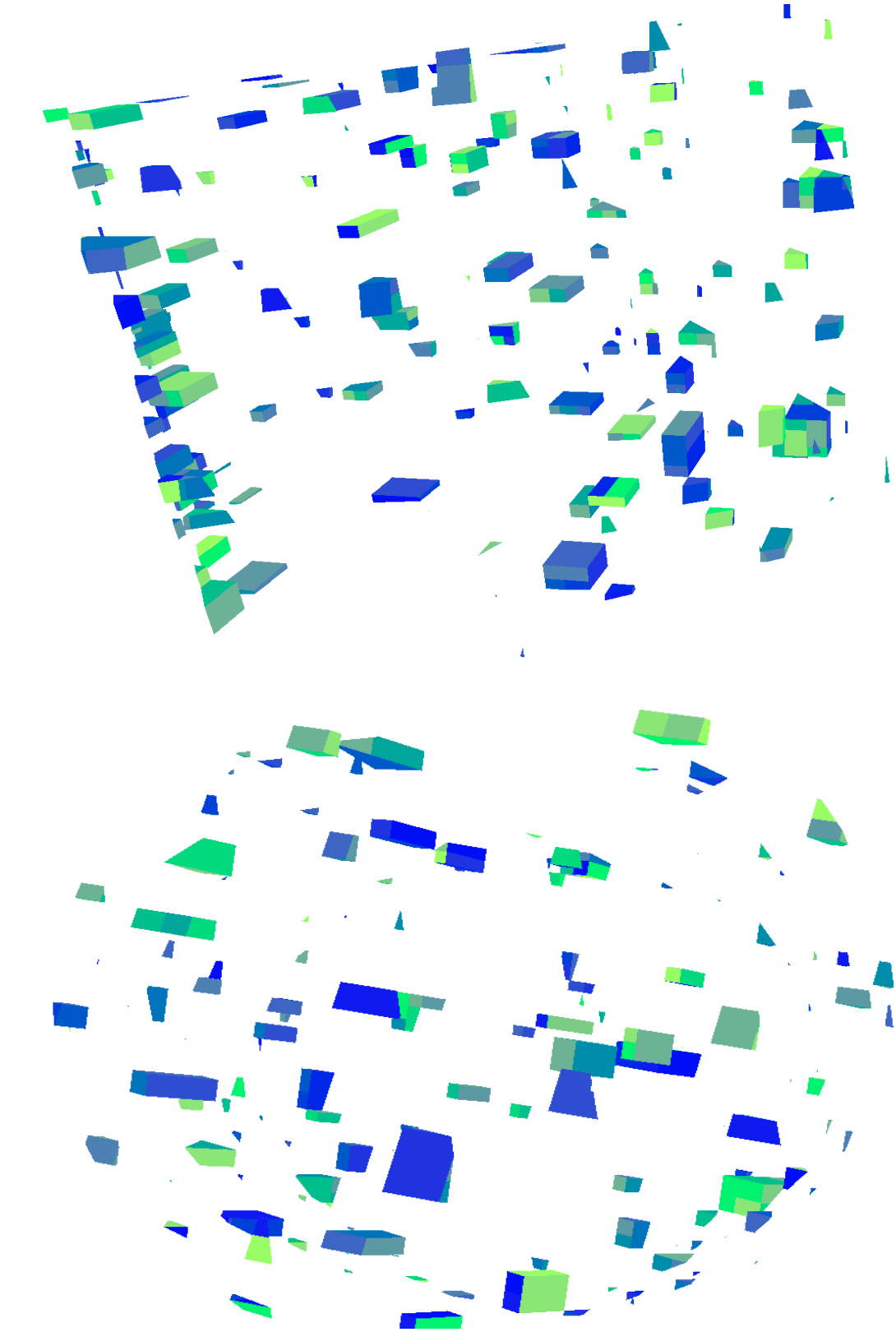

Fig. 7. One fifth of the individual blocks exclude the boundary main block

5.2. Jointed Rock Masses with Less Than 20% Volume of Inner Blocks: Connected Rock

In this section, a joint system with 2.0 times the joint trace length is examined. The joint polygons are produced and blocks are formed. Here, the joint spacing is still the original.

In this case the joint length is relatively small and the joint spacing is relatively large, some very complex concave blocks can be formed. Since more than 80% of the rock volume is connected, the rock blocks are basically confined by the surrounding rock masses. The rock is still stable.

The target block for producing joint polygons and computing blocks is a cube of dimension:

20m × 20m × 20m

As the checking sum, the volume summation of all blocks is 8,000.0000000000 cubic meters. It indicates the whole computation is accurate.

The average joint length ratio in this simulation is $R_{ls} = 7.84$

Total inner block volume is 12.24 % of the total rock volume.

Figure 8 shows the connected main boundary block with 7655 and 7671 polygons respectively.

Figure 9 shows one fifth of the individual blocks excluding the connected boundary main block.

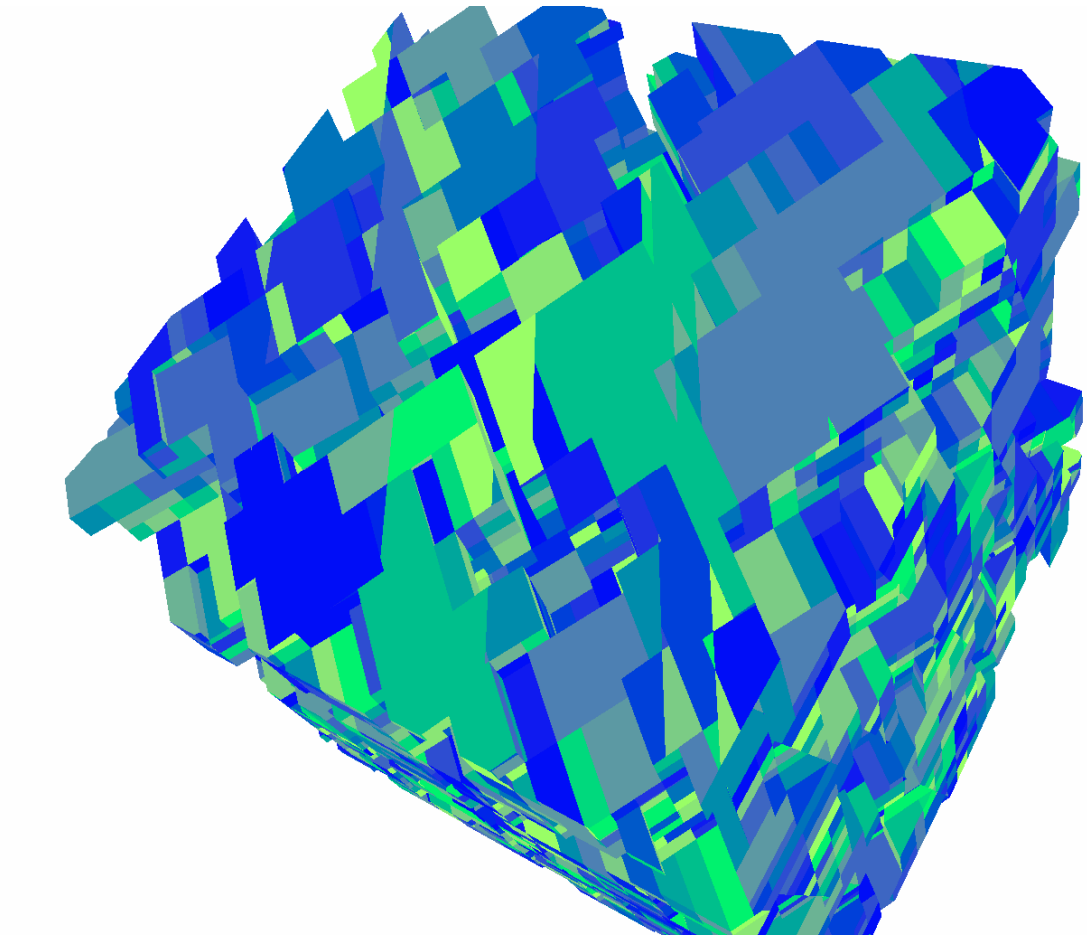

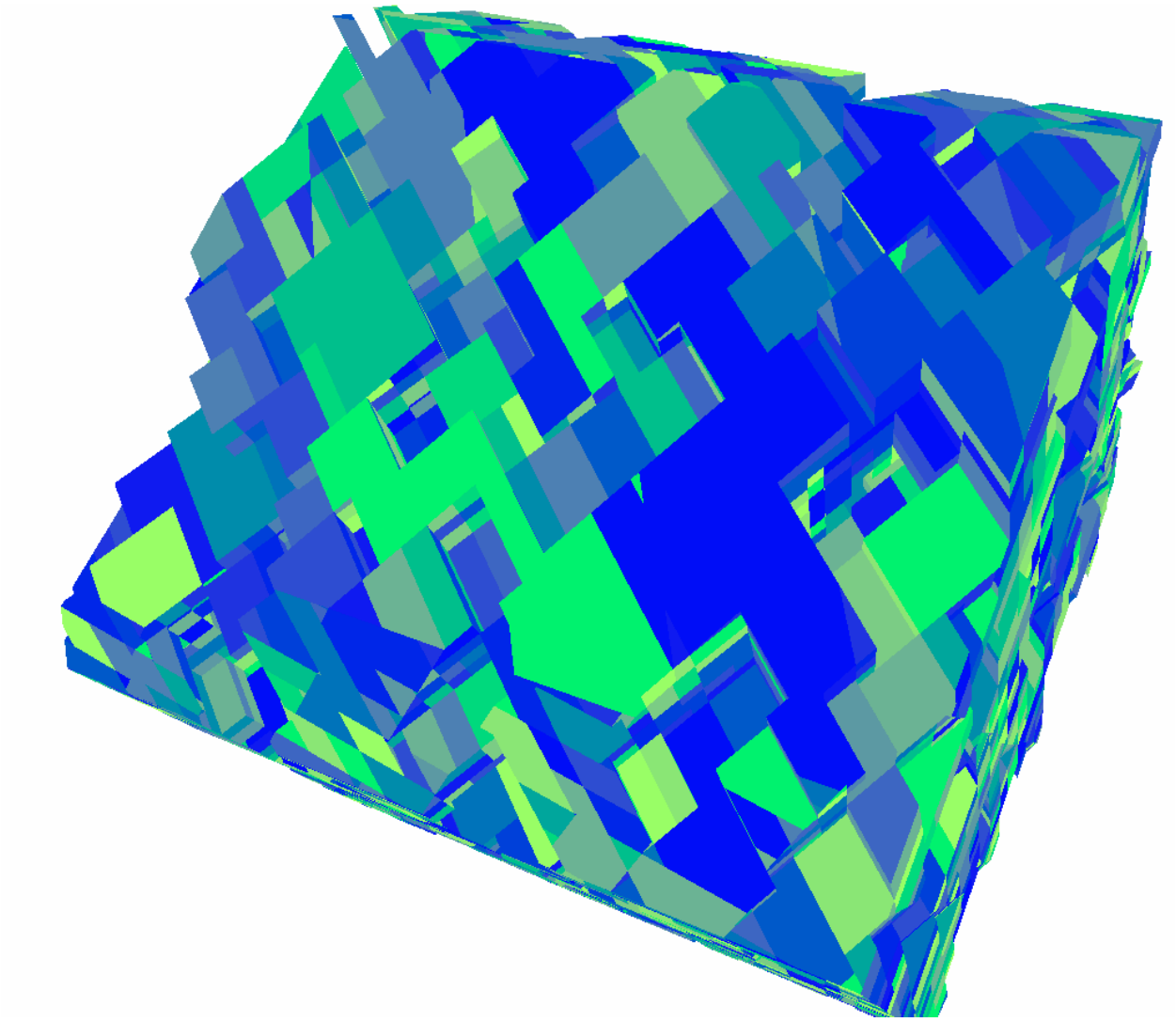

Fig. 8. The single connected main boundary block with 7655 and 7671 polygons

6. BLOCKY OR DISCONNECTED ROCK MASSES

6.1. Jointed Rock Masses with More Than 40% Volume of Inner Blocks: Blocky Rock

Here, the joint spacing is still the original. For the case of 3.0 times joint trace length, joint polygons are produced. Due to the relative long joints, the blocks are relatively simple. There are no very complex major blocks like in the previous case.

Here the target block is a three-dimensional cube with the dimension:
20m × 20m × 20m
As the checking sum, the volume summation of all blocks is as accurate as 8,000.0000000000 cubic meters. This summation kept 14 correct digits. The numbers with double precisions have only 16 digits.

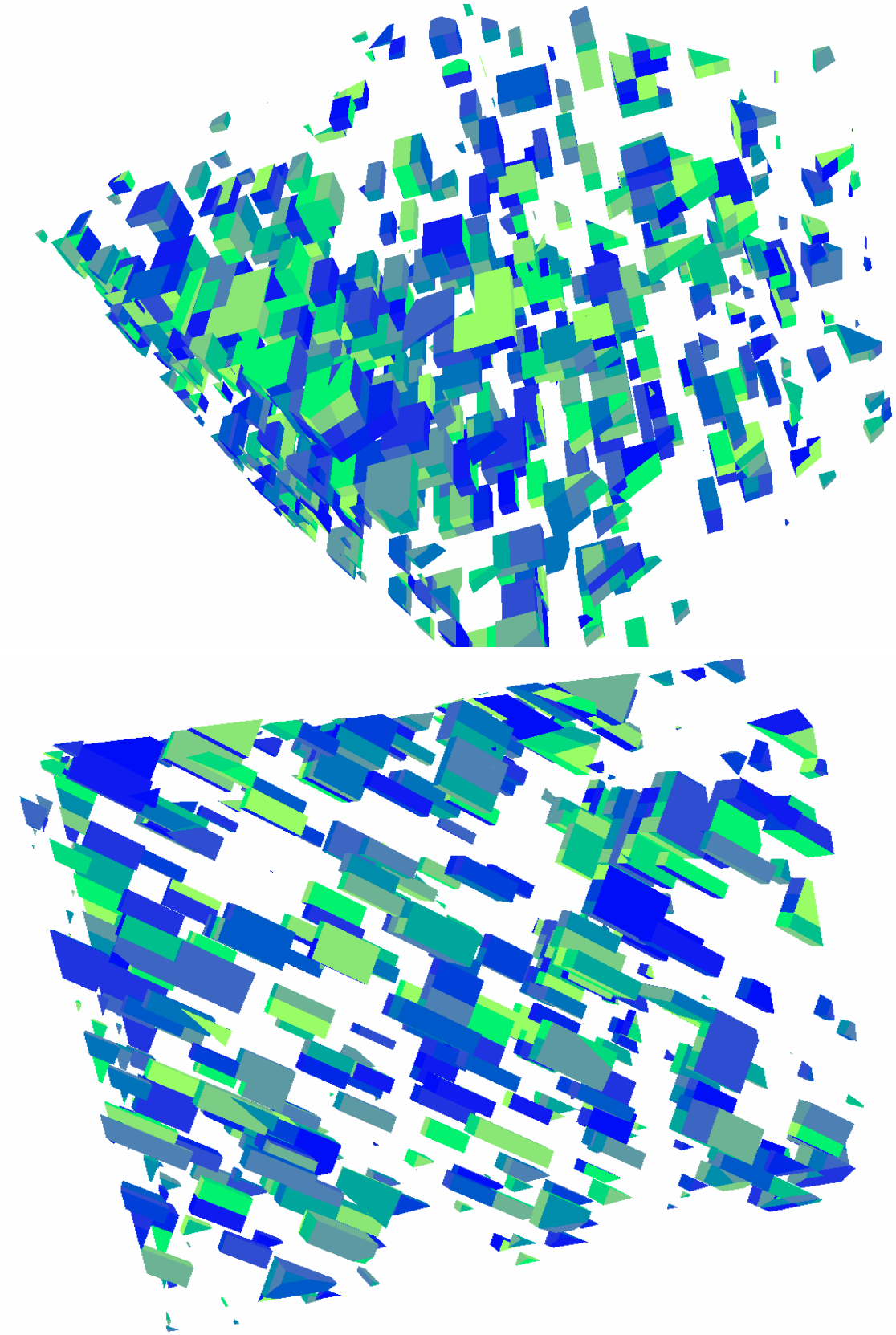

Fig. 9. One fifth of the individual blocks exclude the boundary main block

The average joint length ratio $R_{ls} = 11.11$

The total inner block volume is 44.54 % of the total rock volume.

Figure 10 shows the connected main boundary block with 601 and 561 polygons respectively.

Figure 11 shows one fifth of the individual blocks excluding the connected boundary main block.

Fig. 10. The single connected main boundary block delimited by 601 and 561 polygons

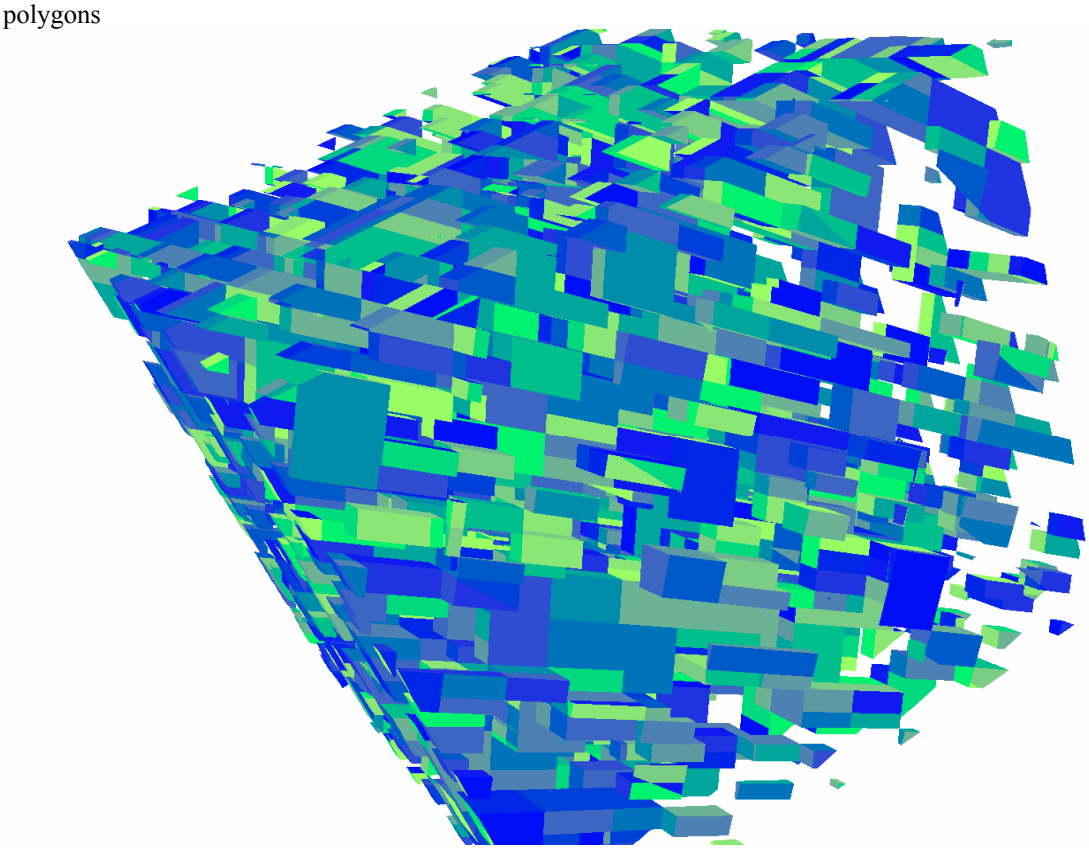

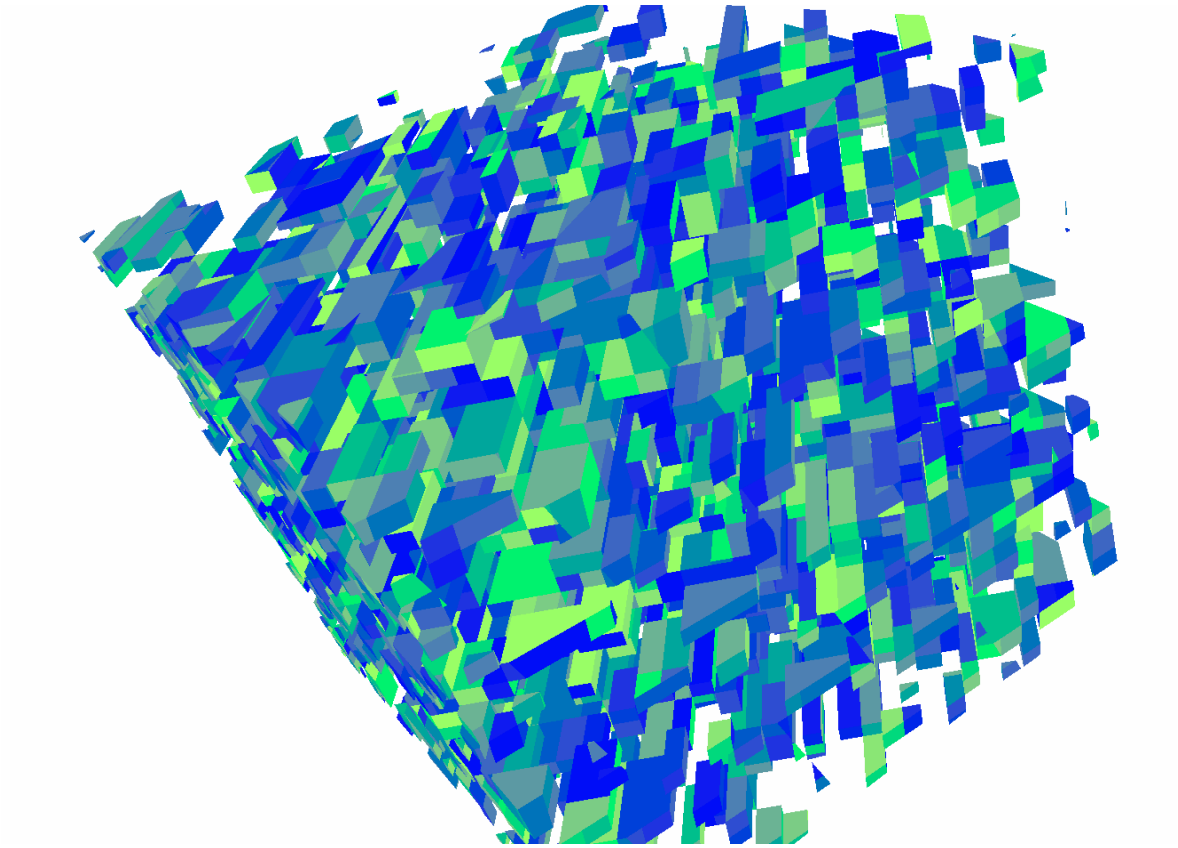

Fig. 11. One fifth of the individual blocks excluding the boundary main block

6.2. Jointed Rock Masses with More Than 60% Volume of Inner Blocks: Blocky Rock

For the case of 4.0 times joint trace length, the average joint length ratio $R_{ls} = 14.83$. Total inner block volume is 65.06 % of the total rock volume. The graphic results are similar with previous Figure 10 and 11.

The volume summation of all blocks is still as accurate as 8,000.0000000000 cubic meters.

7. MINIMUM CONVEX TARGET BLOCK OF FREE SURFACES

7.1. Target Block Is Convex Block

The joint polygons are produced in a space lager than the target block. Target blocks are defined as convex blocks. Convex blocks are simple. It is convenient to compute the part of polygon which is inside of the convex target block. The equations of target block boundary faces are plane equations:

$$A_i x + B_i y + C_i z + D_i = 0 \qquad i = 1, 2, 3, ..., n$$

The equation of target block is

$$A_i x + B_i y + C_i z + D_i \geq 0 \qquad i = 1, 2, 3, ..., n$$

Each produced polygon is trimmed by all boundary face planes $A_i x + B_i y + C_i z + D_i = 0$. If the plane divides the polygon to two sub-polygons, only the sub-polygon satisfying $A_i x + B_i y + C_i z + D_i \geq 0$ keeps.

All boundary faces of the target block are convex polygons same as the produced and trimmed joint polygons. The boundary polygons are also cutting polygons same as the joint polygons. All oriented blocks of the target block form a three dimensional chain in Algebraic Topology. The boundary of this chain is the boundary of target block ad shown by Figure 12.

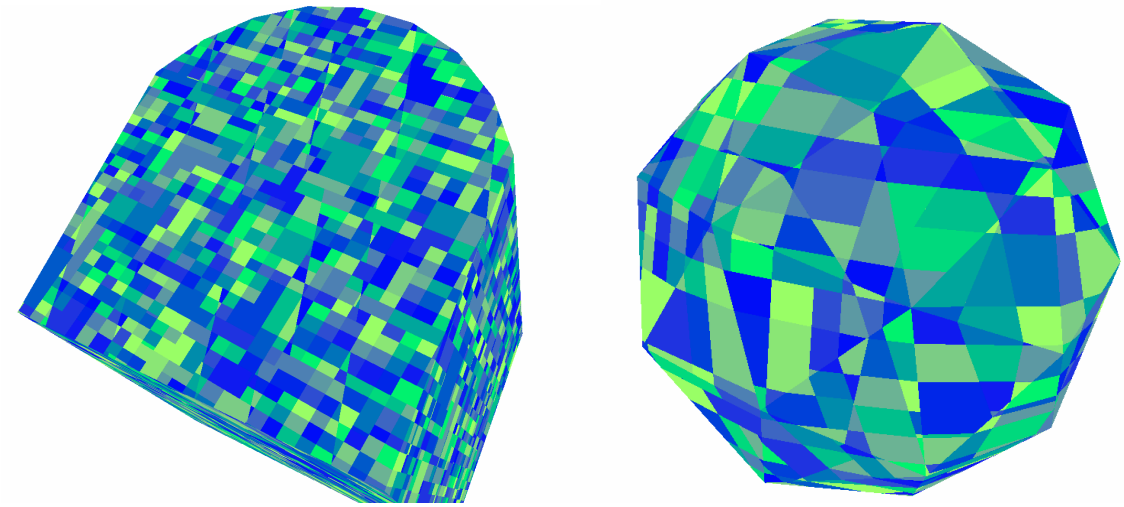

Fig. 12. Different shapes of convex target blocks

7.2. Target Blocks Are Delimited By Their Oriented Boundary Triangles

Since the boundary of the target block is formed by convex polygons. Each polygon can be divided into oriented triangles in a natural way. The rotation directions of the triangles are pointing inside of the target block. Each boundary triangle has three nodes:

$$(x_{i,} \quad y_{i,} \quad z_i) \quad (x_{j,} \quad y_{j,} \quad z_j) \quad (x_{k,} \quad y_{k,} \quad z_k)$$

The plane equations of point $(x, \quad y, \quad z)$ are defined by three points

$$\begin{vmatrix} 1 & x_i & y_i & z_i \\ 1 & x_j & y_j & z_j \\ 1 & x_k & y_k & z_k \\ 1 & x & y & z \end{vmatrix} = o$$

All of the boundary triangle nodes $(x, \quad y, \quad z)$ satisfy the following equation. Any point $(x, \quad y, \quad z)$ of the target block also satisfies the following equation.

$$\begin{vmatrix} 1 & x_i & y_i & z_i \\ 1 & x_j & y_j & z_j \\ 1 & x_k & y_k & z_k \\ 1 & x & y & z \end{vmatrix} \geq o$$

7.3. Computing The Minimum Convex Target Block For Rock Boundaries

The general rock mass boundaries are still polygons. However, real rock masses are generally not a convex block. For example, the rock mass with a tunnel are no longer a convex block. To generate the joint polygons and the blocks inside a target block, the minimum convex target block containing the rock mass can be constructed. Choose any three nodes from the boundary polygons of the rock mass with the condition:

$$(x_{i,} \quad y_{i,} \quad z_i) \qquad (x_{j,} \quad y_{j,} \quad z_j) \qquad (x_{k,} \quad y_{k,} \quad z_k)$$

$$\begin{vmatrix} x_i & y_i & z_i \\ x_j & y_j & z_j \\ x_k & y_k & z_k \end{vmatrix} \neq 0$$

If the following equation is satisfied by all nodes $(x, \quad y, \quad z)$ of all boundary polygons of the rock mass, the plane defined by these three points is a boundary plane of the minimum target block of the rock mass.

$$\begin{vmatrix} 1 & x_i & y_i & z_i \\ 1 & x_j & y_j & z_j \\ 1 & x_k & y_k & z_k \\ 1 & x & y & z \end{vmatrix} \geq o$$

All boundary planes of the minimum convex target block can be found by choosing different groups of three nodes.

8. EXCAVATE FREE SURFACES INSIDE A TARGET BLOCK

8.1. Free Surfaces Are Delimited by Their Oriented Boundary Triangles

The free surfaces of the rock mass are polygons in three dimensional spaces. These polygons are not necessarily convex. However the boundary polygon can be subdivided into oriented triangles. The rotation directions of the oriented triangles are pointing into the rock mass.

The control points of contours can be connected by oriented triangles. Surfaces of slopes, dam foundations, tunnels, whole underground chambers, portals or tunnel intersections can be represented as oriented triangles.

8.2. Conditions of Free Surfaces

As mentioned in the previous paragraph, the boundaries of rock mass are a set of oriented triangles $\bigcup_{i=1}^{n} S_i$. Denote the target block as T. Denote the set of points outside of the target block T as $C(T)$. The boundaries $\partial \bigcup_{i=1}^{n} S_i$ of all oriented triangles of the free surfaces $\bigcup_{i=1}^{n} S_i$ consist of outer edges of the free surfaces. The boundary $\partial \bigcup_{i=1}^{n} S_i$ is in the union of the boundary ∂T of the target block T and the set $C(T)$ outside of the target block T. Intuitively speaking, the input free surfaces will cut through the entire target block. The free surface can not end inside of the target block.

$$\partial(\bigcup_{i=1}^{n} S_i) \subseteq (\partial T \bigcup C(T))$$

The target block is divided by the free surfaces. Two different polygons are input into the polygon cutting code DC:

Boundary oriented triangles of the target block

The oriented triangles of the free surfaces

Blocks are formed. The union of these blocks is the target block. These blocks are divided to two groups: rock mass blocks and the excavated blocks. The excavated blocks are the blocks outside the free surface and should be removed. Here the free surfaces are even not necessarily connected.

8.3. Joint Blocks Trimmed by Free Surfaces

To form all of the joint blocks inside of the target block, three different polygons are input:

Boundary oriented triangles of the target block

The oriented triangles of the free surfaces

Produced joint polygons

All produced joint blocks are inside of the target block. The joint blocks are subdivided blocks of rock mass blocks or excavated blocks. There are two different kinds of joint blocks: joint blocks which are inside a rock mass block and the joint blocks which are inside a excavated block. The joint blocks of the excavated blocks called excavated joint blocks and should be removed.

Here the rotation direction of the oriented triangles of the free surfaces points inside the rock mass. After the joint blocks are formed, the whole free surfaces consist of the joint block boundaries. Based on the polygon orientation of the joint blocks and the triangle orientation of the free surfaces, all of the excavated joint blocks are removed.

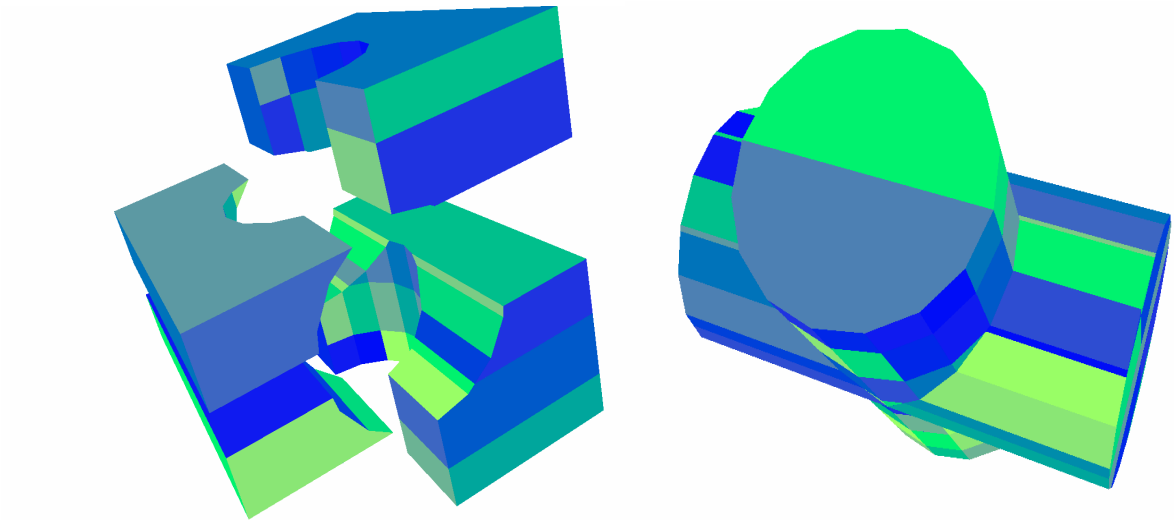

Fig. 13. Tunnel intersection as free surfaces of a cubic target block

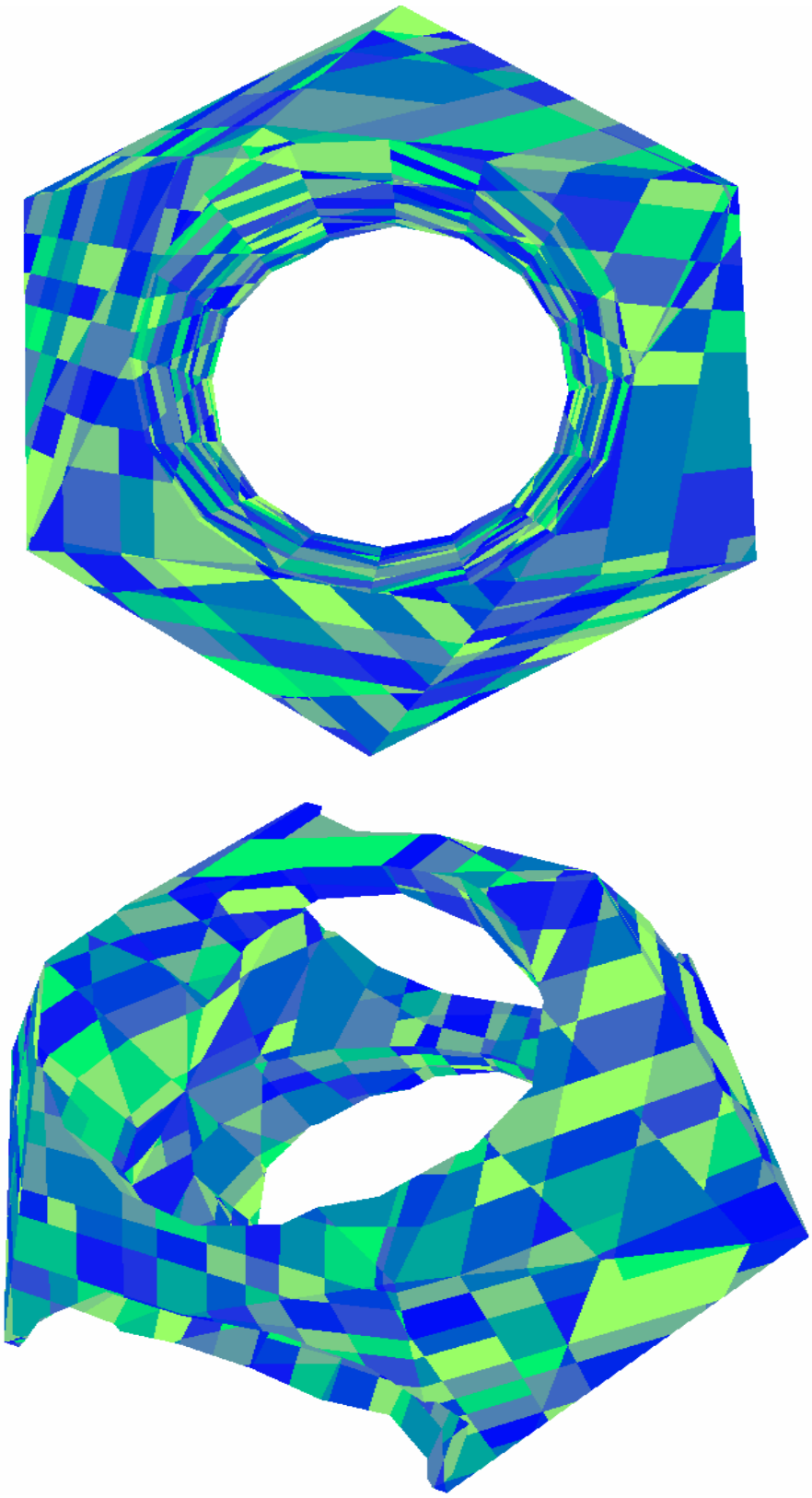

Fig. 14. One tunnel and two tunnels are the free surfaces of 20 face target block

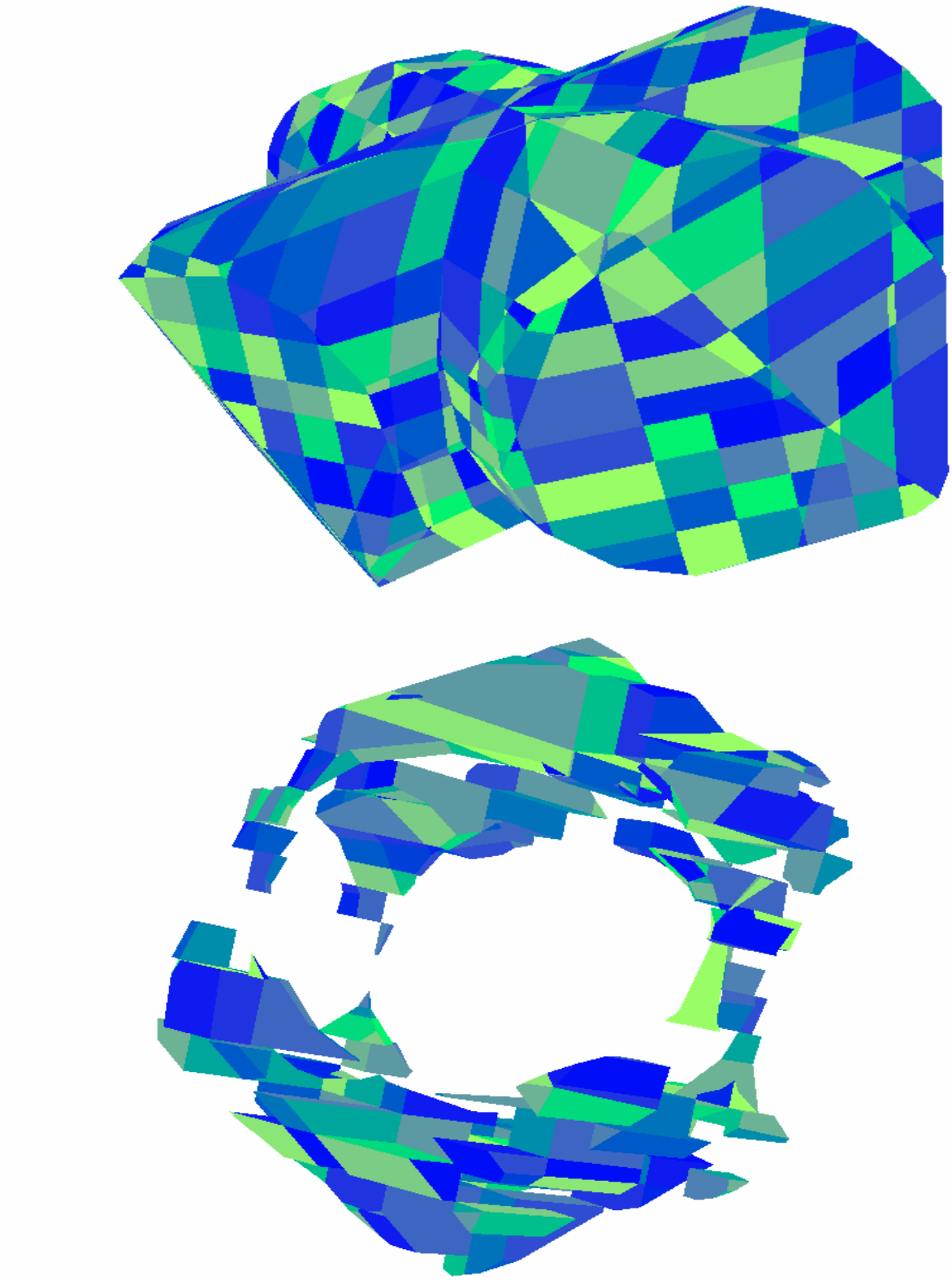

Fig. 15. Removed tunnel intersection and 1/5 of the joint blocks after the excavation of tunnel intersection

Figure 13 shows part of the rock mass joint blocks and the excavated joint blocks. The target block is a cube. The free surfaces are the surfaces of two intersecting tunnels.

Figure 14 shows the rock mass joint blocks. The boundaries of the target block are 20 equal-lateral triangles. The free surfaces are one tunnel surface and two tunnel surfaces respectively.

Figure 15 shows the excavated joint blocks and part of the rock mass joint blocks. The boundaries of the target block are 20 equal-lateral triangles. The free surfaces are the surfaces of two intersecting tunnels.

9. FINDING ALL REMOVABLE BLOCKS OF FREE SURFACES

9.1. Removable Blocks Along a Direction

Given a moving direction vector $\vec{m}$, the removable blocks along vector $\vec{m}$ are defined. A removable block group along vector $\vec{m}$ is the group of joint blocks R_i. The boundaries ∂R_i of the group R_i are polygons P_k. The normal vector of polygon P_k is $\vec{n_k}$. The normal vector $\vec{n_k}$ points the side of the joint blocks of the group. This group of joint blocks is a removable block group along vector $\vec{m}$, if the following equation is satisfied for all its boundary polygons P_k except the free surface polygons.

$$\vec{n_k} \cdot \vec{m} \geq 0$$

There could be very large number of different removable block groups. The removable block groups along the same vector $\vec{m}$ are additive.

If R_i and R_j are removable groups along moving direction vector $\vec{m}$, the union $R_i \cup R_j$ is also removable block group along vector $\vec{m}$.

9.2. Maximum Removable Blocks Along a Direction

Union of all removable block groups along a vector $\vec{m}$ is still a removable block group along the same moving direction vector $\vec{m}$. This union is the maximum removable block group along vector $\vec{m}$. Therefore for a given vector $\vec{m}$, there is only one unique maximum removable block group. It is more convenient to find this unique maximum removable block group.

There may be many removable block groups of a vector. It is too hard to find all of the removable block groups. However, if the maximum removable block group is found, the stability of the rock mass along the vector can be estimated. The maximum removable block group may not be connected.

9.3. Delimiting Maximum Removable Block Group Along a direction

The method of finding the maximum removable block group of a vector $\vec{m}$ is based on the equation:

$$\vec{n_k} \cdot \vec{m} \geq 0$$

This equation has to be satisfied for all its boundary polygons P_k except the free surface polygons.

Starting with all of the rock mass joint blocks on the rock side of the free surfaces, compute the

boundary of all the remaining joint blocks. Using the previous equation, the joint blocks outside of the maximum removable block group are deleted one-by-one. If there are no more joint blocks to be deleted, the remaining joint blocks are the maximum removable block group.

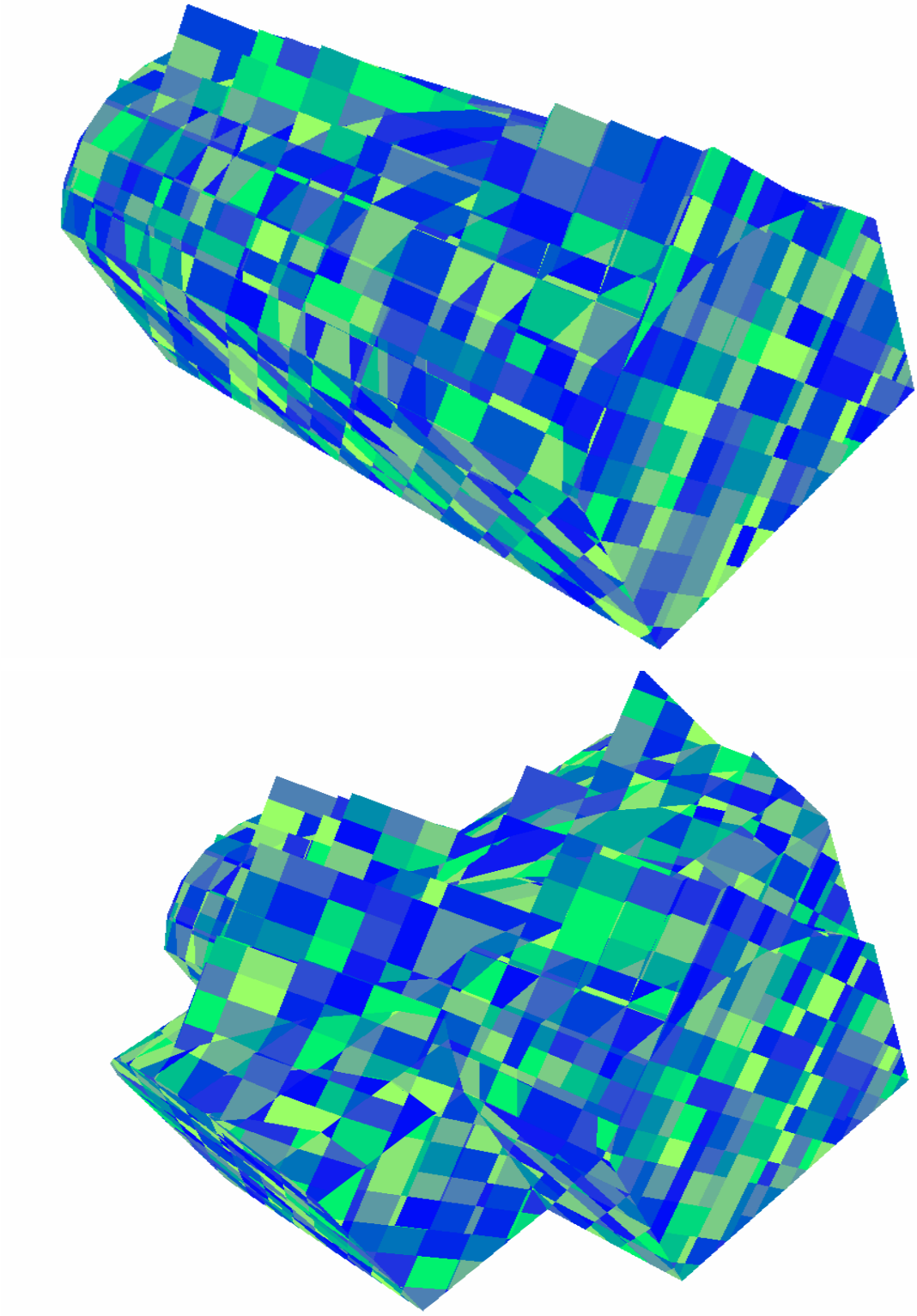

Fig. 16. Maximum removable block groups of tunnel and tunnel intersections of vertically downward vector

Figure 16 shows the maximum removable block groups together with the excavated joint blocks of the vertical downward vector. The free surfaces are the surface of a tunnel and the surfaces of two intersecting tunnels.

9.4. Comparison With Original Key Block Analysis

The following table compares the traditional Key Block method with the polygon cutting method.

Methods	Key Block	Polygon Cutting
Joint system	Joint set	Joint set or individual joints
Free surface	Simple	Complex and general
Block system	Small number of blocks	Large number of blocks
Moving directions	Few moving directions	Large number of moving directions
Finiteness	Infinite	Finite
Secondary removable blocks	No	Yes

The results of the polygon cutting method are consistent with the results of the Key Block method in cases where both methods apply.

ACKNOWLEDGMENT

The author thanks Professor Mary MacLaughlin for her kind help.

REFERENCES

1. Shi, Gen-hua. 2002. Single and multiple block limit equilibrium of key block method and discontinuous deformation analysis. *Stability of Rock Structures, ICADD-5,* 3-46. Beer Sheva, Israel.
2. Shi, Gen-hua. 1999. Applications of discontinuous deformation analysis (DDA) and manifold method. *The Third International Conference on Analysis of Discontinuous Deformation, ICADD-3,* 3-15. Vail, Colorado.
3. Shi, Gen-hua. 1993. Block system modeling by discontinuous deformation analysis. *Computational Mechanics Publications,* Southampton, UK and Boston, USA.

Modified point-to-face frictionless contact constraints for three-dimensional Discontinuous Deformation Analysis (3-D DDA)

Beyabanaki S. A., Jafari A.

School of Mining Engineering, Faculty of Engineering, University of Tehran, Tehran, Iran

This paper was prepared for presentation at *ICADD-7, the Seventh International Conference on Analysis of Discontinuous Deformation*, held in Honolulu, Hawaii, December 10-12, 2005.

ABSTRACT: In the original 3-D DDA method, block contact constraints are enforced using the penalty method. This approach is quite simple, but may lead to inaccuracies which may be large for small values of the penalty number. The penalty method also creates block contact overlap which violates the physical constraints of the problem. These two limitations are overcome by using the Augmented Lagrangian Method which is implemented in 3-D DDA and has been programmed in VC++. This method has been found to model block contact quite well. In this paper 3-D DDA formulation of the three most widely used methods for modeling contacts in numerical methods, namely, the Penalty Method, the Lagrange Multiplier Method, and the Augmented Lagrangian Method is given for point-to-face frictionless contacts and implementation of the Augmented Lagrangian Method into the 3-D DDA is presented by an illustrative example.

10. INTRODUCTION

Discontinuous Deformation Analysis (DDA) method is a relatively new numerical modeling technique that is a member of the family of DEM methods. Shi and Goodman [1] introduce the back-ward approach of DDA to back-calculate the best-fit deformed geometry of a block system from measured displacements and strains. Subsequently Shi [2-4] and shi and Goodman [5] generalized the two-dimensional DDA to include the capability of analyzing the mechanical behavior of block system in a forward approach. DDA has become a rapidly developing numerical method for practical applications.

As DDA draws more and more attention, several modifications and improvements to the original formulas have been proposed to overcome some of its limitations and make it more efficient, suitable and practical to engineering computations. Surface contact kinematics conditions can be enforced by prescribing displacement constraints in order to prevent contact domains from overlapping. In the DDA method, contact sliding is allowed but not interpenetration. The classical Lagrange Multiplier Method and the Penalty Method are the two most commonly used approaches to enforce the surface contact displacement constraints [6]. The penalty technique is used in the original DDA to prevent inter-penetration between blocks. Cai et al. [7] adopted the Lagrange Multiplier methods to fulfill the contact constraints of no penetration and no tension. Lin et al. [8-10] applied the Augmented Lagrangian method instead of the Penalty Method and obtained satisfactory results.

This study presents a new approach to block contacts, namely, the Augmented Lagrangian Method instead of the Penalty Method originally used in 3-D DDA [11-16] for point-to-face frictionless contacts. This allows block-to-block contacts to be enforced more precisely and block contact forces to be determined more accurately. An illustrative example is presented for the single purpose of demonstrating this new approach.

11. THREE-DIMENSIONAL DDA THEORY

Discontinuous Deformation Analysis calculates the equilibrium Equations by minimization of the potential energies of single blocks and contacts between two blocks. To calculate the simultaneous equilibrium equations, deformation functions must be defined. The deformation function calculates the deformation of all the blocks using the displacement of each block centroid. This function is similar to the shape function of Finite Element Method and can present the potential energy of the blocks and the simultaneous equilibrium equations simply.

Assuming all displacements are small and each block has constant stress and constant strain throughout, the displacement (u,v,w) of any point (x,y,z) of a block can be represented by 12 displacement variables. In the 12 variables, (u_0,v_0,w_0) is the rigid body translation of a specific point (x_0,y_0,z_0), r_1 is the rotation angle (radians) of block around z axis, r_2 is the rotation angle of block around x axis, r_3 is the rotation angle of block around y axis, $\varepsilon_x,\varepsilon_y,\varepsilon_z,\gamma_{xy},\gamma_{yz},\gamma_{zx}$ are the normal and shear strains in the block. The displacement of any point (x,y,z) in the block can by represented by Eq. (1).

$$\begin{pmatrix} u \\ v \\ w \end{pmatrix} = \begin{bmatrix} 1 & 0 & 0 & -(y-y_0) & 0 & (z-z_0) & (x-x_0) & 0 & 0 & (y-y_0)/2 & 0 & (z-z_0)/2 \\ 0 & 1 & 0 & (x-x_0) & -(z-z_0) & 0 & 0 & (y-y_0) & 0 & (x-x_0)/2 & (z-z_0)/2 & 0 \\ 0 & 1 & 1 & 0 & (y-y_0) & -(x-x_0) & 0 & 0 & (z-z_0) & 0 & (y-y_0)/2 & (x-x_0)/2 \end{bmatrix} \cdot \begin{pmatrix} u_0 \\ v_0 \\ w_0 \\ r_1 \\ r_2 \\ r_3 \\ \varepsilon_x \\ \varepsilon_y \\ \varepsilon_z \\ \gamma_{xy} \\ \gamma_{yz} \\ \gamma_{zx} \end{pmatrix} \quad (1)$$

In DDA, the equilibrium equation is established by differentiation of the potential energy of the block as with FEM. The stiffness matrix is constructed using the potential energy of a single block and the contacts between two blocks. As DDA is a displacement method like FEM, the equilibrium equations are established by transposition of the constant to the right side, which is calculated by the differentiation of the total potential energy with respect to the displacement variables. Assuming there are n blocks in the defined block system, the simultaneous equilibrium equation has the same form as Eq. (2). In Eq. (2), $K_{ij}(i=1,...,n,\ j=1,...,n)$ is a stiffness matrix which is a 12×12 matrix calculated for a single block and its contact with two other blocks; D_i represents the displacement variables; F_i is the loading on the blocks, distributed to the 12 displacement variables.

$$\begin{bmatrix} K_{11} & K_{12} & K_{13} & \dots & K_{1n} \\ K_{21} & K_{22} & K_{23} & \dots & K_{2n} \\ K_{31} & K_{32} & K_{33} & \dots & K_{3n} \\ \vdots & \vdots & \vdots & \ddots & \vdots \\ K_{n1} & K_{n2} & K_{n3} & \dots & K_{nn} \end{bmatrix} \begin{bmatrix} D_1 \\ D_2 \\ D_3 \\ \vdots \\ D_n \end{bmatrix} = \begin{bmatrix} F_1 \\ F_2 \\ F_3 \\ \vdots \\ F_n \end{bmatrix} \quad (2)$$

12. THE PENALTY METHOD

The Penalty Method was probably the first approach adopted for a constraint enforcing method. This method is discussed by Campbell [17], Felippa [18, 19]. It was originally used by shi [11, 12] in the 3-D DDA method to enforce contact constraints at block interfaces.

Assume there is a spring between point P_1 and entrance plane $P_2P_3P_4$. The distance δ of two sides should be zero after the displacement increment is applied. Therefore:

$$\delta + d\delta = \frac{V_0}{A} + \frac{1}{A}\begin{vmatrix} 1 & u_1 & y_1 & z_1 \\ 1 & u_2 & y_2 & z_2 \\ 1 & u_3 & y_3 & z_3 \\ 1 & u_4 & y_4 & z_4 \end{vmatrix} + \frac{1}{A}\begin{vmatrix} 1 & x_1 & v_1 & z_1 \\ 1 & x_2 & v_2 & z_2 \\ 1 & x_3 & v_3 & z_3 \\ 1 & x_4 & v_4 & z_4 \end{vmatrix} + \frac{1}{A}\begin{vmatrix} 1 & x_1 & y_1 & w_1 \\ 1 & x_2 & y_2 & w_2 \\ 1 & x_3 & y_3 & w_3 \\ 1 & x_4 & y_4 & w_4 \end{vmatrix} \tag{3}$$

that

$$V_0 = \begin{vmatrix} 1 & x_1 & y_1 & z_1 \\ 1 & x_2 & y_2 & z_2 \\ 1 & x_3 & y_3 & z_3 \\ 1 & x_4 & y_4 & z_4 \end{vmatrix} \tag{4}$$

and

$$A = \left(\begin{vmatrix} y_3 - y_2 & z_3 - z_2 \\ y_4 - y_2 & z_4 - z_2 \end{vmatrix}^2 + \begin{vmatrix} x_3 - x_2 & z_3 - z_2 \\ x_4 - x_2 & z_4 - z_2 \end{vmatrix}^2 + \begin{vmatrix} x_3 - x_2 & y_3 - y_2 \\ x_4 - x_2 & y_4 - y_2 \end{vmatrix}^2 \right) \tag{5}$$

let

$$\begin{bmatrix} g_{11} & g_{12} & g_{13} & g_{14} \\ g_{21} & g_{22} & g_{23} & g_{24} \\ g_{31} & g_{32} & g_{33} & g_{34} \\ g_{41} & g_{42} & g_{43} & g_{44} \end{bmatrix}^T = V_0 \begin{bmatrix} 1 & x_1 & y_1 & z_1 \\ 1 & x_2 & y_2 & z_2 \\ 1 & x_3 & y_3 & z_3 \\ 1 & x_4 & y_4 & z_4 \end{bmatrix}^{-1} \tag{6}$$

and

$$\begin{aligned} d\delta = & \begin{bmatrix} g_{12} & g_{13} & g_{14} \end{bmatrix} \begin{bmatrix} u_1 \\ v_1 \\ w_1 \end{bmatrix} \frac{1}{A} + \begin{bmatrix} g_{22} & g_{23} & g_{24} \end{bmatrix} \begin{bmatrix} u_2 \\ v_2 \\ w_2 \end{bmatrix} \frac{1}{A} + \begin{bmatrix} g_{32} & g_{33} & g_{34} \end{bmatrix} \begin{bmatrix} u_3 \\ v_3 \\ w_3 \end{bmatrix} \frac{1}{A} \\ & + \begin{bmatrix} g_{42} & g_{43} & g_{44} \end{bmatrix} \begin{bmatrix} u_4 \\ v_4 \\ w_4 \end{bmatrix} \frac{1}{A} \end{aligned} \tag{7}$$

$$\begin{aligned} \begin{bmatrix} E_i \end{bmatrix}^T &= \begin{bmatrix} g_{12} & g_{13} & g_{14} \end{bmatrix} \begin{bmatrix} T_i(x_1, y_1, z_1) \end{bmatrix} / A \\ \begin{bmatrix} G_j \end{bmatrix}^T &= \begin{bmatrix} g_{22} & g_{23} & g_{24} \end{bmatrix} \begin{bmatrix} T_j(x_2, y_2, z_2) \end{bmatrix} / A + \begin{bmatrix} g_{32} & g_{33} & g_{34} \end{bmatrix} \begin{bmatrix} T_j(x_3, y_3, z_3) \end{bmatrix} / A \\ & + \begin{bmatrix} g_{42} & g_{43} & g_{44} \end{bmatrix} \begin{bmatrix} T_j(x_4, y_4, z_4) \end{bmatrix} / A \end{aligned} \tag{8}$$

then

$$\delta + d\delta = \frac{V_0}{A} + [E_i]^T [D_i] + [G_j]^T [D_j] \tag{9}$$

The potential energy of the normal spring is:

$$\begin{aligned}\Pi_k &= \frac{P}{2}\left(\frac{V_0}{A} + [E_i]^T [D_i] + [G_j]^T [D_j]\right) \times \left(\frac{V_0}{A} + [E_i]^T [D_i] + [G_j]^T [D_j]\right) \\ &= \frac{P}{2}\left(\frac{V_0}{A}\right)^2 + \frac{P}{2}\left([D_i]^T [E_i][E_i]^T [D_i] + [D_j]^T [G_j][G_j]^T [D_j]\right) + P\left(\frac{V_0}{A}\right) \\ &\quad \times \left([D_i]^T [E_i] + [D_j]^T [G_j]\right) + P[D_i]^T [E_i][G_j]^T [D_i]\end{aligned} \tag{10}$$

Denote the stiffness of the spring as P . Minimizing Π_k by taking the derivatives, four 12×12 sub-matrices and two 12×1 sub-matrices are obtained:

$$P[E_i][E_i]^T \rightarrow [K_{ii}] \tag{11}$$

is added to sub-matrix $[K_{ii}]$

$$P[E_i][G_j]^T \rightarrow [K_{ij}] \tag{12}$$

is added to sub-matrix $[K_{ij}]$

$$P[G_j][E_i]^T \rightarrow [K_{ji}] \tag{13}$$

is added to sub-matrix $[K_{ji}]$

$$P[G_j][G_j]^T \rightarrow [K_{jj}] \tag{14}$$

is added to sub-matrix $[K_{jj}]$

$$-\frac{PV_0}{A}[E_i] \rightarrow [F_i] \tag{15}$$

is added to sub-matrix $[F_i]$

$$-\frac{PV_0}{A}[G_j] \rightarrow [F_j] \tag{16}$$

is added to sub-matrix $[F_j]$

The main features of this method are:

- Enforcement of constraints requires no extra equations.
- The solution is easily obtained by simply adding contact components to the stiffness matrix.

- The constraints are only satisfied in an approximate manner and the contact solution depends highly on the choice of the penalty number and the optimal number can not be explicitly found beforehand.
- If the penalty number is too low, the constraints are poorly satisfied, while if it is too large, the simultaneous equilibrium matrix becomes difficult to solve.

13. THE LAGRANGE MULTIPLIER METHOD

The classical Lagrange Multiplier Method was one of the first methods to solve block contact problems. In this method, contact forces are unknowns and must be explicitly calculated.

Let λ be the unknown contact force caused by penetration to a depth, $(\delta + d\delta)$. In the Lagrange Multiplier Method, the strain energy of that contact force is defined as:

$$\Pi_k = \lambda(\delta + d\delta) \tag{17}$$

The penetration distance, $(\delta + d\delta)$, can be expressed in the same form as in Eq. (9) and hence the strain energy is:

$$\Pi_k = \lambda\left(\frac{V_0}{A} + [E_i]^T[D_i] + [G_j]^T[D_j]\right) \tag{18}$$

Since this expression is of first order only in the displacements, the second derivatives vanish and hence there is no contribution to the stiffness matrix K. The contribution to the force matrix F is obtained from the derivatives that is:

$$-\frac{\partial\Pi(0)}{\partial d_{ri}} \rightarrow -\lambda[E_i]^T \tag{19}$$

$$-\frac{\partial\Pi(0)}{\partial d_{rj}} \rightarrow -\lambda[G_j]^T \tag{20}$$

The Lagrange Multiplier (i. e. contact force), λ, is not known and therefore joins the displacement matrix $[D]$ as an unknown in Eqs. (2). The extra equation needed to solve the new system is provided by satisfying the displacement constraints, according to Eq. (9). The simultaneous equilibrium equations (2) are modified as follows:

$$\left[\begin{array}{c|c} [K] & [K_1]^T \\ \hline [K_1] & 0 \end{array}\right]\left[\begin{array}{c} [D] \\ \hline \lambda \end{array}\right] = \left[\begin{array}{c} [F] \\ \hline -\frac{V_0}{A} \end{array}\right]$$

$$[K_1] = [[E_i] \ldots [G_j]] \tag{21}$$

Note that modified simultaneous equations in (21) result from a single contact force λ existing between two blocks. If more contact forces exist, say n_λ contacts, $[K_1]$ will have n_λ rows and

Eqs. (21) will increase by n_λ rows and n_λ columns. The unknown scalar λ is then replaced by an unknown vector with n_λ entries, each of which represents a contact force.

The method allows the contact conditions to be satisfied exactly and from the physical point of view, λ directly represents a contact force and is calculated directly. However, the method has several disadvantages. The number of governing Equations is increased so that extra computational effort is needed to solve the system. The matrix on the left hand side of Eq. (21) may not be positive definite but is non-singular [6]. Furthermore, the matrix contains a zero sub-matrix along its diagonal and in order to obtain a unique solution some special numerical procedures have to be invoked.

14. THE AUGMENTED LAGRANGIAN METHOD

The objective of this method, which was developed in the early nineties, is to minimize the disadvantages of the Penalty and Lagrangian Multiplier Methods by combining the two methods. The method is independent of the magnitude of penalty number and introduces no extra Eq. to the system.

In this method an iterative method is used to calculate the Lagrange Multiplier until the distance, $(\delta + d\delta)$, of penetration of one block into the other is below another minimum specified tolerance.

When using the Augmented Lagrangian Method, the contact force at the contact point can be accurately approximated by iteratively calculating the Lagrange Multiplier λ^*. A first order updated value for λ^* can be written as:

$$\lambda \approx \lambda^*_{k+1} = \lambda^*_k + P(\delta + d\delta) \tag{22}$$

where the penalty number, P, can be variable and does not have to be a very large number as in the Penalty Method. In Eq. (22), λ^* is the Lagrangian Multiplier at the kth iteration and λ^*_{k+1} is the updated Lagrange Multiplier. At the kth iteration, the strain energy, Π_{st}, resulting from the contact force becomes:

$$\Pi_{st} = \lambda^*_k(\delta + d\delta) + \frac{1}{2}P(\delta + d\delta)^2 \tag{23}$$

This Eq. consists of two components. The first component is the strain energy resulting from the iterative Lagrange Multiplier λ^*_k, and the penalty constraint creates the second. The contribution of the second component to the $12n \times 12n$ global stiffness matrix K in Eq. (2) was already covered in section (3), so only the contribution of the first component of Eq. (23) to matrix K is derived in the following sequence of operations.

Denoting this first component as Π^*_{st}:

$$\Pi^*_{st} = \lambda^*_k(\delta + d\delta) = \lambda^*_k\left(\frac{V_0}{A} + [E_i]^T[D_i] + [G_j]^T[D_j]\right) \tag{24}$$

The relevant derivatives of Π^*_{st} are equal to:

$$-\frac{\partial \Pi^*_{st}(0)}{\partial d_{ri}} \rightarrow -\lambda^*_k [E_i]^T \qquad \text{and} \qquad -\frac{\partial \Pi^*_{st}(0)}{\partial d_{rj}} \rightarrow -\lambda^*_k [G_j]^T \tag{25}$$

Which form two 12×1 matrices $-\lambda^*_k [E_i]$ and $-\lambda^*_k [G_j]$ that are added to sub-matrices F_i and F_j, respectively. Note that the λ^* values are known and calculated from the previous iteration. They are distinct from the λ values in Eqs. (19) and (20) which are unknowns in the classical Lagrange Multiplier Method.

For the Augmented Lagrangian Method, the combined contributions of the first and second components of Π^*_{st} to Eqs. (2) are obtained and added to $[K_{ii}]$, $[K_{ij}]$, $[K_{ji}]$, $[K_{jj}]$, $[F_i]$ and $[F_j]$ respectively:

$$P[E_i][E_i] \rightarrow [K_{ii}], \quad P[E_i][G_j] \rightarrow [K_{ij}], \quad P[G_j][E_i] \rightarrow [K_{ji}], \quad P[G_j][G_j] \rightarrow [K_{jj}] \tag{26}$$

$$-\left(\lambda^*_k + \frac{PV_0}{A}\right)[E_i] \rightarrow [F_i] \qquad \text{and} \qquad -\left(\lambda^*_k + \frac{PV_0}{A}\right)[G_j] \rightarrow [F_j] \tag{27}$$

Box (1) summarizes an iterative procedure for Augmented Lagrangian algorithm.

Box(1). Iterative procedure for Augmented Lagrangian algorithm

- **1.0** Initialize $\lambda_1 = 0$
- **2.0** For each iteration k
  - **2.1** Solve for displacements $([K][D] = [F])$
  - **2.2** Compute penalty forces $\left(f^c = \Delta\lambda = P \times d_{\max}\right)$
  - **2.3** Check for convergence
    - IF $(\Delta\lambda \le Tol_1)$ and $\left(\frac{\|[K][D_k] - [K][D_{k-1}]\|}{\|[K][D_{k-1}]\|} \le Tol_2\right)$ THEN
      GOTO 3.0
      END IF
  - **2.4** update Lagrange multipliers $\left(\lambda_{k+1} = \lambda_k + \Delta\lambda\right)$
  - **2.5** GOTO 2.0
- **3.0** END

From a physical point of view, again, the Lagrangian multiplier, λ, represents the contact force along a point of contact between two blocks and the penalty number, P, represents the stiffness of the contact spring. The final exact contact forces can always be obtained by the iterative method even with small initial values of the penalty number.

The precision of the solution depends on residual forces that are produced during the iterative calculations of the contact forces. The criterion for convergence is based on the requirements satisfaction of contact minimum distance of interpenetration and minimum residual forces between block contacts (Box (1)).

In this method however, since a value of λ_k is known at each iteration, there is no increase in the size of the system of equations (2). In addition, the simplicity of the Penalty Method is retained and the disadvantages are minimized.

The main features of this method are:

- The Augmented Lagrangian approach uses a penalty stiffness but iteratively updates the contact traction to impose the contact constraints with a specified precision.
- No additional equations are required.
- Large penalty values are not required; avoiding the ill conditioning of the stiffness matrices. However if the initial penalty number is too small, many iterations are required.
- The constraints are satisfied within a user defined required tolerance.
- The algorithm can be used effectively for applications where the contact pressures become very large in comparison with the material elastic parameters [6].

15. EXAMPLE

The algorithm described in the previous section has been programmed in VC++. To investigate it, sliding along an inclined plane is examined.

This example simulates the sliding of a block along an inclined plane at an angle α to the horizontal direction without considering frictional forces (Fig. 1).

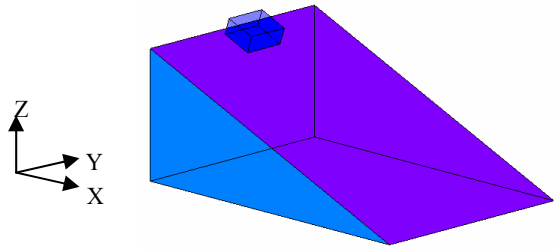

Fig. 1 A single block resting on a inclined plane

Under the action of gravitational force, the displacement s of the block is determined analytically as a function of time t given as:

$$s(t) = \frac{1}{2}at^2 = \frac{1}{2}(g\sin\alpha).t^2 \tag{28}$$

The inclination of the modeled plane is 20 degree and the density, Young's modulus and Poisson's ratio for both blocks are 2.6×103 kg/m^3, 5GPa and 0.25, respectively. The maximum time increment for each time step is 0.01 s.

The accumulated displacements are calculated up to 5 sec. A comparison between the analytical solution in Eq. (28) and DDA solution for different values of the stiffness of the normal contact spring is shown in Fig. 2. Fig. 3 shows the displacements of sliding block in X and Z directions.

The deformation of the block system, using the Augmented Lagrangian Method to enforce the contact interface, after 0, 300, 400 and 500 time steps of 0.01 seconds for P=50MN/m is shown \in Fig 4. It is clear that no block interpenetration occurs here even though the penalty number is

low. Fig. 5 and Fig. 6 show the deformation of the block system, using the classical penalty method, after 0, 300, 400 and 500 time steps of 0.01 seconds for P=500MN/m and P=50MN/m, respectively. It indicates that a small penalty number is unable to enforce the interpenetration constraint.

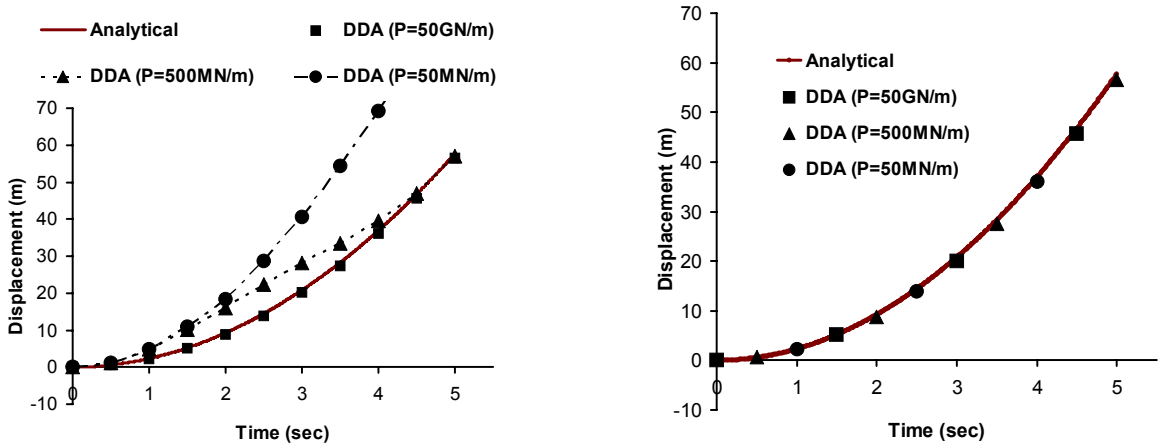

(a) (b)

Fig. 2 Comparison between the analytical solution and DDA results (a) the Penalty method (b) the Augmented Lagrangian method

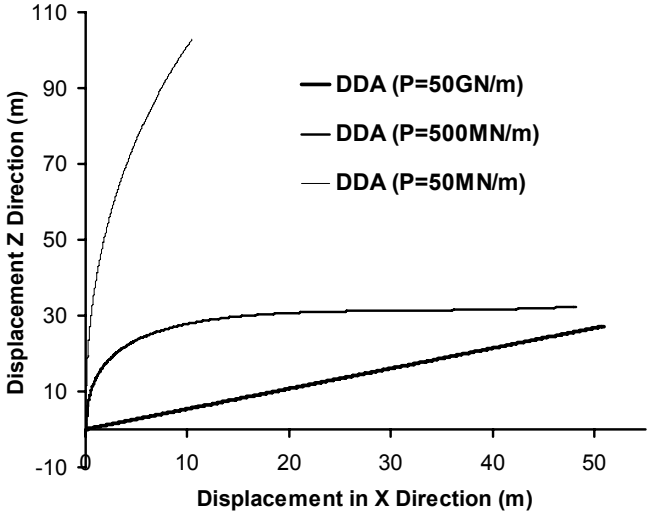

Fig. 3 Sliding block displacements in X and Z directions for Penalty Method

16. CONCLUSION

In the original 3-D DDA method, the Penalty Method is used to enforce block contact constraints. Using the Augmented Lagrangian Method to enforce contact restraints retains the simplicity of the Penalty Method and reduces the disadvantages of the Penalty and classical Lagrange Multiplier Methods. The disadvantages of the Penalty Method are: (1) It creates block contact overlap which violates the physical constraints of the problem. (2) It may lead to inaccuracies which may be large for small values of the penalty number. These two limitations are overcome by using the Augmented Lagrangian Method which

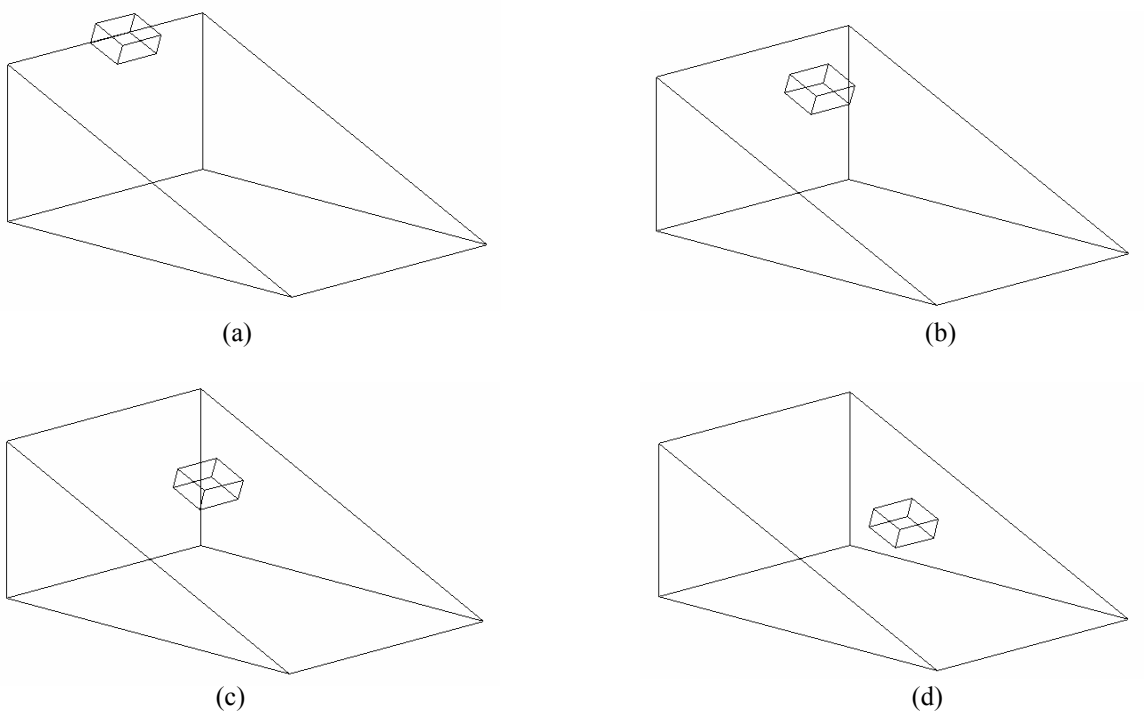

Fig. 4 The deformation of the block system, using the Augmented Lagrangian Method after (a) 0 (b) 300 (c) 400 and (d) 500 time steps of 0.01 seconds for P=50MN/m

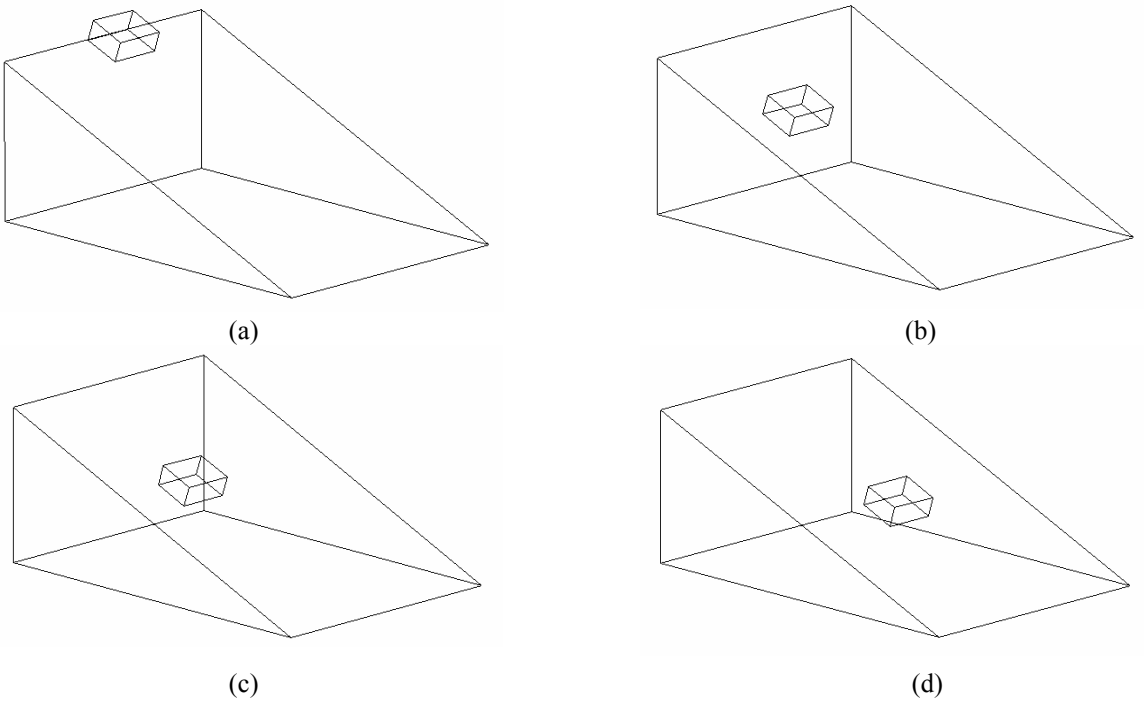

Fig. 5 The deformation of the block system, using the classical penalty method, after (a) 0 (b) 300 (c) 400 and (d) 500 time steps of 0.01 seconds for P=500MN/m

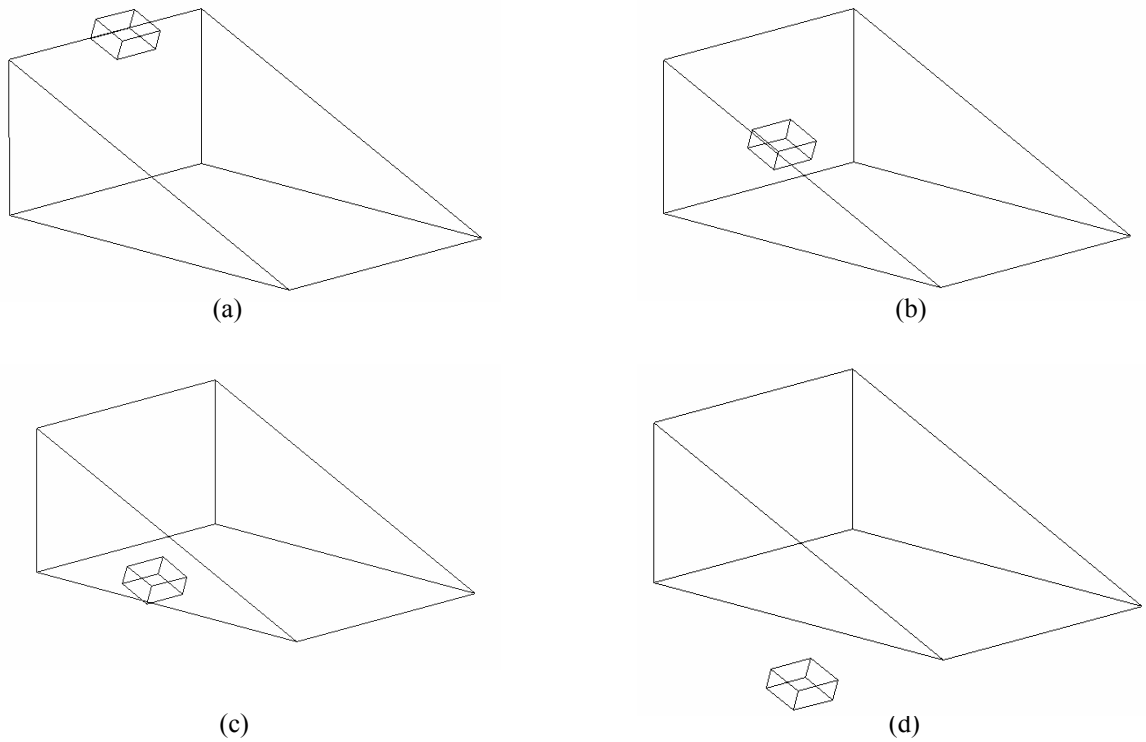

Fig. (6) The deformation of the block system, using the classical penalty method, after (a) 0 (b) 300 (c) 400 and (d) 500 time steps of 0.01 seconds for P=50MN/m

were implemented in the 3-D DDA program for point-to-face frictionless contacts. This method has been found to model block contact quite well.

17. ACKNOWLEDGMENTS

The authors are thankful to the "center of excellence" in the School of Mining Engineering, University of Tehran, which funded this ongoing research.

REFERENCES

1. Shi, G.H. and Goodman R. E. 1985. Two–dimensional discontinuous deformation analysis. *International Journal for Numerical and Analytical Methods in Geomechanics* 9, 541-556.
2. Shi, G.H. 1998. Discontinuous *deformation analysis: a new numerical model for the statics and dynamics of block systems*. PhD thesis, Department of Civil engineering, University of California, Berkeley.
3. Shi, G.H. 1992. Discontinuous deformation analysis: a new numerical model for the statics and dynamics of deformable block structures. *Engineering Computations* 9: 2, 157-162.
4. Shi, G.H. 1993. *Block system modeling by discontinuous deformation analysis*. Southampton UK and Boston USA: Computational Mechanics Publications.
5. Shi, G.H. and R.E. Goodman. 1989. Generalization of two-dimensional discontinuous deformation analysis for forward modeling. *International Journal for Numerical and Analytical Methods in Geomechanics* 13: 4, 359-380.

6. Mohammadi, S. 2003. *Discontinuous mechanics using Finite and Discrete elements*. WIT Press.

7. Cai, Y., G.P. Liang , G.H. Shi and N.G.W. Cook. 1996. Studying on impact problem by using LDDA method. In *Proceedings of the 1st International Forum on discontinuous Deformation Analysis (DDA) and Simulations of Discontinuous Media, Albuq-Verque*, eds. R. Salami et al, 288-294, TSI Press.

8. Lin, C.T., B. Amadei, J. Jung and J. Dwyer. 1996. Extensions of discontinuous deformation analysis for jointed rock masses. *International Journal of Rock Mechanics and Mining Science* 33: 7, 671-694.

9. Lin, C.T., B. Amadei and S. Sture. 1994. Using an Augmented Lagrangian Method and block fracturing in the DDA method. In *Proceedings of Computer Methods and Advances in Geomechanics*, eds. Siriwardane et al, 837-842.

10. Lin, C.T. 1995. *Extensions to the discontinuous deformation analysis for jointed rock masses and other blocky systems*. PhD thesis, Department of Civil engineering, University of California, Berkeley.

11. Shi, G.H. 2001. Three dimensional discontinuous deformation analysis. In *Proceedings of the 38th US Rock Mechanics Symposium, Washington D.C., eds.* D. Elsworth et al, 1421-1428.

12. Shi, G.H. 2001. Three Dimensional Discontinuous Deformation Analysis. In *Proceedings of the 4th Conference on Analysis of Discontinuous Deformation (ICADD-4), Abingdom*, ed. N. Bicanic, 1-21, Balkema.

13. Kong, X. and J. Liu. 2003. Development of three dimensional discontinuous deformation analysis. In *Proceedings of the 6th Conference on Analysis of Discontinuous Deformation (ICADD-6), Abingdom*, ed. M. Lu, 45-54, Balkema.

14. Jiang, Q. H. and M.R. Yeung. 2004. A model of point-to-face contact for Three-Dimensional Discontinuous deformation Analysis. *Rock Mechanics and Rock engineering* 37, 95-116.

15. Liu, J., X. Kong and G. Lin G. 2004. Formulation of the Three-Dimensional Discontinuous Deformation Analysis Method. *Chinese Journal of Mechanics Press* 20: 3.

16. Wu, J.H., C.H. Juang and H.M. Lin. 2005. Vertex-to-face contact searching algorithm for three-dimensional frictionless contact problems. *International Journal for Numerical Methods in Engineering* 63: 6, 876-897.

17. Campbell, J. S. 1974 A penalty function approach to the minimization of quadratics functions in finite element analysis. In *Proceedings of Finite Elements in Engineering*, University of South Wales.

18. Felippa C.A. 1978. Iterative procedures for improving penalty function solutions of algebraic systems. *International Journal of Numerical Methods in engineering* 12, 821-836.

19. Felippa C.A. 1986. Penalty-function iterative procedures for mixed finite element formulations. *International Journal of Numerical Methods in engineering* 22, 267-279.

Dynamic Three-Dimensional Discontinuous Deformation Analysis (3-D DDA) Validation Using Analytical Solutions

Moosavi M., Jafari A., Beyabanaki S.A.
School of Mining Engineering, University of Tehran, Tehran, Iran

This paper was prepared for presentation at *ICADD-7, the Seventh International Conference on Analysis of Discontinuous Deformation*, held in Honolulu, Hawaii, December 10-12, 2005.

ABSTRACT: The Discontinuous Deformation Analysis (DDA) is a powerful numerical method for analysis of discontinuous rock mass behavior. This method can be used to perform static and dynamic analysis. In this paper the validity of 3-D DDA is examined by comparing its solution for dynamic block displacement with analytical solution. Displacement of a single block on an inclined plane subjected to a dynamic loading is studied for both simple form of analytical solution and with respect to the frictional resistance offered by the inclined slope. 3-D DDA predicts accurately the analytical displacements.

1. INTRODUCTION

The Discontinuous Deformation Analysis (DDA) is a numerical model for rock mass behavior [1,2]. Using DDA, one can perform static and dynamic analysis of a block system to obtain solution of large deformation and large displacement.

Before applying dynamic DDA to a full scale problem of a jointed rock slope it is necessary to check whether dynamic DDA displacements are in agreement with the analytical solutions. Hatzor and Feintuch [3] demonstrated the validity of 2-D DDA results for fully dynamic analysis of a single block on an incline subjected to dynamic loading. Dynamic solution for a single block on an incline subjected to gravitational load (constant acceleration), a case which was investigated originally by Sitar & MacLaughlin [4] and Maclaughlin [5] later more developed using the new dynamic code [6]. For a slope inclination of 22.6 degree, four dynamic displacement tests were performed for interface friction angle values of 5, 10, 15 and 20 degrees. The agreement between the analytical and 2-D DDA solution was within 1-2%. Hatzor and Feintuch investigated three different sinusoidal functions of increasing complexity for the dynamic load input function, and checked the agreement between 2-D DDA and derived simple form of analytical solution. A very good agreement between simple form of analytical solution and 2-D DDA was observed in all cases, with errors between 5% to 10%.

Dynamic displacement problem of a block on an incline was studied by Tsesarsky et al. [7, 8] using 2-D DDA analytical solution and shaking table experiments. The results of the validation study showed that DDA solution of an idealized system for which an analytical solution exists is accurate. After these investigations, dynamic 2-D DDA was applied to stability analysis of jointed rock slopes [9, 10].

Three Dimensional Deformation Analysis (3-D DDA) method is still at rearly stage. It has a long development road ahead before it can become a practical analysis tool for engineering problems. Up to now, only a limited amount of work on 3-D DDA has been published [11-26].

In this paper, analytical results are compared with numerical solution of DDA for displacement of a single block which rests on an inclined plane. A short hand version of the analytical equations ignoring the frictional resistance offered by an incline slope inclination was studied for 2-D DDA [3], however but in this research the complete set of equations is studied. Clearly, the analytical validation of the numerical method can only be performed for a single block. In order to validate dynamic displacements, determined by 3-D DDA for a system of blocks comparison with physical models would be necessary. However this study for a single block would be the first necessary step for such research.

2. DDA FUNDAMENTALS

In DDA method, the formulation of blocks is very similar to the definition of a finite element mesh. A finite element type problem is solved in which all elements physically isolated blocks are bounded by pre-existing discontinuities. When the blocks are in contact, Coulomb's law is applied to the contact interfaces, and the simultaneous equilibrium equations are formed and solved at each loading or time increment. The large displacements are the accumulation of incremental displacements and deformation at each time step. Within each time step, the incremental displacements of all points are small, and hence the displacements can be reasonably represented by the first order approximation [27].

2.1. Block Deformation and Displacement

Using complete first order polynomial as displacement function for a block, DDA method assumes that each block has constant strains and stresses in the block. Displacements (u,v,w) of any point (x,y,z) in the i[th] block can be related to twelve displacement variables as:

$$[D_i] = (u_0, v_0, w_0, r_x, r_y, r_z, \varepsilon_x, \varepsilon_y, \varepsilon_z, \gamma_{xy}, \gamma_{yz}, \gamma_{zx})^T \tag{1}$$

where u_0, v_0 and w_0 are rigid body translations at a specific point (x_0, y_0, z_0) within the block, r_x, r_y and r_z are rotation angles of the block with a rotation center (x_0, y_0, z_0) and $\varepsilon_x, \varepsilon_y, \varepsilon_z, \gamma_{xy}, \gamma_{yz}$ and γ_{zx} are normal and shear strains in the block. The complete first order approximation of block displacements takes the following form:

$$(u \;\; v \;\; w)^T = [T_i][D_i] \tag{2}$$

$$[T_i] = \begin{bmatrix} 1 & 0 & 0 & -y' & 0 & z' & x' & 0 & 0 & y'/2 & 0 & z'/2 \\ 0 & 1 & 0 & x' & -z' & 0 & 0 & y' & 0 & x'/2 & z'/2 & 0 \\ 0 & 1 & 1 & 0 & y' & -x' & 0 & 0 & z' & 0 & y'/2 & x'/2 \end{bmatrix} \tag{3}$$

where

$$x' = x - x_0 \quad , \quad y' = y - y_0 \quad , \quad z' = z - z_0$$

2.2. Block Deformation and Displacement

Assuming that n blocks are defined in the block system, the simultaneous equilibrium equations can be written in the matrix form as follows:

$$\begin{bmatrix} K_{11} & K_{12} & K_{13} & \dots & K_{1n} \\ K_{21} & K_{22} & K_{23} & \dots & K_{2n} \\ K_{31} & K_{32} & K_{33} & \dots & K_{3n} \\ \vdots & \vdots & \vdots & \ddots & \vdots \\ K_{n1} & K_{n2} & K_{n3} & \dots & K_{nn} \end{bmatrix} \begin{bmatrix} D_1 \\ D_2 \\ D_3 \\ \vdots \\ D_n \end{bmatrix} = \begin{bmatrix} F_1 \\ F_2 \\ F_3 \\ \vdots \\ F_n \end{bmatrix} \tag{4}$$

Submatrices K_{ii} depend on the material properties of block i and K_{ii}, where $i \neq j$, is defined by the contacts between blocks i and j. Since each block i has twelve degrees of freedom defined by the components of D_i in Eq. (1), each K_{ii} in Eq. (4) is a 12×12 sub matrix. Also, each F_i is a 12×1 sub matrix that represents the loading on block i. The system of Eq. (4) can also be expressed in a more compact form as $KD = F$ where K is a $12n \times 12n$ stiffness matrix, and D and F are $12n \times 1$ displacement and force matrices, respectively. The total number of unknown displacements is the sum of the degrees of freedom of all the blocks.

The total potential energy Π is the summation over all potential energy sources; stresses and forces. The simultaneous equations are derived by minimizing the total potential energy Π of the block system.

$$k_{ijrs} = \frac{\partial^2 \Pi}{\partial d_{ri} d_{sj}} \quad , \quad r, s = 1,2,...,12 \tag{5}$$

$$F_{ir} = -\frac{\partial \Pi(0)}{\partial d_{ri}} \quad , \quad r = 1,2,...,12 \tag{6}$$

The solution to the system of equations (4) is constrained by a system of inequalities associated with block kinematics (e. g. no penetration and no tension between blocks) and coulomb's friction for sliding along block interface. The system of equation (4) is solved for the displacement variables and the final solution to this system is obtained as follow. At first, the solution is checked to see how well the constraints are satisfied. If tension or penetration is found along any contact, the constraints are adjusted by selecting new blocks and constraining positions and a modified version of K and F are formed from which a new solution is obtained. This process is repeated until no tension and no penetration are found along all of the block contacts. Hence, the final displacement variables for a given time step are actually obtained by an iterative process.

3. SINGLE BLOCK ON AN INCLINE - GRAVITATIONAL LOAD ONLY

This case was studied by Jiang &Yeung [18], Liu et al. [19] and Wu et al. [22], which this is a classic example of dynamics. As shown in Fig. 1 a single block rests on an inclined plane at an angle α to the horizontal direction. The friction angle along the contact surface is ϕ. Under the action of gravitational force, displacement s and velocity v of the block are determined analytically as functions of time t and are given as:

$$m\ddot{u} = mg\sin\alpha - m(g\cos\alpha\tan\phi) \tag{7}$$

$$\dot{u}(t) = \ddot{u}t = (g\sin\alpha - g\cos\alpha\tan\phi)t \tag{8}$$

$$u(t) = \frac{1}{2}\ddot{u}t^2 = \frac{1}{2}(g\sin\alpha - g\cos\alpha\tan\phi)t^2 \tag{9}$$

Fig. 2 shows the results computed by 3-D DDA for different friction angles. This figure shows that the analytical solutions agree well with the results computed by 3-D DDA.

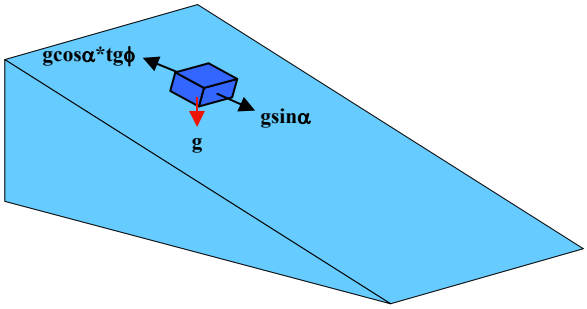

Fig. 1 a block sliding on inclined plane

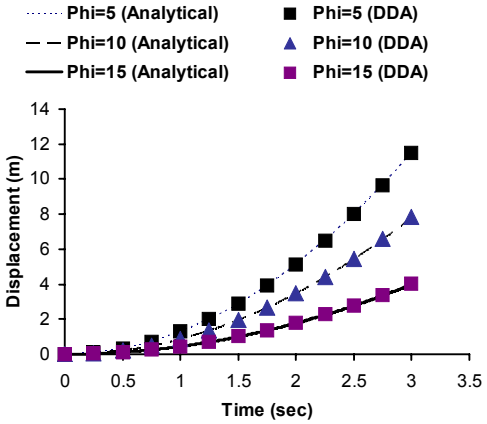

Fig. 2 Comparison between 3-D DDA results and analytical solutions

4. SINGLE BLOCK ON AN INCLINE – DYNAMIC LOAD

Typically, earthquake damage is associated with finite displacement of large discrete masses. Therefore, block performance in a slope should be evaluated in terms of permanent displacements rather than in terms of safety factor derived from pseudo-static analysis. This approach was firstly introduced by Goodman and Seed [28] and by Newmark [29] and is now largely referred to as "Newmark" type analysis.

A Newmark type analysis assumes that relative slope movement is initiated when inertial forces on the potential sliding mass overcome the shear resistance along the sliding plane, the corresponding level of horizontal acceleration known as "yield acceleration". The analysis assumes that the mass will come to rest when it attains zero velocity. The permanent displacement of the sliding mass can then be calculated by integrating the relative velocity of the block during sliding over time. In this study the complete form of the equation is used. It should be reminded that the solution is only valid for a single, rigid, block undergoing sliding deformation.

No damping is assumed in this study.

4.1. The simplest form of a sinusoidal function

In this case, acceleration would have the form:

$$\ddot{u}(t) = k.g.\sin(t) \tag{10}$$

where $\ddot{u}$ is acceleration , t is time, k is a constant coefficient and g is gravitation acceleration. In order to find the velocity and displacement gravity by this acceleration function, the acceleration has to be integrated twice over a range from t_0 to t, where t_0 is the time at which :

$$\ddot{u}(t) = a_y \tag{11}$$

where a_y is defined as the yield acceleration. Goodman and Seed [28] showed that for frictional sliding only, where cohesion along the sliding surface is zero, the down slope, horizontal, yields acceleration for a block resting on a plane with inclination α and friction angle φ is given by:

$$a_y = tg(\varphi_{eq} - \alpha).g \tag{12}$$

where φ_{eq} is a displacement dependent friction angle, which for all practical purposes in rock mechanics could be replaced by φ. The corresponding analytical solution for the velocity $\dot{u}(t)$ and displacement $u(t)$ in simple form are given by:

$$\dot{U} = \int \ddot{U} = k.g.(-\cos(t) + \cos(t_0)) \tag{13}$$

$$U = \int \dot{U} = k.g\left[\int_{t_0}^{t} (-\cos(t))dt + \cos(t_0)(t - t_0) = k.g.[-\sin(t) + \sin(t_0) + \cos(t_0)(t - t_0)]\right. \tag{14}$$

and taking into account the frictional resistance offered by the inclined slope (complete form) are given by:

$$\ddot{U} = g\sin\alpha + kg\sin(t)\cos\alpha - g(\cos\alpha - k\sin(t)\sin\alpha)tg\phi \tag{15}$$

$$\dot{U} = \int \ddot{U} = g.(\sin(\alpha) - \cos(\alpha).\tan(\phi))\int_{t_0}^{t} dt + g.(\cos(\alpha) + \sin(\alpha).\tan(\phi))\int_{t_0}^{t} k.\sin(t)dt \tag{16}$$

$$U = \int \dot{U} = g.(\sin(\alpha) - \cos(\alpha).\tan(\phi))\int_{t_0}^{t} (t - t_0)dt + k.g.(\cos(\alpha) + \sin(\alpha).\tan(\phi))\int_{t_0}^{t} (\cos(\theta) - \cos(t))dt \tag{17}$$

$$U = g.\left[(\sin(\alpha) - \cos(\alpha).\tan(\phi))\left(\frac{t^2}{2} - t_0 \cdot t\right)\right] + k.g.[(\cos(\alpha) + \sin(\alpha).\tan(\phi))(\cos(t_0)(t - t_0) - \sin(t) + \sin(t_0))] \tag{18}$$

Considering a plane inclined at 20°, and $k = 0.5$, the parameters used for the study are shown in table 1.

Table 1. The used parameters for the simplest form of a sinusoidal function

Friction Angle (φ)	**Yield acceleration (a_y)**	**Time at a_y (t_0)**
22°	$0.3426\ m/s^2$	0.0699 sec

Acceleration, velocity and displacement function derived in Eqs. (10), (13)-(16) and (18) are plotted in Fig. 3 for one complete cycle that last 2π seconds.

The input acceleration record for 3-D DDA was the horizontal component only and the other acceleration components were set to zero.

A comparison between the analytical solution and 3-D DDA results for $\Delta t = 0.01s$ is shown in Fig. 4.

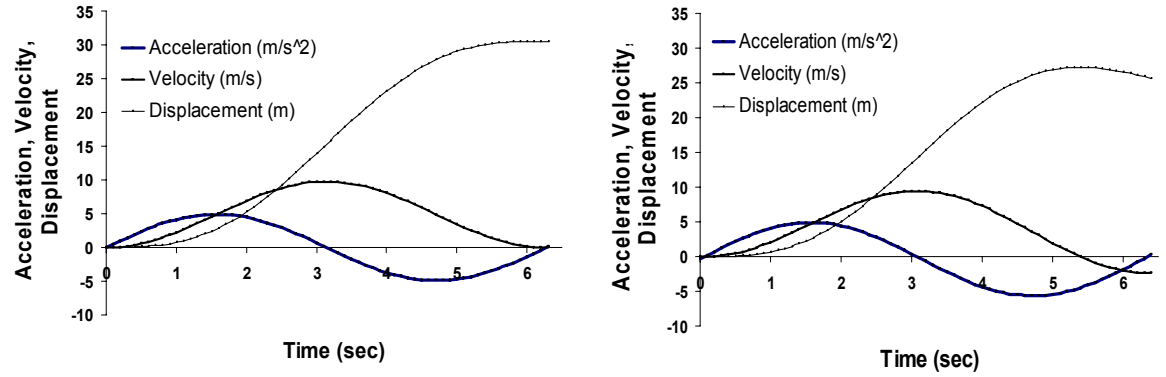

Fig. 3 Analytical solution for acceleration, velocity and displacement $(\ddot{u}(t) = 0.5g.\sin(t))$ a) the simple form b) the complete form

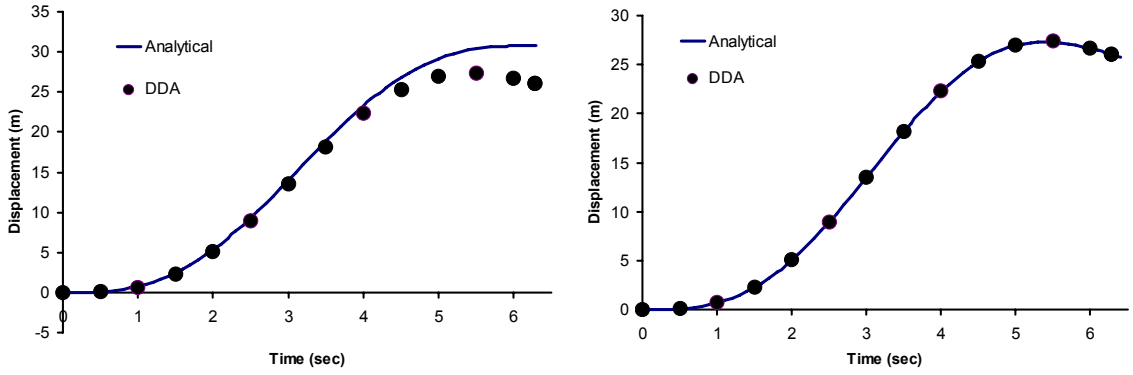

Fig. 4 Comparison between analytical solution and 3-D DDA results $(\ddot{u}(t) = 0.5g.\sin(t))$ a) the simple form b) the complete form

A very good agreement between complete form of analytical solution and 3-D DDA was obtained, while error about 14% in the simple form can be seen and this could probably be improved by optimizing the numerical parameters.

4.2. A harmonic function

The function $\ddot{u}(t) = k.g.\sin(\omega t)$ allows us to model different ground motion frequencies using the parameter ω. The analytical solutions for the velocity and displacement in the simple form are given by:

$$\dot{U} = \int k.g.\sin(\omega t) = \frac{k.g}{\omega}(-\cos(\omega t) + \cos(\omega t_0)) \tag{20}$$

$$U = \int \dot{U} = \frac{k.g}{\omega}[-\frac{\sin(\omega t)}{\omega} + \frac{\sin(\omega t_0)}{\omega} + \cos(\omega t_0)(t - t_0)] \tag{21}$$

and with respect to the frictional resistance offered by the inclined slope are given by:

$$\ddot{U} = g\sin\alpha + kg\sin(\omega t)\cos\alpha - g(\cos\alpha - k\sin(\omega t)\sin\alpha)tg\phi \tag{22}$$

$$\dot{U} = \int \ddot{U} = g(\sin\alpha - \cos\alpha\tan\phi)\int_{t_0}^{t} dt + g(\cos\alpha + \sin\alpha\tan\phi)\int_{t_0}^{t} k\sin(\omega t)dt \tag{23}$$

$$U = \int \dot{U} = g(\sin\alpha - \cos\alpha\tan\phi)\int_{t_0}^{t} (t - t_0)dt + kg(\cos\alpha + \sin\alpha\tan\phi)\int_{t_0}^{t} \frac{\cos(\omega t_0) - \cos(\omega t)}{\omega} dt \tag{24}$$

$$U = g.\left[(\sin(\alpha) - \cos(\alpha).\tan(\phi))\left(\frac{t^2}{2} - t_0 \cdot t\right)\right] + \frac{k.g}{\omega^2}.[(\cos(\alpha) + \sin(\alpha).\tan(\phi))(\omega\cos(\omega t_0)(t - t_0) - \sin(\omega t) + \sin(\omega t_0))] \tag{25}$$

Considering a plane inclined at 20°, $k = 0.75$ and $\omega = 2$, the parameters used for the study are shown in table 2.

Table 2 The used parameters for the harmonic function

Friction Angle (φ)	**Yield acceleration (a_y)**	**Time at a_y (t_0)**
22°	$0.3426\ m/s^2$	0.0233 sec

In Fig. 5 the shape of the acceleration, velocity and displacement functions are plotted. Since $\omega = 2$, a complete cycle lasts π seconds only.

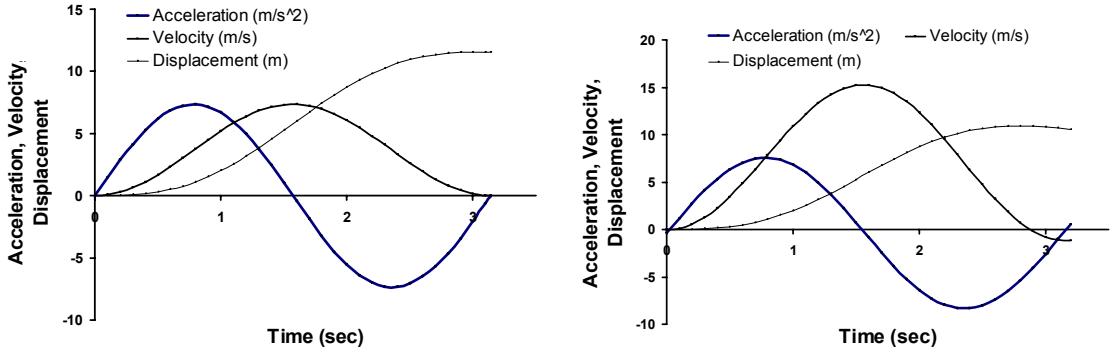

Fig. 5 Analytical solution for acceleration, velocity and displacement $(\ddot{u}(t) = 0.75g.\sin(2t))$ a) the simple form b) the complete form

A comparison between the analytical solution and 3-D DDA results is shown in Fig. 6 for this case. This figure shows that the results computed by 3-D DDA agree well with the analytical solutions and it can be seen that result from 3-D DDA solution is maximum 8% lower than the analytical results in case (a).

4.3. A sum of two sine functions

The influence of higher order terms in a series of sine functions is negligible and therefore we will not proceed our validation effort beyond the sum of three sine functions. Therefore:

$$\ddot{u}(t) = k_1.g.\sin(\omega_1 t) + k_2.g.\sin(\omega_2 t) \tag{26}$$

The corresponding analytical solutions the velocity and displacement in the simple form are given by Eqs. (27) and (28) below:

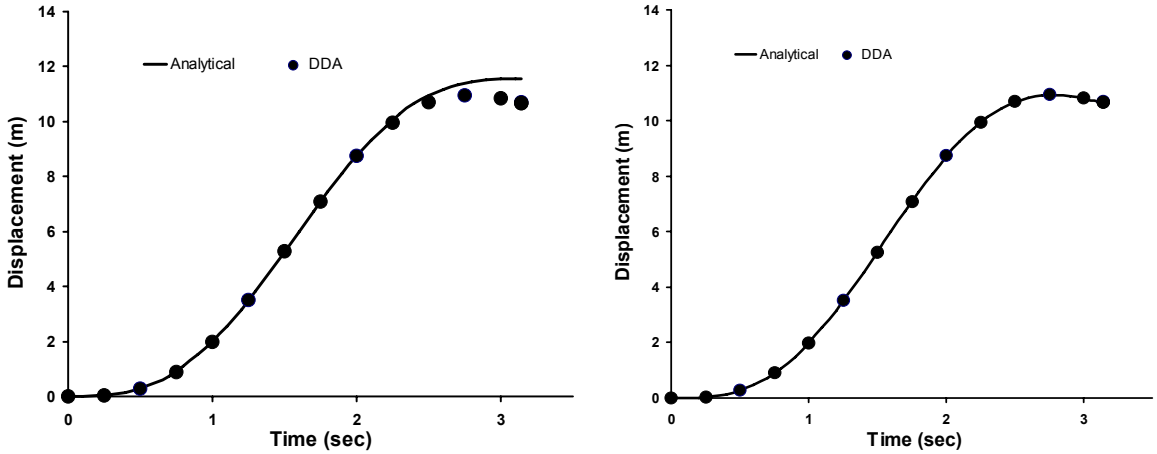

(a) (b)

Fig. 6 Comparison between analytical solution and 3-D DDA results $(\ddot{u}(t) = 0.75g.\sin(2t))$ a) the simple form b) the complete form

$$\dot{U} = k_1.g.(\frac{-\cos(\omega_1 t) + \cos(\omega_1 t_0)}{\omega_1}) + k_2.g.(\frac{-\cos(\omega_2 t) + \cos(\omega_2 t_0)}{\omega_2}) \tag{27}$$

$$U = \frac{k_1.g}{\omega_1^2}\left[-\sin(\omega_1 t) + \sin(\omega_1 t_0)\right] - \frac{k_2.g}{\omega_2^2}\left[\sin(\omega_2 t) - \sin(\omega_2 t_0)\right] + \frac{k_1.g}{\omega_1}.\cos(\omega_1 t_0)\,(t - t_0) + \frac{k_2.g}{\omega_2}\cos(\omega_2 t_0)\,(t - t_0) \tag{28}$$

and taking into account the frictional resistance offered by the inclined slope (complete form) are given by:

$$\ddot{U} = g[\sin\alpha + (k_1 \sin\omega_1 t + k_2 \sin\omega_2 t)\cos\alpha - (\cos\alpha - (k_1 \sin\omega_1 t + k_2 \sin\omega_2 t)\sin\alpha)tg\,\varphi] \tag{29}$$

$$\dot{U} = \int \ddot{U} = g[(\cos\alpha + \sin\alpha\, tg\,\varphi)[\frac{k_1}{\omega_1}(\cos\omega_1 t_0 - \cos\omega_1 t) + \frac{k_2}{\omega_2}(\cos\omega_2 t_0 - \cos\omega_2 t)] + (t - t_0)(\sin\alpha - \cos\alpha\, tg\,\varphi)] \tag{30}$$

$$U = \int \dot{U} = g(\sin\alpha - \cos\alpha\, tg\,\varphi)[\frac{1}{2}(t^2 - t_0^2) - t_0(t - t_0)] + (\cos\alpha + \sin\alpha\, tg\,\varphi)[\frac{k_1 g}{\omega_1^2}(\sin\omega_1 t_0 - \sin\omega_1 t) + \frac{k_2 g}{\omega_2^2}(\sin\omega_2 t_0 - \sin\omega_2 t) + \left(\frac{k_1 g}{\omega_1}\cos\omega_1 t_0 + \frac{k_2 g}{\omega_2}\cos\omega_2 t_0\right)(t - t_0)] \tag{31}$$

Considering a plane inclined at 20°, $k_1 = 0.2$, $k_2 = 0.3$, $\omega_1 = 1$ and $\omega_2 = 2$ the parameters used for the study are shown in table 3.

Table 3. The used parameters for the sum of two sine functions

Friction Angle (φ)	Yield acceleration (a_y)	Time at a_y (t_0)
22°	$0.3426\ m/s^2$	0.0437 sec

Acceleration, velocity and displacement functions for this case are shown in Fig. 7. A comparison between the analytical solution and 3-D DDA results is shown in Fig. 8. At the end of the cycle in Fig. (8a), 3-D DDA solution is about 7% lower than the analytical solution.

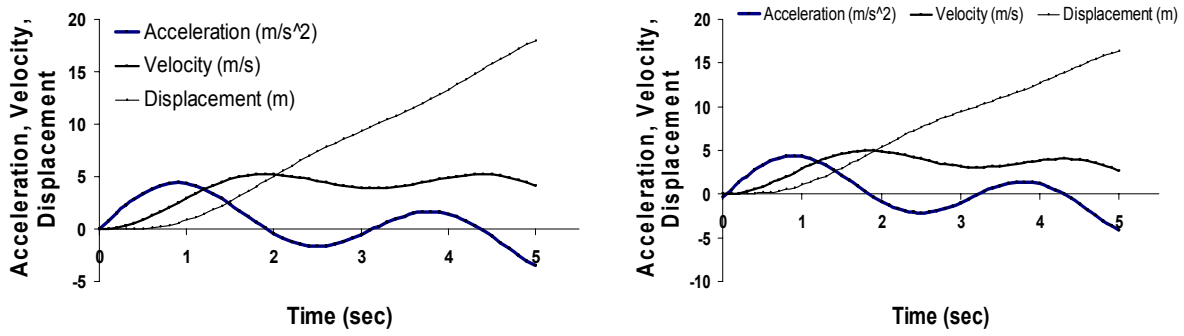

Fig. 7 Analytical solution for acceleration, velocity and displacement $(\ddot{u}(t) = 0.2g.\sin(t) + 0.3g.\sin(2t))$
a) the simple form b) the complete form

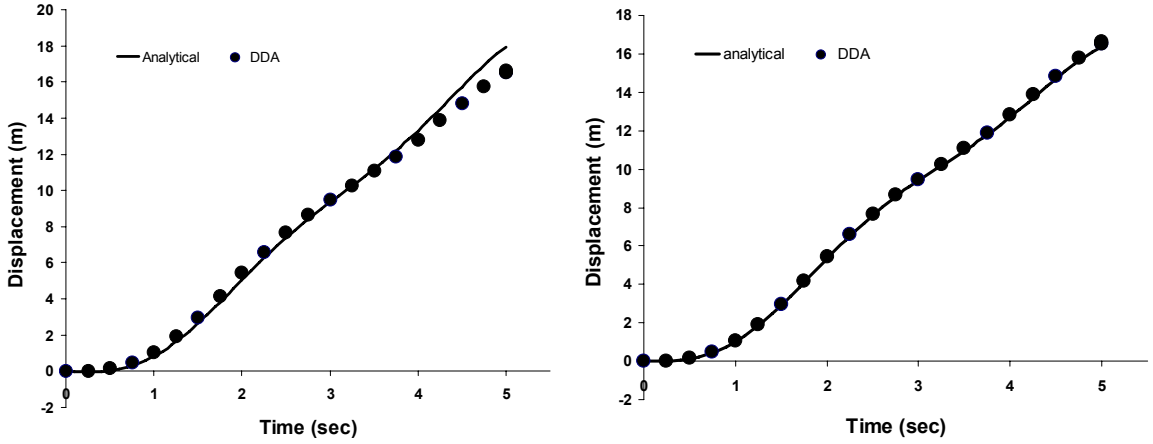

Fig. 8 Comparison between analytical solution and 3-D DDA results $(\ddot{u}(t) = 0.2g.\sin(t) + 0.3g.\sin(2t))$
a) the simple form b) the complete form

5. CONCLUSIONS

In this paper the displacement history of a single block on an incline subjected to dynamic loading was studied. The analysis was performed for a single block resting on a plane inclined to the horizontal for both simple form of analytical solution and taking into account the frictional resistance offered by the inclined slope.

Three different sinusoidal functions with difference complexity considering the dynamic load were investigated. Agreement between 3-D DDA and derived simple and complete form of analytical solution was investigated. The observed agreement in all cases was very good, as

experienced before in 2-D DDA by other researchers. The error was found to be 7% to 14% in 3-D DDA, while previous 5% to 10% error was seen in 2-D DDA. The higher error in this study could probably be improved by optimizing the numerical parameters. For the complete form which the formulation of the analytical solution is obtained taking into account the frictional resistance offered by the inclined slope, the agreement between analytical solution and 3-D DDA was very well in all three different sinusoidal functions. However, the analytical solution is for an ideal condition and can be considered as approximation of a physical problem with various simplifying assumptions including: perfectly rigid block, constant friction, and complete energy conservation.

6. ACKNOWLEDGMENTS

The authors are thankful to the “center of excellence” in the School of Mining Engineering, University of Tehran, which has funded this ongoing research.

REFERENCES

1. Shi, G.H. and R.E. Goodman. 1985. Two–dimensional discontinuous deformation analysis. *International Journal for Numerical and Analytical Methods in Geomechanics* 9: 541-556.

2. Shi, G.H. 1993 *Block system modeling by discontinuous deformation analysis.* Southampton UK and Boston USA: Computational Mechanics Publications.

3. Hatzor, Y.H. and A. Feintuch A. 2001. The validity of dynamic displacement prediction using DDA. *International Journal of Rock Mechanics and Mining Sciences.* 38: 4, 599-606.

4. Sitar, N. and M.M. Maclaughlin M.M. 1997. Kinematics and discontinuous Deformation analysis of Landslide Movement. In *II Pan-American Symposium on Landslides, Rio de Janeiro, 10-14 November 1997.*

5. Maclaughlin, M.M. 1997. *Discontinuous Deformation Analysis of the Kinematics of Landslides.* PhD Dissertation, Dept. of Civil and Env. Enger., Univ. of California, Berkeley.

6. Shi, G.H. 1999. Application of Discontinuous Deformation Analysis and Manifold Method”, In *Proceedings of ICADD-3, Third International Conference of analysis of Discontinuous Deformation, Vail, Colorado*, ed. B. Amadei, 3-15.

7. Tsesarsy, M., Y.H. Hatzor , and N. Sitar, 2002. Dynamic block displacement prediction-validation of DDA using analytical solutions and shaking table experiments. In *Proceedings of ICADD-5, 5th International Conference of Analysis of Discontinuous Deformation, Beer-Sheva, Israel, ed.Y.H. Hatzor,* 195-203.

8. Tsesarsky, M., Y.H. Hatzor, and N. Sitar. 2005. Dynamic Displacement of a Block on an Inclined Plane: Analytical, Experimental and DDA Results. *Rock Mechanics and rock Engineering.* 38: 2, 153-167.

9. Hatzor, Y. H., A.A. Arzi , and M. Tsesarsky. 2002. Realistic dynamic analysis of jointed rock slopes using DDA. In *Proceedings of ICADD-5, 5th International Conference of Analysis of Discontinuous Deformation, Beer-Sheva, Israel, ed.Y.H. Hatzor,* 47-56.

10. Hatzor, Y. H., A.A. arzi , Y. Zaslavsky , and A. Shapira. 2004. Dynamic atability analysis of jointed rock slopes using DDA method: King Herodis Palace, Masada, Israel. *International Journal of Rock Mechanics and Mining Sciences 41*, 813-832.

11. Shi, G.H. 2001. Three dimensional discontinuous deformation analysis. In *Proceedings of the 38th US Rock Mechanics Symposium, Washington D.C*., eds. D. Elsworth et al, 1421-1428.

12. Jang, h.I. and C.I. Lee. 2002. Development of a three dimensional discontinuous deformation analysis technique and its application to toppling failure", In *Proceedings of ICADD-5, 5th International Conference of Analysis of Discontinuous Deformation, Beer-Sheva, Israel, ed.Y.H. Hatzor,* 225-229.

13. Jiang, Q. and M.R. Yeung. 2002. A simplified model of bolt for 3-D discontinuous deformationa analysis method. In *Proceedings of Rock Engineering Problems and Approaches in underground Construction*, eds. Choi et al, 597-502.

14. Yeung, M.R., Q.H. Jiang and N. Sun. 2003. Validation of block theory and three - dimensional discontinuous deformation analysis as wedge stability analysis methods. *International Journal of Rock Mechanics and Mining Science,* 40: 2, 265-275.

15. Jiang, Q. H., M.R. Yeung and N. Sun. 2003. Modelling Groundwater Pressure and Thermal Loading in Three-Dimensional Deformation Analysis. In *Proceedings of International Conference on Coupled T-H-M-C Processes in Geosystems*.

16. Kong, X, and J. Liu. 2003. Development of three dimensional discontinuous deformation analysis. In *Proceedings of the 6th Conference on Analysis of Discontinuous Deformation (ICADD-6)*, ed. M. Lu , 45-54, Balkema.

17. Yeung, M.R., N. Sun , and Q.H. Jiang. 2003. Parametric study of wedge stability using three-dimensional discontinuous deformation analysis, In *Proceedings of the 6th Conference on Analysis of Discontinuous Deformation (ICADD-6)*, ed. M. Lu , 65-74, Balkema.

18. Jiang, Q.H. and M.R. Yeung. 2004. A model of point-to-face contact for Three-Dimensional Discontinuous deformation Analysis. *Rock Mechanics and Rock engineering*, 37, 95-116.

19. Liu, J., X. Kong , and G. Lin. 2004. Formulation of the Three-Dimensional Discontinuous Deformation Analysis Method. *Chinese Journal of Mechanics Press*, 20: 3.

20. Yang, M., T. Fukawa , Y. Ohnishi , S. Nishiyama , S. Miki , Y. Hirakawa , and S. Mori. 2004. The application of 3-dimensional DDA with a spherical rigid block for rockfall simulation. *International Journal of Rock Mechanics and Mining Science*, 41: 3, Paper 2B 25.

21. Yeung, M.R., N. Sun , Q.H. Jiang , and S.C. Blair. 2004. Analysis of large block test data using three-dimensional discontinuous deformation analysis. *International Journal of Rock Mechanics and Mining Science*, 41: 3, Paper 2B 10.

22. Wu, J.H., C.H. Juang , and H.M. Lin. 2005. Vertex-to-face contact searching algorithm for three-dimensional frictionless contact problems. *International Journal for Numerical Methods in Engineering*, 63: 6, 876-897.

23. Wu, J.H., Y. Ohnishi , and S. Nishiyama. 2005. A development of the discontinuous deformation analysis for rock fall analysis. *International Journal for Numerical and Analytical Methods in Geomechanics*, 29: 10, 971-988.

24. Shi, G.H. 2005. Forming Three Dimensional Block System from Statistically Produced Joint Polygons Using Three Dimensional DDA. In *The 40th U.S. Symposium on Rock Mechanics (USRMS): Rock Mechanics for Energy, Mineral and Infrastructure Development in the Northern Regions, Alaska, June 25-29 2005*.

25. Sun, N., M.R. Yeung, C.F. Lee , and Q.H. Jiang. 2005. Design Method Coupling Block Theory and Three-Dimensional Discontinuous Deformation Analysis. In *The 40th U.S. Symposium on Rock Mechanics (USRMS): Rock Mechanics for Energy, Mineral and Infrastructure Development in the Northern Regions, Alaska, June 25-29* .

26. Wu, J.H., Ohnishi Y., Shi G.H. and Nishiyama S. 2005. Theory of Three-Dimensional Discontinuous Deformation Analysis and Its Application to a Slope Toppling at Amatoribashi, Japan. *International Journal of Geomechanics,* 179-195.

27. Lin, C.T., B. Amadei, J. Jung, and J. Dwer. 1996. Extensions of Discontinuous Deformation analysis for Jointed Rock Masses. *International Journal of Rock Mechanics and Mining Sciences*, 33: 7, 671-694.

28. Goodman, R.E., and H.B. Seed. 1995. Earthquake induced displacements in sands and embankments. *J. soil Mech. Foundation Div. ASCE*, 92: SM2, 125-46.

29. Newmark, N.M. 1965. Effects of earthquakes on dams embankments, *Geotechnique*, 15: 2, 139-60.

Analysis and improvement of scheme to detect contacts in 3D blocky systems

WANG, Jianquan

Earthquake Engineering Research Division, School of Civil and Hydraulic Engineering, Dalian University of Technology, Dalian, China

LIU, Jun. and LIN, Gao.

Earthquake Engineering Research Division, School of Civil and Hydraulic Engineering, Dalian University of Technology, Dalian, China

This paper was prepared for presentation at *ICADD-7, the Seventh International Conference on Analysis of Discontinuous Deformation*, held in Honolulu, Hawaii, December 10-12, 2005.

ABSTRACT: DDA (Discontinue Deformation Analysis) and DEM (Discrete Element Method) are two important numerical methods for the analysis of discontinuous media. These methods have been widely applied to the two-dimensional analysis of discontinuous deformation. However, they are limited for three-dimensional analysis of practical rock engineering problems. At present, spheres, bonded spheres or ellipsoids blocks are mainly used in 3D codes, which can not describe the real behavior of more complex blocky system such as fractured rock masses. Contact detection is a key problem in 3D DDA and DEM analysis. The limitations and advantages of the existent contact detection schemes are discussed. Based on the advantages of the existent methods, a new approach called incision body is put forward. The C program codes for 3D DDA are developed. Convex blocks are the basic shape. A concave block can be formed through combining several convex blocks. The simulation examples of block movement are also given in this paper. The simulation result shows that the incision body method is capable of overcoming indeed limitations of the existent methods, can detect 3D block contacts correctly and hence simulate the open-close and slide process of the block masses.

1. INTRODUCTION

Discontinuous deformation analysis(DDA)[1,2] and distinct element method(DEM)[3] are two important numerical approaches which can model effectively rock mass discontinuities, and hence compute the displacements of blocky system, as a result, have been enjoying wide application in rock engineering and other engineering involving blocky system. Although numerous extensions and improvements have been implemented with many papers published, the two methods cannot analyze properly the practical three dimension problems of rock engineering at present because that existent contact detection algorithms cannot get the exact contact relationship sometimes between two 3D rock blocks that contact each other. Up until recently, spheres, bonded spheres and ellipsoids were mainly used as elements or blocks in 3D codes, which can not reveal the real behavior of more angular block system such as fractured rock masses in that joints, fissures and faults intersecting. The real rock block can be convex and

concave, also, can have any numbers of polygons as their faces. In principle, a contact may appear between any two faces of any two blocks, and may exist in any combination of vertices, edges and faces. Direct detection method is implemented through checking every possible contact between faces, edges, vertices that belong to a block and the same that belong to the other block. It has been proved to be excessively time consuming and not been used in code in practice. The preliminary effort to detect 3D contact between blocks was made by Cundall[4] who proposed the common-plane algorithm to detect and represent contacts in system composed of many polyhedral blocks. The common-plane method was developed in [5,6] for face-participant contact, and [7] for fast detection. A further effort was made to analysis the 3D blocky system using the CP method in [8], which was implemented by visual c++ programming. Unfortunately, this algorithm cannot always detect the correct contact relationship between two 3D polyhedral blocks, as was discussed in [9] and also emerged in author's programming practice. Meanwhile, a new scheme named penetration edges[9] was put forward to detect contacts between 3D polyhedral blocks. Although this method explores a new way along which researchers may walk to get a reliable detection method, it still sometimes detects wrong contact type or misses existent contact between two blocks contacted each other. So a robust and reliable algorithm that can detect contact relationship correctly between two real rock blocks is needed at present[10-12].

By analyzing the problems of existing contact detection methods and gathering the advantages of them, this paper proposed a new method, namely incision body method, to detect contacts between 3D rocky blocks more reliably. The algorithm has been implemented in code programmed in visual c++. Numerical examples illustrate the applicability and reliability of the proposed method. Three dimension blocks are assumed to be convex blocks while a concave block can be modeled as a combination of several convex blocks attached to each other.

2. IDEAS AND PROBLEMS OF EXISTING CONTACT DETECTING METHOD

2.1. Direct detection method

Though this method is simple and straightforward, it dose not make use of the inherent geometrical relations between three types of elements, namely vertex, edge and face, of a block. For example, when detecting contacts between block A and block B, because that an edge of block A consists of two vertices, it is not necessary to check for any possible interaction relationship between the edge and geometrical elements of block B if relationship between the two vertices and block B has already been checked. Furthermore, a face of block A consists of several edges and, if two edges of the face contact with an edge of block B, then the face of block A must contact the edge of block B without checking the relation between another edge of the face of block A and the edge of block B. Similarly, because that two faces of block A intersect each other at a certain edge, if the edge of block A contact a vertex of block B, then the two faces of block A must contact the vertex of block B which dose not have to be checked over while detecting possible contacts pertain to the two faces of block A.

Such straightforward relations between three types of elements represent part of geometrical feature of a polyhedral block. These relations should be, and indeed have been, employed to enhance the detecting efficiency by the following more valid methods.

2.2. Common plane(CP) method

Each face of a convex block partitions whole space into two parts, namely, inside part and outside part. The intersection of inside parts of whole faces of a block defines the volume of the block, on which the idea of common plane method based. When detecting contact between block

A and block B, if an element of block A, for example an edge, is located in outside part of a face of block B and the distance between every point on the element of block A and the face of block B is greater than a tolerance, the element can not contact block B. If all elements of block A located in outside of a face of block B and the distance between every convex of block A and the face of block B is greater than a tolerance for contact, the two blocks can not contact. So faces of a block are crucial in detecting contact because they part a block from space in which the other block is located.

The idea of common plane method is based on the assumption that there must exist a plane that can separate two blocks. If two blocks penetrate each other, there also must exist a plane that can separate two penetration sections of two blocks. The plane separate two blocks, namely common plane, is a plane that may be parallel to one face of either block or be not parallel to any face of two blocks. As a result of using common plane, the contact detection between two blocks reduced to detection between a block and a plane. The algorithm to position CP is: "Maximize the gap between the c-p and the closest vertex and minimize the overlap between the common plane and the vertex with the greatest overlap". The algorithm itself defines the correct position of common plane between two blocks contacted each other. During implementing the algorithm in program, an initial position of CP is fixed using centroids of two blocks. The final position of CP is determined based on the initial position. Because that relative positions of two centroids cannot reveal adequately the local shape character of blocks, for instance, the same point can play the centroid of many blocks at the same time that have different shapes, so the initial position of CP cannot always ensure that the final position of CP would be fixed correctly. This problem emerged in author's programming and also has been noticed in [9]. The CP algorithm was improved in [7] to speed up the detecting mainly and get the correct CP position more reliably. But the problem of with the lack of reliability has not been solved by the improvement.

2.3. Penetration edges method

The idea of this method is based on the assumption that there must exist an intersection between two blocks in contact with each other. Since the volume of a block can be seen as a set of space points, so there is a non-empty set of points that is the intersection. The edge or a part of which is located in the non-empty set is called penetration edge. The penetration edge has three realizations: a point of an edge of original block, a part of an edge of original block and a whole edge of original block. Only if the length of a penetration edge is less than a limit, it reduces to a point on the penetration edge.

When two blocks come into contact, combinations of penetration edges on block A and block B determine the type of contact. The advantage of this method is that it can take the local geometrical characteristics of a block into full account and, then, avoid the problem that hindered development of CP method. All kinds of combinations of the penetration edges of block A and block B constitute the universal set of edge-combination. All kinds of contacts constitute the universal set of contact-types. Unfortunately, according to this method, the mapping from edge-combination set to contact-type set is not a one to one mapping. Furthermore, the contact scope of a block is not exact. As a result a contact between two blocks may not be recognized or may be assigned the wrong type.

A reliable contact detection method should satisfy two criteria. Firstly, it should define an exact contact scope for a block. When an element, namely point, edge and face, of another block comes into the scope, a contact occurs between the element and another block. Secondly, it should define a one-one mapping between the universal set of initial information and the universal set of contact-type. For CP method, the initial information includes various relative

positions of CP between two contacted blocks. In algorithm of penetration edges, the initial information is all combinations of penetration edges.

3. IDEA AND PROCEDURE OF INCISION BODY METHOD

The idea of incision body method is similar to the one of penetration edges method. This method detects contact type through identifying the geometrical type of the incision body of each block. There are three geometrical types, namely, point and line and face (a incision body of a block will be looked as a point while it's volume is less than a tolerance).

The incision body of a block is the part of the block that is located in the volume encompassed by outer limit of contact scope of the other block. For block A and block B that contact each other, the incision body of block A is the intersection of Va and Vb' and the incision body of block B is the intersection of Vb and Va'(Va and Vb stand for volume of block A and block B respectively, in the same way, Va' stand for volume of contact scope of block A, Vb' stand for volume of contact scope of block B).

Detecting procedure of this method started by incising block B with planes determined by contact scope of A and getting incision body of block B, then, identifying the geometrical type of the incision body, for example, point; and then getting incision body of block A likewise, for example, line; finally judging contact type, namely, point-line. There are overall 7 contact types, namely, point-point, point-line, point-face, cross line-line, parallel line-line, line-face, face-face.

3.1. Contact scope of a block

In order to detect contact correctly, the contact scope of a block is defined at first. Suppose d0 is the tolerance of contact and d1 is the tolerance of allowable maximum penetration. If distance between two elements is less than d0, the two elements contact each other. Assume that each vertex is the intersection of three faces of a block. The contact scope can be disassembled into four types of sections, as shown in Fig.1. The first type is face-control section. Each face of a block owns one section of this type. This section is a space swept by the face of block when the face slides along it's outward normal direction with length of d0. The second type is edge-control section. It is a part of cylinder. Axis is the line coincided with the edge and height equal to the length of the edge while radius equal to d0. Each edge of a block owns one edge-control section that is formed by subtracting the parts of cylinder that located in space of block and face-control section from the cylinder itself. The third type is point-control section. It is a part of spheroid whose centre is a vertex of block and radius equal to d0. Each vertex of a block owns one such section that is formed by subtracting the parts of spheroid that located in space of block and face-control section and edge-control section from the spheroid itself. The fourth type is penetration section. There is only one such section for a block. It is a space encompassed by all inner faces of a block. Each face of a block owns only one inner face that is formed by sliding the face of block with length of d0 along inward normal direction of the face.

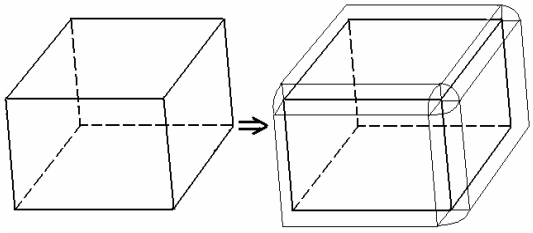

Fig.1. Illustration of contact scope of a block

If an element of a block comes into the contact scope of the other block, contact between the element and the other block occurs.

3.2. Classification of faces

Faces of a block can be classified into three types according to the minimum or maximum distance between the face and other block. The distance from a vertex to a face is defined as:

$$d^v=\mathbf{n}\cdot(V-V_0) \quad (1)$$

where **n** is unit outward vector normal to the face and V_0 is any point on the face, and V is the vertex. The minimum and maximum distances from a block to a face of other block are defined as:

$$d^{min}=\min\{d^v_i\} \quad i=1,2,\ldots,m \quad (2)$$

$$d^{max}=\max\{d^v_i\} \quad i=1,2,\ldots,m \quad (3)$$

where d^v_i is the distance from the i^{th} vertex of a block to the face, and $\min\{\cdot\}$ and $\max\{\cdot\}$ represent minimum and maximum values, respectively, taken over all vertices of a block, and m is the number of vertices of a block. If d^{max} from block A to a face of block B is less than –d1, then the face of block B is an enclosure face. Else if d^{min} from block A to a face of block B is greater than zero, the face of block B is a partition face. If a face of a block is neither an enclosure face nor a partition face, then it is an incision face. When two blocks were detecting, only the incision faces of a block were used to incise the other block to get the incision body of the other block.

If a block has one partition face, then the detection can be implemented only by checking the distances between every element of other block to the face. In fact, the partition face works like a common plane. As a result, the advantage of common plane algorithm is introduced into incision body algorithm in that it is good at taking the local geometrical characteristics of a block into full account.

3.3. Procedure of contact detection

When detecting contact using this method, the whole procedure includes four stages. The first is getting initial incision body of each block by incising twice. The second is getting final incision body of each block by removing the false part of initial incision body from the body itself. The false part of initial incision body of a block is the portion that is located outside contact scope of the other block. The third is judging the types of two incision bodies belong to two blocks. The fourth is getting contact type by combining the types of two incision bodies. Because there are totally seven types of combination, so there are seven types of contact, namely, point-point, point-line, point-face, cross line-line, parallel line-line, line-face, face-face.

In the first stage, in order to get the initial incision body of block A, two types of incising are required, and two types of planes are used in turn. Each plane of the first type used in the first incision is what coincides with a face on block B, whereas each one of the second type used in the second incision is an outer plane of face-control section of a face on block B. The first incising can find all faces of each type of block B and separate penetration section of block A from other three sections, and find key incision faces on block B at the same time. The second incising can get the initial incision body of block A by incising block A with planes determined by the key incision faces on block B. Not all incision faces of a block are used ultimately to determine the initial incision body of the other block. While incising block A with planes determined by faces of block B, there is only one or two key incision faces on block B. If the initial incision body of any block is empty, then the two blocks do not contact each other.

The two blocks cannot contact each other if any initial incision body located outside contact scope of the other block. Whether an initial incision body of a block locates out of the contact scope of the other block, a judging performed in the second stage will decide.

The final incision body of each block is also a convex polyhedron. All kinds of final incision bodies of two blocks constitute the universal set of initial information of this detecting method.

The geometrical type of final incision body will be determined in the third stage. Edges of a final incision body are sorted into four types, namely, original edge, incision edge, original point, incision point. If an edge is conserved without being incised after incising in the first two stage, then it is an original edge that has two vertices. The incision edge has zero or one vertex but the length is greater or equal than d2 (the tolerance for edge length). If length of an incision edge is less than d2, the edge reduces to a point. If the edge has one vertex, it reduces to an original point, else, reduces to an incision point. Let a, b, c, d be the number of original edges, incision edges, original points and incision points of an incision body respectively. So the type of final incision body can be represented with the combination of four numbers, namely, "abcd". There are 16 different of combinations. All combinations and corresponding geometry types are listed in Table 1. The types marked with an asterisk are distinguished in program by confirming the nice form of incision bodies.

In the fourth stage the contact type is determined by combining the two types of two incision bodies.

Table 1: Types of incision bodies

No.	"abcd"	Type
1	0000	empty or face*
2	0001	edge
3	0010	point
4	0002	edge or face*
5	0011	point or face*
6	0020	face
7	0102	edge
8	0111	point or edge*
9	1020	edge
10	010d(d>2)	edge or face*
11	011d(d>1)	point or edge*
12	0204	face
13	0212	point or edge or face*
14	021d(d>2)	point or edge or face*
15	0313	point
16	abcd(a+b>=2)	face

4. NUMERICAL EXAMPLES

The examples presented below have been used to demonstrate how the incision body algorithm can detect contacts between 3D polyhedrons correctly and reliably. The algorithm has been implemented in DDA method.

As the first example, consider the geometry of Fig.2 where a block system, consisting of 3 blocks in the shape of cuboid, rests on ground. Three blocks are numbered 1 to 3 along positive *z*-direction with the fixed bottom block (No.1) having dimensions of 10m×8m×3m and the top two blocks (No. 2 and No. 3) having dimensions of 6m×4m×2m. The top block is subjected to a horizontal force $\boldsymbol{F}$ which linearly increased from 1×10^5N at 0 *sec* to 3×10^5N at 1000 *sec*. $\boldsymbol{F}$ acts in the positive *y*-direction at the centre of a face parallel to the *x*-*z* plane. Four vertices of bottom

face of the bottom block are fixed on ground. The material properties for the three blocks are: Young's modulus E=3160Mpa, Poisson's ratio μ=0.2,ρ=2400kg/m^3. The interface properties are: friction angle ϕ=5, cohesion c=0, tensile strength=0. Figure 4 shows the results of example 1. Block 3 slides continually on top face of block 2 until it topples and comes into contact with block 1. Finally, block 3 departs from block 2 and block 1 successively at 53 *sec* and 55 *sec* respectively. Following departing, block 3 rotates and falls off block 1. This example shows the effectiveness of the algorithm when detecting line-face and face-face types as well as forming new contact and releasing of existent contact.

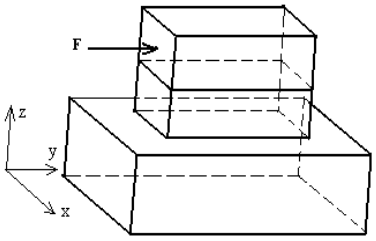

Fig.2. Example 1

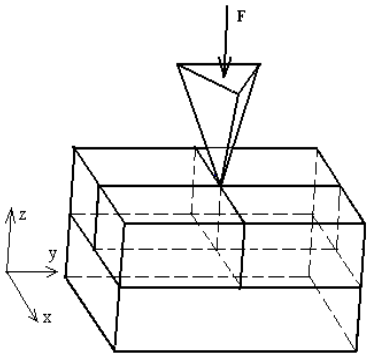

Fig.3. Example 2

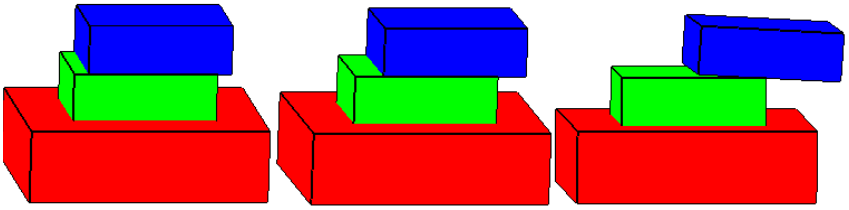

Fig.4a. Example 1 (20s) Fig.4b. Example 1 (30s) Fig.4c. Example 1 (50s)

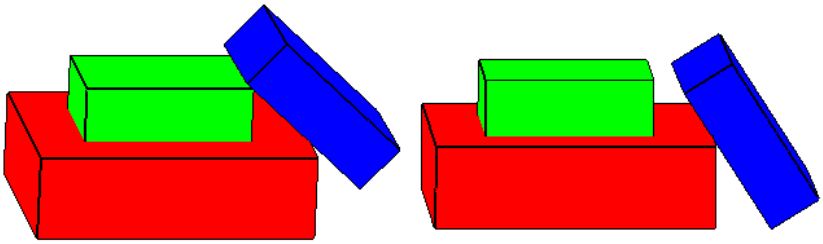

Fig.4d Example 1 (53s) Fig.4e Example 1 (54s)

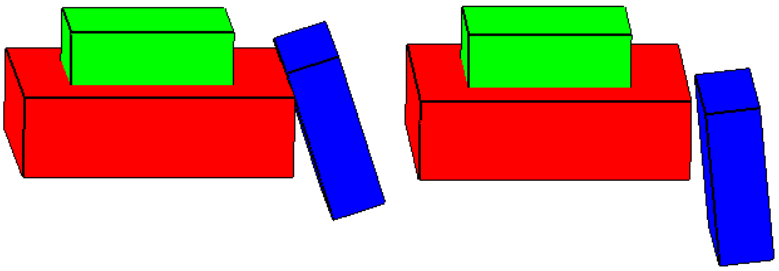

Fig.4f Example 1 (55s) Fig.4g Example 1 (56s)

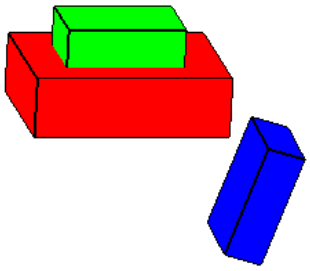

Fig.4h Example 1 (58s)

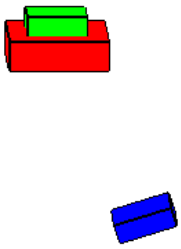

Fig.4i Example 1 (65s)

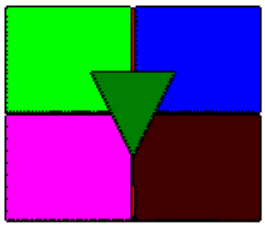

Fig.5a Example 2 (0.4s)

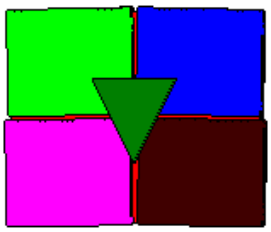

Fig.5b. Example 2 (0.6s)

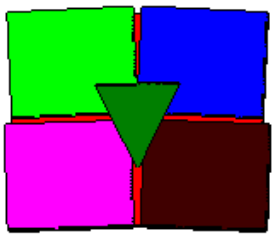

Fig.5c. Example 2 (0.8s)

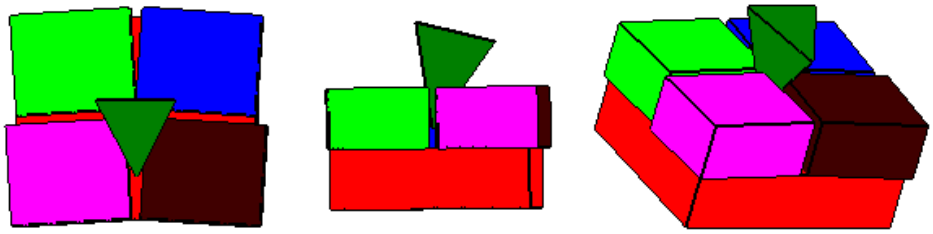

Fig.5d. Example 2 (1.2s)

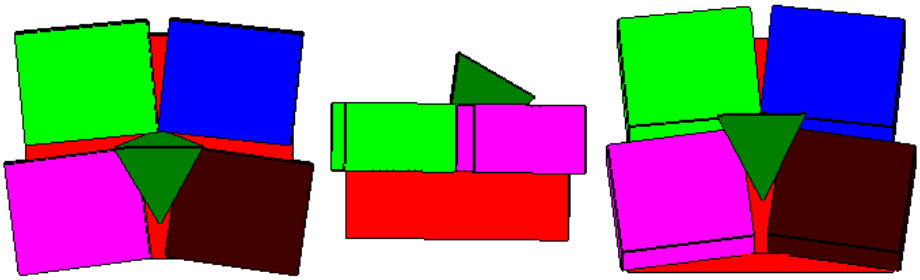

Fig.5e. Example 2 (1.9s)

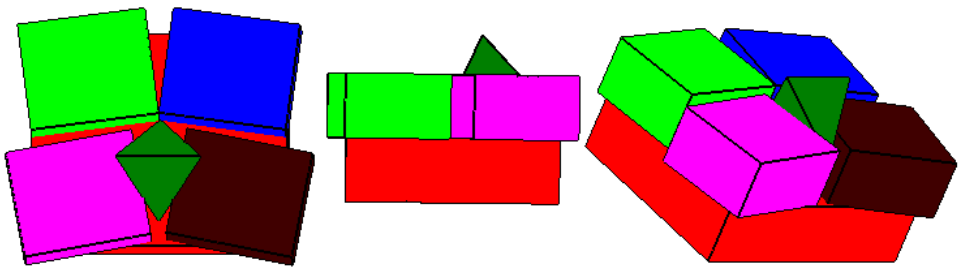

Fig.5f. Example 2 (2.5s)

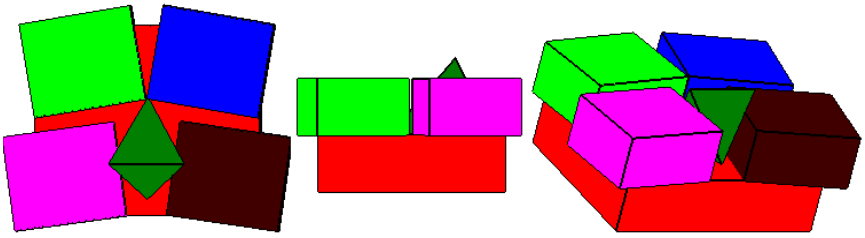

Fig.5g. Example 2 (3.0s)

The second example deals with a six-block system consists of five cuboids and one triangular pyramid, as shown in Fig.3. Six blocks are numbered 1 to 6. The bottom block is numbered 1 and having dimensions of 12m×10m×3m. The top block is numbered 6. It's top face is a isosceles triangle whose base edge has a length of 4m and two sides have a length of $(20)^{1/2}$m. Middle four blocks are numbered 2 to 5 and having dimensions of 6m×5m×3m. Four vertices of bottom face of the bottom block are fixed on ground while the top block is subjected to a vertical force $\boldsymbol{F}$ which keeps 1×10^7N all the time. $\boldsymbol{F}$ acts in the negative z-direction at the centroid of the top face parallel to x-y plane that is horizontal. The blocks and interfaces have the same properties as in the first example. Figure 5 shows the results of example 2. Block 6 splits the middle 4 blocks and squeezes itself into joints in the midst of 4 blocks in little time with concomitant slide and detachment between blocks. This example shows that the algorithm can detect the following types reliably: point-point, point-line, point-face, cross line-line, parallel line-line. Furthermore, it also demonstrates that the algorithm can distinguish different types effectively and detect various contact type transform correctly.

5. CONCLUSIONS

To apply DDA or DEM in resolving practical problems in rock engineering, it is essential to have a reliable 3D contact detection algorithm. But the existing detection algorithms cannot always handle the exact contact relationship between two 3D rock blocks that contact each other. Based on the analysis of ideas and problems of two methods already used in programming, the incision body algorithm is proposed in this paper. Two examples in this paper demonstrate the effectiveness and reliability of the algorithm in detecting contact between polyhedrons.

6. ACKNOWLEDGEMENT

The research presented here is supported by Key Program of National Natural Science Foundation of China (Grant No.50139010) and Natural Science Foundation of Liaoning Province of China(Grant No.20041077). This support is gratefully acknowledged.

REFERENCES

1. Shi, Genhua. 1992. Discontinuous deformation analysis: A new numerical model for the statics and dynamics of deformable block structures. *Engineering Computations*. 9: 157–168.

2. Shi, Genhua. 1997. *Numerical Manifold Method and Discontinuous Deformation Analysis.* 1st ed (in Chinese, Translated by Pei Juemin). Beijing: Tsinghua University Press.

3. Cundall, P.A. 1971. Computer model for simulating progressive large-scale movements in blocky systems. In *Proceedings of the Symposium of the International Society of Rock Mechanics,* Nacy France, Vol. 1, Paper No. II-8.

4. Cundall, P.A. 1988. Formulation of a 3-D distinct element model---Part I, a scheme to detect and represent contacts in system composed of many polyhedral blocks. *Int. J. Rock Mech. Min. Sci. & Geomech. Abstr.* 25: 107–116.

5. Luo, Haining. and Jiao, Yuyong. 1999. Improvement of contact judgement algorithm in 3D DEM. *Chinese J. Rock and Soil Mechanics.* 20: 37–40(in Chinese).

6. Jiang, Q.H., and Yeung M.R. 2004. A model of point-to-face contact for three-dimensional discontinuous deformation analysis. *Rock Mechanics and Rock Engineering.* 37: 95–116.

7. Erfan, G.N., Youssef M.A. Hashash, and Dawei Zhao et al. 2004. A fast contact detection algorithm for 3-D discrete element method. *Computers and Geotechnics.* 31: 575-587.

8. Liu, Jun., and. Kong X.J., and Lin G. 2004. Formulations of the three-dimensional discontinuous deformation analysis method. *Acta Mechanica Sinica.* 20: 270–282.

9. Chen, W.S., Zheng Hong, and Cheng Yungming et al. 2004. Detection of 3D rock block contacts by penetration edges. *Chinese J. Rock Mechanics and Engineering.* 23:565-571(in Chinese).

10. Liu, Jun., and Li Zhongkui. 2004. Current situation and development of DDA method. *Chinese J. Rock Mechanics and Engineering.* 23: 839-845(in Chinese).

11. Chen, W.S., Wang Guiyao, and Liu Hui et al. 2005. Insight into some aspects of discrete element numerical methods for rock mass. *Chinese J. Rock Mechanics and Engineering.* 24:1639-1644(in Chinese).

12. Jing, L., and Hudson, J.A. 2002. Numerical methods in rock mechanics. *Int. J. Rock Mech. Min. Sci.*39:409-427.

DDA Benchmark Testing at UCT – A Summary

Scheele, F. and Bates, B.
Department of Civil Engineering, University of Cape Town, South Africa

ABSTRACT: Discontinuous Deformation Analysis (DDA) was initially developed for use in rock slope engineering and has proved to be very useful in many other fields of engineering. However, its readiness and applicability to real, usually complex, engineering problems is not always apparent. For a number of years the major thrust of DDA research was the development of suitable benchmark tests, to establish points of reference for basic, standard, small-scale problems and thus hopefully, the development of guidelines for the selection of the input control parameters of the computer code.
This paper presents a brief summary of the benchmark tests undertaken in laboratory conditions at UCT since 1998. The paramount sensitivity of the control parameters and the relative insensitivity of the physical characteristics in various situations is presented and discussed. The findings will be demonstrated in a selection of more recent laboratory tests and their equivalent DDA model simulations.

1. INTRODUCTION

In this paper a selected number of DDA benchmark tests are described that have been conducted in Geotechnical Engineering at the University of Cape Town relatively recently. The benchmark tests refer to laboratory model tests that can be used to study the effects of a single chosen value or a combination of chosen values of the control parameters g0, g1, g2 and k01 for the purposes of verification. DDA Version 96, the original implementation of the DDA method developed by Shi [1, 2], was used to simulate the benchmark tests.

2. BENCHMARK TESTING PROCEDURES

2.1. Criteria for selecting Benchmark Tests

Benchmark tests were generally designed with the following criteria in mind:

Simplicity - Discrepancies between the physical test and the computer analysis should be easily identifiable.

Construction accuracy - The model should be designed in such a way that the precision required for reliable results is not greater than the precision allowed by the construction techniques.

Measurement accuracy - The limitations of the data capturing or recording equipment should be taken into account.

Repeatability - The test should be able to be repeated many times to confirm that the results are consistent. Models that are likely to be damaged during testing should be avoided.

	The repeatability of a benchmark test is not only related to the material from which the physical model is made, but also to the variations in the mechanism involved. Tests where small deviations (such as the positioning of blocks) would result in large differences between results should be avoided.
Correspondence to subject -	A physical model should be designed to incorporate aspects which the computer program is validated to simulate. If the complexity of the physical model lies beyond the scope of the computer program, it will be difficult to identify the source of errors.

2.2. Material Properties

The material properties of the 'building' blocks are the Young's modulus, Poisson's ratio, density and the interface friction angle. Both the elastic modulus and Poisson's ratio were generally obtained from the manufacturer's specifications. The density of a material is calculated as the ratio of the mass of a block and its dimensions.

The angle of friction of the interfaces was determined experimentally using a universal tension/compression testing machine (ZWICK) fitted with a direct shear attachment. The experimental set-up is shown schematically in Figure 1.

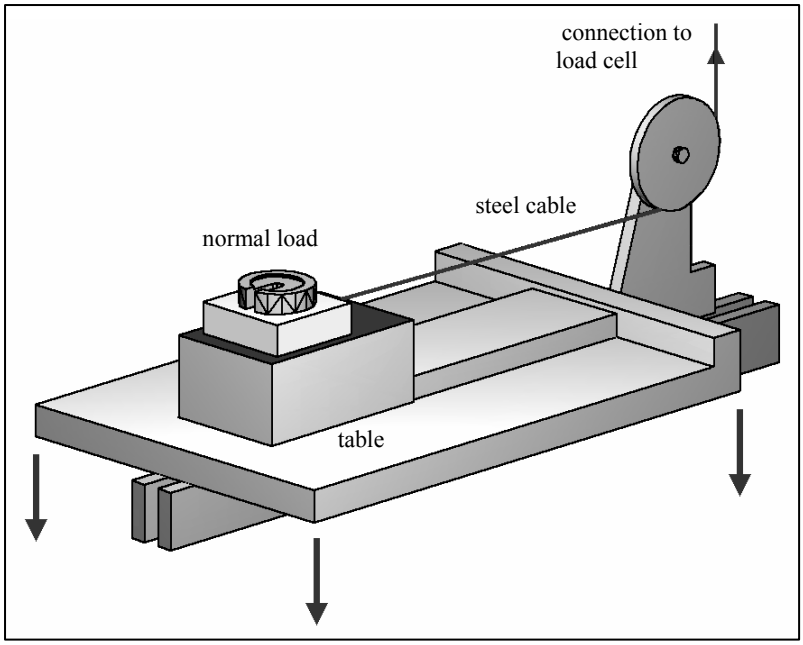

Fig. 1. Test accessory for interface shear investigations

The rate at which shear took place was generally set to 150mm/min in accordance with ASTM D 1894-90 Standard Test Method for Static and Kinetic Coefficients of Friction of Plastic Film and Sheeting [3]. Lower shear rates showed indistinguishable effects on the results. For each friction surface, three normal loads were applied. Three shear tests were then carried out for each of these normal loads.

2.3. Recording of Data

The aim of the benchmark tests was to measure the displacements of the blocks over time once the test was initiated. The overall behaviour of the model was recorded by a high speed digital camera and subsequently, the displacements measured using the respective bitmap images. In addition, stop watches were used to time each experiment, also to identify erroneous runs and to provide general information as to the accuracy of the measuring systems.
Regarding the interface tests rates, loads and displacements were recorded by the ZWICK internal data acquisition system (class 0.5).

3. OVERVIEW OF BENCHMARK TESTS

3.1. Inclined Block Model

The benchmark test (shown in Fig. 2) consists of two components: a set of blocks sitting stationary on a stepped slope and a single, dynamic block sliding down an adjoining steep ramp, striking the stationary blocks in such a way that the blocks fail with suitably large displacements. The modes of failure are a combination of sliding and toppling.

The materials and geometry of the model were selected so that initially the blocks were close to the state of limit equilibrium and thus requiring the same strike resulting in roughly the same velocities with which the blocks were knocked over. This, in turn, guaranteed almost identical and most consistent results each time the test was run.

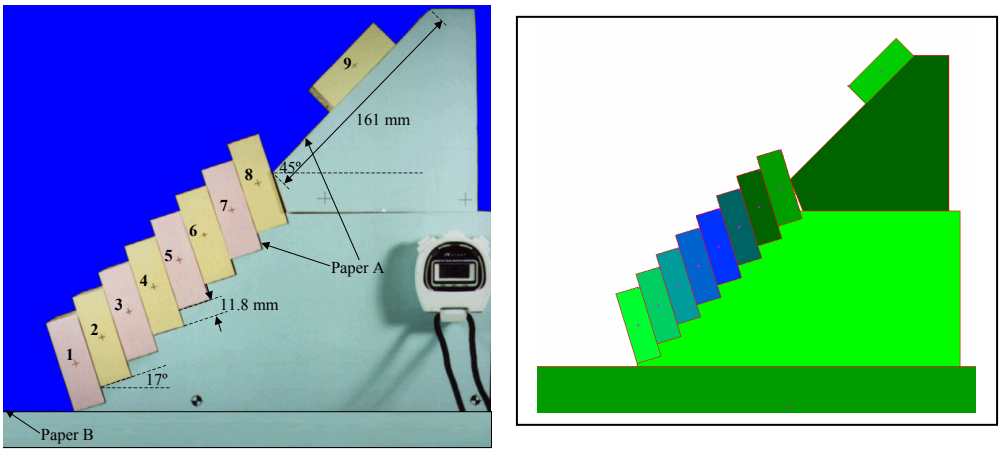

Fig. 2. Physical and DDA model [4,5]

A certain amount of trial and error investigation was required to identify the optimal values for the control parameters k01 and g0. The values k01=0.80, g2=0.001, g1=0.001s and g0=1.5×10^6N/m. (as listed in the overview in Table 1) were found to produce final block configurations which correlated very well with the physical observations.

3.2. Steps Model

A number of PVC blocks were piled up in a staircase type fashion to form six steps. On each step two steel cylinders were placed with one single cylinder at the edge of the highest step (as shown in Figure 3). This cylinder was allowed to roll down, pushing apart the two cylinders located on the lower step. Thus, the momentum was transferred to the cylinder sitting next to the edge, which in turn rolled over to the next lower step. The chain reaction continued until the cylinder hit the ground surface.

In this benchmark test the modes of rolling, colliding and sliding were being investigated.

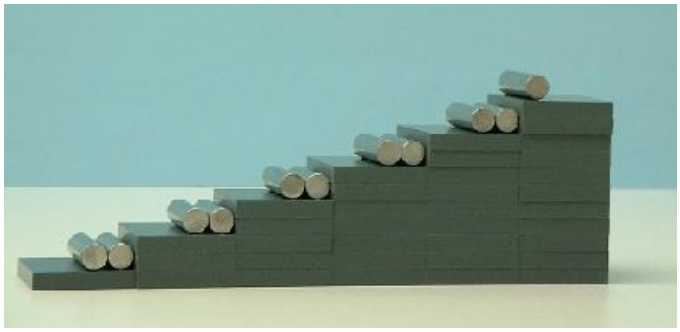

Fig.3. Steps models [6]

The tests showed a high degree of repeatability; the average runtime of the experiments was 1.91s. In numerous simulations the control parameters of k01=1.00, g2=0.001, g1=0.001s and g0=1×10^5N/m were determined matching not only the run time of the physical model but also the displacement behaviour of the cylinders.

3.3. Half Pipe Model

This benchmark test consists of a wooden block with a high precision circular arc cut out. A steel cylinder was placed on the edge of the ramp (as shown in Figure 4). Once the cylinder was released it rolled down along the surface in dampened simple harmonic motion. The cylinder lost energy while rolling from side to side of ever decreasing height until it came to a complete stop in the middle of the half pipe. Adequacy in modeling the modes of sliding and rotational acceleration was being tested.

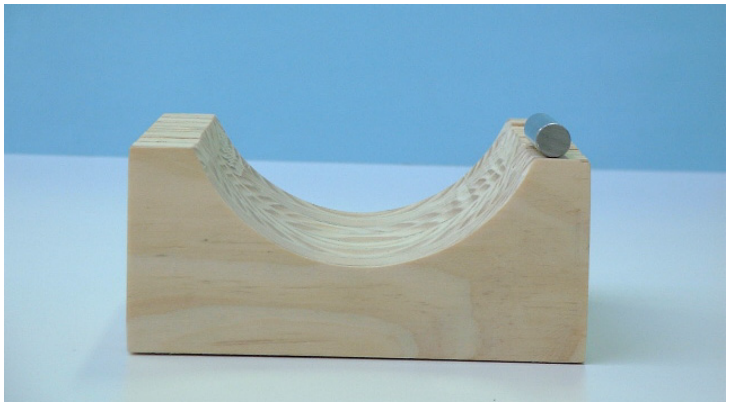

Fig. 4. Concave half pipe [6]

Again as before, the circular ramp as well as the cross-section of the cylinder was approximated by a cyclic polygon containing 200 sides. Attempts were undertaken to represent the circular shapes by a 1000 sided cyclic polygon to reduce inaccuracies.
However, the simulations were in both cases almost identical and in perfect agreement with the observations thus not allowing an adequate assessment of the effects of the number of sides on the results. The following control parameters of k01=1.00, g2=0.001, g1=0.001s and g0=1.3×10^4N/m were eventually employed.

3.4. Domino Run

This benchmark test consists of numerous rectangular PVC blocks lined up at 30mm spacing on a horizontal surface (Figure 5). The first block was allowed to topple into the second block, which in turn toppled, starting a process which continued through the entire line of blocks.

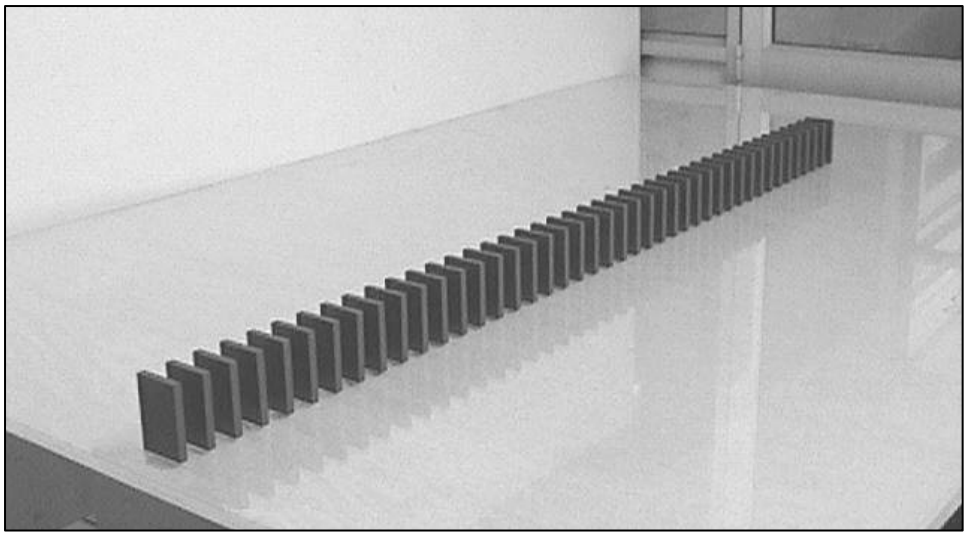

Fig.5. Domino run

The time taken for the physical model to run was calculated by multiplying the number of frames in the video recording by the frame length. An average test time of 1.267 seconds was calculated which is in close correlation with the analytical result.
The behaviour predicted by DDA seemed most realistic with k01=1.00, g2=0.0005, g1=0.001s and g0=500 000 N/m. The time taken here was not closest to the average experimental time (which was obtained with g2=0.002), but cannot be seen as any less accurate in the context of the video recording frame rate.

A comparison between the physical model and the DDA model is shown in Figure 6.

Time (s)	Physical Model	DDA Model
0.00	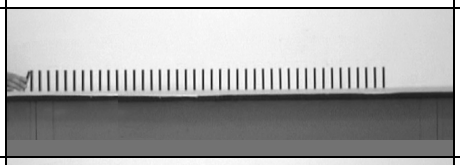	
0.28	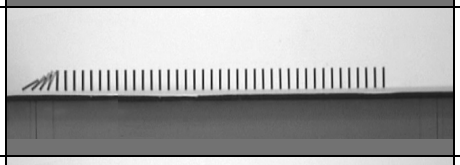	
0.44	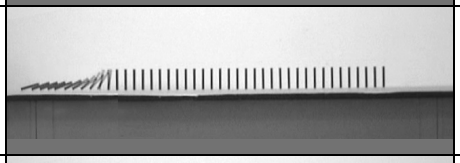	
0.56	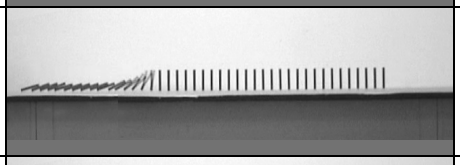	
0.64	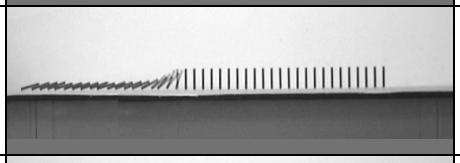	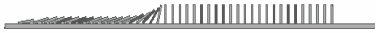
0.76	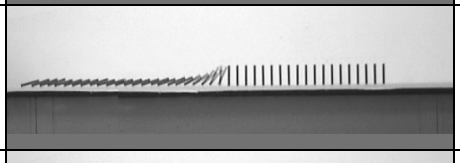	
0.88	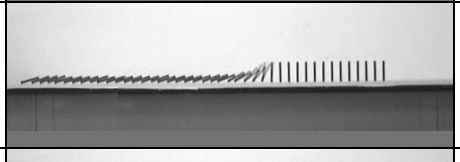	
0.96	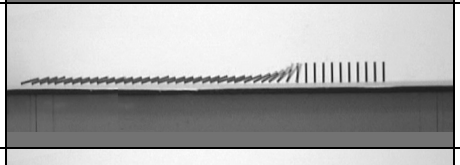	
1.08	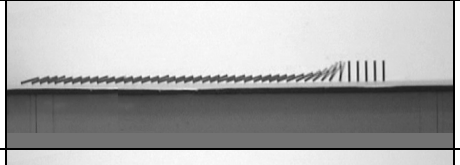	
1.20	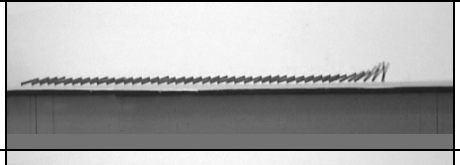	
1.28	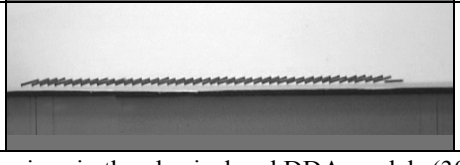	

Fig.6. Toppling behaviour in the physical and DDA models (30mm spacing) [7]

3.5. Rockfall Canopy

Road cuttings in steep rock formations are frequently accompanied by cantilevered canopies. These structures are intended to deflect the impact of rockfalls and to keep the road clear of any debris. This benchmark test was conceived as a simplified representation of a cantilevered rockfall canopy, where the investigation was intended to determine the maximum rock fall height for which the canopy and "rock mass" would remain intact.

In the model the "rock formation" consisted of eighteen identical rectangular blocks in analogy to a jointed rock layer. The canopy was represented by one of four smaller rectangular blocks. A circular cylinder represented a falling boulder. The larger rectangular blocks were made from high-density polyethylene and the smaller blocks from PVC plastic. A release mechanism was constructed to ensure that the falling circular cylinder was consistently dropped from the same position.

In the physical test the block directly above the cantilevered canopy was pushed apart from the adjacent block mass. Successive blocks above this behaved in a similar manner, leaving a consistent failure pattern in the block mass. Different drop heights were tested and the rock fall canopy failed consistently for a drop height of 250mm.

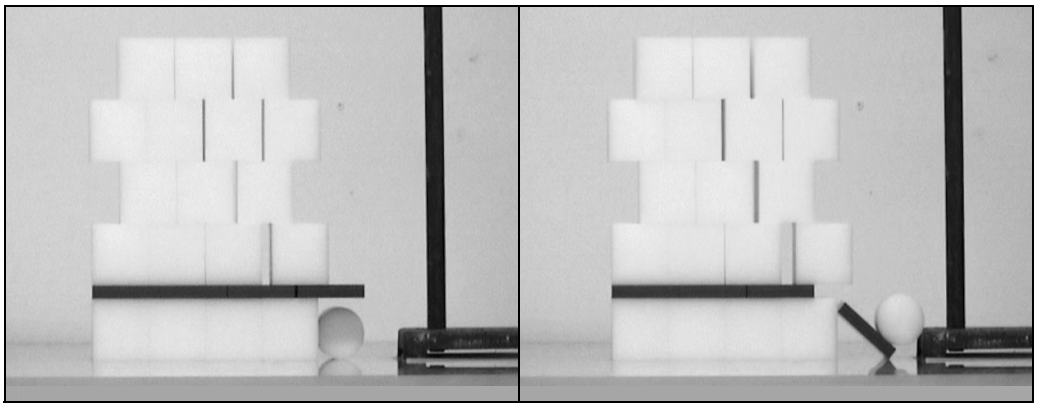

Fig.7. Typical block positions after impact

None of the control parameters tested resulted in a good correlation between the physical and DDA models. The block mass collapsed in all analyses (see also Fig. 8). In the physical test the canopy was dislodged without causing a collapse of the block mass.

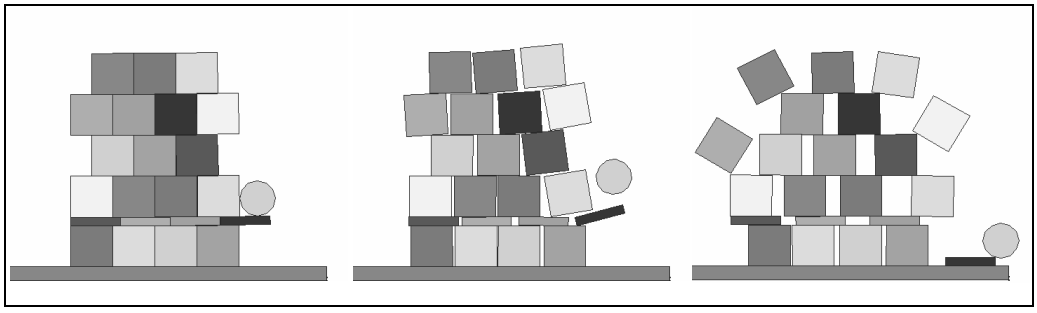

Fig.8. Collapse of block mass for a drop height of 210mm

Since DDA is based on the assumption of uniform strain distributions in each block bending in the canopy and non-uniform strains in the circular block due to impact cannot be modeled resulting in unrealistic energy transfer during the collision.

3.6. Stepped Pyramid Model

This benchmark test was intended to address the rate controlled displacement of a particular block while accurately monitoring the force required. The physical model is set up on a Perspex base consisting of 12 identical polyethylene blocks. The blocks were arranged into five tiers as a symmetrical pyramid. Three spaces in the block arrangement introduced a level of instability (see Figure 9).

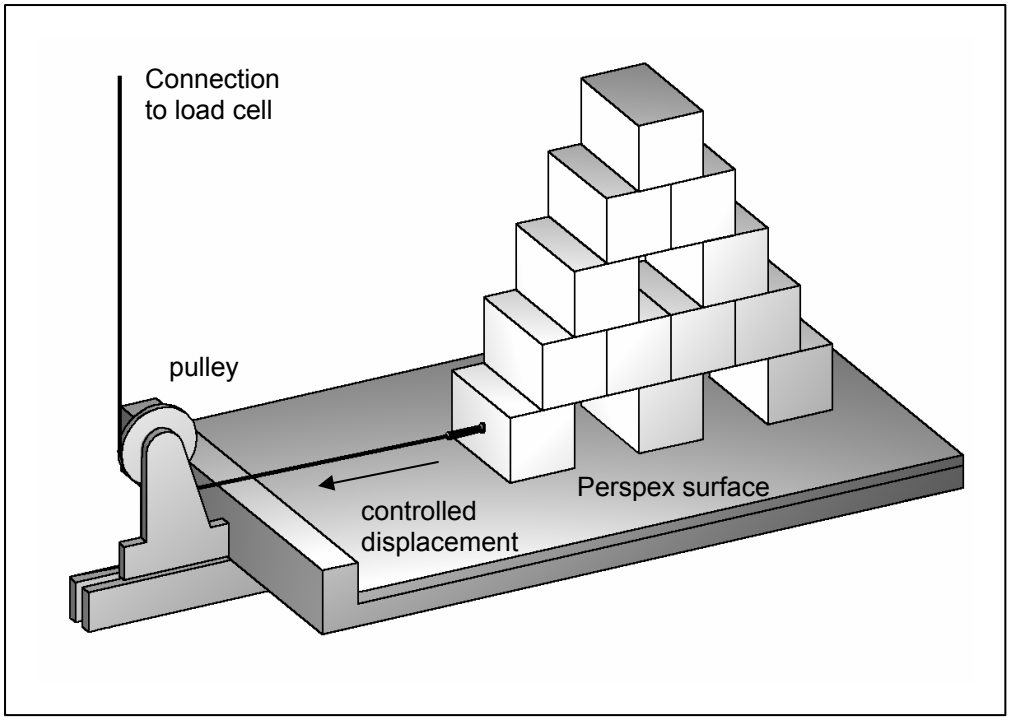

Fig.9. Stepped pyramid

A (key) block on the lowest tier was pulled away from the pyramid (using a steel wire attached to a load cell) causing the structure to collapse. The tensile force was recorded. The test was repeated three times. All three tests showed in principle identical collapse behaviour (see Figure 11). The force-displacement responses are shown in Figure 10. After a displacement of about 12.3mm the key block provided no (zero) support of the pyramid and the structure collapsed.

To achieve matching results the DDA simulation had to be undertaken in two stages: a static analysis with a prescribed displacement of the key block of 12.3mm and a second stage with no set displacements allowing the collapse of the pyramid under self-weight to take place.

The static analysis was run with the control parameters k01=0.00, g2=0.0005, g1=0.5s and g0=2×10^7N/m. In stage two the geometry was input with the key block at a displacement of 12.3mm. The block directly above the key block was also repositioned to reflect the geometry at the end of stage 1. On a qualitative level the results from the static analysis seemed to be more realistic than those from the dynamic analysis.

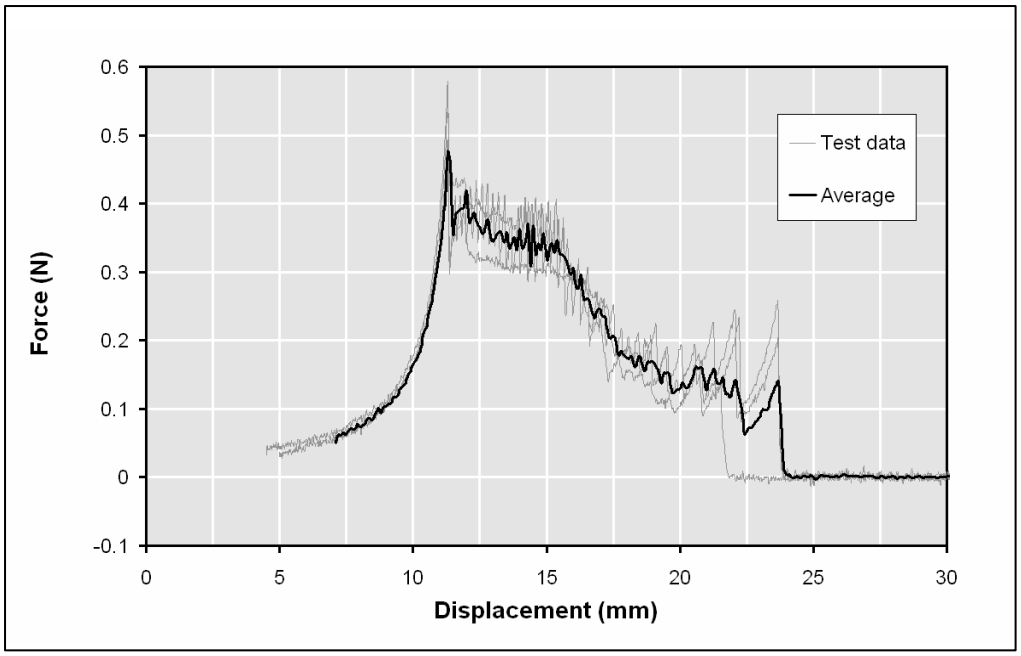

Fig.10. Force-displacement responses with averaged result

The geometry of the physical model and DDA simulations at various displacements of the key block are shown in Figure 11.

4. SUMMARY AND CONCLUSIONS

It appears that DDA, in its basic form (Version 96), is capable of simulating all discussed benchmark tests as long as there are no or low energy collisions involved. Problems involving friction, basic motion and systems with single or multiple blocks of any shape can be simulated comfortably providing good and accurate results. This is in support of the findings of earlier work [8].

Both dynamic and static problems can be solved. The inherent kinetic damping causes the scheme to dissipate energy whilst still accurately simulating the primary response of the test system. However, the real strength of DDA is its ability to solve static problems. In all cases, the accuracy of the solutions of the analyses is highly sensitive to the choice of appropriate values of the control parameters.

Benchmark tests (provided these experimental set-ups and performances are of highest precision and accuracy) are very useful tools if clarity is needed about particularly complex physical processes to be analyzed. This will set the framework for the choice of suitable control parameters. Although it is unlikely that a guideline for the selection of definite values for kinetic damping, k01, and the stiffness of the penalty springs, g0, will ever be developed.

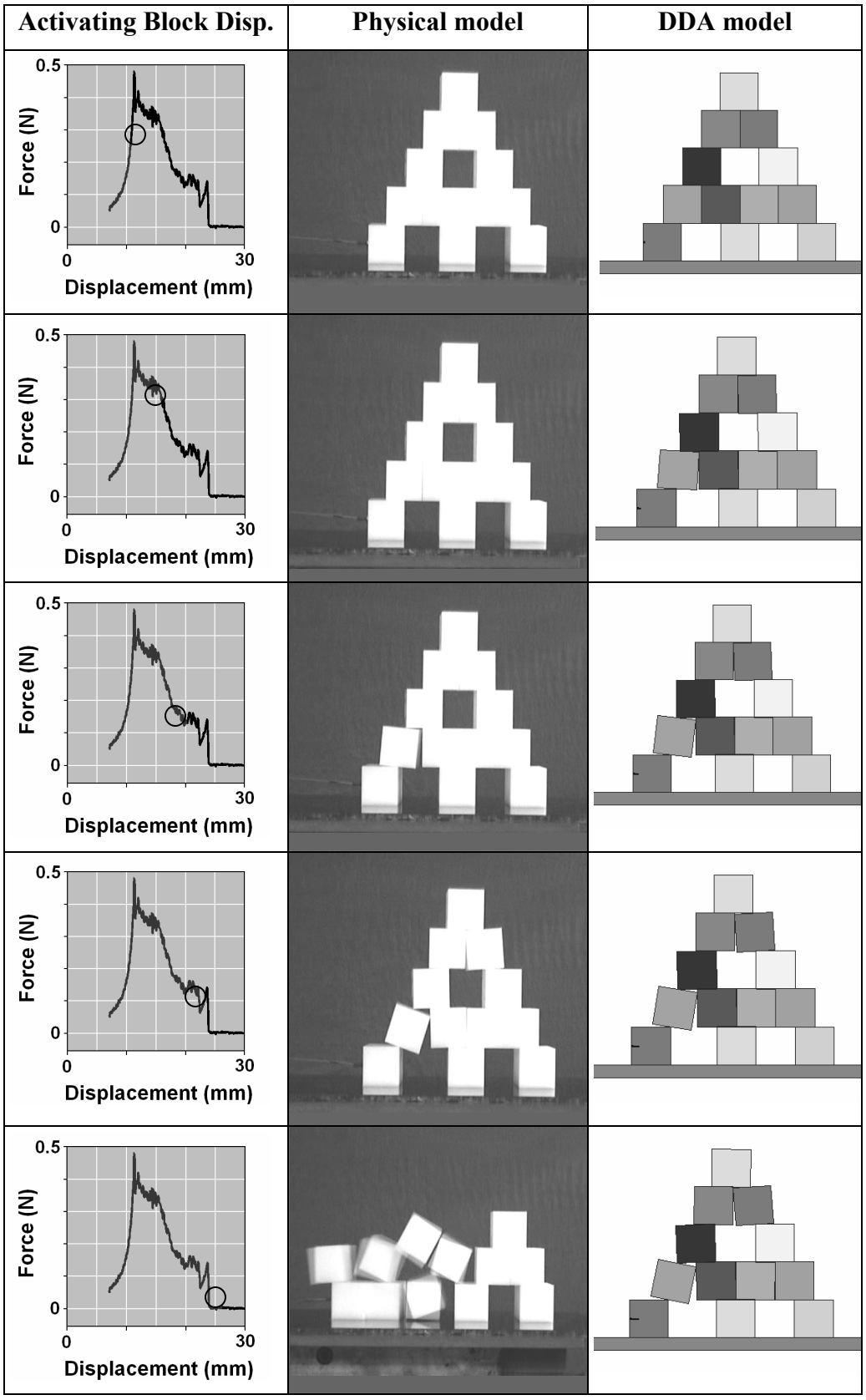

Fig.11. Physical model and DDA simulations at various displacements of the key block [7]

REFERENCES

1. Shi, G.-H. 1996. *DDA Version 96*, 5650 Pointsett Ave., El Cerrito, CA.
2. Yeung, M.R. 1996. *Discontinuous Deformation Analysis Programs: Version 96, User's Manual.* Department of Civil and Environmental Engineering, University of California, Berkeley.
3. ASTM, 1990. *D1894-90: Static and Kinetic Coefficient of Friction of Plastic Film and Sheeting*. Annual Book of ASTM Standards, Philadelphia.
4. Matthews, A. 2000. *The Use of Laboratory Benchmark Tests to Investigate Discontinuous Deformation Analysis*. B.Sc. Thesis, Department of Civil Engineering, University of Cape Town.
5. McBride, A.T. 1998. *Experimental and Numerical Investigation of Discontinuous Deformation Analysis*. B.Sc. Thesis, Department of Civil Engineering, University of Cape Town.
6. Rantloane, L. 2002. *DDA Benchmark Testing*. B.Sc. Thesis, Department of Civil Engineering, University of Cape Town.
7. Bates, B. 2004. *Development and DDA Modelling Of Benchmark Tests.* B.Sc. Thesis, Department of Civil Engineering, University of Cape Town.
8. McBride, A.T. and F. Scheele, 2001. Investigation of Discontinuous Deformation Analysis using Physical Laboratory Models. Proc. 4th International Conference on Analysis of Discontinuous Deformation (ICADD-4), Glasgow, Scotland, UK, pp.73-82.

(This page intentionally left blank.)

Validation of DDA Block Motions and Failure Modes using Laboratory Models

MacLaughlin, M.M.
Geological Engineering Department, Montana Tech of The University of Montana, Butte, Montana, USA
Hayes, M.A.
Halliburton, Denver, Colorado, USA

This paper was prepared for presentation at *ICADD-7, the Seventh International Conference on Analysis of Discontinuous Deformation*, held in Honolulu, Hawaii, December 10-12, 2005.

ABSTRACT: This paper presents a description of and results produced during a small validation project involving comparison of the mechanical behavior of physical models constructed in the laboratory, and equivalent DDA models. Wooden blocks were used in the laboratory experiments, with three different materials along the block interfaces (wood, Teflon, and sandpaper). Two types of models were constructed: 1) sets of three blocks on a single incline, and 2) multiple vertical blocks on a double incline. The single-incline experiments produced a range of results, but in most cases the displacements of the experimental blocks were greater than those of the DDA blocks; two plausible explanations for this are 1) that the friction angle realized in the experiments was lower than originally measured, or 2) that once motion initiated, the friction dropped from a higher static value to a lower dynamic value. The double-incline experiment was designed to demonstrate that the same geometric configuration can display either sliding or toppling failure mode depending on the friction angles of the different surfaces. The DDA results were found to be very sensitive to friction angle and geometry.

1. INTRODUCTION

Discontinuous Deformation Analysis (DDA) is a numerical analysis method used to model the motions of rock masses under a wide range of conditions [1]. DDA allows the user to construct models of blocky materials that recognize different loading conditions and interactions between blocks, accounting for friction along block surfaces. One of the results of the analysis is the expected failure mode, if any, resulting from the modeled conditions.

The primary objective of this research project was to validate DDA, showing that it produces accurate results for known situations. Simple block models were constructed in the laboratory to provide data for comparison with identical models constructed using DDA. The models were designed to demonstrate sliding and toppling failure modes, and the associated block motions were recorded. The models were then replicated in DDA and the motions and failure modes were compared. The overall goal was to elevate confidence in the DDA method, thereby promoting its use in practice as well as research. Itasca's UDEC was used in one portion of the study, providing a comparison of two different numerical methods to the experimental data.

While a significant amount of similar work has been done previously, particularly at Kyoto University [2,3], the University of Capetown [4], Ben Gurion University [5], and Hokkaido University [6], additional validation using physical models is beneficial to the DDA community. This small study is designed to complement and extend the work already undertaken.

2. LABORATORY MODELS

Wooden blocks constructed out of particle board were used to construct the laboratory models. Wood was used because it is much easier to manipulate than rock. Particle board was selected because it displays less anisotropy than standard lumber.

2.1. Material Properties

The properties of the wooden blocks were measured in the laboratory. The density of the wood is 0.7 g/cm^3, which corresponds to a unit weight of 6.9 kN/m^3 (43.8 pcf). Montana Tech's triaxial testing apparatus was used to determine the Young's modulus (28,000 psi) and Poisson's ratio (0.0357). Although these values are much lower than typical values for rock, the models constructed involve extremely small loads on the block and the associated deformations are negligible, so the results are expected to be insensitive to the elastic properties of the material.

The friction angle of the block surfaces was measured using the simple tilt test, as shown in Figure 1(a). In order to incorporate a range of friction values in the models, the block surfaces were covered with sandpaper to increase the friction angle, and with Teflon to decrease the friction angle, as shown in Figure 1(b). The friction angle values observed in the tilt tests are displayed in Table 1. Note that the tilt test measures the friction required for the initiation of motion, which corresponds to the static friction coefficient.

(a) (b)

Figure 1. Tilt tests were performed to measure the friction angle of the block surfaces: (a) tilt test in progress, (b) examples of the three surfaces used: wood (left), Teflon (middle), and sandpaper (right).

Table 1. Average friction angles of the block surfaces measured using the tilt test.

material on surface of lower block	**material on surface of upper block**		
	wood	sandpaper	Teflon
wood	30°	40°	20°
sandpaper	40°	46°	27°
Teflon	22°	36°	18°

2.2. Models

A suite of "single-incline" models was constructed using sets of blocks with the following dimensions: 45° right triangle with 2" sides (2.5" thick), rectangle 2" wide by 2.5" high (2"thick); and rectangle 1" wide by 6" high (2.5" thick). Three sets of the blocks were made, with a different material on the base of each block (wood, sandpaper, and Teflon), as shown in

Figure 2. The blocks were arranged in the configuration shown in Figure 2(a), with the triangle in the front and the tall rectangle in the back, on top of an inclined base block. Nine experiments were recorded for each base block inclination, corresponding to the nine combinations of 3 materials on the base block and 3 materials on the bottom of the set of upper blocks.

Additionally, a "double-incline" model was constructed with multiple thin vertical blocks placed on a base consisting of two inclined planes, a steeper upper incline and a shallower lower incline. The model was designed to demonstrate that the same geometric configuration can display either sliding or toppling failure mode depending on the friction angles of the different surfaces, as discussed in [7]. Toppling requires very tall, thin blocks and a very low friction value between the toppling blocks, both of which were difficult to achieve in the physical models. Only one configuration was constructed, with an upper incline of 75° and a lower incline of 30° The double-incline model is shown in Figure 2(b).

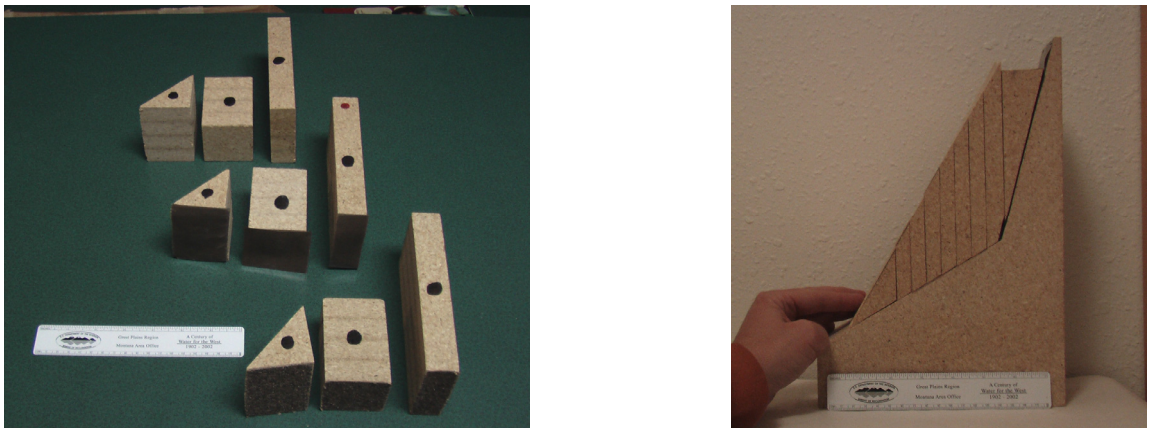

(a) (b)

Figure 2. (a) The sets of blocks used in the single-incline experiments. (b) The double-incline model.

2.3. Data Collection

The block motions observed during the tests were recorded using a 1000 frame-per-second video camera. A mark was made on each block, and the associated horizontal and vertical movements of the mark were measured with the aid of a transparent grid, as shown in Figure 2(b).

Figure 2. The experimental setup, showing the video camera, measurement grid, and blocks.

3. NUMERICAL MODELS

Numerical models were created in DDA that matched the experimental models as closely as possible. The DDA software that was used for the study is the most recent version of UC-Berkeley's *DDA for Windows,* with DDAML input files. Figure 4 shows examples of the DDA models.

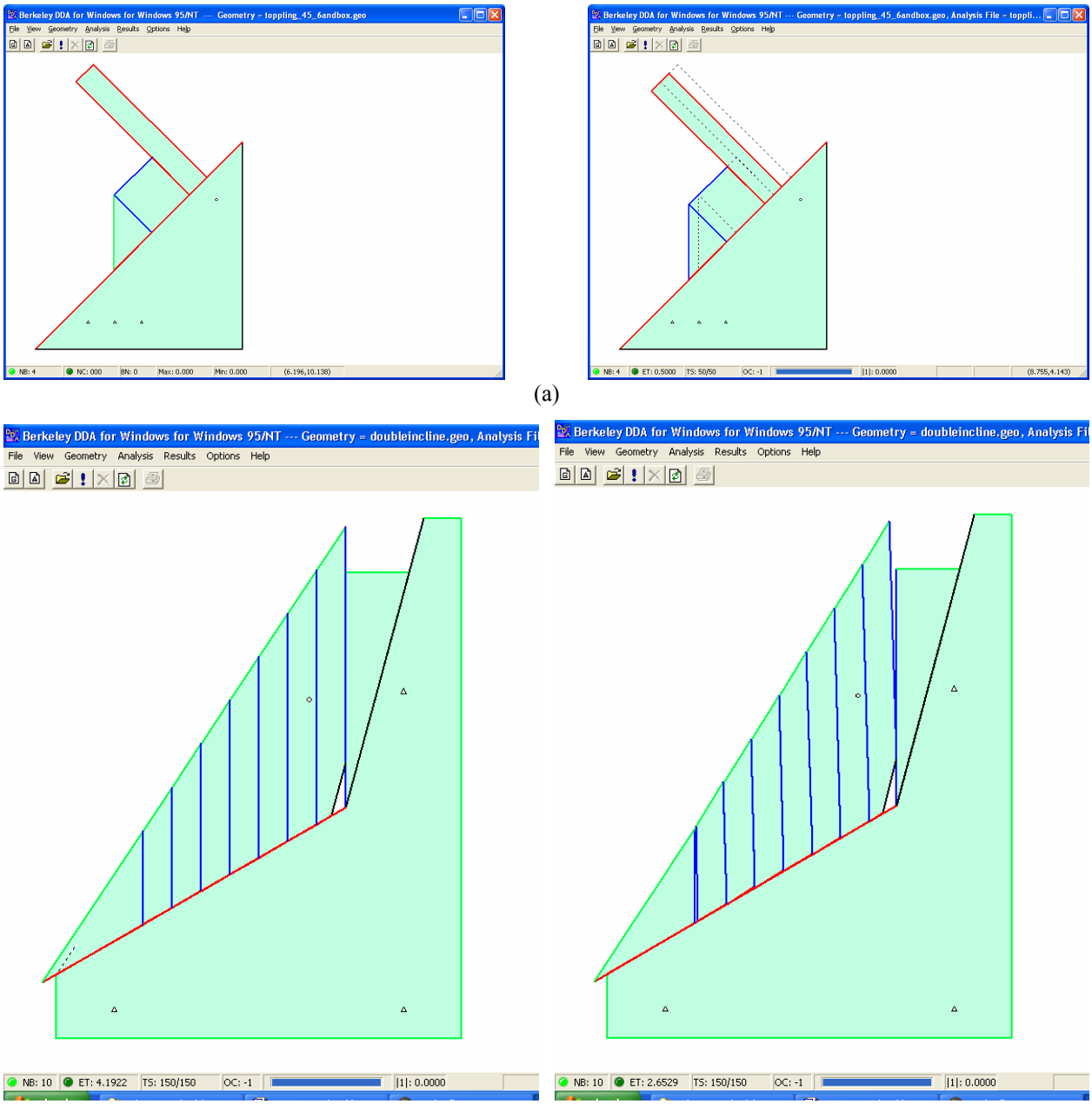

Figure 4. DDA models of (a) one of the single-incline experiments, showing initial (left) and final (right) models; (b) the double-incline experiment, showing one configuration that slides (left) or topples (right) depending on the friction angles on the block surfaces.

4. RESULTS AND DISCUSSION

4.1. Single-Incline Experiments

The results of several of the single-incline experiments are graphed in Figures 5, 6, and 7. The graphs show displacement as a function of time for the experimental and DDA results, and illustrate the range of results observed. The three graphs in each figure represent the displacements of the three blocks in each set (triangle, small rectangle, tall rectangle). All of the figures correspond to the experimental setup with wood material on the surface of the base block, inclined at 30°. Figure 5, 6, and 7 display the results for the set of blocks with wood material, Teflon, and sandpaper along the base, respectively.

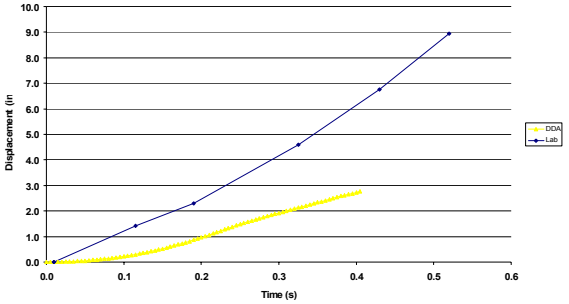

(a)

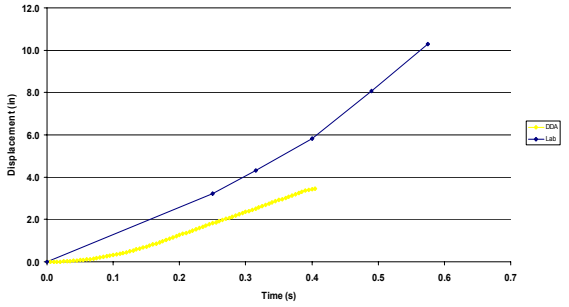

(b)

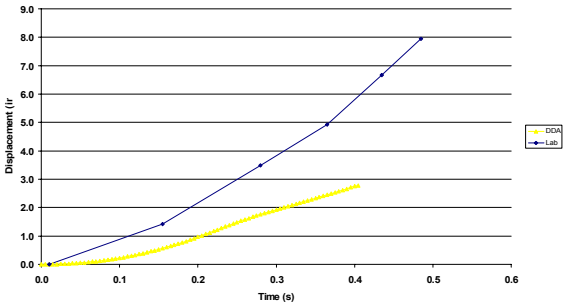

(c)

Figure 5. Graphs of displacement [in] vs. time [s] for the experimental (dark blue) and DDA (light yellow) blocks. The base block is inclined at 30°, with wood material on the surface. The upper blocks also have wood material on the surface of contact. Displacements shown are for (a) triangular block, (b) small rectangle, and (c) tall rectangle.

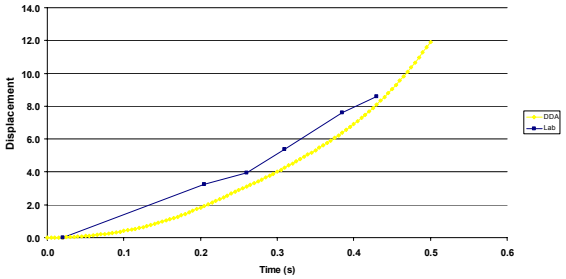

(a)

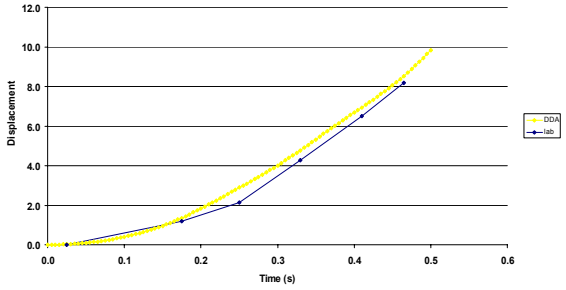

(b)

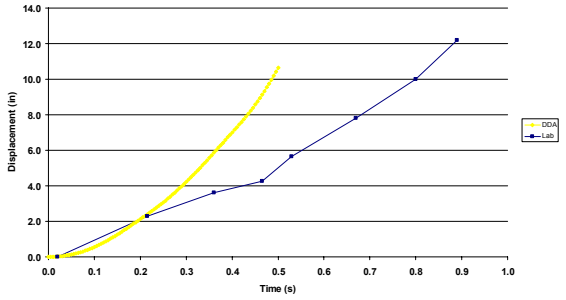

(c)

Figure 6. Graphs of displacement [in] vs. time [s] for the experimental (dark blue) and DDA (light yellow) blocks. The base block is inclined at 30°, with wood material on the surface. The upper blocks have Teflon material on the surface of contact. Displacements shown are for (a) triangular block, (b) small rectangle, and (c) tall rectangle.

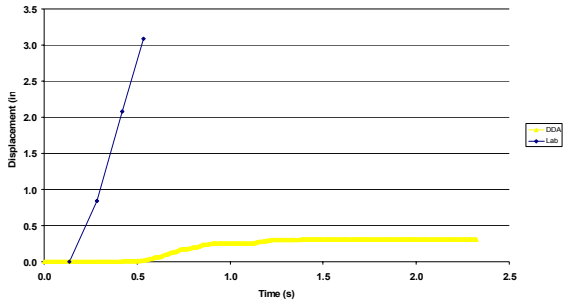

(a)

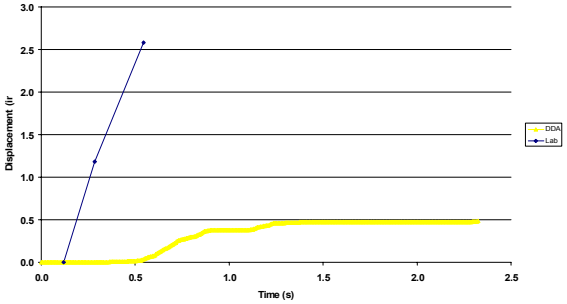

(b)

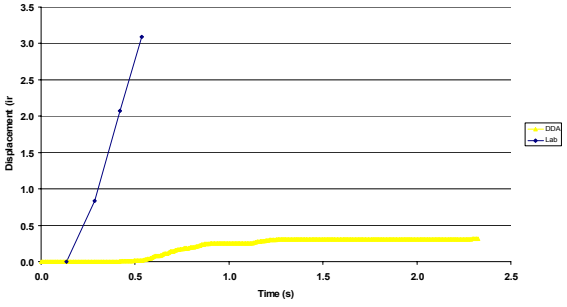

(c)

Figure 7. Graphs of displacement [in] vs. time [s] for the experimental (dark blue) and DDA (light yellow) blocks. The base block is inclined at 30°, with wood material on the surface. The upper blocks have sandpaper material on the surface of contact. Displacements shown are for (a) triangular block, (b) small rectangle, and (c) tall rectangle.

Figure 5, with data for the wood on wood models, is a case in which the friction angle and inclination angle are equal (30°). There is a small driving force due to the tendency of the tall rectangle to topple at an inclination greater than $\tan^{-1}$(base/height). The data show that the displacements of the experimental blocks are greater than the displacements of the DDA blocks. One explanation for this is that the actual friction angle of the wood/wood surface is lower than that measured in the tilt test, which is not unreasonable due to the variability in the block surfaces. The other plausible explanation is that while the static friction angle measured in the tilt test was correct, once the blocks start moving, the friction drops to a lower dynamic value. Note that the experimental data could be used to back-calculate the best-fit friction angle realized in the physical model.

The results displayed in Figure 6 correspond to the Teflon on wood models, with a surface friction angle (20°) significantly lower than the angle of inclination (30°). These results show the best match between the experimental and DDA models, for the triangle and small rectangle blocks. The tall rectangle, however, displaced a great deal more in the DDA model than in the laboratory experiment, probably because of a higher friction value on the real block due to variation in the Teflon or wood material along the surface of contact.

Figure 7 shows the results for sandpaper on wood, a case in which the friction angle (40°) is significantly higher than the angle of inclination (30°). All three of the experimental blocks displaced a great deal more than the DDA blocks. Again, this may be due to a discrepancy between the friction angle measured in the tilt test and that realized in the actual model, either due to variation in the material surfaces (degradation of the sandpaper during the course of the experiments could cause the friction angle to decrease), or the difference between static and dynamic coefficients of friction. In this case in particular, post-experiment re-testing of the friction angle of the surfaces in contact could shed some light on the differences between the physical and numerical models.

4.2. Double-Incline Experiments

As previously mentioned, the double-incline model was designed to demonstrate that the same geometric configuration can display either sliding or toppling failure mode depending on the friction angles of the different surfaces. One set of blocks was constructed with the objective of observing different failure modes when the surface materials were changed. In all of the experiments, the lowest friction angle (18°, corresponding to Teflon/Teflon surfaces) was used on the upper incline to maximize the driving force in the model. The materials along the lower incline and vertical surfaces were varied, with a total of 5 different combinations tested. Table 2 shows the different combinations of materials modeled, along with a comparison of the modes of failure observed in the physical models and predicted using DDA.

Table 2. Modes of failure observed in the models.

Configuration		**Laboratory Model**	**DDA Model**
lower incline friction	**vertical surface friction**		
medium (30°, wood/wood)	medium (30°, wood/wood)	sliding	sliding
medium (30°, wood/wood)	low (20°, Teflon/wood)	sliding	sliding
high (40°, wood/sandpaper)	low (20°, Teflon/wood)	toppling	sliding
high (40°, wood/sandpaper)	medium (30°, wood/wood)	toppling	sliding
high (40°, wood/sandpaper)	high (40°, wood/sandpaper)	toppling/stable	sliding

The results did not correspond very well, since DDA predicted sliding failure mode in all cases, and the physical models displayed toppling failure mode in three of the five cases. This discrepancy was investigated more closely, by 1) re-measuring the friction angles of the surface materials, and 2) measuring the geometry actually achieved in the physical model. The tilt test was again used to measure the friction angles. There was significant scatter in the results, as displayed in Table 3. The actual width of the vertical blocks in the physical model was 0.5”, as opposed to 0.6” in the design.

Table 3. Ranges of friction angles of the block surfaces measured using the tilt test.

material on surface of lower block	**material on surface of upper block**		
	wood	sandpaper	Teflon
wood	20-40°	40-50°	15-25°
sandpaper	38-48°	45-55°	-
Teflon	18-22°	-	12-20°

A number of DDA models were run to determine the degree of sensitivity to the friction angle and geometry of the configuration. It was found that while the results were sensitive to geometry and also to the timestep size and maximum displacement per timestep analysis parameters, they were particularly sensitive to friction angle. In each of the three cases in which the DDA model slid but the physical model toppled, corresponding to the three cases in Table 2 with sandpaper/wood on the lower incline, the DDA models can be made to topple by making small changes in parameter values. For instance, holding everything else constant, the models with wood/Teflon on the vertical surfaces can be made to topple if the upper incline friction angle is reduced by 4° (from 18° to 14°), or if the lower incline friction angle is increased by 1° (from 40° to 41°), or if the vertical surface friction angle is reduced by 1° (from 20° to 19°). All of these are well within the range of values displayed in Table 3. This suggests that precise measurement of the friction angle is critical for accurate results, but due to the inherent variability of material surfaces, this is a very difficult property to pinpoint.

5. CONCLUSIONS

In the experiments involving block motions along a single incline, the displacements of the real blocks were typically greater than those of the DDA blocks. The most likely explanations are that the actual friction angle on the blocks was lower than measured in the tilt tests (and consequently used in the DDA models), or that the real blocks displayed a reduction in friction coefficient from static to dynamic once movement initiated.

The results of the double-incline model study related to sliding vs. toppling failure modes are extremely sensitive to the friction angles of the contacting surfaces. The initial results of several of the DDA models did not match the observed behavior of the physical models, but only very small changes in friction angles were required in order to produce the same failure mode.

Although this validation study did provide some useful results, there was quite a bit of uncertainty associated with it. It would be valuable to repeat the work using more controlled geometries and precisely measured material properties, if resources become available.

ACKNOWLEDGMENTS

This work was supported by Montana Tech's Undergraduate Research Program. The NIOSH-Spokane Research Laboratory provided the 1000 frame-per-second video camera used to record the block motions. Steve Berry helped construct the wooden models and photograph the experiments.

REFERENCES

4. Shi, G. (1993). Block System Modeling by Discontinuous Deformation Analysis, Computational Mechanics Publications: London, England.

5. Ohnishi, Y., Chen, G., & Miki, S. (1995). Recent Development of DDA in Rock Mechanics. In J.C. Li, C.Y Wang, & J. Sheng (eds.), *Proceedings of ICADD-1, The First International Conference On Analysis of Discontinuous Deformation, December 21-23,* p 26-47. Nat'l Central Univ., Chungli, Taiwan, R.O.C.

6. Ohnishi, Y., Chen, G., Ogawa, M., Itoh, T., & Nakai, T. (1999). Comparison between Physical and Manifold Method Models of Discontinuous Rock Masses. In B. Amadei (ed.), *Proceedings of ICADD-3, Third International Conference on Analysis of Discontinuous Deformation – From Theory To Practice, Vail, CO, June 3-4,* pp. 33-56. Alexandria, VA: American Rock Mechanics Association.

7. Scheele, F. and B. Bates (2005). DDA Benchmark Testing at UCT – A Summary, *Proceedings of ICADD-7, the Seventh International Conference on the Analysis of Discontinuous Deformation*, Honolulu, Hawaii, December 10-12, pp. 59-70.

8. Tsesarsky, M, Hatzor, Y.H. & Sitar, N. (2002). Dynamic block displacement prediction validation of dda using analytical solutions and shaking table experiments. In Y. H. Hatzor (Ed.), *Stability of Rock Structures Proceedings of the Fifth International Conference on Analysis of Discontinuous Deformation*, Abingdon: A. A. Balkema, pp. 195-206.

9. Ishikawa, T, Sekine, E. & Ohnishi, Y. (2002). Shaking table tests of coarse granular materials with discontinuous deformation analysis. In Y. H. Hatzor (Ed.), *Stability of Rock Structures Proceedings of the Fifth International Conference on Analysis of Discontinuous Deformation*, Abingdon: A. A. Balkema, pp. 181-188.

10. MacLaughlin, Mary M. Nicholas Sitar, David M. Doolin, and Tracy S. Abbot (2001). Investigation of Slope Stability Kinematics Using Discontinuous Deformation Analysis, *International Journal of Rock Mechanics and Mining Sciences,* vol. 38/5, pp. 753-762.

Comparison of the Deformation of Externally Loaded DDA and UDEC Blocks with an Analytical Solution

Cindy A. Wright

Graduate Research Assistant, Department of Geological Engineering

Mary M. MacLaughlin

Professor, Department of Geological Engineering

Richard P. Donovan

Assistant Professor, Department of General Engineering

Montana Tech of The University of Montana, Butte, Montana, USA

This paper was prepared for presentation at *ICADD-7, the Seventh International Conference on Analysis of Discontinuous Deformation*, held in Honolulu, Hawaii, December 10-12, 2005.

ABSTRACT: In a previous study, the deformation of rectangular blocks due to gravity (volume) loading was tested over a range of block sizes and material properties using UC-Berkeley's *DDA for Windows*. In all cases the percent error between *DDA for Windows* and the exact, analytical solution was negligible. In this follow up study, the rectangular blocks were subjected to an external point load, and again in all cases the percentage of error was negligible. Additionally, *DDA*'s capability to model the deformability of blocks that are not rectangular was validated. In these tests, a trapezoidal shaped block was subjected to an external point load and tested over a range of block sizes and material properties. While the results were insensitive to variations in load, material properties, and height of the block; they were sensitive to changes in block shape. For the scenarios where the width of the top of the trapezoid varied, the percent error was close to 0% for a trapezoid that was almost rectangular to 40% for the case where width at the top of the trapezoid was so small it resembled a triangle. These results quantify and put in question DDA's ability to correctly model the deformation of non-equidimensional blocks due to the stresses and strains within any given block in the analysis being constant across the whole region of the block regardless of shape and size. Because of the error experienced in DDA, a comparison was then performed using Itasca's *UDEC 4.0,* which is a commercially available discrete element method. The same trapezoid parameters were used in the UDEC runs, revealing a 0.05% to 39% error. An additional sensitivity analysis was performed to find the optimum mesh size for the UDEC blocks.

1. INTRODUCTION

Discontinuous Deformation Analysis (DDA) is a numerical method used to model the motions of blocky masses [Shi, 1993]. An important aspect of the analysis of how a material reacts under a loading condition is the deformation that is caused by the load being applied. In DDA the blocks are "simply deformable," which means that stresses and strains within any given block are constant across the whole region of the block regardless of its size or shape; consequently, DDA block deformability is limited and is most accurate for models with more regularly shaped and equidimensional blocks [MacLaughlin and Tinucci, 2000].

Validation of computer applications of DDA is an important part of the software development process. This often involves testing to make sure the program is modeling simple mechanical problems correctly. Simple mechanical problems are used because the data from the numerical

method can then be compared to an exact, analytical solution. To ensure that the program is modeling a complex problem correctly, it must first be verified that it is modeling the smaller parts of the complex problem correctly.

In a previous study, the deformation of rectangular blocks due to gravity (volume) loading was tested over a range of block sizes and material properties using UC-Berkeley's *DDA for Windows*. In all cases the percent error between *DDA for Windows* and the exact, analytical solution was negligible [Duneman et al., 2003]. In this study, DDA's ability to correctly model the deformation of a block experiencing a point load with gravity turned off was tested over a range of sizes of rectangular blocks with different material properties. Additionally, trapezoidal shaped blocks were tested to see if DDA would correctly model a non-rectangular block. The version of DDA software that was used was UC-Berkeley's *DDA for Windows.*

2. ANALYTICAL SOLUTIONS

Two different analytical solutions were used: one for the rectangular block and one for the trapezoidal block. To determine the deformation of the blocks, the analytical solution for the strain that the blocks experienced was solved because strain is defined as the deformation of a body under an applied force. For the rectangular block under a point loading condition with gravity turned off, the definition of strain and stress is [Beer, DeWolf, 2002]:

$$\varepsilon = \frac{\sigma}{\mathrm{E}} \tag{1}$$

where ε = strain, σ = stress, and E = Young's Modulus of Elasticity.

$$\sigma = \frac{\mathrm{P}}{\mathrm{A}} \tag{2}$$

where P = applied force and A = cross-sectional area on which the force is being applied. The analytical solution for axial strain in a rectangular block is:

$$\varepsilon = \frac{\mathrm{P}}{\mathrm{AE}} \tag{3}$$

The lateral strain was found by using:

$$\varepsilon_{Lateral} = -\upsilon \varepsilon_{Axial} \tag{4}$$

where υ= Poisson's Ratio.

The same definition of stress and strain was used for the analytical solution for the strain experienced by a trapezoid, but the deformation of the trapezoid was used to ultimately solve for the strain experienced.

$$u = \int_0^{\mathrm{H}_0} \frac{PH_0 dy}{(b_1 H_0 - (b_1 - b_2)y)E} \tag{5}$$

where b_1 is the initial width of the base and b_2 is the initial width of the top of the trapezoid.

The total change in height *u,* can be found by integrating over the initial height H_0.

$$u = \frac{PH_0}{E}\int_0^{H_0} \frac{dy}{(b_1 H_0 - (b_1 - b_2))y} \tag{6}$$

$$u = \frac{PH_0}{E}\left[\frac{1}{-(b_1 - b_2)}\left(\ln\left|(b_1 - b_2)y + (b_1 H_0)\right|\right)\right]_0^{H_0} \tag{7}$$

After substituting the limits of integration to evaluate the definite integral, the final equation used was:

$$u = \frac{PH_0}{E}\left[\frac{1}{-(b_1 - b_2)}\left(\ln\left|b_2 H_0\right| - \ln\left|(b_1 H_0\right|\right)\right] \tag{8}$$

Since $u = \Delta H$, the total strain in the block can be represented by:

$$\varepsilon = \frac{\Delta H}{H_0} = \frac{u}{H_0} \tag{9}$$

which corresponds to the axial strain for the trapezoid. The lateral strain can be found with the same equation used for the rectangular blocks, Equation 4.

3. NUMERICAL VALIDATION OF DDA

3.1. Parameters Investigated

Both the rectangular and trapezoid blocks were defined with a "base" case that was the starting point of the sensitivity analysis. The base size for the rectangle was 1m x 1m; the trapezoid was 1m wide at the bottom x 0.9m tall with a top width of 0.2m. Thickness was assumed to be 1 unit. The base case material properties for both types of blocks were a modulus of elasticity (E) = 10 GPa and Poisson's ratio (ν) = 0.3. The base case point load was 100N. Figure 1 shows the base case setup.

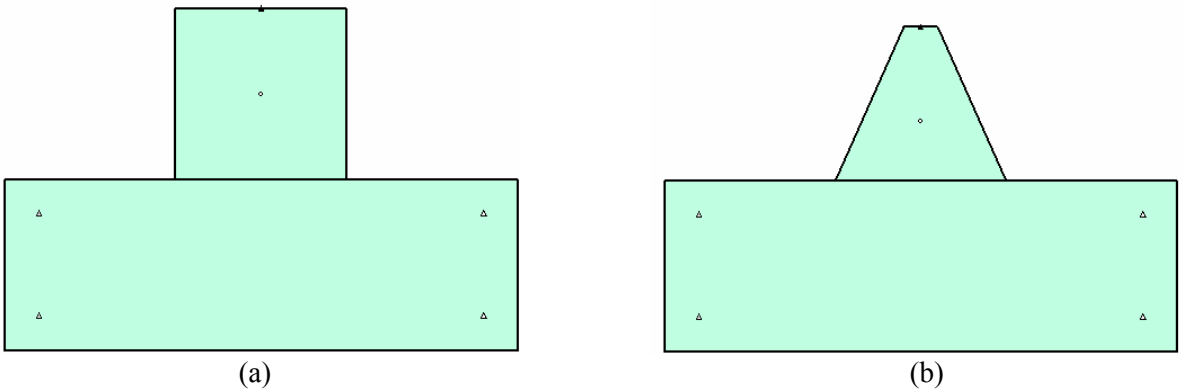

(a) (b)

Figure 1. Examples of block setup a) Rectangular block: 1 m × 1 m; b) Trapezoid blocks: 1 m × 0.9 m x 0.2 m.

The unit weight of the material was 26.487 kN/m^3. DDA was run in dynamic mode with true rotation correction for 100 time steps with gravity turned off. The different parameters investigated for each shape of block are as follows: one run of the base case scenario, one run in which a third block containing the point load was added on top of the block being investigated, one run in which the coordinates were changed on the base case but the size of the blocks stayed the same, two runs with different modulus of elasticity (E) values (1 GPa and 100 GPa), two runs with different Poisson's ratios (ν) (0.15 and 0.45), two runs with different point loads (10N and 1000N), two runs in which the height of the blocks stayed the same but the width changed, two runs in which the width of the block stayed the same but the height changed, and finally two runs were performed in which the block size was changed by a factor of 10 and 0.1. The complete sensitivity analysis consisted of a suite of 15 runs for the rectangular block and for the trapezoidal block, for a grand total of 30 runs.

3.2. Error Calculations

The DDA output file that was used records the coordinates of the vertices of the blocks at the end of each time step. The vertices used to determine the lateral deformation were the x coordinates from the bottom of the block and the vertices used for axial deformation came from the right side top and bottom y coordinates. DDA deformation for both the rectangle and trapezoid is calculated from the original and final dimensions as follows:

$$\varepsilon_{Axial} = \frac{(H_f - H_0)}{H_0} \tag{10}$$

$$\varepsilon_{Lateral} = \frac{(W_f - W_0)}{W_0} \tag{11}$$

From these results the percent error is then calculated by:

$$Percent\_Error = \frac{(\varepsilon_{DDA} - \varepsilon_{Analytical})}{\varepsilon_{Analytical}} \times 100\% \tag{12}$$

EXCEL was then used to perform the calculations.

4. DDA RESULTS AND DISCUSSION

4.1. Results for the Rectangular Block

In all cases with the rectangular blocks the final error was found to be less than 0.15%. A graph showing the final error percentage at time step 100 is shown in Figure 2. Positive error indicates that DDA deformation is greater than the actual solution.

Although the final percent error was near 0%, it is interesting to note in Figure 3 that initially the error percentage oscillates then dampens to 0%, but by the 15th time step all error percentages were oscillating under +/- 1% error. In a previous study it was found that for a dynamic analysis of deformation under gravity loading using DDA, blocks can vibrate for more than 100 time steps [Duneman et al., 2003]. This also seems to be the case for a dynamic analysis of the block experiencing a point load with gravity turned off. The differences in the percent error for the different scenarios are negligible, but the elasticity and the size of the rectangular block were the most sensitive changes made.

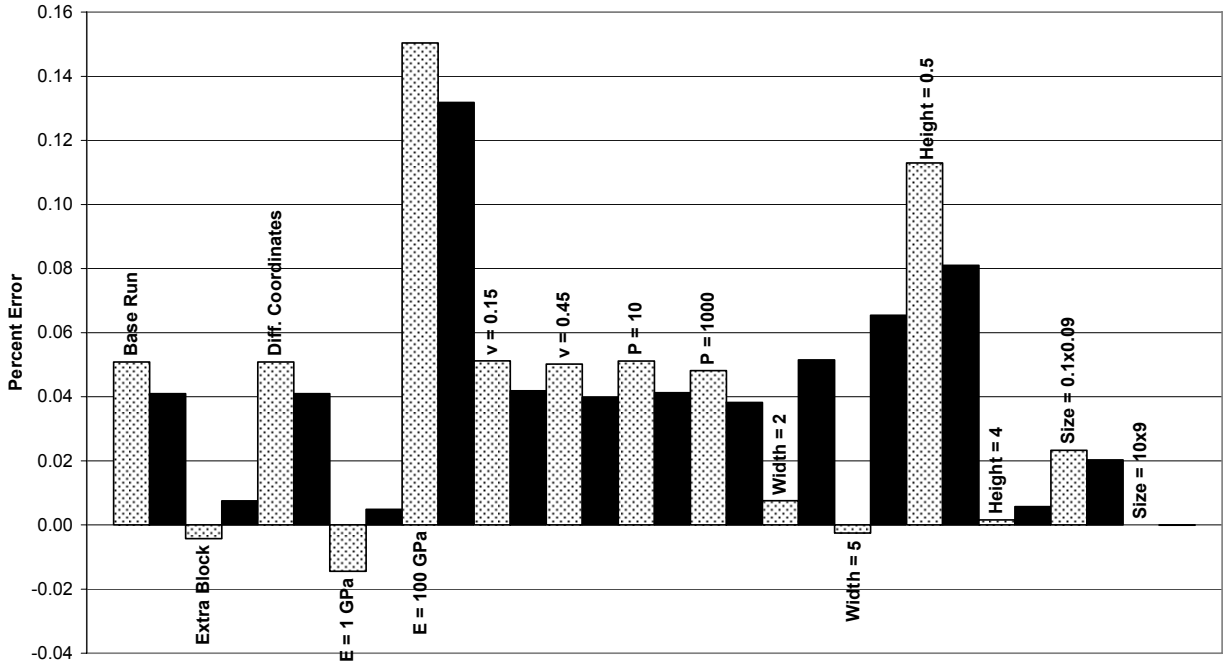

Figure 2. Final percent error for each scenario of the rectangular blocks at time step 100. The black bars are axial strain error and the dotted bars are the lateral strain error.

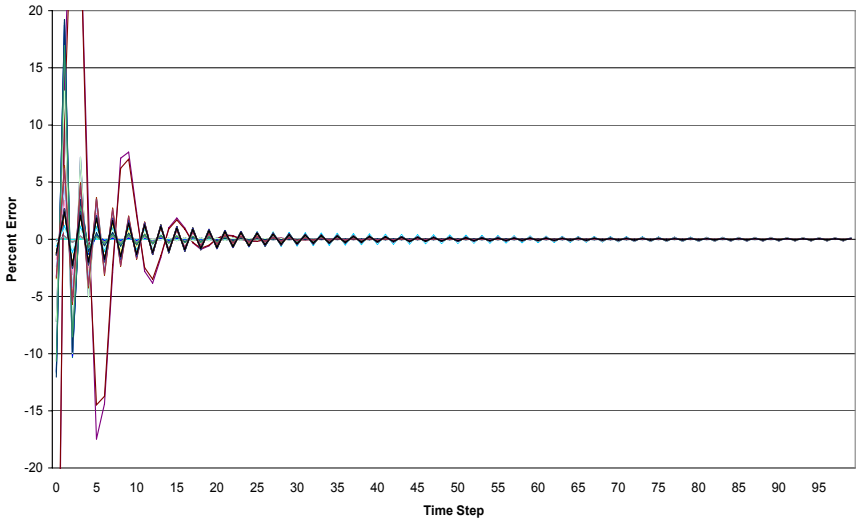

Figure 3. Percent error vs. time step for the different scenarios of the rectangular blocks.

In Figure 3, there is one error graph whose oscillation that has a higher amplitude and lower frequency and does not match the others. This is the plot for the case in which the size of the trapezoid was increased to 10 times the base case size; even though the error is initially greater it can be seen in Figure 2 that the final percent error for this case (the last one plotted) was so close to zero percent that it did not show up on the graph.

4.2. Results for Trapezoidal Block

For most cases with the trapezoidal blocks the error, shown in Figure 4, was 17%. When the width of the bottom of the trapezoid was widened to 2 meters and 5 meters the percent error increased to 29% and 42% respectively.

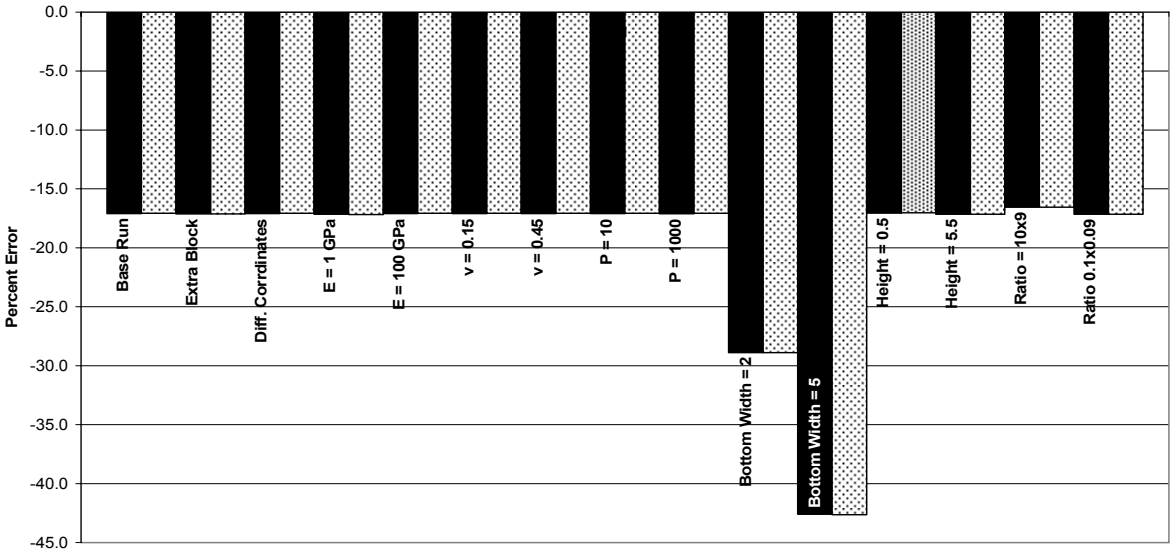

Figure 4. Final percent error for each scenario of the trapezoidal blocks at time step 100. The black bars are axial strain error and the dotted bars are the lateral strain error.

It is difficult to see in Figure 4 because of the scale, but the percent error for the base case and material property differences are not all the same: they do vary by 0.01 to 0.10% error just like the results of the rectangular blocks. Additionally the percent error for the lateral strain (light bars) and axial strain (dark bars) are not all the same; for all the cases there is a 0.01 to 0.10% error difference between the lateral and axial strain. Figure 5 shows that, just like in the rectangular blocks, the percent error oscillates before damping to a more consistent percentage.

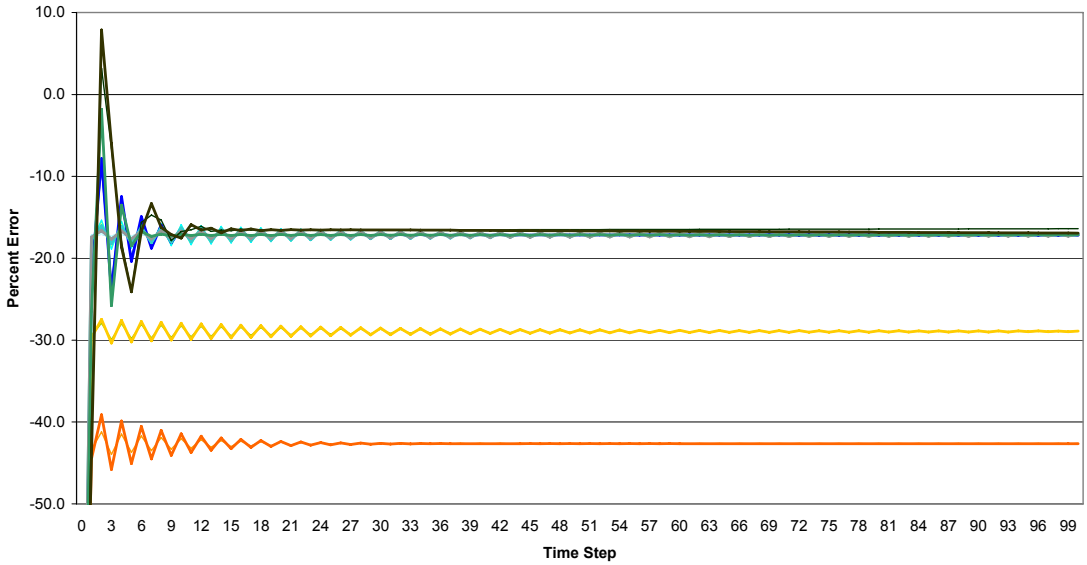

Figure 5. Percent error vs. time step for the different scenarios of the trapezoidal blocks.

Another set of runs was done to further quantify the effect that changing the shape of the trapezoid has on the percent error. The width of the top of the trapezoid was varied while the width of the bottom stayed at 1 m, causing the trapezoid to become either squarer or more triangular as can be seen Figure 6. A graph of the variation in percent error is shown in Figure 7. When the width of the top of the trapezoid was increased to 0.95 m (nearly rectangular shaped) the percent error was less than 0.05%, but when the width of the top of the trapezoid was decreased to 0.05 m (nearly triangular shaped) the percent error was close to 40%. An additional set of runs was performed in which the width of the top and the bottom of the trapezoid were kept at 0.2 m and 1 m respectively while the height was varied. Several of these blocks can be seen in Figure 8 and the results are plotted in Figure 9. For all cases of different heights the percent error was 17%.

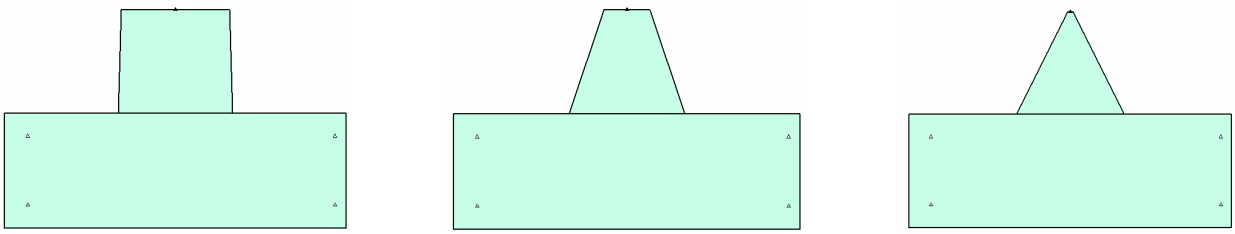

Figure 6. Examples of trapezoids with varying top width (b2), the bottom width is held constant at 1 m.

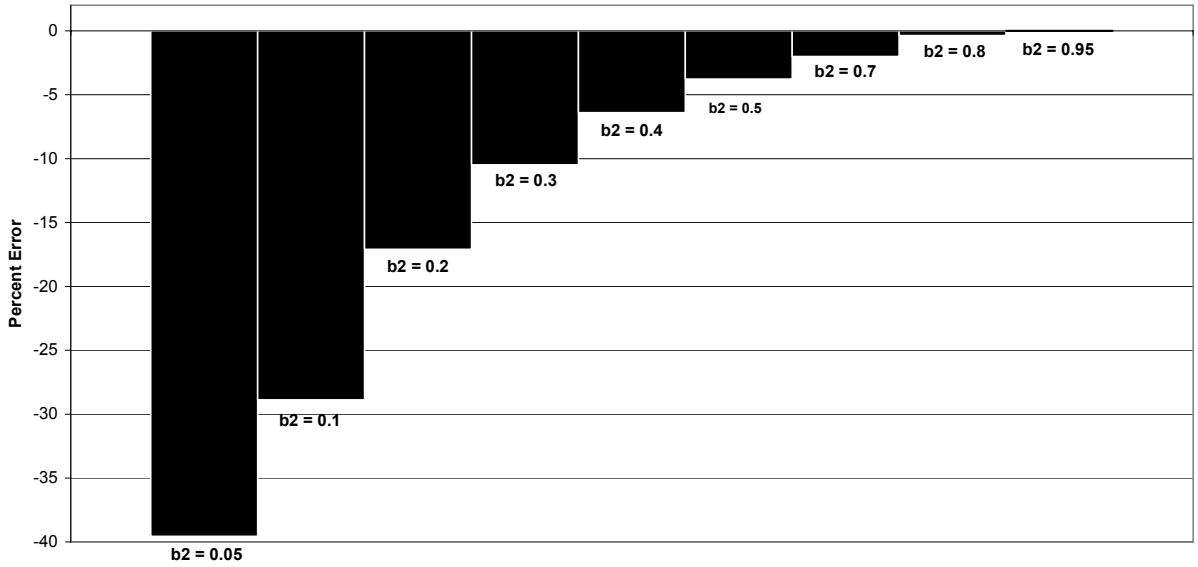

Figure 7. Percent Error vs. different lengths of the variation of the width of the top of the trapezoid (b2)[m], with the bottom width held constant at 1 m.

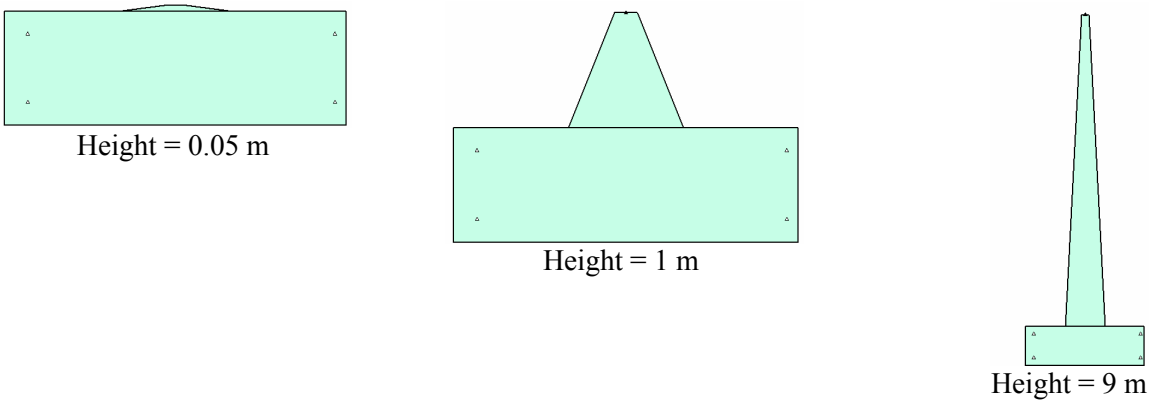

Figure 8. Examples of trapezoids with varying heights, the bottom and top widths are held constant at 1 m and 0.2 m, respectively.

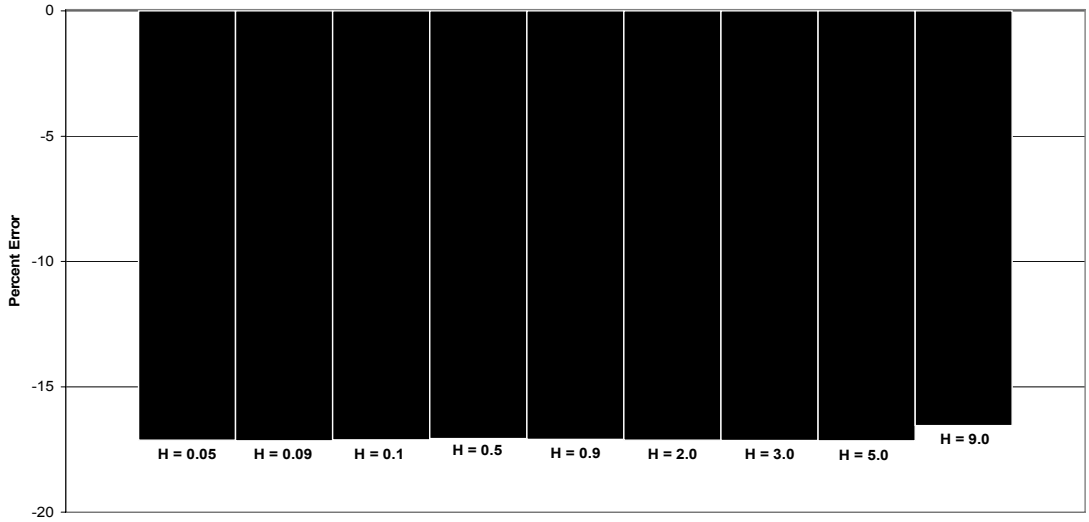

Figure 9. Percent Error vs. different heights of the trapezoid, with the widths of the top and bottom held at 1 m and 0.2 m, respectively.

An interesting observation about the variations of the dimensions of the block is that the results suggest different degrees of sensitivity relative to the direction of the applied load. In Figure 7 when the dimension of the top of the trapezoid (perpendicular to the load) was changed there was a large change in the percent error, but in Figure 9 when the height of trapezoid (parallel to the load) was changed there was a negligible difference in the results.

5. UDEC COMPARISON

UDEC, or Universal Distinct Element Code, is a commercially available program developed by Itasca. It is a 2-dimensional numerical analysis program based on the distinct element method for modeling discontinuous materials. Deformable blocks are subdivided into a mesh of finite-difference zones, and each zone responds according to a prescribed linear or nonlinear stress-strain law; therefore, mechanical changes like stress or strain are calculated in each zone. DDA and UDEC are similar but differ in that blocks in DDA deform due to a superposition of strain modes [Itasca, 2004]. As stated earlier, DDA models stresses and strains within any given block as constant across the whole region of the block regardless of its shape and size [MacLaughlin

and Tinucci, 2000]. In this section, the results of UDEC models of the same trapezoidal block investigation is presented, to allow a comparison between the trapezoid modeled as a whole region, as in DDA, or subdivided into elements, as in UDEC.

UDEC Version 4.0 Double Precision was used to run the models and the same parameters that were used in the DDA models were also used in UDEC. The only difference is that the modulus of elasticity and Poisson's ratio were converted to a shear and bulk modulus in UDEC, because these material properties are preferred in UDEC. A mesh of zones was created using the generate quad command in UDEC with the size of the zones specified to be 0.1 which is $1/10^{th}$ the size of the width of the bottom of the trapezoid, which in most cases is 1 m. The resulting model is shown in Figure 10.

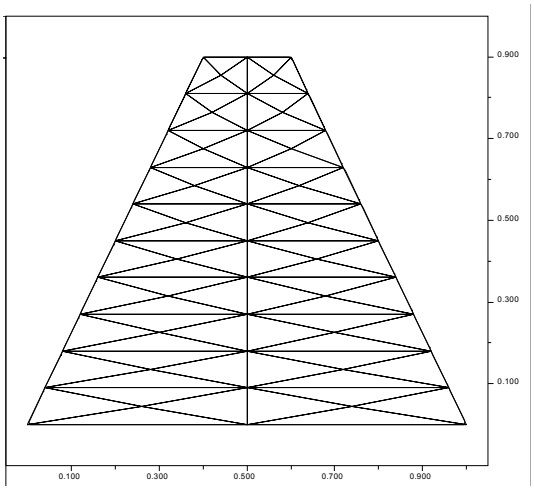

Figure 10. Trapezoid modeled in UDEC with the dimensions of 1m x 0.9 m x 0.2 m with a 0.1 zoning.

Each run was allowed to equilibrate for 40,000 time steps. Figure 11 shows the percent error between the analytical solutions and the UDEC results for the 13 different cases investigated, corresponding to the variation in input parameters.

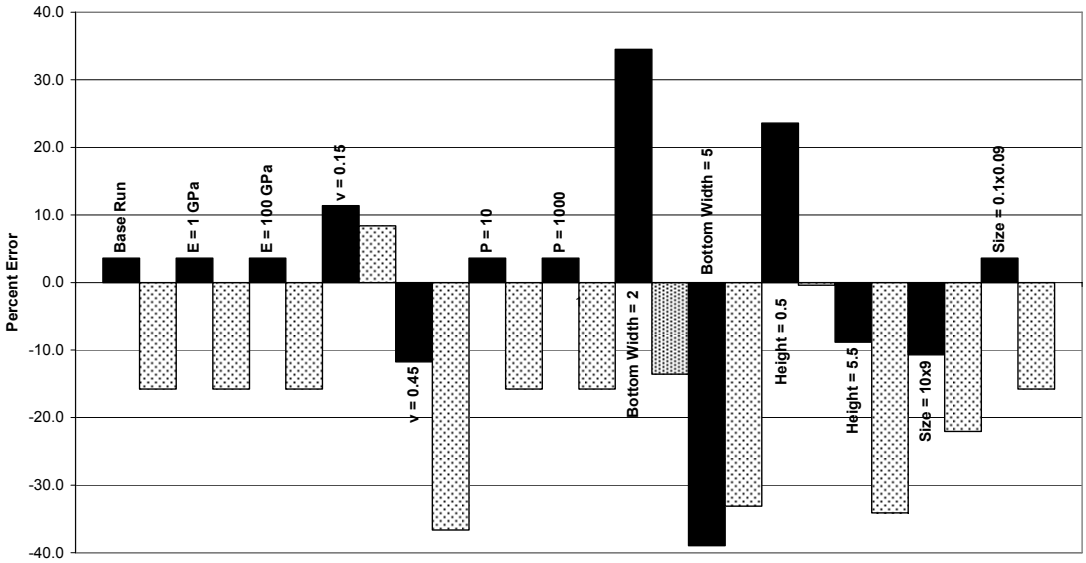

Figure 11. Percent Error between UDEC and Analytical Solution.

The percent error in Figure 11 ranges from 0.5% to 39%. A major difference from the DDA runs is that the axial and lateral errors in UDEC differ from each other while in DDA they were very similar. This can probably be attributed to the zones at the bottom of the block deforming differently than the zones at the top, a feature that is not allowed in DDA. If percent error for all 13 different cases in UDEC are averaged, the average error for UDEC was 12% in the axial direction and 18% in the lateral direction; this is compared to an average of 17% for both lateral and axial in DDA. Although Figure 4 and Figure 11 do not look similar, both the results from UDEC and DDA average to be very similar when looking at a number of different runs.

Since DDA's greatest error came from varying the width of the top of the trapezoid to make it either more equidimensional or more triangular, an additional comparison with UDEC was made to see if similar results could be obtained. Figure 12 shows the results of these runs in UDEC. The lateral error is the lighter bars and axial error is the darker bars. The UDEC runs do not show a consistent variation in error with the change in block shape as was observed in the DDA runs in Fig. 7. The percent error in UDEC ranged from 0.6% to 70%.

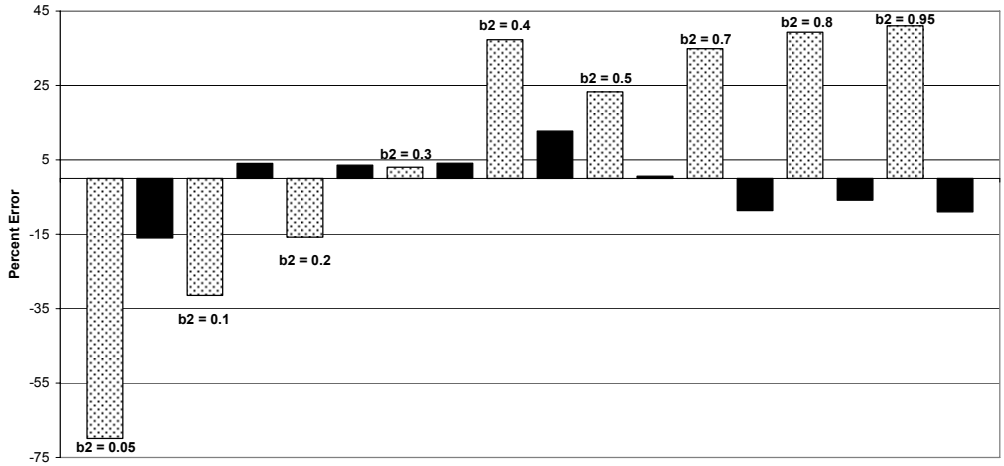

Figure 12. UDEC percent error with varying top width of trapezoid (bottom width held constant at 1 m).

Finally, a sensitivity analysis was run in UDEC using the "base" case trapezoid to see if different results could be obtained through a different degree of meshing. A meshing size of 1 and 0.01 was compared original 0.1 size; creating the different degrees of meshing shown in Figure 13.

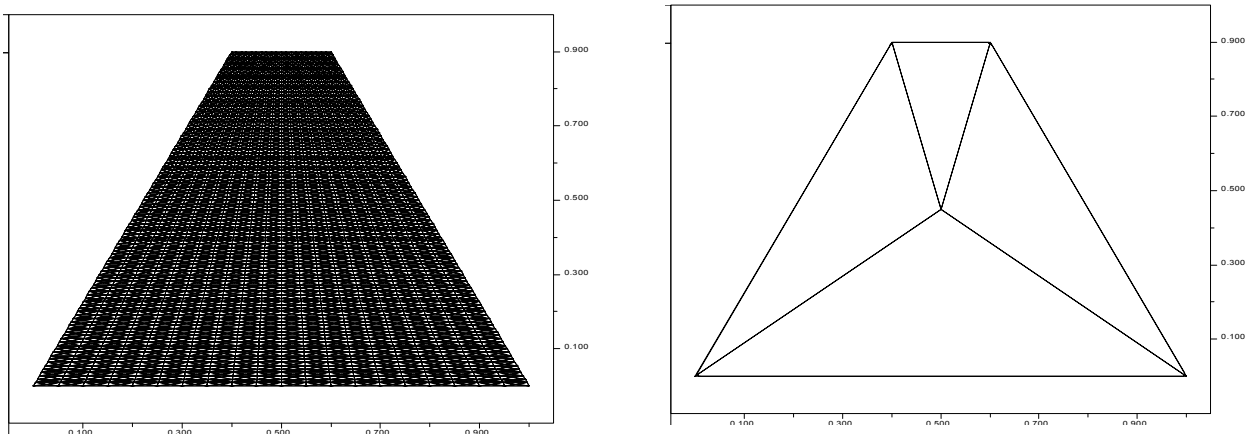

(a) Mesh Size 0.01 (b) Mesh Size 1

Figure 13. Different mesh sizes used in sensitivity analysis (mesh size 0.1 can be seen in Fig. 10).

The results of the sensitivity analysis are shown in Figure 14. The smaller mesh size produced the smallest and most similar error between both the lateral and axial directions. It is suggested in the UDEC manual to use many zones to represent the varying distribution of stress/strain. From the sensitivity analysis it observed that the lateral and axial deformations will be more uniform if more zones are used, but this is not always practical when running large models. Decreasing the mesh size from 0.1 to 0.01 in this small model meant that the time it took the models to equilibrate went from less than 5 seconds for the 0.1 sized zones to almost a ½ hour for the small zones.

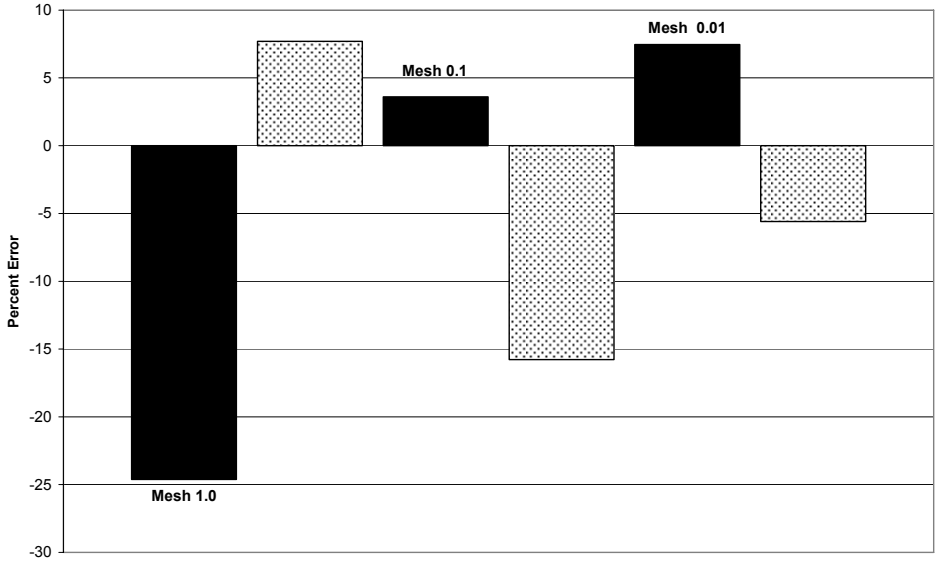

Figure 14. Percent Error of Different Mesh Sizes in UDEC. The black bars are axial strain error and the dotted bars are the lateral strain error.

It is suggested in the UDEC 4.0 User Manual to try and keep the zoning as uniform as possible and avoid long, thin zones with aspect ratios greater than 5:1. When using the *generate quad* command a mesh generator fills the block with triangular-shaped zones based on a single parameter that controls the size of the zones; therefore, when working with non-uniform blocks in UDEC it is difficult to stipulate the sizes of zones in different directions. An example of this would be a block with one side 10 m long and another side only 0.1 m long. If the zone size is too large the smaller side of the block would not have enough zones to adequately show stress/strain in this area; where as if the zones were sized for the 0.1 m side and were smaller there could be too many zones in the entire block and the run time would be quite long and maybe impractical.

6. CONCLUSIONS

The data from the rectangular blocks show that DDA is correctly modeling the deformation in a rectangular block that experiences a point load. This is important because it has now been shown that the DDA solution for total strain in a rectangular block exactly matches the analytical solution for both a point load and gravitational load.

The data gathered from the trapezoidal blocks show that there are limitations of DDA. As stated previously, one of the limitations of DDA is that deformability is limited and works best with equidimensional blocks [MacLaughlin and Tinucci, 2000]. One of the reasons for this is that DDA models stresses and strains within any given block as constant across the whole region of the block regardless of its shape and size, and this is not entirely accurate when dealing with blocks that are non-uniform. Figure 7 shows that the less rectangular the trapezoid becomes the more error is introduced into DDA's ability to model deformation. Interestingly, Figure 9 shows that DDA is not sensitive to the height of the trapezoid. These results corresponds to a previous study that showed that DDA can correctly model the deformation in a more square rectangular block as well as a tall, thin rectangular block [Duneman et al., 2003]. This suggests that the sensitivity to block shape may be directional, relative to the applied load, and further investigation into this would be valuable.

The data from the UDEC analysis shows the zoning the trapezoidal blocks allows for different axial and lateral deformations in the block because each zone can deform independently. When the axial and lateral errors observed in many UDEC runs with blocks of different shapes and properties are averaged and compared to the averaged percent error of the same number of runs in DDA, the resultant percent errors are similar. Additionally, it was shown that the more zones in a UDEC block, the axial and lateral deformations are more similar, but the trade off is that it can take much longer for the models to equilibrate.

7. ACKNOWLEDGEMENTS

This study was jointly funded by the National Science Foundation under grant number 0346458 and the Montana Board of Research and Commercialization Technology under Grant number 04-06 through the University of Montana, Missoula, Undergraduate Research Program. I would like to thank Professor Mary MacLaughlin for the opportunity to come to Montana Tech and work on this project and Professor Rick Donovan for his help with the analytical solutions. Thanks to Dr. Gen-hua Shi for creating DDA and to Dr. David Doolin for implementing DDAML.

8. REFERENCES

1. Shi, G. (1993). *Block System Modeling by Discontinuous Deformation Analysis*, Computational Mechanics Publications: London, England.

2. MacLaughlin, M., Tinucci, J. (2000). *Introduction to Discontinuous Deformation Analysis*, Short Course Notes, 4th North American Rock Mechanics Symposium, Seattle, Washington, July 30, 2000.

3. Beer, F., Johnston, E., DeWolf J. (2002). *Mechanics of Materials, Third Edition*, The McGraw-Hill Companies: New York, New York.

4. Duneman, M., MacLaughlin, M., Donovan, R. (2003). Validation of DDA Block Deformability under Gravity Loading Conditions, *Proceedings of the 6th International Conference on Analysis of Discontinuous Deformation*, Trondheim, Norway, October 5-8 2003.

5. Itasca Consulting Group, Inc. (2004). *UDEC 4.0 User's Manual*, ICG: Minneapolis, MN.

Implementation of a quadratic triangular mesh into the DDA method

Roozbeh Grayeli

Mahab Ghodss Consulting Engineers, Vahid Dastgerdy Ave. Tehran, IRAN P.O.Box: 15815-1791, grayeli@mahabghodss.com

Ali Mortazavi

Assistant Professor, Dept. of Mining & Metallurgical Engineering, Amirkabir University of Technology, Tehran, IRAN, mortazav@aut.ac.ir

ABSTRACT: The Discontinuous Deformation Analysis (DDA) with a second-order displacement function was derived incorporating a six-node triangular mesh in order to enhance DDA's capabilities for use in practical applications. The matrices of equilibrium equations for the second-order DDA are given in detail for program coding. By close comparison with a widely used Finite Element code, the advantages of the modified DDA can be seen clearly. The modified DDA was applied to the analysis of stress distribution around circular tunnels. The obtained results were compared against analytical results as well as the results obtained from a commercial FEM code. A fairly good agreement was achieved between DDA, FEM, and analytical solution.

KEYWORDS: Discontinuous Deformation Analysis, Finite Element Method, Triangular element, High-order function, Rock Mechanics, Blocky media

1. INTRODUCTION

Numerical methods in geomechanics can be classified into two main groups: continuum methods and discontinuous methods. Examples of continuum methods are; the finite element method (FEM), the boundary element method (BEM), and the finite difference method (FDM). . These methods are now fully developed and have been successfully used in many applications. These classical methods, however, face great difficulties when dealing with discontinuous media. Rock mass discontinuities can be modeled in a discrete manner with FEM and BEM methods using special joint elements [1]. However, these methods are incapable of simulating the behavior of blocky media, in particular discontinuous rock mass. On the other hand, discontinuoum methods such as discrete element method (DEM) introduced by Cundall [2], and discontinuous deformation analysis (DDA) established by Shi [3], are now well developed and can be used to simulate the behavior of the discontinuous media. The discontinuous deformation analysis (DDA) method is a promising discontinuoum modeling technique which has great potentials for modeling of blocky systems. Large displacement and deformation are considered under both static and dynamic loading conditions. Various modifications to the original DDA formulation have been reported in the rock mechanics literature [4, 5]. In the original DDA formulation, a

first order polynomial displacement function was assumed for block deformation, which do not allow for variable stress/strain distribution within a block. This approximation precludes the application of the first order polynomial function to problems with significant stress variations within blocks. To overcome this shortcoming, one approach adopted was to glue small blocks together in artificial manner to form a larger block. This approach suffers form large computational time. Ma *et al.* [6], Koo *et al.* [7] and Hsuing [8] implemented the high order displacement function into the DDA algorithm.

Some researchers [9, 10] implemented finite element mesh into the original DDA blocks in order to account for stress variations within the blocks. Moreover, Shi's recent development, the manifold method, was aimed at describing stress distributions within blocks [11]. The manifold method, still retaining most of the DDA's attractive features, can be identified as the generalized finite element and discontinuous deformation analysis method. Additionally, Chen *et al.* developed the high order version of manifold method [12]. This paper presents the implementation of a high order triangular element into the DDA algorithm. The new code was developed in C++ environment problem and to demonstrate the capability of the modified DDA code the typical example of stress distribution around circular tunnels at depth was analyzed. The following sections describe the implementation procedure and the analysis results.

2. DISPLACEMENT APPROXIMATIONS

In the displacement-based finite element method the primary unknown quantity is the displacement field, which varies over the problem domain. In two dimensional plane strain situations, the displacement field is characterized by two global displacement vectors u and v, in the x and y directions respectively. The original DDA algorithm lacks ability to model complex block deformations. This paper presents the implementation of a six node triangular element into the original DDA blocks. The major advantage of these elements is their deformation capability. Moreover, due to their simple geometry, they can easily fit any arbitrary block shape formed by the intersection of pre-existing discontinuities.

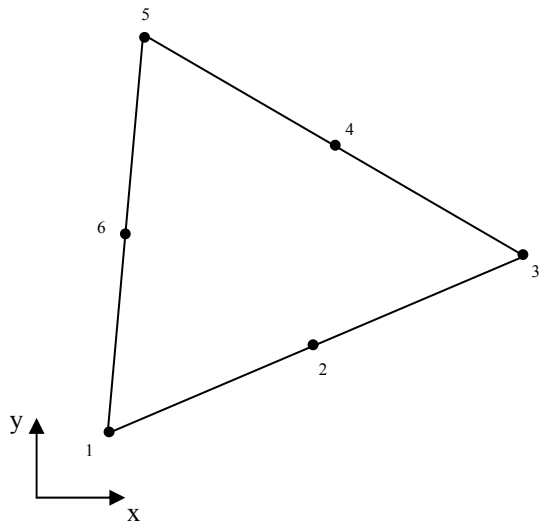

Figure 1 Geometry of the six-node triangular element

Each element consists of 6 nodes and has 12 degrees of freedom in the x and y directions. The displacement vector for the employed element can be represented in a matrix form as below:

$$[D_i] = [u_1 \quad u_2 \quad \cdots \quad u_6 \quad v_1 \quad v_2 \quad \cdots \quad v_6]^T \tag{1}$$

The displacement function of the six-nodded triangular element can be written in the following fashion:

$$\begin{aligned} u &= a_1 + a_2 x + a_3 y + a_4 xy + a_5 x^2 + a_6 y^2 \\ v &= b_1 + b_2 x + b_3 y + b_4 xy + b_5 x^2 + b_6 y^2 \end{aligned} \tag{2}$$

The 12 unknown coefficients $a_1, a_2, \cdots, a_6$ and $b_1, b_2, \cdots, b_6$ can be expressed in terms of nodal displacements by substituting the nodal coordinates into the above equations. The element is positively oriented when six nodes are arranged counter-clockwise and the total displacement field of the element *e* can be written as blow:

$$\begin{bmatrix} u \\ v \end{bmatrix} = [T^{(e)}][X^{(e)}][D^{(e)}] \tag{3}$$

where

$$[T^{(e)}] = \begin{bmatrix} 1 & x & y & xy & x^2 & y^2 & 0 & 0 & 0 & 0 & 0 & 0 \\ 0 & 0 & 0 & 0 & 0 & 0 & 1 & x & y & xy & x^2 & y^2 \end{bmatrix}, \quad [X^{(e)}] = \begin{bmatrix} n_c & n_0 \\ n_0 & n_c \end{bmatrix} \tag{4}$$

and,

$$n_c = \begin{bmatrix} 1 & x_1 & y_1 & x_1y_1 & x_1^2 & y_1^2 \\ 1 & x_2 & y_2 & x_2y_2 & x_2^2 & y_2^2 \\ 1 & x_3 & y_3 & x_3y_3 & x_3^2 & y_3^2 \\ 1 & x_4 & y_4 & x_4y_4 & x_4^2 & y_4^2 \\ 1 & x_5 & y_5 & x_5y_5 & x_5^2 & y_5^2 \\ 1 & x_6 & y_6 & x_6y_6 & x_6^2 & y_6^2 \end{bmatrix}, \quad n_0 = \begin{bmatrix} 0 & 0 & 0 & 0 & 0 & 0 \\ 0 & 0 & 0 & 0 & 0 & 0 \\ 0 & 0 & 0 & 0 & 0 & 0 \\ 0 & 0 & 0 & 0 & 0 & 0 \\ 0 & 0 & 0 & 0 & 0 & 0 \\ 0 & 0 & 0 & 0 & 0 & 0 \end{bmatrix} \tag{5}$$

3. DDA FORMULATION BASED ON THE 2nd ORDER SIX-NODED TRIANGULAR ELEMENT

In the discontinuous deformation analysis method, the equilibrium equations are established by minimizing the total potential energy induced into the system and solved. The total potential energy, Π_t of a the system with N number of nodes has the following form [3]

$$\Pi_t = \frac{1}{2}[D_t]^T [K_t][D_t] + [D_t]^T [F_t] + C \tag{6}$$

where

$$[K_t]=\begin{bmatrix} k_{11} & k_{12} & k_{13} & \cdots & k_{1n} \\ k_{21} & k_{22} & k_{23} & \cdots & k_{2n} \\ k_{31} & k_{32} & k_{33} & \cdots & k_{3n} \\ \vdots & \vdots & \vdots & \ddots & \vdots \\ k_{n1} & k_{n2} & k_{n3} & \cdots & k_{nn} \end{bmatrix}, [D_t]=\begin{bmatrix} d_1 \\ d_2 \\ d_3 \\ \vdots \\ d_n \end{bmatrix}, [F_t]=\begin{bmatrix} f_1 \\ f_2 \\ f_3 \\ \vdots \\ f_n \end{bmatrix} \tag{7}$$

In Eq. (6) C in here is the energy produced by friction force and for the material analysis, F_i is called the loading matrix. Elements K_{ij} and K_{ii} in the coefficient matrix, given by Eq. (6), are 2×2 submatrices and elements d_i, f_i are 2×1 submatrices. By minimizing the total potential energy, Π_t, that is produced by the forces and stresses, the equilibrium equations can be derived. The global system of equations has the form of:

$$[K_t][D_t]=[F_t] \tag{8}$$

For a system with N node, the global stiffness matrix will be $2N\times 2N$ in size. In Eq. (6) the off-diagonal contributions to the system matrix will exist only if the blocks are in contact. In other words, the existence of sub-matrices k_{ij} and k_{ji} is the result of contact between two elements. The following sections demonstrate the determination of various sub-matrices required to set up the global equilibrium equation.

6.1. Stiffness matrix

The strain energy Π_e due to the elastic stresses of element *e* can be written as:

$$\Pi_e=\frac{1}{2}\iint\{\varepsilon\}^T\{\sigma\}dxdy=\frac{1}{2}[D^{(e)}]^T\iint[X^{(e)}]^T[B]^T[E][B][X^{(e)}]dxdy[D^{(e)}] \tag{9}$$

where,

$$\{\sigma\}=[E]\{\varepsilon\}\ ,[E]=\frac{E}{1-\nu^2}\begin{bmatrix} 1 & \nu & 0 \\ \nu & 1 & 0 \\ 0 & 0 & \frac{1-\nu}{2} \end{bmatrix}\ \text{and}\ [B]=\begin{bmatrix} \frac{\partial u}{\partial x} \\ \frac{\partial v}{\partial y} \\ \frac{\partial u}{\partial y}+\frac{\partial v}{\partial x} \end{bmatrix} \tag{10}$$

Hence, by minimizing the above energy function with respect to the displacement variables the stiffness term associated with elastic stresses can be calculated as below and added to the global $[K_t]$ matrix:

$$[X^{(e)}]^T\iint[B]^T[E][B]dxdy[X^{(e)}]\rightarrow[K_{i(r)\,i(s)}]\qquad r,s=1\cdots 6 \tag{11}$$

Where

i(1), the number of the first node of element.
i(2), the number of the second node of element.

i(3), the number of the third node of element.
i(4), the number of the fourth node of element.
i(5), the number of the fifth node of element.
i(6), the number of the sixth node of element.

It should be noted that the elements in $[B_i]$ matrix contain $x^{n_1} y^{n_2}$ terms, where n_1 and n_2 are non-negative integers. It should be realized that the, integration of Eq. (11) is not straightforward. The higher the order of the polynomial functions, the more difficult the integrating would be. Shi [13] proposed the 2D and 3D simplex integration scheme, which allow for the integration of high order polynomials. The presented research has adopted the integration method proposed by Shi [13].

6.2. Initial stress

Initial stresses are often sources of energy within a blocky system. Examples of these stresses are the in-situ ground stress caused by tectonic activities and also stresses due to lack of fit in mechanical applications. In the DDA method, the stresses are accumulated from the previous computational step. Therefore, the potential energy due to initial stresses can be easily implemented into the DDA algorithm. In the first-order DDA, the stresses within an element are considered to be constants. However, in the high-order formulation of DDA developed here, the strains and stresses are no longer constants because the matrix [B] is a function of x and y. The potential energy of the initial constant stresses in an element *e* can be written as below:

$$\Pi_{is} = \iint \{\varepsilon\}^T \{\sigma^0\} dxdy = \left[D^{(e)}\right]^T \iint \left[X^{(e)}\right]^T [B]^T [E][B]\left[X^{(e)}\right] dxdy \left[D_0^{(e)}\right] \tag{12}$$

By minimizing the above energy function with respect to the displacement variables, the following force matrix will be determined which must be added to the global force matrix:

$$-\iint \left[X^{(e)}\right]^T [B]^T [E][B]\left[X^{(e)}\right] dxdy \left[D_0^{(e)}\right] \rightarrow \left[F_{i(r)}^{(e)}\right] \qquad r = 1 \cdots 6 \tag{13}$$

$$-\left[X^{(e)}\right]^T [H]\left[X^{(e)}\right]\left[D_0^{(e)}\right] \rightarrow \left[F_{i(r)}^{(e)}\right] \quad r = 1 \cdots 6$$

Where

i(1), the number of the first node of element.
i(2), the number of the second node of element.
i(3), the number of the third node of element.
i(4), the number of the fourth node of element.
i(5), the number of the fifth node of element.
i(6), the number of the sixth node of element.

and

$$[H] = \iint [B]^T \left[E^{(e)}\right][B] dxdy \tag{14}$$

The calculated $\left[F_i^{(e)}\right]$ matrix is added to the global force matrix.

6.3. Force of Inertia

Denote (u (t), v (t)) as the time-dependent displacement of any point (x, y) in element *e*, the force of inertia per unit area is:

$$\Pi_i = -M\frac{\partial^2}{\partial t^2}\begin{bmatrix} u(t) \\ v(t) \end{bmatrix} = -M\left[T^{(e)}\right]\left[X^{(e)}\right]\frac{\partial^2 D_t}{\partial t^2} \tag{15}$$

where M is the mass per unit area. The potential energy of the inertial force of an element *e* is

$$\Pi_i = -M\left[D^{(e)}\right]^T \iint \left[X^{(e)}\right]^T \left[T^{(e)}\right]^T \left[T^{(e)}\right]\left[X^{(e)}\right]\frac{\partial^2 D_t}{\partial t^2}\, dxdy \tag{16}$$

It is easy to show that the inertial force matrix is of the same form as that of the original DDA then, one can write:

$$\begin{aligned} &\frac{2M}{\Delta t^2}\left[X^{(e)}\right]^T \iint \left[T^{(e)}\right]^T \left[T^{(e)}\right] dxdy \left[X^{(e)}\right] \rightarrow \left[K^{(e)}_{i(r)\,i(s)}\right] \\ &-\frac{2M}{\Delta t}\left[X^{(e)}\right]^T \iint \left[T^{(e)}\right]^T \left[T^{(e)}\right] dxdy \left[X^{(e)}\right]\left[V_0^{(e)}\right] \rightarrow \left[F^{(e)}_{i(r)}\right] \end{aligned} \qquad r,s = 1\cdots 6 \tag{17}$$

where Δt is time interval of a step, and $\left[V_0^{(e)}\right]$ is the element velocity accumulated form previous time step. The integral of $\iint \left[T^{(e)}\right]^T \left[T^{(e)}\right] dxdy$ was calculated using the simplex method outlined by Shi [13].

6.4. Fix point

When a point (x, y) in an element *e* is to be fixed, a very strong constraint spring is used at that point. The energy of the constraint spring can be expressed as:

$$\Pi_f = P\left[D^{(e)}\right]^T \left[X^{(e)}\right]^T \left[T^{(e)}\right]^T \left[T^{(e)}\right]\left[X^{(e)}\right]\left[D^{(e)}\right] \tag{18}$$

where P is the stiffness of the constraint spring. Minimizing the above function with respect to the displacement variables determines the following sub-matrix which must be added to the global stiffness matrix:

$$P\left[X^{(e)}\right]^T \left[T^{(e)}\right]^T \left[T^{(e)}\right]\left[X^{(e)}\right] \rightarrow \left[K^{(e)}_{i(r)\,i(s)}\right] \qquad r,s = 1\cdots 6 \tag{19}$$

$\left[K^{(e)}_{i(r)\,i(s)}\right]$ is added to the global stiffness matrix.

Due to limitation in the length of paper the implementation of the contact matrix and the body loading matrix are not discussed in this paper.

7. VERIFICATION OF THE NEW MODIFIED DDA

The new second-order DDA code was developed in C++ environment. In the following sections the application of the modified DDA is presented for a typical example of Circular tunnel in an Infinite Elastic Medium.

The example presented below is used to demonstrate the displacement distribution around underground opening. This problem verifies displacements for the case of a circular tunnel in an infinite elastic medium subjected to a constant in-situ (compressive) stress. The problem geometry as depicted in Figure 4 and the analytical solutions to the problem are taken from classical Kirsch solution [14].

The stresses σ_r, σ_θ and $\tau_{r\theta}$ for a point at polar coordinate (r, θ) near the tunnel opening of radius 'a' (Figure 2) are given by:

$$\sigma_r = \frac{P_1 + P_2}{2}\left(1 - \frac{a^2}{r^2}\right) + \frac{P_1 - P_2}{2}\left(1 - \frac{4a^2}{r^2} + \frac{3a^4}{r^4}\right)\cos 2\theta \tag{21}$$

$$\sigma_\theta = \frac{P_1 + P_2}{2}\left(1 + \frac{a^2}{r^2}\right) - \frac{P_1 - P_2}{2}\left(1 + \frac{3a^4}{r^4}\right)\cos 2\theta \tag{22}$$

$$\tau_{r\theta} = -\frac{P_1 - P_2}{2}\left(1 + \frac{2a^2}{r^2} - \frac{3a^4}{r^4}\right)\sin 2\theta \tag{23}$$

where P_1, P_2 are far field stress in x and y directions and a is the opening radius.

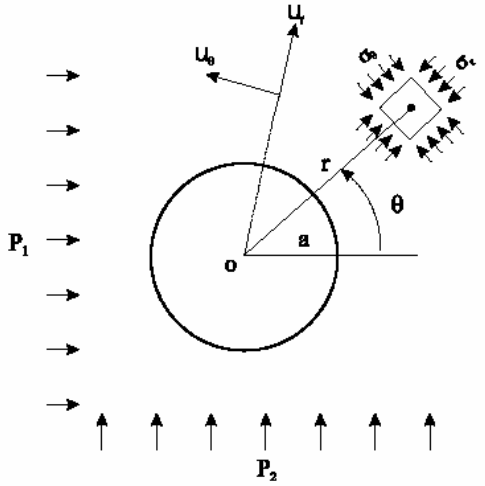

Figure 2. Cylindrical hole in an infinite elastic medium [14]

The radial (outward) and tangential displacement based on solution given in [14], assuming conditions of plane strain are given by:

$$u_r = \frac{P_1 + P_2}{4G}\left(\frac{a^2}{r}\right) + \frac{P_1 + P_2}{4G}\left(\frac{a^2}{r}\right)\left[4(1-\upsilon) - \frac{a^2}{r^2}\right]\cos 2\theta \tag{24}$$

$$u_\theta = -\frac{P_1 - P_2}{4G}\left(\frac{a^2}{r}\right)\left[2(1-2\upsilon) - \frac{a^2}{r^2}\right]\sin 2\theta \tag{25}$$

where G is the shear modulus and ν is the Poisson ratio.

To compare the result of DDA with a commercial FEM code, *Phase*^{2} (the powerful 2D elasto-plastic finite element stress analysis program for underground or surface excavations in rock) is used in this paper. The *Phase*^{2} model and boundary conditions is shown in Figure 3. A similar model was constructed with the modified DDA. The model geometry is illustrated in Figure 4.

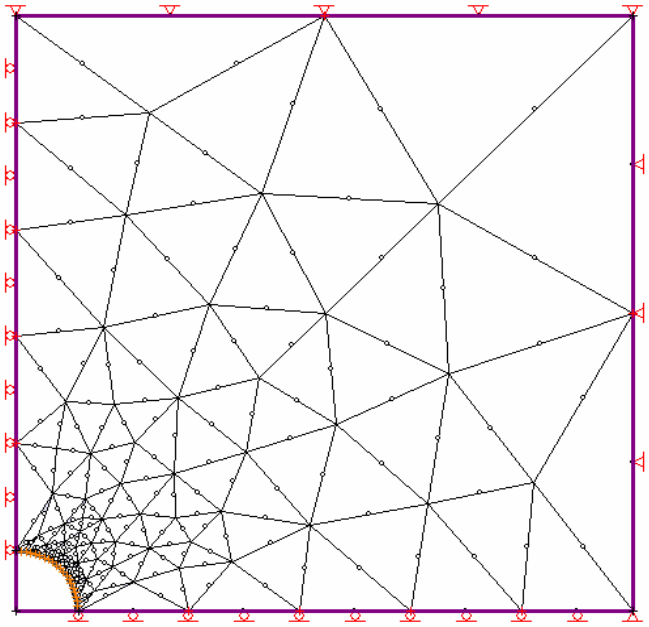

Figure 3 The constructed Phase2 Model and boundary condition

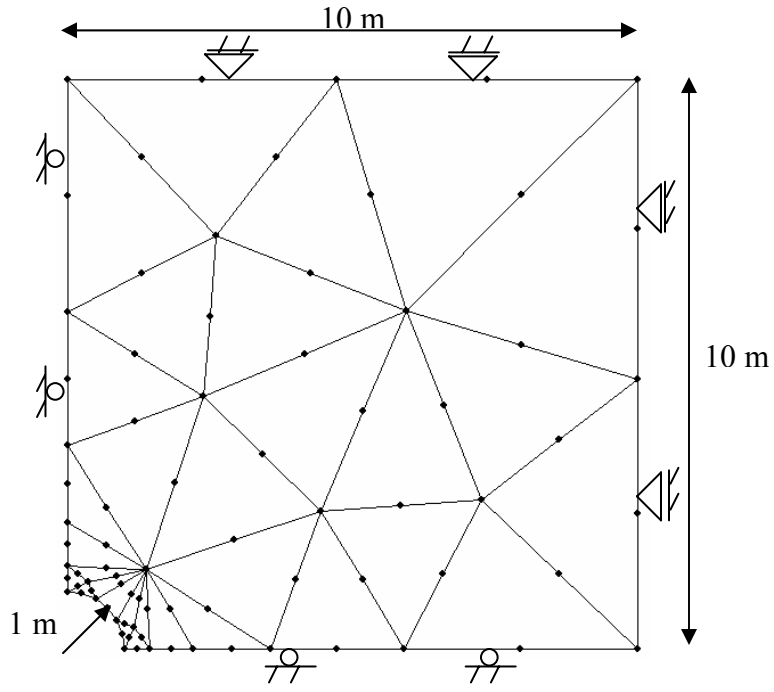

Figure 4 DDA model of a Circular tunnel in an infinite elastic medium

The input data used in the DDA analysis are as below:

$E = 6$ GPa, $\nu = 0.2$, $\sigma_{x0} = \sigma_{y0} = P_1 = P_2 = -30$ MPa and $r =$ 1 m.

Figure 5 shows the radial displacement contours calculated by new DDA. Figure 6 compares the radial displacement distribution obtained from the analytical solution, FEM (Phase2 code), and the modified DDA method.

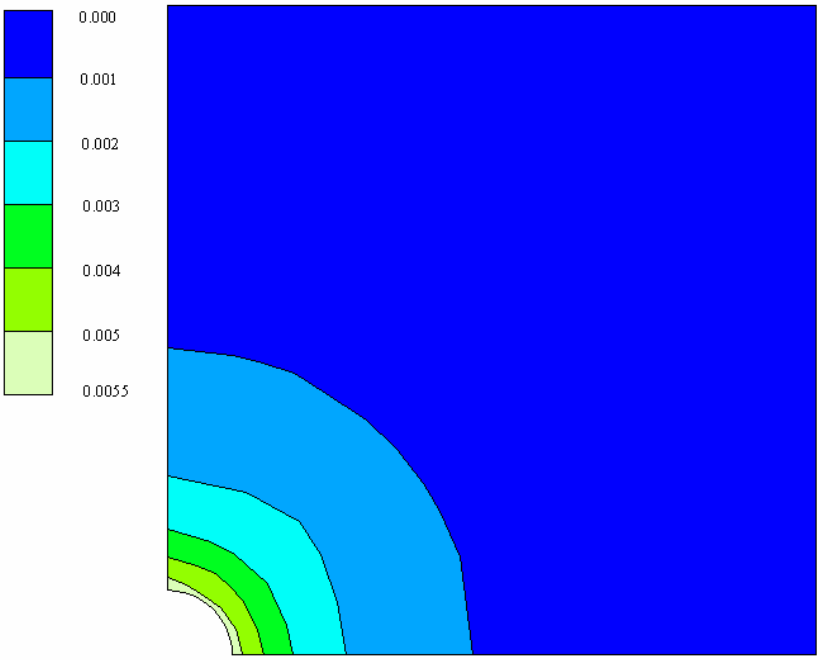

Figure 5 Total displacement distributions around the circular tunnel is calculated by DDA

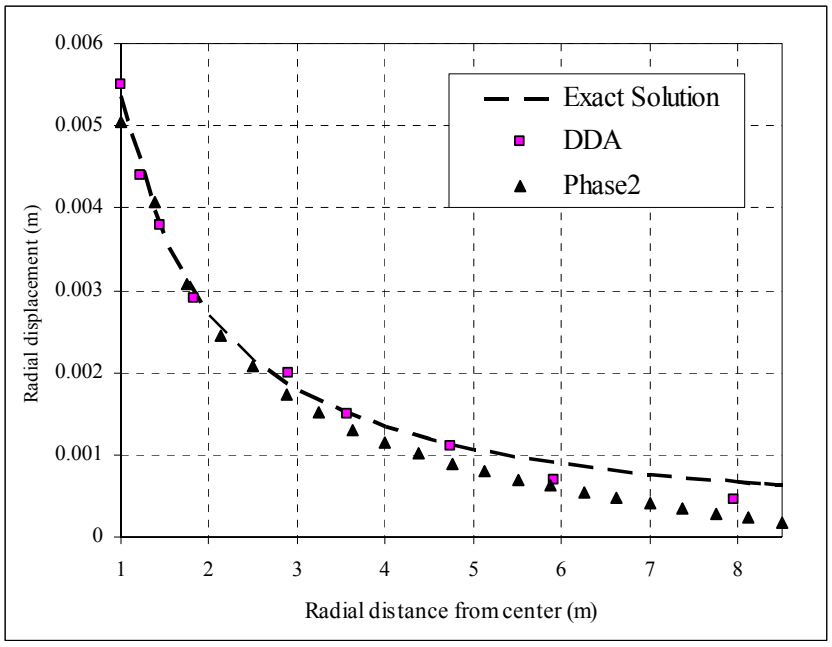

Figure 6 Comparison of u_r distribution for the circular tunnel in an infinite elastic medium

With regard to the obtained results, the modified DDA results are in good agreement with the analytical solution. At a distance of about 5 m from the opening wall the DDA solution slightly diverges from the analytical solution. This is due to a very course mesh used in this area. Comparing the discretization degree of Phase2 and DDA models, it is obvious that DDA with quadratic triangular mesh provides better results than the general CST elements employed within general FEM codes. Accordingly, considering the discontinuum modeling capabilities of DDA, the modified code, with further verifications, has great potential for modelling of practical problems.

8. CONCLUSIONS

The main purpose of using a finite element mesh within each block is to improve its deformation capability. By adding the finite element mesh into each block it is possible to take advantages of the continuum mechanics principles used in FEM and the discontinuum mechanics used by the DDA method. Coupling continuum and discontinuum mechanics allows for simulation of complex problems involving material fracturing, dynamic behavior and fluid flow. In this study, a more powerful version of DDA method was developed using the six-node triangular elements. This enhanced the deformation capability of DDA significantly, thus, making it a more suitable tool for accurate calculations and practical applications. The matrices of equilibrium equations for the high order DDA were outlined in detail for program coding. The successful application of the modified DDA to problem with known solutions was demonstrated. The calculated results show close agreement with the theoretical solutions, however, it is believed that more verification and refinement of the new DDA is required to make it a more useful tool for practical applications.

9. REFERENCE

1. Jing L, Hudson JA. Numerical method in rock mechanics. *International Journal of Rock Mechanics & Mining Sciences 2002*; 39: 409-427.
2. Wang Z, Lia Y, Wang S, Yang Z. Numerical simulation of the geomechanical processes in rock engineering. *International Journal of Rock Mechanics & Mining Sciences 2000*; 37: 499-507.
3. Shi GH, *Block System Modeling by Discontinuous Deformation Analysis*. Computational Mechanics Publication: Southampton. UK. 1993.
4. Lin CT, Amadei B, Jung J, Dwyer J. Extension of discontinuous deformation analysis for jointed rock masses. *International Journal of Rock Mechanics & Mining Sciences & Geomechanical Abstract 1996*; 33: 671-694.
5. Kim Y, Amadei B, Pan E. Modelling the effect of water, excavation sequence and rock reinforcement with discontinuous deformation analysis. *International Journal of Rock Mechanics & Mining Sciences 1999*; 36: 949-970
6. Ma MY, Zaman M, Zhu JH. Discontinuous Deformation Analysis Using the Third Order Displacement Function. *Discontinuous Deformation Analysis (DDA) and simulations of Discontinuous Media*. M. R. Salami and Don Banks Editor, 1996.
7. Koo CY, Chern JC. The development of DDA with third order displacement function. *Discontinuous Deformation Analysis (DDA) and simulations of Discontinuous Media*. M. R. Salami and Don Banks Editor.

8. Hsiung SM. Discontinuous Deformation Analysis (DDA) with nth Order Polynomial Displacement Functions. *38th U.S. Rock Mechanics Symposium*, July 7-10, Washington, DC, 2001.
9. Chang CT, Moteiro P, Nemati K, Shyu K. Behavior of marble under compression. *Journal of Material in Civil Engineering 1996*; 8:157-170 1996.
10. Jing L. Formulation of discontinuous deformation analysis (DDA) an implicit discrete element model for block systems. *International Journal of Engineering Geology 1998*; 49: 371–81.
11. Shi GH, Manifold method, *Discontinuous Deformation Analysis (DDA) and simulations of Discontinuous Media*. M. R. Salami and Don Banks Editor, 1996.
12. Chen G, Ohnishi Y, Ito T. Development of High-Order Manifold Method. *International Journal of Numerical Method in Engineering 1998*; 43: 685-712.
13. Shi GH. Simplex integration for manifold method, FEM, DDA and analytical analysis, *Discontinuous Deformation Analysis (DDA) and Simulation of Discontinuous Media*, TSI Press, Mexico, 1996..
14. Jaeger, J. C., and N. G. W. Cook. *Fundamentals of Rock Mechanics*, 3rd Ed. London: Chapman and Hall, 1976.

(This page intentionally left blank.)

DDA for Elastic Elliptic Element

Y. Ohnishi, S. Nishiyama, and S. Akao
Department of Urban and Environmental Engineering, Kyoto University, Kyoto, Japan
M. Yang
The Japan Research Institute Ltd, Tokyo, Japan
S. Miki
Kiso-Jiban Co., Ltd, Chiba, Japan

This paper was prepared for presentation at *ICADD-7, the Seventh International Conference on Analysis of Discontinuous Deformation*, held in Honolulu, Hawaii, December 10-12, 2005.

ABSTRACT: The Distinct Element Method (DEM) and Discontinuous Deformation Analysis (DDA) implicated a rigid disc element have been often applied to analyzing the behavior of granular materials and ground. However, stress states in materials are not evaluated directly because rigid disc elements have no deformation. We have developed an elastic elliptic element and have introduced to the DDA. The mathematical formulation for the elastic elliptic element has been attempted as an assumption that circular or elliptic element is deformed into an elliptic element. The formulation is also derived in a same manner with the original DDA where an element shape is polygon. In the formulation, main difference between an elliptic element and a polygon element is the treatment of the contact between elements. Judging from the some sample results, it is consider that the elliptic element DDA will be applied to an analysis of the ground behavior with large deformations characterized as a combination of continuous and discontinuous displacement.

1. INTRODUCTION

DEM implicated circular disc elements or spherical ball element is widely used for the analysis of granular mechanics in many fields [1, 2]. DDA implicated circular disc elements or spherical ball elements have been developed [3-5]. It has been also applied to the simulations of tri-axial compression test of granular materials [6], rock falls [7], and so on.

However, circular disc elements and spherical ball elements in these analysis codes are formulated as a rigid block, and many elements are demanded to simulate the behavior of granular materials. These codes have disadvantage that stress states in granular materials are not evaluated directly. In the DDA code, to handle many elements causes practical troubles about computation time and storages. Strictly speaking, it is not true discontinuous deformation analysis, because a rigid disc element has no deformation.

It is consider that deformable particle elements will save the number of elements in simulating the ground behavior with large deformations characterized as a combination of continuous and discontinuous displacement. It is useful to evaluate the stress states in granular materials directly. Therefore, we have introduced a deformable circular disc element to the DDA. In this paper, we have derived a basic formulation of the deformable circular disc element, and present analysis examples and applications.

2. ELLIPTIC DISC ELEMENT FOR DDA

2.1. Element shape function and sub-matrices

The formulation has been made as an assumption that circular and elliptic elements are deformed into elliptic elements. Assuming that (x_0, y_0) is the center of gravity of an elliptic element, the shape of an ellipse is represented by,

$$\begin{aligned} x &= R\ \cos\ s + x_0 \\ y &= R\ sin\ s + y_0 \\ R &= \frac{ab}{\sqrt{b^2\cos^2 s + a^2 sin^2 s}} \qquad 0 \le s \le 2\pi \end{aligned} \tag{1}$$

where a and b are the length of major and minor axis respectively, and s is an angular parameter. When only parallel translation (u_0, v_0) is involved, the displacement (u, v) at any point in the element are given by

$$\begin{pmatrix} u \\ v \end{pmatrix} = \begin{pmatrix} 1 & 0 \\ 0 & 1 \end{pmatrix} \begin{pmatrix} u_0 \\ v_0 \end{pmatrix} \tag{2}$$

When only rotation (r_0) of the element around the center (x_0, y_0) is involved, the shape of an element can exactly be represented by

$$\begin{aligned} x &= R\ \cos(s + r_0) + x_0 \\ y &= R\ sin(s + r_0) + y_0 \end{aligned} \tag{3}$$

For a small rotation r_0, the displacement due to the rotation is simplified

$$\begin{pmatrix} u \\ v \end{pmatrix} = \begin{pmatrix} -(y - y_0) \\ (x - x_0) \end{pmatrix} (r_0) \tag{4}$$

Assuming that (ε_x, ε_y) is the normal strains at the element along X and Y direction respectively. The displacement due to the normal strains are given by

$$\begin{pmatrix} u \\ v \end{pmatrix} = \begin{pmatrix} x - x_0 & 0 \\ 0 & y - y_0 \end{pmatrix} \begin{pmatrix} \varepsilon_x \\ \varepsilon_y \end{pmatrix} \tag{5}$$

When only shear strain (γ_{xy}) is involved, the shape of an element can be expressed by

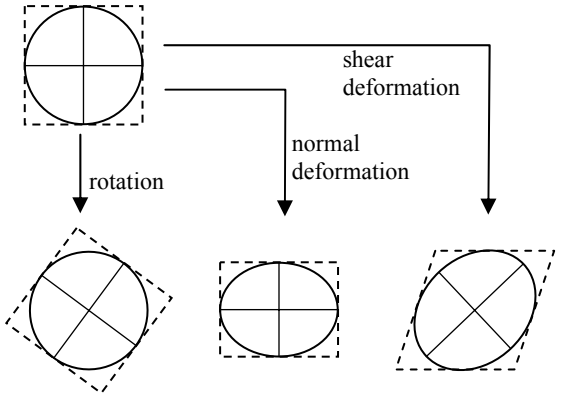

Fig. 1. Rotation and deformation of an ellipse

$$x = R\ \cos\left(s - \frac{\gamma_{xy}}{2}\right) + x_0$$
$$y = R\ \sin\left(s + \frac{\gamma_{xy}}{2}\right) + y_0 \tag{6}$$

Assuming small shear strain γ_{xy}, the displacements are simplified to the following equation.

$$\begin{pmatrix} u \\ v \end{pmatrix} = \begin{pmatrix} \frac{y - y_0}{2} \\ \frac{x - x_0}{2} \end{pmatrix} (\gamma_{xy}) \tag{7}$$

The total displacement (u, v) of the deformable elliptic element is the sum of displacement by parallel translation, rotation, normal strains and shear strain. Adding the matrices of Eq. (2), (4), (5) and (7), the element deformation matrix [$T(x, y)$] is obtained as follow.

$$\begin{pmatrix} u \\ v \end{pmatrix} = \begin{pmatrix} 1 & 0 & -(y - y_0) & x - x_0 & 0 & \frac{y - y_0}{2} \\ 0 & 1 & (x - x_0) & 0 & y - y_0 & \frac{x - x_0}{2} \end{pmatrix} \begin{pmatrix} u_0 \\ v_0 \\ r_0 \\ \varepsilon_x \\ \varepsilon_y \\ \gamma_{xy} \end{pmatrix} \tag{8}$$

$$= [T(x,y)][D]$$

The element deformation matrix [$T(x, y)$] in Eq. (8) is identical to that of a polygon element in original DDA [8]. Therefore, sub-matrices for the inertia force and various loading conditions are derived as a same manner with the original DDA. The differences between elliptic element DDA and polygon element DDA are area integration of an element in calculating sub-matrices. The area integration of an ellipse in Eq. (1) can be obtained analytically. The sub-matrices for the elliptic element are also added to the simultaneous equilibrium equations, and displacement and deformation are computed to solve the simultaneous equilibrium equations.

2.2. Contact between ellipse

In the formulation, main difference between an elliptic element and a polygon element is the treatment of the contact between elements. We have to know all pair of elliptic elements that could possibly collide during calculation. The measure of proximity between elliptic elements is

the characteristic length that is defined in a conventional way. As shown in Figure 2, an ellipse has following relation for any point P on the boundary,

$$L = PF + PF' = 2a \tag{9}$$

where point F and F' are two focuses of an ellipse, and a is the length of major axis. Assume that elliptic elements i and j are in contact. Denote F_i and F_i' are the focuses on the element i. L_{ij} is the minimum length of P_jF_i and P_jF_i', where P_j is the any point along the boundary of the element j. Assuming that a_i is the length of major axis in the element i, following discriminant are easily obtained.

$$\begin{aligned} L_{ij} > 2a_i \quad &\Rightarrow non-contact \\ L_{ij} = 2a_i \quad &\Rightarrow contact \\ L_{ij} < 2a_i \quad &\Rightarrow pentration \end{aligned} \tag{10}$$

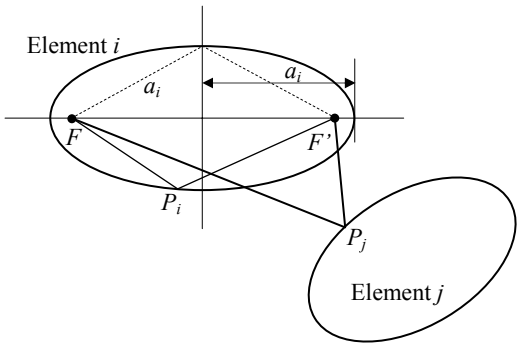

Fig. 2. Judgment of overlap between ellipses

If point P_j is inside the element i, L_{ij} is smaller than $2a_i$. Contrary, if point P_j is out of the element i, L_{ij} is always larger than $2a_i$. In practice, it is difficult to get minimum value of L_{ij} analytically. Therefore, iterative computing technique is used to obtain it. All pairs of elliptic elements, which have possibility to collide, are examined by using this relation.

2.3. Contact sub-matrices between elliptic elements

When inter-penetration is detected between elements after deformation, the penalty spring has to be attached to keep the penetration under allowance value. In this section, the contact sub-matrices for the elliptic element are derived.

Assuming that elliptic element i is just in contact with elliptic element j, these two elements share a common tangent. As shown in Figure 3, point $C_i(x_{ci}, y_{ci})$ and $Cj(x_{cj}, y_{cj})$ are intersections between the line, which is normal to the tangent and runs through the contact point, and the major axis of two elements respectively. Denote $P_i(x_{pi}, y_{pi})$ and $P_j(x_{pj}, y_{pj})$ are the contact points on the element i and j respectively. When inter-penetration occurs, penalty spring will be attached along the line C_iC_j and the penetration value will be controlled. If the penetration value is small, point C_i, C_j, P_i and P_j are assumed to be nearly on a line.

Assuming h_n and h_s are a displacement along the line C_iC_j and being normal to the line C_iC_j respectively, h_n and h_s are given by

$$\begin{pmatrix} h_n \\ h_s \end{pmatrix} = \begin{pmatrix} \cos\alpha & sin\alpha \\ -sin\alpha & \cos\alpha \end{pmatrix} \begin{pmatrix} u \\ v \end{pmatrix} = \begin{pmatrix} \ell_x & \ell_y \\ -\ell_y & \ell_x \end{pmatrix} \begin{pmatrix} u \\ v \end{pmatrix} \tag{11}$$

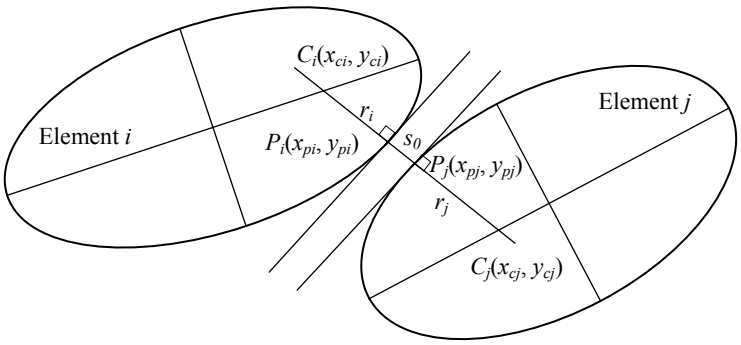

Fig. 3. Contact between elliptic elements

where $sin\alpha$ and $cos\alpha$ are as follows:

$$\begin{aligned} sin\alpha &= \frac{y_{cj} - y_{ci}}{G} = \ell_y \\ \cos\alpha &= \frac{x_{cj} - x_{ci}}{G} = \ell_x \\ G &= \overline{C_i C_j} \end{aligned} \tag{12}$$

The potential energy Π_k contributed to the penalty spring deformation is given by

$$\Pi_k = \frac{1}{2} k_p \left(s_0 + \left(s_j - s_i \right) \right)^2 \tag{13}$$

where k_p is stiffness of the penalty spring and s_0 is initial deformation of the spring. Denoting r_i=C_iP_i and r_j=C_jP_j, deformation s_i and s_j are expressed by

$$\begin{aligned} s_0 &= G - r_i - r_j \\ s_i &= \ell_x u_i + \ell_y v_i = \begin{pmatrix} \ell_x & \ell_y \end{pmatrix} \left[T_i(x_{pi}, y_{pi}) \right] \left[D_i \right] \\ s_j &= \ell_x u_j + \ell_y v_j = \begin{pmatrix} \ell_x & \ell_y \end{pmatrix} \left[T_j(x_{pj}, y_{pj}) \right] \left[D_j \right] \end{aligned} \tag{14}$$

The contact sub-matrices are obtained by minimizing the energy Π_k. By differentiating Eq. (13), we get following sub-matrices:

$$\begin{aligned} & k_p \left[T_i(x_{pi}, y_{pi}) \right]^T \begin{pmatrix} \ell_x & \ell_y \end{pmatrix}^T \begin{pmatrix} \ell_x & \ell_y \end{pmatrix} \left[T_i(x_{pi}, y_{pi}) \right] \rightarrow \left[K_{ii} \right] \\ & k_p \left[T_j(x_{pj}, y_{pj}) \right]^T \begin{pmatrix} \ell_x & \ell_y \end{pmatrix}^T \begin{pmatrix} \ell_x & \ell_y \end{pmatrix} \left[T_j(x_{pj}, y_{pj}) \right] \rightarrow \left[K_{jj} \right] \\ & -k_p \left[T_i(x_{pi}, y_{pi}) \right]^T \begin{pmatrix} \ell_x & \ell_y \end{pmatrix}^T \begin{pmatrix} \ell_x & \ell_y \end{pmatrix} \left[T_j(x_{pj}, y_{pj}) \right] \rightarrow \left[K_{ij} \right] \\ & -k_p \left[T_j(x_{pj}, y_{pj}) \right]^T \begin{pmatrix} \ell_x & \ell_y \end{pmatrix}^T \begin{pmatrix} \ell_x & \ell_y \end{pmatrix} \left[T_i(x_{pi}, y_{pi}) \right] \rightarrow \left[K_{ji} \right] \\ & -k_p s_0 \left[T_i(x_{pi}, y_{pi}) \right]^T \begin{pmatrix} \ell_x & \ell_y \end{pmatrix}^T \rightarrow \left[F_i \right] \\ & k_p s_0 \left[T_j(x_{pj}, y_{pj}) \right]^T \begin{pmatrix} \ell_x & \ell_y \end{pmatrix}^T \rightarrow \left[F_j \right] \end{aligned} \tag{15}$$

Sub-matrices in Eq. (15) are added to the simultaneous equilibrium equations, where $[K_{ij}]$ is 6x6 sub-matrix, and $[F_i]$ and $[F_j]$ are 6x1 sub-matrix.

When friction force or cohesion at the contact prevent shear displacement between elements, the elements have to be locked each other. The sub-matrices for locking shear displacement are also derived from Eq. (11), and the formulation is similar to deriving the contact sub-matrices. The sub-matrices for the lock are given by

$$
\begin{aligned}
&k_s\left[T_i(x_{pi},y_{pi})\right]^T[N]\left[T_i(x_{pi},y_{pi})\right]\rightarrow[K_{ii}]\\
&k_s\left[T_j(x_{pj},y_{pj})\right]^T[N]\left[T_j(x_{pj},y_{pj})\right]\rightarrow[K_{jj}]\\
&-k_s\left[T_i(x_{pi},y_{pi})\right]^T[N]\left[T_j(x_{pj},y_{pj})\right]\rightarrow[K_{ij}]\\
&-k_s\left[T_j(x_{pj},y_{pj})\right]^T[N]\left[T_i(x_{pi},y_{pi})\right]\rightarrow[K_{ji}]\\
&k_s\left[T_i(x_{pi},y_{pi})\right]^T[N]\begin{pmatrix}x_{pj}-x_{pi} & y_{pj}-y_{pi}\end{pmatrix}\rightarrow[F_i]\\
&-k_s\left[T_j(x_{pj},y_{pj})\right]^T[N]\begin{pmatrix}x_{pj}-x_{pi} & y_{pj}-y_{pi}\end{pmatrix}\rightarrow[F_j]\\
&[N]=[I]-\begin{pmatrix}\ell_x & \ell_y\end{pmatrix}^T\begin{pmatrix}\ell_x & \ell_y\end{pmatrix}
\end{aligned}
\tag{16}
$$

where k_s is the stiffness of the shear penalty spring and $[I]$ is 2x2 unit matrix. Sub-matrices in Eq. (16) are also added to the simultaneous equilibrium equations when the lock conditions are satisfied.

3. APPLICATIONS AND EXAMPLES

In order to illustrate effectiveness of the elastic elliptic element DDA, some simulations and a comparison between the results by the rigid disc DDA and the elastic ellipse DDA will be presented.

3.1. Loading test on the ground

First are the simulations of a loading test on the ground. In the simulations, the top face of granular materials was subjected to the loading by moving the plate downward on the materials, and simulations have been made for 5 models in Figure 4. The results after 1000 time step calculations are shown in Figure 4. In the figure, (a) shows the result by the rigid disc DDA, the others shows the results by the elastic ellipse DDA in this work. The thick and thin lines among disc elements in Figure 4(a) indicate the intensity of contact force among elements. Figure 4(b) shows results of the model where a shape of original particle was circular and particles were packed with a hexagonal structure. Figure 4(c), (d) and (e) shows the results of the models where a shape of particle was ellipse. Drawn stress crosses in the figure were normalized by the maximum stress. The parameters used in the simulations are presented in Table 1. In loading, the bearing plate *AB* in Figure 4(a) was moved downward with a constant displacement rate (2.0m/s). In the models, width of a bearing plate was adjusted to being in contact with 3 elements.

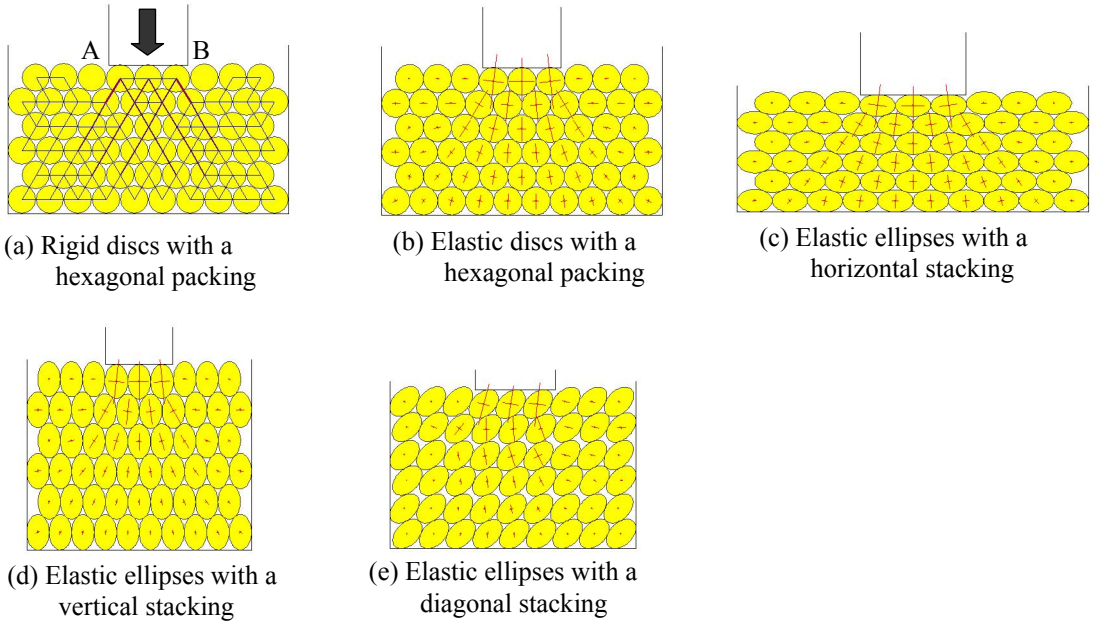

Fig. 4. Displacement and stress (contact force) distribution after 1000 time step calculation

In the elliptic elements model, stresses have remarkably presented anisotropic distributions related to the orientation of particles. It is considered that stress distributions of the results are appropriate. The circular elements in initial state have been deformed into elliptic elements after loading as shown in Figure 4(a). Figure 5 shows the relation between displacement (settlement) of the bearing plate and total contact force acting to the bearing plate. The rigid disc element DDA and the elastic ellipse DDA have showed different force-displacement curves. The force-displacement curves also have depended on a shape of particles, packing structure, and orientation of particles.

Table 1. Parameters for the simulations

	Rigid disc	Elastic disc	Elastic ellipse
Original size(m)	r=1.0(radius)		a=1.25, b=0.8
Density(kg/m^3)	2700		
Young's modulus(GPa)		10.0	
Poisson's ratio		0.45	
Contact spring(MN/m)	100.0		
Friction angle(deg)	0.0		
Max. time increment(s)	0.00005		

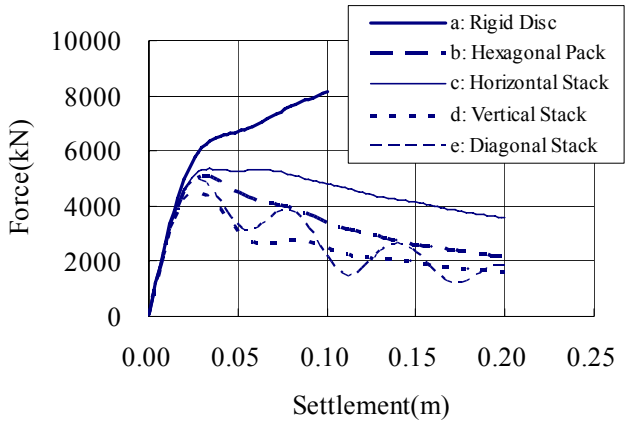

Fig. 5. Relation between force and displacement (settlement) for the simulation models in Figure 4

3.2. Compression test

Second illustrations are the simulations of compression test of the columnar or prismatic specimen. In the simulations, the specimens, its height was 34.775cm, were composed by 780 circular elements with a hexagonal packing structure. A diameter of the elements was 1cm, and its density was 2700kg/m^3. The rigid disc DDA and the elastic ellipse DDA were applied to the simulation. In case of the elastic ellipse DDA, Young's modulus of the elements was 1MPa, and Poisson's ratio was 0.45. A stiffness of the contact spring was 1kN/m^2, and a friction angle between elements was 20 degrees. The specimens were subjected to the monotonic loading by the top and bottom cap with a constant displacement rate (2.0cm/s) as shown Figure 6(a).

Figure 6(a) and (b) show the results after 5000 time step calculations by the rigid disc DDA and the elastic ellipse DDA respectively. In the both results, each displacement of the specimen was about 1.0cm. In case of the rigid disc DDA, two diagonal shear slip lines were observed, however shear slip lines were obscure in the results by the elastic ellipse DDA. Figure 6(c) shows the relations between displacement of the end cap and total contact force acting to the end cap. The diagonal shear slip lines in Figure 6(a) became visible around the peak *B* on the force-displacement curve in Figure 6(c). The displacement of granular materials, which are composed of rigid particles, is represented by an accumulation of slippages among particles. In case of elastic particles, both a slippage among particles and the deformation of particles contribute to the displacement. It is considered that relative slippages among elastic particles are small than that among rigid particles for the same displacement. Therefore, shear slip lines were obscure in the results by the elastic ellipse DDA.

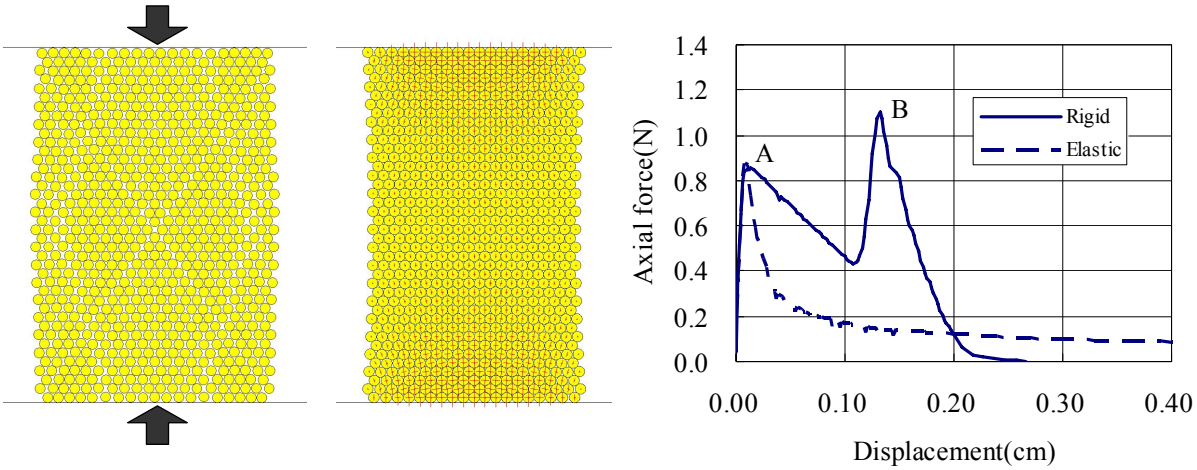

(a) Rigid disc elements (b) Elastic elliptic elements (c) Relation between axial force and displacement

Fig. 6. Deformation of the specimen after axial loading and the relation between axial force and displacement

4. CONCLUSIONS

In this work, an elastic elliptic element for the DDA has been developed, and applicability to geotechnical problems was presented. A comparison between the results by the rigid disc DDA and the elastic ellipse DDA was also presented.

The following conclusions can be obtained;

(i) The mathematical formulation for the elastic elliptic element has been attempted as an assumption that circular or elliptic element is deformed into an elliptic element. The formulation is also derived in a same manner with the original polygon DDA.

(ii) The applicability to geotechnical problems of the elastic ellipse DDA have been confirmed by the simulations. It appears that the elastic ellipse DDA will be applied to an analysis of the ground behavior with large deformations characterized as a combination of continuous and discontinuous displacement.

REFERENCES

11. Cundall, P.A. and O.D.L. Strack. 1979. A discrete numerical model for granular assemblies. *Geotechnique.* 29, No.1, 47-65.

12. ITASCA Consulting Group, Inc. 1995. *PFC-3D and Manuals*.

13. Ohnishi, Y. and S. Miki. 1993. Analysis of Granular Mechanics by DDA. In *DDA Research and Development Committee 8th meeting*. 35-38.

14. Ohnishi, Y. and S. Miki. 1996. Development of Circular and Elliptic Disc Elements for DDA. In *Proceedings of the First International Forum on Discontinuous Deformation Analysis (DDA) and Simulations of Discontinuous Media, Berkeley, 12-14, June 1996*, eds. M.R. Salami and D. Banks, 44-51.

15. Ohnishi, Y., S. Nishiyama and S. Miki. 2003. Development of Spherical Element for DDA and Its Application. In *Proceedings of the Conference on Computational Engineering and Science, 8(1), Tokyo*. 171-176.

16. Ishikawa, T., K. Tamaki, Y. Ohnishi and S. Miki. 2004. Numerical simulation of shear tests with DDA considering change of pore pressure in granular materials. In *Proceedings of the ISRM International Symposium 3rd ARMS, Kyoto*, eds. Y. Ohnishi and K. Aoki. 1227-1232.

17. Fukawa, T., Y. Ohnishi, S. Nishiyama, M. Yang, H. Fukumori, K. Yonezu and S. Miki. 2004. The application of 3-dimensional DDA with spherical rigid block to rockfall simulation. In *Proceedings of the ISRM International Symposium 3rd ARMS, Kyoto*, eds. Y. Ohnishi and K. Aoki. 1243-1248.

18. Shi, G.H. and R.E. Goodman. 1984. Discontinuous deformation analysis. In *Proceedings of the 25th U.S. Symposium on Rock Mechanics, Evanstone*, eds. C. H. Dowding and M. M. Singh. 269-277.

Preliminary consideration for analyzing ground deformation due to fault movement

OSADA, M.
Geosphere Research Institute, Saitama University, Saitama, JAPAN
TANIYAMA, H.
Department of Civil and Environmental Engineering, Saitama University, Saitama, JAPAN

This paper was prepared for presentation at *ICADD-7, the Seventh International Conference on Analysis of Discontinuous Deformation*, held in Honolulu, Hawaii, December 10-12, 2005.

ABSTRACT: This paper provides preliminary consideration for analyzing ground deformation resulting from fault movements by using discontinuous deformation analysis (DDA) technique. This is one of the applications of DDA to practical subject. As a first step, we examined the characteristics of fault movements from previous studies. As it turned out, it is necessary to consider the influence of dynamic friction on ground deformation. Then the procedure for incorporating the effect of velocity-dependent friction into DDA program is introduced. These considerations give a better idea to modeling of real properties of rocks and sediments and to setting boundary conditions and analytical conditions.

1. INTRODUCTION

Recently, construction of nuclear power plant on soft ground comes under review in Japan. In most situations, soft grounds are underlain by hard basement rocks with some faults and/or fractures in varying degrees. Larger faults can easily be detected by geographical and geological information. Therefore, an important structure can be set at a place of safety away from such large faults. However, there is no guarantee not to move relatively minor faults developed within a construction site. To discuss the right and wrong of the construction, it is necessary to study ground deformation due to fault movement.

To do this, we are considering using discontinuous deformation analysis as a tool to evaluate an extent of ground deformation. For studying ground deformation due to fault movement, numerical methods on the basis of elastic dislocation theory [e.g., 1] and finite element method [e.g., 2] have been used. However, it is known that discontinuous deformation behaviors are distinguished when deformations on the surface along a fault were investigated by field surveys and by excavating trenches. Therefore these kinds of discontinuous deformations should be considered in a numerical simulation. Konagai and Johansson [3] have developed two-dimensional Lagrangian particle finite difference method for analyzing large deformations of soils. This method is useful to analyze ground deformation with a dip-slip fault. But actual shear behavior is three dimensional one. Thereby we choose discontinuous deformation analysis (DDA), which is expected to extend into three dimensional one [e.g., 4 - 6].

This paper summarizes the extent of ground deformation resulting from faulting and discusses how a model should be constructed and how analytical conditions should be set in this numerical simulation.

2. TWO REPRESENTATIVE EXAMPLES FOR DISCONTINUOUS DEFORMATIONS

Firstly, two representative examples are introduced to show that the ground has been deformed associated with earthquake surface faults. One is a world-famous fault, Neodani Fault, and another is Nojima Fault.

2.1. Neodani Fault

This fault is exposed to the textbook of Scholz [7, p.162], and is one of the earthquake surface faults at the 1891 Nobi Earthquake (8.0 Richter magnitude). Even now, the fault scarp can clearly be seen at Midori district in Neodani village. This fault scarp was formed as a result of block movement along the fault. Figure 1(a) shows cross section of the fault in the conservation center constructed on the part of the fault. Vertical displacement over 6 m can be seen and soft grounds are cut by the fault. Figure 1(b) shows the schematic drawing of relative movement around this district. The triangular part, which is pinched between nearly N-S and NW-SE faults including Mt. Nishi uplifted repeatedly by every earthquakes, was displaced upward associated with sinistral oblique slip of the fault, as like Mode III fracture. It is just evidence that this part is formed by block movement.

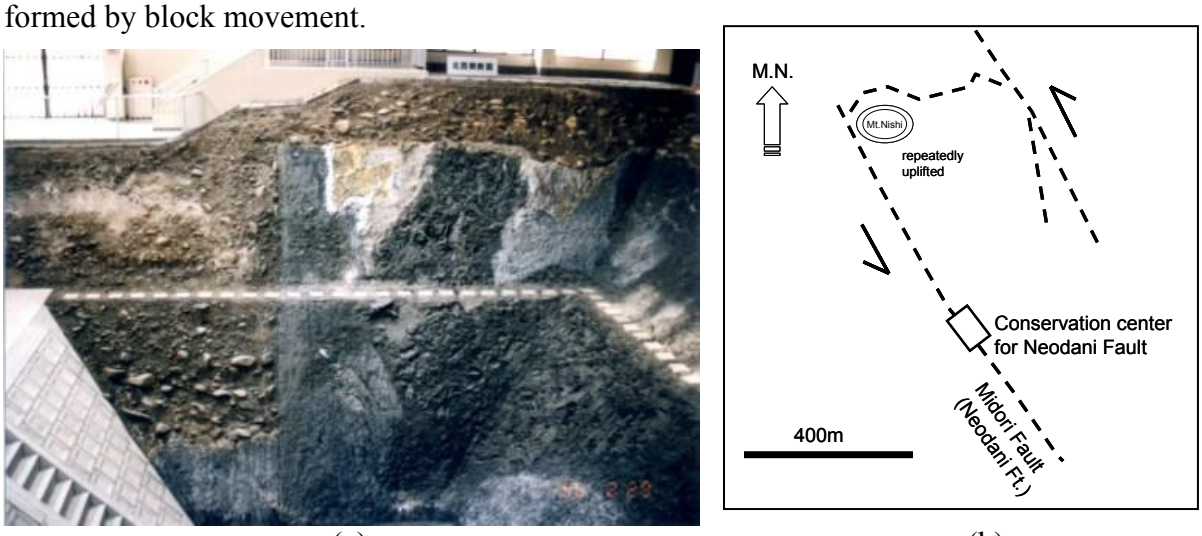

(a) (b)

Figure 1. Neodani Fault. (a) photograph of cross-section at trench taken in the conservative center, (b) schematic drawing of the fault movement.

2.2. Nojima Fault

The Hyogoken-Nanbu Earthquake (7.2 Richter magnitude) hit the metropolitan area around Kobe in the early morning of 17 January 1995. An earthquake surface fault, Nojima Fault, came out along western shoreline of Awaji Island, which is located at south-west of the epicenter. Figure 2 is photographs taken in the conservation center of Nojima Fault. It can be seen local differences in displacement. In Figure 2(a), apparent vertical displacement occurs along one surface of this fault. On the other hand, the fault branches into two surfaces with different vertical displacements as shown in Figure 2(b).

It is thought that these kinds of discontinuous movements in ground are not special, rather dominant near the earth's surface because a number of faults and fractures are developed near the surface. Therefore, it is necessary to direct the eye to also these kinds of discontinuous behavior in order to consider the displacement behavior of surface ground for constructing important structures on the surface.

(a)

(b)

Figure 2. Photographs of Nojima Fault taken in the conservation center. (a) a fault plane with apparent vertical displacement of ca.50 cm. (b) a fault is diverged into two faults with different displacements.

3. EXTENT OF THE IMPACT FOR FAULT MOVEMENT

In order to construct a model for analyzing ground deformation, some relationships about fault characteristics are needed to be considered:

- length versus width
- length versus displacement
- effect of thickness of covering sediments

3.1. Relation between fault length and fault width

There are a lot of previous researches studying about relationships between fault length and fault width in fields and laboratories. From field surveys, it is often reported that zones with high fracture density can be found in the vicinity of relatively large faults [e.g., 8]. Fracture distribution along the Atera fault has been investigated by Ohshima and Yoshida [9]. They found that the width of a zone with high fracture density is about 250 m measured vertical to the fault. It is thought that their results indicate the width of process zone [10] associated with initial and reactivated faulting. It is certain that the mechanically weak zones are formed along a fault. These fractures presumably help a fault branch easily when an earthquake occurs.

In addition, Hitomi et al. [11] provides an interesting result about positional relationship between earthquake surface faults and their lineaments. They investigated ten earthquake surface faults of Japan, and 'maximum discrepancies', which are maximum differences in distance between fault traces (lineaments) and earthquake surface faults observed, were measured. The results show that maximum discrepancies are within 300 m for dip-slip faults of 93% and within 100 m for strike-slip faults of 86%. For plain part of dip-slip faults, the maximum value extends to 800 m. This is good and practical information for estimating the extent of the impact of fault movement.

3.2. Relation between fault length and maximum displacement

Displacements along a fault taper off gradually towards both the fault tips [12]. Scholz et al. [10] concludes that fault growth is a self-similar process in which fault displacement scales linearly with fault length. Displacement – length data with wide range of fault length are compiled by Schulz and Fussen [13].

The relationships between fault length and maximum fault displacement are primarily obtained from normal faults. Sano et al. [14] investigated the extent of the damage of 1999 Chi-Chi Earthquake in Taiwan, and reported that main thrust fault may be diverged into many smaller faults in the footwall of the fault. This description is consistent with the result of Hitomi et al. [11]. Lately, Davis et al. [15] investigated the relation between fault length and maximum fault displacement in the Ostler Fault, New Zealand, and then concluded that their data display the similar scaling.

3.3. Effect of thickness of covering sediments

Generally, elastic properties of sediments are smaller than those of basement rocks. When a fault is propagating into soft sediments, deformation pattern is expected to be changed depending upon the thickness of surface ground. This effect is examined with simulated materials like clay or sand. Tani and Oyama [16] conducted shear experiments using dry sand at varying thickness up to 400 mm. They found that widths of shear bands, which are defined by the distance from fault to the rim of Riedel shear, decrease a little bit as it becomes thick. The ratio of the width to the thickness of 400 mm is about unity.

The knowledge mentioned above is summarized conceptually in Figure 3.

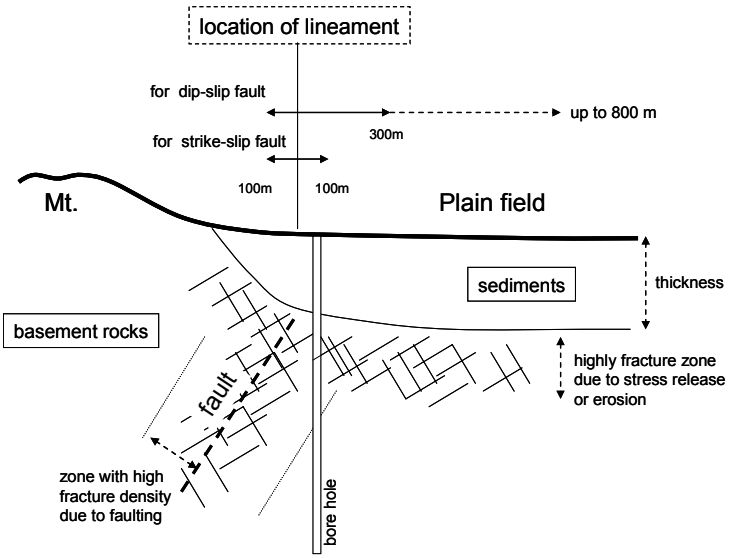

Figure 3. Conceptual model in the vicinity of a fault covered by sediments.

4. CONSTRUCTION OF MODEL FOR DDA

It is very difficult to simulate all the processes happening when an earthquake occurs. Here analytical domain for numerical simulation must be limited only the vicinity of the ground surface including hard basement rocks. The width of model can be determined on the basis of the results from Hitomi et al. and so on. Physical properties of basement rocks and grounds can be estimated from the information of borehole logging data and seismic profile data. And the thickness of covering sediments can also be given using the same information. Problem to be solved is how a forced displacement should be applied to the bottom of the analytical domain. Generally, the coefficient of friction is velocity-dependent. So this effect should be considered.

4.1. Velocity-dependent friction

Displacement rate along a fault is very high and in the order of 1m/sec. It is well known that the coefficient of friction is velocity-dependent. Although DDA scheme is dynamic analysis, the coefficient of friction is treated to be constant. Therefore the effect of velocity on friction should be built onto DDA code.

The frictional behavior of many rocks has been described by a slip distance and/or slip rate dependent constitutive laws. One possible constitutive equation is slip rate dependent constitutive law developed by Dieterich [17] and Ruina [18]. Their constitutive equation is given by Kanagawa [19] in the following simple way:

$$\mu = \frac{\tau}{\sigma} = \mu_0 + a \ln\left(\frac{V}{V_0}\right) + b\Theta \tag{1}$$

$$\frac{d\Theta}{dt} = -\frac{V}{L}\left\{\Theta + \ln\left(\frac{V}{V_0}\right)\right\} \tag{2}$$

where a, b, and L are experimentally determined constants, V is the slip velocity, τ, σ, and μ are shear stress, normal stress, and the coefficient of friction when the velocity is V. Θ is state variable of sliding surface, V_0 is the velocity at which the steady state friction is μ_0. In case of steady state $d\Theta/dt = 0$, the state variable at a steady state is

$$\Theta^{ss} = -\ln\left(\frac{V}{V_0}\right) \tag{3}$$

where the subscript ss shows steady state. By substituting (3) into (1), the coefficient of friction at a steady state can be written

$$\mu^{ss} = \mu_0 + (a-b)\ln\left(\frac{V}{V_0}\right) \tag{4}$$

Accordingly, the steady state friction velocity dependence is

$$\frac{d\mu^{ss}}{d(\ln V)} = a - b \tag{5}$$

and can be determined by experimental measurement of μ^{ss} at two different sliding velocities. In case that $a-b>0$, the frictional behavior is referred to as velocity-strengthening, and on the other hand, as velocity-softening in case that $a-b<0$. This constitutive equation does not

include the effect of velocity-independence in friction under very high velocity as pointed out by Shimamoto et al. [20]. As a first step of research, it is sufficient to use this constitutive equation.

4.2. Modification of DDA code

In DDA program, the velocity V at each contact edge is expressed by shear displacement in each time step. Because the shear displacements are obtained in open-close calculation before solving the equilibrium equation, it is easy to update the coefficient of friction at each contact edge. At this moment, V_0 is the velocity of each contact edge at the beginning of each time step.

Obviously, it is necessary to obtain the coefficient of friction for wide ranges of velocity by laboratory experiments and so on. Although one of the authors conducted shear experiments using large specimens for the purpose of evaluating rock slope stability [21], shear displacement is insufficient in order to obtain dataset of velocity and dynamic friction. In addition to previous shear experiments, Ichiba et al. [22] conducted experimental works on rapid flow of granular materials. This kind of result is expected to provide the information about velocity-dependent friction as an alternative method.

5. FURTHER WORKS

Philip and Megard [23] reported about 1969 Pariahuanca Earthquake in central Peru. They described detail deformational structures such as open fractures, en echelon shears and folds on Quaternary moraines and terraces. According to these descriptions, we need to learn about the three-dimensional deformation characteristics around a fault.

As a final goal of this study, mitigation measures should be proposed from an engineering point of view. Tani and Oyama [16] have proposed very interesting ideas which are to improve the surface ground so that ground deformation is dispersed and the individual displacements along faults are minimized. These ideas should be evaluated quantitatively using DDA method.

ACKNOWLEDGEMENT

This study was funded by JNES (Japan Nuclear Energy Safety Organization). This support is gratefully acknowledged.

REFERENCES

1. Ohtsuka, Y. 1978. Numerical analysis of ground or rock mass deformation associated with the displacement of earthquake fault, *Journal of Japanese Society of Engineering Geology*, Vol.19, No.2, 9-18 (in Japanese).
2. Kajikawa, S. and Y. Wakizaka. 1999. Displacement of ground surface caused by movement of faults buried undera alluvium and diluvium, In *Proceedings of Japanese Society of Engineering Geology*, 5-8 (in Japanese).
3. Konagai, K. and J., Johansson. 2001. Two Dimensional Lagrangian Particle Finite Difference Method for Modeling Large Soil Deformations, *Structural Eng./ Earthquake Eng*. 18(2), 91s-95s.
4. Shi, Gen-hua. 2003. Rock global stability estimation by three dimensional blocks formed with statistically produced joint polygons, In *Proceedings of ICADD-6, Development and Application of Discontinuous Modelling for Rock Engineering*, ed. Ming Lu, 3-11,Balkema.

5. Yeung, M.R., Jiang, Q.H. and Sun, N. 2003. Validation of block theory and three-dimensional diccontinuous deformation analysis as wedge stability analysis methods, *Int. Jour. Rock Mech. Min. Sci.*, Vol.40, 265-275.

6. Jiang, Q.H. and M.R. Yeung. 2004. A model of point-to-face contact for three-dimensional discontinuous deformation analysis, *Rock Mech. Rock Engng.*, 37(2), 95-116.

7. Scholz, C.H. 1990. *The mechanics of earthquakes and faulting*, Cambridge Univ. Press, 439pp.

8. Kojima, K., Y. Ohtsuka, and T. Yamada. 1981. Distributions of fault density and "fault dimension" in rockmass and some trials to estimate them, *Journal of Japanese Society of Engineering Geology*, Vol.22, No.1, 88-103 (in Japanese).

9. Oshima, A. and H. Yoshida. 2004. Character of fracture and influence area by active fault movement – A case study of the Atera fault, central Japan–, In *Proceedings of Japanese Society of Engineering Geology*, 325-328 (in Japanese).

10. Scholz, C.H., N.H.Dawers, J.-Z.Yu, and M.H. Anders. 1993. Fault growth and fault scaling laws: preliminary results, *Journal of Geophysical Research,* Vol.98,No.B12, 21951-21961.

11. Hitomi, Y., S. Shinagawa and Y. Wakizaka. 2000. Positional relationship between earthquake fault and their lineaments, In *Proceedings of Japanese Society of Engineering Geology*, 265-268 (in Japanese).

12. Muraoka, H. and H. Kamata. 1983. Displacement distribution along minor fault traces. *Journal of Structural Geology*, 5, 483-495.

13. Schultz, R.A. and H.Fossen. 2002. Displacement-length scaling in three dimensions: the importance of aspect ratio and application to deformation bands, *Journal of Structural Geology* , Vol.24, 1389-1411.

14. Sano, M., A.Nakasuji, and M.Taniuchi. 2000. Outline of earthquake faults caused by Chi-Chi earthquake in Taiwan. In *Proceedings of Japanese Society of Engineering Geology*, 261-264 (in Japanese).

15. Davis, K., D.W.Burbank, D.Fisher, S.Wallace, and D.Nobes. 2005. Thrust-fault growth and segment linkage in the active Ostler fault zone, New Zealand. *Jour. Struct. Geol.*, 27, 1528-1546.

16. Tani, K. and Y. Oyama. 2001. Analysis of shear zones structures developed in strike-slip fault ruptures and proposal of mitigation measures against structural damage by earthquake faulting, In *Proceedings of Japanese Society of Engineering Geology*, 47-50 (in Japanese).

17. Dieterich, J.H. 1979. Modeling of rock friction. 1.Experimental results and constitutive equations. *Jour. Geophys. Res.*, 84, 2161-2168.

18. Ruina, A. 1983. Slip instability and state variable friction laws, *Jour. Geophys. Res.*, 88, 10359-10370.

19. Kanagawa,K. 1996. Effects of pressure solution on the frictional properties of rocks: Experimental investigations, *Tectonics and Metamorphism (The Hara Volume)*, SOUBUN Co. Ltd., 304-313 (in Japanese).

20. Shimamoto,T., A.Tsutsumi, E.Kawamoto, M.Takahashi, R.Aoyagi, and Y.Ohtomo. 1996. Fault rocks and fault rheology: their progress and future perspectives, *Tectonics and Metamorphism (The Hara Volume)*, SOUBUN Co. Ltd., 314-331 (in Japanese).

21. Osada, M., Shrestha, S. K., T. Kajiyama and K.Yamaguchi. 2004. Application of Rock Mass Integration Method (RMIM) with DDA modeling in Rock Slope Stability, In *3rd ARMS, Contribution of Rock Mechanics to the New Century*, Kyoto, Dec., 1257-1262.

22. Ichiba k., K. Iwashita and M. Oda. 2005. Experimental study on stress ratio in rapid granular shear flow, *Powders & Grains*, Garcia-Rojo, Herrmann and McNamara (eds.), 751-755.

23. Philip, H. and F. Megard. 1977. Structural analysis of the superficial deformation of the 1969 Pariahuanca Earthquakes (Central Peru), *Tectonophysics*, 38, 259–278.

Dynamic back analysis of structural failures in archeological sites to obtain paleo-seismic parameters using DDA

Kamai, R. and Hatzor, Y.H.

Department of Geological and Environmental Sciences, Ben Gurion University of the Negev, Beer – Sheva, 84105, Israel.

This paper was prepared for presentation at *ICADD-7, the Seventh International Conference on Analysis of Discontinuous Deformation*, held in Honolulu, Hawaii, December 10-12, 2005.

ABSTRACT: The numerical Discontinuous Deformation Analysis (DDA) method was used for back analysis of structural failures in archaeological sites along the active Dead Sea rift system in Israel and preliminary constraints on historical seismic ground motions were obtained.

Two validations were first performed for calibration purposes: 1) The well studied case of a block on an inclined plane was re-studied and a much greater accuracy was obtained for the dynamic case with respect to previous publications, 2) The dynamic displacement of the foundation of a structure was simulated by inducing time-dependant displacements into the foundation block and studying the response of the overlying block.

Two case studies are presented in the paper, in which historic masonry structures were modeled and both synthetic and real earthquake records were applied as loading functions. The response of the structures was studied up to the point of incipient failure in a mechanism similar to the one observed in the field.

In both case studies the dynamic analysis was found to provide more complete and accurate results than the pseudo-static solution. Therefore, we believe that such an approach can be employed, where relevant, to provide constraints on paleo-seismic ground motions and consequently on expected PGA values in seismically active regions.

1. INTRODUCTION

1.1. Research Objectives

In this research we present an alternative method for obtaining strong ground-motion data: by back analysis of structural failures in archaeological sites using numerical analysis by the DDA method [1]. The results of this research will provide constraints on PGA estimates, generated by the existing seismological strong motion catalogue in Israel.

In this work we focus on man-made masonry structures such as towers and arches, where hewn stones forming the building create an initial geometrical network of reference. When failure is confined to displaced blocks within an otherwise intact structure, block displacement is measurable and a mechanical analysis is possible; this can not be achieved in a completely collapsed structure. Therefore, several archaeological sites In Israel were examined for confined structural failure, and two case studies were chosen for the preliminary analysis: The Nabatean cities of Avdat and Mamshit.

2. VALIDATIONS

DDA Validation studies were performed for calibration purposes only, all with respect to analytical solutions. Section 2.1 repeats cases that have been validated before, yet sometimes with greater accuracy here. Section 2.2 is a new development of a validation that has never been performed before.

2.1. Block on an Incline

Block displacement as a function of time has been studied by many researchers, since a well known analytical solution for displacement of a point mass is readily available. The case of a single block on an incline is perhaps the most studied [2].

2.1.1. Gravitation only

For a single block resting on a plane inclined at an angle α with friction along the interface ϕ, and subjected to gravitational acceleration g, the analytical solution for displacement d as a function of time t is given by:

$$d(t) = \frac{1}{2}at^2 = \frac{1}{2}\left(g\sin\alpha - g\cos\alpha\tan\phi\right)t^2 \quad (1)$$

The inclination of the modeled plane is 28° (Figure 1), and five friction angles are studied, ϕ =5°, 10°, 15°, 20°, 25°. The accumulated displacements are calculated up to 1sec.
Comparison between analytical and DDA solutions is shown in Figure 1.

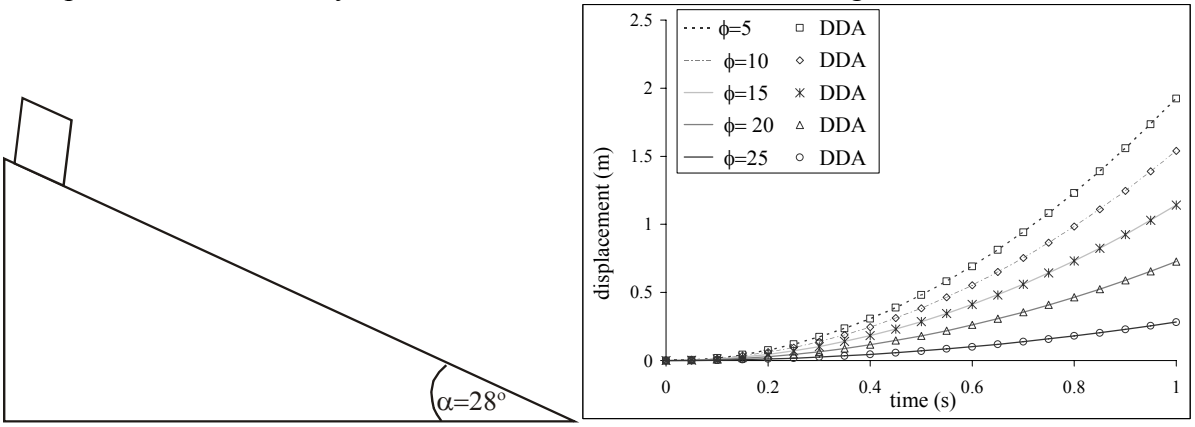

Figure 1.**A.** The model used for DDA validations of a block on an incline **B.** Block displacement – gravitational loading only. Comparison between analytical (solid line) and DDA (symbols) solutions.

2.1.2. Dynamic loading

The case of a single block on an inclined plane, subjected to both gravitational load and horizontal sinusoidal acceleration, has first been examined by Hatzor and Feintuch [3] for an acceleration function consisting of a sum of up to three sines. Hatzor and Feintuch found that the accuracy of DDA prediction was within 15% of the analytical solution, provided that the numerical control parameters g1, g2 were carefully optimized, without application of any damping [(1)].

(1) Note that in the analytical solution published by Hatzor and Feintuch (2001), the resisting force during sliding for $a_t > a_{yield}$ was neglected in the double integration.

Tsesarsky et al. [4] broadened the investigation and compared DDA results with physical results of shaking table experiments, for which an introduction of 1.5% damping was found to reduce the error significantly.
In this section, the presented validation is for an acceleration function of one sine only.
The displacement *d* of the block at any time *t* is determined by double integration on the acceleration, with θ as reference datum:

$$d = \int_{\theta}^{t} v = \iint_{\theta} a = g\left[\left(\sin\alpha - \cos\alpha\tan\phi\right)\left(t^2/2 - \theta t\right)\right] +$$

$$+ \frac{ag}{\varpi^2}\left[\left(\cos\alpha + \sin\alpha\tan\phi\right)\left(\varpi\cdot\cos(\varpi\theta)(t-\theta) - \sin(\varpi t) + \sin(\varpi\theta)\right)\right] \qquad (2)$$

where θ is the elapsed time from beginning of shaking until yield acceleration is reached and block motion ensues.
The model is similar to the one presented in Figure 1, but with a plane inclination of 20°. Three friction angles are studied: ϕ =20°, 22°, 30°, and the accumulated displacements are computed. Figure 2.A displays the case of $\alpha=\phi=20°$, for which yield acceleration is zero, and displacement is calculated for more than a full cycle of the input sinusoidal earthquake. The higher friction angles, ϕ =22°,30° have θ = 0.089sec. and 0.1802sec. respectively, which complicates the analytical solution after half a cycle. For that reason, the accumulated displacements in Figure 2.B for ϕ =22° and 30° are calculated up to ~2.5 seconds.

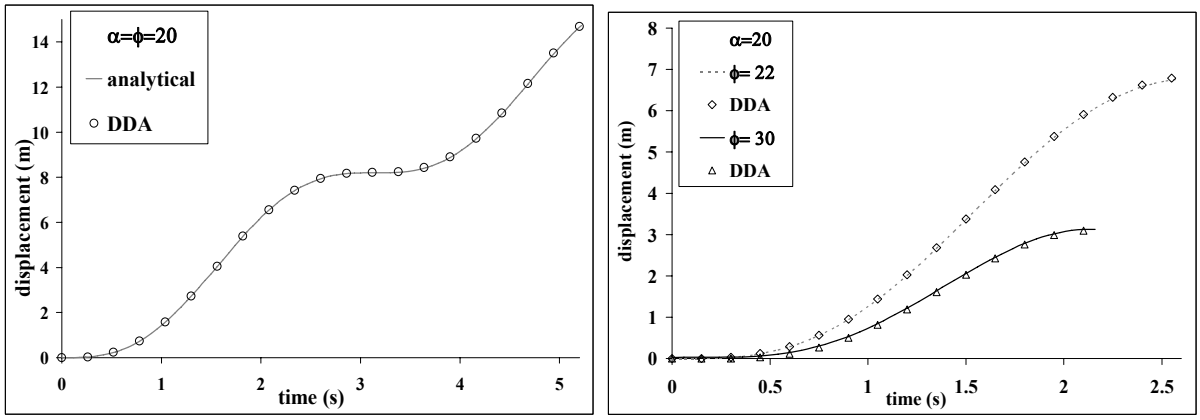

Figure 2.**A.** Block displacement versus time, for the case of α=ϕ=20. Comparison between analytical (solid line) and DDA (symbols) solutions. **B.** Block displacement versus time, for the case of α<ϕ.

Figure 2.**A** and **B**. present a comparison between DDA and analytical solutions. The obtained agreement is remarkable, with maximum displacement errors ranging between 0.2% and 0.9%. The time-step size is kept constant in all DDA runs, 0.002 sec.

2.2. Block response to induced displacements in the foundation

DDA allows application of time-dependant displacements to "fixed" points in the mesh which are defined and positioned by the user. We use this feature to simulate seismic ground motions at the foundation and to investigate the response of a masonry structure, later in this work.
We start with a validation. The purpose of this validation is to examine the accuracy of this DDA feature by comparing it to an analytical solution which is developed here for the response of a single block resting on a block which is subjected to a time-dependent displacement function.
For the validation, the block system consisted of three blocks: the fixed foundation block (no.0), the induced block (no.1), and the responding block (no.2) (see Figure 3). The displacement function for block 1 was in a form of a cosine function, starting from 0:

$$d(t) = D(1-\cos(2\pi\omega t)) \quad (3)$$

and the corresponding response of block 2 was investigated.

In order to compare between DDA and the analytical solution, the mode of failure of the analyzed block in DDA had to be constrained to sliding in one direction only without rotation or vertical motions. One way for constraining DDA to one degree of freedom in our case is by generating a block system in which block 2 has limited motion options. The block system was generated therefore such that the responding block had a very slender geometry and therefore its preferred displacement mode was one dimensional sliding with no rotation or bouncing, namely one degree of freedom, as in the analytical solution.

Figure 3. The DDA block system which constrains Block 2 to one degree of freedom – horizontal sliding only. Block 0 is the foundation block, Block 1 receives the dynamic input motion (horizontal – cyclic), and Block 2 responds.

2.2.1. The analytical solution

The analytical solution for this case must be computed in time steps, since the relative velocity and the direction of the force are dependant on each other. The analysis was performed by Matlab 7.0.
Figure 3 presents two blocks: The basement block (Block 0) is fixed, Block 1 is subjected to a horizontal displacement input function, and Block 2 responds dynamically.
The only force acting on Block 2 other than gravity is frictional, which immediately determines its acceleration:

$$m_2 a_2 = F_{friction} \quad (4)$$

$$\downarrow$$

$$m_2 a_2 = \mu \cdot m_2 g \quad (5)$$

$$\downarrow$$

$$a_2 = \mu \cdot g \quad (6)$$

The direction of the driving force is determined by the direction of the relative velocity between Blocks 1 and 2 (v_1*). When Block 1 moves to the right relative to Block 2, the frictional force pulls Block 2 in the same direction, and determines the sign of a_2.
When Block 2 is at rest in relation to Block 1, the friction force is determined by the acceleration of the Block 1 (a_1). The threshold acceleration, under which the two blocks move in harmony, is equal to the friction coefficient multiplied by the gravitation acceleration (μg). When the acceleration of Block 1 passes the threshold value, the frictional forces act in the same direction as a_1.
The positive direction is determined by the sign convention in Figure 3, and the relative velocity of Block 1 is given by:

$$v_1^* = v_1 - v_2 \tag{7}$$

The direction of the acceleration of Block 2 is set by the following boundary conditions and inequalities:

$$\begin{array}{llll} \textit{if} \quad v_1^* = 0 & \textit{and} \quad |a_1| < \mu g & & a_2 = a_1 \\ & \textit{and} \quad |a_1| > \mu g & \textit{and} \quad a_1 > 0 & a_2 = \mu g \\ & & \textit{and} \quad a_1 < 0 & a_2 = -\mu g \\ \textit{if} \quad v_1^* \neq 0 & & \textit{and} \quad v_1^* > 0 & a_2 = \mu g \\ & & \textit{and} \quad v_1^* < 0 & a_2 = -\mu g \end{array} \tag{8}$$

2.2.2. The numerical analysis

A sensitivity analysis for amplitude, frequency and friction was performed. Accumulating displacement of Block 2 was calculated, and comparison between DDA and Matlab results are presented in Figure 4.

Figure 4.**A** presents the response of Block 2 to changing amplitudes of motion (D), with constant input frequency of 1Hz. The accumulating displacement is in direct proportion to the amplitude, as expected. Note that the three displacement curves follow the periodic behavior of the induced displacement function (T = 1 sec.), and that divergence between curves starts after 0.25 sec., where the displacement function has an inflection point.
Figure 4**.B** presents the response of block 2 to changing frequencies. Although the displacement amplitude is constant (2cm), the acceleration amplitude ($A=D\omega^2$) increases with increasing frequency (Eq. 2). The displacement curves follow the different periods of motion, and the accumulating displacement is in direct proportion to the amplitude of the acceleration.
Figure 4.**C** presents the response of Block 2 to changing friction coefficients, with a constant displacement function of *D=0.5m, f=1Hz*. Note that the accumulating displacement is in direct proportion to the friction coefficient up to 0.5sec., where the induced displacement function changes direction. After that point the accumulating displacement of μ=0.6 is larger than μ=1, since the high friction works in both directions: forward and backward. Note that μ=0.1 and μ=0.6 follow the periodic behavior of the displacement function, whereas μ=0.6 is in a delay of about 0.25sec.

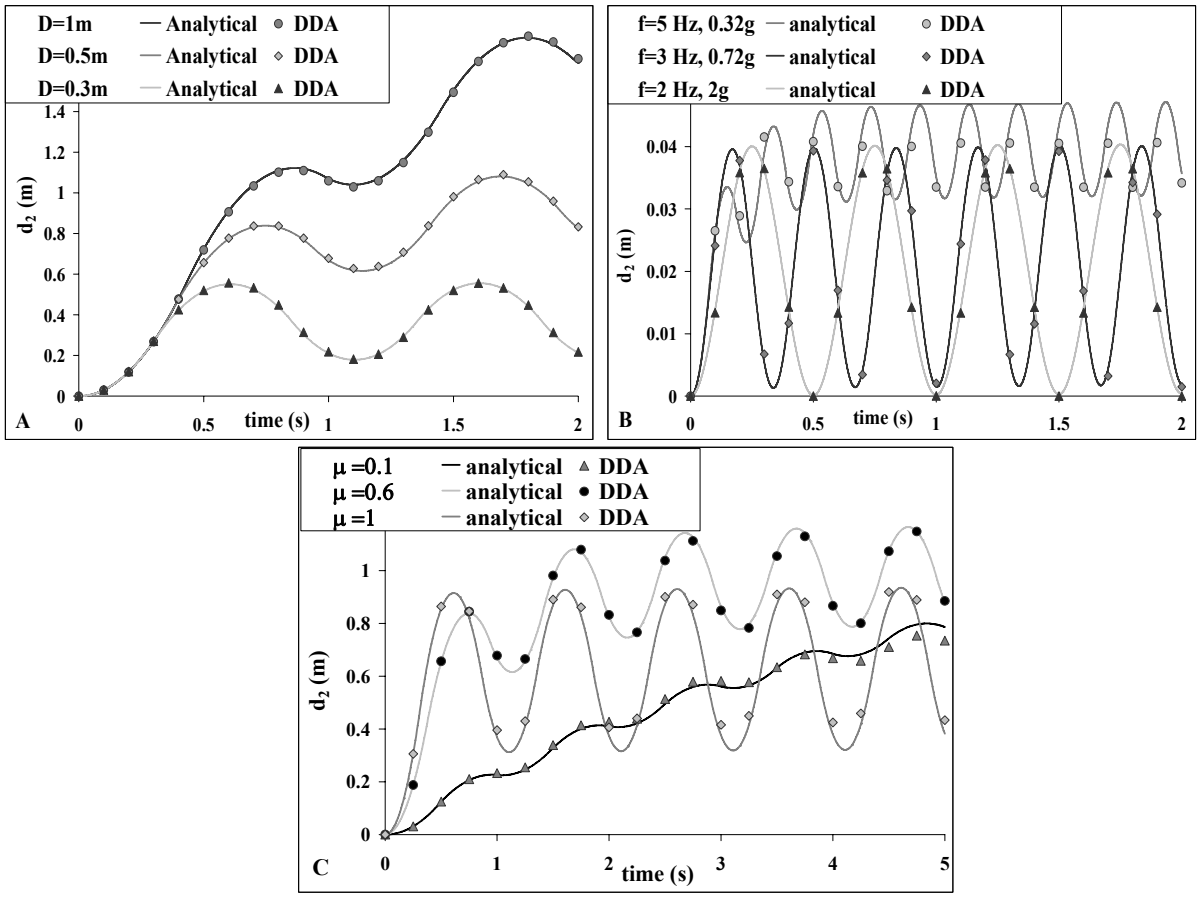

Figure 4.**A.** Response of Block 2 to displacement input of *f*=1Hz.Comparison between analytical (line) and DDA (symbols) solutions for different amplitudes of motion. **B**. Response of Block 2 to displacement input of *D*=0.02m. **C.** Response of block 2 to displacement input of *D*=0.5m, *f*=1Hz.

A remarkable agreement can be seen in all three figures. DDA follows the analytical results in all cases, with changing friction coefficients, amplitudes, and frequencies of motion.

3. TWO CASE STUDIES

The applicability of dynamic DDA for back analysis of historical failures in masonry structures was tested in two archeological sites in Israel. Original building stones were sampled and transported to the Rock Mechanics Laboratory of the Negev at Ben-Gurion University. Lab tests were performed in order to obtain physical and mechanical properties of intact rock as well as block interface friction parameters. Test results are summarized in Table 1.

Table 1. Mechanical properties of original building block material.

Mechanical property	Avdat	Mamshit
Density (Kg/m^3)	2555	1890
Porosity (%)	5	30-38

Dynamic Young's modulus (GPa)	54.2	16.9
Dynamic Poisson's ratio	0.33	0.37
Dynamic Shear modulus (GPa)	20.3	6.17
Interface friction angle	35	35

3.1. Masonry Arch: results from Mamshit

A unique structural failure is noticed in a tower at the corner of the Eastern Church at the Nabatean city of Mamshit (Figure 5A), where a key stone has slid downwards out of a still standing arch (Figure 5.B). In the tower, dated back to the second half of the 4th century AD [5], the outer walls and the arched doors were built of excellent ashlars, while the interior walls were built of large squared blocks, with an occasional filling of smaller stones and earth cement (Figure 5.A) [5].

Figure 5. The damaged arch at Mamshit. **A.** The arch is embedded in a very heterogenic wall. **B.** The Keystone has slid 4cm downwards while the rest of the arch remained intact.

3.1.1. Numerical solution

Modeling the embedded arch was a challenging task because of the heterogeneity in block material shape and size (Figure 5.A). Because of material heterogeneity DDA material lines were assigned to the arch blocks in order to assign different mechanical parameters to the arch and the wall (Figure 6). Different mesh configurations and material properties were tested in order to find the conditions in which forward modeling results would fit as closely as possible the observed failure pattern in the field. The selected mesh configuration is a simple, consistent masonry wall, in which the heterogeneity is represented by lower density and stiffness than those of the hewn stones forming the arch (Figure 6).

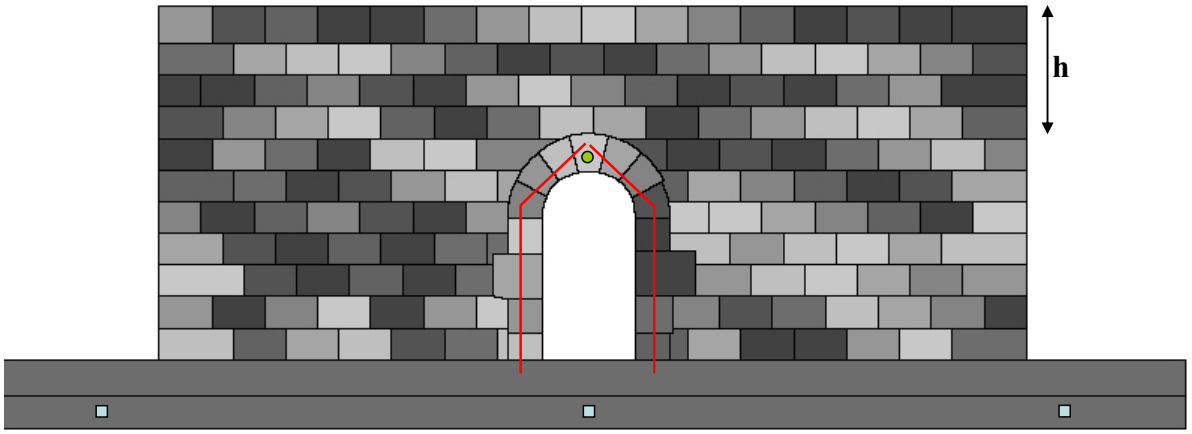

Figure 6. The final mesh configuration for the embedded arch in Mamshit. The uniform masonry wall rests on two blocks: the lower is fixed, and the overlying block can be subjected to time-dependant displacements. The height of the wall above the arch is *h*.

Two different loading mechanisms were examined: In the first, referred to here as 'dis. mode', the foundation block was subjected to time-dependant displacements, while in the second, all block centroids were subjected to time-dependant accelerations, a loading mechanism that has been studied before in DDA and is referred to as 'qk. mode' here.

Repeated runs of the problem revealed that the dis. mode, although validated successfully in a two-block problem, does not provide satisfactory results for a multiple block system, where over 100 blocks respond to the induced motion of a single block at the foundation.
Figures 7 and 8 display the difference in forward modeling with the dis. vs. qk. mode. In both cases the block system was loaded with a sinusoidal input function. In displacement mode the keystone undergoes upward displacement, and the entire block system is deformed, whereas in quake mode the keystone moves downwards and the rest of the mesh stays intact.

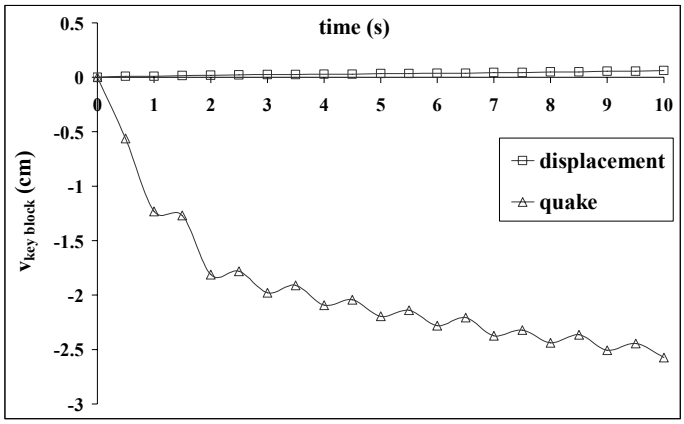

Figure 7. Influence of loading mode on keystone displacement. A=0.32g (D=8cm), f=1Hz.

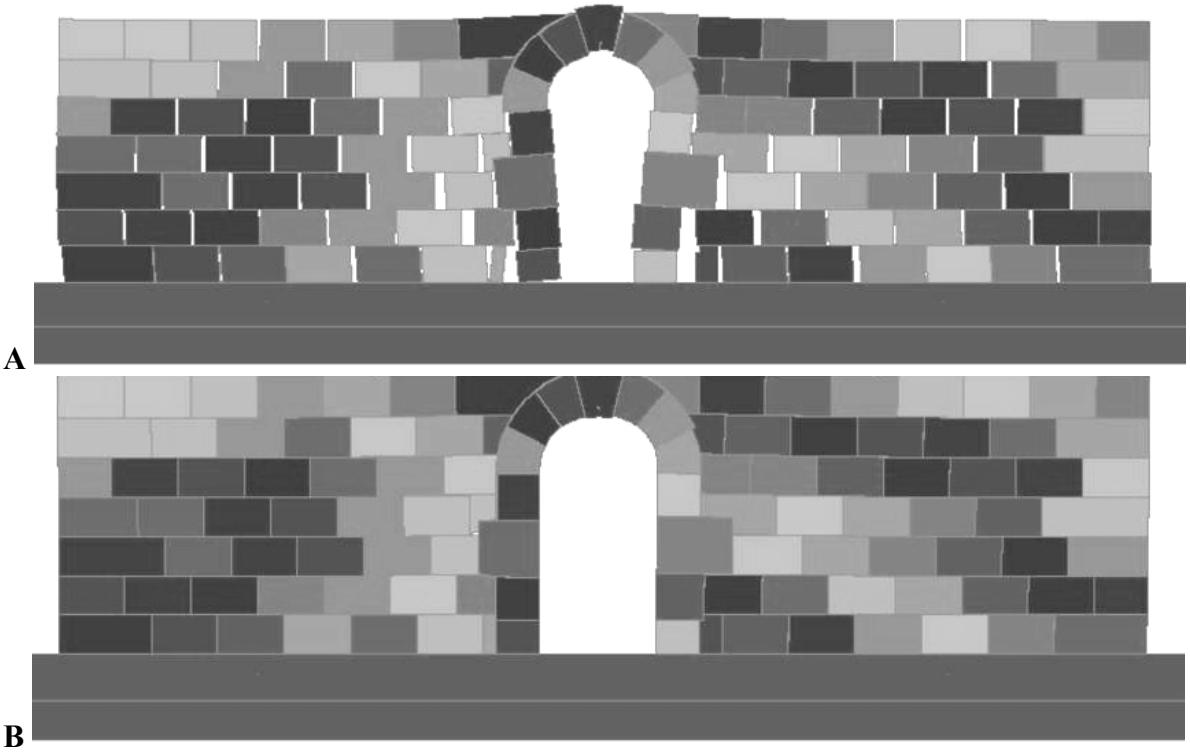

Figure 8. Response of the Mamshit block system to an earthquake with A=0.32g (D=8cm), f=1Hz. **A.** dis. mode **B**. qk. mode.

A sensitivity analysis for the block system (Figure 6) was performed with over 50 runs. Overburden, stiffness of blocks in the structure surrounding the arch, numerical damping (k01), and motion parameters (Amplitude and frequency) were examined. Results are presented in Figures 9 and 10, where the downward vertical displacement of the key-stone is plotted vs. time. Unless mentioned otherwise, the mechanical parameters of the block system are: ϕ_{arch}=35, ϕ_{wall}=40, E_{arch}=17GPa, E_{wall}=1MPa, h=0, and the analysis is performed in qk. mode. In most simulations, the input function (either acceleration or displacement) was of a sinusoidal form. A real earthquake record was used for comparison, in which the Nuweiba 1995 record, recorded in Eilat and de-convoluted to rock response (see Hatzor et al. 2004 [6] for details on this earthquake record), was scaled to different amplitudes (results are presented in Figure 10.B).

Figure 9 displays the structural response to different structural and numerical parameters. Clearly from Figure 9.A the downward displacement of the keystone became possible only after the collapse of all overlying layers, most probably due to relaxation of arching stresses. Figure 9.B implies that a difference of four orders of magnitude between the arch and wall materials is required to obtain the desired deformation, and for the deformation to be restricted to the arch only. This large difference might seem exaggerated, but a close inspection of Figure 5.A reveals the large heterogeneity and diversity of the wall, where spaces between wall-blocks are filled with soft filling materials. The soft filling materials allow for large deformations under low stresses, and drastically reduce the stiffness of the wall. We believe therefore that a 1MPa wall stiffness is reasonable.

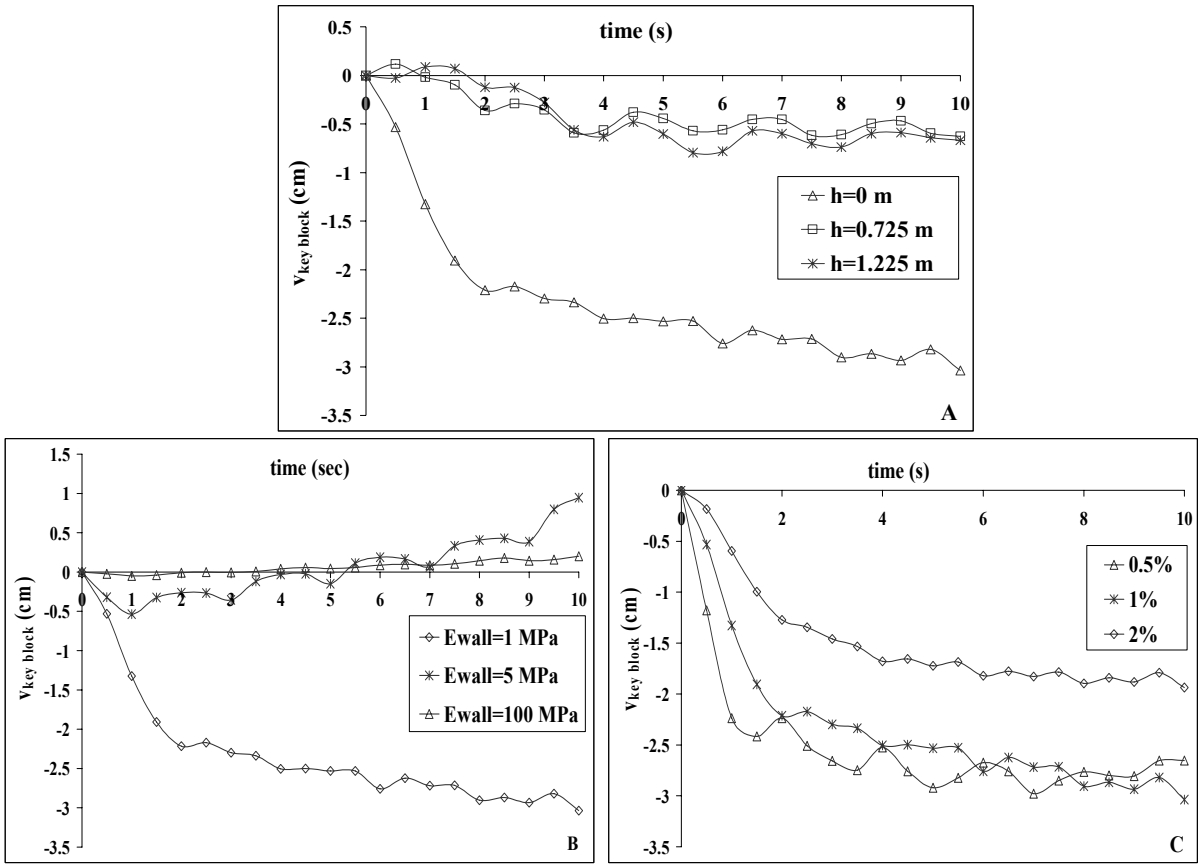

Figure 9.**A.** Influence of overburden (*h*). *A*=0.5g, *f*=1.5Hz. **B.** Influence of block stiffness in surrounding wall. *A*=0.5g, *f*=1.5Hz. **C.** Influence of numerical damping (k01). *A*=0.5g, *f*=1.5Hz.

In Validations of simple cases where DDA results are compared with analytical solutions, the analysis should be fully dynamic (k01 = 1). However, it was found that in the case of a large block-system, consisting of many blocks, some energy dissipation is required for obtaining realistic results. On the basis of field and experimental studies Hatzor et al. 2004 and Tsesarsky et al. 2005 [4, 6] found that 2% velocity damping should be sufficient. Figure 9.C suggests that for the Mamshit case, the ideal amount of damping is 1%, since 2% damping reduces the displacement unnecessarily, while 0.5% damping produces stronger keystone fluctuations. When no damping is applied (k01=1), the analysis results in complete destruction of the structure.

Figure 10 displays the influence of input-motion parameters on keystone displacement. It can be seen from Figure 10.A that while a relatively low amplitude (*A*=0.1g) results in a small displacement, a high amplitude (*A*=1g) results in strong fluctuations and in a shift in the accumulated displacement direction after ~4 sec. The best fit amplitude for this block system seems to be around 0.5g.

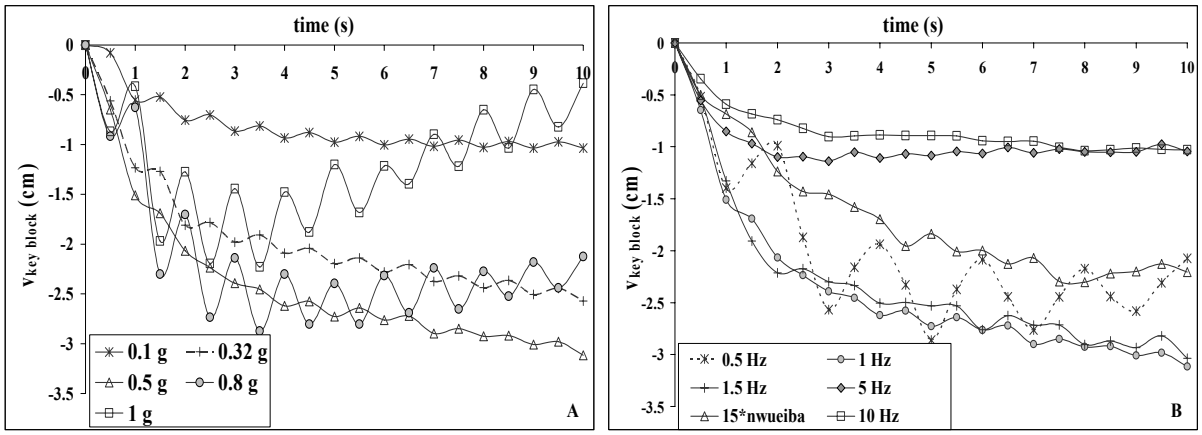

Figure 10.**A.** Influence of amplitude. *f*=1Hz. **B.** Influence of frequency. *A*= 0.5g.

A very interesting behavior is displayed in Figure 10.B: the ideal frequency seems to be around 1Hz, while a low frequency (eg. 0.5Hz) results in strong fluctuations and a high frequency (eg. 5Hz and 10Hz) results in "locking" of the structure, and very little displacement.
The structure response to the real Eq. record of Nuweiba 1995, amplified by 15 (PGA~0.6g) is also displayed in Figure 10.B. It can be seen that the behavior of the block system is not significantly different when a range of frequencies and additional vertical accelerations are introduced, meaning, that the results of the synthetic records are valid enough to be discussed and analyzed further.

Figure 11 displays the dynamic block system response to what we believe is the best fit earthquake, with *A*=0.5g and *f*=1Hz. The accumulating downwards displacement of the keystone is 3.11cm.

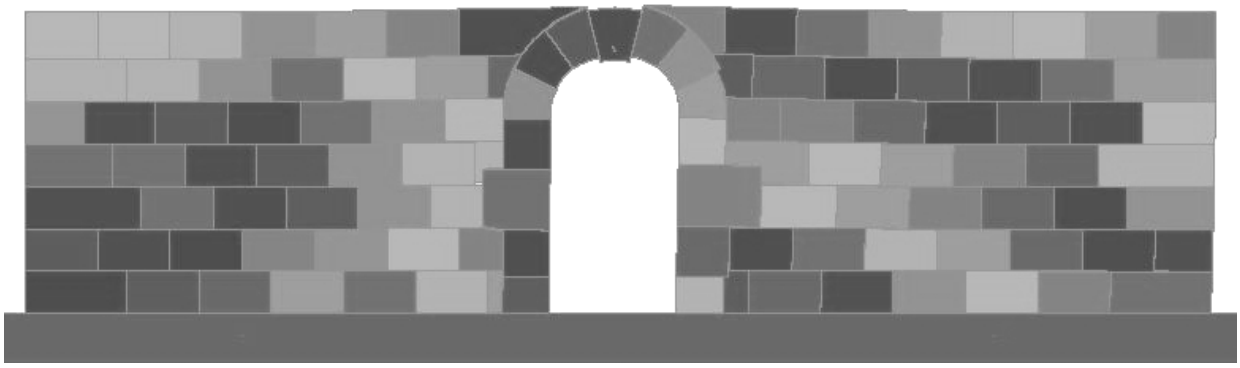

Figure 11. The result of the dynamic block system response under an earthquake with *A*=0.5g and *f*=1Hz. The accumulating downwards displacement of the keystone is 3.11cm.

3.2. A block on a plane: results from Avdat

Five blocks are displaced from the western wall of a Roman tower at the Nabatean city of Avdat (Figure 12). The tower, dated to 294 AD, was founded directly on bedrock, and has risen to a height of 12m, from which only 6m are left standing today [7].

Figure 12.**A.** The Roman tower in Avdat, a view of the western wall. The displaced blocks are numbered for reference. **B.** The displaced blocks.

3.2.1. Numerical solution

The numerical analysis of the roman tower at Avdat was performed on a block system representing the tower's northern wall, to best capture the observed westerly sliding of the three corner stones.

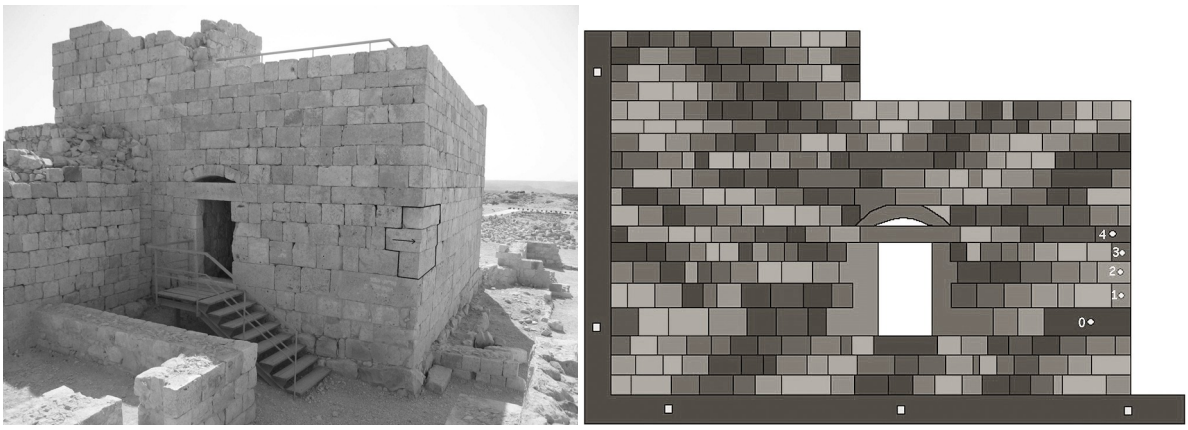

Figure 13.**A.** The northern wall of the roman tower at Avdat. The five corner blocks are marked and their displacement direction is displayed with an arrow. **B.** The DDA block system for the tower at Avdat. Five fixed points (squares) are assigned to the confining block, and five measurement points (circles) are assigned and numbered on corner blocks. 1,2 and 3 are three of the displaced blocks.

The block system, displayed in Figure 13.**B**, was generated using program DC of DDA [1]. The DC mesh includes the entrance door and the confining block on the left side, which represents the later added structure that restricts lateral movements to the left (Figure 13.**A.**). The confining block was fixed by five fixed points, and the displacement of the five corner blocks was

measured: three of the analyzed blocks (1,2, and 3 from Figure 12.**A**), one above (4) and one below (0). The structure consists of one set of mechanical parameters, presented in Table 1.

The location of the displaced blocks at mid height of the wall and not at the top, where normal stresses on the frictional surfaces are at minimum, is in contradiction with the basic physical principals of a pseudo-static analysis, which would predict greater displacement of the upper-most stones. Therefore, a simulation without the confining wall was performed in order to analyze the basic behavior of the structure. The analysis predicts the exact observation that is noticed in the field, though with greater expansion, in which all blocks in the doorway level, on both sides, are displaced outwards (Figure 14).
This result might indicate arching caused by the doorway on both sides, which reduces normal stresses, and allows for block displacement in the relaxed "abutments", in mid-height of the structure. This interesting result, again, demonstrates the extensive treatment of a dynamic solution to such a multi-block problem, versus the restricted and limited analytical approach.

A sensitivity analysis for amplitude and frequency was performed, and results are presented in Figures 15 and 16, where the average horizontal displacement (D_h) of the five measurement points is plotted vs. time. All simulations were performed with 1% damping and a synthetic sinusoidal acceleration record.

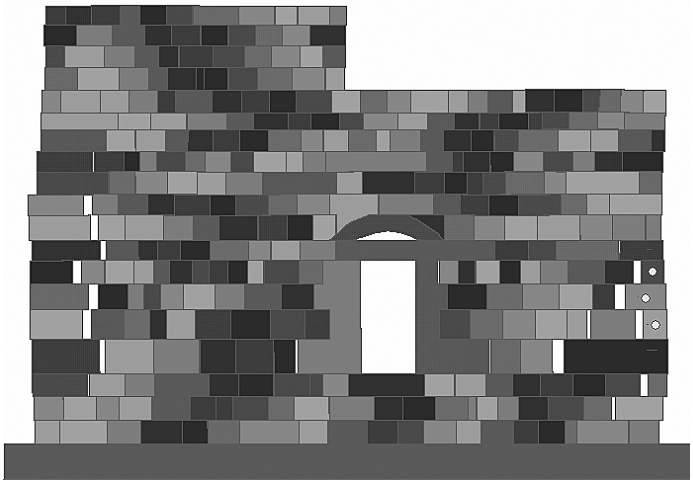

Figure 14. A simulation without a confining wall predicts the exact height of displaced blocks as is observed in the field. A=1.5g, f=5Hz.

Figure 15.**A** displays the influence of the amplitude on structural response, under f=5Hz. The two curves of A=0.8g and A=1g are erratic and intersect. Figure 15.**B.** displays the influence of frequency structural response. There is no clear trend, though it seems that displacement increases with increasing period of motion (decreasing frequency), due to longer periods of high acceleration.
Searching for the best fit set of parameters for Avdat is not as straight forward as in the previous case of the arch at Mamshit. There is no merit in comparing total block displacements since the blocks move back and forth, and do not follow a consistent trend; their total displacement depends on the duration of motion, which is unknown. Furthermore, relative displacements

between the blocks might obscure the observed total amount of displacement in the field and make the comparison meaningless.

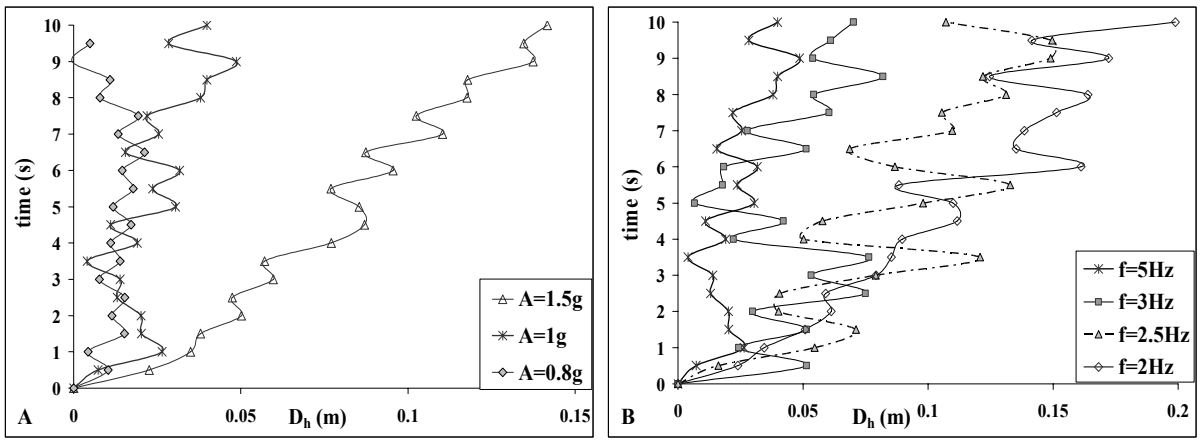

Figure 15.**A.** Influence of amplitude. f = 5Hz. **B.** Influence of frequency. A=1g.

Figure 16.A and B display the final result of two different runs, in which only the corner blocks are displaced while the rest of the structure remains intact. Both simulations were performed with no input vertical motions (Av = 0). In Figure 16A the horizontal acceleration amplitude (Ah) is 1g and frequency (f) is 3Hz. The resulting horizontal displacement (Dh_avmax) is 8cm. In Figure 16.B Ah is 1.5g, f is 5Hz., and Dh_avmax is 14cm. We believe these two sets of parameters represent the best approximation that can be reached with a 2-D, numerical, back analysis of the historical earthquake that caused the observed damage in Avdat. A determination of the single, best fit set of parameters to this case study is not attempted here because of the above mentioned limitations, although the graphical output in Figure 16A better fits field measurements.

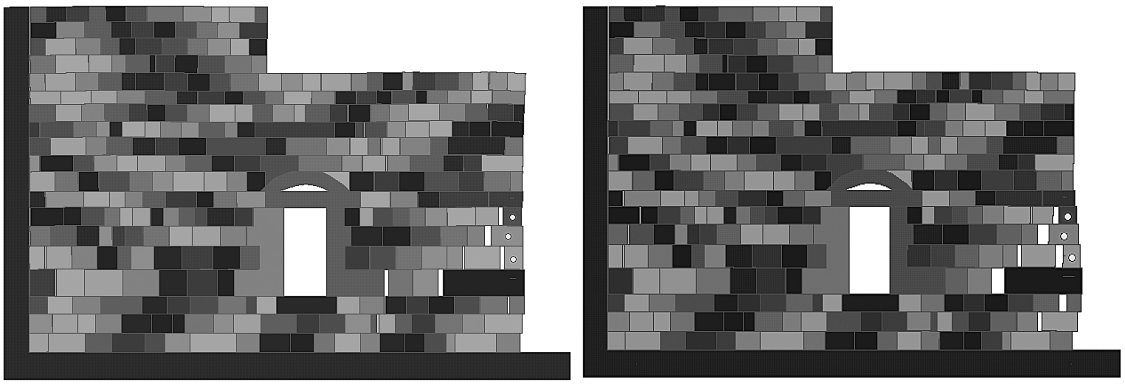

Figure 16. Best – fit simulations of the Avdat earthquake A. A_h= 1g, A_v=0, f =3Hz. $D_h\_av_{max}$=8cm. **B.** A_h=1.5g, A_v=0, f= 5Hz. $D_h\_av_{max}$=14cm.

4. SUMMARY AND CONCLUSIONS

This paper describes back analysis of two earthquake induced failures in two archeological sites in the Negev, Israel, that are dated back to the 3rd and 4th centuries AD. The sites may have been subjected to more than one earthquake tremor in their history, but separation to individual seismic events is beyond the resolution or scope of this study. Back analysis is performed by subjecting the structures to simple, harmonic, dynamic loading functions and structural response is discussed in terms of displacement evolution of selected structural elements: keystone in the case of an arch (Mamshit site), and corner stones in the case of a tower (Avdat site).

4.1. General conclusions

- 2D-DDA successfully duplicated structural damage that was detected and measured in the field, after the block system was generated correctly with adequate boundary conditions and material properties.
- We found that the best style of input motion for structural analysis is "quake mode" where all block centroids are loaded with time dependent acceleration simultaneously. While this loading mechanism is reasonable for a jointed rock mass, it is less adequate for masonry structures. Nevertheless, it provides a better deformation picture than simulations where the entire structure responds to an input displacement at the foundation block ("displacement mode").
- Clearly, application of "quake" mode does not allow for wave propagation phenomena such as amplification, de-amplification, etc. to take place when the motion is transferred from bedrock to the structure. Further research is required to resolve the significance of rock-structure interaction processes when masonry structures are founded on stiff rock, for forward numerical modeling.
- As a result of applying "quake" mode and a harmonic sinusoidal function the obtained ground-motion parameters may be higher than reasonably expected (eg. 1g at Avdat). Therefore, we do not argue at this stage for exact historical ground motion restoration, but focus on the structural behavior and failure patterns that are obtained, and compare them to field observations.
- The sensitivity analysis performed with DDA demonstrates the importance of the dynamic structural response, thus stressing the role of the duration and frequency of ground motion. This is a strong proof for the partial determination of motion by the value of PGA, often used in the fields of seismic hazard assessment and design.
- We wish to emphasize that over-all structure response is as important as local displacement measurements. Therefore, graphical output of the deformed mesh configuration is as valuable as the quantitative measurement point data, since it enables us to understand the evolution of the structural damage and the dominant failure modes.

4.2. Back analysis of masonry arch (Mamshit)

- We found that downward displacement of the keystone was only possible after the collapse of overlying layers. A process that must have caused relaxation of arching stresses.
- We found that most damage resulted from horizontal motions and that the significance of vertical motions was negligible.

- We found that most of the accumulated keystone displacement took place in the first two seconds of the motion; therefore much longer runs are not necessary. This result may also suggest the duration of the earthquake that caused the detected damage.
- Our best estimate for the horizontal amplitude and frequency of the earthquake that caused the damage in Mamshit is 0.5g, and 1 Hz respectively. Resolution of the date and number of events is beyond the scope of this paper.

4.3. Back analysis of masonry tower (Avdat)

- 2D analysis of corner stones in the tower ignores in plane rotations, which may play a significant role in the dynamic deformation of the structure.
- A very unique structural failure in Avdat, in which mid-height blocks have been laterally displaced, is duplicated perfectly by dynamic DDA. The results provide and insight into the structural dynamic behavior, which could not have been achieved by a different analysis approach, certainly not by a pseudo-static approach.
- We found two possible sets of dynamic input motion that could have generated the observed failure in the field: A) A_h = 1g, f = 3Hz; B) A_h = 1.5g, f = 1.5Hz. The best fit set of parameters is not determined conclusively since a meaningful and finite comparison measure such as total block displacement will not portray the failure mechanism properly, as blocks move back and forth, sometimes with no obvious trend, and so total displacement is a matter of time frame.

5. ACKNOWLEDGMENTS

Dr. Gen-hua Shi is thanked for providing us with his latest version of DDA (2003). Dr. Zvika Zuk from Israel Nature and Parks Authority and Dr. Tali Gini of Israel Authority of Antiquities are thanked for supervising block sampling and measurements in the field. Finally, Dr. Shmulik Marco of Tel Aviv University is thanked for joint field trips and stimulating discussions.

6. REFERENCES

(1) Shi, G.-H. 1993. *Block System Modeling by Discontinuous Deformation Analysis.* Southhampton, UK: Computational Mechanics Publication.

(2) MacLaughlin, M.M. and D.M. Doolin. 2005. Review of validation of the Discontinuous Deformation Analysis (DDA) method. *Int. J. Numer. Anal. Meth. Geomech.* 29:

(3) Hatzor, Y.H. and A. Feintuch. 2001. The validity of dynamic block displacement prediction using DDA. *Int. J. Rock Mech. Min. Sci.* 38: 599-606.

(4) Tsesarsky, M., Y.H. Hatzor and N. Sitar. 2005. Dynamic displacement of a block on an inclined plane: Analytical, experimental and DDA results. Technical note. *Rock Mechanics and Rock Emgineering.* 38: 2,153-167.

(5) Negev, A. 1988. The Architecture of Mampsis*. Quedem. monographs of the institute of archaeology.* ed.

(6) Hatzor, Y.H., A.A. Arzi, Y. Zaslavsky and A. Shapira. 2004. Dynamic stability analysis of jointed rock slopes using the DDA method: King Herod's Palace, Masada, Israel. *Int. J. Rock Mech. Min. Sci.* (in press):

(7) Negev, A. 1997. The Architecture of Oboda*. Quedem. monographs of the institute of archaeology.* ed.

Earthquake response analysis of a rock-fall by discontinuous deformation analysis

T. Sasaki, I. Hagiwara, K. Sasaki & S. Horikawa
Rock Engineering Lab., Suncoh Consultants Co., Ltd., Tokyo, Japan
Y. Ohnishi & S. Nishiyama
School of Urban & Environment Engineering, Kyoto University, Kyoto, Japan
R. Yoshinaka
Saitama University, Saitama, Japan

ABSTRACT: This paper describes the simulation of rock-falls caused by earthquakes in October 1994 in Niigata Prefecture using discontinuous deformation analysis (DDA). It introduces the formulation of viscous damping on contact of blocks by a Voigt-type model and the velocity-energy ratio for the rock-fall models based on DDA theory. The paper also proposes a method of inputting the earthquake accelerations in DDA and compares the method with actual rock-fall phenomena. The results show qualitative agreement, and so the method is applicable to physical phenomena.

1. INTRODUCTION

Earthquakes are known to trigger rock-falls at rock slopes and earthquakes are common in Japan. Furthermore, rock slopes are often close to rail lines, roads and private houses. The Niigata Prefecture Chuetsu earthquake that struck on October 23, 1994 and the Genkai earthquake offshore of Hakata City in Japan caused heavy losses of life and are still fresh in people's memory. It is important to predict such disasters and to take measures before earthquakes strike in order to protect life and industrial activity. With this background, we are studying the applicability of DDA by examining small-scale rock-fall models using earthquake response analysis. The present study investigates the optimum values of parameters in a model of actual rock-falls of natural large rock slopes that occurred in Niigata Prefecture. The study focuses on the input of earthquake acceleration time history, and considers the damping effects of contact between blocks by a Voigt-type model based on DDA theory [1]. The numerical results of DDA are compared with actual measurements at the site.

2. OUTLINE OF THE THEORY

2.1 *Governing equation of motion*

The governing equation of the potential energy Π^{sys} for large deformations of continuous and discontinuous elastic bodies is given by:

$$\Pi^{sys} = \sum_{i=1}^{n} \Pi^{(block)i} = \sum_{i=1}^{n} \left(\Pi^{i} + \sum_{j=1}^{m} \Pi_{PL}^{i,j} \right) \tag{1}$$

The first term on the right side of Eq. (1) is the potential energy of the continuum part, and the second term is the potential energy of the contact between blocks. The first term is given by:

$$\Pi^i = \int_V \frac{\rho^c}{\rho^0}\left[\tau_{ij}^* \delta D_{ij} - \frac{1}{2}\sigma_{ij}\delta(2D_{ik}D_{kj} - v_{k,i}v_{k,j})\right]dV - \int_\Gamma \bar{t}\cdot u d\Gamma - F(x,y)\int_V [\rho(\dot{b} - \ddot{u}) - c\dot{u}]\cdot dV \quad (2)$$

The first term of Eq. (2) is the strain energy of the velocity field, the second term is the surface traction energy, and the third term is the energy of the inertia force and damping force, where, ρ^0: density before deformation, ρ^c: density after deformation, τ_{ij}^*: Kirchhoff stress velocity, D_{ij}: deformation velocity tensor, σ_{ij}: Cauchy stress, $\ddot{u}$: acceleration, $\dot{u}$: velocity, ρ: unit mass, *b*: body force, *c*: viscosity coefficient, $\bar{t}$: surface traction force, *V*: volume of a block, and Γ: surface area of a block.

The second term on the right side of Eq. (1) is the potential energy of the contact between discontinuous planes, and is evaluated by the least squares method by using a penalty as follows:

$$\Pi_{PL}^{i,j} = \frac{1}{2}k_N[(u^j - u^i)\cdot n]^2 - \frac{1}{2}k_T[u_T^j - u_T^i]^2 \quad (3)$$

where, k_N: penalty coefficient in the normal direction, k_T: penalty coefficient in the shear direction, $(u^j - u^i)\cdot n$: amount of penetration in the normal direction, u_T: amount of slip in the shear direction, and *n*: direction cosine of the contact plane.

DDA (Shi, 1984) is formulated from Eq. (1) using the kinematic equations based on Hamilton's principle and minimized potential energy expressed by:

$$M\ \ddot{u} + C\ \dot{u} + K\ u = F \quad (4)$$

where, *M*: mass matrix, *C:* viscosity matrix, *K*: stiffness matrix, F: external force vector, $\ddot{u}$: acceleration, $\dot{u}$:velocity, and *u*: displacement of the center of a block.

The kinematic equation of motion Eq. (4) is solved by Newmark's β and γ method (Hilbert, 1993) by using parameters β = 0.5 and γ = 1.0, and the algebraic equation for the increase in displacement is solved for each time increment by the following three equations [2, 3]:

$$\tilde{K}\cdot\Delta u = \tilde{F} \quad (5)$$

where,

$$\tilde{K} = \frac{2}{\Delta t^2}M + \frac{2\eta}{\Delta t}M + \frac{\rho^c}{\rho^0}[K_e + K_s] \quad (6)$$

$$\tilde{F} = \frac{2}{\Delta t}M\cdot\dot{u} + (\Delta F - \sum\int\sigma dv) - M\alpha(t) \quad (7)$$

where, Δu: incremental displacement, K_e: stiffness matrix of linear term, K_s: initial stress matrix caused by rigid rotation, and $\alpha(t)$: time history of earthquake acceleration.

2.2 *Viscosity matrix of a body and contact friction*

The viscosity matrix of a body *C* in Eq. (4) can be rewritten as follows in terms of viscosity η_e and mass matrix *M*:

$$C = \eta_e M \quad (8)$$

The physical meaning of viscosity η_e is the damping of the rock itself, the viscosity of air around the rock surface and the vegetation on the surface of the rock slope.

On the other hand, in earthquake response analysis it is conventional to prevent the reflection of seismic waves from the boundary to the blocks in the analysis area by using dash pot damping

elements as shown in Figure 1. We therefore introduce Voigt-type viscous damping elements between blocks as shown in Figure 2. The original DDA developed by Shi (1989) was formulated by defining penalty parameters for the normal direction P_n and the shear direction P_s. We also introduced parameters for the normal damping η_{pn} and the shear damping η_{ps} based on the original DDA theory. In the case of Voigt-type damping, the penetration d and the velocity strain $d/\Delta t$ are expressed by:

$$f_t = f_p + f_\eta = pd + \eta_p \cdot \dot{d} = pd + \eta_p \frac{d}{\Delta t} \tag{9}$$

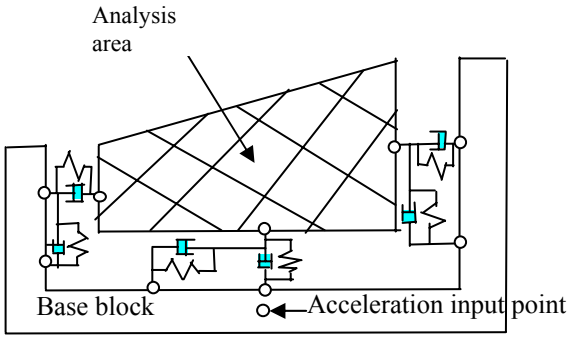

Fig. 1. Boundary condition of earthquake response analysis

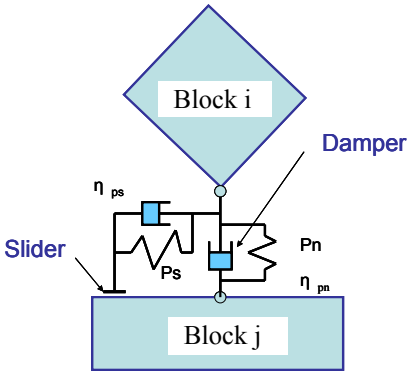

Fig. 2. Voigt-type viscous damping of friction

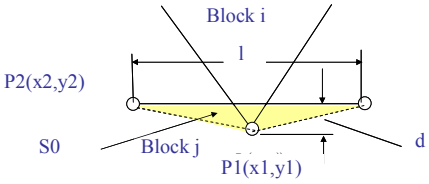

Fig. 3. Mechanism of block contact by penalty

The total reaction force of the penetration f_t is expressed as the summation of the force by penalty f_p and the force by dash pot f_η as follows:

$$f_t = f_p + f_\eta = pd + \frac{\eta_p}{\Delta t} d = (p + \frac{\eta_p}{\Delta t}) d \tag{10}$$

The potential energy of the penetration between blocks considering contact viscous damping is expressed by:

$$\Pi_{p\eta} = f_t d = \frac{1}{2}(p + \frac{\eta_p}{\Delta t}) d^2 \tag{11}$$

The quantity of penetration between blocks d is defined by:

$$d = \left([E_i][D_i] + [G_j][D_j] + \frac{S_0}{l} \right) \tag{12}$$

where, S_0: area of the penetration triangle in Figure 3, and l: length of the contact edge respectively.

The unknown parameter of the center of gravity of a block is expressed by:

$$\{D_i\} = \{\, u_0 \;\; v_0 \;\; r_0 \;\; \varepsilon_x \;\; \varepsilon_y \;\; \gamma_{xy} \,\} \tag{13}$$

The contact matrix between blocks is expressed by:

$$\begin{aligned}[E_i] &= \frac{1}{l}(y_2 - y_3 \quad x_3 - x_2)[T_i(x_1, y_1)] \\ [G_j] &= \frac{1}{l}(y_3 - y_1 \quad x_1 - x_3)[T_j(x_2, y_2)] \\ &\quad + \frac{1}{l}(y_1 - y_2 \quad x_2 - x_1)[T_j(x_3, y_3)]\end{aligned} \tag{14}$$

The displacement matrix of a block is defined by:

$$[T_i] = \begin{bmatrix} 1 & 0 & -(y-y_0) & (x-x_0) & 0 & (y-y_0)/2 \\ 0 & 1 & (x-x_0) & 0 & (y-y_0) & (x-x_0)/2 \end{bmatrix} \tag{15}$$

Substituting Eq. (12) into Eq. (10), the total reaction force of the penetration f_t is given by:

$$f_t = (p + \frac{\eta_p}{\Delta})\left([E_i][D_i] + [G_j][D_j] + \frac{S_0}{l} \right) \tag{16}$$

Substituting Eq. (16) into Eq. (11), the potential energy of the penetration between blocks considering the contact viscous damping is expressed by:

$$\begin{aligned}\Pi_{p\eta} &= \frac{1}{2}(p + \frac{\eta_p}{\Delta})d^2 = \frac{1}{2}(p + \frac{\eta_p}{\Delta})\left([E_i][D_i] + [G_j][D_j] + \frac{S_0}{l} \right)^2 \\ &= \frac{1}{2}(p + \frac{\eta_p}{\Delta})([D_i]^T[E_i]^T[E_i][D_i] + [D_j]^T[G_j]^T[G_j][D_j] + 2[D_i]^T[E_i]^T[G_j][D_j] \\ &\quad + \frac{2S_0}{l}[E_i][D_i] + \frac{2S_0}{l}[G_j][D_j] + \frac{S_0^2}{l^2})\end{aligned} \tag{17}$$

Minimizing the potential energy by deriving the penetration d, the stiffness matrix of penetration between blocks is expressed by Eq. (18) and superposes the global stiffness matrix:

$$\begin{aligned}&(p + \frac{\eta_p}{\Delta})[E_i]^T[E_i] \to [K_{ii}], \; (p + \frac{\eta_p}{\Delta})[E_i]^T[G_j] \to [K_{ij}] \\ &(p + \frac{\eta_p}{\Delta})[G_j]^T[E_i] \to [K_{ji}], \; (p + \frac{\eta_p}{\Delta})[G_j]^T[G_j] \to [K_{jj}]\end{aligned} \tag{18}$$

The external force of the contact is expressed by Eq. (19), and also superposes the global external forces:

$$-\frac{S_0}{l}(p + \frac{\eta_p}{\Delta})[E_i]^T \to [F_i], \; -\frac{S_0}{l}(p + \frac{\eta_p}{\Delta})[G_j]^T \to [G_j] \tag{19}$$

The relations between displacements, velocities and accelerations at an arbitrary point of a block at time t in step i are expressed by the following three equations, respectively:

$$u_i = [D_i] = \frac{\Delta t^2}{2}\frac{\partial^2[D(t)]}{\partial t^2} + \Delta t \frac{\partial [D(t)]}{\partial t} \tag{20}$$

$$\dot{u}_i = \frac{\partial [D(t)]}{\partial t} = \frac{2}{\Delta t}[D_i] - \frac{\partial [D(t-\Delta t)]}{\partial t} = \frac{2}{\Delta t}[D_i] - \dot{u}_{i-1} \tag{21}$$

$$\ddot{u}_i = \frac{\partial^2[D(t)]}{\partial t^2} = \frac{2}{\Delta t^2}[D_i] + \frac{2}{\Delta t}\frac{\partial [D(t-\Delta t)]}{\partial t} = \frac{2}{\Delta t^2}[D_i] - \frac{2}{\Delta t}\dot{u}_{i-1} \tag{22}$$

3. NUMERICAL EXAMPLES

3.1. Analytical models and parameters

In order to examine the applicability of the earthquake response analysis by using DDA, a numerical example model is created for a rock slope along the Shinano River which was fractured by the Niigata Prefecture Chuetsu earthquake on October 23, 2004. The analyzed rock slope was measured after it had collapsed by aerial survey and ground surface survey. These surveys were done to clarify the mode of falling slope, the distance traveled by rock blocks from the slope, the time taken for the rock blocks from the toe of the slope, and the relation between the parameters in the analysis.

Figure 4 shows the geological features near the slope and the epicenter of the Chuetsu earthquake. The modeled slope is located 8 km from the epicenter and the rock slope consists of Tertiary deposit inclined at 20 to 25 degrees to the horizontal elevation. Figure 5 shows the topography after collapse. The size of collapsed rock blocks ranges from 2 and 3 meters to 10 meters. The collapsed rock blocks traveled 100 to 150 meters at the toe of the slope. Figure 6 shows a sectional view of the analyzed slope. The height of the slope is almost 145 meters, the width of collapsed rock is almost 500 meters, and the volume of collapsed rock is estimated to be about 500,000 m^3.

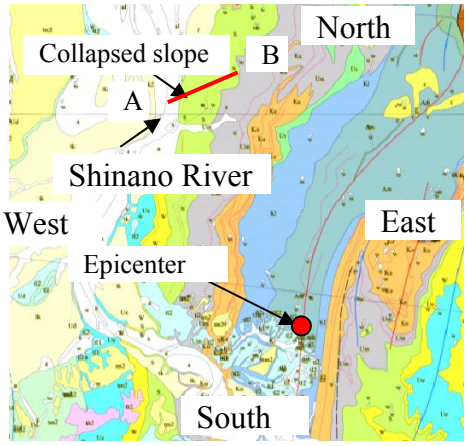

Fig. 4. Geological features around the slope

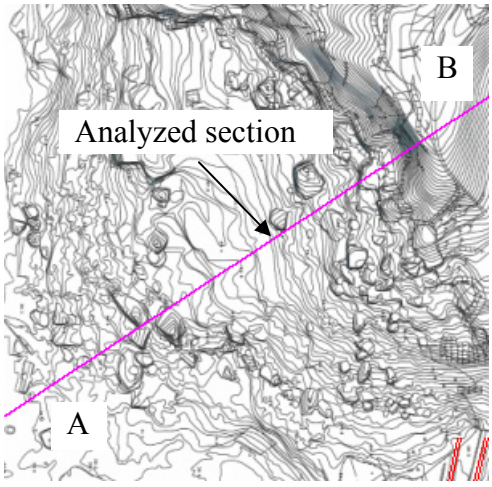

Fig. 5. Topography after collapse

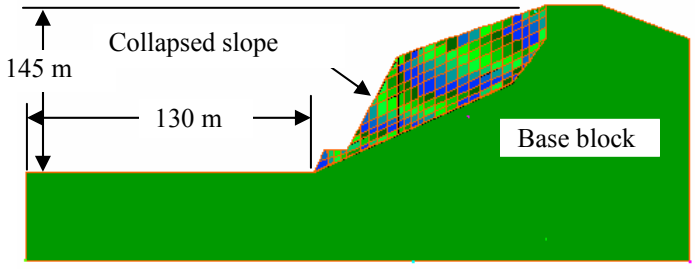

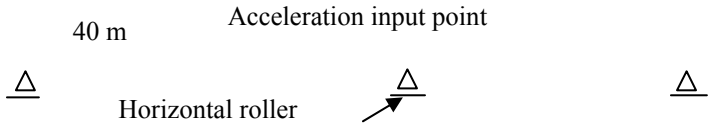

Fig. 6. Section of the analytical model (Section A-B)

Figure 7 show the acceleration record of the Chuetsu earthquake near the collapsed slope measured by Niigata University (NIG019, 37.30, 138.8, East–West and up–down). Figure 8 shows the Fourier spectrum of acceleration, revealing large amplitude of over 200 Gal in the east–west direction at the frequency of 1.5 to 5 Hz. On the other hand, the up–down wave of amplitude was 150 Gal, independent of frequency.

The position of acceleration of seismic waves in the model is defined as the center in the horizontal direction of the slope and 10 meters from the bottom of the base block in the vertical direction. The boundary condition of the base block is adopted in the horizontal roller condition at the bottom of the block.

In reality, the actual collapsed rock slope contained blocks of various sizes, and so it is very difficult to estimate the block size before collapse. Therefore, in order to distinguish the difference in collapse mode between large and small block sizes, we set up two models as shown in Figure 9. The size of the large block model was set to 5 to 10 meters (model-1) and that of the small one to 2 to 3 meters (model-2).

The material properties and parameters used in the analysis are shown in Table 1. The elastic modulus of the slope is estimated to be 1 to 3 GPa and the unit mass to be 20 to 25 kN/m^3. We analyzed the models using these parameters.

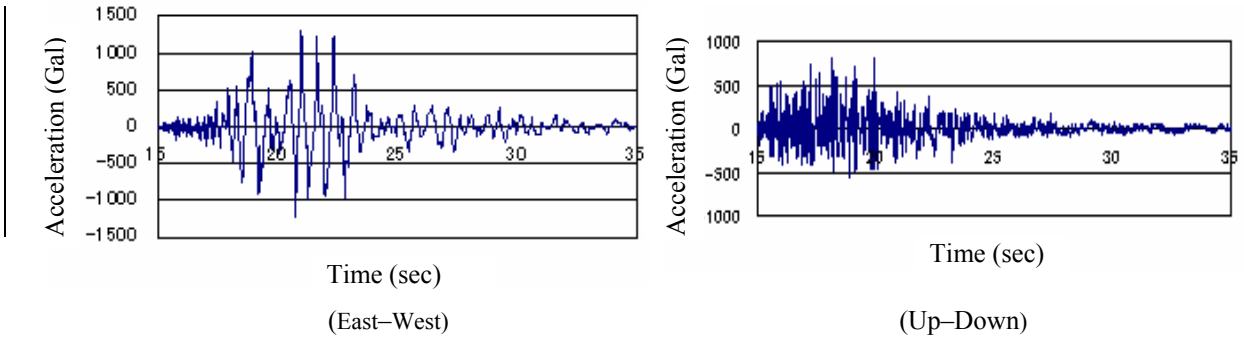

Fig. 7. Input acceleration of Chuetsu earthquake (NIG019, 37.30, 138.8)

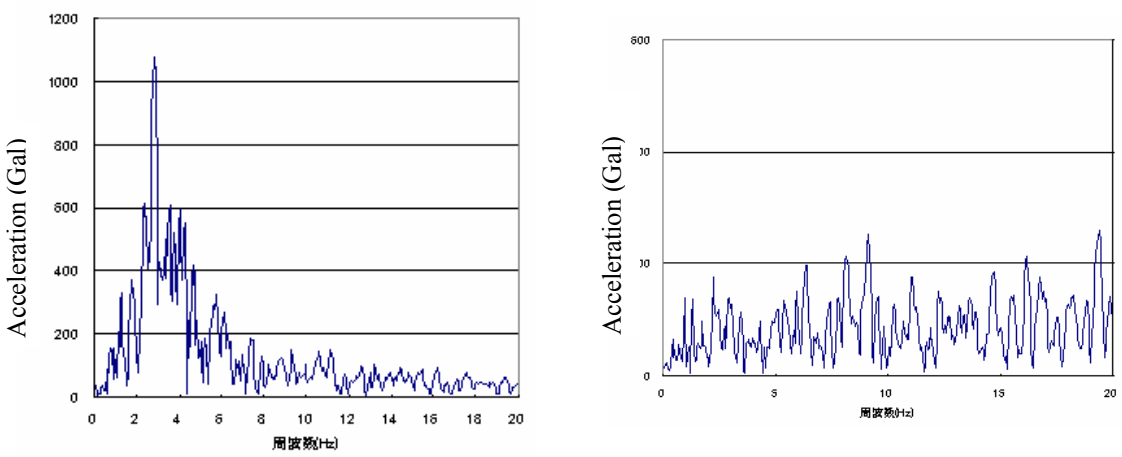

(East–West) (Up–Down)

Fig. 8. Fourier spectrum of acceleration

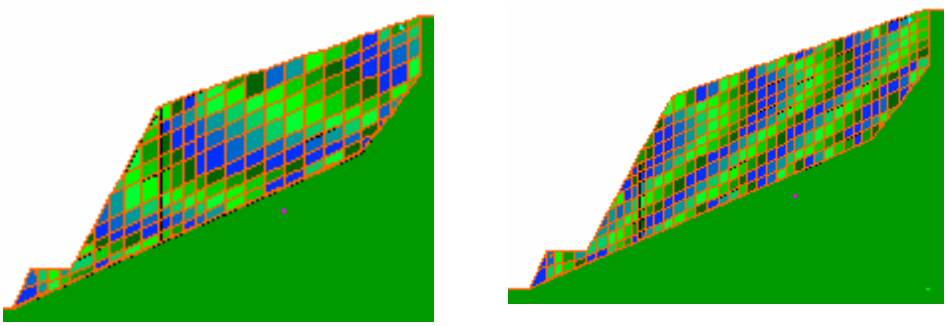

(a) Large block model (Model-1) (b) Small block model (Model-2)

Fig. 9. Models of different block size

Table 1. Material properties and parameters

Items	Parameters	
Time increment	0.001 second	
Elastic modulus	3 GPa	1 GPa
Unit mass	25 kN/m^3	20 kN/m^3
Poisson's ratio	0.30	
Friction angle, Cohesion	ϕ=30°, c=0.2 MPa	
Penalty coefficient (Normal) Penalty coefficient (Shear)	2 GN/m^3 0.5 GN/m^3	
Viscosity (Block body)	5 %×(unit mass)×sec	
Viscosity (Normal contact) Viscosity (Shear contact)	5%×(Penalty Pn)×sec 10%×(Penalty Ps)×sec	
Velocity – energy ratio	Rock VS Rock: 0.80 Rock VS Soil: 0.40	

In order to compare the distance of collapse from the slope toe, two unit masses is set up and the viscosity of the block itself is defined as 5% of the unit mass [4, 5]. The viscosity of the block contact is defined as 5% and 10% of each of the normal and shear penalty coefficients respectively. The velocity-energy ratio is defined as 80% and 40% for the rock vs. rock and the rock vs. soil respectively.

3.2. Analytical results

Figure 10 shows the deformation of Case-1 (Model-1, E = 3 GPa, 25 kN/m^3) and Case-3 (Model-2, E = 3 GPa, 25 kN/m^3) after 5, 10 and 15 seconds, respectively. The lines in the figures show the trace of blocks. From these results, the rock slope started to collapse at the crest of the slope and the blocks were pushed out toward the toe of slope from the top of the slope. The collapsed blocks moved along the surface of the base block and reached 90 meters from toe of the slope after 15 seconds. The blocks at the center of the slope moved within the body. These modeled behaviors agreed well with the observations. Comparing Case-1 and Case-3, the distance traveled from at the slope toe was greater in Case-3 than Case-1. This result shows that smaller blocks traveled further than larger blocks in the model. The reason for this result is that the friction forces between the base block and the collapsed blocks is smaller for small blocks than for large blocks.

Figure 11 shows the result of Case-2 (Model-1, E = 1 GPa, 20 kN/m^3) and Case-3 (Model-2, E = 3 GPa, 25 kN/m^3). The unit mass of Case-2 is 20 kN/m^3, which is 80% of that of Case-1. Therefore, the friction between the base block and collapsed blocks is smaller than in Case-1. The distance traveled from the slope toe is 10 to 15 meters longer than in Case-1.

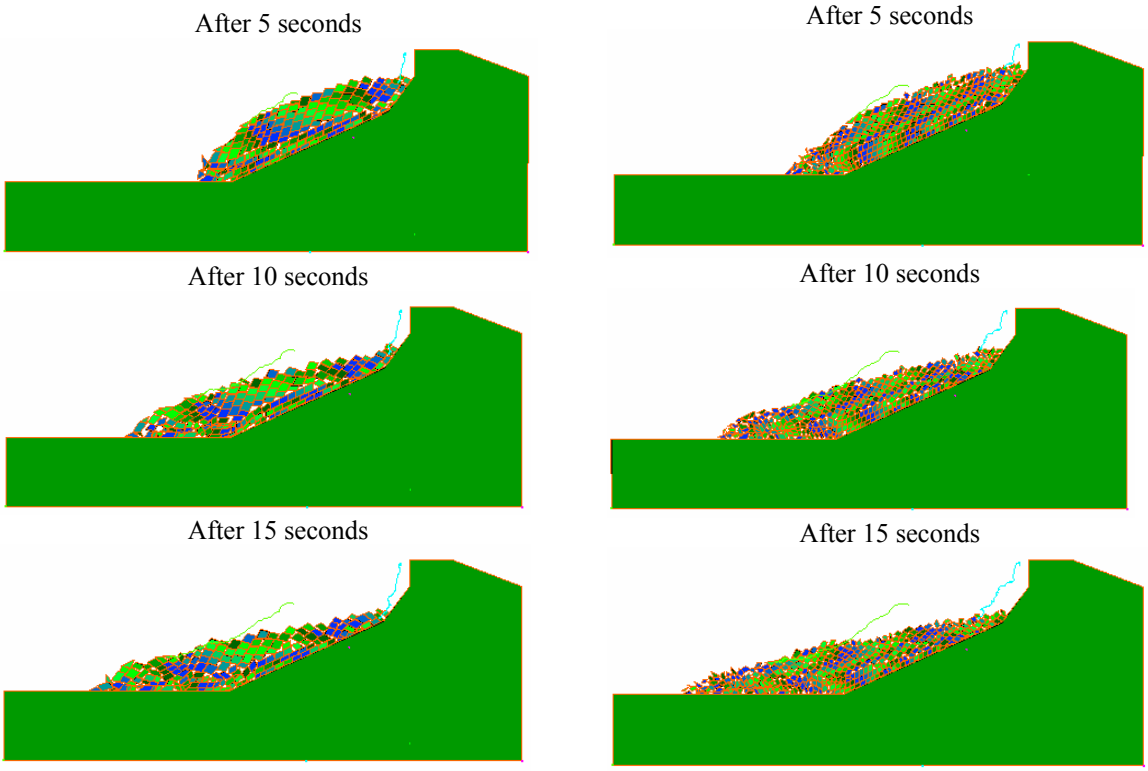

(Case-1, E = 3 GPa, 25 kN/m^3) (Case-3, E = 3 GPa, 25 kN/m^3)

Fig. 10. Comparison of difference of block size

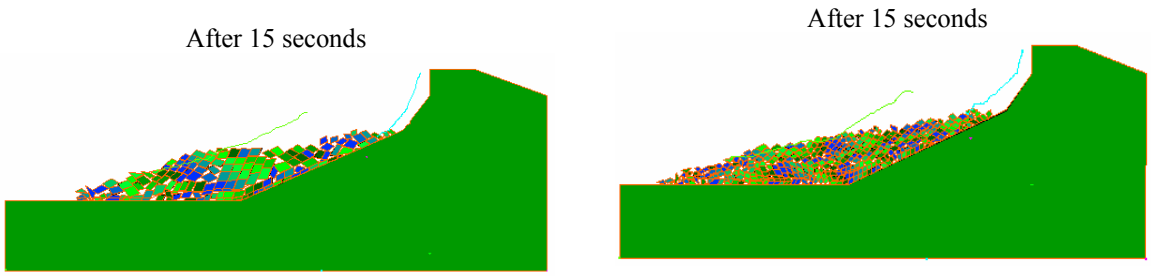

(Case-2, E = 1 GPa, 20 kN/m^3) (Case-4, E = 1 GPa, 20 kN/m^3)

Fig. 11. Comparison of difference of elastic modulus of blocks

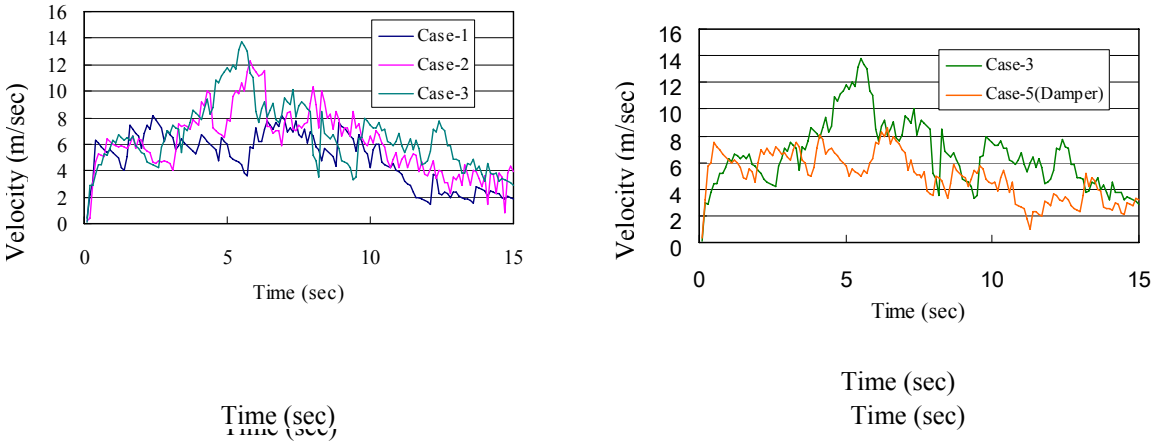

Time (sec) Time (sec)

(a) without contact viscosity (b) with contact viscosity

Fig. 12. Comparison of velocities of block with contact viscosity

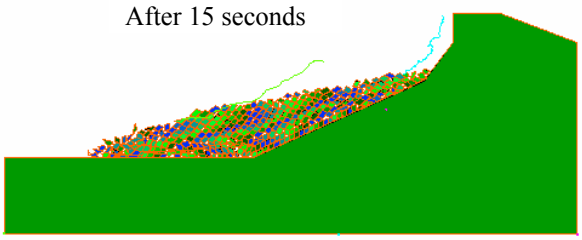

Fig. 13. Deformation with contact viscosity (Case-5)

Figure 12(a) shows block velocities with elapsed time at toe of the slope. In the case of the same block size, the blocks of small unit mass travel faster than the blocks of large unit mass. In the case of small block size, the average velocity of blocks is slightly higher than in the case of large block size. Figure 12(b) compares the velocities of Case-3 (no contact viscosity) and Case-5 (with contact viscosity). Figure 13 shows the deformation of Case-5 after 15 seconds with contact viscosity. The coefficients of the viscosities of contacts are assumed to be 5% of the normal and 10% of the shear direction penalty coefficients.

Regarding the effects of contact viscosity, it is evaluated that the velocity of the block of Case-5 is one-third that of Case-3 after 5 seconds, and that the distance traveled from the slope top is 5% shorter than in Case-3. This is due to velocity-proportional damping in the Voigt-type viscosity model.

4. CONCLUDING REMARKS

We introduced a contact viscous damping model based on the DDA theory, ignoring the additional reaction forces between blocks at the boundary. We presented an earthquake response analysis using the DDA model for the rock slope fall caused by the Niigata Prefecture Chuetsu earthquake in October 2004. The numerical results were compared with the topography of the collapsed slope, and the results agreed well with the actual rock fall phenomena.

The principal influences of the parameters in the analysis for the distance traveled are the block shape and unit mass. The effect of the viscosity of block contact is reduced at higher speed of blocks during contact. The DDA results show that the parameters adequately model the rock slope collapse caused by an earthquake.

However, the actual rock fall behavior is a three-dimensional phenomenon, so the relation between two and three dimensions needs to be clarified. It is also important to analyze the characteristics of earthquake wave acceleration at the slope.

ACKNOWLEDGMENT

The authors thank Dr. Gen Hua Shi for many informative discussions.

REFERENCES

1. Shi G.H. 1989. Block system modeling by discontinuous deformation analysis, *Univ. of California*, Berkeley, Dept. of Civil Eng. August.
2. Hilbert L.B. Jr., et al. 1993. A new discontinuous finite element method for interaction of many deformable bodies in geomechanics, U.C. Berkeley.
3. Shi G.H.. 2002. Single and multiple block limit equilibrium of key block method and discontinuous deformation analysis, *Proc. of ICADD-5*, pp. 3–43, BALKEMA.
4. Hatzor Y.H., A.A. Arzi and M. Tsesarsky. 2002. Realistic dynamic analysis of jointed rock slopes using DDA, *Proc. of ICADD-5*, pp. 47–56, BALKEMA.
5. Tsesarsky M. and Y.H. Hatzor. 2002. Dynamic block displacement prediction-validation of DDA using analytical solutions and shaking table experiments, *Proc. of ICADD-5*, pp. 195–203, BALKEMA.
6. Sasaki T., et al. 2004. Earthquake response analysis of a rock falling model by Discontinuous Deformation Analysis, In *Proc. of the ISRM Symp. 3rd Asia Rock Mechanics Symp.*, *Kyoto, 1-3 December 2004*, eds. Y. Ohnishi et al., pp. 1267–1272, Millpress.

Influence of input parameters on energy loss in free fall tests with DDA

Ishikawa, T. and Miura, S.
Hokkaido University, Sapporo, Hokkaido, Japan
Ohnishi, Y.
Kyoto University, Kyoto, Kyoto, Japan

This paper was prepared for presentation at *ICADD-7, the Seventh International Conference on Analysis of Discontinuous Deformation*, held in Honolulu, Hawaii, December 10-12, 2005.

ABSTRACT: According to some past researches, it was reported that in case of applying DDA to the full dynamic problem such as impact problems, if input parameters, e.g. time increment and penalty coefficient, are not appropriate, accidental energy loss caused by numerical errors occurs in the results. This paper examines the relationships between input parameters and energy loss at the collision between two objects by performing free fall tests of a block with DDA under a variety of experimental conditions, and studies how to select appropriate input parameters according to the analytical condition to decrease the numerical errors. As the results, it is revealed that as a necessary and sufficient condition for the precise DDA simulations of full dynamic problems, it is indispensable to set some specific input parameters about contact computation within the proper range which is determined according to analytical conditions.

1. INTRODUCTION

Geotechnical materials such as sand and gravel are an assembly of granular particles. The mechanical behavior of granular materials is extremely complicated because it would be mainly ruled by a lot of non-linear factors due to the discrete and non-homogeneous internal structure, or disorderly particle alignment. In general, experimental research such as model test and element test would be adopted for investigating the mechanical behavior of granular materials in comparison with numerical simulations. However, it is hard to separate one factor from the others based on experimental research because it is almost impossible to control experimental condition precisely and exclude an individual difference between test samples completely in laboratory tests. Meanwhile, numerical simulation has an advantage that it can examine the mechanical behavior of geotechnical materials in terms of micromechanics as well as controlling an arbitrary experimental condition accurately, compared with experimental research. Accordingly, numerical simulation (numerical experiment) has been widely utilized to examine the geotechnical problem which is hard to be reproduced by real laboratory tests these days.

Especially, from the viewpoint of the mechanics of granular materials, discontinuous models seem to be appropriate for simulating the mechanical behavior of granular materials caused by the movement of constituent particles. This is because discontinuous analyses assume granular materials as discontinuum and consider the granularity of geotechnical materials. In discontinuous modeling, the movement of an individual particle can be microscopically traced under both kinematic and static constraint conditions which consider the mechanics of granular

materials and the discontinuum mechanics. Therefore, discontinuous analysis has been recently applied to various kinds of the mechanical behavior of granular materials, for example, liquefaction of saturated granular soils [1], settlement of railway ballast under cyclic loading [2], and designing of rockfall prevention works [3].

In discontinuous analysis such as Distinct Element Method (DEM) [4] and Discontinuous Deformation Analysis [5], when two elastic or rigid elements come in contact, a frictional slider, elastic springs and viscous dashpots are created at the contact point. The results of numerical simulation with discontinuous analysis are sensitive to the input parameters concerned with contact between elements. The reason for this is that contact mechanism in discontinuous analysis plays an important role in not only the transmission mechanism of external force and kinetic energy at collision but also the stability of computation or the convergence for iterative calculation. Accordingly, it is indispensable for improving the prediction accuracy of discontinuous analysis to examine the influence of the input parameters concerning contact mechanism on the transmission of kinetic energy at the collision between two objects in case of analyzing the mechanical behavior of granular materials, where many blocks come in contact repeatedly during simulations.

2. OBJECTIVES OF RESEARCH

This paper presents a fundamental study to improve the reliability of numerical simulation in case of applying DDA to the mechanical behavior of granular materials.

The objectives of this paper are:

- to examine the relationships between input parameters and the transmission mechanism of kinetic energy at the collision between two objects.
- to show how to select appropriate input parameters according to the analytical condition to decrease the numerical errors.

In this paper, a series of free fall tests using a regular polygon block are performed with two-dimensional DDA under a variety of experimental conditions altering block materials, falling heights, ball diameters, etc. Based on the results, the influence of input parameters on the prediction accuracy of numerical simulations is evaluated in terms of the correctness in transmission of kinetic energy. Then, the validity of the method for selecting input parameters in DDA simulations is examined.

3. ANALYTICAL ASSIGNMENT IN DDA SIMULATION

3.1. Input Parameters in DDA

DDA, which is based on the minimizing potential energy, is a dynamic analytical method for the discontinuous assemblages. The movements of each block are the cumulative displacements for each time step, and the deformation property of a DDA block is linear elastic in this paper. When two DDA blocks come in contact during computations, contact springs are introduced to prevent blocks from penetrating to each other as shown in Figure 1. Contact damping is not necessary in the calculations to maintain the stability of computation, and it makes the physical meaning of input parameters in DDA clearer than in DEM. Hence, DDA is expected as a method to solve the contact problem of discontinuum and simulate the mechanical behaviors of discontinuous blocks after contact.

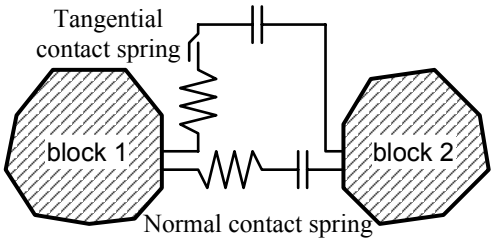

Fig. 1. Contact mechanism of DDA.

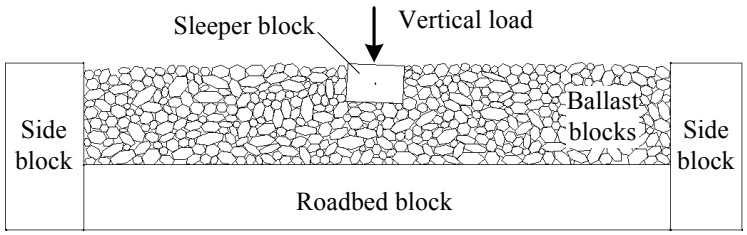

Fig. 2. DDA model of ballasted railroad track.

In discontinuous analysis, the contact computation plays an important role. DDA introduces the methodology called "Open-close iteration," to set the correct contact spring patterns of block systems and calculate the approximated contact forces for each contact pair under the rule keeping "no-penetration, no-tension criterion between two blocks." Some specific input parameters controlling numerical calculation, namely "reference length (*w0*)," "displacement allowed ratio (*DAR* or *G2*)," "maximum time increment ($\Delta t_{\max}$)," and "stiffness of normal contact spring (k_n)," are employed to consider the convergence efficiency of time integration and derive the correct solution about the contact behaviors simultaneously. These control parameters are most difficult to be decided among all designated analytical conditions because most of the parameters cannot be obtained by experimental results. Moreover, the problems with lots of blocks and complicated contacts such as the mechanical behavior of granular materials are very sensitive to these control parameters. Therefore, the selection of control parameter has a significant effect on computational results in simulating the mechanical behavior of granular materials.

Moreover, the time integration method introduced in DDA is one of the Newmark-type approaches [6]. The Newmark-type time integration guarantees the unconditional stability of numerical computation if the parameters satisfy the specific conditions. Accordingly, the Newmark-type approach can be good to analyze static problems because with large time increment the simulation results approach to the static state fast and remain stable. However, when DDA is applied to the full dynamic problem such as impact problems, the numerical simulation may not attain the correct solution in theory according to the analytical conditions. This is because for example, in case of employing larger time increment in the block collision simulation, accidental energy loss caused by numerical errors, namely "algorithmic damping," occurs in the results [7]. Although DDA introduces Open-close iteration to control the size of time increment during contact computation, it is not small enough to neglect the algorithmic damping. Accordingly, the small time increment should be employed to the dynamic problem in order to diminish the numerical errors during time integration.

3.2. Simulations of Granular materials

This section presents a numerical simulation of railroad ballast under cyclic loading as an example of analytical assignments in applying DDA to the mechanical behavior of granular materials. Figure 2 shows the element meshes of DDA models before loading. The DDA model is composed of some polygon blocks, named "ballast blocks," which represent andesite ballast particles and rectangular blocks, named "a sleeper block" which represents an aluminum sleeper, named "a roadbed block" which represents steel roadbed and named "side blocks" which represent a rigid soil container. Vertical loads with constant amplitude between the maximum value $P_{\max}$ of 2kN and the minimum value of 0.5kN was repeatedly applied to the center of the sleeper block as shown in Figure 2. The waveform was triangular, and the number of loading cycles was five. Furthermore, the gravity force was applied to the DDA model throughout the

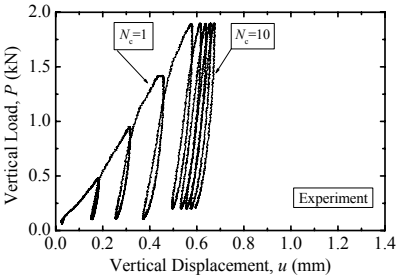

Fig. 3a. Experiment.

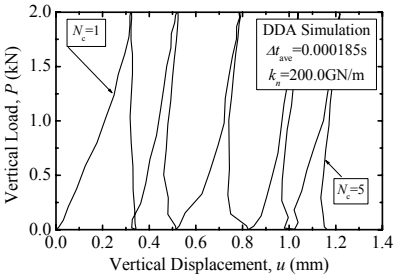

Fig. 3b. Simulation (k_n=200GN/m).

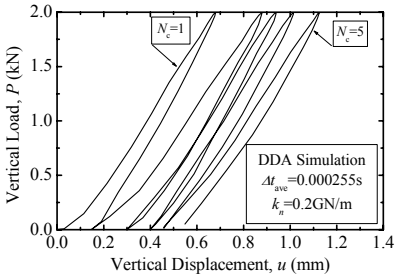

Fig. 3c. Simulation (k_n=0.2GN/m).

simulation. "Analysis type index" or "Kinetic damping parameter [8]" (k01) was set equal to 0.0, and so the DDA simulations were performed under quasi-static conditions. For further details about analytical conditions, the paper [9] is to be referred.

The applicability of DDA to the cyclic plastic deformation of railroad ballast was examined. Figure 3 shows the relations between the vertical load P and the vertical displacement u of the sleeper comparing analytical results derived from the DDA simulation with experimental results. It is observed that the load-displacement relation of analytical results in Figure 3b differs from that of experimental results (Figure 3a) in the elasto-plastic deformation at unloading process. In DDA simulations as shown in Figure 3b, the vertical displacement increases progressively not only at loading but also at unloading, though the vertical displacement of experimental results decreases at unloading. Accordingly, at the above-mentioned analytical conditions, DDA may not simulate railroad ballast under cyclic loading well.

Then, one of the control parameters, namely "stiffness of normal contact spring (k_n)," was changed to improve the prediction accuracy of DDA simulations. Figure 3c shows the load-displacement relations under cyclic loading obtained from DDA simulations which decreases k_n from 200.0 GN/m to 0.2 GN/m, together with their average time increments. It is recognized that the difference in the stiffness of normal contact spring has a considerable influence on the simulation results, and that in adopting the k_n value of 0.2 GN/m, the analytical results are similar in the shape of load-displacement relation to experimental results compared with in adopting the k_n value of 200.0 GN/m because the vertical displacement decreases at unloading like experimental results. This example demonstrates that the selection of unsuitable parameter may cause wrong computational results.

Beside, Figure 3 shows that with the decrement of the k_n value, the average time increment increases. Here in this paper, the time increment is not given as one of input parameters, but the average time increment is derived from DDA simulations. Consequently, in case of a long term simulation for granular materials, selecting small stiffness of normal contact spring has an outstanding advantage. On the other hand, as mentioned above, a small time increment should be employed to avoid the numerical errors caused by algorithmic damping. Also, a large stiffness of normal contact spring should be selected so as to prevent blocks from penetrating to each other. Accordingly, it is indispensable for the precise and efficient simulation of granular materials to select a well-balanced stiffness of normal contact spring.

4. FREE FALL TEST

Some researchers investigate the influence of input parameters on the analytical results by simple and basic simulations [10]. In this paper, a series of free fall tests using a regular polygon block

are performed with two-dimensional DDA program to evaluate the influence of input parameters on the prediction accuracy of numerical simulations in terms of the correctness in transmission of kinetic energy.

4.1. Numerical Models

Free fall test simulations under plane-strain condition were performed while changing analytical conditions such as materials of a ball and/or a reflector plate, falling heights H, ball diameters D. The schematic diagram of DDA models is shown in Figure 4. The test implement is composed of only two DDA blocks, namely a "ball block" which represents a free falling ball and a "reflector block" which represents a fixed reflector plate. At the begging of each simulation, the ball block, which shape was a regular octagon and which diameter was 40 mm or 60 mm, was placed so as to turn a certain angle of the ball block downward. In the simulations, a ball block at the height of 0.2 m, 0.4 m and 0.6 m from the upper surface of the reflector block falls by the gravity force G of 9.8 m/s^2 and collides with the reflector block. Here, the initial velocity of the ball block is zero. Consequently, the contact type between two blocks is vertex-to-edge contact as shown in Figure 5a.

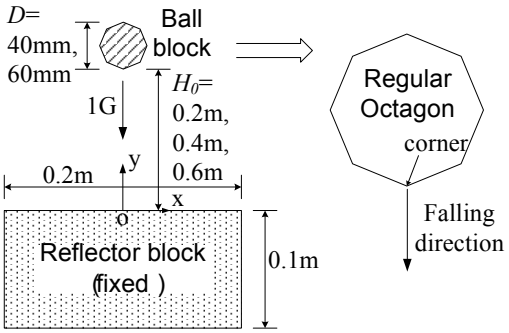

Fig. 4. Schematic Section of DDA model.

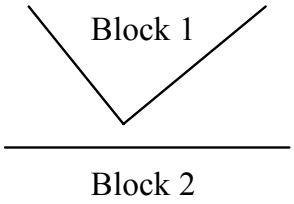

Fig. 5a. Vertex-to-edge contact.

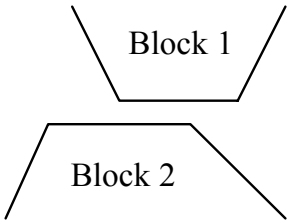

Fig. 5b. Edge-to-edge contact.

Table 1. Material Properties of DDA Model.

Block Material	Unit Mass γ g/cm^3	Young's Modulus E GPa	Poisson's Ratio ν	Cohesion C_μ kPa	Friction Angle ϕ_μ deg.	Input *COR*
Andesite	2.70	20.0	0.1	0	0	1.0
Iron	8.00	210.0	0.3	0	0	1.0

Free fall test simulations in this paper assume to be the perfectly elastic collision problem where the energy conservation law holds good. Therefore, the material properties of blocks and the interface properties of block edges were selected as shown in Table 1. As for the material properties, the parameters γ, E and ν were set referring to the material properties of andesite and iron. As for the interface properties, both ϕ and C_μ were set equal to zero assuming frictionless dynamic contact problems only in vertical direction. Besides, as for one of input parameters in DDA simulations, the coefficient of restitution *COR* which represents the energy dissipation of mechanical energy at the collision between two objects, was set equal to 1.0.

4.2. Coefficient of Restitution

In this paper, the coefficient of restitution is used as an index to evaluate the influence of the input parameters on the transmission of kinetic energy at the collision between two objects. For this purpose, the output *COR* is calculated by Eq. (1).

$$COR = \sqrt{H_1 / H_0} \tag{1}$$

Where H_0 = initial falling height, H_1 = maximum rebounded height after first collision.

Some examples of DDA simulations which differ in the average time increment Δt_{ave} are shown in Figure 6. Here, the average time increment Δt_{ave} is defined as the elapsed time while two blocks keep contact divided by total number of time steps during the contact. The relationships between vertical positions of a ball block and elapsed time differ according to the average time increment. In the DDA calculations assuming the perfectly elastic collision between two blocks, the mechanical energy should conserve, and then the fallen ball block ought to return to the original position. However, in Figure 6, the simulation that employs larger time increment does not obey the energy conservation law, though the simulation using smaller time increment keeps it. This indicates that the potential energy dissipation mechanism, that is "algorithmic damping," exists in DDA in case of using larger time increment as aforementioned. Therefore, computational errors were evaluated by comparing the input *COR* with the output *COR* obtained from analytical results. The successful DDA simulation, which can obtain the correct output *COR* value, is defined as the simulation in case the difference in both *COR* is less than 2.0 %.

Before turning to a closer examination of analytical results in next chapter, a few remarks should be made concerning the shape of a ball block. In this paper, the ball block which shape was a regular octagon was mainly used, and it was set so that the corner of a ball block hit with a

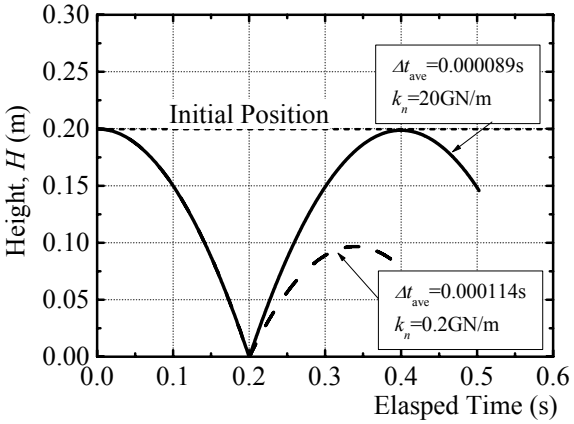

Fig. 6a. Simulation results "success" and "loss" .

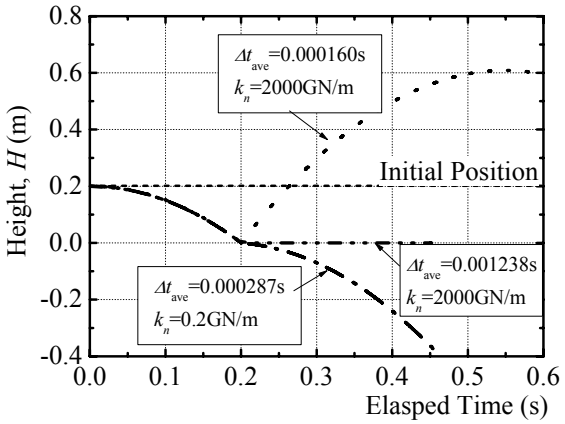

Fig. 6b. Simulation results "stay," "over" and "penetration".

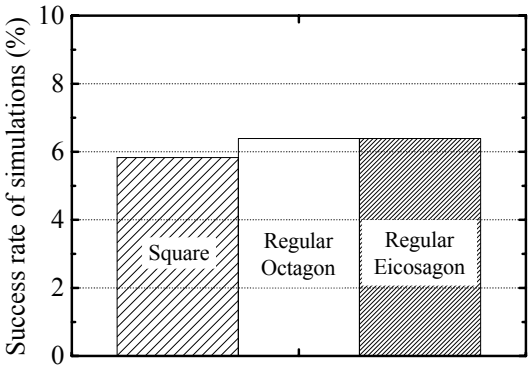

Fig. 7a. Influence of block shape on success rate.

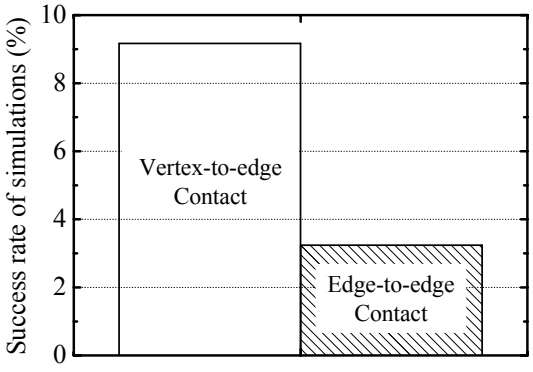

Fig. 7b. Influence of contact type on success rate.

reflector block. Then, as a preliminary investigation, the influence of the difference in the block shape and the aspect of the polygon corner on the analytical result of free fall test simulations was examined. Figure 7a compares the success rate of DDA simulations which used a variety of block shapes, while Figure 7b compares the success rate of DDA simulations which contact type is vertex-to-edge contact with that of edge-to-edge contact (Figure 5b). From these results, it is recognized that the difference in the block shape has a little influence on the success rate, and that the success rate in case of vertex-to-edge contact is higher than that of edge-to-edge contact.

5. RESULTS AND DISCUSSIONS

This chapter will discuss the relationships between the analytical precision of DDA simulations and some input parameters including the aforementioned control parameters.

5.1. Cause of Different Rebound Type

The analytical results can be divided into five types as one successful simulation and four unsuccessful simulations, namely "penetration," "stay," "over" and "loss", as shown in Figure 6. Here, the state called "penetration" is such a simulation that a ball block penetrates through a reflector block, the "stay" is such a simulation that a ball block clings to the surface of a reflector block the "over" is such a simulation that a ball block rebounds over the initial position and the "lack" is such a simulation that a ball block does not return to the initial position after collision. Hereinafter, "penetration," "stay" and "over" are called "ill-condition" in the mass. Table 2 shows the number of the successful DDA simulations and the unsuccessful DDA simulations among 6 kinds of DDA simulations which differ in the combination of D, i.e. D = 40, 60 mm, and H_0, i.e. H_0 = 0.2, 0.4, 0.6 m, under keeping the other analytical conditions like k_n and MD constant. Here, the maximum allowed displacement MD is defined as "displacement allowed ratio (DAR or $G2$)" multiplied by "reference length ($w0$)." So, if the number is 6, the success

Table 2. Classification of DDA simulation results.

Material Property	k_n (GN/m)	MD(=$w0$×$G2$) (mm)								
		0.126	0.210	0.294	0.420	0.840	1.260	1.680	2.520	3.360
Ball: Andesite Reflector: Andesite	0.2	(1)								
	2.0							1	1	
	20.0				1	4	2	2	2	
	200.0				3	6	2	2	2(1)	(1)
	2000.0		(2)	(2)	1(1)	2(3)	1(3)	(6)	(4)	(6)
Ball: Andesite Reflector: Iron	0.2	(1)								
	2.0							1	1	
	20.0				1	4	2	2	2	
	200.0				3	6	2	2	2(1)	(1)
	2000.0		(1)	(1)	1(1)	2(4)	1(5)	(4)	(5)	(6)
Ball: Iron Reflector: Andesite	0.2	(5)	(3)		(2)	(1)				
	2.0									
	20.0					1	1	2	2	
	200.0				3	6	2	2	2	
	2000.0		2		4	6	2	2(1)	2(2)	(4)
	0.2	(5)	(3)		(2)	(2)				
	2.0					1	1	2	2	

rate of DDA simulations is 100%. Besides, in Table 2, a figure without parenthesis is total number of successful DDA simulations under the designated analytical conditions, and a figure in parenthesis is total number of ill-conditioned simulations. An underlined figure means total number of simulations which results in "penetration." From the table, the following tendencies may be founded;

- The suitable combination of k_n and MD for successful DDA simulations may lie in some specific range. For example, under the analytical condition in this paper, the best-suited combination is MD = 0.84 mm and k_n = 200 GN/m.
- The appropriate k_n value depends on the material property of a ball block, though it has a little influence on the material property of a reflector block. Under the analytical condition in this paper, the appropriate k_n value in using an iron ball block is about 10 times of the appropriate k_n value in using an andesite ball block.
- In case of setting both k_n and MD in comparatively small value, the DDA simulation results in "penetration" state. In case of setting both k_n and MD in comparatively large value, the DDA simulation results in "stay" or "over" state.

These results indicate that the control parameters such as k_n and MD have a serious influence on the transmission of kinetic energy at the collision between two objects in applying DDA to the full dynamic contact problem.

5.2. Relation between k_n and Material Property

The influence of material properties such as γ, E and ν on the selection of appropriate k_n value is examined under keeping input parameters except the variable input parameter constant. Figure 8 shows the range of the appropriate k_n value against various densities of a ball block and various Young's moduli of a ball block. With increasing the density of a ball block, the appropriate k_n value gradually increases. On the other hands, the variation in Young's modulus E of a ball block has little effect on the appropriate k_n value. In addition, another investigation confirms that the variation in Poisson's ratio ν of a ball block also has little effect on the appropriate k_n value. From these results, it is revealed that the appropriate k_n value mainly depends on the mass of a ball block in a variety of material parameters.

5.3. Relation between MD and Δt_{ave}

The relation between the output COR values and the Δt_{ave} values is examined to show the proper

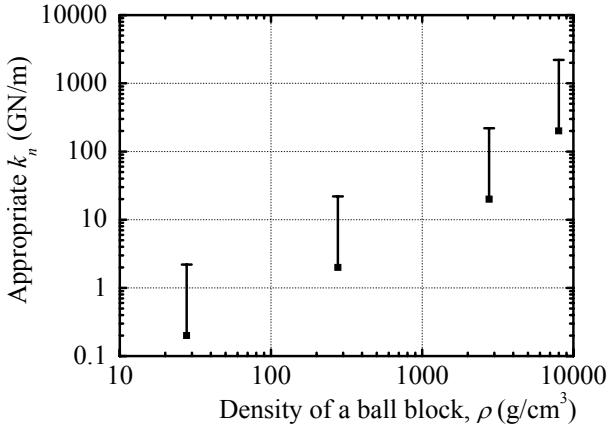

Fig. 8a. Influence of density on k_n.

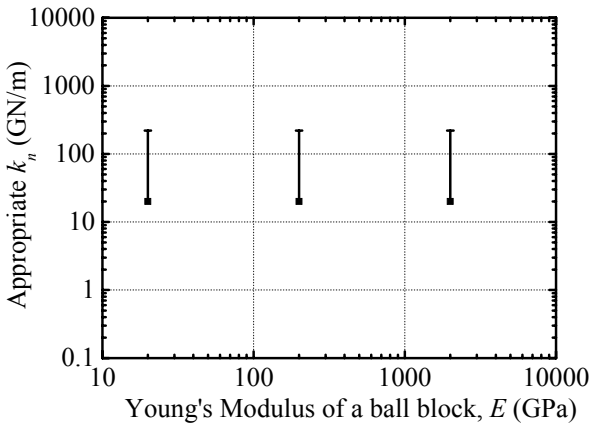

Fig. 8b. Influence of Young's modulus on k_n.

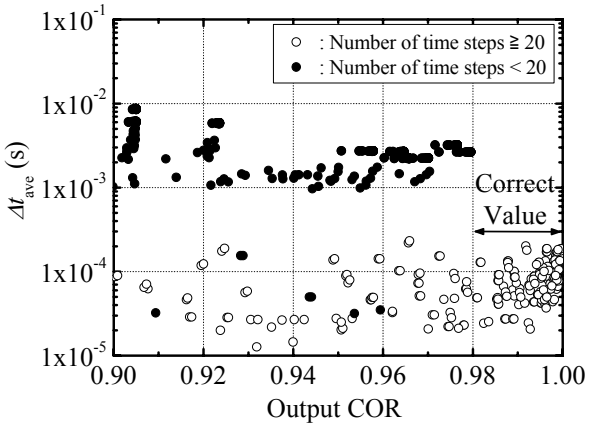

Fig. 9. Relations between output *COR* and Δt_{ave}.

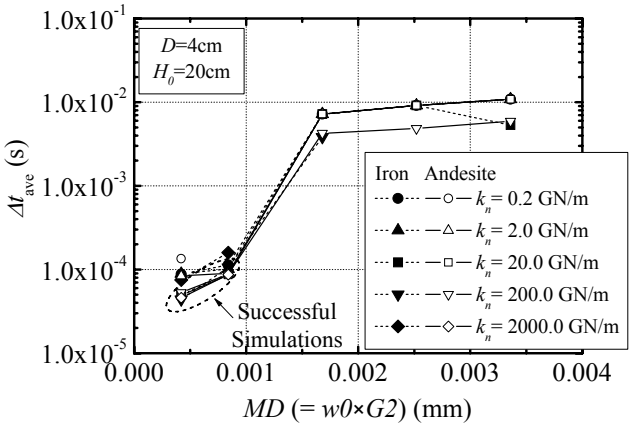

Fig. 10. Relations between *MD* and Δt_{ave}.

range of time increment for decreasing numerical errors during contact computation. Figure 9 shows the relations between the output *COR* and the Δt_{ave} derived from all DDA simulations except the simulations which results in "penetration," "stay" and "over" states. The correct output *COR* values can be obtained when the Δt_{ave} takes the comparatively small value of 1.3×10^{-5}~2.3×10^{-4}sec. However, some cases cannot obtain the correct *COR* value, even if the Δt_{ave} is in the above range. Moreover, there is a tendency to increase time increment extremely when the total number of time steps during contact is more than 20 steps, and consequently the correct output *COR* values cannot be obtained. These indicate that the employment of the small time increment is necessary condition for the successful DDA simulation.

Next, the method to keep time increment in the aforementioned proper range by selecting appropriate input parameters according to the analytical condition is examined. Figure 10 shows the relations between the maximum allowed displacement *MD* and the Δt_{ave} at the respective k_n values, comparing the analytical results in case of an iron ball vs. an iron plate with those in case of an andesite ball vs. an andesite plate. The Δt_{ave} tends to increase with the increment of the *MD*, irrespective of the k_n value, and the Δt_{ave} is highly sensitive to the *MD* compared with the sensitivity to the k_n. Besides, the difference in the *MD*-Δt_{ave} relations due to the material properties on cannot be discerned. From these results, it is recognized that setting time increment to the appropriate value needs to control the maximum allowed displacement *MD*, which is defined as "displacement allowed ratio (*DAR* or *G2*)" multiplied by "reference length (*w0*)." Accordingly, in case of employing both the same *MD* and the same k_n, the analytical results are the same, regardless of the selection of *G2* or *w0* values. This tendency has already been confirmed in this free fall test simulations.

5.4. Relation between k_n and Δt_{max}

The preceding sections illustrate that the k_n and Δt_{ave}(*MD*) plays an important role in the transmission mechanism of external force and kinetic energy at collision and the stability of contact computation. In this section, the relations between k_n and Δt_{ave} are examined to attain the correct numerical solution in theory according to the analytical conditions.

Figure 11 shows the relationships of an iron ball and an andesite ball, respectively. In case DDA simulations can obtain the correct output *COR* value, the Δt_{ave} value is confined within the limits according to the k_n value, and the minimum limit of Δt_{ave} has a tendency to increase gradually

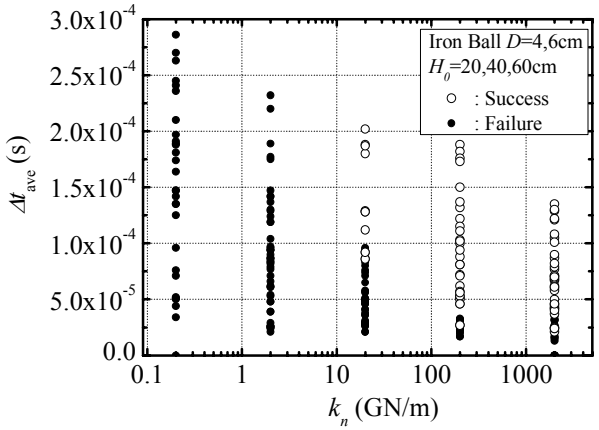

Fig. 11a. Relations between k_n and Δt_{ave} of an iron ball.

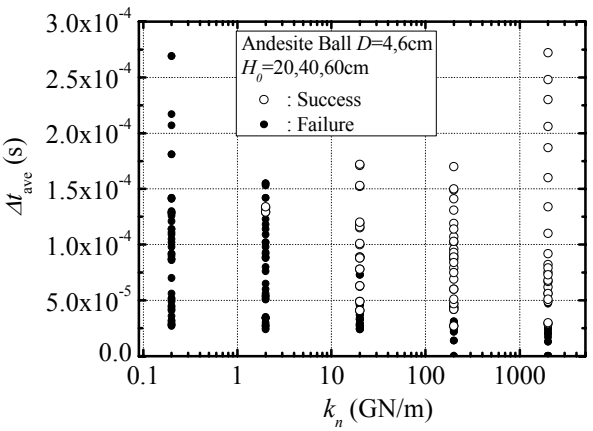

Fig. 11b. Relations between k_n and Δt_{ave} of an andesite ball.

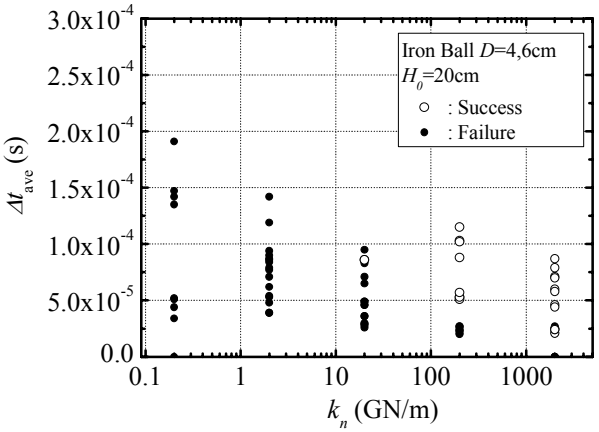

Fig. 12a. Relations between k_n and Δt_{ave} of H_0 = 20cm.

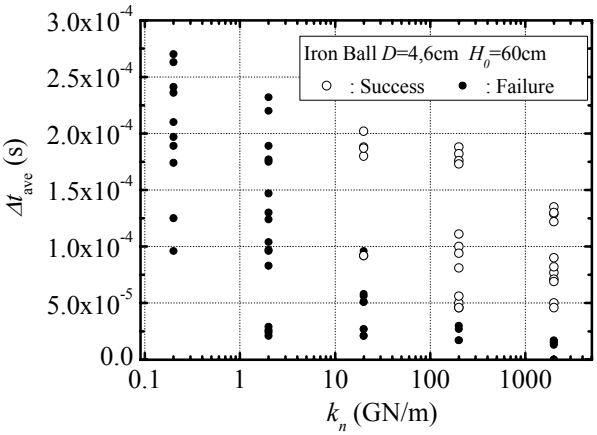

Fig. 12b. Relations between k_n and Δt_{ave} of H_0 = 60cm.

with the decrement of the k_n. Besides, it is recognized that the proper range of Δt_{ave} is influenced by the material properties like density. Especially, as for the maximum limit of Δt_{ave}, there seems to be a considerable difference due to the material properties. The important points from the above considerations are summarized as follows. There is some possibility of not obtaining the correct numerical solution in theory in case of employing extremely small time increment, while too large time increment leads to the wrong solutions as the error due to algorithmic damping cannot be neglected. Therefore, it is a necessary and sufficient condition for the precise DDA simulations of full dynamic problems that time increment lies in the proper range from the minimum value to the maximum value, which are determined by the material properties and the k_n value.

Figure 12 also shows the relationships of an iron ball, comparing analytical results of H_0 = 20 cm with those of H_0 = 60 cm. In spite of no difference in all analytical conditions except falling height between both figures, Figure 12a is different from Figure 12b. Accordingly, it is recognized that the difference in the falling height of a ball block, that is the kinetic energy of a ball block, influences the proper range of Δt_{ave}, and that both the minimum limit of the appropriate Δt_{ave} and the width of the proper Δt_{ave} range increase with increasing the kinetic energy of a ball block before collision. This indicates that other factors except the control

parameter previously mentioned influence the transmission mechanism of kinetic energy at collision, and another potential energy dissipation mechanism besides "algorithmic damping" may exist in DDA. For example, it is said that the "Open-close iteration" can cause unreal contact behaviors as the tensile forces and too large contact forces are generated if control parameters, e.g. "criteria of opening (*f0*)" and "criteria of open-close (*f1*)", are not appropriate [11]. In this paper, though both the *f0* value and the *f1* value are fixed, the penetration length at collision is closely related to the kinetic energy of colliding objects. Therefore, these control parameters ought to be adjusted to the kinetic energy of a ball block so as to diminish the numerical errors during contact computation as much as possible. However, it needs further investigation concerned with the influence of these control parameters on the transmission of kinetic energy at the collision between two objects

6. CONCLUSION

The following conclusions can be obtained;

(vii) The control parameters such as k_n and *MD* have a serious influence on the transmission of kinetic energy at collision in applying DDA to the full dynamic contact problem.

(viii) The suitable combination of k_n and *MD* for successful DDA simulations may lie in some specific range.

(ix) The appropriate k_n mainly depends on the mass of a ball block, though it has a little influence on the material property of a reflector block.

(x) The Δt_{ave} tends to increase with the increment of the *MD*, irrespective of the k_n value, and the Δt_{ave} is highly sensitive to the *MD* compared with the sensitivity to the k_n.

(xi) Setting time increment to the appropriate value needs to control the maximum allowed displacement *MD*, which is defined as *G2* multiplied by *w0*.

(xii) There is some possibility of not obtaining the correct numerical solution in theory in case of employing extremely small time increment, while too large time increment leads to the wrong solutions as the error due to algorithmic damping cannot be neglected.

(xiii) As a necessary and sufficient condition for the precise DDA simulations of full dynamic problems, it is indispensable to put time increment within the proper limitation which is determined by material properties and k_n.

(xiv) The difference in the falling height of a ball block, that is the kinetic energy of a ball block, influences the proper range of Δt_{ave}.

(xv) Other factors except k_n and Δt_{ave} influence the transmission mechanism of kinetic energy at collision, and another potential energy dissipation mechanism besides "algorithmic damping" may exist in DDA.

ACKNOWLEDGEMENT

The authors would like to thank Dr. Takeshi Sasaki, Suncoh Consultants Co. Ltd. for many invaluable discussions and suggestions.

REFERENCES

1. Zeghal, M. and U.EI. Shamy. 2004. Dynamic response and liquefaction of saturated granular soils: a micro-mechanical approach. In *Proceedings of Cyclic Behaviour of Soils and Liquefaction Phenomena, Bochum, 31 March – 02 April 2004*, eds. Th. Triantafyllidis, 589–602. Rotterdam: Balkema.
2. Saussine, G., C. Cholet, P.E. Gautier, F. Dubois, C. Bohatier and J.J. Moreau. 2004. Modelling ballast under cyclic loading using Discrete Element Method. In *Proceedings of Cyclic Behaviour of Soils and Liquefaction Phenomena, Bochum, 31 March – 02 April 2004*, eds. Th. Triantafyllidis, 649–658. Rotterdam: Balkema.
3. Fukawa, T., Y. Ohnishi, S. Nishiyama, S. Uehara and S. Miki. 2005. Three dimensional discontinuous deformation analysis for rockfall simulation. In *Proceedings of the 11th International Conference of IACMAG, Torino, 19 – 24 June 2005*, eds. G. Barla and M. Barla, Volume 3: 513–520. Bologna: Patron editore.
4. Cundall, P.A. and O.D.L. Strack. 1979. A discrete numerical model for granular assemblies. *Geotechnique.* 29(1): 47–65.
5. Shi, G.H. and R.E. Goodman. 1984. Discontinuous Deformation Analysis. In *Proceedings of the 25th U.S. Symposium on Rock Mechanics,* 269–277.
6. O`Sullivan, C. and J.D. Bray. 2001. A comparative evaluation of two approaches to discrete element modeling of particulate media. In *Proceedings of the 4th International Conference on the Analysis of Discontinuous Deformation, Glasgow, 6 – 8 June 2001*, eds. N. Bicanic, 97–110. Glasgow: University of Glasgow.
7. Ishikawa, T., Y. Ohnishi, J.H. Wu and S. Nishiyama. 2003. Modeling for energy dissipation in free fall tests of spherical stone with discontinuous analysis. In *Proceedings of Soil and Rock America 2003, Cambridge, 22 – 23 June 2003*, eds. P.J. Culligan et al., 1105–1110. Essen: Verlag Gluckauf GambH.
8. McBride, A. and F. Scheele. 2001. Investigation of discontinuous deformation analysis using physical laboratory models. In *Proceedings of the 4th International Conference on the Analysis of Discontinuous Deformation, Glasgow, 6 – 8 June 2001*, eds. N. Bicanic, 73–82. Glasgow: University of Glasgow.
9. Ishikawa, T., K. Kobayashi, E. Sekine, and Y. Ohnishi. 2005. Evaluation of the effect of particle shape on the bearing capacity of railroad ballast with discontinuous analysis. In *Proceedings of the 7th International Conference on the Bearing Capacity of Roads, Railways and Airfields, Trondheim, 27 – 29 June 2005*, [1/1(CD-ROM)52].
10. Doolin, D.M. and N. Sitar. 2002. Displacement accuracy of discontinuous deformation analysis method applied to sliding block. *J. Engineering Mechanics.* 1158–1168.
11. Wu, J.H. 2003. Numerical analysis of discontinuous rock masses using discontinuous deformation analysis. In *Doctoral Dissertation*, Kyoto University, 62.

Numerical Simulation of Bench Blasting by 2D-DDA Method

Yang Jun
Ning You-jun
State Key Laboratory of Explosion Science and Technology, Beijing Institute of Technology, Beijing, China

This paper was prepared for presentation at *ICADD-7, the Seventh International Conference on Analysis of Discontinuous Deformation*, held in Honolulu, Hawaii, December 10-12, 2005.

ABSTRACT: Rock blasting is a large deformation, large displacement process, accompanying with both dynamic and static effects, blocks in the discontinuous rock medium may be fractured by explosive impulsive loads. DDA method meets the characteristics of rock blasting and the blasting fragment size can be forecasted by this method. In order to simulate rock blasting process exactly, plastic constitutive relation is added to the initial edition of 2D-DDA code and energy dissipation is taken into account. A typical rock bench blasting is calculated by the extended code and the blasting fragment size is analyzed.

1. PREFACE

Since the method of Discontinuous Deformation Analysis was put forward by Doctor Shi Gen-hua, it has been developed a lot and now is used in various fields, such as rock and soil engineering, water conservancy projects and so on. For the numerical simulation of rock blasting, DDA has its superiority in theory compared with traditional numerical methods such as FEM and DEM. DDA meets the characteristics of rock blasting [1]: large deformation, large displacement, accompanying with both dynamic and static effects, the calculated media is discontinuous block system and the blocks may be fractured by explosive impulsive loads. As both joints in the initial rock medium and new cracks generated by the effect of explosive loads can be calculated by DDA method, the blasting fragment size forecast can be done by this method.

However, DDA hasn't been playing an important role in the simulation of rock blasting until now and only a little work in this field has been down. Zhu Chuan-yun, Jiang Qing-hu [2], Liu Hong-yan [3] etc. have calculated blasting funnel using 2D-DDA method. In their work, the simple elastic constitutive relation was used and the dissipation of energy was not considered. A.Mortazavi and P.D.Katsabanis simulated bench blasting process with extended 2D-DDA code and achieved satisfying result [4], but the calculated model was limited in static state and the simulated pile differs from the practical pile. It is obvious that simple constitutive relation can't meet the characteristic of the association of dynamic and static effects of rock blasting. For the initial edition of 2D-DDA code, the friction among blocks is the main way of the consumption of energy and obviously it's not enough, the energy dissipation can't be ignored. In order to simulate rock blasting exactly, the author may try to solve both of the two problems, and a way of forecasting blasting fragment size is put forward in this paper. Then a typical rock bench blasting with a consideration of over drilling is calculated with the extended code and the result is analyzed.

2. CODE EXTENSION

2.1. Plastic Constitutive Relation

As Drucker-Prager yield criterion is the revise of Mohr-Coulomb yield criterion, the effect of ambient pressure σ_2 to the yield of rock medium is taken into account and this criterion can also reflect the effect of shear stress to the expansion of volume [5]. So this yield criterion is to be used in the extension of the initial edition of 2D-DDA code. This criterion can be expressed as follows:

$$f = \alpha I_1 + J^{1/2} - K = 0 \tag{1}$$

Where I_1 is the first invariant of stress tensor, J_2 is the second invariant of deviator stress tensor, α, K are material parameters, their relations to cohesion c and angle of internal friction ϕ are:

$$\alpha = \frac{2\sin\phi}{\sqrt{3}(3-\sin\phi)}$$

$$K = \frac{6c\cos\phi}{\sqrt{3}(3-\sin\phi)}$$

The linear strain-hardening plastic constitutive relation is added to the 2D-DDA code and the two dimensional Drucker-Prager yield criterion is used.

2.2. Energy Dissipation

In the initial DDA method, the friction among blocks is the main way of the consumption of energy [6] and for the one order displacement function DDA code, fracture of blocks can't be calculated. In order to calculate rock blasting with DDA method, the dissipation of energy is taken into account according to the calculation of suppositional cracks.

While a block is under plastic condition according to the Drucker-Prager yield criterion, the plastic constitutive relation is used.

Because the expansion of rock medium is limited [5], if a block expands above a certain ratio that's permitted, it is considered to be fractured and a crack is recorded. For this fractured block, it can't bear tensile stress [7], so the tensile stresses of the block should be set zero and the increase of the strain of this block in this time step should be ignored.

When a block doesn't expand as much as that ratio, if a certain principal stress is bigger than the tensile strength of the rock medium, the block is considered to be fractured and a crack is recorded. This principal stress should be set zero and the increase of the corresponding principal strain of this block in this time step should be ignored.

When a block doesn't grow as much as that ratio, if a certain principal stress is bigger than the compressive strength of the rock medium, the block is considered to be fractured and a crack is recorded. This principal stress should be set the value of the compressive strength and the increase of the corresponding principal strain of this block in this time step should be ignored.

Because rock media's strength may grow a lot under the condition of high strain increasing ratio [5], the tensile strength and compressive strength may be multiplied by 10 while the strain increasing ratio is bigger than 10^4.

So in each time step, stresses and increased strains in this time step in x-axis, y-axis and the shear direction should be transformed to the principal directions and the transforming angle should be recorded for the backward transformation [8].

2.3. Blasting Fragment Size Forecast

With the consideration of the above records of suppositional cracks and the open and close conditions of the initial joints, the blasting fragment size can be forecasted.

In the fractured area (Fig.1) of the blasted rock media [9], if the number of suppositional cracks is n_1 in a certain initial block, it is supposed to be fractured into 2^{n_1} smaller blocks and the area of each of the smaller blocks is:

$$S = (\frac{1}{2})^{n_1} S_0 \qquad (2)$$

Where S_0 is the initial average area of the blocks in the jointed rock media. If a block is still felted to n_2 other blocks, the area of the felted bigger block is:

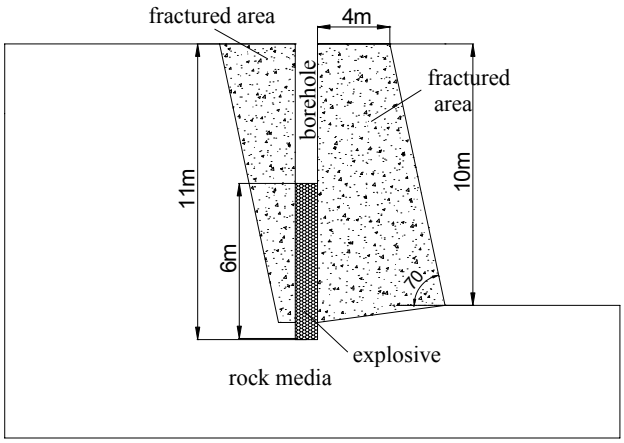

Fig.1 Typical rock bench

$$S = (n_2 + 1)S_0 \qquad (3)$$

Where S_0 is the initial average area of the blocks in the jointed rock media. If a block is not suppositional fractured and is not felted to any other block, the area of this block after blasting is the same as that before blasting:

$$S = S_0 \qquad (4)$$

The representative dimension l of each block is calculated by the assumption that all the blocks before and after blasting are equilateral triangle, so l can be calculated by the following formula:

$$l = 2\sqrt{\frac{1}{\sqrt{3}}S} \qquad (5)$$

The proportion of the total area of blocks which have the same representational dimension to the total area of blocks in the fractured area can be gotten:

$$\beta = \frac{n_l S}{N S_0} \times 100\% \qquad (6)$$

Where n_l is the number of blocks which have the representative dimension of l and S is the corresponding block area. N is the total number of blocks in the fractured area and S_0 is the initial average area of the blocks in the jointed rock media.

To define Γ is the proportion of the total area of blocks which have the representational dimension smaller than l, so Γ can be calculated as follows:

$$\Gamma = \sum \beta_i \tag{7}$$

Where β_i is the proportion of all the blocks which have the same but smaller representational dimension than l.

Then a Γ-l curve can be drawn and this curve reveals the blasting fragment size distribution.

3. SIMULATION OF A TYPICAL ROCK BENCH BLASTING

3.1. Simulation of a Typical Rock Bench Blasting

The sketch map of the calculated typical rock bench is shown in Fig.1. As the fragmental zone is not going to be calculated, the diameter of the borehole is 2.5 times [9] of the initial borehole, it's 500 mm. The rock media is granite, and the material parameters of rock media [10] and the joint parameters are shown in Table 1 (2600 $kg \cdot m^{-3}$ =4382.26 $lb \cdot yd^{-3}$).

Table 1. Material parameters

	Density ρ $kg \cdot m^{-3}$	Yong modulus E_p / GPa	Poisson ratio ν	Friction angle $\theta / °$	Cohesion c MPa	Tensile strength σ_t / MPa	Compressive strength σ_p / MPa
rock media	2600	62	0.22	60	50	18	155
joints	-	-	-	45	2	0.5	-

In A.Mortazavi and P.D.Katsabanis's work, the effect of stress wave to the blast is ignored and only the blasting products' effect is calculated. In this paper, both of the above two effects are going to be taken into account by the method of compositing the two load history together.

The sketch map of the composition load history acted on the borehole wall where the explosive effects directly (6 m (6.5617 yd) at the bottom) is shown in Fig.2. On the borehole wall where the explosive doesn't effect directly (5 m (5.4681 yd) at the top), the load will gradually start in 2 ms with the dissipation of the peak value to zero in the direction to the borehole mouth. All the loads on the bore hole will finish in 6 ms.

The peak value of explosion pressure of 2 $^{\#}$ rock explosive is [9]:

$$P_H = \frac{1}{4}\rho_0 D_H{}^2 = 3240 MPa$$

Where $\rho_0 = 1g/cm^3$ (2123.89 $lb \cdot yd^{-3}$) is the density of the explosive, $D_H = 3600 m/s$ (3937 yd/s) is the explosion velocity. As the crush zone is not going to be calculated, according to the

effecting area of the load and the theory that most energy is consumed in the crush zone [9], the real peak value is:

(note – Figure 2 removed because it would not convert to .pdf)

Fig.2 Load history

$$P_1 = \frac{1}{10}(\frac{r_0}{r_f})P_H = 130MPa$$

Where r_0 is the radius of the initial borehole and r_f is the radius of the borehole with out the consideration of crush zone. The ratio $\frac{1}{10}$ is used because of the dissipation of the energy for crush in this zone.

As the effect of explosion products is taken into account, the turning point time and the ending time of the load are $t_2 = 0.2ms$ and $t_3 = 6ms$. The peak value time $t_1 = 10vs$ and turning point pressure $P_2 = 30MPa$ is decided by the explosion shock load itself.

In the calculation, according to the weak plastic character of granite, the Yong modulus under plastic condition is 0.8 times of that under elastic condition, and the maximum expansion ratio of each block is 0.1%.

The initial joints in the rock media and representative moments of the simulation are shown in Fig.3. Compared with the initial edition of 2D-DDA code in which elastic constitutive relation is used and the energy dissipation is not taken into account, the control of the blocks is obviously improved. The movement of the blocks in the bench displays the real bench blasting quite well. But the control is still not enough: the fractured area is lager than that in theory; the flying rocks are not fully controlled.

The blocks that should fall and form the blasting pile may be out of control if the calculation goes on and the energy dissipation is not enough. For the reflection of the boundary to the stress wave, the free surface on the top is disturbed by the explosive load.

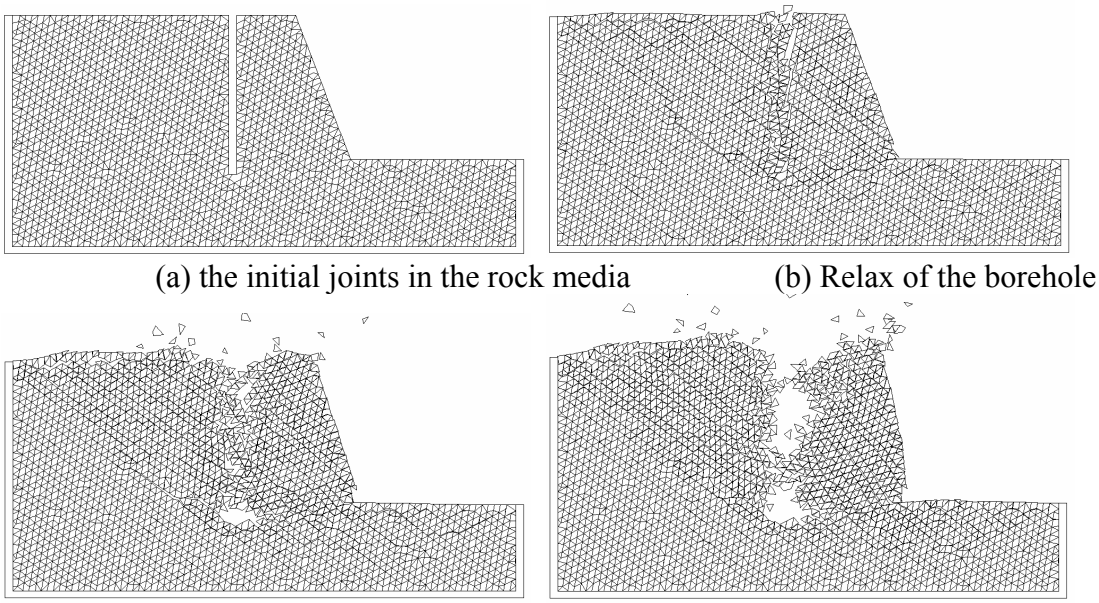

(a) the initial joints in the rock media (b) Relax of the borehole

(c) Flying rocks (d) To fall down

Fig.3 Initial joints and representative moments

3.2. Fragment Size Analysis

By the fragment size forecast method mentioned above, the Γ-l curve is shown in Fig.4. The initial average area of the blocks in the jointed rock media is $0.11\,m^2$ ($0.1316\ yd^2$), and the initial average representative dimension is $0.50\,m$ ($0.5468\ yd$).

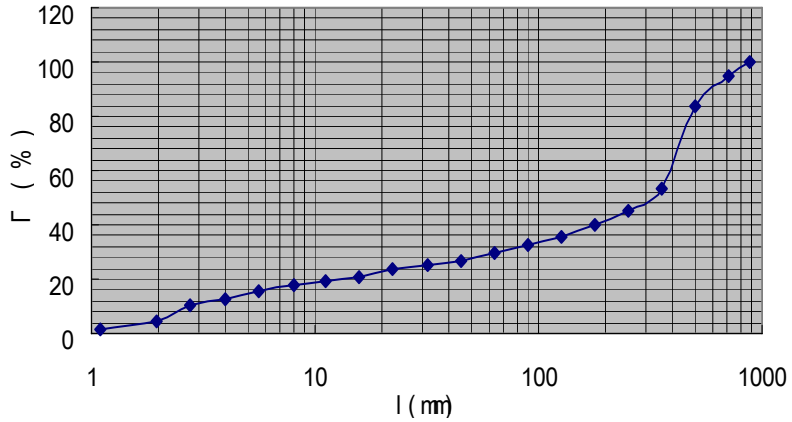

Fig.4 Blasting fragment size forecast

4. CONCLUSIONS

According to the simulation result of the typical rock bench blasting, it's feasible to simulate rock blast with DDA method, especially for the forecast of blasting fragment size distribution.

By adding plastic constitutive relation and energy dissipation to the initial edition of 2D-DDA code, A new method to solve complex static-dynamic problem such as rock blasting by DDA is presented.

However, the beneficial tentative work in this paper is still not satisfied and some more work should be done for the following reasons.

(xvi) Because of the constitutive relation of rock is very complex in reality, it need to take a precise and practical elastic-plastic constitutive relation through a lot of test.

(xvii) The energy dissipation method in the above work is primary and not precise. In order to solve eventually the problem, we can develop high order displacement function DDA with the calculation of real cracks and energy dissipation among blocks [4].

(xviii) For the simulation of rock blasting, how to get the real explosive load history and put it into the simulation work should be studied, maybe we can turn to FEM method. For the calculation of impulsive loads, absorbing boundary should be developed.

REFERENCES

1. Jun Yang, Jin Qian-kun and Huang Feng-lei. 1999. *Rock blasting Theory Model and Its Numerical Simulation*. Beijing: Science Press.
2. Qing-hui Jiang and Zhu Chuan-yun. 2004. Discontinuous deformation analysis for dynamics and its application in modeling of blasting throwing process. *J. Engineering Blasting.* 10: 5-8.
3. Hong-yan Liu, Yang Jun and Chen Peng-wan. 2004. Simulation of the process of explosion funnel formulation by means of discontinuous deformation analysis. *J. Engineering Blasting.* 6: 17-20.
4. A.Mortazavi and P.D.Katsabanis. 2001. Modeling burden size and strata dip effects on the surface blasting process. *J. Rock Mechanics and Mining Sciences.* 38: 481-498.
5. Mei-feng Cai, He Man-chao and Liu Dong-yan. 2002. *Rock Mechanics and Engineering*. Beijing: Science Press.
6. Gen-hua Shi. 1997. *Numerical Manifold Method and Discontinuous Deformation Analysis*. Beijing: Tsinghua University Press.
7. Ji-shan Xu. 1981. *Strength Theory and Its Application.* Wuhan: Water and Electricity Conservancy Press.
8. Zhi-lun Xu. 1980. *A Concise Course in Elasticity*. Beijing: Higher Education Press.
9. Jun Yang, Chen Peng-wan and Hu Gang. 2004. *Modern Blasting Technology.* Beijing: Beijing Institute of Technology Press.
10. Henrych, J. 1987. *Explosion Dynamics and Its Application.* Beijing: Science Press.

(This page intentionally left blank.)

Numerical simulation of Startup and the Whole Process Characteristics of Qianjiangping Landslide with DDA Method

Aiqing Wu, Xiuli Ding
Yangtze River Scientific Research Institute, Wuhan, China, 430010
Huizhong Li
Three Gorges Institute of Survey and Research, CWRC, Yichang, China, 443003
Gen-hua Shi
1746 Terrace Drive, Belmont, CA 94002, USA

ABSTRACT: With advantages of real time variable employment and large discontinuous deformation simulation for DDA method, and on the basis of field geological investigation and its mechanical parameters study, the numerical simulation of startup and a whole sliding process of Qianjiangping Landslide has been carried out by use of DDA method. The corresponding criterion for startup of a landslide has been established, and the whole process characteristics have been analyzed based on the calculation results. It is shown that the main reason of landslide is the reduction of mechanical parameters of controlled sliding surfaces in the landslide body resulted from rainfall and rise of reservoir water level. The landslide belongs to thrust load caused landslide. Compared to the actual process characteristics and the spatial morphology of the Qiangjiangping landslide, it has been proved that the simulation results by DDA are quit reasonable and acceptable. In addition, the most valuable progress is that methods adopted in this paper supply a new way for stability study of landslide or other geotechnical engineering.

1. INTRODUCTION

On July 13 of 2003, a foundation rock landslide called Qianjiangping landslide, with the total volume of about $20.4\times10^6 m^3$, happened in the left bank of Qinggan River in Zigui County, located in the Three Gorges Reservoir area . When it happened, the front of sliding body was thrust to the right bank of Qinggan River and 30m high water wave formed, which resulted in the collapse of houses, the block of Qinggan River, and a serious loss of lives and property.

The geologic features and startup mechanism of Qianjiangping landslide was paid attention by society because it is located in the Three Gorges reservoir area and happened in the time no more than 2 weeks after the storage of Three Gorges reservoir up to 135m elevation.

The research of landslide deformation and failure mechanism by the use of numerical methods is one of the main research aspects for landslide problems in recent years. There exist many difficulties in studying the startup and the whole sliding process of landslide with existed numerical methods because they are not able to employ the real time variable in the model or to simulate discontinuous deformation in large scale during calculation.

DDA method in its mechanical principles has overcome the shortages mentioned above, and has the potential usage to simulate the startup and whole sliding process of a landslide which, in author's view, should be a very important milestone to realize clearly what the true mechanism is

in a landslide[1-5]. On the basis of field geological investigation and its mechanical parameters study, the numerical simulation of startup and process characteristics of Qianjiangping Landslide has been carried out, and some important mechanical deformation mechanism and landslide philosophy have been revealed with use of DDA numerical modeling in this paper.

2□ MAIN FEATURES OF QIANJIANGPING LANDSLIDE

2.1 Process of landslide

There was a obvious sign of deformation appeared before about 15~18 days of landslide: probably on June 27, at the north-east side of rear of sliding body, a crack occurred in the wall of a house with the elevation of 350m ; at the south-west side of sliding body, a crack of 3~6cm wide occurred in the road of 280m elevation and increased to 10cm wide on July 4, forming a steep ridge of approximately 10cm high.

Before 14 hours of landslide, another crack of 0.5cm wide appeared at the elevation of 140m of the sliding body, and 3~5cm wide cracks were also found in the gentle slope at the elevation of 182m. At 24:20 of July 13, massive sliding happened.

2.2 Spatial morphology and scale

Qianjiangping landslide is in arm-chair shape in general, the rear edge is in arc shape, while the sides fan out and the front is also in arc shape, as shown in Fig. 1.

The front elevation of sliding body is 94.7m before sliding and 170m after sliding, and the front is 600m wide; the rear is 350□405m in elevation, 380m in width and 1150m in longitudinal length. The influenced area covers 0.68×106m^2 in total, with average thickness of 30m and volume of 20.40×10^{6}m^3.

2.3 Characteristics of micro-topography

The typical micro-topography of landslide consists of rear edge cliff, massive sliding zone, sliding terrace (gentle slope), sliding sidewall and pinnate-tension joints (groove), barrage and dammed lake, slide tongue and landslide tension influenced zone, etc.

Fig. 1. Spatial morphology of landslide

The rear edge cliff is located on the rear of sliding body with the elevation from 330m to 405m and in arc shape. The bedding rock, smooth and planar and behaved as the bottom sliding surface in foundation of the landslide is revealed , with attitude of 140□30°. Its exposed area is with width of about 380m and length of 180m.

The slide front tongue, shaped with anti-dip stratum, is formed by high speed sliding of landslide and thrust to the right bank of the Qinggan River. Its material consists mainly of rock blocks, contented with soil and produced by foundation rock cracking, and pebbles from original

riverbed on the top of the front tongue, which indicates that movement of the lower foundation rock had occurred.

2.4 Others

According to the scrapes and slickenside grooves on the rear sliding surface, the sliding direction is as the same as the bed rock orientation basically, and it can be determined as NE130°. The sliding distance was about 150m. The volume of landslide sliding into water was $2.40\times10^6 m^3$ accounting to 1/9~1/8 of the total. Water wave of 23 25m in height was formed at the front of landslide. Based on the monitoring information obtained by seismometer station, the maximum sliding velocity is estimated as 16m/s.

3. GENERAL GEOLOGY CONDITIONS

The exposed strata of sliding area belong to Niejiashan Group of Jurassic System (J_{1-2n}), residual deposits (Q^{dl+el}) and riverbed alluvial layer (Q^{al}) of quaternary system. Niejiashan Group (J_{1-2n}) is composed mainly of massive sandstone filled with feldspar and quartz, and siltsand mixtured with a small amount of clayrock and mudstone.

The strike of the slope in the sliding area is accordant with the geologic structure with orientation in the strata of 130° 15° 33°. The dip of the strata from top to the toe of the slope is varied gradually, steep as 33° in the rear edge at the top to 15° at Qinggan river side, seeing Fig. 2.

(note – Figure 2 removed because it would not convert to .pdf format)

Two groups of joints, namely SN and EW, developed in the sliding area. They have played an important role to form side walls and rear tension cracks during landslide.

Rock samples with sliding face contained have been taken from landslide field, and tested in laboratory. The shear strength for the upper sliding surface, f=0.25 c=0.05MPa, and for material in the lower part of sliding body, f=0.37~0.40 C=0.023~0.09MPa.

4. BLOCK SYSTEM AND PARAMETERS IN DDA MODEL

4.1 Block system

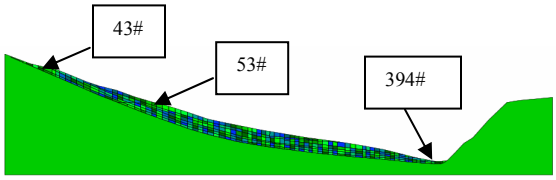

Fig. 3. Block system in DDA model

According to the geological condition of the landslide, the bock system, formed by different sliding surfaces and joints, has been obtained as in Fig. 3.

4.2 Properties assignment

In order to conduct flexibly different simulations involved in running cases and the corresponding parameters, different material regions and block boundaries have been pre-determined individually prior to properties assignment of the block system. For deformation properties, 4 regions in total, where three in the sliding body including one which located below the reservior water level at 135m in elevation, and one for the sliding foundation; for shear strength in block boundaries or sliding faces, 11 types in total.

Parameters in each material region and block boundary or potential sliding surface can be assigned individually. It is convenient to conduct deformation analysis of the block system in different conditions.

4.3 Parameters

In order to get reasonable parameters for the landslide analysis, relative considerations which include aspects of geological conditions, rock and soil mechanical tests and parameters back analysis for the landslide have been conducted comprehensively. Parameters used in DDA model are listed in table 1, where material parameters (1) refers to the general running condition of the slope (not considering the influence of rainfall and storage of reservoir to parameters) , and parameters (2) refer to the parameters which have been reduce to an extent by water seepage of storage of reservoir at 135 water level and rainfall.

Table 1 Parameters used in DDA

Calculation conditions	Deformation properties		Strength properties along general block boundaries		Strength properties along the main sliding faces	
	E (GPa)	μ	ϕ(°)	C(MPa)	ϕ(°)	C(MPa)
Parameter (1)	0.5~1.0	0.35	18~23	0.03~0.06	18~23	0.02~0.05
Parameter (2)	0.5~1.0	0.35	18~20	0.03~0.05	12~15	0.02~0.03
Sliding foundation	2.0	0.25				

5. STARTUP OF LANDSLIDE

5.1 Criterions

For a potential landslide, there is a direct criterion to judge if a landslide occurs. It can be expressed as: for a given load condition, there is a determined sliding surface in the sliding body, and all above the sliding surface would have a massive sliding failure. This means that any part in the sliding body would have obvious displacement and velocity. In DDA model, some particular blocks in sliding body at different positions, i.e. upper part, middle part and lower part of the land slide, are chosen as monitoring points. If all monitoring points have obvious displacement and velocity at time t, then the landslide may occur.

In this paper, three blocks, 43#, 53#,and 394# in figure 3, have been chosen as monitoring points. From curves of displacement and velocity versus time of these points obtained by DDA modelling, the startup of landslide can be determined.

5.2 Conditions of landslide startup

With the established DDA block system, the deformation and failure mechanism of the landslide in three cases have been carried out respectively.

(1) Not consider storage of the reservoir

Parameter (1) in table 1 is used. Curves of displacement and velocity versus time of monitoring points in sliding body are shown in Fig. 4. It is shown that the landslide at this condition is stable although there are obvious deformation and velocity at the upper part of the slope for blocks 43# and 53# at first, but the block 394# at the lower part show a very little displacement and velocity. In this case, the startup of landslide does not occur.

(2) Water lever in the reservoir rises to 135m, and parameters remain unchanged

In this case, parameter (1) in table 1 and the submerged unit weight in the material region below the 135m water lever are used. The corresponding curves are shown in Fig. 5. From Fig. 5, it is shown that the startup of landslide does not occur.

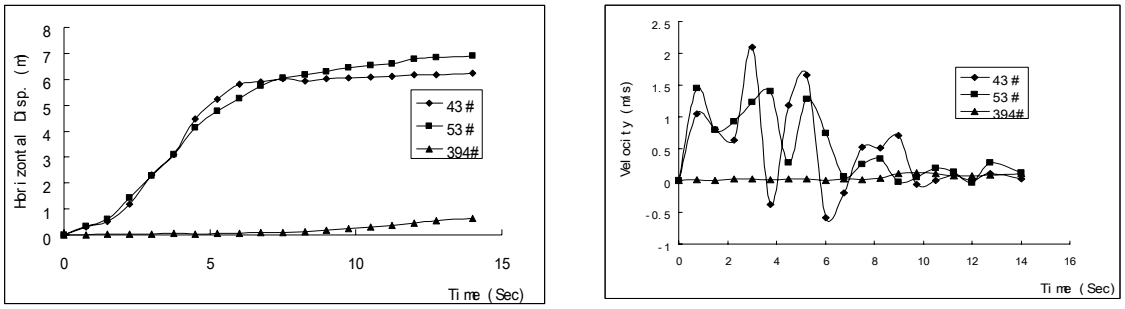

□a□ Horizontal displacement versus time (b) Velocity versus time

Fig. 4. Calculation results in case (1)

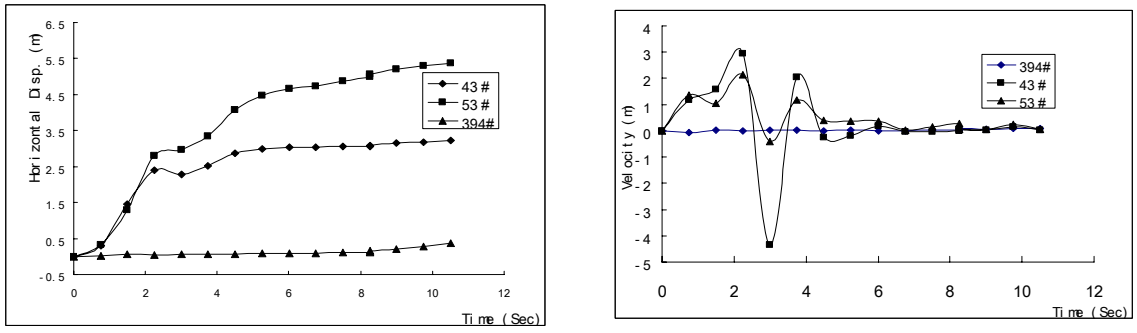

(a) Horizontal displacement versus time (b) Velocity versus time

Fig. 5. Calculation results in case (2)

(3) Water lever in the reservoir rises to 135m, and parameters decreased to some extent

As the reason of storage of the reservoir and heavy rainfall, mechanical parameters in landslide may be decreased by the effect of water seepage. Parameter (2) in table 1 is used, and the corresponding curves are shown in figure 6. It is shown that at beginning of deformation (time interval of OA), displacement and velocity for blocks 43#, and 53# are obvious, but very little for block 394# at lower part of the landslide. It means the startup of landslide does not occur. After time interval OA, there are obvious increasing of displacement and velocity of block 394#, and velocities in three blocks behave nearly a same level immediately after time A. It means that the startup of the landslide occurs.

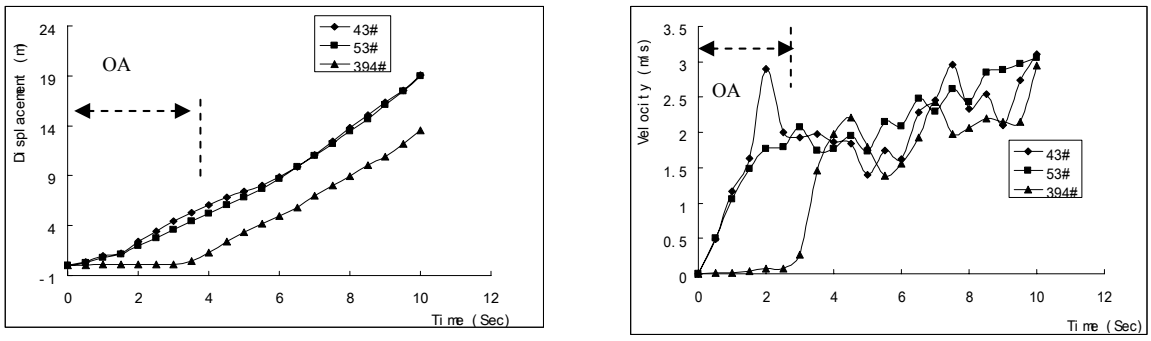

(a) Displacement versus time (b) Velocity versus time

Fig. 6. Calculation results in case (3)

6 PROCESS CHARACTERISTICS

According to numerical analysis with DDA method, the whole process of landslide can be divided into three periods, shown as in Fig. 7 and Fig. 8.

(1) Startup of landslide

There are obvious deformation at the rear edge and upper part of the landslide. The shear failures between blocks near the surface of the upper slope occur, and there are severe deformation and stress concentration in compression at the slope toe. The displacement and velocity at toe is very small, seeing part curve of 394# in figure 8 within time interval OA.

(2) Rapid sliding period

When deformation of the landslide develops to an extent, compression failure at the toe occurs. Local blocks at the toe of the slope have been thrust to the air, and shear movement of the landslide occurs. Immediately a whole landslide is induced with comparative increasement of displacement and velocity at each monitoring blocks, shown in Fig. 7(a) and Fig. 8 within time interval AB. By calculation, the maximum velocity of the three chosen blocks is 5m/s.

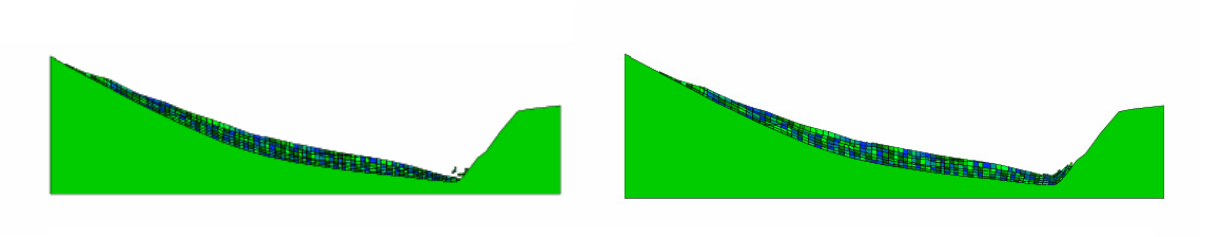

(a) After 15000 steps (b) after 50000 steps

Fig. 7 Deformation pattern of block system

(3) Velocity reduction and cease of the landslide

Following sliding down of the landslide, the potential energy of the landslide is decreased, and the front tongue become anti-sliding. The velocity of landslide reduces gradually and the landslide stop at last, shown in Fig.7(b) and Fig. 8 within time interval BC. The total duration of the landslide is about 40 seconds and the maximum sliding distance is 105m.

7 CONCLUSIONS

On the basis of field geological investigation and its mechanical parameters study, the numerical simulation of startup and a whole sliding process of Qianjiangping Landslide has been carried out by use of DDA method. The corresponding criterion for startup of a landslide has been established, and the whole process characteristics have been analyzed based on the calculation results. It is shown that the main reason of landslide is the reduction of mechanical parameters of controlled sliding surfaces in the landslide body resulted from rainfall and rise of reservoir water level. The landslide belongs to thrust load caused landslide. Compared to the actual process characteristics and the spatial morphology of the Qiangjiangping landslide, it has been proved that the simulation results by DDA are quit reasonable and acceptable. In addition, the most valuable progress is that methods adopted in this paper supply a new way for stability study of landslide or other geotechnical engineering.

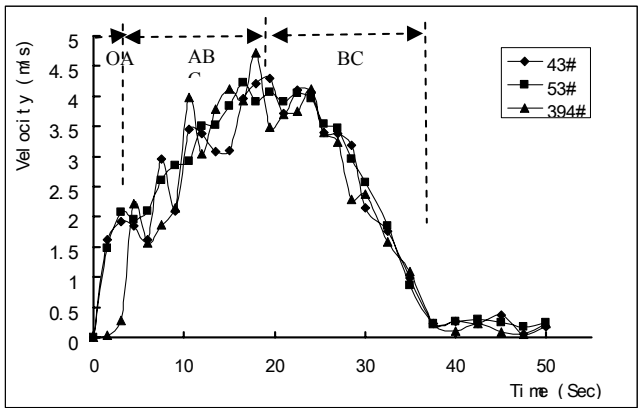

Fig.8. Sliding velocity versus time during the whole process

REFERENCES

[1] Shi G.H. and R E Goodman. 1985. Two dimensional discontinuous deformation analysis. Int. *J. for numerical and analytical methods in geomechanics.* Vol.9:541-556.
[2] Shi G.H.1988., *Discontinuous deformation Analysis –a new numerical method for the static and dynamics of block system.* PhD Thesis, Dept. Civil Engng., Univ. of California, Berkeley.
[3] Dong X.S., A.Q.Wu & F. Ren. 1996. A Preliminary Application of Discontinuous Deformation Analysis (DDA) to the Three Gorges Project on Yangtze River,Chian. In *Proc. of*

the First International Forum on Discontinuous Deformation Analysis (DDA) and Simulations of Discontinuous Media,1996,Albuquerque, TSI Press, 310-318.
[4] Wu A.Q. & Z.J. Huang. 2002. Stability analysis for rock blocks in Three Gorges Project. In *Proc. of 5th Int. conference on Analysis of Discontinuous Deformation, 2002*, 95-100,A.A.Balkema Publishers.
[5] Ding X.L., J. Fu, Z.H.Dong & A.Q.Wu. 2003. Stability study on the surrounding rock of the underground powerhouse in Shui Buya project by DDA. In *Proceedings of the 6th International Conference on Analysis of Discontinuous Deformation, 5-8 October 2003*, 75-78,Trondheim, Norway.

Preliminary Research on Solving Large Displacement Problems by Numerical Manifold Method with Fixed Mathematical Meshes

Su Haidong
School of Civil Eng. & Mechanic, HUST, Wuhan, China
DDA Center, Yangtze River Scientific Research Institute, Wuhan, China
Xie Xiaoling
Dept. of Material and Structure, Yangtze River Scientific Research Institute, Wuhan, China

This paper was prepared for presentation at *ICADD-7, the Seventh International Conference on Analysis of Discontinuous Deformation*, held in Honolulu, Hawaii, December 10-12, 2005.

ABSTRACT: According to the fact that mathematical meshes are independent of structure boundaries in numerical manifold method (NMM), Gen-hua Shi, the inventer of NMM, proposes an idea that large deformations of solid structures can be computed by means of NMM with fixed mathematical meshes, similar to Eulerian description approach in point of the characteristic that material particle moves in fixed meshes. In this paper, an attempt is made to compute large displacements of structures using fixed rectangular mathematical meshes and 1-order polynomial cover functions. Following the time steps, equations of NMM for large deformations are adopted. After each time step is completed, deformed boundaries of the structures are intersected with fixed mathematical meshes to generate new manifold elements. Several approaches are presented to compute initial stresses. The results of large deflection of a cantilever beam show the feasibility of NMM with fixed meshes, and indicate that more research should be further done on the approach of precisely computing initial stresses in the structures.

Key words: numerical manifold method, fixed mathematical meshes, large displacement problems, initial stress load

1. INTRODUCTION

Solving problems in spatial description is also called Eulerian approach whose typical feature is that material particle moves in fixed meshes. Compared with the substance description (Lagrangian approach) which is usually adopted in solid mechanics, Eulerian approach is very attractive because the fixed meshes will not be distorted with the deformed material (structures), so computational accuracy unlikely descends when too large deformations occur.

As for finite element method (FEM) of solid mechanics, it is difficult to implement moving structures in fixed meshes. Because the meshes must strictly satisfy boundaries of the structures, and fixing meshes implies that the boundaries can not move. Whereas in numerical manifold method (for short NMM) [1], the feature that meshes are independent of structure boundaries offers the possibility of solving geometrically nonlinear problems (large displacements or large deformations of structures) in fixed meshes.

In NMM, two independent mesh systems are introduced. One is physical mesh system defining real material boundaries as the integration fields, another is mathematical mesh system defining

only the numerical approximations. Separation of the two mesh systems results in the manifold elements of arbitrary shape.

The manifold method computations follow the time steps. The approach to implement moving structure in fixed meshes, proposed by Shi, is that the deformed boundaries (physical meshes) are intersected with fixed mathematical meshes to generate new manifold elements after each time step is completed. In this paper we shall call the NMM with this procedure as NMM with fixed mathematical meshes, for short, fixed-mesh NMM.

Besides the forementioned advantage of keeping computational accuracy, another important significance of fixed-mesh NMM in the future may consist in the fluid-solid coupling analyses considering large deformation of structure and large disturbance of fluid, because it may be convenient to solve the coupling problems when treating both fluid field and solid structure in the same background meshes. Furthermore, studying fixed-mesh NMM is also the requirement of NMM itself, because in Lagrangian description approach, when high-order manifold method is adopted by increasing the order of polynomial functions in covers, very large deformations can result in the incompatibility of the straight mesh edges with the deformed meshes[2], and then incorrect deformations such as separation of element edges can be observed.

This paper makes an attempt to solve problems of large displacements, restricting the study to the case of isotropic linear-elastic material of continuum for the sake of simplicity. With fixed rectangular mathematical meshes and 1-order polynomial cover functions, it is implemented that structures move in the meshes. In the end of the paper, large deflection results of a cantilever beam illustrate the feasibility of the fixed-mesh NMM.

To avoid confusions, in the following text we shall only designate meshes as mathematical meshes.

2. EQUATIONS OF NMM

The manifold method computations follow the time steps. The quasi-static equations at each load step (or time) for linear-elastic material are given (from $t=i$ to $t=i+1$) as

$$[K]\{\Delta d_{i+1}\} = \{F\} - \int_{\Omega} [B]^T \{\sigma_i\} d\Omega \quad (1) \qquad \{d_{i+1}\} = \{d_i\} + \{\Delta d_{i+1}\} \quad (2)$$

$$\{\sigma_{i+1}\} = \{\sigma_i\} + [E][B]\{\Delta d_{i+1}\} \quad (3)$$

where $[K]$, $[B]$,$[E]$,$\{F\}$,$\{d\}$ and $\{\sigma\}$ denote stiffness matrix, strain matrix, elasticity matrix, load vector (F is the total load which is already applied by the time of $i+1$), displacement vector and stress vector, respectively. Expressions of these matrices and vectors can be referred to Ref. 1.

Eq. (1) is the equilibrium equation in which $\int_{\Omega} [B]^T \{\sigma_i\} d\Omega$ represents initial stress load. Eq. (2) means modification of the coordinates of structures, indicating $[B]$, $[K]$, $\{F\}$ are all computed in the current configuration. Eq. (3) means superposing stresses as initial stresses for the next step.

The above equations differ greatly from classical FEM formulas for large deformation computation [3], because $[K]$ and $[B]$ are identical to those of small deformation problems, involving neither complicated nonlinear terms nor equilibrium iterations usually appearing in FEM processes. One can directly use program codes for small deformations to carry out the

entire procedure conveniently. Nevertheless, these equations demand that incremental displacements of each step should be small enough to neglect the second order displacements. The requirement leads to a problem: in FEM, a relatively large load can be applied in a time step and unbalanced forces can be eliminated in an iterative way, while in NMM, time of each step should be small and consequently times of solving linear system equations may increase a lot. Fortunately inertia dominant equilibrium equations are presented in Ref. 1, introducing inertial effect to Eq. (1) as

$$([K]+[K_g])\{\Delta d_{i+1}\} = \{F\} + \{F_g\} - \int_{\Omega} [B]^T \{\sigma_i\} d\Omega \qquad (4)$$

where, $[K_g]$and $\{F_g\}$ are stiffness matrix and load vector respectively caused by inertial forces. Eq. (4) can be used to compute dynamic problems with large deformations. Considering the statics is the ultimate stabilized state of dynamics, energy reduction should be introduced, such as velocity multiplying an appropriate constant. When using Eq. (4), the condition number of the linear system equations in each step is good enough for iteration solver, so computational time is saved.

In order to improve computational accuracy, 1-order cover functions are used in this paper. Because of the shape arbitrariness of manifold elements, simplex integration method [1] which can give the accurate result is usually adopted in NMM. However the requirement of integrand being polynomial functions about x and y results in the difficulties of formulation and programming. As a foundation of this paper, approaches are obtained to develop expressions of high-order NMM matrix and to automatically form program codes in Ref. 4.

3. MANIFOLD ELEMENT GENERATION

According to the idea of fixed-mesh NMM, deformed boundaries of the structures have to be intersected with the fixed mathematical meshes to generate new manifold elements after a time step is completed. One may doubt if this generation procedure is carried on for many times, the additional much computational amount is involved. In fact the procedure costs much less time than generation of FEM meshes. For example, similar intersecting operations have been done by Shi to cut 2800 three-dimensional blocks of DDA, and only 30 seconds are spent in a computer with 2GHz Pentium-M CPU. As to NMM, there are still better approaches to reduce more computation time. So generally speaking, generation of manifold elements does not increase a lot of computation amount.

Two-dimensional manifold element generation program written by Shi is adapted to rectangular mathematical meshes in this paper. In fixed-mesh NMM additional works must be done as follows:

(xix) Before the computation starts, original mathematical meshes are established. They should cover the entire area in which structures may move throughout the whole computation procedure.

(xx) Vertices in the boundaries of the structure should be refined to ensure the accuracy of intersecting operations for many times.

(xxi) In each step, only mathematical meshes covering current structure boundaries are to be considered. So current active meshes should associate with the original mathematical

meshes to ensure that stresses of elements and velocities of nodes can be transferred from the current time step to the next step.

4. DEFINITION OF INITIAL STRESSES

After the renewal of configurations and the generation of new manifold elements, displacements of structures are transferred from the previous time step to a new step. The difficulty is the computation of the initial stress load in Eq. (1). Initial stresses are essential to the fixed-mesh NMM. We will encounter the problem of how to calculate exactly the stress distribution after a time step is completed. Because of the movement of material, shape of the manifold element in each mathematical mesh varies along with the time step, and part of material may enter a new mesh. Therefore two problems should be solved: one is how to superpose stresses in a manifold element as shown in Eq. (3), and another is the transference of the stresses when material enters a new mesh.

4.1. Stress superposition

As for polynomial cover functions of displacements, stresses in manifold elements are also in the form of polynomial functions. Some approaches are presented and discussed in detail for the computation of coefficient matrix of stresses in the following.

- Approach a: coefficient superposition

Stresses in manifold elements are written as

$$\{\sigma\} = [E]\{\varepsilon\} = [E][B]\{d\} = [E][N]\{t\} \qquad (5)$$

where $[N]$ is the coefficient matrix, $\{t\}$ is the vector of polynomial functions. Eq. (5) means that the strain $\{\varepsilon\}=[B]\{d\}$ can be expressed in the form of $[N]\{t\}$. So in Ref. 5, stress superposition is actually the superposition of coefficient matrix $[N]$ with respect to homogeneous material. Then initial stress load $\int_{\Omega} [B]^T \{\sigma\} d\Omega$ is calculated using simplex integration method.

This approach is simple and the computing procedure is stable, yet the results of large deflection of cantilever beams have considerable error compared with the analytic solutions because this approach does not consider the effect of the configuration change when superposing stresses.

- Approach b: inversion formula method

In this paper inversion formula method is presented which performs well in Lagrangian approach. As for 1-order polynomial cover functions, stresses of manifold element are distributed as 2-order polynomial functions in rectangular mathematical meshes. Therefore, six points are selected in each manifold element to compose a group of stress points, such as three points around the element centroid and another three midpoints between them as shown in Fig. 1.

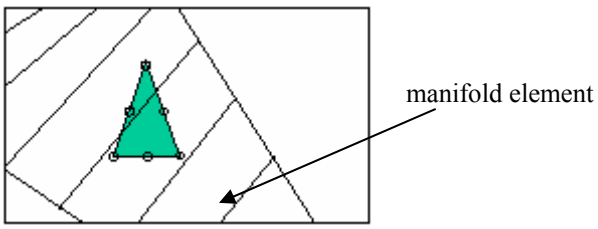

Fig.1. Six stress points of a manifold element in a mesh

When a time step is completed, accumulated stresses of these six points are computed respectively according to Eq. (3), and the accumulated stress of any point in a mesh can be interpolated using shape functions of six-node triangular element. So the stress vector in the mesh can be written as

$$\begin{Bmatrix}\sigma_x\\ \sigma_y\\ \tau_{xy}\end{Bmatrix}=\begin{bmatrix}\sigma_x^1 & \cdots & \sigma_x^6\\ \sigma_y^1 & \cdots & \sigma_y^6\\ \tau_{xy}^1 & \cdots & \tau_{xy}^6\end{bmatrix}\begin{Bmatrix}L_1\\ L_2\\ L_3\\ L_4\\ L_5\\ L_6\end{Bmatrix}=\begin{bmatrix}\sigma_x^1 & \cdots & \sigma_x^6\\ \sigma_y^1 & \cdots & \sigma_y^6\\ \tau_{xy}^1 & \cdots & \tau_{xy}^6\end{bmatrix}\begin{bmatrix}c_{11} & \cdots & c_{16}\\ \vdots & \vdots & \vdots\\ c_{61} & \cdots & c_{66}\end{bmatrix}\begin{Bmatrix}1\\ x\\ y\\ x^2\\ xy\\ y^2\end{Bmatrix}=\begin{bmatrix}a_{11} & \cdots & a_{16}\\ a_{21} & \cdots & a_{26}\\ a_{31} & \cdots & a_{36}\end{bmatrix}\begin{Bmatrix}1\\ x\\ y\\ x^2\\ xy\\ y^2\end{Bmatrix}=\begin{bmatrix}\ N_s\ \end{bmatrix}\begin{Bmatrix}\ t\ \end{Bmatrix} \qquad (6)$$

where, the shape functions of six-node triangular element, L_1 to L_6 are rewritten according to polynomial functions, and then right multiply the matrix of stresses to obtain polynomial coefficient matrix $[N_s]$. Thus the stress distribution formula is deduced inversely from the accumulated stresses of the six points.

After the above procedure is finished, stress points should move to the positions of the new configuration in which the next time step will be computed. Moving positions is very important. If positions do not shift, this approach will return to the above coefficient superposition approach and lead to large errors. However, when large displacements occur, stress points may move outside the mathematical mesh and may be not suitable for describing stresses in that mesh. To solve this problem, alternate operations of stress points are designed as follows:

(a) In a time step, incremental stresses of stress points are computed in current positions and superposed with the existent total stresses.

(b) Coefficient matrix $[N_s]$ is obtained according to Eq. (6).

(c) Stress points are relocated, and their accumulated stresses are computed via $[N_s]\{t\}$.

(d) Compute the new coordinates of these stress points in the new configuration.

(e) Go to (a) for a new time step.

- Approach c: least-squares method

Actual computations indicate that stresses in an element will become too complicated to be described via a group of six stress points when too large deformations occur. Thus approach b is not appropriate because differences become significant when using various groups of stress points.

Therefore an improved method is adopted. More stress points are selected in a manifold element to obtain coefficient matrix $[N_s]$ using least-square fit to 2-order polynomial distributions. We require only substituting the least-squares formula for inversion formula of Eq. (6) in the second step of the above alternate operations in which other procedures need not change.

4.2. Transfer initial stresses when material enters a new mesh

It is necessary to consider transference of initial stresses when material enters a new mathematical mesh. Small blocks are the tools for the transference in this paper.

When complicated boundaries of material are encountered in the procedure of manifold element generation, some small blocks often appear which occupy much less area in a mathematical mesh, such as 1% to 5% proportion to the whole area of the mesh. These small blocks will lead to an ill-conditional system matrix. A usual solution is attaching the small block to its peripheral mesh in which the area of manifold element is large enough, and displacements and stresses of the small block are controlled by the mesh [5].

As for the fixed-mesh NMM, when material boundaries enter a new mesh, a small block definitely appears at once as shown in Fig. 2. Calculation error would occur if initial stresses of these small blocks are neglected during the integration of initial stress load. The approach is treating the small block as the stretching part of the manifold element of the mathematical mesh to which the small block is attached, so strain matrix of the mesh is used for integrations of initial stress load and the new mesh does not work.

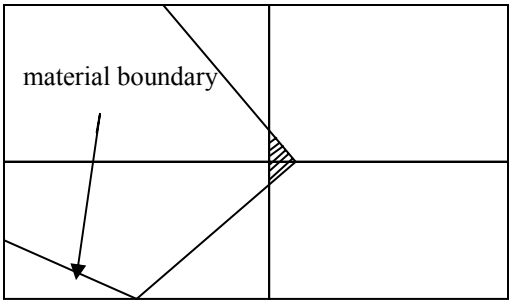

Fig.2. Small blocks (dashed area) in new mathematical meshes

Along with the deformations of material, the area of the small block may increase to the extent exceeding the proportion (1% to 5%), and the block may be controlled by the new mesh to which it belongs. When this happens, the stress coefficient matrix $[N_s]$ of the old mesh to which the small block has been attached is transferred to the new one. Then the procedure of initial stresses computation in the new mesh will continue from the third step of the above alternate operations.

5. NUMERICAL EXAMPLE OF LARGE DEFLECTION OF A CANTILEVER BEAM

Based on the two-dimensional program written by Shi, the above procedures have been carried out through implementation of Fortran codes. We consider a cantilever beam whose original position is shown in Fig. 3 in which the background rectangular frames represent the fixed mathematical meshes. The length of the beam is 10m, with both height and width are 1m. The Young's modulus E is 3×10^5 kN/m^2, and Poisson's ratio ν is 0.2. The beam is subjected to a concentrated force P at the midpoint of the section of the free end, which is always downward vertically. Load of 12.5kN is applied in a time step.

When using approach b to define initial stresses, it is observed that the relative errors compared with the analytic solutions are not over 3% when the vertical displacement of the free end gets to 5~6m. However when the load reaches about P=700kN, deformations of the beam begin to oscillate and then computation fails. It is found that distribution of the stresses in the elements become complicated when too large deformations occur.

Approach c is then used. More stress points are selected for the least-squares method. Table 1 gives the results of several steps, and corresponding deformations are shown in Fig. 3. The relative errors are all under 2%, indicating that the precision increases somewhat. Larger load can be computed, but oscillation still comes when P>900kN.

This example implies that it is feasible to compute large displacement problems using fixed-mesh NMM. However, the approaches in this paper are not good enough to precisely describe the distribution of stresses in any cases, so when the deformations become too large, the initial stress load is not accurate and the computation becomes instable.

Table 1. Displacements of the midpoint at the free end of the cantilever beam

P (kN)	Horizontal displacements—u (m)			Vertical displacements—v (m)		
	Numerical solutions	Analytic solutions[6]	Relative error (%)	Numerical solutions	Analytic solutions[6]	Relative error (%)
125	0.16	0.16	0.00	1.63	1.62	0.62
250	0.57	0.56	1.79	3.04	3.02	0.66
500	1.61	1.60	0.63	4.96	4.94	0.40
750	2.60	2.55	1.96	6.10	6.03	1.16
875	3.02	2.97*	1.65	6.50	6.46*	0.59

* results of Lagrangian approach (the analytic solution of P=875kN is not presented in Ref. 6)

Fig.3. Deformation of the cantilever beam

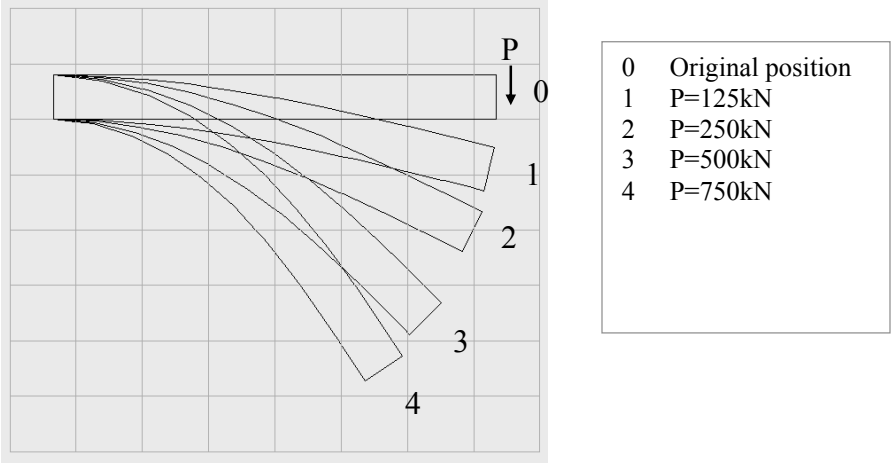

6. CONCLUSION

In this paper, an attempt is made to solve large displacement problems using NMM with fixed mathematical meshes, and the given results of a cantilever beam indicate that the approach is effective. However, at present it is still a problem of how to accurately describe stresses of the manifold elements. This paper presents several approaches to solve the problem. They are effective to some extent and will fail when very large deformations occur. So it can be deduced that better results will be obtained in the dynamic occasions when rigid motion is dominant.

The accurate computation of stresses is most important to the fixed-mesh NMM in which material moves through the meshes. Relevant solutions presented in this paper are rough and some improvements can be made in the future. One potential way is the modification of

coefficient superposition approach. It is found that this method is stable to compute very large displacements even if the relative error is considerable (up to 20%). So if something could be done to consider the effect of the configuration change when superposing stresses, the approach might be the ultimate solution.

Although the study of this paper is preliminary, the purpose of presenting the possibility of fixed-mesh NMM is achieved. One can see that fixed-mesh NMM has both the advantage of tracing material particle in Lagrangian description and the virtue of fixed mesh in Eulerian description. Therefore the study is attractive even if there is a long way to go.

ACKNOWLEDGEMENT

The research is done under the guidance of Dr. Gen-hua Shi and Professor Yu-ying Huang. Thanks for their great helps.

REFERENCES

1. Shi, G.H. 1996. Manifold Method. In *Proceedings of the First International Forum on Discontinuous Deformation Analysis and Simulations of Discontinuous Media*, *Berkeley, California, USA, 12-14 June, 1996*, 52-204.
2. Su, H.D., Xie, X.L. & Chen, Q. 2004. Application of NMM in solving large displacement problems (in Chinese). Acta Mechanica solida sinica, Chinese journal of solid mechanics. Vol.25 S.Issue, 88-92.
3. Yin, Y.Q. 1987. *Fundamental theory of nonlinear finite element method for solid mechanics.* (in Chinese). 1st ed. Beijng: Beijing University Press & Tsinghua University Press.
4. Su, H.D., Xie, X.L. & Liang, Q.Y. 2003. Automatic programming for high-order numerical manifold method. In *Proceedings of the 6th International conference on analysis of Discontinuous Deformation, Trondheim, Norway, 5-8 October, 2003*, 153-157.
5. Lu, M. 2002. High-order manifold method with simplex integration. In *Proceedings of the 5th International conference on analysis of Discontinuous Deformation*, 2002, 75-83.
6. Liu, Z.X., Sun, Y. & Wang, G.Q. 2000. *Computational solid mechanics* (in Chinese). 1st ed. Shanghai: Shanghai Jiaotong University Press.

Formulation of high-order numerical manifold method and fast simplex integration based on special matrix operations

Lin Shaozhong
DDA Center, Yangtze River Scientific Research Institute, Wuhan, China
Qi Yongfeng
Dept. of Material and Structure, Yangtze River Scientific Research Institute, Wuhan, China
Su Haidong
Dept. of Material and Structure, Yangtze River Scientific Research Institute, Wuhan, China
DDA Center, Yangtze River Scientific Research Institute, Wuhan, China

This paper was prepared for presentation at *ICADD-7, the Seventh International Conference on Analysis of Discontinuous Deformation*, held in Honolulu, Hawaii, December 10-12, 2005.

ABSTRACT**:** The simplex integration is commonly used in the numerical manifold method (NMM) for accurate integration. But in high-order NMM a difficulty is encountered by adopting the simplex integration since all integrands have to be explicitly expressed in the polynomial form. In this paper the formulations of element matrices (stiffness matrix, load matrix, *etc*) of high-order NMM are derived by using the special matrix operations including Kronecker product, Hadamard product and vectorization, therefore the terms of element matrices are expressed explicitly in matrix product form in which the integrands are only the product of polynomial bases, resulting in a convenience of implementation of the simplex integration and development of codes. Also given in the paper is a recursive simplex integration formula, with which much less computation is required and the integrals of all polynomial bases of lower order are incidentally obtained after the integral of the polynomial base of the highest order has been computed. Based on the derived formulae, a program of high-order NMM for elastic stress analysis of 3-D continua is developed and verified by examples.

Key words: numerical manifold method, high-order cover function, formulation of element matrices, fast simplex integration, special matrix operations

1. INTRODUCTION

The manifold element is basic element in numerical manifold method (Shi, 1996), whose formulation is similar to that of the finite element. However, different from the finite element, the manifold element may have complex shape. The integration on the complex domain is simplified to numerical or analytical integration on several simplexes. If numerical integration is adopted, the number of integration points will rapidly increases with the order of the cover function becoming higher. The simplex integration proposed by Shi (1996) is an analytical integration and commonly used in NMM. But in high-order NMM a difficulty is encountered by adopting the simplex integration since all integrands have to be expressed explicitly in polynomial form. Basing on the simplex integration and triangular mathematical meshes, Lu (2001,2002) derived explicit polynomial expressions of the integrand of terms of the element matrices for 2-D high-order NMM. But the derivation is tedious since the formulae are manually carried out by the fundamental matrix multiplication. To avoid the complicated derivation, Kourepinis et al (2003) proposed a strategy, whereby the coefficients and base exponents of the

polynomial function of terms of the geometric matrix are stored in a multi-dimensional array, and then the polynomial coefficients of the integrand of terms of the element stiffness matrix are determined by the fundamental matrix multiplication. With the help of the Mathematica software, Su et al (2003) presented a simple method for automatic producing of subroutine codes for 2-D and 3-D high-order element matrices, but the codes are very long in the case of high-order cover function.

Different from the works of Lu, Kourepinis and Su, in this paper the terms of element matrices of high-order NMM are derived by using the special matrix operations and the integrands are expressed explicitly in product form of polynomial bases convenient for implementation of the simplex integration and development of codes. A recursive formula for fast simplex integration proposed by the first author is also introduced. The matrices, e.g. point loading matrix, fixed point matrix, which are not in integration form, are referred to Shi (1996) and not listed in the paper.

2. ELEMENT DISPLACEMENT

2.1. Cover function

The polynomial cover displacement functions on cover C_i can be expressed as:

$$\begin{Bmatrix} u_i(x,y,z) \\ v_i(x,y,z) \\ w_i(x,y,z) \end{Bmatrix} = \sum_{j=1}^{m} t_{cj}(x,y,z) D_{ij} \tag{1}$$

Where $D_{ij} = \{u_{ij}, v_{ij}, w_{ij}\}^{\mathrm{T}}$ are unknowns; t_{cj} are polynomial bases, e.g. $1, x, y, z$, etc. For a complete N-order cover function, the number of terms of the cover function m=(N+1)(N+2)(N+3)/6.

2.2. Element displacement function

Assuming that the manifold element e is the intersection of n covers, the global displacements are written as:

$$\begin{Bmatrix} u(x,y,z) \\ v(x,y,z) \\ w(x,y,z) \end{Bmatrix} = \sum_{i=1}^{n} W_i(x,y,z) \begin{Bmatrix} u_i(x,y,z) \\ v_i(x,y,z) \\ w_i(x,y,z) \end{Bmatrix} = \sum_{i=1}^{n} \sum_{j=1}^{m} N_{ij}(x,y,z) D_{ij} \tag{2}$$

In which

$$W_i(x,y,z) = \sum_{\xi=1}^{n} f_{i_\xi} t_{w\xi}(x,y,z) = F_i^{\mathrm{T}} T_w \quad \square$$

$$F_i = \{f_{i_1}, f_{i_2}, \cdots, f_{i_n}\}^{\mathrm{T}} \quad \square \quad T_w = \{t_{w1}, t_{w2}, \cdots, t_{wn}\}^{\mathrm{T}},$$

$$N_{ij} = t_{cj} W_i = t_{cj} F_i^{\mathrm{T}} T_w = F_i^{\mathrm{T}} T_j \quad \square$$

$$T_j = t_{cj} T_w = \{t_{j_1}, t_{j_2}, \cdots, t_{j_n}\}^{\mathrm{T}}, \; t_{j_\xi} = t_{cj} t_{w\xi}, \xi = 1 \sim n .$$

Where W_i is weight function; F_i and T_w are the polynomial coefficient and base set of W_i, respectively. Using finite element mesh as mathematical mesh, W_i and n are the shape function and number of nodes of the finite element, respectively. In NMM the mathematical mesh and the

physical mesh are independent each other. Therefore simply shaped finite elements can be utilized to define the mathematical mesh, such as 3-node triangular element and 4-node rectangular element in 2-D, 4-node tetrahedral element and 8-node cuboidal element in 3-D, whose shape function can be expressed explicitly in polynomial form.

2.3. *Partial derivative of displacement function*

As seen in Eq.(2), the partial derivative of displacement function depends on the partial derivative of N_{ij}. Let $x_\alpha(\alpha=1,2,3)$ denote x, y, z, respectively, then

$$N_{ij,\alpha}=\frac{\partial N_{ij}}{\partial x_\alpha}=F_i^{\mathrm{T}}\frac{\partial T_j}{\partial x_\alpha}=F_i^{\mathrm{T}}(C_{j\alpha}\circ T_{j\alpha})=(F_i\circ C_{j\alpha})^{\mathrm{T}}T_{j\alpha} \tag{3}$$

Where $T_{j\alpha}=\{T_{j_1\alpha},T_{j_2\alpha},\cdots,T_{j_g\alpha}\}^{\mathrm{T}}$ is the polynomial base set of the partial derivative and $C_{j\alpha}$ is a constant vector resulted from the partial differentiation on the base set T_j. Zero terms are included in $C_{j\alpha}$. The symbol "$\circ$" stands for the Hadamard product of matrices. Let $A=[a_{rs}]$ and $B=[b_{rs}]$ be of the same order, then $A\circ B=[a_{rs}b_{rs}]$.

3. ELEMENT STIFFNESS MATRIX AND MASS MATRIX

The submatrix of the element stiffness matrix is written as:

$$K_{ijkl}=\int_v B_{ij}^{\mathrm{T}}DB_{kl}\mathrm{d}v,\quad i,k=1\sim n\ ;\ j,l=1\sim m \tag{4}$$

Where D =[d_{pq}] is the elastic matrix and B_{ij} is the geometric matrix. For 3-D continua,

$$B_{ij}=\begin{bmatrix} N_{ij,1} & 0 & 0\\ 0 & N_{ij,2} & 0\\ 0 & 0 & N_{ij,3}\\ N_{ij,2} & N_{ij,1} & 0\\ 0 & N_{ij,3} & N_{ij,2}\\ N_{ij,3} & 0 & N_{ij,1}\end{bmatrix}=\sum_{\alpha=1}^{3}A_\alpha N_{ij,\alpha} \tag{5}$$

$$A_1=\begin{bmatrix}1&0&0\\0&0&0\\0&0&0\\0&1&0\\0&0&0\\0&0&1\end{bmatrix},\quad A_2=\begin{bmatrix}0&0&0\\0&1&0\\0&0&0\\1&0&0\\0&0&1\\0&0&0\end{bmatrix},\quad A_3=\begin{bmatrix}0&0&0\\0&0&0\\0&0&1\\0&0&0\\0&1&0\\1&0&0\end{bmatrix} \tag{6}$$

The submatrix is rewritten as:

$$\begin{aligned}K_{ijkl}&=\int_v(\sum_{\alpha=1}^{3}A_\alpha N_{ij,\alpha})^{\mathrm{T}}D(\sum_{\beta=1}^{3}A_\beta N_{kl,\beta})\mathrm{d}v\\&=\sum_{\alpha=1}^{3}\sum_{\beta=1}^{3}\int_v A_\alpha^{\mathrm{T}}DA_\beta N_{ij,\alpha}N_{kl,\beta}\mathrm{d}v\end{aligned} \tag{7}$$

The (r,s)-th term of the K_{ijkl} can be expressed as:

$$(K_{ijkl})_{rs} = \sum_{\alpha=1}^{3}\sum_{\beta=1}^{3}\int_v d_{pq} N_{ij,\alpha} N_{kl,\beta} \mathrm{d}v,\ \ p = k_{3(r-1)+\alpha}, q = k_{3(s-1)+\beta} \tag{8}$$

In which the indicator set $(k_1, k_2, \cdots k_9) = (1,4,6,4,2,5,6,5,3)$. For 2-D continua, the indicator set $(k_1, k_2, k_3, k_4) = (1,3,3,2)$ and $p = k_{2(r-1)+\alpha}, q = k_{2(s-1)+\beta}, \alpha = 1 \sim 2, \beta = 1 \sim 2$.

Let $d_{pq} = D_{pq}^{\mathrm{T}} T_d$ be a polynomial function, then the term of K_{ijkl} can be expressed as:

$$\begin{aligned}(K_{ijkl})_{rs} &= \sum_{\alpha=1}^{3}\sum_{\beta=1}^{3}\int_v D_{pq}^{\mathrm{T}} T_d \ (F_i \circ C_{j\alpha})^{\mathrm{T}} T_{j\alpha} \ (F_k \circ C_{l\beta})^{T} T_{l\beta} \mathrm{d}v \\ &= \sum_{\alpha=1}^{3}\sum_{\beta=1}^{3}[D_{pq} \otimes (F_i \circ C_{j\alpha}) \otimes (F_k \circ C_{l\beta})]^{\mathrm{T}} \int_v (T_d \otimes T_{j\alpha} \otimes T_{l\beta}) \mathrm{d}v\end{aligned} \tag{9}$$

Where D_{pq} is coefficient matrix and T_d is base set. The symbol "$\otimes$" represents the Kronecker product of matrices. Let $A = [a_{rs}] \in R^{m_a \times n_a}, B = [b_{\alpha\beta}] \in R^{m_b \times n_b}$, then the terms of $(A \otimes B)$ have expression $(A \otimes B)_{(r-1)m_b+\alpha,(s-1)n_b+\beta} = a_{rs} b_{\alpha\beta}$.

As seen in Eq. (9), the integrands are only the product of the polynomial bases and can be integrated directly by the simplex integration. The following formulae are the same.

If D is constant, Eq. (9) is reduced to

$$(K_{ijkl})_{rs} = \sum_{\alpha=1}^{3}\sum_{\beta=1}^{3} d_{pq} \ k_{\alpha\beta} \tag{10}$$

$$k_{\alpha\beta} = \int_v N_{ij,\alpha} N_{kl,\beta} \mathrm{d}v$$

$$= (F_i \circ C_{j\alpha})^{\mathrm{T}} \int_v T_{j\alpha} T_{l\beta}^{\mathrm{T}} \mathrm{d}v \, (F_k \circ C_{l\beta}) \tag{11}$$

Furthermore for isotropic material,

$$(K_{ijkl})_{rs} = \lambda \, k_{rs} + G \, k_{sr} + \delta_{rs} G \sum_{\alpha=1}^{3} k_{\alpha\alpha} \tag{12}$$

Where λ and G are the Lame's constants, δ_{rs} is the Kronecker Delta operator.

Let ρ be constant density of material and I is identity matrix, the mass matrix has also a simple expression:

$$M_{ijkl} = \rho \, I \int_v N_{ij} N_{kl} \mathrm{d}v = \rho \, I \, F_i^{\mathrm{T}} \int_v T_j T_l^{\mathrm{T}} \, \mathrm{d}v \, F_k \tag{13}$$

4. ELEMENT EQUIVALENT LOAD

4.1. Body load

Let constant body load per unit volume be $Q = \{q_x, q_y, q_z\}^{\mathrm{T}}$. The submatrix of the body load matrix is expressed as:

$$R_{ij} = \int_v N_{ij} \mathrm{d}v \, Q = F_i^{\mathrm{T}} \int_v T_j \mathrm{d}v \, Q \tag{14}$$

4.2. Face load

Let face load applied at element surface A be a polynomial function $P = \{p_x, p_y, p_z\}^{\mathrm{T}} = P_f T_f$. The submatrix of the face load matrix is expressed as:

$$R_{ij} = \int_A N_{ij} P \mathrm{d}A = P_f \int_A T_f T_j^{\mathrm{T}} \mathrm{d}A \, F_i \tag{15}$$

Where P_f is coefficient matrix and T_f is base set.

4.3. Initial stress

Let initial stress vector in the manifold element be a polynomial function $\sigma_0 = ST_\sigma$. The submatrix of the load matrix is expressed as:

$$R_{ij} = \int_v B_{ij}^{\mathrm{T}} \sigma_0 \mathrm{d}v = \sum_{\alpha=1}^{3} A_\alpha^{\mathrm{T}} S \int_v T_\sigma T_{j\alpha}^{\mathrm{T}} \mathrm{d}v \, (F_i \circ C_{j\alpha}) \tag{16}$$

Where S is coefficient matrix and T_σ is base set.

The r-th term of R_{ij} can be expressed as:

$$(R_{ij})_r = \sum_{\alpha=1}^{3} R_{k_{3(r-1)+\alpha}} \tag{17}$$

$$R = S \int_v T_\sigma T_{j\alpha}^{\mathrm{T}} \mathrm{d}v \, (F_i \circ C_{j\alpha}) \tag{18}$$

4.4. Initial strain

Let initial strain vector in manifold element be a polynomial function $\varepsilon_0 = ET_\varepsilon$. If each term of D is a polynomial function, then we have expression $D = D_d (I_d \otimes T_d)$. Here E and D_d are coefficient matrices, T_ε and T_d are base sets, $\mathrm{I_d}$ is identity matrix of a same order as D. As the symmetry of D and $(I_d \otimes T_d) B_{ij} = B_{ij} \otimes T_d$, the submatrix of the load matrix is expressed as:

$$\begin{aligned} R_{ij} &= \int_v B_{ij}^{\mathrm{T}} D \varepsilon_0 dv \\ &= \int_v B_{ij}^{\mathrm{T}} (I_d \otimes T_d)^{\mathrm{T}} D_d^{\mathrm{T}} E T_\varepsilon \mathrm{d}v \\ &= \int_v (B_{ij} \otimes T_d \otimes T_\varepsilon)^{\mathrm{T}} \mathrm{d}v \, \overrightarrow{D_d^{\mathrm{T}} E} \\ &= [\sum_{\alpha=1}^{3} A_\alpha \otimes \int_v (T_d \otimes T_\varepsilon) N_{ij,\alpha} \mathrm{d}v]^{\mathrm{T}} \overrightarrow{D_d^{\mathrm{T}} E} \\ &= [\sum_{\alpha=1}^{3} A_\alpha \otimes \int_v (T_d \otimes T_\varepsilon) T_{j\alpha}^{\mathrm{T}} \mathrm{d}v \, (F_i \circ C_{j\alpha})]^{\mathrm{T}} \overrightarrow{D_d^{\mathrm{T}} E} \end{aligned} \tag{19}$$

Where the symbol "→" represents the vectorization of matrix row by row. If D is constant, the r-th term of R_{ij} is reduced to

$$(R_{ij})_r = \sum_{\alpha=1}^{3} R_{k_{3(r-1)+\alpha}} \tag{20}$$

$$R = DE \int_v T_\varepsilon T_{j\alpha}^{\mathrm{T}} \mathrm{d}v \, (F_i \circ C_{j\alpha}) \tag{21}$$

5. ELEMENT STRESS AND STRAIN

After the displacement coefficients D_{ij} have been computed, the stress and strain of the manifold element can be computed as follows:

$$\sigma = D\varepsilon, \quad \varepsilon = \sum_{i=1}^{n}\sum_{j=1}^{m} B_{ij} D_{ij} \tag{22}$$

Substituting Eq. (3) into Eq. (22), the strain can be rewritten in a polynomial form similar to $\varepsilon = ET_{\varepsilon}$ as an initial strain for next time step:

$$\varepsilon = \sum_{j=1}^{m}\left(\sum_{i=1}^{n}\begin{bmatrix} u_{ij}(F_i \circ C_{j1})^{\mathrm{T}} & 0 & 0 \\ 0 & v_{ij}(F_i \circ C_{j2})^{\mathrm{T}} & 0 \\ 0 & 0 & w_{ij}(F_i \circ C_{j3})^{\mathrm{T}} \\ v_{ij}(F_i \circ C_{j1})^{\mathrm{T}} & u_{ij}(F_i \circ C_{j2})^{\mathrm{T}} & 0 \\ 0 & w_{ij}(F_i \circ C_{j2})^{\mathrm{T}} & v_{ij}(F_i \circ C_{j3})^{\mathrm{T}} \\ w_{ij}(F_i \circ C_{j1})^{\mathrm{T}} & 0 & u_{ij}(F_i \circ C_{j3})^{\mathrm{T}} \end{bmatrix}\right)\begin{Bmatrix} T_{j1} \\ T_{j2} \\ T_{j3} \end{Bmatrix} \tag{23}$$

6. RECURSIVE FORMULA FOR SIMPLEX INTEGRATION

The integral of polynomial base $x^{m_x} y^{m_y} z^{m_z}$ on an oriented simplex *v* is expressed as:

$$\int_v x^{m_x} y^{m_y} z^{m_z} \mathrm{d}v = \frac{(n_v - 1)!\,vol}{(m_x + m_y + m_z + n_v - 1)!} s_{m_x, m_y, m_z} \tag{24}$$

Where n_v and *vol* is the number of vertices and the volume of the simplex, respectively.

For segment: n_v =2, *vol*= oriented length of the segment;

For triangle: n_v =3, *vol*= oriented area of the triangle;

For tetrahedron: n_v =4, *vol*= oriented volume of the tetrahedron.

Also basing on the special matrix operation, a recursive formula for s_{m_x, m_y, m_z} was derived [Lin, 2005]

$$\begin{cases} s_{i,0,0} = \sum_{\alpha=1}^{i} C_{i-1}^{\alpha-1} e_{\alpha,0,0}\, s_{i-\alpha,0,0}, \quad i = 1 \sim m_x \\ s_{i,j,0} = \sum_{\beta=1}^{j} C_{j-1}^{\beta-1} \sum_{\alpha=0}^{i} C_i^{\alpha} e_{\alpha,\beta,0}\, s_{i-\alpha,j-\beta,0}, \quad i = 0 \sim m_x, j = 1 \sim m_y \\ s_{i,j,k} = \sum_{\gamma=1}^{k} C_{k-1}^{\gamma-1} \sum_{\beta=0}^{j} C_j^{\beta} \sum_{\alpha=0}^{i} C_i^{\alpha} e_{\alpha,\beta,\gamma}\, s_{i-\alpha,j-\beta,k-\gamma}, i = 0 \sim m_x, j = 0 \sim m_y, k = 1 \sim m_z \end{cases} \tag{25}$$

In which, $s_{0,0,0} = 1$, $C_i^{\alpha} = \dfrac{i!}{\alpha!(i-\alpha)!}, i \geq \alpha$,

$e_{\alpha,\beta,\gamma} = (\alpha + \beta + \gamma - 1)! E^{\mathrm{T}}(X^{(\alpha)} \circ Y^{(\beta)} \circ Z^{(\gamma)})$

$$X=\begin{Bmatrix}x_1\\x_2\\\vdots\\x_{n_v}\end{Bmatrix},\ Y=\begin{Bmatrix}y_1\\y_2\\\vdots\\y_{n_v}\end{Bmatrix},\ Z=\begin{Bmatrix}z_1\\z_2\\\vdots\\z_{n_v}\end{Bmatrix},\ E=\begin{Bmatrix}1\\1\\\vdots\\1\end{Bmatrix}$$

In which x_i, y_i, z_i are the vertex coordinates of the simplex. $X^{(\alpha)}$ denotes the α-th power of Hadarmard product of matrix X. The recursive formula requires much less computation than the Shi's formula and the integrals of all polynomial bases of lower order are incidentally obtained after the integral of the polynomial base of the highest order has been computed. $e_{\alpha,\beta,\gamma}$ is computed before the implementation of the recursive calculation. $X^{(\alpha)} \circ Y^{(\beta)} \circ Z^{(\gamma)}$ is also computed by a recursive procedure.

7. NUMERICAL EXAMPLE

Based on the derived formulae, a program of high-order NMM is developed for elastic stress analysis of 3-D continua by using 8-node cuboidal element mesh as mathematical mesh. The formulae and program have been verified by analytical and numerical examples.

Fig.1 shows a gravity dam with width of 20m, elastic modulus of $10^6 N/m^2$ and Poisson's ratio of 0.2. The mathematical mesh is shown in *Fig*.2. The manifold element mesh, *i.e.* the intersection of physical mesh (dam) and the mathematical mesh, is shown in *Fig*.3. The mesh for FEM computation is shown in *Fig*.4.

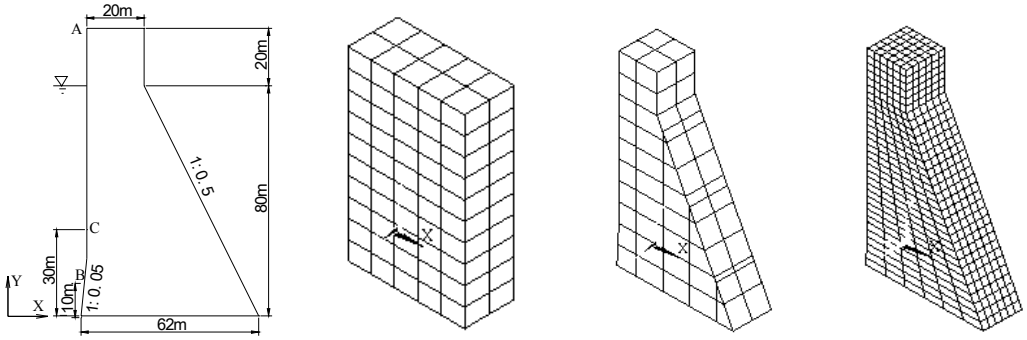

Fig.1 Section of Dam Fig.2 Mathematical mesh Fig.3 Manifold elements Fig.4 Mesh of FEM

The displacement and stress at the action of reservoir water pressure are computed by NMM and FEM and compared in *Tab*.1. It can be seen that the results of 0-order cover function are far from the FEM solutions. When the order increases, the results approximate to the FEM solutions and the stress σ_x at point *C* reaches to the water pressure at the same point.

Tab.1 Comparison of solutions of NMM and FEM

	FEM	NMM		
		0-order	1-order	2-order
u at point A (m)	0.181	0.170	0.180	0.181
σ_y at point B (MPa)	1.121	0.752	1.113	1.147
σ_x at point C (MPa)	-0.494	-0.445	-0.487	-0.501

8. CONCLUSION

The formulation of high-order NMM with the help of the special matrix operations makes the derivation and code development convenient such providing a sound base for application and p-version adaptive analysis of NMM. Besides of the program for stress analysis, a program for transient temperature analysis has been developed. The derivation presented in this paper is based on an assumption of all covers with cover functions of same order. However the derivation procedure is also suitable for the case of different covers associated with cover functions of different order.

ACKNOWLEDGEMENT

The authors gratefully acknowledge the encouragement of Dr. Shi Gen-hua.

REFERENCES

1. Kourepinis, D., Bićanić, N. & Pearce, C.J. 2003. A higher-order variational numerical manifold method formulation and simplex integration strategy. In Proceedings of the 6th International conference on analysis of Discontinuous Deformation: 145-151, Trondheim, Norway, 5-8 October, 2003.
2. Lin, S.Z. 2005. Recursive Formula for Simplex Integration. Journal of Yangtze River Scientific Research Institute 2005(3): 32-34.
3. Lu, M. 2001. Complete N-order polynomial cover function for manifold method. SINTEF Report,STF22 F01139.
4. Lu, M. 2002. High-order manifold method with simplex integration. In Proceedings of the 5th International conference on analysis of Discontinuous Deformation: 75-83, 2002.
5. Shi, G.H. 1996. Manifold Method. In Proceedings of the First International Forum on Discontinuous Deformation Analysis and Simulations of Discontinuous Media: 52-204, Berkeley, California, USA, 12-14 June, 1996.
6. Shi, G.H. 1996. Simplex integration for Manifold Method, FEM, DDA. In Proceedings of the First International Forum on Discontinuous Deformation Analysis and Simulations of Discontinuous Media: 205-262, Berkeley, California, USA, 12-14 June, 1996.
7. Su, H.d., Xie, X.L. & Liang, Q.Y. 2003. Automatic programming for high-order numerical manifold method. In Proceedings of the 6th International conference on analysis of Discontinuous Deformation: 153-157, Trondheim, Norway, 5-8 October, 2003.

Data Compression using Manifold Method

Fang, Xi-sheng
Ohlone College, Fremont, CA, U.S.A
Tu, Guo-fang
Graduate University, Chinese Academy of Sciences, Beijing, China
Wang, Ying
Graduate University, Chinese Academy of Sciences, Beijing, China
Shi, Gen-hua
DDA Company, Belmont, CA, U.S.A.

This paper was prepared for presentation at *ICADD-7, the Seventh International Conference on Analysis of Discontinuous Deformation*, held in Honolulu, Hawaii, December 10-12, 2005.

ABSTRACT: Manifold Method [1] is not only widely used in rock science, mechanical engineering, but also used in information sciences and data communications. The results introduced here briefly demonstrate that how this numerical analysis can be applied in sound and image compression, and the results discussed here also show that manifold method can be regarded as a fundamental method of computation in scientific field.

1. DATA COMPRESSION

Compression refers to storing data in a format that requires less space than original. Compression is important for today's data communications for faster transmission and less space on storage devices. Compression tools scan the data files to reduced un-necessary space without recovery problems. Typical compression methods can reduce the size of most files from 50% to 90%.

Sound is recorded as continuous waves with multi-frequency range. One of most popular sound compression methods is MP3, which belongs to lossy compression category, and which becomes today's audio standard [2]. Its transformation stream is split into multiple channels, each channel into a frame of samples, each frame into frequency sub-bands, and each sub-band into blocks. Each block is using a modified Digital Cosine Transformation (MDCT) [3] to reduce those waste frequency space to reach comprising results.

Due to nature of lossy algorithms, audio quality suffers when a file is decompressed and recompressed (generational losses). For MP3, the limitations also include (1) limited maximum frame size (320 kbps), which leads to unavoidable degradations of sounds quality. (2) Inoptimal window sizes, which brings time/frequency resolution either 576 samples for a long block, or 192 samples for a short block, and it is limiting the frequency resolution, and also the coding efficiency. (3) Hybrid transform scheme (MDCT on top of the 32 sub-bands produced by quadrature Mirror Filters of layer II), which introduces some noise that cannot be totally removed. However the popularity of those programs makes us thinking some easier and more efficient way to improve the algorithms by introduce manifold methods.

2. MANIFOLD METHOD

The term “manifold” here comes from the topological manifold and differential manifold. The Manifolds connect many individual folded domains together to cover the entire material volume. Then, the global behavior can be computed by functions defined in local covers. The new method has separated and independent mathematical covers and physical mesh: the mathematical covers define only the fine or rough approximations; as the real material boundary, the physical mesh defines the integration fields.

The mathematical covers are chosen by users, and consist of finite overlapping covers, which occupy the whole material volume. The physical mesh includes the boundaries of the material volume, joints, blocks and the interfaces of different material zones. The physical mesh represents material conditions, which cannot be chosen artificially. Both mathematical covers and physical meshes form the physical cover system. If the joints or block boundaries divide a mathematical cover to two or more completely disconnected domains, those domains are defined as physical covers. Therefore the physical covers are the subdivision of the mathematical covers by discontinuities.

For the manifold method, the cover displacement functions are independently defined on individual physical covers. Local displacement functions can be connected together to form a global displacement function on the whole material volume. The global displacement function is general and flexible enough to represent the wide variety of continuous or discontinuous materials located within moving boundaries.

Even the one-dimensional numerical manifold method can still show the easy way of approximations to general curves. The cover functions $u_i(x)$ defined on physical cover U_i

$$u_i(x) \quad x \in U_i \tag{1}$$

can be constant, linear, high order polynomials or locally defined series. These cover functions are connected together by the weight functions $w_i(x)$

$$\begin{aligned} w_i(x) &\geq 0 \quad x \in U_i \\ w_i(x) &= 0 \quad x \notin U_i \end{aligned} \tag{2}$$

with

$$\sum_{x \in U_j} w_j(x) = 1. \tag{3}$$

The meaning of the weight functions $w_i(x)$ is weighted average, which is to take a percentage from each cover function $u_i(x)$ for all physical covers U_i containing x

Using the weight functions $w_i(x)$ a global function $F(x)$ on the whole physical cover system is defined from the cover functions

$$u(x) = \sum_{i=1}^{n} w_i(x) u_i(x). \tag{4}$$

3. MANIFOLD METHOD IN DATA COMPRESSION APPLICATION

To simplify our model, let us discuss single audio channel only here. The wave is discrete sampled and dynamic range (amplitude) is captured based on DCT, where only cosine is used to

avoid uncertainty by introducing sine function. To avoid discontinuity MDCT added overlap of sampling process. Based on this, Manifold Method gives additional flexibility including varying lengths of frames, and varying sizes of windows. In each physical cover, discrete samples are recorded and stored. The sound is recreated using interpolation of the resulting discrete digital data. The above 1-D representation of Manifold Method provides a stable and efficient numerical method for data capture analysis for sound wave.

For two dimensional manifold computation, the cover displacement functions $u_i(x,y)$ and $v_i(x,y)$ defined on the physical cover U_i

$$u_i(x,y), \qquad (x,y) \in U_i \tag{5}$$

$$v_i(x,y), \qquad (x,y) \in U_i \tag{6}$$

can be constant, linear, high order polynomials or locally defined series (such as Fourier series as our wave form). These cover displacement functions are connected together by the weight functions $w_i(x,y)$

$$\begin{aligned} &w_i(x,y) \geq 0, && (x,y) \in U_i \\ &w_i(x,y) = 0, && (x,y) \notin U_i \end{aligned} \tag{7}$$

with

$$\sum_{(x,y)\in U_j} w_j(x,y) = 1$$

Using the weight function $w_i(x,y)$, the global displacement functions on the whole physical cover system are defined from the cover displacement functions. The global displacement functions $u(x,y)$ and $v(x,y)$ on the whole material body are two global functions:

$$\begin{Bmatrix} u(x,y) \\ v(x,y) \end{Bmatrix} = \sum_{i=1}^{n} w_i(x,y) \begin{Bmatrix} u_i(x,y) \\ v_i(x,y) \end{Bmatrix} = \sum_{i=1}^{n}\sum_{j=1}^{m} \left[T_{ij}(x,y)\right]\left\{D_{ij}\right\}$$

$$= \sum_{i=1}^{n} \left[T_i(x,y)\right]\left\{D_i\right\} \tag{8}$$

$$\left[T_{ij}(x,y)\right] = \begin{pmatrix} t_{12j-1}(x,y) & t_{12j}(x,y) \\ t_{22j-1}(x,y) & t_{22j}(x,y) \end{pmatrix}, \quad \left\{D_{ij}\right\} = \begin{Bmatrix} d_{i2j-1} \\ d_{i2j} \end{Bmatrix} \tag{9}$$

$$\left[T_i(x,y)\right] = \begin{pmatrix} T_{i1} & T_{i2} & \dots & T_{im} \end{pmatrix}, \quad \left\{D_i\right\} = \begin{Bmatrix} D_{i1} \\ D_{i2} \\ \vdots \\ D_{im} \end{Bmatrix} \tag{10}$$

The displacement matrix $[T_i(x,y)]$ can be given in the following form:

$$\begin{aligned}\left[T_i(x,y)\right] &= \begin{pmatrix} T_{i1} & T_{i2} & \ldots & T_{im} \end{pmatrix} \\ &= \begin{pmatrix} t_{11}(x,y) & t_{12}(x,y) & t_{13}(x,y) & \ldots & t_{12m-1}(x,y) & t_{12m}(x,y) \\ t_{21}(x,y) & t_{22}(x,y) & t_{23}(x,y) & \ldots & t_{22m-1}(x,y) & t_{22m}(x,y) \end{pmatrix}\end{aligned} \tag{11}$$

where the subscript "i" represents the i-th cover.

Each intersection domain of physical covers is defined as an element e. If an element e is not in cover U_i, $T_i(x,y)=0$.

$$\begin{aligned} T_i(x,y) &\neq 0, \qquad e \in U_i \\ T_i(x,y) &= 0, \qquad e \notin U_i \end{aligned} \tag{12}$$

Element e is the intersection of covers $U_{e(1)}, U_{e(2)}, \ldots, U_{e(q)}$, then

$$\begin{aligned} T_i(x,y) &\neq 0, \qquad e \in U_{e(r)} \\ T_i(x,y) &= 0, \qquad e \notin U_{e(r)} \end{aligned} \tag{13}$$

$$\begin{aligned}\begin{Bmatrix} u(x,y) \\ v(x,y) \end{Bmatrix} &= \sum_{r=1}^{q} w_{e(r)}(x,y) \begin{Bmatrix} u_{e(r)}(x,y) \\ v_{e(r)}(x,y) \end{Bmatrix} \\ &= \sum_{r=1}^{q} \sum_{j=1}^{m} \left[T_{e(r)j}(x,y)\right] \left\{D_{e(r)j}\right\} \\ &= \sum_{r=1}^{q} \left[T_{e(r)}(x,y)\right] \left\{D_{e(r)}\right\}, \quad (x,y) \in e\end{aligned} \tag{14}$$

In each element, weight function $w_i(x,y)$ has an analytical representation, which is either constant number or a differentiable elementary function. Therefore, global displacement function $(u(x,y), v(x,y))$ in the element e often has analytical representation. Very often, cover functions $u_i(x,y)$ and $v_i(x,y)$ are represented as series, the coefficients of each term of the series are the unknown d_{ij}

$$\begin{Bmatrix} u_i(x,y) \\ v_i(x,y) \end{Bmatrix} = \sum_{j=1}^{m} \begin{pmatrix} f_{ij}(x,y) & 0 \\ 0 & f_{ij}(x,y) \end{pmatrix} \begin{Bmatrix} d_{i2j-1} \\ d_{i2j} \end{Bmatrix} \tag{15}$$
$$(x,y) \in U_i$$

On cover U_i, $(u_i(x,y), v_i(x,y))$ are the displacements of point (x,y) on x any y direction respectively, the cover displacement functions $(u_i(x,y), v_i(x,y))$ often take one of the following : The constant function on cover U_i

$$\begin{Bmatrix} u_i(x,y) \\ v_i(x,y) \end{Bmatrix} = \begin{pmatrix} 1 & 0 \\ 0 & 1 \end{pmatrix} \begin{Bmatrix} d_{i1} \\ d_{i2} \end{Bmatrix} \tag{16}$$

The complete first order approximation on cover U_i

$$\begin{Bmatrix} u_i(x,y) \\ v_i(x,y) \end{Bmatrix} = \begin{pmatrix} 1 & 0 & x & 0 & y & 0 \\ 0 & 1 & 0 & x & 0 & y \end{pmatrix} \begin{Bmatrix} d_{i1} \\ d_{i2} \\ d_{i3} \\ d_{i4} \\ d_{i5} \\ d_{i6} \end{Bmatrix} \tag{17}$$

Here x and y should be represented as cosine function expansion with its coefficients to be computed by least square method as follows.

Denote $\begin{pmatrix} u(x,y) & v(x,y) \end{pmatrix}^T$ as approximation of any point (x,y) of the element e. Here e is the intersection of q covers $U_{e(1)}, U_{e(2)}, ..., U_{e(q)}$. Denote $\begin{pmatrix} r(x,y) & s(x,y) \end{pmatrix}^T$ as function of any point (x,y) of the element e.

The displacement function is

$$\begin{Bmatrix} u(x,y) \\ v(x,y) \end{Bmatrix} = [T_{(e)}(x,y)]\{D_{(e)}\} \tag{18}$$

where

$$[T_{(e)}(x,y)] = \begin{pmatrix} T_{e(1)} & T_{e(2)} & T_{e(3)} & \dots & T_{e(q)} \end{pmatrix}$$

$$\{D_{(e)}\} = \begin{Bmatrix} D_{e(1)} \\ D_{e(2)} \\ D_{e(3)} \\ \vdots \\ D_{e(q)} \end{Bmatrix} \tag{19}$$

The least square integration is of element e is

$$\Pi_m = \frac{1}{2}\iint_A \begin{pmatrix} u(x,y)-r(x,y) & v(x,y)-s(x,y) \end{pmatrix} \begin{Bmatrix} u(x,y)-r(x,y) \\ v(x,y)-s(x,y) \end{Bmatrix} dx\,dy \tag{20}$$

$$\Pi_m = \frac{1}{2}\iint_A \begin{pmatrix} u(x,y) & v(x,y) \end{pmatrix} \begin{Bmatrix} u(x,y) \\ v(x,y) \end{Bmatrix} dx\,dy + \iint_A \begin{pmatrix} u(x,y) & v(x,y) \end{pmatrix} \begin{Bmatrix} r(x,y) \\ s(x,y) \end{Bmatrix} dx\,dy$$
$$+ \frac{1}{2}\iint_A \begin{pmatrix} r(x,y) & s(x,y) \end{pmatrix} \begin{Bmatrix} r(x,y) \\ s(x,y) \end{Bmatrix} dx\,dy \tag{21}$$

$$\Pi_m = \frac{1}{2}\iint_A \{D_{(e)}\}^T [T_{(e)}(x,y)]^T [T_{(e)}(x,y)]\{D_{(e)}\}dxdy + \{D_{(e)}\}^T \left[\iint_A [T_{(e)}(x,y)]^T \begin{Bmatrix} r(x,y) \\ s(x,y) \end{Bmatrix} dx\,dy \right]$$
$$+ \frac{1}{2}\iint_A \begin{pmatrix} r(x,y) & s(x,y) \end{pmatrix} \begin{Bmatrix} r(x,y) \\ s(x,y) \end{Bmatrix} dx\,dy \tag{22}$$

After minimization of the least square integration, the element matrix is

$$\iint_A [T_{(e)}(x,y)]^T [T_{(e)}(x,y)]\,dx\,dy \tag{23}$$

i.e.,

$$\iint_A \begin{Bmatrix} [T_{e(1)}]^T \\ [T_{e(2)}]^T \\ [T_{e(3)}]^T \\ \vdots \\ [T_{e(q)}]^T \end{Bmatrix} \left([T_{e(1)}] \quad [T_{e(2)}] \quad [T_{e(3)}] \quad \ldots \quad [T_{e(q)}] \right) dx\,dy \tag{24}$$

The free term matrix is

$$\iint_A [T_{(e)}(x,y)]^T \begin{Bmatrix} r(x,y) \\ s(x,y) \end{Bmatrix} dx\,dy$$

$$= \iint_A \begin{Bmatrix} [T_{e(1)}]^T \\ [T_{e(2)}]^T \\ [T_{e(3)}]^T \\ \vdots \\ [T_{e(q)}]^T \end{Bmatrix} \begin{Bmatrix} r(x,y) \\ s(x,y) \end{Bmatrix} dx\,dy \tag{25}$$

Then

$$\iint_A [T_{e(r)}(x,y)]^T [T_{e(s)}(x,y)]\,dx\,dy \quad \rightarrow \quad [K_{e(r)e(s)}], \tag{26}$$

$$r,s = 1,2,3,\ldots,q.$$

$$\iint_A [T_{e(r)}(x,y)]^T \begin{Bmatrix} r(x,y) \\ s(x,y) \end{Bmatrix} dx\,dy \quad \rightarrow \quad \{F_{e(r)}\} \tag{27}$$

$$r,s = 1,2,3,\ldots,q.$$

Assume the number of physical covers is n, and there are $2m$ unknowns in each physical cover,

$$D_i = \begin{Bmatrix} d_{i1} \\ d_{i2} \\ d_{i3} \\ d_{i4} \\ \vdots \\ d_{i2m-1} \\ d_{i2m} \end{Bmatrix}, \qquad i = 1,2,\ldots,n. \tag{28}$$

The least square function has the form

$$\Pi = \frac{1}{2}\begin{pmatrix} D_1^T & D_2^T & D_3^T & \dots & D_n^T \end{pmatrix}\begin{pmatrix} K_{11} & K_{12} & K_{13} & \dots & K_{1n} \\ K_{21} & K_{22} & K_{23} & \dots & K_{2n} \\ K_{31} & K_{32} & K_{33} & \dots & K_{3n} \\ \vdots & \vdots & \vdots & \ddots & \vdots \\ K_{n1} & K_{n2} & K_{n3} & \dots & K_{nn} \end{pmatrix}\begin{Bmatrix} D_1 \\ D_2 \\ D_3 \\ \vdots \\ D_n \end{Bmatrix}$$

$$+\begin{pmatrix} D_1^T & D_2^T & D_3^T & \dots & D_n^T \end{pmatrix}\begin{Bmatrix} F_1 \\ F_2 \\ F_3 \\ \vdots \\ F_n \end{Bmatrix} + C. \tag{29}$$

Because each cover has $2m$ degrees of freedom, each sub matrix K_{ij} in the coefficient matrix given by equation is a $2m \times 2m$ matrix. D_i and F_i are $2m \times 1$ sub matrices, where D_i represents the displacement variables $(d_{i1}d_{i2}d_{i3}d_{i4}...d_{i2m})^T$ of physical cover i. From the formulation of Π, the previous formula can be written as a symmetric representation,

$$K_{ij} = K_{ji}^T \tag{30}$$

The equilibrium equations are derived by minimizing the least square function Π. The i-th row of following equation consists of $2m$ linear equations

$$\frac{\partial \Pi}{\partial d_{ir}} = 0, \qquad r = 1,2,3,4,...,2m, \tag{31}$$

The r-row, s-column element of K_{ij} is

$$\frac{\partial \Pi}{\partial d_{ir}\partial d_{js}}, \qquad r,s = 1,2,3,4,...,2m, \tag{32}$$

The r-row element of F_i is the derivative of Π at value 0, namely all variables $D_1,...,D_n$ equal to zero.

$$\frac{\partial \Pi(0)}{\partial d_{ir}}\Big|_{D_1,...,D_n=0}, r = 1,2,3,4,...,2m, \tag{33}$$

Where d_{ir} is the displacement variable of cover i. The matrix of obtained simultaneous equilibrium equations is same as the matrix of quadratic form

$$\begin{pmatrix} K_{11} & K_{12} & K_{13} & \dots & K_{1n} \\ K_{21} & K_{22} & K_{23} & \dots & K_{2n} \\ K_{31} & K_{32} & K_{33} & \dots & K_{3n} \\ \vdots & \vdots & \vdots & \ddots & \vdots \\ K_{n1} & K_{n2} & K_{n3} & \dots & K_{nn} \end{pmatrix}\begin{Bmatrix} D_1 \\ D_2 \\ D_3 \\ \vdots \\ D_n \end{Bmatrix} = \begin{Bmatrix} F_1 \\ F_2 \\ F_3 \\ \vdots \\ F_n \end{Bmatrix}. \tag{34}$$

For material analysis, F_i is the loading on cover i distributed to the $2m$ displacement variables. Sub-matrix K_{ii} depend on the material properties of cover i and K_{ij} , where $i \neq j$ is defined by the overlapping or contact between cover i and cover j.

This directly leads 2-D image compression.

References:

[1] Shi, G-H.. 1997. *Working Forum on Manifold Method of Material Analysis, Volume 2,* US Army Corps of Engineer.

[2] Brandenburg, K. and G. Stoll. 1994. ISO-MPEG-1 Audio: A Generic Standard for Coding of High-Quality Digital Audio, *Journal of the Audio Engineering Society,* 42: 780-792.

[3] Princen, J. P. and A. P. Bradley. 1986. Analysis/Synthesis Filter Design Based on Time Domain Aliasing Cancellation, *IEEE Transaction on Acoustics, Speech and Signal Processing,* ASSP-34, 1153-1161.

Upper and lower bound solution with hybrid-type penalty method

Hirohisa Ohki
Department of Civil Engineering, Hosei University, Koganei, Tokyo, Japan
Norio Takeuchi
Department of Art and Technology, Hosei University, Koganei, Tokyo, Japan

This paper was prepared for presentation at *ICADD-7, the Seventh International Conference on Analysis of Discontinuous Deformation*, held in Honolulu, Hawaii, December 10-12, 2005.

ABSTRACT : Hybrid-type penalty method (HPM) assume the linear displacement field with rigid displacement, rigid rotation and constant strain in each sub-domain and introduce subsidiary condition about the continuity of displacement into the framework of the variational expression with Lagrange multipliers. This compatibility of the displacement on the intersection boundary is approximately introduced using the penalty as a spring constant which is applied to the Lagrange multiplier. Present method can be deal with the fracture on the intersection boundary and yielding in the each element at the same time.

1. INTRODUCTION

This paper presents new approach for the upper and lower bound solution for limit analysis. Present method (HPM : Hybrid-type penalty method) introduce hybrid displacement model based on the modified principle of virtual work. In this model, subsidiary conditions are introduced into the framework of the variational expression with Lagrange multipliers. Physical meaning of the Lagrange multiplier is equal to the surface force on the intersection boundary. Then, the concept of the spring of RBSM (Rigid Bodies-Spring Model) is applied to the Lagrange multiplier. Compatibility of the displacement on the intersection boundary is approximately introduced using the penalty as a spring constant. Therefore, the displacement filed can be assumed for each element without restraining by the condition of compatibility. So that, we assume the linear displacement field with rigid displacement, rigid rotation and constant strain in each sub-domain. And it can be introduced the slip by the same algorithm of RBSM without processing the double node. Because the surface force on the intersection boundary between two adjacent sub-domains is obtained and displacement field is defined independently in each sub-domain. Also, present method is satisfied the continuity of surface force and mechanism. So that, it can be obtained the upper bound solution. And more, present method can estimate the stiffness in each sub-domain. Namely, we can obtain the lower bound solution to consider the plasticity condition in each sub-domain. Using by the present method, it is possible to obtained the upper and lower bound solution for limit analysis.

2. GOVERNING EQUATION AND HYBRID-TYPE PENALTY METHOD

2.1. Governing equation

We consider the solution of the governing equations of solid mechanics that can be written as

$$\boldsymbol{L}^t\boldsymbol{\sigma} + \boldsymbol{f} = 0, \quad \boldsymbol{\sigma} = \boldsymbol{D}\boldsymbol{\varepsilon}, \quad \boldsymbol{\varepsilon} = \boldsymbol{L}\boldsymbol{u} \quad \text{in } \Omega \tag{1}$$

where, u is the displacement vector, ε and σ are the stress and strain vectors, respectively. $\boldsymbol{D}$ is constitutive stress-strain matrix, and $\boldsymbol{f}$ is the vector of constant body force. The matrix $\boldsymbol{L}$ contains the differential operators. Ω is the domain area or volume with boundary$\Gamma = \Gamma_u \cup \Gamma_\sigma$. Γ_u is the boundary where the displacements are given and Γ_σ is the boundary where the traction forces are given. In these boundaries, following conditions are satisfied.

$$\boldsymbol{T} = \boldsymbol{n}\boldsymbol{\sigma} = \overline{\boldsymbol{T}} \ \text{ on } \Gamma_\sigma \ , \ \boldsymbol{u} = \overline{\boldsymbol{u}} \ \text{ on } \Gamma_{\mathrm{u}} \tag{2}$$

where $\overline{T}$ the prescribed traction forces at the boundary Γ_u , $\overline{u}$ the prescribed displacement at the boundary Γ_u, and $\boldsymbol{n}$ is the outward unit normal vector on the domain boundary.

By multiplying eq.(1) of infinitesimal virtual displacements δ_u, it will be integrated as following:

$$\int_\Omega \delta\boldsymbol{u}^t(\boldsymbol{L}^t\boldsymbol{\sigma} + \boldsymbol{f})d\Omega = 0 \quad (\delta\boldsymbol{u} = 0 \ \text{ on } \Gamma_{\mathrm{u}}) \tag{3}$$

We should choose the arbitrary set of virtual displacement such that the geometrical boundary conditions Γ_u are not violated. Integrating by parts the first term in eq.(3) yields the well-known the principle of virtual work such that

$$\int_\Omega [\boldsymbol{L}\delta\boldsymbol{u}]^t\boldsymbol{\sigma}d\Omega - \int_\Omega \delta\boldsymbol{u}^t\boldsymbol{f}d\Omega - \int_{\Gamma_\sigma} \delta\boldsymbol{u}^t\ \boldsymbol{T}d\Gamma = 0 \tag{4}$$

The domain Ω will be discretion by the finite number of the sub-domain $\Omega^{(e)}$ as follows (see Fig.1):

$$\Omega = \bigcup_{e=1}^{M} \Omega^{(e)} \ \text{ where } \ \Omega^{(\mathrm{e})} \cap \Omega^{(\mathrm{r})} = 0 \quad (\mathrm{e} \neq \mathrm{r}) \tag{5}$$

where$M$is the total number of sub-domains $\Omega^{(e)}$which will be surrounded in closed boundary $\Gamma^{(e)}$.

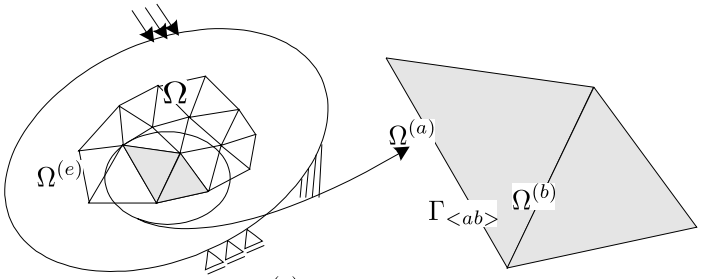

[1]
[2] Fig.1. Sub-domain $\Omega^{(e)}$ and boundary $\Gamma_{<ab>}$ between sub-domain $\Omega^{(a)}$ and $\Omega^{(b)}$

The discrete counterpart of the principle of virtual work (4) will be given by

$$\sum_{e=1}^{M}\left(\int_{\Omega^{(e)}} [\boldsymbol{L}\delta\boldsymbol{u}]^t\boldsymbol{\sigma}d\Omega - \int_{\Omega^{(e)}} \delta\boldsymbol{u}^t\boldsymbol{f}d\Omega\right) - \int_{\Gamma_{<\sigma>}} \delta\boldsymbol{u}^t\bar{\boldsymbol{T}}d\Gamma = 0 \tag{6}$$

As shown as Fig.1, the boundary $\Gamma_{<ab>}$ is the intersection between sub-domain $\Omega^{(a)}$ and $\Omega^{(b)}$.

$$\Gamma_{<ab>} = \Gamma^{(a)} \cap \Gamma^{(b)} \tag{7}$$

In the principle of virtual work of hybrid-type, subsidiary condition on the boundary will be shown:

$$\hat{\boldsymbol{u}}^{(a)} = \hat{\boldsymbol{u}}^{(b)} \quad \text{on } \Gamma_{<ab>} \tag{8}$$

This subsidiary condition is expressed by the following equation using Lagrange multiplier $\boldsymbol{\lambda}$:

$$H_{<ab>} = \delta \int_{\Gamma_{<ab>}} \boldsymbol{\lambda}^t (\hat{\boldsymbol{u}}^{(a)} - \hat{\boldsymbol{u}}^{(b)}) d\Gamma \tag{9}$$

where $\hat{\boldsymbol{u}}^{(a)}$ and $\hat{\boldsymbol{u}}^{(b)}$ are the displacements on the boundary. Substituting (9) into (6), the equation of virtual work of hybrid-type is expressed by

$$\begin{aligned} \sum_{e=1}^{M} \left(\int_{\Omega^{(e)}} [\boldsymbol{L}\delta\boldsymbol{u}]^t \boldsymbol{D} [\boldsymbol{L}\boldsymbol{u}] d\Omega - \int_{\Omega^{(e)}} \delta\boldsymbol{u}^t \boldsymbol{f} d\Omega - \int_{\Gamma_\sigma} \delta\boldsymbol{u}^t \boldsymbol{T} d\Gamma \right) \\ - \sum_{s=1}^{N} \left(\delta \int_{\Gamma_{<s>}} \boldsymbol{\lambda}^t (\hat{\boldsymbol{u}}^{(a)<s>} - \hat{\boldsymbol{u}}^{(b)}_{<s>}) d\Gamma \right) = 0 \end{aligned} \tag{10}$$

where N is the total number of adjacent element boundary.

Lagrange multiplier $\boldsymbol{\lambda}$ is equal to traction force on the intersection boundary $\Gamma_{<ab>}$ as follows:

$$\boldsymbol{\lambda} = \boldsymbol{T}^{(a)}(\hat{\boldsymbol{u}}^{(a)}) = -\boldsymbol{T}^{(b)}(\hat{\boldsymbol{u}}^{(b)}) \tag{11}$$

where $\boldsymbol{T}^{(a)}$ and $\boldsymbol{T}^{(b)}$ are the traction forces on the intersection boundary between $\Omega^{(a)}$ and $\Omega^{(b)}$.

2.2. Independent linear displacement field

In this paper, we assume the following independent linear displacement field $\boldsymbol{u}^{(e)}$ with rigid displacement, rigid rotation and constant strain in each sub-domain.

$$\boldsymbol{u}^{(e)} = \boldsymbol{N}_d{}^{(e)} \boldsymbol{d}^{(e)} + \boldsymbol{N}_\varepsilon{}^{(e)} \boldsymbol{\epsilon}^{(e)} \tag{12}$$

Where, $\boldsymbol{d}^{(e)}$ is the displacement vector which has the rigid displacement and the rigid rotation at a typical point within the sub-domain, $\boldsymbol{\epsilon}^{(e)}$is the constant strain vector within the sub-domain and $\boldsymbol{N}_d{}^{(e)}$ and $\boldsymbol{N}_d{}^{(\epsilon)}$ is a linear interpolation function respectively. And each coefficient is follows:

$$\boldsymbol{N}_d^{(e)} = \begin{bmatrix} 1 & 0 & -(y - y_p) \\ 0 & 1 & (x - x_p) \end{bmatrix} \quad , \quad \boldsymbol{d}^{(e)} = \lfloor u_p, v_p, \theta_p \rfloor^t$$

$$\boldsymbol{N}_d^{(e)} = \begin{bmatrix} x - x_p & 0 & \dfrac{y - y_p}{2} \\ 0 & y - y_p & \dfrac{x - x_p}{2} \end{bmatrix} \quad , \quad \boldsymbol{\varepsilon}^{(e)} = \lfloor \varepsilon_x, \varepsilon_y, \gamma_{xy} \rfloor^t$$

The displacement field (12) expresses by using the displacement at a typical point in each sub-domain. In RBSM(Rigid Bodies-Spring Model), it is introduced into the concept of spring between the surface force and the relative displacement on the boundary$\Gamma_{<ab>}$, and estimated to total energy by using work of surface force with spring. Then, applying Lagrange multipliers $\boldsymbol{\lambda}$ to the idea of RBSM, the surface force $\boldsymbol{\lambda}_{<ab>}$ of boundary between sub-domain $\Omega^{(a)}$ and $\Omega^{(b)}$ is able to express as follow:

$$\boldsymbol{\lambda}_{<ab>} = \boldsymbol{k} \cdot \boldsymbol{\delta}_{<ab>} \tag{13}$$

where, $\boldsymbol{k}$ is the spring constant matrix, $\boldsymbol{\delta}_{<ab>}$is relative displacement vector of sub-domain boundary$\boldsymbol{\Gamma}_{<ab>}$, $\boldsymbol{\lambda}_{<ab>}$ is Lagrange multiplier vector which has the components corresponding to the surface force vector. In equation of virtual work of hybrid-type, it is necessary to set a large number for the spring constants. This will be demanded to approximate the continuity of

displacement on sub-domain boundary. Therefore, the spring constants will be dealt with the penalty numbers as follow:

$$\boldsymbol{k} = \boldsymbol{p} \tag{14}$$

where, $\boldsymbol{p}$ is a matrix with penalty function.

The virtual displacement δ_u is expressed by the following equation.

$$\delta\boldsymbol{u} = \boldsymbol{N}_d\delta\boldsymbol{d} + \boldsymbol{N}_\varepsilon\delta\boldsymbol{\varepsilon} \tag{15}$$

Eq.(12) and (15) can be replaced by

$$\boldsymbol{u}^{(e)} = \boldsymbol{N}^{(e)}\boldsymbol{U}^{(e)}, \qquad \delta\boldsymbol{u}^{(e)} = \boldsymbol{N}^{(e)}\delta\boldsymbol{U}^{(e)} \tag{16}$$

Then, (16) gives the following expression.

$$\boldsymbol{L}\boldsymbol{u}^{(e)} = \boldsymbol{L}\boldsymbol{N}^{(e)}\boldsymbol{U}^{(e)} = \boldsymbol{B}^{(e)}\boldsymbol{U}^{(e)} \tag{17}$$

Substituting (12), (13), (14), (16) and (17) into (10), it can be obtained as following final conclusion of the discretion governing equation for whole domain.

$$\delta\boldsymbol{U}^t\left(\sum_{e=1}^{M}\boldsymbol{K}^{(e)} + \sum_{s=1}^{N}\boldsymbol{K}_{<s>}\right)\boldsymbol{U} - \delta\boldsymbol{U}^t\left(\sum_{e=1}^{M}\boldsymbol{P}^{(e)}\right) = 0 \tag{18}$$

Namely, eq.(18) is resulted the following simultaneous linear equations. Where, $\boldsymbol{K}$ and $\boldsymbol{P}$ is follows:

$$\boldsymbol{K} = \sum_{e=1}^{M}\boldsymbol{K}^{(e)} + \sum_{s=1}^{N}\boldsymbol{K}_{<s>} \quad , \quad \boldsymbol{P} = \sum_{e=1}^{M}\boldsymbol{P}^{(e)} \tag{19}$$

where, each coefficient is follows:

$$\boldsymbol{K}^{(e)} = \int_{\Omega^{(e)}} (\boldsymbol{B}^{(e)})^t\boldsymbol{D}^{(e)}\boldsymbol{B}^{(e)}\, d\Omega$$

$$\boldsymbol{K}_{<s>} = \int_{\Gamma_{<s>}} \boldsymbol{B}^t_{<s>}\boldsymbol{k}\boldsymbol{B}_{<ab>}\, d\Gamma$$

$$\boldsymbol{P}^{(e)} = \int_{\Omega^{(e)}} (\boldsymbol{N}^{(e)})^t\boldsymbol{f}\, d\Omega + \int_{\Gamma_\sigma} (\boldsymbol{N}^{(e)})^t\bar{\boldsymbol{T}}\, d\Gamma$$

3. HANDLING OF FRACTURE

3.1. Fracture on the intersection boundary

In case of Mohr-Coulomb's condition, yield function f is expressed by:

$$f = \tau^2 - (c - \sigma_n \tan\phi)^2 \tag{20}$$

where, c, ϕ, σ and τ is cohesion, the angle of internal friction, surface force of the tangential and normal directions, respectively. Yield function f and plasticity potential Q is expressed by:

$$f(\boldsymbol{\lambda}) = 0 \quad , \quad Q(\boldsymbol{\lambda}) = 0 \tag{21}$$

where, $\boldsymbol{\lambda}$ is the surface force on the intersection boundary. In each intersection boundary, we assume the relation of the surface force-relative displacement which is the generally law of the plastic flow. So, the increment of relative displacement $\Delta\delta$ after the plasticity condition is expressed by:

$$\Delta\boldsymbol{\delta}^p = \mu\frac{\partial Q}{\partial\boldsymbol{\lambda}} \tag{22}$$

where, Δ is the quantity of increment and superscript p is the plasticity condition. Expressing the superscript e before the plasticity condition, relative displacement in the element is follows:

$$\Delta\boldsymbol{\delta}^e = \Delta\boldsymbol{\delta} - \Delta\boldsymbol{\delta}^p \tag{23}$$

On the other hand, the relation of surface force-relative displacement before the plasticity condition is expressed by:

$$\boldsymbol{\lambda} = \boldsymbol{k}^e \cdot \boldsymbol{\delta}^e \tag{24}$$

Substituting (22) and (23) into (24), it can be obtained the increment surface force.

$$\Delta\boldsymbol{\lambda} = \boldsymbol{k}^e \left(\Delta\boldsymbol{\delta} - \mu \frac{\partial f}{\partial \boldsymbol{\lambda}} \right) \tag{25}$$

and more, plasticity condition is follows:

$$\frac{\partial f}{\partial \boldsymbol{\lambda}} \boldsymbol{\Delta\lambda} = 0 \tag{26}$$

Arranging the above equation, we obtain the relation of the increment of surface force and relative displacement as follows:

$$\Delta\boldsymbol{\lambda} = \boldsymbol{k}^{ep} \cdot \Delta\boldsymbol{\delta} \tag{27}$$

where, $\boldsymbol{k}^{ep}$ is follows:

$$\boldsymbol{k}^{ep} = \left(\boldsymbol{k}^e - \frac{\boldsymbol{k}^e \dfrac{\partial f}{\partial \boldsymbol{\lambda}} \dfrac{\partial Q}{\partial \boldsymbol{\lambda}} \boldsymbol{k}^e}{\dfrac{\partial f}{\partial \boldsymbol{\lambda}} \boldsymbol{k}^e \dfrac{\partial Q}{\partial \boldsymbol{\lambda}}} \right) \tag{28}$$

In the above eq.(28), it obey the associated flow rule if $f \equiv Q$. Following equation is the plasticity stiffness matrix which concerning Mohr-Coulomb's condition. When the surface force extends to the yield surface, it moves on the yield surface using the following equation.

$$\begin{aligned} \boldsymbol{k^{ep}} = & \begin{bmatrix} k_n & 0 \\ 0 & k_t \end{bmatrix} \\ & -\frac{1}{F} \begin{bmatrix} k_n^2 \{(c - \lambda_n tan\phi) tan\phi\}^2 & k_n k_t \lambda_t (c - \lambda_n tan\phi) tan\phi) \\ sym. & k_t^2 \lambda_t^2 \end{bmatrix} \end{aligned} \tag{29}$$

where,

$$F = k_t \cdot \lambda_t^2 + k_n \{(c - tan\phi \cdot \lambda_n) \cdot tan\phi\}^2$$

3.2. Yielding in each element

In case of Mohr-Coulomb's condition, yield function g is expressed by:

$$g = \sigma_1 - \sigma_3 + 2c\cos\phi - (\sigma_1 + \sigma_3)\sin\phi \tag{30}$$

where, $\sigma_1, \sigma_2, \sigma_3$ is major, intermediate and minor principal stress, respectively. Yield function g and plasticity potential Φ is expressed by:

$$g(\boldsymbol{\sigma}) = 0 \quad , \quad \Phi(\boldsymbol{\sigma}) = 0 \tag{31}$$

where, $\boldsymbol{\sigma}$ is the stress in the element. In each element, we assume the relation of the stress-strain which is the law of the plastic flow. So, in this study, strain increment $\Delta\varepsilon$ after the plasticity condition is expressed by:

$$\Delta\boldsymbol{\varepsilon}^p = \eta\frac{\partial g}{\partial\boldsymbol{\sigma}} \tag{32}$$

where, Δ is the quantity of increment and superscript p is the plasticity condition. Expressing the superscript e before the plasticity condition, strain in the element is follows:

$$\Delta\boldsymbol{\varepsilon}^e = \Delta\boldsymbol{\varepsilon} - \Delta\boldsymbol{\varepsilon}^p \tag{33}$$

On the other hand, the relation of stress-strain before the plasticity condition is expressed by:

$$\boldsymbol{\sigma} = \boldsymbol{D}^e \cdot \boldsymbol{\varepsilon}^e \tag{34}$$

Substituting (32) and (33) into (34), it can be obtained the increment stress.

$$\Delta\boldsymbol{\sigma} = \boldsymbol{D}^e\left(\Delta\boldsymbol{\varepsilon} - \eta\frac{\partial g}{\partial\boldsymbol{\sigma}}\right) \tag{35}$$

and more, plasticity condition is follows:

$$\frac{\partial g}{\partial\boldsymbol{\sigma}}\boldsymbol{\Delta\sigma} = 0 \tag{36}$$

Arranging the above equation, we obtain the relation of the increment stress and strain as follows:

$$\boldsymbol{\sigma} = \boldsymbol{D}^{ep} \cdot \boldsymbol{\varepsilon}^e \tag{37}$$

where, $\boldsymbol{D}^{ep}$ is follows:

$$\boldsymbol{D}^{ep} = \left(\boldsymbol{D}^e - \frac{\boldsymbol{D}^e\dfrac{\partial g}{\partial\boldsymbol{\sigma}}\dfrac{\partial\Phi}{\partial\boldsymbol{\sigma}}\boldsymbol{D}^e}{\dfrac{\partial g}{\partial\boldsymbol{\sigma}}\boldsymbol{D}^e\dfrac{\partial\Phi}{\partial\boldsymbol{\sigma}}}\right) \tag{38}$$

In the above eq(38), it obey the associated flow rule if $g \equiv \Phi$. Following equation is the plasticity stiffness matrix which concerning Mohr-Coulomb's condition. When the element stress extends to the yield surface, it moves on the yield surface using the following equation.

$$\boldsymbol{D}^{ep} = \frac{1}{(1+\nu)}\begin{bmatrix} \dfrac{1-\nu}{1-2\nu} - \dfrac{{S_1}^2}{S} & \dfrac{\nu}{1-2\nu} - \dfrac{S_1S_2}{S} & -\dfrac{S_1S_3}{S} \\ & \dfrac{1-\nu}{1-2\nu} - \dfrac{{S_2}^2}{S} & -\dfrac{S_2S_3}{S} \\ sym. & & \dfrac{1-\nu}{2(1-2\nu)} - \dfrac{{S_3}^2}{S} \end{bmatrix} \tag{39}$$

where, each coefficient is follows:

$$S_1 = \frac{E}{(1+\nu)(1-2\nu)}\Big\{(1-\nu)S_{xx} + \nu S_{yy}\Big\}$$
$$S_2 = \frac{E}{(1+\nu)(1-2\nu)}\Big\{(1-\nu)S_{yy} + \nu S_{xx}\Big\}$$
$$S_3 = \frac{E}{2(1+\nu)}\tau_{xy} \quad , \quad S = S_1S_{xx} + S_2S_{yy} + S_3\tau_{xy}$$

Namely, in this study, on the intersection boundary, it's deal with the relation of the surface force-relative displacement. On the other hand, in each element, it's deal with the relation of stress-strain.

4. NUMERICAL EXAMPLE

4.1. Plate with V-notched subjected tensile load

Fig.2 shows the analysis model and mesh division with the V-notch tension specimen. The considered area is quarter-sized because of symmetry. Boundary conditions are shown in Figure. It's analyzed under the condition of plane stress. The material properties are shown in Table 1.

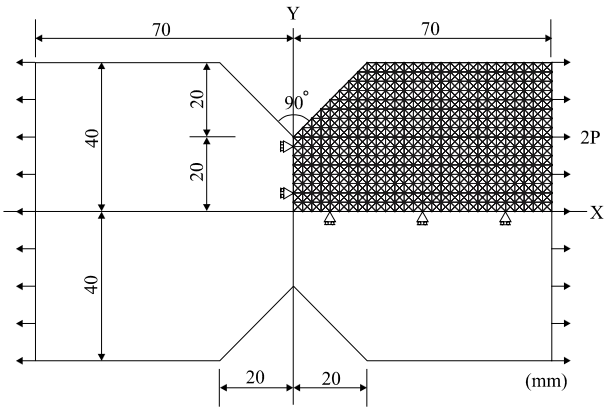

Fig.2. Analysis model and mesh division

Table 1. Material properties

Young's Modulus (KN/mm^2)	196.2
Poison's ratio	0.3
Yield Stress (KN/mm^2)	294.3
Angle of internal friction	0

Fig.3 shows the slip line and deformation that considered the fracture on the intersection boundary. It arise the slip line near the V-notch in early stage. And then, it's broken the boundary of left side. Finally, slip line arising the V-notch form along the hatched line.

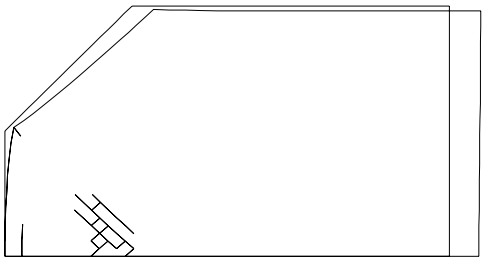

Fig.3. Slip line and deformation (6.79KN)

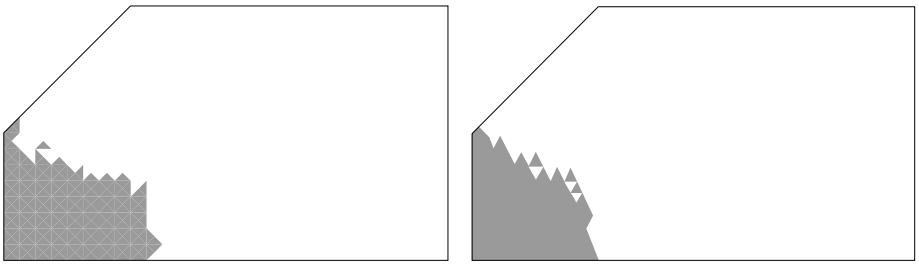

Fig.4. Yield Area (HPM:7.00KN, FEM:7.01KN)

Fig.4 shows the yield area that considered the yielding in each element. Comparing HPM and FEM, it shows much the same pattern. Fig.5 shows the slip line and yielding area that considered the fracture on the intersection boundary and yielding in each element at the same time. As a result, progress of fracture is seen toward the boundary from the V-notch.

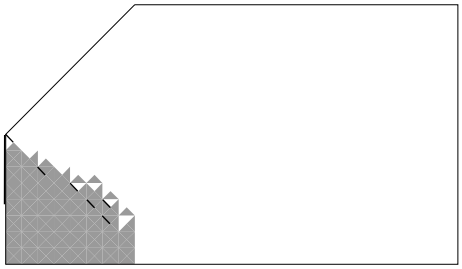

Fig.5. Slip line and Yielding Area (6.79KN)

Fig.6 shows the relation of Load-Displacement. And the collapse load is shown in Table 2. In this figure, each line is indicated follows. Limit analysis is one point broken line. Fracture of intersection boundary(Boundary) is interrupted line. Yielding in each element(Element) is broken line. Fracture of intersection boundary and yielding in each element(Boundary+element) is full line. We obtain the similar collapse load in each case. As a reason, this model is broken by tension fracture.

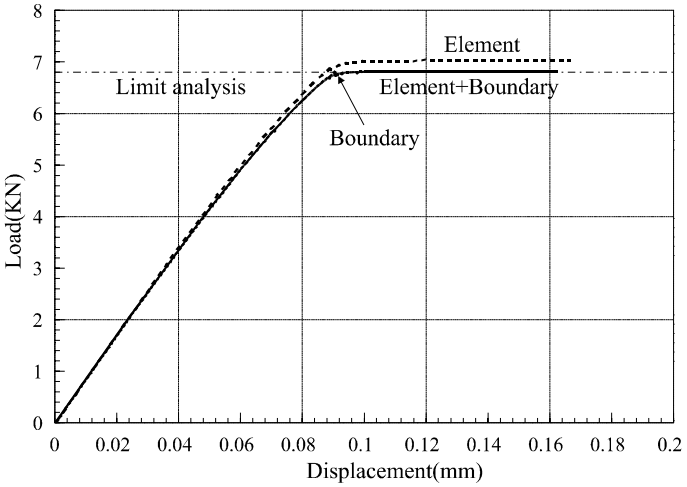

Fig.6. Relation of Load-Displacement

Table 2. Result of Collapse Load (KN)

type	HPM	FEM	Limit

			Analysis
Boundary	6.79	-	6.79
Element	7.00	7.01	
Element+Boundary	6.79	-	

4.2. Bearing capacity

We try to exam the problem of the bearing capacity. Fig.7 shows the analysis model and mesh division. The considered area is half-sized because of symmetry. It's analyzed under the condition of plane strain. The material properties are shown in Table 3.

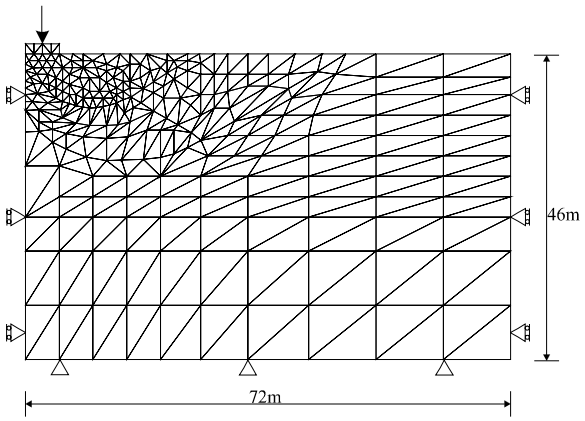

Fig.7. Analysis model and mesh division

Table 3. Material properties

Young's Modulus (KN/mm^2)	98.1
Poison's ratio	0.3
Shear Stress (KN/mm^2)	9.81
Angle of internal friction	30
Specific weight (KN/mm^3)	17.16

Fig.8 shows slip line that considered the fracture on the intersection boundary. In the early stage, it arise the slip line near the loading platform. It shows the tendency to make progress along the slip surface. Finally, it forms the slip line.

Fig.9 show the yield area that considered the yielding in each element. In this case, it shows much the same pattern to the model of fracture on intersection boundary.

Fig.10 is the model of considering on the intersection boundary and yielding in each element at the same time. It shows the slip line and yield area. In the early stage, it seems the progress of fracture near the loading platform. And in the collapse load, fracture has spread in the whole region.

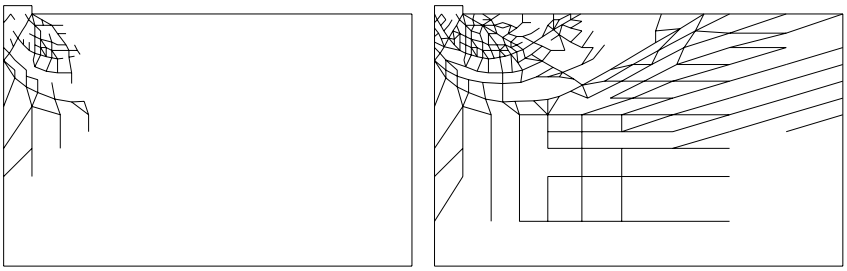

Fig.8. Slip line (50.0KN, 195.84KN)

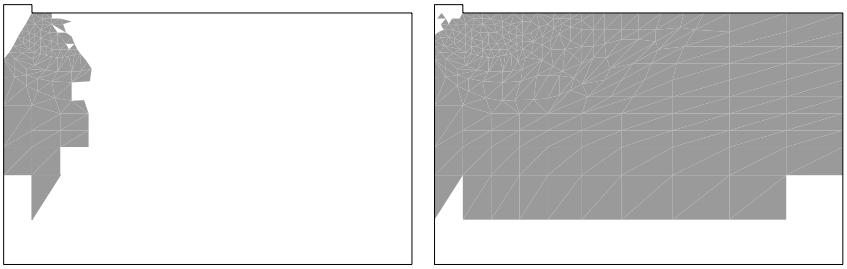

Fig.9. Yielding Area (50.17KN, 154.91KN)

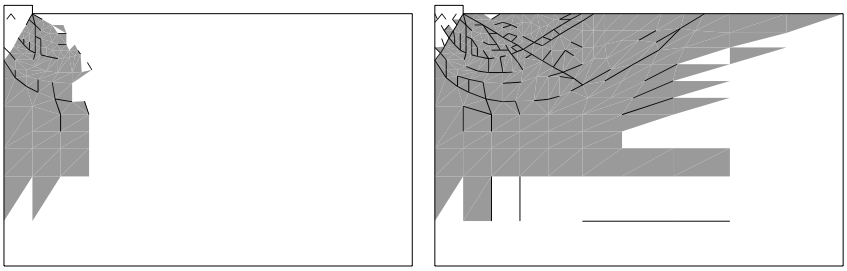

Fig.10. Slip line and Yielding Area
(50.21KN, 99.87KN)

Fig.11 show the relation of Load-Displacement. And the collapse load is shown in Table 4. In this figure, each line is indicated follows. The bearing capacity is one point broken line. Fracture of intersection boundary(Boundary) is interrupted line. Yielding in each element(Element) is broken line. Fracture of intersection boundary and yielding in each element(Boundary+Element) is full line. As shown as in figure, model of dealing the fracture on the intersection boundary, this solution exceed the bearing capacity. And also, model of dealing the fracture on intersection boundary and yielding in each element at the same time, this solution dip form the limit bearing capacity. So, it's obtained the upper and lower bound value. Therefore, true solution exists between upper bound value and lower bound value(hatching area).

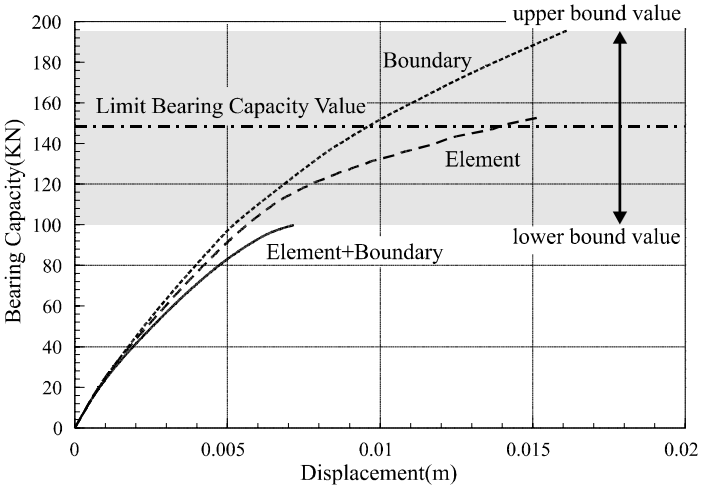

Fig.11. Relation of Load-Displacement

Table 4. Result of Collapse Load (KN)

type	HPM	Bearing Capacity
Boundary	195.84	147.63
Element	154.91	
Element+Boundary	99.87	

5. CONCLUSION

This paper presents the new approach for the upper and lower bound solution for limit analysis by using HPM. Present method is satisfied the continuity of surface force and collapse feature. So that, it is known to obtain the upper bound solution. And more, present method can estimate the stiffness matrix in each sub-domain. Namely, we can obtain the upper bound and lower bound solution considers the plasticity condition in each element.

In this study, we try to apply the plasticity condition in each element and show the two numerical models. As a result, we obtain the upper and lower bound solution. So, true solution exists the between upper bound value and lower bound value. Therefore, present method can be deal with the fracture on the intersection boundary and yielding in the each element at the same time.

REFERENCES

1. T.Kawai, *New element models in discrete structural analysis, J. of the Society of Naval Architects of Japan No. 141, pp187-193, 1977.*
2. N.Takeuchi,H.Ohki,A.Kambayashi and M.Kusabuka, *Non-linear analysis by using discrete model applied penalty method in hybrid displacement model, Transactions of Japan Society for Computational Engineering and Science Paper No. 20010002, 2001.*
3. Y.Yamada and N.Yoshimura, *Plastic stress-strain matrix and its application for the solution of elastic-plastic problems by the finite element method, Int. J. Mech. Sci. Pergamon Press. 1968. Vol.10. pp.343-354.*

4. Y.Yamada, *Application for the Matrix method, structural engineering for numerical analyzing, Tokyo university publishing company, pp.174-175, 1972*
5. R.Hill, *J. Mech. Phys. Solids 1, 19 (1952)*
6. Abdul-Hamid Soubra, *Upper-Bound Solutions for Bearing Capacity of Foundations, Journal of geotechnical and geoenvironmental engineering, January 1999. pp59-68.*

Material nonlinear analysis using hybrid-type penalty method assumed second-order displacement field

Riichi Mihara
Graduate School of Art and Technology, Hosei University (JIP Techno-Science Co.), Tokyo, Japan
Norio Takeuchi
Department of Art and Technology, Hosei University, Tokyo, Japan

This paper was prepared for presentation at *ICADD-7, the Seventh International Conference on Analysis of Discontinuous Deformation*, held in Honolulu, Hawaii, December 10-12, 2005.

ABSTRACT: We proposed the hybrid type penalty method (HPM) which applied the concept of the penalty method to the principle of hybrid type virtual work. HPM applies the concept of the spring of RBSM in Lagrange multiplier and assume independent displacement field to each sub-domain. In the nonlinear analysis by using HPM, a result equal to FEM is obtained about elastic deformation, and a result with a collapse pattern and limit load equal to Rigid-Bodies Spring Model is obtained. This paper reports the analysis for crack initiation problems by using HPM with the second-order displaced field.

1. INTRODUCTION

We proposed the hybrid type penalty method (HPM) which applied the concept of the penalty method to the principle of hybrid type virtual work. This model has succeeded the advantage of RBSM that discrete limit analysis can be performed efficiently and the accuracy of an elastic solution improves.

In the hybrid displacement model, the compatibility of the displacement is loosened a little and it introduces into variational formulation, using Lagrange multiplier to the subsidiary condition. In HPM, the concept of the spring of RBSM (Rigid Bodies-Spring Model) is applied to the Lagrange multiplier. Compatibility of the displacement on the intersection boundary is approximately introduced using the penalty function as a spring constant. So that, HPM can assume a displacement field independent in sub-domain. Therefore, HPM doesn't share degree of freedom by the node like FEM, and the node is used only to recognize the shape of sub-domain.

We analyzed the crack initiation problems using linear displacement field which has rigid displacement and strain for arbitrary point in the sub-domain. In this analysis, the displacement for the elastic problems had the same accuracy as the constant strain element of FEM, and the collapse load for the elasto-plastic problems had the same accuracy as the limit load of RBSM existed.

HPM assumes a displacement field independent in sub-domain and because compatibility requirements of the intersection boundary on adjacent sub-domain are secured by using the penalty method, the displacement field can be assumed regardless of the shape of sub-domain. However, excellent accuracy was not obtained when shape other than the triangle were used at the linear displacement field, and the division of arbitrary shape was difficult. To solve such a problem, it proposes the method of applying the second-order displacement field where the inclination of the strain was added to HPM.

First, the brief formulation of this model is shown. Secondarily, the example of analyzing an easy state of the stress and the stress concentration problem, etc. is shown.

2. GOVERNING EQUATION AND HYBRID-TYPE VIRTUAL WORK

2.1. Governing equation

Let $\Omega \subset \mathbb{R}^{n_{dim}}$, with $(1 \leq n_{dim} \leq 3)$, be the reference configuration of a continuum body with smooth boundary $\Gamma := \partial\Omega$ and closure $\overline{\Omega} := \Omega \cup \partial\Omega$. Here $\mathbb{R}^{n_{dim}}$ is the n_{dim} dimensional Euclidean space.

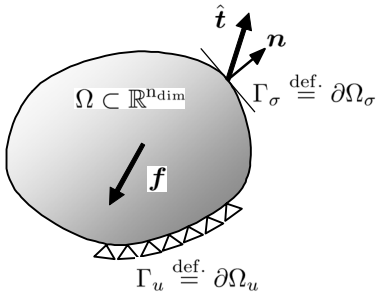

Fig. 1. Reference configuration Ω and smooth boundary $\partial\Omega$

The local form of the equilibrium equation for a deformable body can be written by

$$\operatorname{div} \boldsymbol{\sigma} + \boldsymbol{f} = 0 \quad \text{in} \quad \Omega \tag{1}$$

$$\boldsymbol{\sigma} = \boldsymbol{\sigma}^t \qquad \text{in} \quad \Omega \tag{2}$$

where $\boldsymbol{f} : \Omega \to \mathbb{R}^{n_{dim}}$ is the body force per unit volume, $\boldsymbol{\sigma} : \overline{\Omega} \to \mathbb{S}$ is the Cauchy stress tensor respectively. Here $\mathbb{S} = \mathbb{R}^{(n_{dim}+1)\cdot n_{dim}/2}$ is the vector space of symmetric rank-two tensor and $\boldsymbol{e}_i$ is the standard base vector of $\mathbb{R}^{n_{dim}}$, so that the stress tensor becomes $\boldsymbol{\sigma} = \sigma_{ij}\boldsymbol{e}_i \otimes \boldsymbol{e}_j$, where $\otimes$ denotes a tensor product. $\boldsymbol{u} : \overline{\Omega} \to \mathbb{R}^{n_{dim}}$ is a displacement field of particles with reference position $\boldsymbol{x} \in \Omega$. We write $\boldsymbol{u}(\boldsymbol{x})$ and denote the infinitesimal strain tensor by

$$\boldsymbol{\varepsilon} = \boldsymbol{\nabla}^s \boldsymbol{u} \overset{\text{def.}}{=} \frac{1}{2}\left[\boldsymbol{\nabla}\boldsymbol{u} + (\boldsymbol{\nabla}\boldsymbol{u})^t\right] \tag{3}$$

where $\boldsymbol{\nabla} := (\partial/\partial x_i)\boldsymbol{e}_i$ is the differential vector operator, $\boldsymbol{\nabla}^s$ shows the symmetry part of $\boldsymbol{\nabla}$.
In what follows, we assume that the boundary $\Gamma = \Gamma_u \cup \Gamma_\sigma$.

$$\overline{\Gamma} = \overline{\Gamma_u \cup \Gamma_\sigma} \ , \ \Gamma_u \cap \Gamma_\sigma = \emptyset \tag{4}$$

Here $\Gamma_u := \partial_u\Omega \subset \partial\Omega$ where displacement are prescribed as

$$\boldsymbol{u}|_{\Gamma_u} = \hat{\boldsymbol{u}} \ \text{(given)} \tag{5}$$

Where as $\Gamma_\sigma := \partial_\sigma\Omega \subset \partial\Omega$ where tractions $t := \sigma n$ are prescribed as

$$\boldsymbol{\sigma}|_{\Gamma_\sigma}\hat{\boldsymbol{n}} = \hat{\boldsymbol{t}} \ \text{(given)} \tag{6}$$

Here $\hat{n}$ is the field normal to the boundary Γ_σ. The constitutive equation to the elastic body is provided as follows by the use of the elasticity tensor $\boldsymbol{C}$.

$$\boldsymbol{\sigma} = \boldsymbol{C} : \boldsymbol{\varepsilon} \tag{7}$$

2.2. Virtual work equation (weak forms)

We let $\mathbb{U}$ denote the space of admissible displacement field, define as

$$\mathbb{U} \stackrel{\text{def.}}{=} \{\boldsymbol{u} : \Omega \to \mathbb{R}^{\text{n}_{\text{dim}}} \mid \boldsymbol{u}|_{\Gamma_u} = \hat{\boldsymbol{u}}\} \tag{8}$$

And, let $\mathbb{V}$ denote the space of admissible virtual displacement field, define as

$$\mathbb{V} \stackrel{\text{def.}}{=} \{\delta\boldsymbol{u} : \Omega \to \mathbb{R}^{\text{n}_{\text{dim}}} \mid \delta\boldsymbol{u}|_{\Gamma_u} = \boldsymbol{0}\} \tag{9}$$

We can now use Equation (1) and integrate volume of the body to give a weak statement of the static equilibrium of the body as,

$$\delta W := \int_{\Omega} (\text{div}\,\boldsymbol{\sigma} + \boldsymbol{f}) \cdot \delta\boldsymbol{u}\, dV = 0 \quad {}^{\forall}\delta\boldsymbol{u} \in \mathbb{V} \tag{10}$$

A more common and useful expression can be derived to give the divergence of the vector $\boldsymbol{\sigma}\delta\boldsymbol{u}$ as,

$$\text{div}(\boldsymbol{\sigma}\delta\boldsymbol{u}) = (\text{div}\boldsymbol{\sigma}) \cdot \delta\boldsymbol{u} + \boldsymbol{\sigma} : \text{grad}\ \delta\boldsymbol{u} \tag{11}$$

Using this equation together with the Gauss theorem enable Equation (10) to be rewritten as,

$$\int_{\Omega} \boldsymbol{\sigma} : \text{grad}\delta\boldsymbol{u}\, dV - \int_{\Omega} \boldsymbol{f} \cdot \delta\boldsymbol{u} dV - \int_{\Gamma_\sigma} \hat{\boldsymbol{t}} \cdot \delta\boldsymbol{u}\, dS = 0 \quad {}^{\forall}\delta\boldsymbol{u} \in \mathbb{V} \tag{12}$$

This equation is virtual work equation. If $\boldsymbol{u}$ is the weighing function, this is a weak forms. It is $\mathbb{U} \subset \mathbb{H}^1(\Omega)$ and $\mathbb{V} \subset \mathbb{H}^1(\Omega)$ where denotes the Sobolev space $\mathbb{H}^1(\Omega)$ of function possessing space integrable derivatives.

2.3. Hybrid-type virtual work equation

Let Ω consist of M sub-domains $\Omega^{(e)} \subset \Omega$ with the closed boundary $\Gamma^{(e)} := \partial\Omega^{(e)}$ as shown in Figure 2.

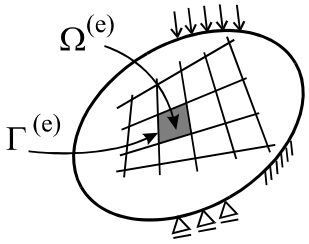

Fig. 2. Sub-domain $\Omega^{(e)}$

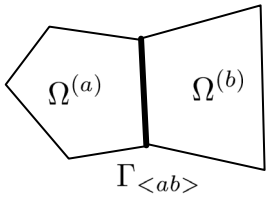

Fig. 3. Common boundary $\Gamma_{<ab>}$ of sub-domain $\Omega^{(a)}$ and $\Omega^{(b)}$

That is,

$$\Omega = \bigcup_{e=1}^{M} \Omega^{(e)} \text{ here }, \ \Omega^{(r)} \cap \Omega^{(q)} = 0 \quad (r \neq q) \tag{13}$$

In what follows, we assume that the closure $\overline{\Omega}^{(e)} := \Omega^{(e)} \cup \partial\Omega^{(e)}$.

We let $\Gamma_{<ab>}$ denote the common boundary in two sub-domain $\Omega^{(a)}$ and $\Omega^{(b)}$ adjoined as shown in Figure 3, define as,

$$\Gamma_{<ab>} \stackrel{\text{def.}}{=} \Gamma^{(a)} \cap \Gamma^{(b)} \tag{14}$$

Relative to $\widetilde{\boldsymbol{u}}^{(a)}$ and $\widetilde{\boldsymbol{u}}^{(b)}$ which are the displacement on the intersection boundary $\Gamma_{<ab>}$ in sub-domain $\Omega^{(a)}$ and $\Omega^{(b)}$,

$$\widetilde{\boldsymbol{u}}^{(a)} = \widetilde{\boldsymbol{u}}^{(b)} \ \text{ on } \ \Gamma_{<ab>} \tag{15}$$

This subsidiary condition is introduced into the framework of the variational expression with Lagrange multipliers $\boldsymbol{\lambda}$ as follows:

$$H_{ab} \overset{\text{def.}}{=} \delta \int_{\Gamma_{<ab>}} \boldsymbol{\lambda} \cdot (\widetilde{\boldsymbol{u}}^{(a)} - \widetilde{\boldsymbol{u}}^{(b)}) \, dS \tag{16}$$

where $\delta(\bullet)$ shows the variation of $(\bullet)$.

The hybrid type virtual work equation can be described as follows about N intersection boundary.

$$\sum_{e=1}^{M} \left(\int_{\Omega^{(e)}} \boldsymbol{\sigma} : \mathrm{grad}(\delta \boldsymbol{u}) dV - \int_{\Omega^{(e)}} \boldsymbol{f} \cdot \delta \boldsymbol{u} \, dV \right) - \sum_{s=1}^{N} \left(\delta \int_{\Gamma_{<s>}} \boldsymbol{\lambda} \cdot (\widetilde{\boldsymbol{u}}^{(a)} - \widetilde{\boldsymbol{u}}^{(b)}) \, dS \right) - \int_{\Gamma_\sigma} \hat{\boldsymbol{t}} \cdot \delta \boldsymbol{u} \, dS = 0 \quad {}^{\forall}\delta \boldsymbol{u} \in \mathbb{V} \tag{17}$$

Physical meaning of the Lagrange multiplier $\boldsymbol{\lambda}$ is equal to the surface force on the intersection boundary $\Gamma_{<ab>}$.

$$\boldsymbol{\lambda} = \boldsymbol{t}^{(a)}(\widetilde{\boldsymbol{u}}^{(a)}) = -\boldsymbol{t}^{(b)}(\widetilde{\boldsymbol{u}}^{(b)}) \tag{18}$$

where $\boldsymbol{t}^{(a)}$ and $\boldsymbol{t}^{(b)}$ are the surface force on the intersection boundary $\Gamma_{<ab>}$ in sub-domain $\Omega^{(a)}$ and $\Omega^{(b)}$.

3. INDEPENDENT SECOND-ORDER DISPLACEMENT FIELD

In the interests of simplicity, we consider the two-dimensional displaced field $\boldsymbol{u} \in \mathbb{U}$with n_{dim} = 2 is considered. Paying attention to a arbitrary domain $\Omega^{(e)}$, Taylor's expansion of the displacement $\boldsymbol{u}(\boldsymbol{x})$ is carried out about Point $\boldsymbol{x}_P = (x_P, y_P) \in \Omega^{(e)}$ as follows:

$$\boldsymbol{u}^{(e)} = \boldsymbol{u}^P + (x - x_P)\boldsymbol{u}_x^P + (y - y_P)\boldsymbol{u}_y^P + \frac{1}{2}(x - x_P)^2 \boldsymbol{u}_{xx}^P + \frac{1}{2}(y - y_P)^2 \boldsymbol{u}_{yy}^P + (x - x_P)(y - y_P)\boldsymbol{u}_{xy}^P + \cdots \tag{19}$$

here ,

$$(\bullet)_x = \frac{\partial}{\partial x}(\bullet) \ , \ (\bullet)_y = \frac{\partial}{\partial y}(\bullet) \ , \ (\bullet)_{xy} = \frac{\partial^2}{\partial x \partial y}(\bullet) \ , \ (\bullet)_{xx} = \frac{\partial^2}{\partial x^2}(\bullet) \ , \ (\bullet)_{yy} = \frac{\partial^2}{\partial y^2}(\bullet)$$

Here, $(\bullet)^P$ indicates the value of the physical quantity in point x_P. The second-order displaced filed can take even the second-order term of Taylor's expansion, and can set the first degree and the second degree differentiation of a displacement as a degree of freedom. However, the stress analysis often needs the check on the strain and stress. It is convenient if the rigid displacement and the slope of strain in Point x_P, and the strain express.

Denoting the component of the displacement to the x and y direction by u and v, strain and its derivative are given by

$$u_x = \varepsilon_x \ , \ u_{xx} = (\varepsilon_x)_x \ , \ u_{xy} = (\varepsilon_x)_y \ , \ v_y = \varepsilon_y \ , \ v_{yy} = (\varepsilon_y)_y \ , \ v_{yx} = (\varepsilon_y)_x$$

$$\frac{1}{2}(u_y + v_x) = \gamma_{vy} \ , \ \frac{1}{2}(u_y + v_x)_x = (\gamma_{vy})_x \ , \ \frac{1}{2}(u_y + v_x)_y = (\gamma_{vy})_y (v_x - u_y) = \theta$$

So that the second-order displacement field in the arbitrary sub-domain $\Omega^{(e)}$ becomes

$$u^{(e)} = u^P - Y^{(e)}\theta^P + X^{(e)}\varepsilon_x^P + \frac{1}{2}Y^{(e)}\gamma_{xy}^P + \frac{1}{2}(X^{(e)})^2(\varepsilon_x^P)_x + \frac{1}{2}(Y^{(e)})^2(\gamma_{xy}^P)_y$$

$$-\frac{1}{2}(Y^{(e)})^2(\varepsilon_y^P)_x + X^{(e)}Y^{(e)}(\varepsilon_x^P)_y \tag{20}$$

$$\begin{aligned} v^{(e)} &= v^P + X^{(e)}\theta^P + Y^{(e)}\varepsilon_y^P + \frac{1}{2}X^{(e)}\gamma_{xy}^P \\ &+\frac{1}{2}(Y^{(e)})^2(\varepsilon_y^P)_y + \frac{1}{2}(X^{(e)})^2(\gamma_{xy}^P)_x \\ &-\frac{1}{2}(X^{(e)})^2(\varepsilon_x^P)_y + X^{(e)}Y^{(e)}(\varepsilon_y^P)_x \end{aligned} \tag{21}$$

here ,

$$\left.\begin{aligned} X^{(e)} &= x - x_P \\ Y^{(e)} &= y - y_P \end{aligned}\right\} \tag{22}$$

where u^P , v^P , θ^P show the displacement for x, y direction, and the rigid rotation at point x_P. Equation (20) and (21) can be described as follows by the matrix form.

$$\boldsymbol{u}^{(e)} = \boldsymbol{N}_d^{(e)}\boldsymbol{d}^{(e)} + \boldsymbol{N}_\varepsilon^{(e)}\boldsymbol{\varepsilon}^{(e)} + \boldsymbol{N}_g^{(e)}\boldsymbol{\varepsilon}_x^{(e)} \tag{23}$$

Here, each coefficient is shown below

$$\boldsymbol{d}^{(e)} = \lfloor u^P, v^P, \theta^P \rfloor^t, \ \boldsymbol{\varepsilon}^{(e)} = \lfloor \varepsilon_x^P, \varepsilon_y^P, \gamma_{xy}^P \rfloor^t \ , \ \boldsymbol{\varepsilon}_x^{(e)} = \lfloor (\varepsilon_x^P)_x, (\varepsilon_y^P)_y, (\varepsilon_x^P)_y, (\varepsilon_y^P)_x, (\gamma_{xy}^P)_x, (\gamma_{xy}^P)_y \rfloor^t$$

$$\boldsymbol{N}_d^{(e)} = \begin{bmatrix} 1 & 0 & -Y^{(e)} \\ 0 & 1 & X^{(e)} \end{bmatrix}, \ \boldsymbol{N}_\varepsilon^{(e)} = \begin{bmatrix} X^{(e)} & 0 & Y^{(e)}/2 \\ 0 & Y^{(e)} & X^{(e)}/2 \end{bmatrix}$$

$$\boldsymbol{N}_g^{(e)} = \begin{bmatrix} (X^{(e)})^2/2 & 0 & X^{(e)}Y^{(e)} & -(Y^{(e)})^2/2 & 0 & (Y^{(e)})^2/2 \\ 0 & (Y^{(e)})^2/2 & -(X^{(e)})^2/2 & X^{(e)}Y^{(e)} & (X^{(e)})^2/2 & 0 \end{bmatrix}$$

In the displacement field used with this paper, the degrees of freedom are rigid displacement, strain and its gradient at the arbitrary point in the sub-domain. The displacement field is expressed with this model using the parameter in the arbitrary point in each sub-domain, so that the displacement is not defined by the node such as displacement model of FEM. Therefore, an arbitrary polygon, a polyhedron, and a curved surface body can be used as sub-domain without limiting the element shape.

4. DISCRETIZATION EQUATION

4.1. Lagrange multiplier and penalty

Physical meaning of the Lagrange multiplier $\boldsymbol{\lambda}$ is equal to the surface force on the intersection boundary as described in Chapter 2. Generally, in a hybrid-type variational principle, this multiplier is dealt with as an unknown parameter.

Since it has the meaning that Lagrange multiplier $\boldsymbol{\lambda}$ is the surface force on the boundary $\Gamma_{<ab>}$ in sub-domain $\Omega^{(a)}$ and $\Omega^{(b)}$, the surface force is defined as follows:

$$\boldsymbol{\lambda}_{<ab>} = \boldsymbol{k} \cdot \boldsymbol{\delta}_{<ab>} \tag{24}$$

Here, $\boldsymbol{\delta}_{<ab>}$ shows relative displacement on the sub-domain boundary $\Gamma_{<ab>}$, and it is shown in two dimensional problem as follows.

$$\begin{Bmatrix} \lambda_{n<ab>} \\ \lambda_{t<ab>} \end{Bmatrix} = \begin{bmatrix} k_n & 0 \\ 0 & k_t \end{bmatrix} \begin{Bmatrix} \delta_{n<ab>} \\ \delta_{t<ab>} \end{Bmatrix} \tag{25}$$

where, $\delta_{n<ab>}$, $\delta_{t<ab>}$ are relative displacement in the normal and the tangential direction to the sub-domain boundary $\Gamma_{<ab>}$. Similarly, $\lambda_{n<ab>}$, $\lambda_{t<ab>}$ are Lagrange multipliers in the normal

and tangential direction of the surface forces. The hybrid type penalty method can be described as follows by penalty function p use as coefficient k.

$$k_n = k_t = p \tag{26}$$

4.2. Relative displacement and subsidiary condition

The subsidiary condition shown by equation (16) can be described with a local coordinate system along the sub-domain boundary as follows.

$$\boldsymbol{R}_{<ab>}\widetilde{\boldsymbol{u}}^{(a)} = \boldsymbol{R}_{<ab>}\widetilde{\boldsymbol{u}}^{(b)} \text{ on } \Gamma_{<ab>} \tag{27}$$

Here, $\boldsymbol{R}_{<ab>}$ is a coordinate transform matrix to change from a global coordinate system to the local coordinate system. $\boldsymbol{R}^{(a)}_{<ab>}$, $\boldsymbol{R}^{(b)}_{<ab>}$ are the geometric transformation in each area of the common boundary $\Gamma_{<ab>}$ in sub-domain $\Omega^{(a)}$ and $\Omega^{(b)}$.

$$\boldsymbol{R}_{<ab>} = -\boldsymbol{R}^{(a)}_{<ab>} = \boldsymbol{R}^{(b)}_{<ab>} \tag{28}$$

Therefore, relative displacement is shown as follows:

$$\boldsymbol{\delta}_{<ab>} = \boldsymbol{R}^{(a)}_{<ab>}\widetilde{\boldsymbol{u}}^{(a)} + \boldsymbol{R}^{(b)}_{<ab>}\widetilde{\boldsymbol{u}}^{(b)} = \sum_{l=1}^{2}\boldsymbol{R}^{(l)}_{<ab>}\widetilde{\boldsymbol{u}}^{(l)} \tag{29}$$

Equation (16) can be described as follows by the use of the relation between these and the relation of equation (24).

$$H_{ab} = -\delta\int_{\Gamma_{<ab>}} \boldsymbol{\delta}^t_{<ab>}\cdot\boldsymbol{k}\cdot\boldsymbol{\delta}_{<ab>}\, dS \tag{30}$$

4.3. Discretization equation by matrix form

When equation (17) is rewritten by the matrix form to make the discretization equation, it is possible to describe it as follows:

$$\sum_{e=1}^{M}\left(\int_{\Omega^{(e)}}[\boldsymbol{L}\delta\boldsymbol{u}]^t\boldsymbol{D}\boldsymbol{L}\boldsymbol{u}dV - \int_{\Omega^{(e)}}\delta\boldsymbol{u}^t\boldsymbol{f}dV - \int_{\Gamma_\sigma}\delta\boldsymbol{u}^t\hat{\boldsymbol{T}}dS\right) + \sum_{s=1}^{N}\left(\delta\int_{\Gamma_{<s>}}\boldsymbol{\delta}^t\boldsymbol{k}\boldsymbol{\delta}\, dS\right) = 0 \tag{31}$$

In a plane stress of two dimensions, each coefficient is as follows:

$$\boldsymbol{L}^t = \begin{bmatrix}\dfrac{\partial}{\partial x} & 0 & \dfrac{\partial}{\partial y}\\ 0 & \dfrac{\partial}{\partial y} & \dfrac{\partial}{\partial x}\end{bmatrix},\quad \boldsymbol{D} = \frac{E}{1-\nu^2}\begin{bmatrix}1 & \nu & 0\\ \nu & 1 & 0\\ 0 & 0 & \dfrac{1-\nu}{2}\end{bmatrix},\quad \boldsymbol{f} = \begin{Bmatrix}f_x\\ f_y\end{Bmatrix},\quad \boldsymbol{u} = \begin{Bmatrix}u\\ v\end{Bmatrix},\quad \delta\boldsymbol{u} = \begin{Bmatrix}\delta u\\ \delta v\end{Bmatrix},\quad \hat{\boldsymbol{T}} = \begin{Bmatrix}\hat{t_n}\\ \hat{t_t}\end{Bmatrix}$$

Here, E and ν are the elastic coefficient and Poisson ratio. f_x and f_y show the body force in the direction of x and y, u and v are the displacements of the direction of x and y, δu and δv are virtual displacement in the direction of x and y, $\hat{t}_n$, $\hat{t}_t$ are the given surface force in the normal and tangential direction on the boundary.

The displacement shown by the second order function in Equation (23) is substituted for Equation(31). Similarly, we assumed virtual displacement as follows:

$$\delta\boldsymbol{u}^{(e)} = \boldsymbol{N}^{(e)}_d\delta\boldsymbol{d}^{(e)} + \boldsymbol{N}^{(e)}_\varepsilon\delta\boldsymbol{\varepsilon}^{(e)} + \boldsymbol{N}^{(e)}_g\delta\boldsymbol{\varepsilon}^{(e)}_x \tag{32}$$

To make the discretization equation, equation (23) and equation (32) are changed as follows.

$$\boldsymbol{u}^{(e)} = \boldsymbol{N}^{(e)}\boldsymbol{U}^{(e)}\,,\ \delta\boldsymbol{u}^{(e)} = \boldsymbol{N}^{(e)}\delta\boldsymbol{U}^{(e)} \tag{33}$$

here ,

$$\boldsymbol{U}^{(e)} = \lfloor \boldsymbol{d}^{(e)}, \boldsymbol{\varepsilon}^{(e)}, \boldsymbol{\varepsilon}_x^{(e)} \rfloor^t\,,\ \delta\boldsymbol{U}^{(e)} = \lfloor \delta\boldsymbol{d}^{(e)}, \delta\boldsymbol{\varepsilon}^{(e)}, \delta\boldsymbol{\varepsilon}_x^{(e)} \rfloor^t\,,\ \boldsymbol{N}^{(e)} = \lfloor \boldsymbol{N}_d^{(e)}, \boldsymbol{N}_\varepsilon^{(e)}, \boldsymbol{N}_g^{(e)} \rfloor$$

Therefore, the following expression is obtained.

$$\boldsymbol{L}\boldsymbol{u}^{(e)} = \boldsymbol{L}\boldsymbol{N}^{(e)}\boldsymbol{U}^{(e)} = \boldsymbol{B}^{(e)}\boldsymbol{U}^{(e)} \tag{34}$$

here ,

$$\boldsymbol{B}^{(e)} = \boldsymbol{L}\boldsymbol{N}^{(e)}$$

When one dimension array that arranges all degree of freedom in the area is assumed to be $\boldsymbol{U}$, the degree of freedom $\boldsymbol{U}^{(e)}$ concerning the sub-domain $\Omega^{(e)}$ is shown as follows:

$$\boldsymbol{U}^{(e)} = \boldsymbol{\mathcal{A}}^{(e)}\boldsymbol{U} \tag{35}$$

Here, $\boldsymbol{\mathcal{A}}^{(e)}$ is a procession who relates all degree of freedom in the area and degree of freedom in the attention sub-domain. Similarly, virtual displacement is described as follows:

$$\delta\boldsymbol{U}^{(e)} = \boldsymbol{\mathcal{A}}^{(e)}\delta\boldsymbol{U} \tag{36}$$

On the other hand, the relative displacement $\boldsymbol{\delta}_{<ab>}$ is described as follows:

$$\boldsymbol{\delta}_{<ab>} = \boldsymbol{B}_{<ab>}\boldsymbol{U}_{<ab>} \tag{37}$$

Here, $\boldsymbol{B}_{<ab>}$, $\boldsymbol{U}_{<ab>}$ are described as follows:

$$\boldsymbol{B}_{<ab>} = \lfloor \boldsymbol{R}_{<ab>}^{(a)}\boldsymbol{N}^{(a)}\ ,\ \boldsymbol{R}_{<ab>}^{(b)}\boldsymbol{N}^{(b)} \rfloor\,,\ \boldsymbol{U}_{<ab>} = \lfloor \boldsymbol{U}^{(a)}\ ,\ \boldsymbol{U}^{(b)} \rfloor^t$$

When one dimension array that arranges all degree of freedom in the area is assumed to be $\boldsymbol{U}$, the degree of freedom $\boldsymbol{U}_{<ab>}$ of the sub-domain boundary $\Gamma_{<ab>}$ can be described as well as equation (35) as follows:

$$\boldsymbol{U}_{<ab>} = \boldsymbol{\mathcal{M}}_{<ab>}\boldsymbol{U} \tag{38}$$

Here, $\boldsymbol{\mathcal{M}}_{<ab>}$ is a procession which relates all degree of freedom in the area to degree of freedom concerning the attention sub-domain boundary. Similarly, virtual displacement is described as follows:

$$\delta\boldsymbol{U}_{<ab>} = \boldsymbol{\mathcal{M}}_{<ab>}\delta\boldsymbol{U} \tag{39}$$

The following is obtained by substituting these relation for Equation (31).

$$\delta\boldsymbol{U}^t\left(\sum_{e=1}^{M}\boldsymbol{K}^{(e)} + \sum_{s=1}^{N}\boldsymbol{K}_{<s>}\right)\boldsymbol{U} - \delta\boldsymbol{U}^t\left(\sum_{e=1}^{M}\boldsymbol{P}^{(e)}\right) = 0 \tag{40}$$

here ,

$$\boldsymbol{K}^{(e)} = (\boldsymbol{\mathcal{A}}^{(e)})^t\int_{\Omega^{(e)}}(\boldsymbol{B}^{(e)})^t\boldsymbol{D}^{(e)}\boldsymbol{B}^{(e)}\,dV\,\boldsymbol{\mathcal{A}}^{(e)} \tag{41}$$

$$\boldsymbol{K}_{<s>} = \boldsymbol{\mathcal{M}}_{<s>}^t\int_{\Gamma_{<s>}}\boldsymbol{B}_{<s>}^t\boldsymbol{k}\boldsymbol{B}_{<s>}\,dS\,\boldsymbol{\mathcal{M}}_{<s>} \tag{42}$$

$$\boldsymbol{P}^{(e)} = (\boldsymbol{\mathcal{A}}^{(e)})^t\left(\int_{\Omega^{(e)}}(\boldsymbol{N}^{(e)})^t\boldsymbol{f}\,dV + \int_{\Gamma_\sigma}(\boldsymbol{N}^{(e)})^t\boldsymbol{T}\,dS\right) \tag{43}$$

Since Virtual displacement $\delta \boldsymbol{U}$ of equation (40) is arbitrary, we obtain the following discretized equations.

$$\boldsymbol{K}\boldsymbol{U} = \boldsymbol{P} \tag{44}$$

Here, $\boldsymbol{K}$ and $\boldsymbol{P}$ are as follows.

$$\boldsymbol{K} = \sum_{e=1}^{M} \boldsymbol{K}^{(e)} + \sum_{s=1}^{N} \boldsymbol{K}_{<s>} \tag{45}$$

$$\boldsymbol{P} = \sum_{e=1}^{M} \boldsymbol{P}^{(e)} \tag{46}$$

The discretization equation of this model becomes a simultaneous linear equation shown in equation (44). Left coefficient matrix $\boldsymbol{K}$ consists of stiffness in the sub domain and subsidiary condition on the intersection boundary for the adjacent sub-domain. The discontinuous phenomenon of opening etc. can be expressed without changing degree of freedom by changing the value of $\boldsymbol{k}$ of equation (42) to zero.

5. NUMERICAL EXAMPLE

5.1. Thickness hollow circular cylinder subjected internal pressure

First, to verify the accuracy of the elasticity solution, we analyze the thickness hollow circular cylinder subjected internal pressure (Refer to Figure 4.) Pressure p_0 in inside diameter r_1 and externals r_2, elastic coefficient E, and Poisson ratio ν are as shown in figure. Moreover, the boundary condition made both ends a roller. We showed the value of the penalty and it was shown that the error margin became small if 10^3 times or more the elastic coefficient was used. In this paper, the penalty used 10^6 times the elastic coefficient.

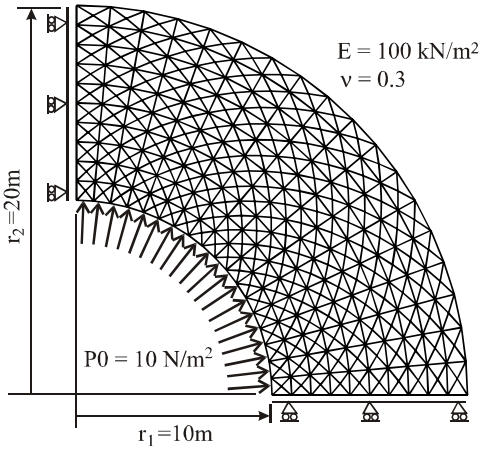

Fig. 4. Thickness hollow circular cylinder subjected internal pressure

The influence that the number of partitions and the element shape give the result is examined. The cylinder 1/4 was taken out as shown in Figure 4. Moreover, the quadrangle was used and divided so that the direction of the circumference and radial may become 9:5. In addition, one quadrangle was crossing divided. Figure 5 assumed a horizontal axis and the number of elements and the spindle were assumed to be a ratio to the elasticity solution concerning displacement. A quadrangle sign is a result of the linear displacement field in the triangulation division model. A round sign is a result of the second-order displacement field in the triangulation division model.

A triangle sign is quadrangle division model and a result of the second-order displacement field. It agreed when the triangulation division model was used by a result of FEM and very high accuracy. On the other hand, because the formulation of displacement has not been suited, quadrangle division model is low some accuracy. However, it settles to the error margin of 0.1% or less by doing the element division in detail.

Figure 6 is displacement distribution concerning radial of quadrangle division model. A horizontal axis is assumed to be a radial distance, and the spindle assumes radial to be displacement. Moreover, the value that is excluded and dimensionless made by inside diameter r_1 is indicated. The solid line shows an analytical solution. A round sign shows radial displacement by HPM. The error margin is 0.5% or less in all parts.

Figure 7 compares radial sub-domain conspiring power σ_r and sub-domain stress σ_θ in the direction of the circumference with an analytical solution. A horizontal axis uses the value that is excluded and dimensionless made by inside diameter r_1. The spindle uses the value that is excluded and dimensionless made by pressure on the inside. The solid line shows an analytical solution. A round sign shows radial displacement by HPM. It became the error margin of 0.1% or less in all both stresses, the points.

Figure 8 shows the VonMises stress. As for this model, the expression by the color contour is also possible as shown in figure because the element conspiring power is requested.

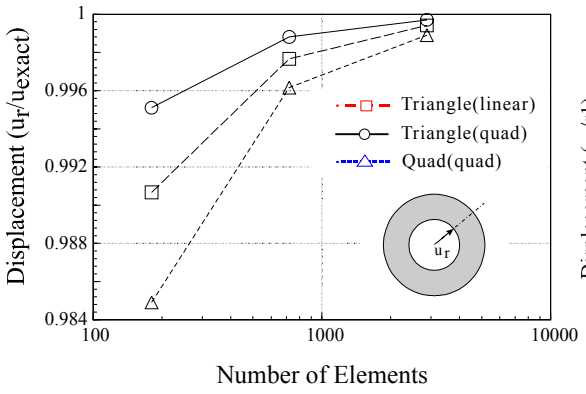

Fig. 5. Settling situation of radial displacement by area division

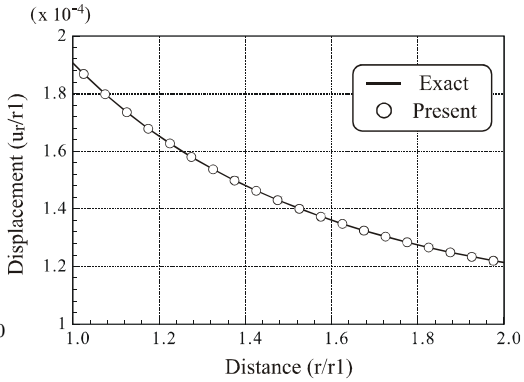

Fig. 6. Radial displacement distribution (quadrangle division)

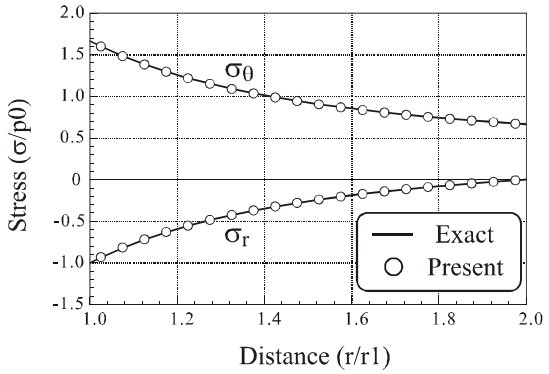

Fig. 7. Radial and circumference direction stress distribution (quadrangle division)

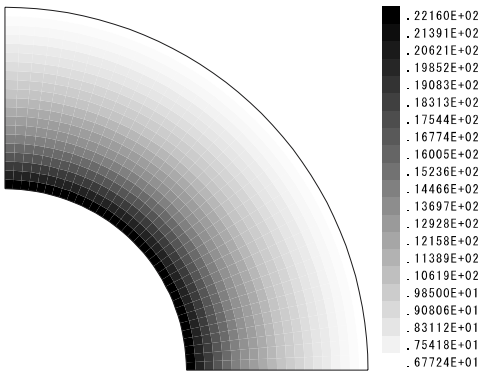

Fig. 8. Contour of VonMises stress (quadrangle division)

5.2. Plate with round hole subjected tensile load

Secondarily, the pull problem of monotony that has a round hole is analyzed as a stress concentration problem. Figure 9 shows an analytical model. It analyzed it by 1/4 models. Figure shows the area division. On the left, it is the quadrangle division model. Upper right is the triangulation division model. The left under is the subdivided model. Lower right is the Voronoi division model.

Table 1 is a table where perpendicular displacement of A point and the horizontal displacement of C point were compared with FEM. A triangulation division model by HPM and an analytical result by FEM were corresponding. However, some error margins were caused in the quadrangle division model. This is because the number of partitions is rough compared with the triangulation division model, and accuracy improves by expanding the number of partitions.

Figure 10 is a displacement mode of the subdivided model and the Voronoi division model. There is no difference that both are big. However, the gap according to the penalty value is caused because the displacement between elements is continuously done by using the penalty.

Table 2 shows the result of comparing the stress concentration coefficients. The value with the largest triangular element is indicated. In the theory solution, FEM is 2.32, and BEM is 2.31. A triangular element of HPM reached almost the same value. Some accuracy has decreased because quadrangle division is rough division. However, it agreed almost in the re-mesh model.

Figure 11 is the horizontal stress distribution chart in the A-B section of the subdivided model. The horizontal stress indicates the value that is excluded and dimensionless made by an nominal stress. The spindle shows the position, and a horizontal axis is a value of (horizontal stress σ_x / nominal stress σ_n).

Figure 12 is a contour that showed the horizontal stress distribution of the subdivided model and the Voronoi division model. Both similar distribution tendencies are shown. A similar tendency is obtained about the triangulation division model and FEM. However, when the destruction between elements is handled, it is necessary to do by using the surface force requested by equation (24).

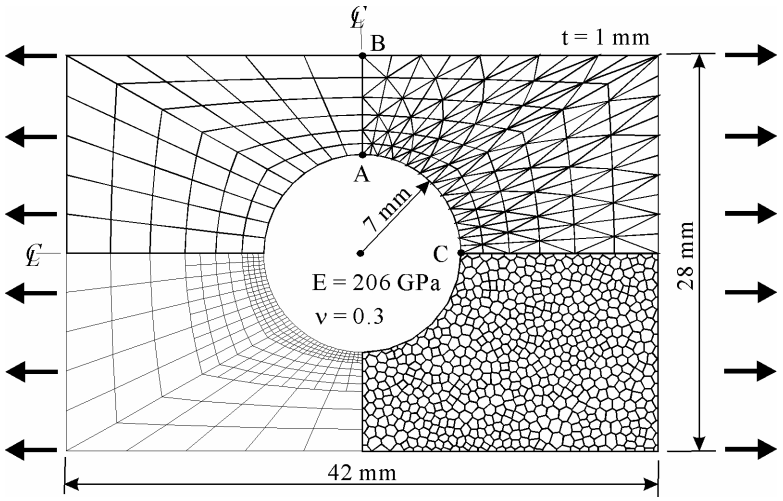

Fig. 9. Plate with round hole subjected tensile load

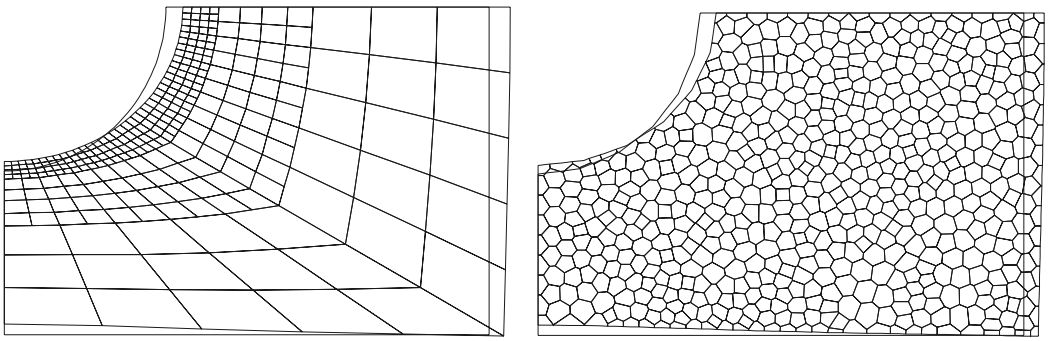

(a) Subdivided model (b) Voronoi division model

Fig. 10. Displacement mode

Table 1. Comparison of displacement (mm)

Method	Division	A point	C point
HPM	Triangle	0.0895	0.153
	Quadrangle	0.0718	0.138
	Subdivision crack	0.0815	0.147
	Voronoi	0.0749	0.141
FEM	Triangle	0.0895	0.153

Table 2. Stress concentration coefficient

Method	Division	Coefficient
HPM	Triangle	2.32
	Quadrangle	1.79
	Subdivision crack	2.17
	Voronoi	2.06
FEM	Triangle	2.31
	Quadrangle	2.29
Analytical solution (Howland)		2.16

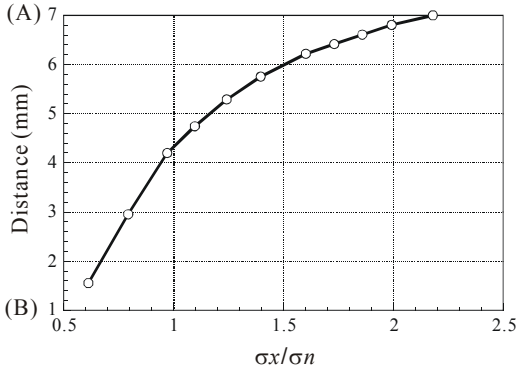

Fig. 11. Horizontal stress distribution in A-B section (subdivision crack)

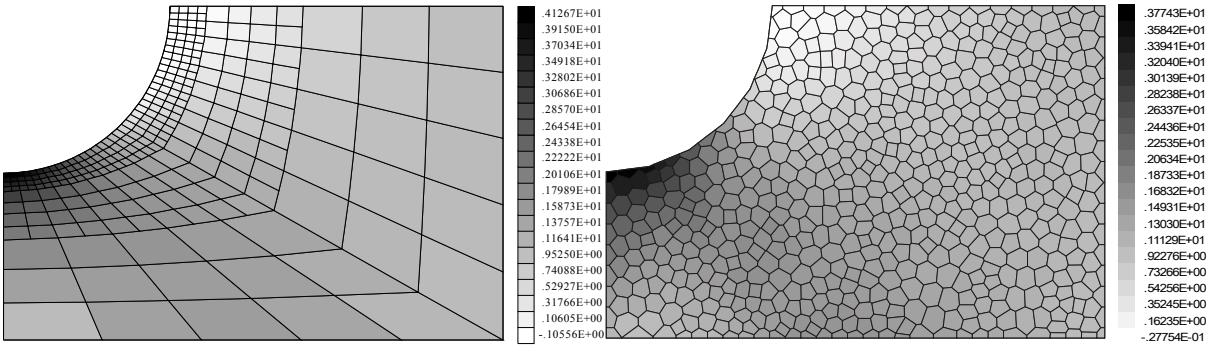

(a) Subdivided model (b) Voronoi division model

Fig. 12. Horizontal stress distribution

6. CONCLUSION

In this paper, it proposed the second-order displacement field where the gradient of the strain was assumed to be degree of freedom as a displacement field of HPM. In addition, the piece of the problem becoming it of types of the same stress field and the stress concentration, etc. was analyzed. As a result, the triangulation division model of HPM obtained the same level accuracy as FEM.

HPM divides a whole area into sub-domain, and the displacement field is defined independently in each sub-domain. At this time, the node of the sub-domain doesn't have degree of freedom from the use only to recognize shape like FEM. Therefore, the middle node need not be installed like FEM. In a word, the displacement field of high-order can be applied by the same number of partitions as the linear displacement field.

Moreover, if the second-order displacement field are used, the Voronoi polygon can be used. This means an arbitrary area can be subdivided as shown by the example of the numerical analysis as the node doesn't worry. In the problem that strong non-linear appears locally, it is thought that the improvement of accuracy can be attempted by divide again partial.

In this paper, only the elasticity problem was taken up as an analysis example. The analysis that applies this technique to a non-linear problem is scheduled to be done in the future.

REFERENCES

1. T.Kawai, New element models in discrete structural analysis, J. of the Society of Naval Architects of Japan No. 141, pp187-193, 1977.
2. K.Washizu, Variational Method in Elasticity and Plasticity, Pergamon, 1975
3. N.Takeuchi,H.Ohki,A.Kambayashi and M.Kusabuka, Non-linear analysis by using discrete model applied penalty method in hybrid displacement model, Transactions of Japan Society for Computational Engineering and Science Paper No. 20010002, 2001.
4. C.Frits and H.Feenstra, DIANA User’s Manual, TNO, 2002
5. R.Mihara, N.Takeuchi and M.Kusabuka, Development of hybrid-type penalty method assumed second-order displacement field, Journal of Structural Engineering, 2005. Vol.51A. pp.249-257.

The Progression of Non-continuous deformation structural analysis

Li Jiuhong
Xi'an University of Technology, Xi'an, Shaanxi, P.R. China 710048
Ren Ruirui Yang Jusheng
Xi'an University of Technology, Xi'an, Shaanxi, P.R. China 710048

This paper was prepared for presentation at *ICADD-7, the Seventh International Conference on Analysis of Discontinuous Deformation*, held in Honolulu, Hawaii, December 10-12, 2005.

ABSTRACT: Continuous, discontinuous, Continuous—discontinuous medium mechanics models adopted in the stress analysis are introduced systematically. Various kinds of theory and numerical methods in the physics of numerical simulation of three models represent the mainstream and direction of stress analysis nowadays. The appearance of the high, big, precise and new-type structures shows that this old and brand-new proposition still has wide prospects. This paper describes its current situation and development of the non-continuous deformation structure analysis. The contents and methods are introduced overall.

KEYWORDS: continuous medium, numerical simulation, stress analysis, mechanics model

In the field of engineering structural stress analysis, great challenges and development opportunities exist at the same time. With the development of modern industrial technology and the effort of challenging the nature, it appears in the area of aviation, astronavigation, navigation, energy, architecture, water conservation, traffic, and environment, there are a lot of high, large, precise, and new structures, such as large-scale and high-speed airplanes and ships, spacecrafts, deep immerged underground engineering, high speed railway and vehicle, TGP hydroelectric station, frozen ground project for Qing-zang railway, and South-to-North water diversion hydroelectric and rock project, etc. Because the original theory and method can not meet the higher technical requirements of strength, rigidity, satiability, reliability and economy to those new structures, non-continuous deformation structural analysis has been the necessary method to solve those problems.

1. CONTINUOUS-DISCONTINUOUS DEFORMATION MODEL

Taking subject investigated as calculation model with continuous medium, and studying quantity relationship of its balance and motion state with analytic method of continuous function (Ewler, 1753), constitute the basic theory of continuous medium mechanics in the physics [12,13]. The fluid mechanics, solid mechanics and air mechanics developed from this theory took continuous assumption as their hypothesis, and deepen the mater composition of subject investigated (also called "material") and physics character. Therefore, they formed an integrated theory system respectively, which advanced the progress of engineering technology. This article only discusses the related issues of deformable solid mechanics.

A screw and the earth crust are both deformable solid, which is called “structure” in the project. Structure strength, rigidity, and stability are the common characters of study content. The abstraction of material physics and structural character derives mechanics branches such as material mechanics, structural mechanics, elastic mechanics, plastic mechanics, visco-elestic and visco-plastic mechanics, rheopectic system mechanics, strength theory, and fluid and solid coupling [1, 2, 3, 10, 11]. The application in metal, concrete, geotechnology, alloy, and rubber can bring two mechanics models.

Flawless model: macro model for continuous medium. From seventeen century (R.Hooke 1966) to the Second World War (R.V.Mises, 1913 and T.Von.Karman, 1939), the representation is elastic theory, plastic theory, stability theory [17, 18, 19, 20];

Defect model: macro model for discontinuous medium. From the World War II to 80's in twenty century, the representation is fracture mechanics (A.A.Griffith,1921), damage mechanics (L·M·Kachanov,1958) [32,35,36,37,38,39,44];

Taking the strength problems of concrete material, which is widely employed in the structure engineering as an example, concrete contains lots of micro-crack, air bubble, pore before loading, so it isn’t a strict continuous integrity. During construction, the appearance and extend of yield and crack, the lost bearing capability and deformation of structure can be all defined as “the damage of concrete”. Treated with continuous macro model, the experiments show that under the multi-axis load, the strength of concrete does not only have relationship with single compress, tension, and shearing stress, its strength principal must also consider the influence of the interrelationship of each stress component to concrete, which should be expressed as stress condition function. As the practice character of concrete material and strength is a very complicated problem, it has relationship with factors such as physics mechanics character, matching ration, load character of aggregate and mortar, which will takes different load conditions under different load. So, there isn’t a model that can express the strength problems of real concrete under all conditions now. Even if such a mathematic model is created, it is difficult to apply it to the real project because of complexities. Concrete is a mushy medium with defect in natural condition. After loading, it breaks with the checking-development-expansion of micro-crack until macro-crack appears [38,39,40,41,45,47,61,62,63,68,69,70,71]. The constitutive model established on the basis of the stated continuous medium mechanics theory has a widely application value. However, strictly to say, it can not reflect the breaking fact of concrete material. The damage mechanics and fracture mechanics established on the basis of discontinuous macro model, on the basis of internal variable dissipative theory and thermodynamics, changes with method of macroscopic, microscopic and the combination of macroscopic and microscopic [79,80,83]. With the development of experiment method and simulation, some theories and works expose the internal law of damage-break with defect, developing a new situation for research on damage rules and constitutive relationship in past 30 years. And it brought the damage mechanics and the physics, mathematics models. There are a lot of numerical articles and research results [40, 45, 48, 49, 50, 56, 57, 58]. However, no result can reflect the character of concrete completely, and the theory is not mature. This article will not discuss and quote.

In conclusion, there is no theory that can express the character of concrete accurately, but each theory has its feature and application range. There are a lot of results of values. During the development of theory, some compound theories appear, for example, elesto-plastic damage fracture model, plastic fracture model, plastic damage model, and boundary face model, micro-

face model, neural network material model and so on. The result is that the ideal model is becoming more complicated that they have little contribution to raise precision and application in engineering.

2. NUMERICAL ANALYSIS IN PROJECT

2.1. No matter what physical model the practice problems idealized to, the stress analysis for engineering structure, in mathematics term, can all be concluded in control of differential equation of engineering science under given boundary conditions, which is called the boundary value problem of differential equation. The unified mathematic expression is: $L\phi = q$ (in the D domain); $\phi_s = \tilde{\phi}$ (on the S boundary, $S \in D$); q is the function of known or unknown ϕ, and L is linear or nonlinear differential operator.

There are three methods for the answer of boundary value problems, that is, analytic solution, numerical solution, and experimental solution. Analytic solution is the exact solution of boundary value problem. Exact solution can be obtained only when the questions of elastic, plastic and visco static-dynamics mechanics are simple and classic [1, 2, 3, 4]. Before the computer came into use, for complicated practice boundary problems, we can only simulate its experiment-analogical answer with physical method such as mechanical, optics. For example, electrical analogue method, flash spotting, membrane analogy and so on [4, 10, 11]. The numerical answer of continuous medium can be divided into numerical answer of differential equation and numerical answer of discrete model. Numerical answer of differential equation is to discrete the differential equation by mathematic way, change the equation to linear or nonlinear algebraic equation, and express the infinite degrees of freedom (continuous medium) with finite degrees of freedom (discrete model), and solve the approximate value on given point (or mesh) of discrete model which meet boundary condition, for example, numerical integrating, weighting resident method, finite difference method, Rayleigh-Litz method, calculus of variation, Galerkin method and so on. Or lower the differential equation to boundary integral equation to solve the numerical answer of boundary integral equation with immediate integration or indirect integration method. Numerical solution of discrete model is to divide the calculating model (solution field) on physics-mathematics, connect the continuous body to discrete aggregate with finite element on finite nodes (in field or on the boundary), and solve numerical approximate answer of nodes or equations with algebraic equation [5, 6, 7, 8, 9]. The problem solving process from accuracy to approximate promoted the development of engineering technology, and it is a milestone in human history since we start knowing the objective world. On objective meaning, it is a basic method to evaluate all process of future objective world in quantity. It has a magnificent meaning to technical economy and society development.

2.2. Numerical answer of discontinuous medium discrete model appears earliest in slicing rigid body model in rock body engineering, for example rigid body element method (Cundall, 1971), and block element method (Shi Gen-Hua, 1983), which belong to rigid body without considering the deformation of element. Based on slicing rigid body model in substance, they can reflect the displacement of fault, interlayer, crack, joint and no-continuous discontinuity and motion condition. Discrete element model considering the deformation of element of deformable body, for example spring element method for rigid body (Kawai,1977) and deformable body element method (Shi Gen-Hua,1992) are all slicing deformation model [26,27,28]. Rigid spring element method is to express the deformation of block element with the deformation cumulated on the

spring. The dominant equation is similar to finite element method, so it is also called rigid element method. Deformable block element adopts discontinuous deformable block model with character of finite element method, the motion analysis of block is similar to that of rigid discrete element, and the solution in each time is similar to that of finite element. On the basis of stated method, Zhuo Jia-shou advanced the boundary element discrete model on the basis of Kawai rigid spring element (1993), replace the spring with boundary element to reflect the different deformation of different kinds of element, and deduced interface stress formula on arbitrary point on anisotropic body interface, it can solve the numerical analysis problems for isotropy and anisotropic continuous-discontinuous medium engineering structure [28, 29, 30, 85, 86, 87]. Numerical manifold method (Shi Gen-hua, 1991; Lin De-zhang, 1992), non-element method or non-mesh method (Belytschko, 1994), unified numerical manifold method (Shi Gen-hua, 1996), create a new way to solve unified continuous-discontinuous problems.

3. FROM FEM TO EFM

R.W. Clough established the finite element method frame in 1960,then O.C.Zienkiewicz (1965), E.L.Wilson (1973) and other people established some remarkable works in general field question and software development aspect [5,6,7,8,9]. K.H.Huebner said, “The finite element method, as one analytical method, had achieved its top and is impossible to expect other theatrical development or breaks through. Certainly, the future development will include more widespread applications in the practical fields, will increase understanding to the special and important aspects, furthermore will improve and enhance essential skill of finite element method" in his book “The Finite Element for Engineers" published in 1975. J.H.Argyris□C.A.Brebbia and Bian Xuehuang, those scholars’ remarkable contribution in promoting the numerical physical model and Mathematics theoretical analysis in application aspect and software market development has proved Huebner’s judgment.

The entire metamorphic solids are non-continuous medium if judged microscopically. The non-continuity of macroscopic continuous medium contains two kinds of basic questions. First, the destruction performance and crack in non-continual body with the discontinuity surface opens□cuts and slips. Second, the produce and expand of crack in continual body.

Along with formation and the development of the diffusion, furcation, muddy and fuzzy theory, many kinds of numerical analysis in non-continuous medium solid mechanics method have been developed and then the unified continuous and the non-continuous medium question numerical method laterally based on the basic thought of finite element in the continuous medium since early 90’s [30,27,91]. To solve the macroscopic non- continuous problem, there are five technical methods currently. They are: Elastic-plastic break mechanics model numerical method (FEM, BEM, WRM, COV and so on); Elastic-plastic damage mechanics model numerical method (PDM, BEM, WRM, COV and so on); non-continuous block body model numerical method (DEM, SEM, RSM, DDM, IEM) and so on; Flow shape element method (FEM + COVER); Element free method (EFM). Among those method, Flow shape element method is the extension of the finite element method [96, 97], which has introduced mathematical and physical grids to define the numerical solution precision (for example with triangle unit) and to solve the territory boundary and the crack surface; which has replaced "the unit" and "the point" with mathematical and the physical Cover. Using three physical covers to define "the flow shape unit", that is replaced the pitch point of unit with the physical cover, replaced the unit boundary with the cover intersection, and replaced the unit with the cover. The manifold unit public space

which is isolated by the crack, the surface, the boundary and so on may have different pitch points, therefore may reflect the break and display the non- continuity [279,280,281,282,203]. Thus it has realized the unification of continuity and the non-continuity. But the element free method does not have the unit and the grid concept.

4. COMPLEX VARIABLES MESHLESS METHOD

EFM has been developed for more than 20 years. Because its flexibility in variable approach, introduction of border, energy integral, many kinds of meshless method have been presented and named differently. In the course of its development, most mathematics scholar put forward approaching function with move least square method. The one that relatively popular is Element Free Galerkin Method (namely EFGM) nowadays. It constructs inserting value function by moving least square method [196,197], to solve algebraic equation of question from the principle of differential equation. The advantages of EFGM are: self-adaptation analysis that does not need to construct the net again; simple pre-process; smooth calculation result in succession; and more precise numerical value. As a kind of new numerical analysis technology, it had the initiative in theory and formed intact framework and system tentatively. But there are also the following problem exists:

4.1. As the spot integration that does not need the background grid, it still lacks of essential theory to support and the precision is reduced.

4.2. Each spot needs to be calculated shape function and its derivative in every operation, also involves the matrix inversion, and must use the higher order Gauss integral in each background integral grid, which leads to large amount work of calculation and longer time in machine-hour.

4.3. There are many influence factors to solution precision, including pitch point density of distribution, basis function order, weight function selection and size of its influence territory. Also the uncertainty of the boundary condition introduction and so on.

With the problems that the distribution nodes are too much with the scalar moving least-square approximation, the moving least-squares method with complex variables is proposed recently [131,277]. The advantages of this method are: the number of the undetermined constants in the trial function is decreased; the two-dimensional problem of Meshless method is possible to take few pitch points; to each spot, the points contained in its tight territory are greatly reduced. At the same time the ill-conditioning equation system won't be formed and the precision gets improved and less amount work of calculation.

The complex variables meshless method based on complex variable moving-least squares method will have the following advantages such as less distribution nodes, higher precision as well as faster calculation. It will also solve the problem with the scalar meshless method. In order to simulate the localization phenomenon of crack top field, the enriched meshless method with complex variables is proposed. It could solve the crack problem better, enhanced the precision of solution of complex variable meshless method [277].

5. THE COUPLING OF NUMERICAL ANALYSIS METHOD

The meshless method has superiority that the finite element method has not, but its shortcomings happen to be the advantage of finite element method. Therefore, using the coupling of the two

methods, "makes up for one's deficiency by learning from others' strong points", will broad its application prospect.

The finite element method in such aspects as the theory, the method, the application, and the software development is quite consummate. With the development of CAD and its visualization, multimedia and network technology, and FEM application in the computation analysis, the visualized analysis software system of FEM occupies the mainstream and leader status in terms of quantity and the value of application. There is more than 400 international well-known finite element software of which the more famous are NASTRAN, MARC, ASKA, ADINA, GTSTRUDL, ANSYS, ABAQUS, and SAP. Their formidable computation character, the design essence and high visualized degree in the pre and post-processing system, have been approved by the international engineering projects and taken as the standard [283]. Fully using this market superiority, maintaining, consummating, enhancing, expanding the functionality and the application scope of finite element software unceasingly, will have the significant technological economic value.

The coupling of finite element method either with the weighting remaining method or with the boundary method has been obtained exciting accomplishment [209,225,284,285,286,287¸288,290]. Belytschko is the first person who proposed coupling method of meshless method and the finite element method. It divides the solve territory to meshless and the finite element method subfield, and defines suitable coupling displacement function to guarantee the continual displacement of contact surfaces between two subfield. However, Huerta used the conductive coupling way, used the approaches or the interpolating function iteration approximating function formed by the pitch points in the border area corresponding to meshless method and the finite element method respectively. Cheng Yumin, Li Jiuhong proposed coupling of complex variable meshless method and the finite element method, which divides the solve territory to the complex variable meshless method and the finite element method subfield. These two subfields will use the complex variable method and the finite element method to establish fundamental equation separately, and establish hypothesized finite element in the subfield intersection point, then form the unified solution equation through two subfields interfaces condition. This method retained advantage of meshless method as it can match point at random; the interface can be irregular. This method enhances the solution precision of meshless method, thus increased the solution precision of the whole subject. It solved the existing problems of Belytschko and the Huerta's coupling method basically. But the error is big nearby the interface region [277].

6. CONCLUSION

6.1. The continuous medium numerical method, take the finite element method for example, in theory, application, software development aspect and so on has reached mature. At present the important question is to expand its application domain, continually perfect software functionality, especially strengthen the application visualization and the simulation technology to make its contact surface friendlier.

6.2. The non- continuous medium numerical method is still pre-mature theoretically. Taking damaged mechanics and break mechanics for example, the theory and the method of processing flaw model still need massive experiment to consummate, constitute the unified destruction numerical model and theory frame.

6.3. Manifold Method and meshless method lays the foundation for the Continuous and Non-Continuous unified mathematical model, but only has preliminary achievement on the two-dimensional problems. It has not been possible to promote the mature software, and the actual project application has been still in exploration stage. It is far behind finite element method, the boundary method and other numerical methods in terms of application level.

6.4. The question of how to introduce function of dealing with the non- continual problem in the rich FEM commercial software to unify continuous and non- continuous should be considered emphatically in current solid mechanics. From this point of view, the research and the corresponding software development of the coupling question of manifold method and meshless method with the FEM has more development value.

REFERENCES:

[1]Qian Weichang,Ye Kaiyuan. *Elastic mechanics*, Beijing: Science press, 165(in Chinese).

[2]Н·И·Мусхелищвил, *some basic problems of mathematics elastic mechanics*, 195(in Russian)

[3] Xu Zhilun, *elastic mechanics*, Beijing: Higher education press, 1990(in Chinese).

[4] Malvern L.E., *Introduction to the mechanics of a continuous medium*, prentice Hall, Inc. 1969

[5] Huebner K.H., *the FEM for Engineers*, 1983, national defense press (in Chinese)

[6] HOLAND IVAR and KOLBEN BELL, *FEM in stress analysis*, prentice hall, 1972.

[7] Brebbia C.A., *Finite Element Systems* (A Handbook), McGraw-hill, 1985.

[8] Rao S.S., *the FEM in Engineering*, McGraw-Hill, 1982.

[9] Zienkiewiz O.C., *The finite element method in engineering science*, McGraw-Hill, 1971.

[10]Timoshenko S., J.N.Goodier, *theory of Elasticity, Education* press*,* 1951(in Chinese).

[11]Zienkiewicz O.C., Y.K.Cheung, *the FEM in structural and continuum mechanics*, McGraw-hill, 1967

[12] Feng Kang, Shi zhongci, *the mathematics theory of elasticity structure*, Beijing, Science press, 1984(in Chinese).

[13] Qian Weichang, Variational, *approach and FEM*, Science press, 1980 (in Chinese)

[14] Xu cida, Hua Bohao, *the method and program of FEM in solid mechanics,* Water and electricity press 1983(in Chinese)

[15] Wang Xucheng, *FEM*, Tsinghua university press, 2003(in Chinese).

[16] Zhu bofang, *the principle and application of FEM*, Water and electricity press, 1979(in Chinese)

[17] Washizu K., *Variation methods in elasticity and plasticity*, Paragon press Ltd, 1982.

[18] Zuo Jiashou, *the principle of broad sense variation in elasticity and plasticity*, Water and electricity press, 1989(in Chinese)

[19] Zuo Jiashou, *foundation of non-linear solid mechanics*, water and electricity press, 1996(in Chinese)

[20] Owen D.R.J., E.Hinton, *FEM in plasticity—Theory and Practice*, Pine ridge press, Suanswa, UK, 1980.

[21] Goodman R.E., G.H.Shi, *block theory and its application to rock engineering*, Prentice—Hall Inc, 1985.

[22] Kawai K., New Hiscrete structural models and Generalization of the method of limit analysis, *Finite Element in Nonlinear mechanics*, NIT, Tronheim, 1977, 885—906

[23] Chen W.F., A.D.Pan, *Finite Element and finite Block Method in Geomechanics*, ASME publication, 1990, 669—675

[24] Xong Z., Q. Lingxi. Rigid Finite Element and Limit Analysis, *Acta Mechanics Sinica*, 9(2), 1993, 156—162

[25] Qian Lingxi, Chang Xong. *Rigid body FEM in structure analysis*, 1991(in Chinese)

[26] Zhuo Jianshou,Zhao Ning. Rigid body-spring FEM of static and dynamic analysis in discontinuous medium, *J. of Hehai University*, 21(5), 1993, 34—43(in Chinese)

[27] Shi Genhua, Numerical manifold method, *Prof. of IFDDA 96*,Tsi Press, Berkeley Califorria,1996,52—204.

[28] Zhao Ning, Zhuo Jiashou. 3D nonlinear interface element analysis of structure, *J. of Hehai University*, 23(2), 1995, 23—35(in Chinese)

[29] Fang Yiling, Zhuo Jiashou, Chang Qing, The interface element method in arbitrary shape element, *Engineering mechanics*, 5(2), 1998, 27—37(in Chinese).

[30] Zhuo Jiashou, *Interface element method of discontinuous medium mechanics,* Science publication, 2000(in Chinese).

[31] Carroll M.M., The tendency and good opportunity of study in solid mechanics, *Mechanics progress*, 16(4), 1986.517—527(in Chinese).

[32] Chaboche J.L., Continuum Damage Mechanics, Part I—General Concepts, *J. of Applied Mechanics*, 55, 1988, 59-63.

[33] Kachanov L.M., *Introduction to continuum damage mechanics*. Martinus Nijhoff Publishers, Dordrecht, 1986

[34] Malvern L.E., *Introduction to the mechanics of a continuous medium*, Prentice Hall, Inc., 1969

[35] Hong Kezhi, *Nonlinear continuous medium mechanics*, Tsinghua university press, 1989(in Chinese)

[36] Kuang, Zhenbang, *The basic of nonlinear continuous medium mechanics*, Xi'an Jiaotong University press, 1989(in Chinese)

[37] Gerstle W.H., A.R., P.Gergely, *The fracture mechanics of bond in reinforced concrete*, Corcell University, Department of structural, Report 81-10/655c,1981

[38] Lemaitre J., A continuous damage mechanics model for ductile fracture, *J. of Eng. Materials and Tech*., 107, Jan., 1985, 83-89

[39] Li Hao, Ou Yangping. *Progress of damage mechanics, Mechanics and conctruct*, 1982, 100-104(in Chinese)

[40] Liu Baozhen, Yan Ronggui, Inquire into model of broken rock mechanics, *J. of rock-soil engineering*, 3(4), 1981(in Chinese)

[41] Yu Tianqing, Divide into sectional linear damage model of concrete, *Crack and strength of rock and concrete*, 1985(in Chinese)

[42] Chen Zhida, *Reasonable mechanics*, mining industry university press, 1986(in Chinese)

[43] Wang Ren, *Stickiness fluid FEM in the large deformation of lane*, 17(2), 1985(in Chinese)

[44] Li Hao, *Damage mechanics*, Huazhong energy. Inst.press, 1986(in Chinese)

[45] Xie Heping, Chen Zhida. Inquire into model of rock continuous damage mechanic, *J. of coal*, 1986, 569(in Chinese)

[46] Xie Heping, *BEM of nonlinear large deformation* 9(12), 1988, 1087(in Chinese)

[47]Han Dajian, The application of plastic, fracture and damage mechanics in concrete structure, *Mechanics and practice*,10(1),1988(in Chinese)

[48] Lemaitre J., How to use damage mechanics, *Nuclear eng. And design*, 80, 1984, 233-245.

[50]Lee C., F.A.Cozzarelli, K.Burke, One-dimensional stain-dependent creep damage in homogeneous materials, *Int. J. nonlinear mechanics*, 21(4), 1986, 303-314.

[51] Chang T.C., C.H.Popelar, G.H.A.Staab, A damage model for creep crack growth, *Int. J. of fracture*, 32, 1987, 157-168

[52] Ashby M.F., Creep fracture, Proc. IUTAM symp. *Creep in structure*, 1980 368

[53] Krajcinovic D., Creep of structure, *J. of structure mechanics*, 11(1), 1983, 1-11

[54] Martison R.H., J.J.Hartog, G.C.Knollman. On the damage field near crack tips in a filled polymer, *Experimental mechanics*, 22(9), 1982, 329-335.

[55] Leckie F.A., E.T.Onat, *IUTAM Colloquium "physical nonlinearities in structural analysis"* Berlin, 1981, 140-155.

[56] Sidoroff F., *IUTAM Colloquium "Physical nonlinearities in structural analysis"*, Berlin, 1981, 237-244

[57] Hult J., J.Janson, Fracture mechanics and damage mechanics-A Combined approach, *J. of mechanics application*, 1, 1977, 69-84

[58] Krajcinovic D., Distributed damage theory of beam in pure bending, *J. applied mechanics,* 46, 1979, 592-596

[59] Xu Jishan, *Strength theory and its application*, Water and electricity press, 1981(in Chinese)

[60] Sidoroff F., *IVTAM Colloquium "physical nonlinearities in structural Analysis"*, Berlin, 1981, 237-244

[61] J Lemaitre.A., a Continuous damage mechanics model for ductile fracture, *J. of Eng. Material & Technology*, 107, 1985, 83

[62] Krajcinovic D., Constitutive equations for damage materials, *J. of applied mechanics*, 50, 1983,355

[63] Marigo,J.J. Modeling of brittle and fatigue damage for elastic material by Growth of micro voids, *Eng. fracture mechanics,* 21(4), 1985, 861□874

[64] Bui H.D. A.Ehrlachar, *The steady state propagation of a damaged zone of an elastic brittle*, Solid, ICF-6, 2, 1984

[65] Bui H.D., A.Ehrlachar, *Propagation of damage in elastic and plastic solid*[R].Solid, ICF-5, 2, 1983, 86-89

[66] Kamesware R., Creep damage under stationary random loading, *J. App. Mechanics, Trans. of ASME*, 44, 1977, 763-764.

[67] Krajcinovic D., Statistical aspects of the continuous damage theory, *Int. J. solids structures*, 18(7), 1982, 551-562.

[68] Sih G.C., Some basic problems in fracture mechanics, *Energy Fracture mechanics*, 5, 1973, 365-377.

[69] Kachanov L.M., *about crack growth problem under creep condition* (in Russian), Probl. Mekh. Spl. Sredy, Moscow, 1969

[70] Saanouni K., J.L.Chaboche, C. Bathias, on the creep crack growth prediction by a local approach, *J. of Eng. fracture Mechanics,* 25(516), 1986, 677-691

[71] Charinteri A., A. R. Ingraffea, Fracture mechanics of Concrete, *Material characterization and testing*, Martinus Nijhoff Publishers, 1984

[72] Mazars J., *Mechanical damage and fracture of concrete structures*, ICF-5, 4, 1983

[73] Popovics S., Fracture mechanism in concrete, How much do we know, *Proc. of SME*, 95, EM3, 1969, 531-544

[74] Carpinteri A., Numerical modeling of damage and fracture in concrete, *ICF-6,* 4, 1984.

[75] Bazant Z.P., B·H·Oh, *concrete fracture via stress-strain relations*, Northwestern University, Report, 82-7, 1981

[76] Frantziskonis G., C.s.Desai, constitutive model with strain softening, *Int. J. solid structure*, 23(6), 1987, 733-768

[77] Ewalds H.L., R.J.H. Wanhill, *Fracture mechanics*, The Netherlands, 1984,226

[78] Cottrell A.H., Theory of brittle fracture in steel and similar materials, *Trans. Of AIME*, 212, 1958,192

[79] Zheng changing, *initial study of tenacity fracture micro-mechanics and its application*, northwest industry university publication, 1988(in Chinese)

[80] Yang wei, Micro-theory of damage mechanics, *Discussion of damage mechanize in China*, 1985(in Chinese)

[81] Wang yunjia, Xing jibo, *Dispersed element method and its application in rock-soil mechanics*, Northeast Industry University press, 1991(in Chinese)

[82] Zhu Yiwen, Discontinuous deformation analysis of large deformation problems, *J. Wuhan Uni. of water-elestricity*, 1997(in Chinese)

[83] Yang wei, *Macro-micro fracture mechanics*, National industry press, 1995(in Chinese)

[84] Zhuo Jiashou, *Foundation of nonlinear solid mechanics*, Water-electricity press, 1996(in Chinese)

[85] Zhang Qing, Zhuo Jiashou, Stress element model of interface element method in anchor rock, *J. of rock-soil engineering* ,20(5),1998,50-53(in Chinese)

[86] Fang Yilin, Zhuo Jiashou, Interface element method of heat conduct problems, *J. Hehai University*, 26(4), 1998, 87-91(in Chinese)

[87] Wang Weibiao, Wu Qingxi, Zhuo Jiashou, Random interface element method of 2D problems, *J. of Hehai University*,27(4),1999,111-115(in Chinese)

[88] Goodman R.E., R.L.Taylor, T.L.Brekke, A model of the mechanics of jointed rock, *J. of Soil Mechanics and foundation division, ASCE, ASM3,* 1968, 94

[89] Desai C.S., B.K.Nagaraj, Modeling for cyclic normal & shear behavior of interfaces, *J. of Eng. Mechanics, ASCE*, 114(EM7), 1988, 1198-1217

[90] Zaman M.M., C.S. Deasi, E.C. Drumm, Interface model for dynamic soil-structure interaction, *J. of Geotechnical Eng., ASCE*,110(GT9),1984,1257-1273

[91] Shi G.H., R.E. Goodman, Discontinuous deformation analysis, *Proc. 25th US symposium on rock mechanics*, 1984, 269-277

[92] Gerrard C.M., Elastic model of rock masses having one, two, three sets of joint, *Int. of rock mech. and min. eng. sic. And geo mech*. abstr, 19(1), 1982

[93] P Cundall.A., a computer model for simulating progressive large scale movements in blocky rock systems, *Proc. Symp rock fracture (ISRM),* Nancy, 1971.

[94] Ke Te-chih, The Issue of rigid-body rotation in DDA, *DDA & simulations of discontinuous media, Albuquerque*, New Mexico, USA, 1996, 318-325

[95] Kachanov M.L., Micro crack model for rock inelasticity, *Thesis of PH.D. Of Rutgers Uni. Piscataway*, 1980

[96] Shi Gen-Hua, Simplex integration for manifold method, DDA & analysis method, *Proc of IFDDA 96*, Tsi Press, Berkeley, Califoria,USA,1996,206-260

[97] Mary M., Maclaughlin and Nicholas Sitar, *Rigid body rotation in DDA, DDA and simulations of discontinuous Media*, Tsi Press, Albuquerque, New Mexico, USA,1996, 620-635

[98] Kawai T., N.C.Chango, *A discrete element analysis of beam bending problems in colluding the effects of shear deformation*, Seisan venkyn, 29(4), 1977, 165-168

[99] Bath K.J., S. Bolourchi. Large displacement analysis of 3D beam structures, *Int. J. Num. Math. Eng.*, 14, 1979, 961-986

[100] Givelli L.A., C.A.Felippa, a 3D nonlinear Timoshenko bean based on the core- congruent formulation, *Int. J. Num. Meth.Eng.,*36(21),1993,3647-3673

[101] Ngo D., A.C. Scordelic, *FEM of Reinforced Concrete beams*, AOI J. 64(3), 1967, 152-163

[102] Ji Xing, Zang Yuelong, Cheng Yuming, *The progress and general program of BEM*, Tongji Uni. press.1997(in Chinese)

[103] Belytschko T et al. Meshless method: An overview and recent developments, *Comp Methods Apply Mech. Energy.*, 139, 1996, 3-47

[104] Li Shaofan, Liu W.K. Mesh free and particle methods and their applications, *Applied Mechanics Review,* 55, 2002, 1-33

[105] Lucy L. B., A numerical approach to the-testing of the fission hypothesis, *The Astron J*, 8(12), 1977, 1013-1024

[106] Lancaster P., Salkauskas K. Surfaces generated by moving least square methods, Math compute, 37, 1981, 141-158

[107] Babuska I., Melenk J M, the partition of unity method, *Int. J. of Numerical Math Energy*,40,1997,727-758

[108] Liu W. K, Jun S, Zhang Y.F., Reproducing kernel particle methods, *Int. J. Numerical Methods Energy*, 20,1995, 1081-1106

[109] Nayroles B. et al. Generalizing the finite element method: diffuse approximation and diffuse elements, *Compute Mech.*, 10, 1992, 307-318

[110] Belytschko T et al. Element-free Galerkin methods, *Int. J. Numerical Methods Energy*, 37, 1994, 229-256

[111] Duarte C. A., Oden J.T., Hp clouds-a meshless method to solve boundary-value problems, *Technical Report 95-05, Texas Institute for Computational and Applied Mathematics*, University of Texas at Austin.1995

[112] Onarte E, A finite point method in computational mechanics, *Int. J. Numerical Methods Energy*, 39, 1996, 3839-3866

[113] Atluri S.N., Zhu T.L., A new meshless local Petrov-Galerkin (MLPG) approach in computational mechanics, *Computational Mechanics* 22, 1998, 117-127

[114] Atluri S.N., Zhu T.L., The meshless local Petrov-Galerkin (MLPG) approach for solving problemsin elasto-statics,. *Computational Mechanics*, 25, 2000, 169-179

[115] Atluri S.N., Zhu T.L., New concepts in meshless methods, *International Journal for Numerical Method in Engineering* 47(1-3), 2000, 537-556

[116] Atluri S.N., Kim H.G. et al, A critical assessment of the truly meshless local Petrov-Galerkin (MLPG) and local boundary integral equation (LBIE) methods, *Computational Mechanics 24*,1999,348-372.

[117] Liu W. K., Chen Y., Uras R. A., Chang C. T., Generalized multiple scale reproducing kernel particle[J], *Compute methods apply mech. engrg*,139,1996,91-157.

[120] Idelsohn S.R., Onate E.,Calvo N.,Del Pin F., The meshless finite element method, *Int. J. numerical methods engrg,* 58, 2003, 893-912

[121] Hao S., Park H.S., Liu W.K. Moving particle finite element method, *Int. J. numeric methods eng*.,53(8), 2002,1937-1958.

[122] Atluri S.N., Sladek J. et al, The local boundary integral equation(LBIE)and it's meshless implementation for linear elasticity[J]. *Computational Mechanics* 25, 2000, 1180-198.

[123] Zhu T. Zhang J. D., Atluri SN, A local boundary integral equation(LBIE)method in computational mechanics, and a meshless discretization approach[J]. *Computational mechanics*, 21, 1998, 223-235

[124] Zhu Tulong, Zhang Jindong, Atluri SN.,A meshless numerical method based on the local boundary integral equation (LBIE) to solve linear and non-linear boundary value problems[J]. *Engineering analysis with boundary elements*, 23, 1999, 375-389.

[125] Zhu T., Zhang J.D., Atluri S.N., A meshless local boundary integral equation (LBIE) method for solving nonlinear problems[J]. *Computational mechanics*, 22, 1998, 174-186

[126] Mukherjee Y.X.,Mukherjee S. The boundary node method for potential problems, *International journal for numerical methods in engineering* 40, 1997, 797-815

[127] Kothnur V.S., Mukherjee S., Mukherjee Y.X., Two dimensional linear elasticity by the boundary node method, *International journal of solids and structures* 36, 1999, 1129-1147

[128]Chati M.K., Mukherjee S., Mukherjee Y.X., The boundary node method for three-dimensional linear elasticity[J].*International journal for numerical methods in engineering* 46,1999,1163 -1184.

[129]Mandar K.Chati and Subrata Mukherjee., The boundary node method for three-dimensional problems in potential theory, *Int.J.numer.meth.engng.*47, 2000, 1523-1547

[130] Chati M.K., Mukherjee S., Paulino G. H., The meshless hyper singular boundary node for three-dimensional potential theory and linear elastic problems[J]. *Engineering analysis with boundary elements*, 25, 2001, 639-653

[131]Cheng Yuming, Chen Meijuan. Meshness method of boundary integration in elasticity mechanics [J], *J. of mechnics*, 2, 2003, 181-186(in Chinese)

[132] Swegle J.W., Hicks D.L., Attaway S.W. Smoothed particle hydrodynamics stability analysis [J], *J Compout Phys*, 116, 1995, 123- 134.

[133]Dyka C.T. Addressing tension instability in SPH methods[R].*Technical report NRL/MR/6384*, NRL, 1994

[134]Jhhnson G.R., Stryk R.A., Beissel S R., SPH for high velocity impact computations, *Compute methods apply mech. Engrg.* 139, 1996, 347-3730

[135]Belytschko T., Gu L.,Liu Y.Y. Fracture and crack growth by element-free Galerkin Methods, *Model simulate master science engrg*, 2, 1994, 519-534.

[136] Dolbow J., Belytschko T., Numerical integration of the Gaierkin weak form in meshfree Methods, *Compute. Mech.,* 23, 1999, 219-230

[137] Belytschko T., Krongauz Y. et al. Smoothing and accelerated computations in the element free Galerkin method [J], *J.comput.appl.math*, 74, 1996, 111-126.

[138] Krongauz Y., Belytschko T., EFG approximation with discontinuous derivatives, *Int. J. numerical methods engrg.* 41, 1998, 1215-1233

[139] Belytschko T., Gu L., Lu Y.Y. Fracture and crack growth by element free Galerkin methods [J]. *Modeling simu. mater.sci.eng.* 2, 1994, 519-534

[140] Lu Y.Y.,Belytschko T. Element-free Galerkin methods for wave propagation and dynamic fracture[J]. *Compute. Methods app. mech.Engrg,* 126, 1995, 131-153

[141] Ponthot J.P., Belytschko T., Arbitrary Lagrangian-Eulerian formulation for element-free Galerkin method, *Compute Methods appl.mech.Engrg*, 152, 1998, 19-46

[142] Krysl P., Belytschko T., Analysis of thin shells by element-free Galerkin method, Compute Mech., 17, 1995, 26-35

[143] Belytschko T., Lu Y.Y. Gu L., Tabbara M. Element-free Galerkin methods for static and dynamic fracture [J]. *International journal of solids and structures*, 32, 1995, 2547-2570.

[144] Sukumar N., Moran B., Black T., Belytscbko T. An element-free Galerkin method for three-dimensional fracture mechanics, *Comput.Mech,* 20, 1997, 170-175

[145] Belytschko T., Organ D., Gerlach C. Element-free galerkin methods for dynamic fracture in concrete [J]. *Compute Methods app. Mech. energy,* 187, 2000, 385-399

[146] Xu Y., Saigal S., An Element Free Galerkin analysis of steady dynamic growth of a mode I crack in elastic-plastic materials, *International journal of sounds and structures*, 36, 1999, 1045-1079

[147]Kargarmovin M.H, Toussi H.E, Faribotz S.J., Elasto-plastic element-free Galerkin method, *Comput. mech*, 2003

[148]Bouillard Ph, Seleau S., Element-free Galerkin solutions for helmholtz problems: formulation and numerical assessment of the pollution effect, *Comput. Methods app. mech.engrg*, 162, 1998, 317-335

[149]Lee S.H, Yoon Y.C. An improved crack analysis technique by element-free Galerkin, *International journal for numerical methods in engineering,* 56, 2003, 1291-1314

[150]Fleming M., Chu Y.A., Moran B., Belytschko T. Enriched element free Galerkin methods for crack tip fields, *International journal for numerical methods in engineering*,40,1997,1483-1504

[151]Beissel S., Belytschko T. Nodal integration of the element free Galerkin method [J] *Comput. Methods app. mech. engrg,* 139, 1996, 49-74

[152]Smolinski P., Palmer T. Procedures for multi-time step integration of element free Galerkin methods for diffusion problems [J]. *Comput. Struct,* 77, 2000, 171-183

[153]Mukherjee Y.X.,Mukherjee S. On boundary conditions in the element-free Galerkin Methods [J], *Comput. Mechanics,* 19, 1997, 264-270.

[154]Alves M.K, Rossi R., A modified element-free Galerkin method with essential boundary conditions enforced by an extended partition of unity finite element weight function [J]. *International journal for numerical methods in engineering* 57, 2003, 1523-1552

[155]Kaljevic I., Saigal S., An improved element free Galerkin formulation [J]. *International journal for numerical methods in engineering* 40, 1997, 2953-2974

[156]Krysl P., Belytschko T. ESFLIB: A library to compute the element free Galerkin shalSe functions [J]. *Comput. Methods app. mech. engrg*, 190, 2001, 2181-2205

[157]Krysl P., Belytschko T. Element-free Galerkin method convergence of the continuous and discontinuous shape functions [J]. *Comput. Methods app. mech.engr*g, 148, 1997, 257-277

[158]Gavete L.,Falcon S.,Ruiz A., An error indicator for the element free Galerkin method [J], *Eur. J. of mech. A/Solids*, 20, 2001, 327-341.

[159]Duarte C.A, Oden J.T. an h-p adaptive method using clouds [J]. *Comput. meth. app. mech. engrg*, 139, 1996, 237-262

[160]Babuska I., Melenk J. M. The partition of unity finite element method: basic theory and applications [J]. *Comput. meth. app. mech. Engrg*, 139, 1996, 289-314,

[161]Chen J.S., Pan C., Wu C.T., Liu W.K., reproducing kernel particle methods for large deformation analysis of non-linear structures [J], *Computer meth.appl.mech.engrg*, 139, 1996, 195-227

[162]Li S., Liu W.K., Moving east-square reproducing kernel method (I), Methodology and Convergence [J], *Comput. meth.appl.mech.engrg,* 143, 1997, 113-154

[163]Li S., Liu W.K., Moving least-square reproducing kernel method Part II Fourier analysis [J], *Comput. meth. Appl.mech.engrg,* 139, 1996.159-193

[164]Chen J.S., Yoon S., Wang H.P. Liu W.K., An improved reproducing kernel particle method for nearly incompressible finite elasticity [J], *Comput. meth.appl.mech.engrg,* 181, 2000, 117-145

[165]Voth T.E., Christon M. A. Discretization errors associated with reproducing kernel methods[J].*dimensional domains*[J],*Comput.meth.appl.mech.engrg*,190,2001,2429-2446.

[166]Liew K.,Ng T.,Wu Y. Meshfree method for large deformation analysis-A reproducing kernel partical approach[J].*Engrg.structure,*24,2000,543-551.

[167]Shangwu X., Liu W.K., Cao J. On the utilzation of the reproducing kernel particle method for the numerical simulation of plane strain rolling [J].*Int. journal of machine tools and manufacture*, 43, 2003, 89-102.

[168]Chen J.S., You Y.,Meng X. A reproducing kernel method with nodal interpolation property [J].I*nternational journal for numerical methods in engineering*, 56, 2003, 935-960

[169]Hah W, Meng X. Error analysis of the reproducing kernel particle method [J]. *Comput. Meth. App. Mech. Engrg*, 190, 2001, 6157-6181.

[170]Onarte E, Idelsohn S., A mesh-free finite point method for advective-diffusive transport and fluid flow problems. *Comput. Mech.*21, 1998, 283-292

[171] Buhmann M.D. Radial Basis Functions [J]. Acta numerica, 2000, 1-38

[172]Franke C., Schaback S. Convergence order estimates of meshless collocation methods using Radial Basis Functions [J]. *Advances in computational mathematics*, 8, 1998, 381-399

[173]Wu Z.M, Hon Y.C. Convergence error estimate in solving free boundary diffusion problem by radial basis functions method [J]. *Engineering analysis with boundary elements*, 27, 2003, 73-79

[174]Wang J.G., Liu G.R. On the optimal shape parameters of radial basis functions used for 2-D meshless methods [J].*Comp. meth. App. mech. egrg*, 191, 2002, 2611-2630

[175]Wang J., Liu G. A point interpolation meshless method based on radial basis functions [J].*Int. journal for num. methods in egineering*, 54, 2002, 1623-1648.

[176]Zhang Jianming, Yao Zhenhan, Li Hong., A hybrid boundary node method [J].*Int. journal for num. methods in engrg*.,53, 2002, 51-763.

[177]Belytschlo T,,Organ D. Coupled finite element-element-free Galerkin method[J].*Comp. Mech.* 17,1995,86-195.

[178]Hegen D. Element-free Galekin methods in combination with finite element approaches [J].Com. method App. Mech.engrg.135, 1996, 143-166

[179]Liu GR, Gu YT. Coupling of element-free Galerkin and hybrid boundary element methods using modified variation formulation [J].Comp. Mech. 26(2), 2000, 166-173

[180]Liu G R, Gu Y., Meshless local petrov-Galerkin (MLPG) method in combination with finite element and boundary element approaches[J],*Comp.mechanics*,26,2000,536-546.

[181]Antonio Huerta, Sonia Fernadez-Mendez, Enrichment and coupling of the finite element and meshless methods[J].*Int. journal for num. methods in Engrg*.,48,2000,1615-1636.

[182]Gu Y., Liu G.R. A coupled element-free galerkin /boundary element method for stress analysis of two-dimension solid [J].*Comp. method in Appl.mech.eng.*190, 2001, 4405-4419

[183]Rao B., Rahman S. A coupled meshless-finite element method for fracture analysis [J].*Int. journal of pressure vessel & piping,* 78, 2001, 647-657

[184]Xiao Q., Dhanasekar M. Coupling of FE and EFG using collocation approach [J], *Adv. in engrg. Software*, 33, 2002, 507-515.

[185]Chen T, Raju I. A coupled finite element and meshless local Petrov-Galerkin method for two-dimensional potential problems [J].*Comp. meth. App. mech. engrg*, 192, 2003, 4533-4550

[186]SongKngzu,Lu Mingwan,Zhang Xong. Meshless method in solid mechanics [J], *Mechanics progress,* 30(1), 2000, 55-65(in Chinese)

[187]Zhang xong, Song Kangzu, Lu mingwan, The progress and application in the study of meshness method[J], *J. compute mechanics*,20(6) 2003,731-741(in Chinese)

[188]Jiang hongdao,Cao guojin. Current situation and trends in meshless study and application [J], *Mechanics progress*, 34(4), 2002, 526-534(in Chinese)

[189]Zhang Suochun, The method of smoothed partial hydromechanics [J], *compute physics,* 13(4), 1996, 385-397(in Chinese)

[190]Bei Xinyuan,Yue zhongwu,3D SPH program and its application in high speed collide problem[J],*compute physics*,14(2),1997,155-166(in Chinese)

[191]Liu X.,Lu M.W.Zhang X. Numerical analysis of singular problems using the partition of unity method[J]. *European comp. mechanics (ECCM'99)*, Munchen, Germany, 1999

[192]Song K.Z., Zhang X. Meshless method based on collocation for elasto-plastic analysis [J].*Proceedings internal conference on computational engineering & science.* August, 20-25, 2000

[193]Zhang X., Song K.Z., Lu M.W. Meshless methods based on collocation with radial basis function [J].*comp. mech.* 26(4),2000,333-343.

[194]Xiong Zhang, Xiao-Hu Liu, K.ang-Zu Song and Ming-Wan Lu, Least-squares collocation meshless method [J].*Int. J. numer. meth. engrg.* 51, 2001, 1089-1100.

[195]Li Mei'e, Zhang Ling. The progress of reproducing kernel partial method [J], *mechanics progress*, 32(4), 2002, 535-544(in Chinese)

[196]Zhang Xong, Hu Wei, Weighted least-square meshless method [J], *J.mechanics,* 35(4), 2003, 425-431(in Chinese)

[197]Zhang Xong,Song Kangzu,Lu mingwan. Weighted remains method of radial potential function [J], *J.mechanics,* 35(1), 2003, 43-49(in Chinese)

[198]Lou Luliang,zeng Pan. The factor analysis of influences solving precision in meshness mechanics [J], *compute mechanics*, 20(3), 2003, 313-319(in Chinese)

[199]Cai Yongchang, Zhu Hehua. Meshness local Petrov-Galerkin method based on the Voronoi structure [J], *J. mechanics* 35(2), 2003, 187-193 (in Chinese)

[200]Cai Yongchang, Zhu Hehua. Meshness method and automatic set point technology in rock-soil engineering numerical calculation, *Rock-soil mechanics,*24(1),2003,21-24(in Chinese)

[201]Long Shuyao,Xu Jingxiao. Local integral equation method in elasticity mechanics [J], *J.mechanics,* 32(5), 2000, 566-577(in Chinese)

[202]Zhang X. A., 2D meshness model for jointed rock structures [J], *Int. J. numerical Methods Engrg*. 47(10), 2000, 1649-1661

[203]Kou Xiaodong, zhou Weiyuan, The approximate computation in crack of Arch Dams using element free methods[J],*J. water conservancy,*10,2000, 28-35(in Chinese)

[204]Zhang Weixing, Pang Hui. Element free method of compute plate based on elasticity foundation [J], *Engineering mechanics*, 17(3), 2000, 138—144(in Chinese)

[205]Pang Zuohui,Ge Xiuren. The application of meshness Galerkin method in slope excavate [J], *Rock- soil mechanics,* 20(1), 1999, 61-64(in Chinese)

[206]Chen Jian, Wu linzhi, Du Shanyi. *The calculation of stress intensity factor using element free method along single crack material plate*[J],17(5),2000,139-144(in Chinese)

[207]Zeng Qinghong,Lou Detang. Meshness method solving stable permeate problem [J], *J. calculate mechanics*, 20(4), 2003, 440-445(in Chinese)

[208]Guo Juan,Tao Zhi. MPS meshness method of nonlinear problem [J], *J. Beijing aviation-spaceflight University,* 29(1), 2003, 83—86(in Chinese)

[209]Zhang Yanjun, Wang Sijing. FEM and EFGM compling method in 2D continuous porous medium [J], *Calculate physics*, 20(2), 2003, 142-146(in Chinese)

[210]Lou Luliang, Zeng Pan. Meshness analysis in stress high gradient problem [J], *J. applied mechnics*, 19(2), 2002, 121-124(in Chinese)

[211]Yuan Zhen, Li Ziran. The expand simulating tired crack with meshless method [J], *Engrg.mech.*19 (1), 2002, 25-28(in Chinese)

[212]Long Shuyao, Analysis of beam based on nonlinear foundation using meshless local Petro-Galerkin method [J], *Quarter J.mechanics*, 23(4), 2002, 547-551(in Chinese)

[213]Wuodong, Tang Guohuan, The application of meshness method in elasticity-plasticity problem[J], *J. solid mechanics*,22(4),2001,361-.367(in Chinese)

[214]Wuodong,Tang Guohuan, The application of meshness method in elasticity-plasticity problem[J], *J. solid mechanics*,20(4),2001,462-.466(in Chinese)

[215]Pang Zuohui, Zu Xueming, EFGM solving engage problems [J], *J. Hehai University* 28(4), 2000, and 54-58 (in Chinese)

[216]Pang zuohui, GeXiuren, EFGM simulating discontinuous face [J], *J. Engrg. Geology,* 8(3), 2000, 364-368(in Chinese)

[217]Pang Zuohui,Ge Xiuren. Two complement about EFGM [J], *J. rock mechanics and engrg.* 18(5), 1999, 581-584(in Chinese)

[218]Xia Daohang, Wu Zuoren etc. *General function analysis* [M].Beijing: Higher education press, 1979(in Chinese)

[219]Timoshenko S.P., Goodier J.N. Theory of elasticity [M] (Third edition), McGraw-Hill Inc., 1970

[220]Rao B.N., Rahman S, an Enriched Meshless Method for Nonlinear Fracture Mechanics [M]. *International Journal for numerical methods in engineering*, 2004, 59, 0001-0027.

[221]Dolbow J. An extended FEM with discontinuous enrichment for applied mechanics[D].

PhD thesis of Northwest University, USA, 1999

[222]Daux C., Moes N., Dolbow J., Sukumar N., Belytschko T. Arbitrary branched and intersecting cracks with the extended finite element method[J].Int. J. numeric. meth. Engrg. 48, 2000, 1741-1760

[223]Dolbow J., Moes N., Belytschko T. an extended finite element method for modeling crack growth with frictional contact [J]. Comput. meth. App. mech engrg, 190, 2001, 6825-6846

[224]Anderson T.L. *Fracture mechanics: Fundamentals and application*s [M] (First Ed.). CRC Press, 1999

[225]Cheng Yuming, Shen Zhuyan, Peng Miaojuan. Weighted random and FEM compiling method solving elasticity mechanics Problems [J]. *J. Civil engrg*. 33(4), 2000(in Chinese)

[226]Cheng Yumin, Peng Miaojuan, The coupling method of boundary and finite elements for a nonlinear problem of structural engineering [M], in: *Theory and applications of boundary element methods,* (Zhenhan Yao and M. Tanaka eds.), International academic publishers, 1998

[227]T.Von Karman. The Engineer Grapples with Nonlinear Problems[R]. *Bulletin of the American mathematical society*, 46(8), 1940, 615-683

[228]Bathe K.J. and Wilson E.L. *Numerical methods in finite element anal*ysis [M].Prentice-Nill, Inc, 1976

[229]Zienkiewicz O.C.and Morgan K. Finite element and approximation [M].*John Wiley & Sons,* Inc, 1983

[230]Owen D.R.J, Hinton E. Finite element in plasticity, *Theory and Practice* [M].Pine ridge Press, 1982

[231]Yin Youquan, *Introduction of nonlinear FEM in solid mechanics* [M].Beijing: Beijing University press, 1986(in Chinese)

[232]Wang Honggang. *Hot elasticity* [M], Tsinghua university press, 1986(in Chinese)

[233]Zhou Weiyuan. Higher rock mechanics [M], Water conservancy and waterpower press, 1990(in Chinese)

[234]Dong Zheren, *Principle and application of nonlinear FEM in reinforced concrete* [M].Railway press, 1993(in Chinese)

[235]Dong Yuli, *Foundation of concrete nonlinear mechanics* [M].Construct industry press, 1997(in Chinese)

[236]Jiang Jianjing. Nonlinear FEM of reinforce concrete [M].Shaanxi technology press, 1994(in Chinese)

[237]Yin Youquan, Zhang hong, NOLM program of stress deformation and stability analysis in elasticity and plasticity of rock-soil system[C].Thesis of geology study (third album), Beijing university press, 1985(in Chinese)

[238]Dragon A.and Mroz Z. A continuum model for plastic-brittle behavior of concrete [J].*Int. J. Engineering science*, 17, 1979, 121-137

[239]Wang Ren, Liang Beiyuan. Viscosity fluid FEM of large deformation of tunnel [J], J. mechanics, 17, 1985(in Chinese)

[240]Lan Labao, Wang Ren. Inverted fold FEM model of elasticity and plasticity[C].*Thesis of 0-o g0eology mechanics study*, Beijing university press,1985(in Chinese).

[241]Yang Jusheng, Lan Shengrui, Li Jiuhong. Three axises non-ratio loading experiment of concrete and struck- tural crack analysis[C].*Thesis of structural engineering and vibration,* Tsinghui university press,2000,23—35(in Chinese).

[242]Yang Jusheng, Li Jiuhong, Guo Yongzhong. Study of finite element analysis for non-elasticity damage of concrete structure[C], *Thesis of structural engineering and vibration*, Tsinghua univ. Press. 2000, 36-45(in Chinese)

[243]Li Jiuhong, Lan Shengrui, Yang Jusheng. Three-Dimensional Nonlinear FEA under Cracking of Concrete Structure [J].*International Symposium on New Development in Concrete science and Technology*, Nanjing, 1995.

[244]Lan Sheng,Yang Jusheng, The Space structural of blast furnace[R]. *International conference on mechanics of solids and materials engineering*, Singaper, 1995

[245]Xu Hanzheng, Yang Jusheng. 3D elasticity-plasticity crack analysis of concrete structure [J], *Engrg. Mechanics*, 1, 1996, 400-404(in Chinese)

[246]Yang Jusheng, LiJiuhong, Guo Yongzhong, The damage cracking Model of brittle material in numerical analysis[R]. Computer method and advances in geomechanics, *3 Ninth international conference of the association for computer method and advances in geomechanics*, 1997

[247]Lan Shengrui, Yang Jusheng. Nonlinear FEM of Arch Dam I: Constitutive relationship [J]. *Advances in engineering software*, 28, 1997

[248]Lan Sheng,Yang Jusheng, Nonlinear FEM of Arch Dams: Nonlinear analysis [J]. Advances in Engineering software, 28, 1997

[249]Yang Jusheng, Li Jiuhong, Liu Hua. Damage-distroy compling model of brittle material [J], *J. rock mechanics and engineering*, 17, 1998, 749—754(in Chinese)

[250]Li Jiuhong,Yang Jusheng. Nonlinear finite element analysis for elasticity-plasticity of rock body [J], J. rock mechanics and engineering, 19(1), 1999, 707—711(in Chinese)

[251]Balmer G.G., Shearing strength of concrete under high triaxial stress-computation of Mohr's envelope as a curve [R], *Bur.Reclam.Struct.Res.Lab.Rep.Sp□23*, 1949

[252]Drucker D.C., A definition of stable inelastic material [J]. *J. App. Mech., 26, ASME* Trans, 81, 1995

[253]Bresler B, Pister K.S. Strength of concrete under combined stress [J], *J. Am.Coner.Inst*, 55, 1958

[254]Willam K.J, Warnke E.P. Constitutive model for the triaxial behavior of Concrete [J].*Int. Assoc. Eng. Sem*, 1974

[255]Ottosen N.S. Failure and elasticity of concrete [R], Dan Atom Energy Comm. Res Estab Ris Eng Dept. Ris□M□1801, Roskilole, Denmark, July, 1975

[256]Hsieh S.S, Ting E.C, Chen W.F., An elastic fracture model for concrete[R].*Proc.3d Eng. Mech. Div. Spec. Conf.ASCE.*, Austin, Tex, 1979

[257]Guo Zhenhai, Wang chuanzhi. Study of intensity and destroy standard of concrete under multi-axises stress [J]. *J. Civil engineering,* 3, 1991(in Chinese)

[258]Yu Mohong., Study of Double-shears stress intensity [M]. Xi'an Jiao tong university public comp., 1988(in Chinese)

[259]Yu Mohong, *Double-shears theory and application* [M], Science press, 1998(in Chinese)

[260]Jiang Jianjing, He xiaogang. Present situation and prospects of constitutive relationship of concrete [J].Engrg. Mechanics, 1993(in Chinese)

[261]Darwin D, Pecknold D., A Nonlinear biaxial stress strain law for concrete [J], *ASCE 103(EM2)*, April, 1997

[262]Kupfkr H, Gerstle K.H., Behavior of concrete under biaxial stresses [J], *ASCE, 99(EM4*), Aug. 1973

[263]Ottosen N.S., Constitutive model for short-time loading of concrete [J], *ASCE, 105(EM1*), 1997

[264]Gerstle K., *Simple formulation of biaxial concrete behavior* [J]. I. J. Jan, Feb.1981.

[265]Stankowski T., Gerstle K. Simple formulation of concrete behavior under multiracial load histories [J].*ACIJ, march-april*, 1985

[266]Chen W.F., Plasticity in Reinforced Concrete [M]. *Mc-Graw-hill,* 1982

[267]Hsieh S.S., Ting E C and Chen W F., A plastic fracture model for concrete [J]. *Int. J. solids structure*, 18(3), 1982.

[268]Hen D J and Chen W F., A no uniform hardening plasticity model for concrete material[J].*Mach. of materials*, 4,1985

[269]Vermeer P. A. and Borst R. Non□associated plasticity for soils [J], *Concrete & rock, Heron,* ACIJ, March 1976

[270]Dong Yuchuan, Xie Heping. Damage structure modelof higher pressure concrete [J] , *Mechanics and practice*,6,1996(in Chinese)

[271]Valanis K C., Theory of visco-plasticity without a yield surface [J]. *Archiwum mech. Stocssowanej*, 23, 1971

[272]Bazant E.P, Bhat D.P. End chronic theory of inelasticity and failure of concrete [J].*ASCE, 102(EM4)*, Aug 1976

[273]Ye Xianguo, *Deformed experiment study of concrete intensity factor under three axises higher pressure* [D], Tsinghua University, 1988 (in Chinese)

[274]Lan shengrui, Ynag Jusheng, Regional cracking model in FEA of reinforced concrete [J]. Int. symposium of concrete engineering (Nanjing, China), 3, 1991

[275]Li Jiuhong, Three axises experiment of concrete and the 3D nonlinear FEM permitting crack [D].Xi'an Univ. of tech., 1994(in Chinese)

[276]Li Jiuhong, Researches on meshless method with complex variables and applications [D] .PhD thesis, Xi'an Univ. of tech., 2004(in Chinese)

[277]Zhao Qin. Researches on meshless method application and influences of solving precision [D].Master thesis, Xi'an Univ. of tech., 2005(in Chinese)

[278]Kou Xjaodong, Zhou Weiyuan. Tracking crack expansion by element free method [J], *J. rock-soil mechanics and Engrg.19 (1)*, 2000, 18□23 (in Chinese)

[279]Zhou Weiyuan, Yang Roqong, Tan Gongrui. Manifold method and its application in engineering [J].*J. rock mechanics and engineering,* 15(3), 1996, 211-218(in Chinese)

[280]Zhou Weiyuan, Kou Xiaodong, Element free method and its application [J], *J. rock mechanics and Engrg*, 30(2), 1998, 193-202(in Chinese)

[281]Kou Xiaodong, Yang Ruo Qong,Shen Dali, Zhou Weiyuan. *The application in crack calculation of Xiao wan Arch Dams using element free methods*[J],Yunnan hydropower,16(1),2000,71-76(in Chinese)

Japanese underground research laboratory project and prediction of rock mass behavior around deep shafts and galleries using continuous and discontinuous models

Sato, T., Mikake, S., Nakama, S. and Seno, Y.
Japan Atomic Energy Agency, Mizunami, Gifu, Japan
Mori, T. and Iwano, K.
Kajima Corporation, Chofu, Tokyo, Japan
Gohke, M. and Tada, H.
Shimizu Corporation, Etchujima, koto-ku, Tokyo, Japan

This paper was prepared for presentation at *ICADD-7, the Seventh International Conference on Analysis of Discontinuous Deformation*, held in Honolulu, Hawaii, December 10-12, 2005.

ABSTRACT: A couple of one thousand meter deep shafts and research galleries at several levels will be excavated in granite for the Mizunami Underground Research Laboratory (MIU) Project. Research on the deep geological environment will provide the basis for R&D on geological disposal of high-level radioactive waste. The site of the MIU project is located in Mizunami City, Gifu Prefecture, in the central part of the main island of Japan. Surface-based investigations including geological mapping, seismic reflection surveying and borehole investigations, and site preparation for the MIU project started in 2002. The shafts reached 150 m depth in September 2005. Mechanical investigations include in situ hydraulic fracturing testing and laboratory tests on core samples. Numerical analysis using continuum and discontinuous models: MBC (Micro-mechanics based continuum model), Crack tensor model and FRACOD (fracture propagation code), were also performed to predict mechanical stability of openings and support systems, and rock mass behavior around openings. In these analyses, an EDZ (Excavation Damaged Zone) due to blasting and excavation was considered.

1. INTRODUCTION

One of the features of the geological disposal policy in Japan is the establishment of Underground Research Laboratories (URLs). The URLs must be distinct from an actual disposal facility, as outlined in the Atomic Energy Commission (AEC) report [1]. Research on the deep geological environment will provide the basis for R&D on geological disposal of high-level radioactive waste. The AEC stipulated that research at the underground laboratories should also contribute to Japan's scientific research on the geological environment.

URL projects conducted by the Japan Atomic Energy Agency (JAEA) are directed towards improving the reliability of geological disposal technologies and developing advanced safety assessment methodologies. It will ensure that the implementation of geological disposal is based on a thorough scientific and technological basis. The URLs in these projects are classified into purpose-built generic URLs as described in the OECD/NEA report [2], and are distinct from on-site (site-specific) URLs to be constructed at potential waste disposal sites. In order to cover the general geological environment in Japan, two URLs, one for crystalline rock

and another for sedimentary rock have been planned, one is the Mizunami Underground Research Laboratory (MIU), the other is the Horonobe Underground Research Laboratory (Hnb-URL) [3, 4]. One purpose of this plan is to confirm the technical reliability of the geological disposal methods, as indicated by the Second Progress Report [5].

The site of the URL project for crystalline rock is located in Mizunami City, Gifu. The regional geology consists of Tertiary and Quaternary sedimentary rocks overlying Cretaceous granitic basement. The conceptual design of the MIU at present is as follows.

- Two 1000 m shafts, the Main Shaft (6.5m ϕ) and the Ventilation Shaft (4.5m ϕ);
- Two experimental levels, the Main Stage at 1000 m and the Middle Stage, at 500 m depth;

The site of the URL project for sedimentary rock is located at Horonobe, Hokkaido, north of the main island of Japan. The geology consists of Tertiary sedimentary rocks. Conceptual design for the Hnb-URL at present is as follows.

- Two 500-m shafts and one Ventilation shaft;
- One experimental level, the Main Stage at around 400 m depth;

As of July 2003, shaft portals were being constructed at Mizunami, and land development work had started at Horonobe.

In the earliest stage of the MIU project, surface-based investigations were carried out at the Shobasama site, also in Mizunami City. However, given that planning permission was obtained for the Underground Research Laboratory (URL) from Mizunami City for the lease of city-owned land (MIU construction site), it was decided that the URL facilities should be constructed at this site. Then, investigations continued on the geological research and prediction analysis. Surface-based investigations including geological mapping, seismic reflection surveying and borehole investigations, followed by site preparation for the MIU project, started in 2002 at the MIU construction site. Layouts of the shafts and galleries were determined considering design and construction constraints, schedule, results of surface-based investigations and the investigation plans for characterization of the geological environment and engineering technologies in the next phase.

In the surface-based investigation phase of the MIU project, rock mechanics investigations including in situ hydraulic fracturing and laboratory tests on core samples were performed. Numerical analyses using continuum and discontinuous models; i.e., MBC (a Micro-mechanics Based Continuum model), a Crack tensor model and FRACOD (fracture propagation code) were performed to predict the mechanical stability of openings and support systems and the rock mass behavior around openings. In this analysis, an EDZ (Excavation Damaged Zone) due to blasting and excavation were considered in same cases.

This paper describes the design and construction of the Mizunami Underground Research Laboratory, and the predicted rock mass behavior around the deep underground openings using the above analytical methods and data mainly from the Shobasama site.

2. MIZUNAMI UNDERGROUND RESEARCH LABORATORY

2.1. Basic design conditions

The URL project for crystalline rock is located in Mizunami City, Gifu Prefecture, in the central part of Honshu, the main island of Japan (Fig. 1). The MIU facility and related surface plant will be constructed on land in Akeyo-cho leased from Mizunami City. The site area is about 7.8 hectares and located in the Intergarden of Tono Frontier Science Research City. This area has a

number of public facilities that draw many people to the area. This situation may affect or constrain traffic flow to the site during execution of the programme, depending on circumstances.

The shafts and galleries of the MIU project will be excavated in the late Cretaceous Toki Granite. The Toki Granite has been faulted, and subjected to several episodes of uplift and subsidence in the Miocene to Pliocene, indicated by the lacustrine and marine sedimentary formations unconformably overlying the granite. The thickness of the sedimentary formations in this area is about 170 m.

The size and shape of shafts and galleries were determined based on considerations of efficiency and economics of excavation, the machinery and materials to be transported in the shafts and in the galleries and needed at the investigation sites. Figure 2 shows the layout of the MIU facility.

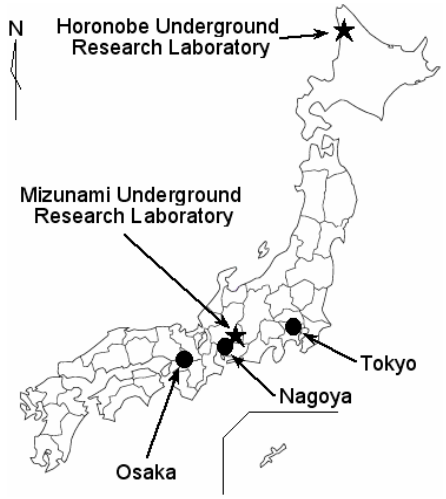

Fig. 1. Location of Underground Research Laboratories

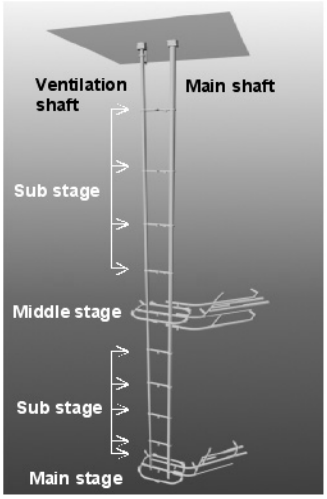

Fig. 2. Conceptual design of Mizunami URL.

One purpose of the MIU project is to confirm the technical reliability of the geological disposal methods, indicated by the Second Progress Report [5] mentioned above. An underlying design guideline is that the maximum depth likely for a disposal facility is 1000 m, in the case of hard rock. For this reason the target depth of geoscience research at the MIU is also 1000 m. Therefore, the MIU shafts will extend to 1000 m depth and research galleries will be constructed as deep as 1000 m, as specified in the Master Plan of the MIU Project [3].

2.2. Design of the MIU facility

Figure 3 shows the plan for surface facilities constructed for shaft excavation. Soundproof panels and materials will be used to enclose equipment at surface, especially the headframes and thus to control excessive noise from the construction and operational activities.

For the shafts, support system designs were based on the rock classification determined from core observation and determination of the physical and mechanical properties of the rock by analyses of core samples. The methodology is the same as the one used for design of highway and railway tunnels in Japan [6, 7]. Calculations using theoretical analysis were performed to check support stress intensity and normal strain of the rock. Therefore, 2-D FEM analysis was performed to understand mechanical stability of the rock and design the rock support requirements [8]. Standard cross-sections of the Main Shaft to illustrate the main design elements for different rock mass classifications are shown in Figure 4. The thickness of the

concrete liner is 40 cm for each shaft. In the case of CL and D rock mass classifications, H-section steel supports (125H) will be installed in the concrete liner. Steel liner plate will also be added in the case of E type rock.

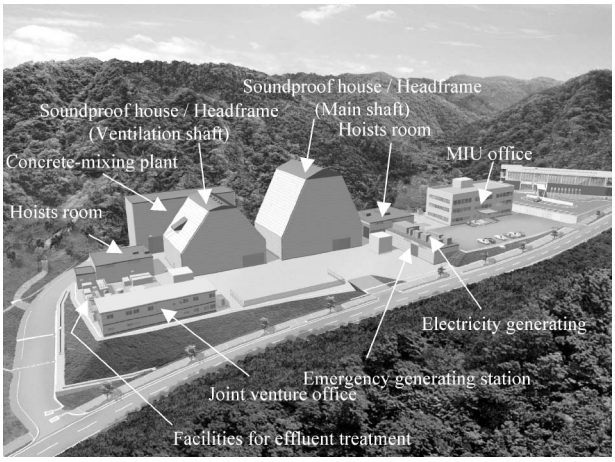

Fig. 3. Conceptual layout of surface facilities.

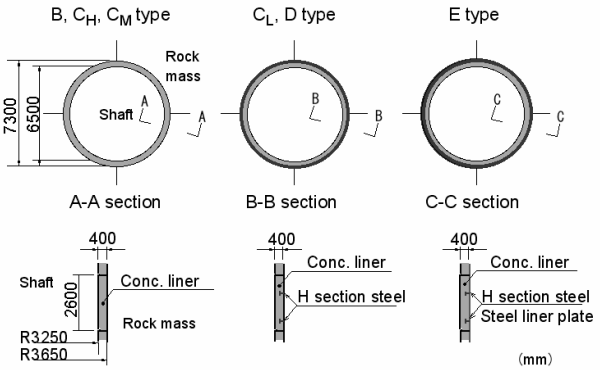

Fig. 4. Standard cross section of Main Shaft.

2.3. Construction plan

- Activities in the main parts of the shaft

Although there are several shaft excavation methods, basically they are grouped into blasting methods (long-step method, short-step method, NATM (New Austrian Tunneling Method), etc.), and mechanical excavation methods (Raise boring, free cross section excavation machines, etc.). The short-step method, performed over a single step (full face) with step length ranging approximately from 1.0 to 2.5 m was selected for rapid excavation and because of actual, proven application in many excavations with poor rock conditions in Japan. It was initially planned that drilling, blasting, mucking, and shaft lining would be carried out every cycle. However, because the ratio of mucking time to excavation cycle time will increase with depth, we adopted a 2 bucket mucking system, and 2 consecutive drill, blast and mucking steps (1.3 m + 1.3 m) and 1 shaft-lining step (2.6 m) per cycle to optimize cycle time for the excavations. There are three hours allotted for geoscience investigations, such as geological mapping, photography of shaft walls, etc., in the excavation cycle time.

- Measurement items

Convergence measurements and geological mapping of the excavation face are considered to be requirements for daily safety management. These will be performed during excavation of all galleries and intersections of shaft and galleries.

The following measurement items will be applied in typical geologic formations about every 50 m in the shafts. These measurements will also be performed in two sections in each gallery.

(a) Convergence measurements, rock mass displacement measurement
(b) Measurement of rock bolt axial stress
(c) Stress measurement of supports

The following measurements will be performed in each excavation cycle in the shafts and galleries and in the connections between the shafts and galleries.

(a) Photography of shaft walls by digital camera

(b) Geological mapping (geological features, rock mass classification, RMR, weathering, alteration, structure (type, geometry, strike and dip, filling materials in fractures and faults), seepage, etc.)
(c) Infrared thermograph of shaft walls using a digital camera
(d) Measurement of groundwater inflow rate and geochemical analysis of sampled water
(e) Groundwater sampling and measurement of physico-chemical parameters (Temp, pH, Eh, EC, DO), of seepage from shaft walls using water collection rings.

Measures to limit inflow of groundwater and mitigate rock bursts will be applied in the excavation of openings, especially in the deeper parts of the MIU. Analytical approach and in situ measurements have been performed to provide information of these phenomena.

3. NUMERICAL ANALYSIS

3.1. Models and code

- MBC model

The Micromechanics-Based Continuum (MBC) model, proposed by Yoshida and Horii [9], is based on a continuum theory for material whose properties are dominated by the presence or generation/growth of micro-structural elements. In order to represent a rock mass with many joints as an equivalent continuum, a representative volume element (RVE) is defined. Although the size of the RVE is much smaller than that of the analytical area, it is much larger than the micro-structural characteristics of jointed rock masses. In the RVE, the average stress and average strain are defined. The relationship between the stress and the strain in the RVE depends on the size, density and strike of joints included, which are the reason for any anisotropic behavior. In the analysis of excavation of rock with joints, opening/shear slippage will become the dominant mechanism of rock mass behavior. Though stress in the stress field will be released during excavation of a gallery, the stress field will continue compressing. In the MBC model, joints with undulations are modeled, in which opening of joints are represented by start of shear slippage when Coulomb's friction conditions are satisfied.

- Crack tensor model

Oda formulated an equivalent elastic stress-strain relation of jointed rock mass in terms of crack tensors [10]. In this formulation, the crack tensors, proposed by Oda, are symmetric, second- and fourth-rank tensors depending on density, orientation, and size of cracks, which are commonly observed in actual rock mass [11, 12]. In order to make the theoretical formulation simple, it is assumed that the crack can be replaced by a set of parallel plates connected by two elastic springs; i.e. normal and shear springs.

- FRACOD

A fracture propagation code, FRACOD, developed by FRACOM Ltd is a two-dimensional computer code that was designed to simulate fracture initiation and propagation in elastic and isotropic rock media. The code employs the Displacement Discontinuity Method (DDM) principles. It predicts the explicit fracturing process, including fracture sliding/opening, fracture initiation and fracture propagation in rock masses [13, 14].

3.2. Input parameters

- In situ stress

Hydraulic fracturing tests were performed to characterize in situ stress field in and around the site for construction of Mizunami Underground Research Laboratory using four 1000 m deep

vertical boreholes, three boreholes at the Shobasama site and one borehole at the MIU construction site [15]. Figures 5 shows the results of hydraulic fracturing tests in the vicinity and at the MIU construction site. The results shown in Figure 5 indicate that the stress magnitudes increase with depth. It is considered that the stresses are affected by small structures in the hanging wall of the Tsukiyoshi fault. Three zones are identified: 0 to 300 m, $\sigma H>\sigma h>\sigma v$; 300 to 700 m, $\sigma H>\sigma h=\sigma v$; 700 to 1000 m, $\sigma H>\sigma v>\sigma h$. In the hanging wall of the Tsukiyoshi fault, the in situ stress state may be different compared to stress in the footwall of the fault (800 to 1000 m: $\sigma v\geq\sigma H>\sigma h$). The results from Shobasama site shows the profiles of the in situ stress state determined by hydraulic fracturing tests in the MIZ-1 borehole. Stress decoupling observed at the Shobasama site is also observed at the MIU construction site. Two zones are identified: an upper zone (200 to 600 m), $\sigma H>\sigma h\geq\sigma v$ (reverse faulting state); and a lower zone (600 to 1000 m), $\sigma H\geq\sigma h>\sigma v$ (strike-slip faulting state).

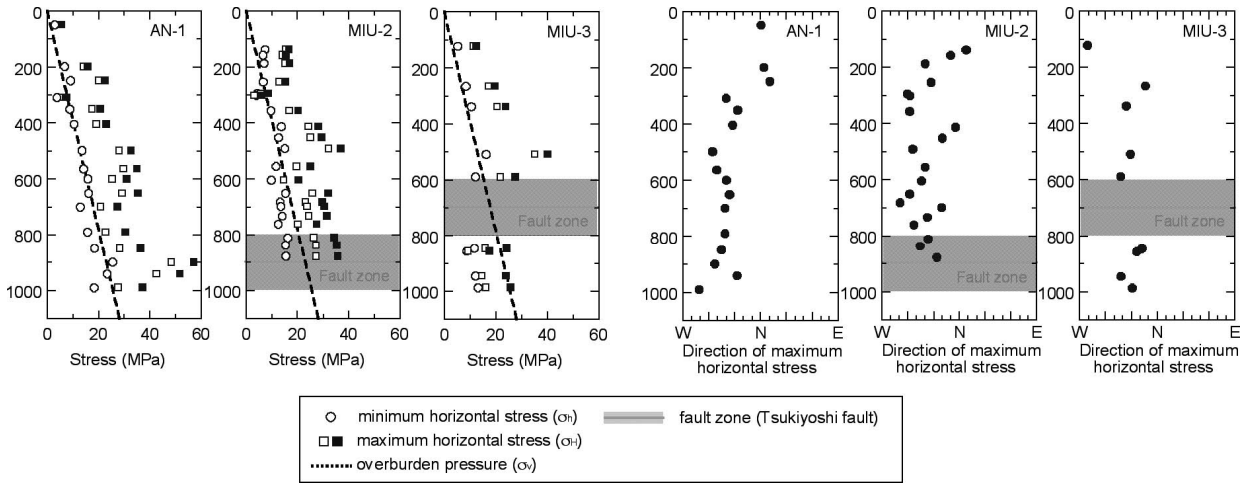

(a) Horizontal principal stresses (b) Direction of maximum horizontal stress

Fig. 5. Results of hydraulic fracturing tests near the construction site (Shobasama site).

Rock stress contours at the Shobasama site were determined based on 3D FEM analysis considering geological structures, including the large fault, known as the Tsukiyoshi fault [16]. The boundary conditions for the following analysis were set based on 3D FEM analysis. Input data for analysis at the MIU construction site was set directly based on the results of the hydraulic fracturing tests in the MIZ-1 borehole. Table 1 shows input parameters of the in situ stress used for analyses.

Table 1. Parameters of in situ stress

	Depth (m)	σhmin (MPa)	σhmax (MPa)	Drection of σhmax
Shobasama site	GL-200	17.9	15.0	N4W
	GL-500	25.0	14.3	N41W
	GL-945	21.2	1.4	N18W
MIU construction site	GL-500	11.7	21.3	N45W
	GL-1000	15.1	22.4	N45W

- Mechanical properties of rock

Young's modulus, Poisson's ratio, share strength and internal friction angle were determined based on the results of laboratory tests on core samples. In the case of analysis at the Shobasama site, input data on the properties of intact rock were 49.4 GPa, 0.34, 33 MPa and 33

degrees, respectively. The data for the fracture zone of the Tsukiyoshi fault, modeled as if it was intersected by the deeper part of Main shaft were 3.5 MPa, 0.36, 33 MPa, and 33 degree, respectively. At the MIU construction site, core samples were obtained to assess the rock mass classification. Input data for analysis were varied according to the expected rock mass classification at the target section of the shafts and galleries.

- Geometry and properties of joints

Parameters of joint include strike/dip, length, density (spacing), friction angle and dip angle are required for input in MBC model. Crack tensor was calculated from strike/dip and density of joint. These parameters are also needed for FRACOD analysis. These data come from borehole TV observations at the boreholes. Table 2 shows parameters of joint geometry for 2D analysis of MBC and FRACOD. Zone 1 - 4 in the granite are identified based on the results of hydraulic fracturing test. Joint sets are determined by stereo net for joints direction. Table 3 shows second- and fourth-rank crack tensor for 2D analysis for the Main shaft.

Table 2. Parameters of joint geometry for 2D analysis of MBC and FRACOD

	Parameters	Granite				Fault	
		Zone 1	Zone 2	Zone 3	Zone 4	Upper side of the Fault	Lower side of the Fault
Joint Set ①	Strike & Dip angle	N89E /4NW	N41E /75SE	N84E /62SE	NS /4E	N88W /84SW	N10E /19SE
	Distance (m) D	0.10	0.20	0.23	0.98	0.08	0.61
	Length (m) L	0.24	0.35	0.38	0.85	0.21	0.65
	Undulation angle (°)α	10°	10°	10°	10°	10°	10°
	Friction angle (°)φ	25.5°	25.5°	25.5°	25.5°	25.5°	25.5°
Joint Set ②	Strike & Dip angle		N87W /51NE	N85E /44NW	N47E /65SE	N59E /70SE	N65E /61NW
	Distance (m) D		0.30	0.43	0.15	0.25	0.15
	Length (m) L		0.44	0.54	0.30	0.40	0.30
	Undulation angle (°)α		10°	10°	10°	10°	10°
	Friction angle (°)φ		25.5°	25.5°	25.5°	25.5°	25.5°
Joint Set ③	Strike & Dip angle		NS /4E				N88W /84SW
	Distance (m) D		3.45				0.10
	Length (m) L		1.71				0.24
	Undulation angle (°)α		10°				10°
	Friction angle (°)φ		25.5°				25.5°

Table 3. Crack tensor for 2D analysis of the Main Shaft.

Crack tensor	Granite Zone 2 (GL-500m)	Fault Lower side of the Fault (GL-1000m)
$\begin{bmatrix} F_{11} & F_{12} \\ F_{21} & F_{22} \end{bmatrix}$	$\begin{bmatrix} 0.296 & -0.021 \\ -0.021 & 0.394 \end{bmatrix}$	$\begin{bmatrix} 0.293 & -0.073 \\ -0.073 & 0.307 \end{bmatrix}$
$\begin{bmatrix} F_{1111} & F_{1122} & F_{1112} \\ F_{2211} & F_{2222} & F_{2212} \\ F_{1211} & F_{1222} & F_{1212} \end{bmatrix}$	$\begin{bmatrix} 0.209 & 0.087 & -0.013 \\ 0.087 & 0.307 & -0.008 \\ -0.013 & -0.008 & 0.087 \end{bmatrix}$	$\begin{bmatrix} 0.217 & 0.076 & -0.031 \\ 0.076 & 0.231 & -0.042 \\ -0.031 & -0.042 & 0.076 \end{bmatrix}$

Joint properties, including normal stiffness and shear stiffness are needed for all models and analysis. Additionally, strength of joint and Mode I and Mode II toughness are necessary for FRACOD analysis. Mechanical properties of joints were determined based on the result of

joint shearing tests on core samples, including natural joints. Table 4 shows mechanical properties of the joints for FRACOD analysis. As the stress level of joint shearing tests are low compared to in situ stress state, normal and shear stiffness of joints are calculated from compressive strength (JCS), coefficient of roughness (JRC) and permanent friction angle. Input data of parameter depending on the shear stiffness of joint and parameter depending on the shear stiffness of joint for the crack tensor model are 16,000 MPa and 17,700 MPa in the Zone 2 at the 500 m depth and 10,500 MPa and 17,700 MPa in the lower side of the Tsukiyoshi fault, respectively.

Table 4. Parameters of joint properties for 2D analysis of FRACOD.

Fracture toughness	Mode I toughness K_{Ic} (MPa $m^{1/2}$)	1.73
	Mode II toughness K_{IIc} (MPa $m^{1/2}$)	3.07
Joint	Shear stiffness Ks (GPa/m)	1200
	Normal stiffness Kn (GPa/m)	3920
	Friction angle f_j (degree)	33
	Cohesion c (MPa)	33
	Dilation angle f_d (degree)	2
Fresh fracture	Shear stiffness Ks (GPa/m)	3099
	Normal stiffness Kn (GPa/m)	13800
	Friction angle f_j (degree)	33
	Cohesion c (MPa)	33
	Dilation angle f_d (degree)	2

- EDZ

An excavation disturbed zone is defined as the rock zone adjacent to the gallery that has been mechanically damaged directly by excavation. We define this zone as the Excavation Damaged Zone (EDZ). This zone is considered to be dependent on the excavation method, such as mechanical or blasting excavation [17]. So far, in-situ experiments on an EDZ induced by mechanical and blasting excavation have been carried out at Tono Mine and Kamaishi Mine [18]. The results, from seismic survey investigations, have shown that a low P-wave velocity layer is present in the walls adjacent to the excavations. This is interpreted to be the EDZ. The layer extends about 0.3 m into the walls of the gallery in the case of mechanical excavation and about 0.8 m in the case of blasting. Several cases considering an EDZ were analyzed using the MBC model and the Crack tensor model. The EDZ was defined along the periphery of the gallery, and the parameters were the width of the EDZ and joint density in the zone.

3.3. Mesh layout

The shaft and galleries are modeled as circular with an excavation diameter of 7.3 m and a hood shape of 3 m × 3 m, respectively. A 40 cm thick concrete liner is set in the shaft. Several cm to ten cm thick layers of shotcrete and rock bolting, according to the rock mass classification, are set in the gallery. A rock mass of 50 m × 50 m was modeled around the shaft and gallery by numerical analysis. An EDZ with a width of 80 cm and 30 cm was included adjacent to the shaft and gallery in the analysis using the MBC and Crack tensor models.

3.4. Result of analysis

Figures 6 to 8 show the comparison, illustrating the results for numerical analyses using the data from the Shobasama site, expressing distribution of rock mass displacement, fracture opening and local safety factor around the Main Shaft at a depth of about 500 m [16, 19]. The MBC model, the Crack tensor model and FRACOD analysis estimated maximum displacements of 2.8

mm, 5.1 mm and 2.8 mm, respectively, in the case without ground support. The modeling and analysis also indicated that it is likely that spalling will occur at 500 m depth. The principal direction of spalling will be NE and SW, and the depth of spalling would be less than 0.8 m into the shaft walls. It is also predicted that 80 % of the shaft walls may experience spalling or loosening of rock blocks with localized block falls.

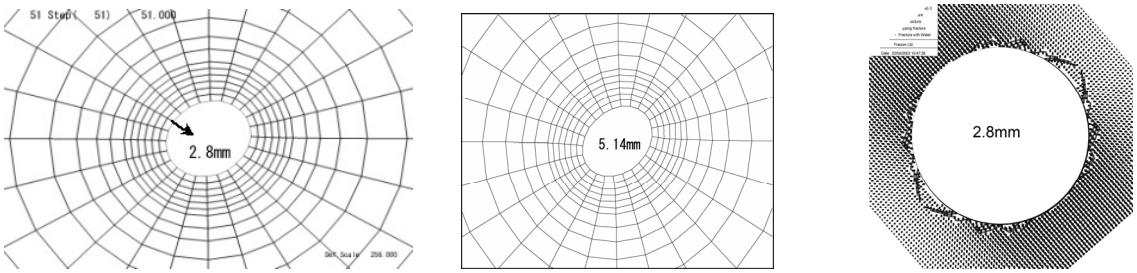

a) MBC model b) Crack tensor model c) FRACOD analysis

Fig. 6 Estimated distribution of rock mass displacement around the Main Shaft at a depth of about 500m.

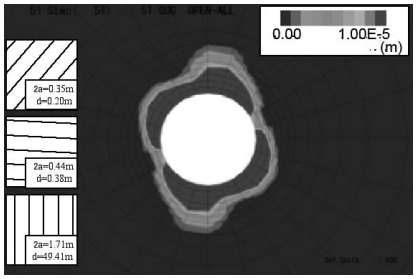

(No estimation)

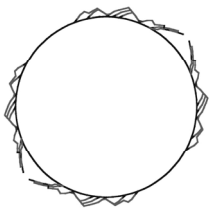

a) MBC model b) Crack tensor model c) FRACOD analysis

Fig. 7 Estimated development of fracture opening and distribution around the Main Shaft at a depth of about 500m.

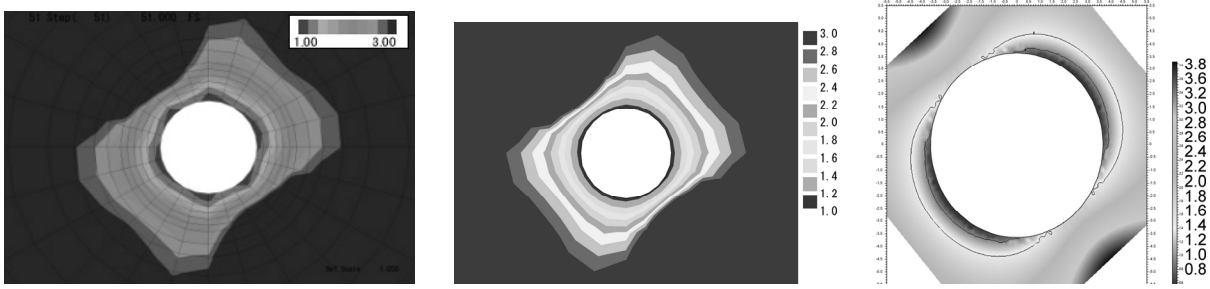

a) MBC model b) Crack tensor model c) FRACOD analysis

Fig. 8 Estimated development of local safety factor around the Main Shaft at a depth of about 500m.

Figures 9 - 11 shows the distribution of rock mass displacement, fracture opening and local safety factors around the Main shaft at a depth of about 1000 m in the fracture zone of the Tsukiyoshi fault [16, 19]. The MBC model, the Crack tensor model and FRACOD analysis estimated maximum displacements of 35.5 mm, 36.3 mm and 43.8 mm, respectively in the case an unsupported system, that is one without ground support. Large displacements were estimated due to the low elastic modulus of the fracture zone in the Tsukiyoshi fault. It is expected that the shaft at 945 m depth in the Tsukiyoshi fault would be unstable without support. A tensile failure zone would develop in the N18W and S18E directions and extend 3-4 m into the shaft wall. Tensile fractures and loose rock blocks are expected in the tensile failure zone. A spalling zone

oriented N72E and S72W will develop and may extend 0.8 m into the walls. Falls of large and small rock blocks are expected from the spalling zone. In addition, anisotropic rock properties from shearing along the fault might cause buckling and sheet loosening within the breakout zone.

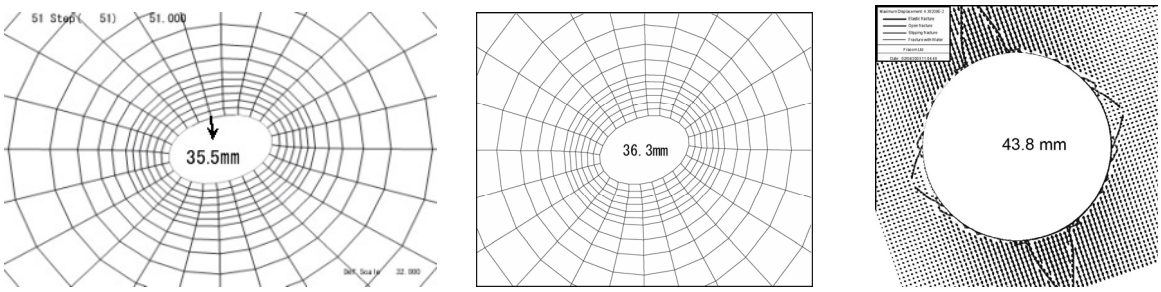

a) MBC model b) Crack tensor model c) FRACOD analysis

Fig. 9 Estimated distribution of rock mass displacement around the Main Shaft at a depth of about 1000m.

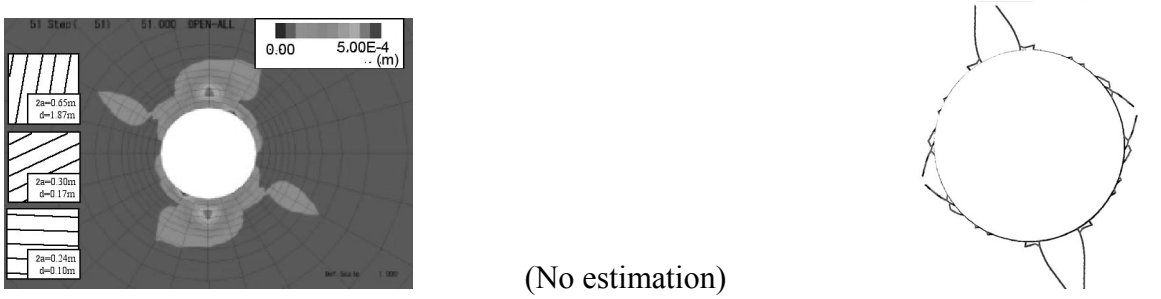

a) MBC model b) Crack tensor model c) FRACOD analysis

Fig. 10 Estimated development of joint opening and distribution around the Main Shaft at a depth of about 1000m.

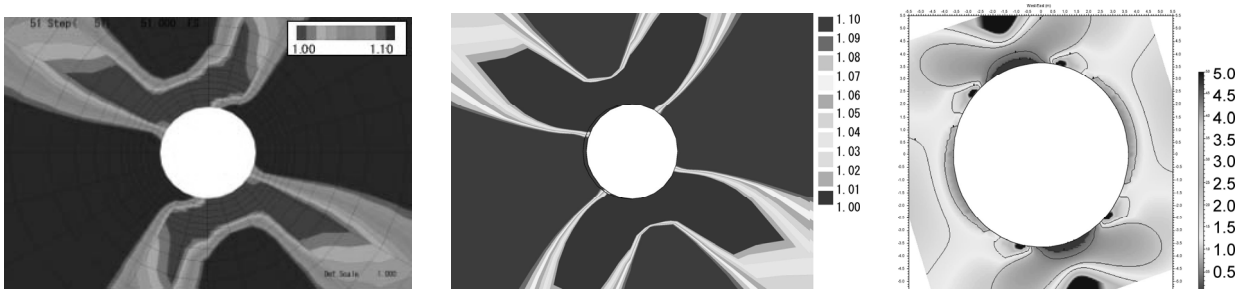

a) MBC model b) Crack tensor model c) FRACOD analysis

Fig. 11 Estimated development of local safety factor around the Main Shaft at a depth of about 1000m.

Maximum rock mass displacements, distribution of joints and safety factors estimated by the models and analysis are in good agreement in the case of intact rock at the depth of 500 m and for the fracture zone of the Tsukiyoshi fault at about 1000 m depth.

Excavation damage and development of an EDZ (Excavation Damaged Zone) was considered in the MBC model and Crack tensor model using Shobasama data at the depth of 500 m [16]. The EDZ models included the initiation of new joints and propagation of existing joints. The joints that are generated due to excavation were empirically assumed to develop tangentially to the gallery walls. Figure 12 shows the results of analysis using the MBC model considering an EDZ developed due to blasting. The results indicate that propagation of existing joints will play a fundamental role in the rock mass behavior due to excavation.

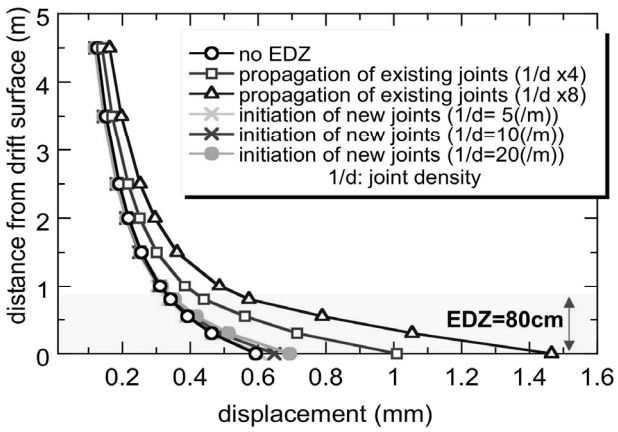

Fig. 12 Parametric analysis for EDZ using MBC model at the depth of 500 m depth.

4. SUMMARY

This paper describes the design and construction of the Mizunami Underground Research Laboratory for crystalline rock, and the predicted rock mass behavior adjacent to the deep underground openings using the MBC model, the Crack tensor model and FRACOD analysis.

Details of the design of shafts and galleries were determined, and the excavation plans, including geotechnical measurement to be performed during shaft sinking, are also described. By July 2003, the entrances to the shafts were constructed, and excavation of the lower part of the shaft entrances started in March 2004. The shafts reached 180 m depth in October 2005.

Numerical analysis using the MBC and Crack tensor models with data from the MIU construction site were performed in the Surface-based Investigation Phase of the MIU project to understand rock mass behavior due to excavation of shaft and gallery. The results of discontinuous analysis, FRACOD analysis agrees with that of continuous models despite the contrasting high and low elastic modulus of the rock. Almost all the results indicated that the joints modeled in these analyses play an important role for rock mass behavior due to excavation and safety of openings. The results of analysis will be compared to the geotechnical measurements in the shaft and galleries. Excavation disturbed zone experiments will also be performed in the Operation Phase in the MIU Project.

REFERENCES

1. Atomic Energy Commission, Japan. 2000. Long-Term Program for Research, Development and Utilization of Nuclear Energy (Unofficial Translation).
2. Nuclear Energy Agency / Organization for Economic Co-operation and Development. 2001. The Role of Underground Laboratories in Nuclear Waste Disposal Programmes.
3. Japan Nuclear Cycle Development Institute. 2001. Horonobe Underground Research Laboratory Project, Plan of surface-based Investigation. *JNC Technical Report, JNC TN1410 2001-001*.
4. Japan Nuclear Cycle Development Institute. 2002. Master Plan of the Mizunami Underground Research Laboratory Project. *JNC Technical Report*, *JNC TN7410 2003-001*.
5. Japan Nuclear Cycle Development Institute. 2000. Second Progress Report on Research and Development for the Geological Disposal of HLW in Japan, H12: Project to Establish

the Scientific and Technical Basis for HLW Disposal in Japan. *JNC Technical Report, JNC TN1410 2000-001 ~ 004*.

6. Japan Highway Public Corporation. 1998. Third-Volume Tunnel Construction Major Designing Points. 1998.10, in Japanese.
7. Japan Railway Construction Public Corporation. 1996. Design and Construction Guideline for NATM. *Japan Railway Construction Public Corporation*, 1996.3, in Japanese.
8. T. Sato, S. Mikake, M. Sakamaki, K. Aoki, S. Yamasaki, N. Shigeta and S. Takeda. 2003. Underground Research Laboratories in JAPAN – What are the Important Factors for Facilities Design. *Proceedings of ICEM'03: The 9th International Conference on Environmental Remediation and Radioactive Waste Management, Oxford, England, September 21-25, 2003*, ICEM03-4736. Rotterdam: Balkema.
9. Yoshida, H. and Horii, H., 2004. Micromechanics-based continuum model for a jointed rock mass and excavation analysis of a large-scale cavern, *Int. Jour. of Rock Mech. & Min. Science*, Vol.41, Issue 1, pp.119-145.
10. Oda, M. 1988. An experimental study of the elasticity of mylonite rock with random cracks. *International Journal of Rock Mechanics and Mining Science & Geomechanical Abstract*, Vol.25, No.2, pp.59-69.
11. Oda, M. 1983. A method for evaluating the effect of crack geometry on the mechanical behavior of cracked rock masses. *Mechanics of Materials*, 2, pp.163-171.
12. Oda, M. 1988. A method for evaluating the representative elementary volume based on joint survey of rock masses. *Canadian Geotechnical Journal*, Vol.25, pp.440-447.
13. Shen, B. and Stephansson, O., 1993. Modification of the G-criterion of crack propagation in compression. *Int. J. of Engineering Fracture Mechanics*. 47(2), pp.177-189.
14. Shen, B. 2002. FRACOD Version 1.1, User's manual. FRACOM Ltd.
15. Nakama, S., Sato, T. and Kato, H., 2005. Status of study on in-situ stress in the Mizunami Underground Research Laboratory Project, In *Proceedings of the 40th U.S. Rock Mechanics Symposium: Alaska Rocks 2005, Alaska, June 25-29, 2005*, eds. G. Chen et al, CD-ROM 05-887.
16. Mori, T., Iwano, K., Morikawa, S., Tabei, K., Nakama, S., Nakama, S. and Sato, T., 2004. Analysis of Deep Tunnel Excavation in Consideration of Joint Opening Phenomena, *Proceedings of the 3rd Asian Rock Mech. Symposium, 2004, 11/30-12/2, Kyoto Japan*, pp. 567-572.
17. Sato, T., Kikuchi, T. and Sugihara, K., 2000. In-situ experiment on excavation disturbed zone induced by mechanical excavation in Neogene sedimentary rock at Tono mine, central Japan, *Engineering Geology*, 56, pp. 97-108.
18. Sato, T., Matsui, H., Kikuchi, T., Sugihara, K. and Okubo, S., 1998. Seismic Velocity Structure of EDZ around the Drifts at the Kamaishi and Tono Mines in Japan, *Sci. Basis Nucl. Waste Manag*. XXI, pp.813-820.
19. Stephansson, O., Shen, B., Rinne, M., Backers, T., Koide, K., Nakama. S., Ishida, T., Moro, Y. and Amemiya, K., 2003. Geomechanical evaluation and analysis of research shafts and galleries in MIU Project, Japan. *Proceedings of the 1st Int. Symposium on Underground Environment, 3/17-18, 2003, Kyoto Japan*, pp.39-49.

Progressive shear band model for soil retaining wall problems

Septanika, E.G. and Brinkgreve, R.B.J.
Faculty of Civil Engineering and Geosciences, Delft University of Technology, The Netherlands
Plaxis BV, Delft, The Netherlands

ABSTRACT: Modeling of failure in geomaterials requires an adequate description of shear-banding phenomena. Discontinuous approach provides a tool that describes displacement jumps across a surface of failure in a proper way. However, the onset/propagation criterion and the orientation also play an important role towards a robust modeling of progressive growth of the shear band. The novelty of the present paper are: (i) the use of the gradient of incremental-displacement to determine the direction of discontinuity, and (ii) the onset/propagation criterion, i.e. the insertion of discontinuous displacement mode into the continuum element, is based on the average equivalent plastic strains. Moreover, for reliable predictions of the global peak and residual loading capacity a pressure-sensitive constitutive model has been considered. Discontinuous approach employing in this paper is according to the strong discontinuity approach in the context of the Partition of Unity (Extended Finite Element) Method (PUM/XFEM). The capability of the present approach is illustrated by considering smooth & rough soil retaining wall problems.

1. INTRODUCTION

The incorporation of discontinuous displacement mode into inelastic deformed continua provides a proper description of localized deformation phenomena, in which the failure zones are represented as a surface of zero thickness. In the so-called Strong Discontinuity (or Embedded Crack) Approach (SDA), displacement jumps are locally embedded without affecting neighboring elements (e.g. with a fixed crack formulation [1-5], with a rotating crack formulation [6,7]). Further, in the so-called Partition of Unity (or Extended Finite Element) Method (PUM/XFEM), displacement jumps are global degrees of freedom that can not be condensed out on the element level (e.g. based on linear elastic fracture mechanics [8], based on cohesive zone approach [9,10]).

As pointed out by e.g. Meschke and Dumstorff [11], once a discontinuity is inserted into an element the direction is held fixed for the rest of calculation. If the predicted direction is incorrect, severe locking may occur which possibly leads to unreasonable results (e.g. [12]). This paper employs the PUM/XFEM framework and technology as described in Wells and Sluys [9] as the point of departure. In contrast to the aforementioned papers, this paper uses the onset/propagation of shear band based on a threshold value of an equivalent plastic strain applied to the element touched by the shear band tip. To account for a more stable orientation of the shear band, the present approach utilizes the averaged gradient of incremental displacements instead of employing the (non-local) principal stresses. (Note: to remedy locking, Meschke and Dumstorff [11] applied a rotating crack concept in the context of the SDA approach, and the total potential energy criterion for the crack propagation). Moreover, in the present approach discrete shear band at the element level is treated as a special purposed interface element in which no double nodded is being used. In contrast to the classical double-noded interface approach in geomechanics, the constitutive behavior at the shear band is now governed by a traction-jump relation, instead of using a traction relative-displacement relation.

Special attention is first paid on the onset/propagation criterion and shear band orientation in Section 2. Then, a short description of discrete shear band model in the context of the PUM/XFEM is presented in Section 3. Finally, the capability of the present approach is illustrated in Section 4 by considering soil retaining wall problems.

2. ONSET/PROPAGATION & ORIENTATION

The Strong Discontinuity Approach (SDA) and the Partition of Unity Method (PUM/XFEM) provide an efficient and effective tool for describing localization/discontinuity phenomena in inelastic deformed continua. However, for a successful analysis the initiation and propagation of localization/discontinuity (a so-called onset/propagation criterion) also play an important role. As described by Ortiz *et al.* [13], in a non-homogeneous situation the acoustic tensor **A** may strongly vary inside an element. Motivated by the previous work of Ortiz *et al.*, the present paper considers an onset/propagation criterion in an "average" sense.

2.1. Onset/propagation criterion

In a homogeneous stress-strain situation, the inception of a shear band into inelastic deformed continuum elements can be simply according the vanishing of the determinant of the acoustic tensor (e.g. [14]). For a general non-homogenous situation the initiation is however very crucial, since the further growth of localized zone will depend on the state of stress-strain at the onset moment and on the initial orientation of the shear band. The initiation can be done by means of:

- introducing a small crack or defect zone in the finite element mesh (e.g. [11]),
- the acoustic tensor criterion, applied to the element touched by a trigger point (e.g. [9]).

Next, the propagation criterion which determines the further growth of the localized zone during the loading progress can be categorized into:

- a local material instability criterion, e.g. based on det(**A**)=0 criterion at the element center [13], based on an average stress criterion [9],
- a global instability criterion, e.g. based on a linear elastic fracture mechanics approach [10,15], based on the maximum total potential energy criterion [11].

In contrast to [9-11,13,15], for both initiation and propagation the present paper employs a global instability criterion based on an average equivalent plastic strain γ_{eq}^{p}. A discrete shear band is inserted element-wisely as soon as γ_{eq}^{p} exceeds a certain threshold value. The orientation of the shear band is based on the gradient of incremental displacements as described below.

2.2. Orientation of the shear band

Based on a global criterion, the resulting direction of shear band is no longer the local bifurcation direction. Instead, it can be thought of as an approximation of the general trend towards further localization & failure. For the present gradient approach, an incremental displacement function $\Delta V \equiv \Delta V(\mathbf{x})$ is first generated based on the nodal solutions $\{\mathbf{\Delta V_i}\}$. The Gaussian value at (ξ,η,ζ) is then interpolated using the element shape function matrix **N**, i.e.

$$\Delta V(\xi,\eta,\zeta) = \mathbf{N}\ \{\mathbf{\Delta V_i}\} \tag{1}$$

Next, the gradient simply follows from the derivatives of ΔV with respect to the spatial coordinates. To obtain more reliable information for the initial orientation, the incremental displacements around the tip have been averaged using a Gaussian weight function

$$w = \frac{1}{(2\pi)^{3/2} l^3} \exp\left(-\frac{r^2}{2l^2}\right) \tag{2}$$

where w is the weight function, r is the distance from the tip, and l determines how fast the weight function decays from the tip. For the propagation direction, one can simply use the local incremental displacement gradient based on the element in front of the tip.

3. BACKGROUND OF THE EMPLOYED DISCONTINUOUS APPROACH

3.1 Kinematics of discontinuous field & Finite element formulation

The point of departure is the PUM/XFEM as described in e.g. [9]. For the damaged elements the nodal displacements **u** and the strains **ε** can be expressed as

$$\mathbf{u} = \mathbf{Na} + \mathcal{H}_\Gamma(\mathbf{x})\mathbf{Nb} \tag{3}$$

$$\boldsymbol{\varepsilon} = \nabla^s \mathbf{u} = \mathbf{Ba} + \mathcal{H}_\Gamma(\mathbf{x})\mathbf{Bb} + \delta_\Gamma(\mathbf{x})(\mathbf{RN})\mathbf{b} \quad \text{with} \quad \mathbf{B} = \nabla^s \mathbf{N} \tag{4}$$

where **N** is a shape function matrix, **a** and **b** represent the regular nodal displacements and the enhanced displacements (jumps), $\mathcal{H}_\Gamma$ is the Heaviside function and δ_Γ is the Dirac-delta distribution centred at the failure surface. **R** is a matrix containing the components of the normal vector **n**.

The finite element formulation is derived by employing two separate weak equations [9]. Using discrete formulations of displacements & strains, the discrete weak equations can be expressed as

$$\int_\Omega \mathbf{B}^T \boldsymbol{\sigma}\, d\Omega = \int_{\Gamma_u} \mathbf{N}^T \mathbf{t}_u\, d\Gamma \quad \& \quad \int_{\Omega^+} \mathbf{B}^T \boldsymbol{\sigma}\, d\Omega + \int_{\Gamma_d} \mathbf{N}^T \mathbf{t}\, d\Gamma = \int_{\Gamma_u} \mathcal{H}_{\Gamma_d}\, \mathbf{N}^T \mathbf{t}_u\, d\Gamma \tag{5}$$

where $\boldsymbol{\sigma}$ is the Cauchy stress tensor in a vector notation, $\mathbf{t}_u$ is external traction forces along the boundary Γ_u and **t** is the tractions at discontinuity Γ_d. Assuming drained behavior (no pore water pressure change), the stress rate $\dot{\boldsymbol{\sigma}}$ and the traction rate $\dot{\mathbf{t}}$ can be expressed in terms of the rate of regular nodal displacements and the rate of jumps. After substitutions of the rate equations into the above discretised weak equations and linearization, one arrives at an incremental-iterative finite element formulation (for more detail please refer to [9]).

3.2 Elasto-plastic model for intact soil & discontinuity

A general governing equation for the intact soil & for discontinuity can be formulated as

$$\dot{\boldsymbol{\sigma}} = \mathbf{D}^e (\dot{\boldsymbol{\varepsilon}} - \dot{\boldsymbol{\varepsilon}}^p), \quad \dot{\boldsymbol{\varepsilon}}^p = \dot{\lambda} \frac{\partial g}{\partial \boldsymbol{\sigma}}, \quad f = f(\boldsymbol{\sigma}, q) \le 0, \quad \dot{\lambda} \ge 0, \quad \dot{\lambda} f = 0, \quad \dot{\lambda} \dot{f} = 0 \tag{6}$$

$$\dot{\mathbf{t}} = \mathbf{T}^e (\dot{\mathbf{b}}_\Gamma - \dot{\mathbf{b}}_\Gamma^p), \quad \dot{\mathbf{b}}_\Gamma^p = \dot{\lambda}_\Gamma \frac{\partial \mu}{\partial \mathbf{t}}, \quad \phi = \phi(\mathbf{t}, \kappa) \le 0, \quad \dot{\lambda}_\Gamma \ge 0, \quad \dot{\lambda}_\Gamma \phi = 0, \quad \dot{\lambda}_\Gamma \dot{\phi} = 0 \tag{7}$$

where: $\dot{\boldsymbol{\varepsilon}}$ and $\dot{\boldsymbol{\varepsilon}}^p$ are the strain rate and the plastic part of the strain rate, $\dot{\lambda}$ is the rate of plastic multiplier, f and g are the yield function and the plastic potential function, q is an internal

variable to accommodate e.g. hardening behavior; $\mathbf{D}^e$ is the elastic stiffness tensor, $\mathbf{T}^e$ represents the pseudo stiffness matrix of the interface, $\mathbf{b}^p$ represents the "plastic part" of the jump, $\mathbf{b}_\Gamma$ represents the total jump, $\dot{\lambda}_\Gamma$ is the rate of plastic multiplier at discontinuity, ϕ and μ are the discrete yield function and the plastic potential function of discontinuity, κ is an internal variable related to e.g. the state of sliding/cracking at discontinuity. By applying the consistency condition $\dot{\phi}=0$, the plastic multiplier $\dot{\lambda}_\Gamma$ can now be computed as

$$\dot{\phi} = \left(\frac{\partial \phi}{\partial \mathbf{t}}\right)^T \dot{\mathbf{t}} + \frac{\partial \phi}{\partial \kappa}\dot{\kappa} = 0, \quad \dot{\kappa} \equiv \dot{\lambda}_\Gamma \mathrm{H}(\mathbf{t}), \quad \dot{\lambda}_\Gamma = \frac{\left(\frac{\partial \phi}{\partial \mathbf{t}}\right)^T \boldsymbol{D}^e \dot{\mathbf{b}}}{h + \left(\frac{\partial \phi}{\partial \mathbf{t}}\right)^T \boldsymbol{D}^e \frac{\partial \Psi}{\partial \mathbf{t}}}, \quad h = \frac{\partial \phi}{\partial \kappa}\mathrm{H}(\mathbf{t}) \tag{8}$$

3.3 Initial stresses

To account for the gravity loading and lateral stresses, the initial stresses are determined using the standard K0-procedure (eventually including water effects as defined in a phreatic table). In the present implementation the undrained behavior at discontinuity is not yet included, so the pore pressures are kept constant. Further, when using more advanced soil models an initial pre-consolidation state has to be determined to define the initial position of the cap yield surface. If the material is over-consolidated the information over the Over-Consolidation Ratio (OCR), the Pre-Overburden Pressure (POP) and the stress ratio in the normally consolidated state $K0^{NC}$ are also required to define the proper initial state in the soil at the onset/propagation of discontinuity.

4. NUMERICAL EXAMPLE

The present approach has been implemented into the PLAXIS Finite Element Code for Soil and Rock Analyses. For illustration purposes, the present approach has been applied to describe Mode-II failure in 2D case by employing the elastic perfectly-plastic Mohr-Coulomb soil. The analysis is performed using 6-noded triangular elements (Note: in a similar retaining wall problem Constant Strain Triangular (CST) elements are used [16,17]). Based on the discrete Mohr-Coulomb formulation, the following simplified relation can be derived (with k_n & k_s are the pseudo stiffness at discontinuity, φ_i is the frictional angle at discontinuity & h is the softening modulus) governing the traction-jump relation at the shear band

$$\begin{Bmatrix} \dot{t}_n \\ \dot{t}_s \end{Bmatrix} = \begin{bmatrix} \mathrm{k_n} & 0 \\ -\mathrm{k_n}\tan\varphi_\mathrm{i} & -\mathrm{h} \end{bmatrix} \begin{Bmatrix} \dot{b}_n \\ \dot{b}_s \end{Bmatrix} \tag{9}$$

Note: (i) this simplified relation also satisfies the consistency condition $\dot{\phi}=0$, and (ii) for non-frictional material $\varphi_i=0$, it simply leads to $\Delta \dot{t}_n = k_n \Delta \mathrm{b_n}$ and $\Delta \dot{t}_s = -h \Delta \mathrm{b}_s$.

Next, the present example considers a soil retaining wall problem taking into account for initial stresses from the gravity loading and K0-procedure. In the passive wall case, the wall is pushed into the soil. In this non-uniform stress field, localization in the continuum takes place progressively starting from the most critically stressed points and propagating in the direction favoring material bifurcations (e.g. see also [16,17]).

(i) Pre-peak situation

During the loading progress: plastic regions, principal stresses, & incremental displacements are monitored and shown in Fig.1(a)-1(c). The initial principal stresses due to gravity loading and K0 coincide with the vertical and horizontal axis. Due to a small prescribed displacement at the right edge (pushing the wall into the soil) the first plastic region is found at the toe of the wall, while the principal stresses are slightly rotated as shown in the Fig.1(a). Further increase of the prescribed displacement leads to a further growth of the plastic region and further rotation of the principal stresses. On the other hand the incremental displacement plot is showing two distinct regions in which incremental displacement on the right upper wedge starts to dominate the global deformation picture (a hint for the possible sliding mechanism) as shown in Fig.1(b). Around the peak load, plastic zone around the shear band has been completely formed. Moreover, a very clear sliding mechanism is shown by the incremental displacements plot in Fig.1(c) - while from the principal stresses plot neither the localization nor the direction is clearly shown. This also shows the ability of incremental displacements for detecting the failure mechanism in the present case.

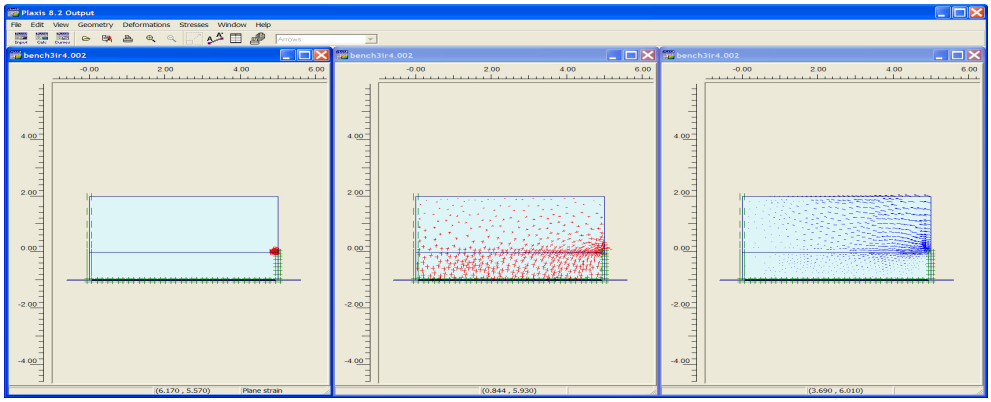

Fig.1(a). Plastic region, principal stresses and incremental displacements plot at the onset of the plasticity around the toe of the wall.

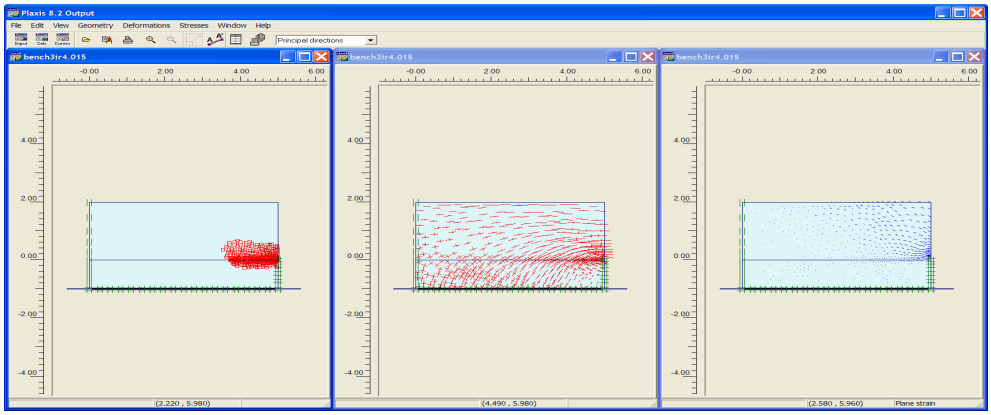

Fig.1(b). Plastic region, principal stresses and incremental displacements plot at about 50% of the peak load.

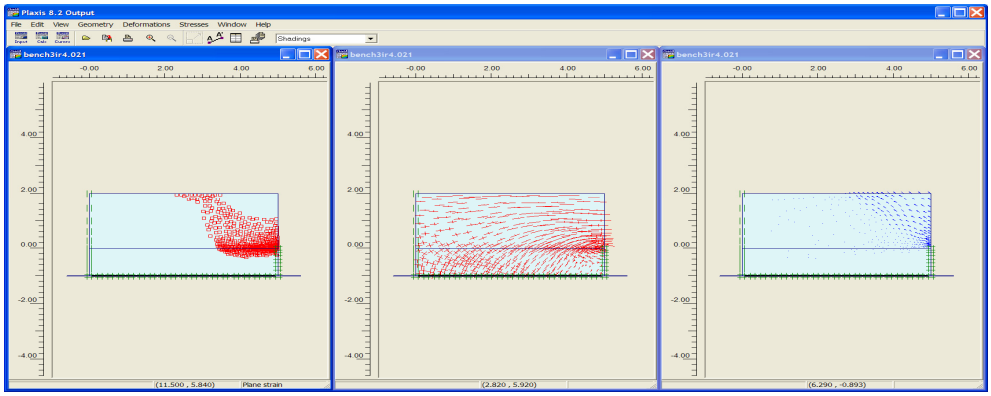

Fig.1(c). Plastic region, principal stresses and incremental displacements plot around the peak load.

(ii) Simulation of passive retaining wall test

Using the previous pre-peak investigation, the formation and the growth of the shear band in a passive wall test is now simulated. The orientation of the shear band at the toe is computed at the end of each (converged) iteration. The orientation according to the gradient approach changes with the increase of γ_{eq}^{p} - until it reaches a "stable" value (i.e. being characterized as a threshold value for γ_{eq}^{p}). The first shear band is inserted in the toe element as soon as the orientation has reached its stable value. Further, the propagation of the shear band for the next element (in front of the tip) is based on a slightly lower threshold value. The force-displacement curve in the present passive smooth retaining wall problem is shown in Fig.2, and the deformed mesh is shown in Fig.3.

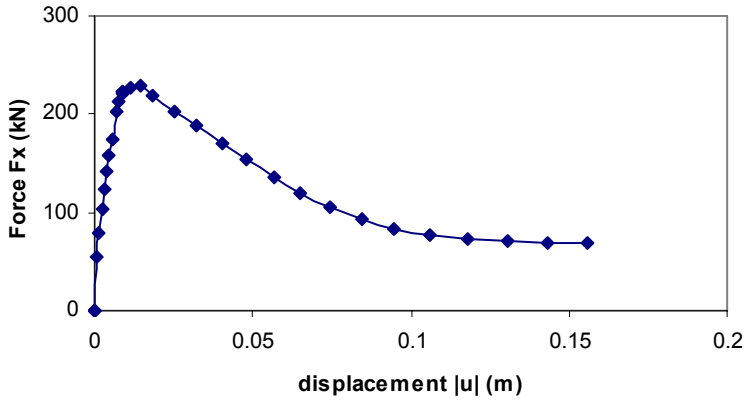

Fig.2. Force-displacement in passive wall test (c=30 kPa, φ=20°, γ = 16 kN/m^3, wedge depth is 2m); F_x at peak ≈ 230 kN, F_x residual (at c = 0) ≈ 70 kN.

(a) (b)

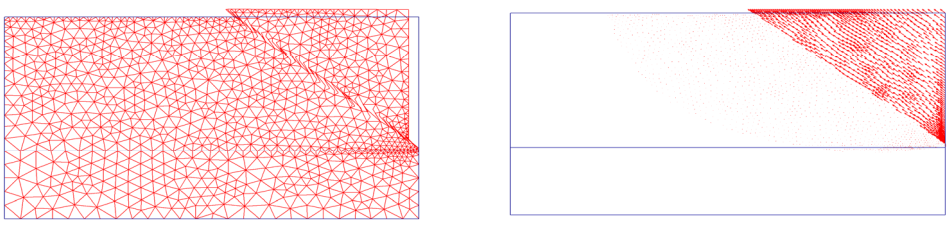

Fig.3. (a) Deformed mesh, (b) Displacement plot/sliding mechanism.

The wedge solutions can be approximated as: F_x at peak (c maximum) ~ 236 kN, F_x residual (when c = 0) ~ 66 kN & the wedge inclination is $\theta^p_{wedge} = \pi/4 - \varphi/2 = 35^o$. According to the present gradient approach: $\theta^p_{wedge} \sim 37^o$ with respect to the horizontal axis. It can be seen that the overall load-displacement behavior in Fig.2 is (qualitatively) in agreement with the classical wedge solution. Since the slip-line around the toe is not exactly straight, the differences with respect to the wedge solution are reasonable. Further, the capability of the present onset/propagation and direction approach has also been evaluated in the so-called rough passive wall case (Fig.4). In contrast, the rough wall case predicts a curved (discrete) shear band, i.e. due to the fixed vertical movement at the wall. The accuracy of the present approach has also been investigated and compared to a non-local continuum approach, as reported in Vermeer *et al.* [18]

(a) (b)

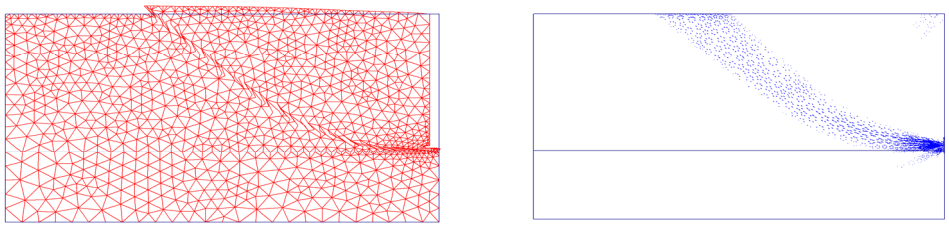

Fig.4. (a) Deformed mesh, (b) Shear band orientation based on the gradient of incremental displacements.

5. CONCLUSIONS

An application of discrete shear band approach in the context of the PUM/XFEM has been presented. This type of discrete shear band can be inserted across the soil elements in a mesh-independent manner, during the progress of analysis. To remedy locking, the onset/propagation has been based on an equivalent plastic shear strain threshold - at which the orientation has reached its stable value. The onset direction is based on the non-local averaged gradient of displacement increments, while the propagation direction on the local gradient of incremental displacements. The capability of the present discrete shear band model has been demonstrated by considering shear band initiation and propagation in soil retaining wall problems. The corresponding global peak and residual load have been compared to the classical wedge solution. Moreover, the present approach is also capable of simulating the initiation & propagation of a curved shear band path in a passive rough wall problem. More works will be performed in the future to further evaluate the capability of the present approach, for describing localization & failure phenomena in geomaterials.

REFERENCES

1. Simo J.C., Oliver J. and Armero F. 1993. An analysis of strong discontinuous induced by strain-softening in rate-independent inelastic solids. *Comput. Mech.* 12:277-296.
2. Armero F. and Garikipati K. 1996. An analysis of strong discontinuities in multiplicative finite strain plasticity and their relation with the numerical simulation of strain localization in solids. *Int. J. Sol. Struct.* 33(20):2863-2885.
3. Oliver J., Cervera M. and Manzoli O. 1999. Strong discontinuities and continuum plasticity models: the strong discontinuity approach. *Int. J. Plast*. 15(3):319-351.

4. Regueiro R.A. and Borja R.I. 1999. A finite element method of localized deformation in frictional materials taking a strong discontinuity approach. *Fin. Elem. Anal. Des.* 33:283-315.
5. Jirasek M. and Zimmermann T. 2001. Embedded crack model: Part 1: Basic formulation, Part 2: Combination with smeared cracks. *Int. J. Num. Meth. Eng.* 50:1269-1305.
6. Mosler J. and Meschke G. 2003. 3D modeling of strong discontinuities in elastoplastic solids: Fixed and rotating localization formulations. *Int. J. Num. Meth. Eng.* 57:1553-1576.
7. Mosler J. and Meschke G. 2004. Embedded cracks vs. smeared crack models: A comparison of elementwise discontinuous crack path approaches with emphasis on mesh bias. *Comput. Meth. Appl. Mech. Eng.* 193:3351-3375. (Spec. issue on Computational Failure Mechanics).
8. Moes N., Dolbow J. and Belytschko T. 1999. A finite element method for crack growth without remeshing. *Int. J. Num. Meth. Eng.* 46:131-150.
9. Wells G.N. and Sluys L.J. 2001. A new method for modeling cohesive cracks using finite elements. *Int. J. Num. Meth. Eng.* 50(12):2667-2682.
10. Moes N. and Belytschko T. 2002. Extended finite element method for cohesive crack growth. *Eng. Fract. Mech.* 69:813-833.
11. Mesche G. and Dumstorff P. 2004. Discontinuous representation of brittle failure. *Proceedings of 2nd International Symposium on Continuous and Discontinuous Modeling of Cohesive Frictional Materials* 2004, Stuttgart. 339-352.
12. Simone A., Askes H. and Sluys L.J. 2004. Incorrect initiation and propagation of failure in non-local and gradient-enhanced media. *Int. J. Sol. Struct.* 41:351-363.
13. Ortiz M., Leroy Y. and Needleman A. 1987. A finite element method for localized failure analysis. *Comput. Meth. Appl. Mech. Eng.* 61:189-214.
14. Rudnicki J.W. and Rice J.R. 1975. Conditions for the localization of deformation in pressure sensitive dilatant materials. *J. Mech. Phys. Solids*. 23:371-394.
15. Zi G. and Belytschko T. 2003. New crack-tip elements for X-FEM and applications to cohesive cracks. *Int. J. Num. Meth. Eng.* 57: 2221-2240.
16. Borja R.I. and Lai T.Y. 2002. Propagation of Localization Instability under Active and Passive Loading. *J. Geotech. Geoenv. Eng.* 128(1):64-75.
17. Regueiro R.A. and Borja R.I. 2001. Plane strain finite element analysis of pressure sensitive plasticity with strong discontinuity. *Int. J. Sol. Struct.* 38:3647-3672.
18. Vermeer P.A., Vogler U., Septanika E.G. and Stelzer O. 2004. A strong discontinuity method without locking. *Proceedings of 2nd International Symposium on Continuous and Discontinuous Modeling of Cohesive Frictional Materials* 2004, Stuttgart. 381-396.

Foundation Stability Analysis of Anchor Dam

Kottenstette, J. T.
US Bureau of Reclamation, Denver, Colorado, USA

This paper was prepared for presentation at *ICADD-7, the Seventh International Conference on Analysis of Discontinuous Deformation*, held in Honolulu, Hawaii, December 10-12, 2005.

ABSTRACT: The Anchor Dam reservoir basin is located in cavernous marine sediments. These sediments are folded, faulted, and solutioned such that reservoir water exits through sinkholes at rates ranging from 300 to 2000 ft^3/s. However, during extreme flooding, the reservoir could fill quickly and in an uncontrolled manner for the first time. Historically, concrete arch dam failures have occurred most often during first filling as a result of foundation deficiencies. This dam is founded on hard sandstone with well-defined continuous bedding plane partings and joints that form blocks within the abutments. These foundation and hydrologic conditions could create significant risks to the downstream public. This paper examines the foundation stability in the event of a rapid uncontrolled first filling that could occur during extreme flooding. Loading conditions include the weight of the blocks, water forces on foundation block planes, and structural foundation loads generated by the dam and reservoir.

1. INTRODUCTION

The Bureau of Reclamation (Reclamation) owns a significant number of large concrete dams, and these structures are continually being evaluated through our Dam Safety Program. This paper reviews the approach used to evaluate the foundation stability for Anchor Dam.

Anchor Dam, located on the South Fork of Owl Creek approximately 40 miles west of Thermopolis, Wyoming, is a constant-radius concrete arch dam with a structural height of 208 feet, a hydraulic height of 146 feet, and a crest length of 660 feet. The spillway is an uncontrolled, ogee-crested overflow weir notched in the central part of the dam with a crest elevation of 6441 and a crest length of 100 feet. The outlet works consists of two 30-inch-diameter conduits through the dam at an elevation of 6345 feet adjacent to the left end of the spillway [1]. The foundation does not include a drainage curtain, which is a unique condition relative to other Reclamation dams.

The most distinctive feature of Anchor Dam is the extensive system of sinkholes that exist throughout the floor of the reservoir. During construction of the dam, several deep solution cavities were discovered in the foundation immediately upstream of the dam, and several sinkholes were found in the reservoir area. The solution cavities were excavated, cleaned out, and backfilled with concrete and grout. The sinkholes were filled with impervious material. However, when the reservoir was first filled in 1961, many additional and larger sinkholes developed that drained the reservoir into the deep regional groundwater table more than 1000 feet below the existing river channel. Over the following years, numerous attempts were made to investigate, fill, treat, and isolate the sinkholes by constructing dikes within the reservoir to minimize further reservoir losses, but these efforts showed limited success. The reservoir still has not filled to capacity, and any water temporarily stored behind the dam drains away. The dam is currently operated to provide flood control and to extend the irrigation season with what water can be stored.

1.1. Background

Preconstruction, the geological and geotechnical investigations for Anchor Dam (1957-1960) did not evaluate potentially unstable foundation blocks. The construction reports and maps were focused more directly on evaluating and controlling seepage under the dam, bedrock permeability, and development of monitoring criteria for the grouting program. In the 1950s, geotechnical analysis typically did not include identification of potentially removable foundation blocks as failure modes.

After construction, investigations focused on seepage issues in the reservoir. The Dam Safety Engineering Geologic Report for Anchor Dam [2] and the Geologic/Geotechnical Engineering Technical Memorandum [3] focused on seepage in the reservoir and did not evaluate the stability of the foundation relative to the geologic structure and the potential for this structure to create unstable foundation blocks. Neither of these investigations evaluated the potential for unstable foundation blocks resulting from increases in uplift pressures and arch thrusts caused by rapid first filling during extreme flooding. However, the geologic structure of Anchor Dam, in conjunction with the topography, relatively shallow excavation trench, and the lack of foundation drains, creates potentially unstable foundation blocks. The bottom of the excavation is coincident with the large bedding plane exposure in the upper part of the left abutment (looking downstream) as shown in Fig. 1. [1]. Thus, Reclamation's Dam Safety Office funded this investigation to improve our understanding of the potential risks for, and reduce our uncertainty relative to, the foundation stability of Anchor Dam.

1.2. Scope

This paper describes the detailed foundation analysis of the left abutment of Anchor Dam, with particular focus on foundation stability during extreme flood loadings. The geologic characterizations are limited to data directly influencing the formation of the foundations block. Data on the regional geology and other site conditions are not included due to the length limitation for the paper and the focus on block analysis methods. Anchor Dam has no dynamic stability issues due the inability of the reservoir to retain water. A brief description of Reclamation's approach to dynamic stability is provided, though no such analysis was conducted for Anchor Dam.

The following procedures are required to complete a detailed foundation analysis.

(xxii) Characterize the rock foundation with particular attention to the rock structure and the potential for conditions to promote development of unstable foundation blocks.
- **(a)** Map and survey discontinuities in the rock structure that form foundation blocks.
- (b) Define the orientation and location of block-forming features (for Anchor Dam joint sets A and B, and bedding).
- (c) Estimate continuity of block-forming features.
- (d) Estimate the shear strength for possible slide planes.

(xxiii) Define foundation loads for the blocks.
- **(a)** Static structural loads (in the case of Anchor Dam, these are the forces from the arch dam including gravity, reservoir, and temperature loads).
- **(b)** Water forces on foundation block planes generated by the reservoir.
- **(c)** Foundation block weights.
- (d) Dynamic earthquake structural and foundation loads (these were not needed at Anchor Dam).

(xxiv) Analyze foundation stability.
- (a) Calculate the static limit equilibrium safety factor.

(b) Estimate foundation block displacements for earthquake loads (this step was not needed for Anchor Dam).

2. ROCK STUCTURE

Discontinuities in the rock mass structure control the foundation stability of concrete dams. A review of the geologic data (historical geologic reports, geologic mapping, foundation mapping, and original construction photographs) and a site visit were performed in July of 2004. A preliminary foundation evaluation indicated that a more detailed evaluation of specific features was warranted. A second field trip was completed in August of 2005. This trip provided additional traditional geologic and photogrammetric surveys of the abutment topography and geologic discontinuities.

The dam is founded on Tensleep sandstone, which consists of fine- to medium-grained, hard, slightly weathered sandstone. This unit forms high cliffs around the dam, and has two well defined joint sets and a set of bedding plane partings. This geologic structure is visible from great distances. The sandstone beds vary in thickness from thin beds (less than 1 foot thick) to massive beds (no bedding plane partings for 50 feet) with local discontinuous cross-bedding in the mass. The bedding dips approximately 35 degrees to the southwest (upstream and into the right abutment) nearly parallel to the excavation cut of the left abutment. Local 5- to 10-foot thick beds of interbedded dolomite are present. Tensleep sandstone is resistant to erosion, but it is highly permeable due to closely spaced open joint and solution cavities in the dolomite interbeds. "During construction, several solution cavities were discovered and backfilled with concrete. The foundation was pressure grouted to reduce seepage. A syncline within the reservoir area along with high angle reverse faults has created the joint sets in the abutments. The beds are overturned and the fracture system is very well developed. The reservoir floor is very cavernous and the reservoir is unable to hold water" [4].

Three dolomite beds were exposed during foundation excavation. The lowest of the dolomite beds, beneath the central part of the dam, contained solution cavities and solution breccia consisting of sandstone and dolomite rubble. The rubble was cleaned out and the cavities were backfilled with 2,000 cubic yards of concrete. A second dolomite bed is on the right side of the foundation, and the top of this bed is at an elevation of 6395 feet. It contained solution cavities that were also backfilled with concrete. A third dolomite bed is located in the foundation at about an elevation of 6440 feet, but no solution cavities were observed in this bed [1].

2.1. Mapping Rock Structure Discontinuities

The foundation rock under Anchor Dam was characterized in terms of the discontinuity structure controlling the block geometry under the dam and in the abutments. Existing geological data provided orientation data on the three dominant block-forming discontinuities, joint sets A, B, and C (bedding). Prominent features of these sets were located on the construction geology foundation maps.

Potentially removable foundation blocks require significant continuity in the bounding planes, such that the blocks are formed without significant bridges of solid rock crossing block boundaries. The August 2005 geologic mapping effort helped tie the downstream abutment data to the existing foundation maps, which did not extend downstream any significant distance. The August 2005 effort focused on defining specific block boundaries (both location and orientation), estimating continuity, and evaluating joint roughness and infilling. A photogrammetric survey [5, 6] of the left and right abutments also was performed. The mapping effort involved three days of field work that included setting targets for photogrammetry, surveying the targets for control, taking calibrated photographs, and conventional mapping of geologic features on each abutment.

In general, the orientation data collected in August 2005 correlated reasonably well with the discontinuity orientation data extracted from review of the existing foundation data. The field mapping of the rock structure was incorporated into a three dimensional (3-D) foundation model. Up to 20 feet elevation differences in the downstream topography between the existing records and the close range photogrammetry were measured. The photogrammetric data was therefore critical in defining the potentially unstable foundation blocks.

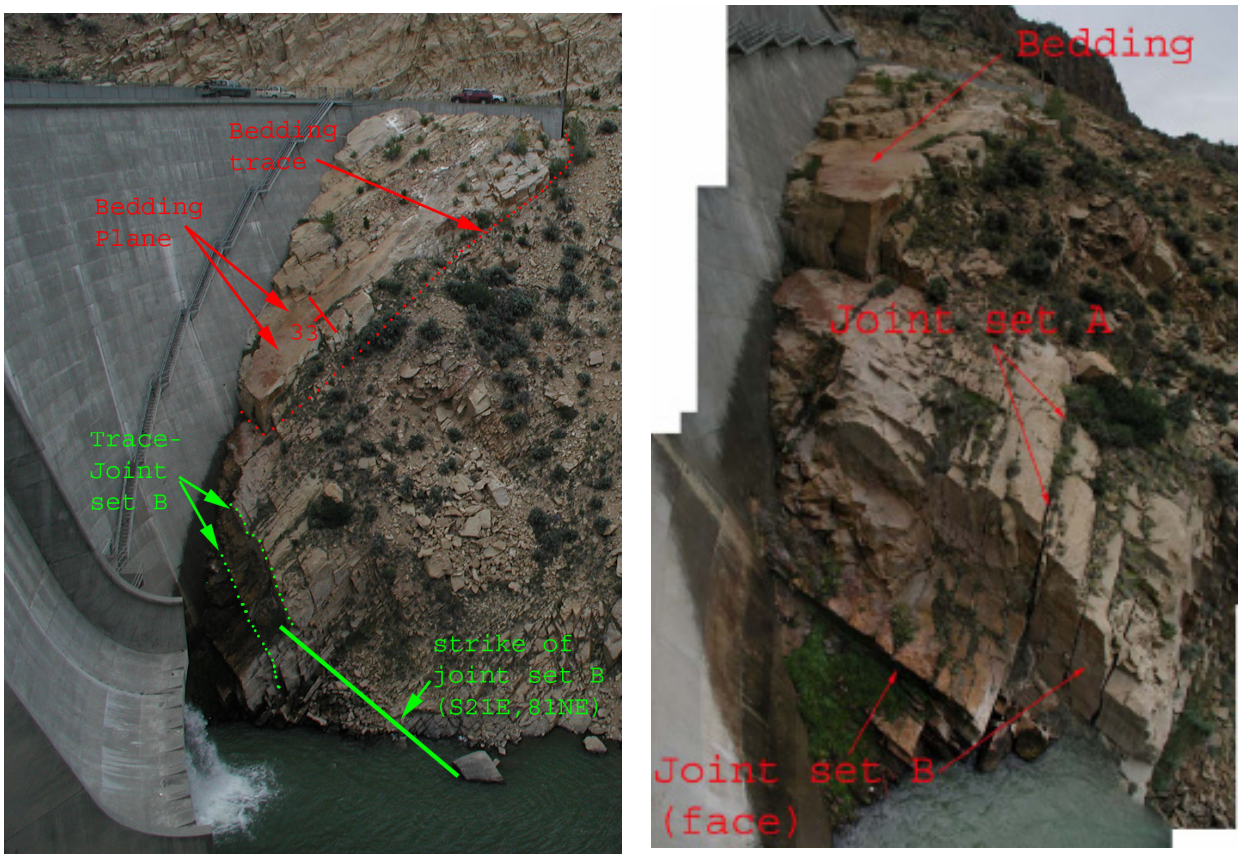

Fig. 1. Photos Showing Major Discontinuities in the Left Abutment of Anchor Dam (by P. Shaffner, 2004).

The three block-forming discontinuities in the vicinity of the dam are highlighted in Fig. 1. This structure consists of the west limb of a northwest-southeast trending anticline. Discontinuity sets on both abutments are similarly oriented. The intersection of these orientations with the topography and the variability in spacing and continuity make the stability issue unique to each abutment. The mapping effort confirmed the previous judgments that the left abutment is the primary concern because the bedding plane partings parallel the abutment slope and daylight a short distance downstream. Also, the spacing is smaller and the continuity is greater for all three discontinuity sets on the left abutment.

2.2. Defining Foundation Blocks

The geometric evaluation of the abutments at Anchor Dam indicated that potentially unstable foundation blocks are possible on both abutments; however, the geologic and topographic features in conjunction with the foundation contact create less stable conditions on the left abutment. The dominant joint orientations and local topography of the left abutment results in small blocks with large foundation contact areas. This condition results in large dam loads acting on the blocks.

The geometric shape and location of the left abutment foundation blocks were modeled using a 3-D CADD system. Fig. 3 shows a plan and several sections through the left abutment. As shown in Fig. 3, the upper left portion of the dam is founded on a relatively thin (10-foot thick) slab of sandstone. Block B is the critical block because the dam is founded below Block A, and Block C is too deep to daylight completely downstream. The terms "daylighting" and "to daylight" refer to the intersection of the geologic discontinuities (joints) with the topographic surface. When discontinuities in the abutment intersect or reach the ground surface they are said to daylight. Block C requires an additional side plane (Joint Set A) to cut the block off (see the blue labelled trace in the plan (top left) of Fig. 3). The orientation of this side plane significantly increases the safety factor since the thrust of the dam provides a large component of load normal to the plane. In addition, planes of Joint Set A are not as continuous as the bedding plane partings. Fig. 3 section C-C shows that the dam is founded on the orange bedding plane. The red bedding plane is only 10 feet below the foundation contact and daylights close to the dam forming a relatively small foundation block. The plan view (top left-Fig. 2) shows the area of Block B (the red daylighting trace).

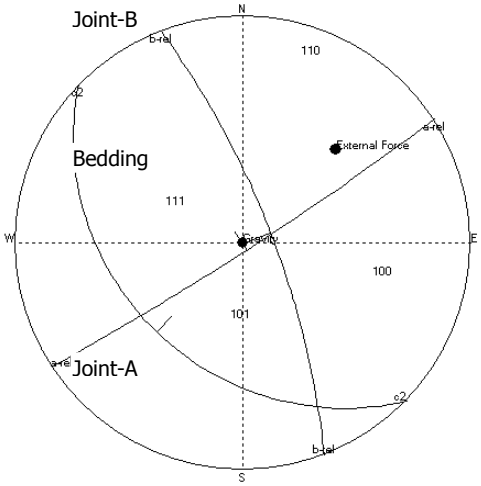

Fig. 2. Lower Hemisphere Joint Plane Projection

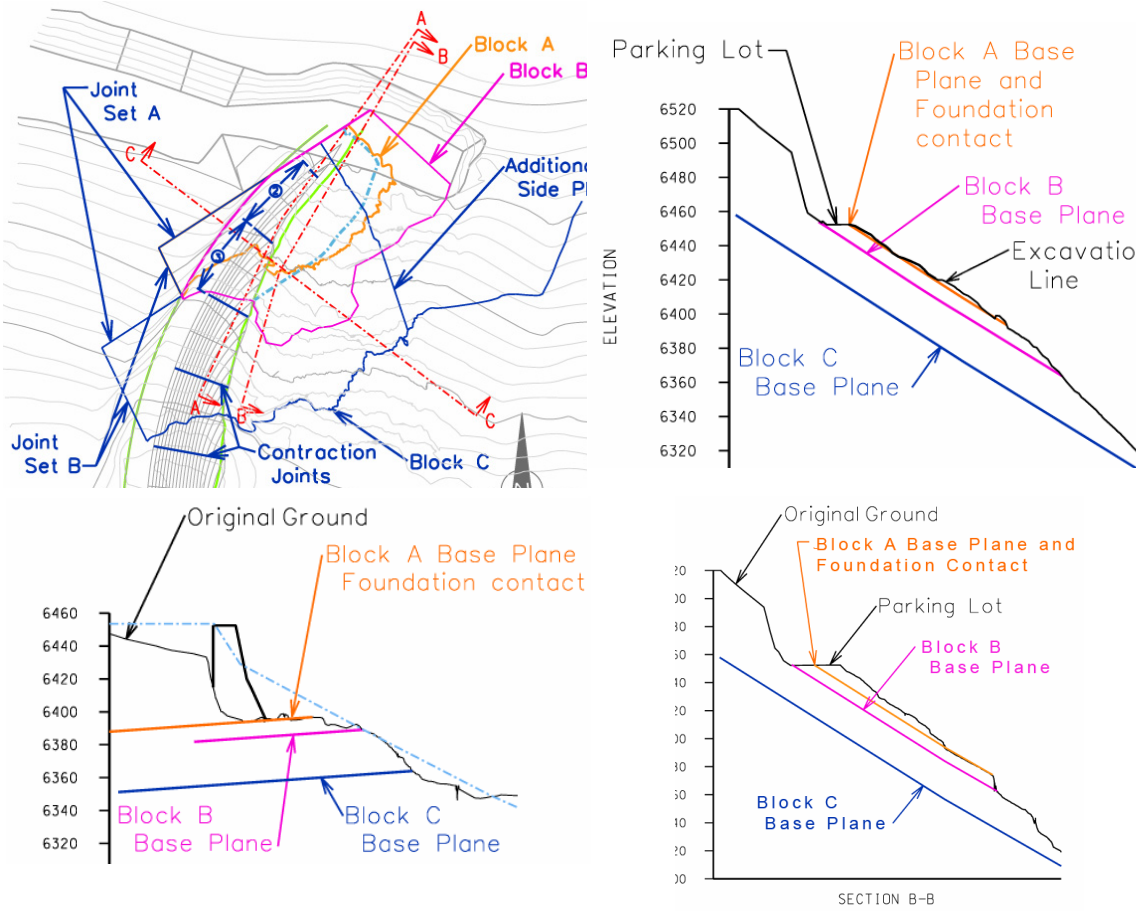

Fig. 3. Anchor Dam Left Abutment Plan and Sections.

2.3. Estimation of Shear Strength

Small blocks have slid off a near surface bedding plane downstream of the dam in this location, suggesting that the bedding plane feature has a shear strength friction angle between 30 and 35 degrees. Harza described the abutments as follows: "The attitude of strata on the left abutment, with the dip of the beds out of the slope, has resulted in some gravitational loosening of the rock mass exposed at the surface on the left side of the valley, seen as characteristic blockiness with local raveling and small-scale block-sliding. This situation has probably been exacerbated by freeze-thaw action. These conditions are in marked contrast to those found on the right side, where the exposed sandstone is seemingly more intact, less broken, and more massive" [3]. These conditions were noted during the 2004 and 2005 site visits. Reclamation's Geologist (Rebecca Heisler) found several examples of radial fracture patterns and related blast holes while mapping the abutments during the 2005 site visit. She pointed out that basting during construction could have contributed to the small scale sliding of rock pieces associated with Block A. Thus, the friction angle could actually be higher than that estimated by the small scale sliding.

3. FOUNDATION LOADS

3.1. Static Structural Loads

Structural loads were calculated from a finite element analysis by summing the forces at foundation contact nodes. These loads were provided by the structural engineers. The critical left abutment foundation block (Block B) is in contact with dam blocks 2 and 3. Table 1 lists foundation loads from dam blocks 2 and 3. These loads include gravity, reservoir, temperature, and silt loads from the structural analysis.

Two reservoir water levels were evaluated:

- The Spillway Crest Elevation at a reservoir water level (RWL) of 6441 feet with a recurrence interval of about 200 years.
- The start of overtopping at a RWL of 6453.5 feet with a recurrence interval of about 2000 years.

Table 1. Static Structural Loads

Load Cases	X (lbs force) East	Y(lbs force) North	Z (lbs force) Up
RWL 6441 ft—Spillway Crest	20448880	22912790	-13831060
RWL 6453.5 ft – Start Of Overtopping	28031600	28794200	-13831660

3.2. Earthquake Loads

Earthquake loading conditions are usually provided by the structural analysis group in the form of a time history set of the loads resulting from a dynamic finite element analysis of the structure. However, the dynamic loads were not developed for Anchor Dam because the probability of having a major earthquake at the same time as an extreme flood is too remote to cause a significant safety concern.

3.3. Water Pressures on Foundation Block Planes

Experience suggests that water pressures within a fractured rock foundation will react quickly to changes in reservoir level. Water forces on the foundation block are assumed to act normal to the block boundaries. These block boundaries are defined by the geologic discontinuities forming the block. The location and shape of the 3-D phreatic surface in the abutments must be modeled to make it possible to calculate the water pressures acting on the foundation block

planes. The fracture system creates complex variations in the water pressure profile. In practice, we typically do not have the data to account for most of these complexities. Thus, we commonly make the following simplifying assumptions about the phreatic surface.

- It is coincident with the reservoir level at the upstream dam-foundation contact.
- It drops sharply in the downstream direction toward the drainage curtain (if present).
- The drop from the reservoir to the drainage curtain is linear unless uplift pressure measurements are available and provide a better estimate of the hydraulic gradient.
- Abutment seepage points are assumed to be on the phreatic surface.
- The phreatic surface between uplift measurements (uplift pipes and seepage points) is linear.
- Drainage curtain effectiveness is characterized by measured uplift pressure profiles when available.
- There is a 67% reduction to the differential head at the drainage curtain, provided that:
    - Reliable uplift profile data is not available, and
    - Physical evidence indicating that the drains are functioning well.
- The tailwater level forms the downstream boundary condition.

A 3-D water surface model can be generated based on these assumptions. The reservoir and tailwater boundary conditions are easy to estimate. The drainage curtain and its effectiveness are typically evaluated by inspection and by comparing the available uplift profiles.

Anchor Dam does not have seepage data, a drainage system, or set of uplift pressure measurements. The reservoir leaks so badly that typical data needed to estimate foundation pressure under full reservoir load is not available.

The phreatic surface at Anchor Dam is based on three simple assumptions. The 1st and 2nd are the reservoir and tailwater boundary conditions described above. The 3rd assumption is based on establishment of three points along the downstream trace of foundation Block B. These points are common to the base plane and to the topography (i.e., they are on the daylighting trace that defines the intersection of the base plane surface with the topographic surface). These points include the lowest point on the daylight trace, the highest point, and one point in between that was needed to define a sharp direction change caused by the topographic surface. The daylighting trace is thought to act as a "natural drain" for water pressures beneath the bedding plane parting. There is significant uncertainty surrounding the rapid first filling condition that is being modeled because of the total lack of performance data, the lack of a foundation drain system below the dam, and the complex geologic setting. The uncertainty associated with the water pressures was addressed by setting an upper and lower bound on the effectiveness of the natural drain provided by the daylighting trace.

- The upper bound: the bedding plane intersection is 100% effective (i.e., the phreatic surface drops linearly from the reservoir to the ground elevation at the daylighting intersection).
- The lower bound: the bedding plane intersection is 70% effective (i.e., the phreatic surface drops linearly from the reservoir to the drain elevation defined by:
    - De=RWL-0.7*(RWL-Ge) where

- De is the effective phreatic surface elevation for points on the daylighting trace.
- RWL is the reservoir water surface elevation, and
- Ge is the ground elevation at the point on the daylighting intersection.

In 2003, Reclamation purchased a computer program (Water Pressure Program NB.exe) [7] from Dr. Gen-hua Shi that can be used to estimate water forces acting on foundation wedges. The water pressure data described above is input into the program and a triangulated water surface is generated. The water surface input data consists of points (easting, northing, and elevation) on the water surface. These points are either part of a break-line string or a random point. The "break-line" string prevents the mesh triangles from crossing the break line. Typical break-line data are:

- the reservoir rim contour corresponding to the RWL in combination with the upstream foundation contact,
- the drainage curtain (if constructed), and
- the tailwater contour.

The water level point data defines a water surface (a topological triangulated mesh). The block boundaries and topographic surfaces are also entered into the program using the Block Theory [9] system of joint plane and free face orientations and locations (dip; dip direction; and x, y, and z locations), and block pyramid codes . These geometric elements are used in calculating water pressures on all block surfaces.

The two reservoir loading conditions (Section 3.1), combined with the upper and lower bound for the natural drain effectiveness, results in four phreatic surfaces and four stability estimates. The water pressure program "NB.exe" was executed four times to calculate block water forces. The program calculated the water loads for all block planes and free faces. Table 2 lists these load cases and the corresponding water forces. Fig. 4 shows results from the foundation water pressure evaluations.

Table 2. Water Force Estimates for Block B on the Left Abutment

RWL 6441 feet: The Spillway Crest: (Recurrence Interval Of 200 yrs)						
6441	Drain Efficiency 100 % on Bedding Plane Int.			Drain Efficiency 70 % on Bedding Plane Int.		
Plane	X (east)	Y (north)	Z (up)	X (east)	Y (north)	Z (up)
Base	-66973.64092	-69353.2354	148461.9887	-80313.82594	-83167.40138	178033.4794
Release-a	16060.26066	-24730.6327	2061.994743	16144.36915	-24860.14842	2072.793526
Release-b	17480.46416	6710.121507	5017.110602	19756.68492	7583.880793	5670.414267
Total	-3.34E+04	-8.74E+04	1.56E+05	-4.44E+04	-1.00E+05	1.86E+05
RWL 6453.5 feet: The Start of Overtopping (Recurrence Interval Of About 2000 yrs)						
Base	-90234.12148	-93440.16813	200024.0235	-108865.1143	-112733.126	241323.7678
Release-a	22903.27104	-35267.94463	2940.576462	23133.13713	-35621.90738	2970.089226
Release-b	20983.50327	8054.812234	6022.52639	23608.53014	9062.465641	6775.941746
Total	-4.63E+04	-1.21E+05	2.09E+05	-6.21E+04	-1.39E+05	2.51E+05

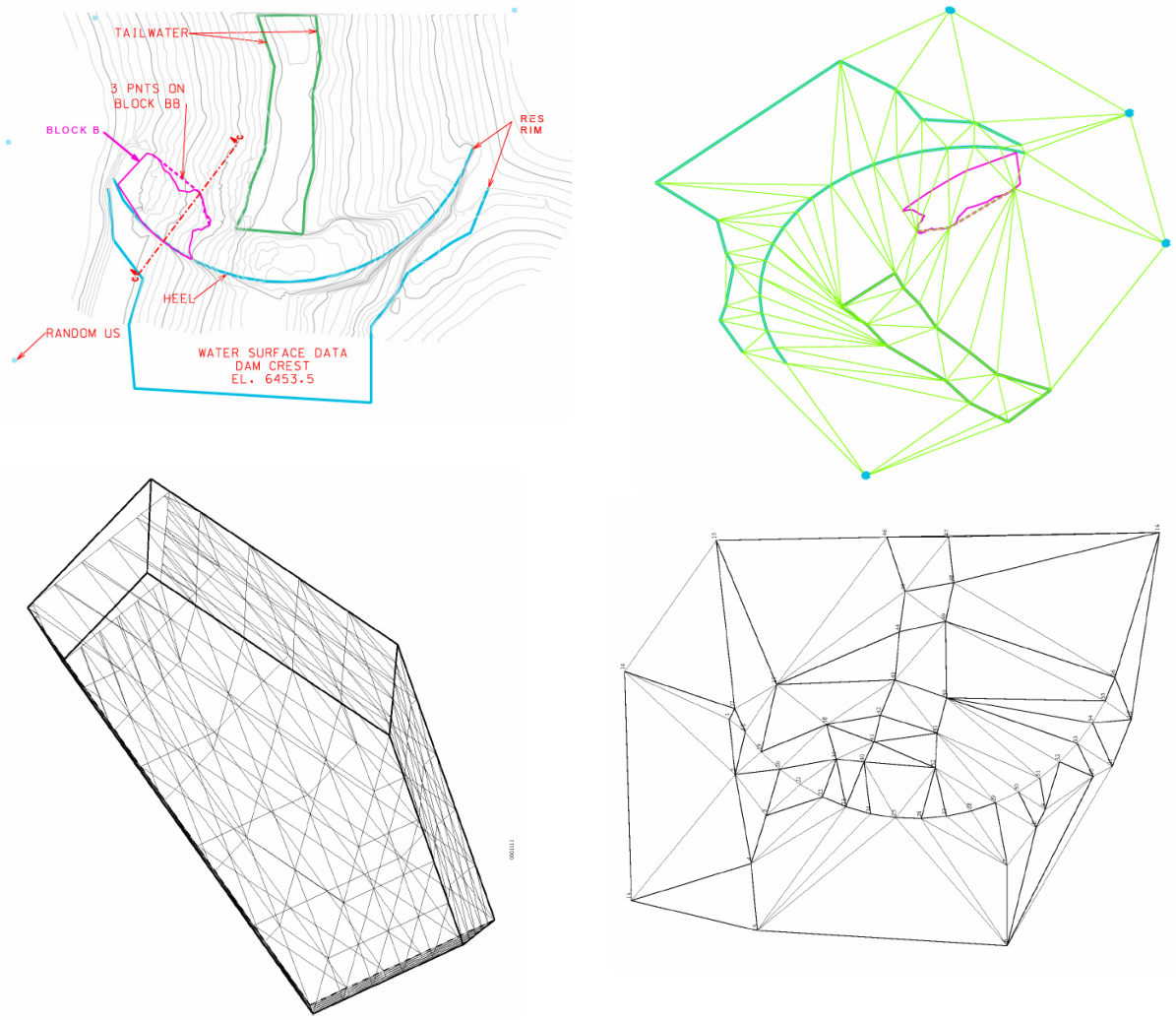

Fig. 4. Phreatic Surface Geometry: The top two graphics show the break line data drawn using a CADD system. The triangular meshes are of the water surface. The two the lower figures are output from NB.exe. The lower left figure is an isometric of Block B showing the intersection of the water surface and the block planes for RWL 6453.5

The water forces on the free faces may need to be ignored if the block is above tailwater, or included for the potion of the block that is below tailwater. Results are not automatically evaluated for these conditions. As such, the calculated loads must be carefully evaluated and only the appropriate components should be included in the stability calculations.

A clear understanding of these geometric shapes is very important because errors in the surfaces can create significantly different results, and one may include or exclude the various components incorrectly. The Anchor Dam water loads are limited to the two upstream release planes and the base plane. All free face loads were ignored because the block is above tailwater. Water forces at the dam contact were conservatively ignored (they would increase the normal stress on the bedding plane parting)

3.4. Block Weight

Due to the complex topography surfaces, the block weight is typically calculated by subtracting the topographic surface from the block surface and calculating the volume with the surfacing tools provided in most CADD systems. The block volume for the critical Anchor Dam

foundation block is 109350 cubic feet, based on this method. The block volume based on simplified topography is 65150 cubic feet, which was also calculated as part of the NB.exe output. The large difference is caused by the difference between the two topographic surfaces; the one used in the NB.exe or Pantechnica Workshop is much simpler, it ignores all the rock downstream of the toe above the foundation contact. The large volume was used in the analysis because the CADD system values are thought to be more realistic.

4. FOUNDATION ANALYSIS

4.1. Static Stability

The foundation stability of large concrete dams founded on rock, like Anchor Dam, depends on the geometry and shear strength of the foundation discontinuities in relation to the structure geometry and topography. The stability of the arch is dependent on the stability of the abutment. At Anchor Dam, Block B comprises a potentially unstable condition.

The foundation analysis for Anchor Dam is based on a 3-D limit equilibrium evaluation of the critical foundation block (Block B). The analysis did not include earthquake loads. The analysis assumes:

- A rigid block.
- The foundation is uncoupled from the structure (i.e., the analysis does not include interaction between the dam and the foundation block).

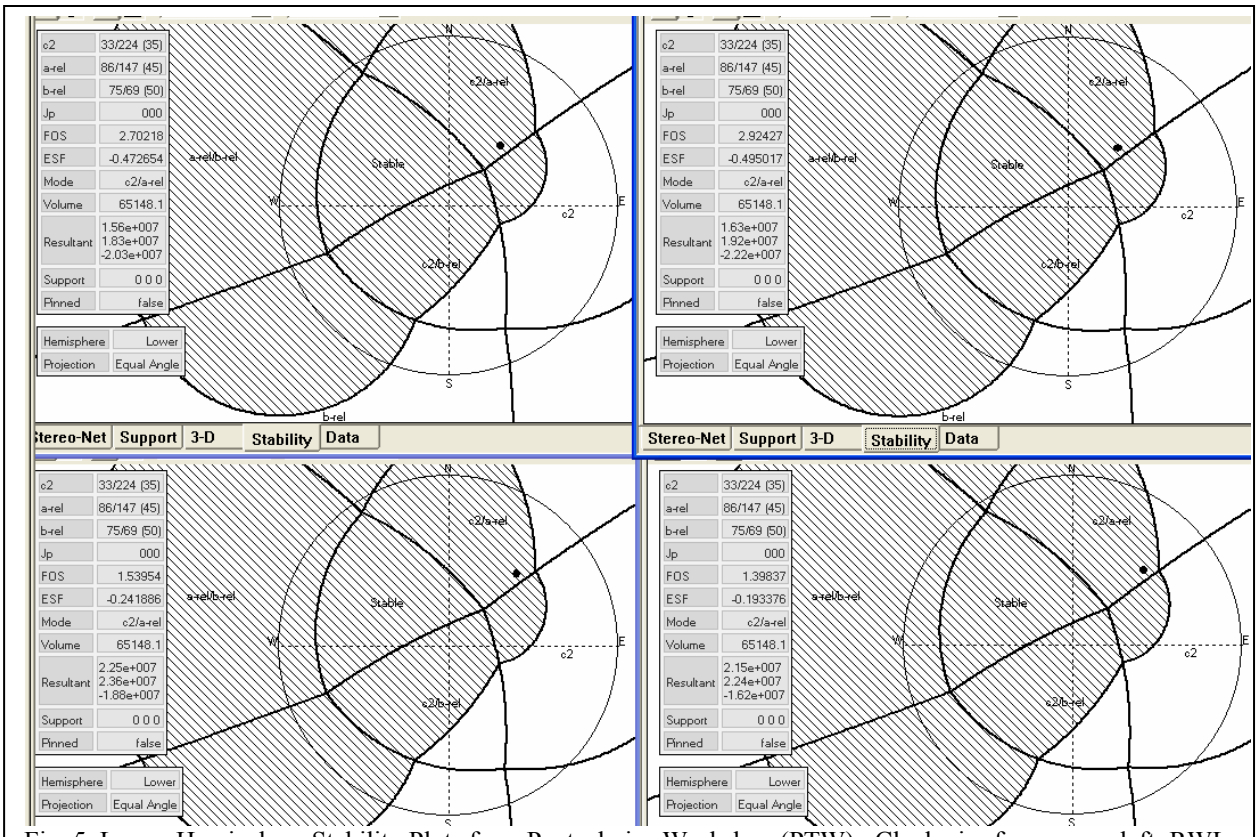

Fig. 5. Lower Hemisphere Stability Plots from Pantechnica Workshop (PTW). Clockwise from upper left: RWL 6441 and 70% drainage, RWL 6441feet and 100% drainage, RWL 6453.5 feet and 70% drainage, RWL 6453.5 feet and 100% drainage.

The second assumption is thought to be conservative because the foundation is free to move toward the dam without the dam providing any resistance and no redistribution of stress is allowed to occur. If the foundation is not stable, the structural analysis may be looked at in more detail and a coupled analysis may be required.

This uncoupled type of analysis can be effectively examined using a stereographic friction cone plot [8]. Goodman and Shi developed a computer program (at University of California, Berkeley, 1985) that creates this plot from appropriate Block Theory parameters. The plot incorporates all the critical elements into a single graphical interpretation of the 3-D limit equilibrium stability analysis. This plot also provides the sliding mode and the orientation of the resultant force relative to the friction cone. Reclamation currently uses a program called the PanTechnica Workshop with the KeyBlock Slope module [9] for this type of analysis. Fig. 4 is a stereographic projection of all relevant features needed to define the limit equilibrium condition of block sliding for all four load cases.

Fig. 5 includes all block theory data used in developing the projection. The following list provides some insight for understanding this stereographic projection.

- Geometric features are projected on this plane such that the lines or vectors show up as points. The location of each point defines the orientation of the vector. Planes are plotted as circles. Block pyramids are plotted as polygons formed by arc segments instead of straight lines.
- This type of projection uses a horizontal reference plane.
- The plane projections divide the projection space into regions representing the various sliding modes (single-plane sliding, double-plane sliding, lifting, and stable without friction).
- The friction cone defining the limit of equilibrium based on the assigned friction angle is shaded. When the resultant force plots in the shaded region, the safety factor is above one and the block is considered stable.
- The orientation of the resultant relative to the orientation of the planes defines the sliding mode.
- The mathematical value of the safety factor is the sum of the resisting forces divided by the sum of the driving forces. This value is calculated by the program and listed on the plot.

4.2. Dynamic Earthquake Stability Analysis

The earthquake loading condition is usually an important one and Reclamation uses a computer program *Keyblock Codes of Dynamic Newmark Method* "NM1.exe" to estimate rigid block displacements under dynamic loads. Reclamation purchased this program from Dr. Shi in September 1998. This is mentioned for completeness, because as mentioned previously the earthquake was not an important loading condition for the Anchor Dam study and thus no results were generated.

5. CONCLUSIONS

The as-excavated foundation topography of the Anchor Dam foundation, in conjunction with the existing natural topography immediately upstream and downstream, create a "free" surface that combines with geologic discontinuities in the foundation to form potentially removable foundation blocks. Block B in the left abutment is a small block, about 10 feet thick. This block is not constrained by a side plane. It is the most critical block at the site. The stability plot

indicates stable with friction. The sliding mode is: double-plane siding on the bedding plane the joint release plane. Most of the normal force is on the bedding plane. The effectiveness of the natural drain (100% vs. 70%) did not significantly affect the safety factor. The safety factor ranges from 2.9 to 2.7 for the spillway crest. The safety factor ranges from 1.54 to 1.40 for the dam crest. Foundation conditions will change significantly with overtopping flows. A risk assessment is planned to evaluate appropriate actions that may be required to protect the downstream population from a remote flood event that could create stability issues, including potential dam overtopping. Flooding of this magnitude is rare and allows some time for evacuation, which is unlike the case for earthquake-related failures.

6. ACKNOWLEDGEMENTS

Reclamation's Dam Safety Office supported and funded this effort. I also would like to thank several other Reclamation coworkers who have participated in this effort particularly: Matt Jones, Rebecca Heisler, Kamy Deputy, Pete Shaffner, Tom Scobell, Chris Powell, Dave Martinez, and Gregg Scott.

REFERENCES

1. Reclamation. 1962. *Technical Record of Design and Construction, Anchor Dam.* Bureau of Reclamation, Denver CO.
2. Goodson & Associates, Inc. November 1981. *Engineering Geological Report for Anchor Dam, Pick-Sloan Missouri Basin Program, Wyoming Upper Missouri Region.* Bureau of Reclamation, Denver CO.
3. Harza Engineering Company. May 1993. *Technical Memorandum on Analysis of Geological and Geotechnical Issues, TM-HV-3620-1.* Bureau of Reclamation, Denver CO.
4. Reclamation. March 2002. *Preliminary Hydrologic Loadings for Comprehensive Facility Review, Anchor Dam.* Bureau of Reclamation, Denver CO.
5. Eos Systems. 2004. *PhotoModeler 5.* 30th ed.
6. Intergraph Corp.2005. *Z/I ImageStation Products, MGE Terrain Analyst, MGE Image Analyst.*
7. Shi, G-h. 2003 *Water Pressure Program BN.exe*.
8. Goodman. R. E. and G-h Shi. 1985. *Block Theory and Its Application to Rock Engineering*
9. PanTechnica Corp. 2003. *PTWorkshop Key Block - PTWorkshop, iVec, KBSlope modules-Ver. 2.0,* Chaska, (MN).

The Application of DDA to Practical Rock Engineering Problems: Issues and Recent Insights

Ohnishi, Y. and Nishiyama, S.
Kyoto University, Kyoto, Japan
Sasaki,T.
Suncoh Consultants Co. Ltd., Japan
Nakai, T.
Earth-tech Toyo Co.Ltd., Japan

This paper was prepared for presentation at *ICADD-7, the Seventh International Conference on Analysis of Discontinuous Deformation*, held in Honolulu, Hawaii, December 10-12, 2005.

1. INTRODUCTION

Japan is susceptible to numerous types of natural disasters, such as rock falls and landslides induced by earthquakes and intensive rains, resulting in roads, railways and public houses on slopes being damaged and closed. Now about 25000 slopes are identified to be potentially unstable. Ministry of construction and transport announced that these unstable slopes should be taken care as soon as possible to establish the safe and comfortable country. In order to protect against unstable slopes, it is very important to take prior countermeasures. Some government agencies intended to change their conventional safety codes for rock slope and rock fall and to include modern numerical methods. DDA is one of the candidate tools to analyze rock slope stability problems and to use for designing such countermeasure structures. However, in DDA analyses, how we can determine necessary parameters is not clear yet and engineers are still skeptical to use DDA in design works.

Fig. 1 [1] shows an example of DDA analyses. This rock slope failed in March, 1999 and its falling process was recorded by a video camera. DDA analysis was done to estimate the failure mechanism, but we encountered the difficulties of determining many parameters involved in the DDA calculation. Some parameters are obtained by various tests, but some are determined by try and error process. Final results of calculation gave us a lot of hints how the combination of blocks interactively moved.

Parameters used in DDA are rock mass densities, elastic moduli of rock blocks, the penalty coefficients, viscosity (damping) of blocks, joint friction coefficient, velocity energy ratio, time increment, allowable displacement in a time increment and so on. Who can determine these parameters with confidence?

Here, we will discuss the feature of DDA in relation to the basic equations with respect to rock-fall phenomenon and some new parameters to be considered in an earthquake dynamic problem. In this discussion, we simply focused on the relationship between numerical stability, calculation precision and the parameter characteristics in DDA calculations. Although we pick up a rock-fall phenomenon as an example, the discussion can be extended to general DDA analysis.

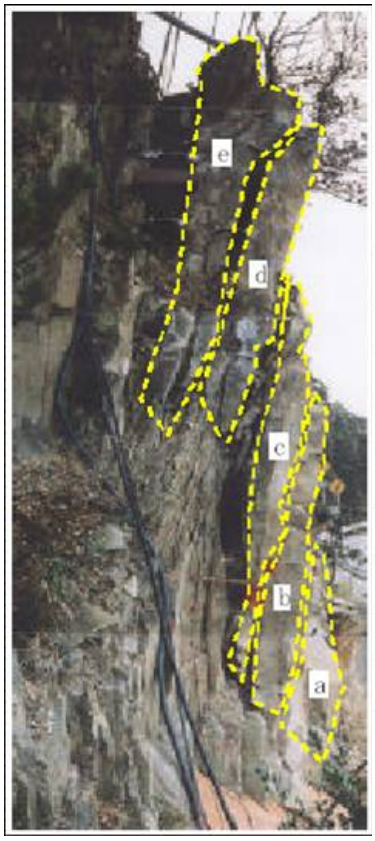

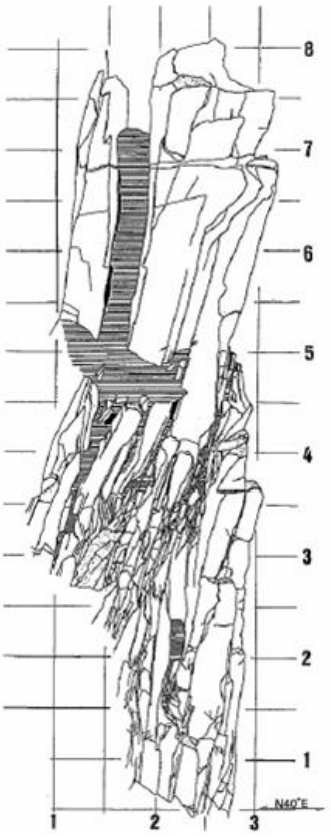

Fig. 1(a) Rock slope before failure Fig. 1(b) Sketch of jointed rock mass

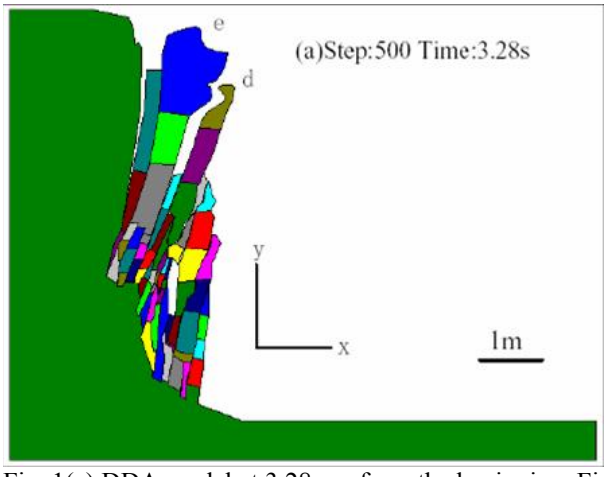

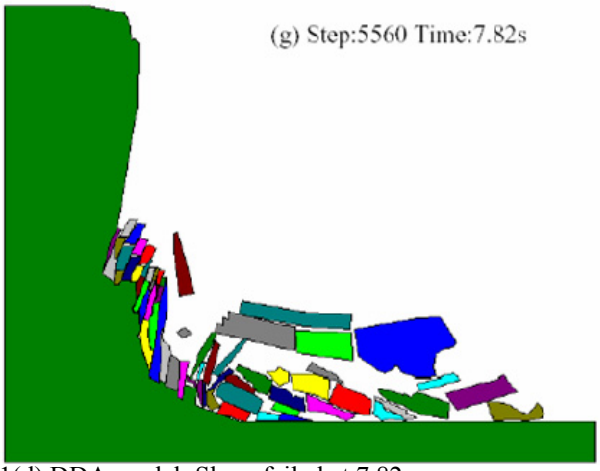

Fig. 1(c) DDA model at 3.28 sec from the beginning Fig. 1(d) DDA model: Slope failed at 7.82sec

2. DDA PARAMETERS

In order to get an accurate solution for a complex rock condition in DDA analyses, we should know how the equation behaves and how the DDA parameters interact in the problems.

Here we discussed the parameters for DDA analysis as follows.

(1) Damping effects and viscosity
(2) Energy loss before and after contact or collision
(3) Concerning the balance of numerical stability in the kinematic equation
(4) Viscous damping boundary for dynamic earthquake analysis

2.1. KINEMATIC EQUATIONS OF MOTION (Basic Equation)

DDA (Shi, 1984) [2] is formulated from Eq. (1) using the kinematic equations based on Hamilton's principle and minimized potential energy expressed by:

$$M\ddot{u} + C\dot{u} + Ku = F \tag{1}$$

where, M: mass matrix, C: viscosity matrix, K: stiffness matrix, F : external force vector, $\ddot{u}$: acceleration, $\dot{u}$: velocity, and u: displacement of the center of a block.

Although the original DDA do not include viscosity term, the viscosity matrix of a body C in Eq. (1) can be rewritten as follows in terms of viscosity η_e and mass matrix M:

$$C = \eta_e M \tag{2}$$

The physical meaning of viscosity η_e is the damping of the rock and rock mass itself and also is extended to other viscous effects.

The kinematic equation of motion Eq. (1) is solved by Newmark's β and γ method (Hilbert, 1993) by using parameters $\beta = 0.5$ and $\gamma = 1.0$, and the algebraic equation for the increase in displacement is solved for each time increment by the following three equations [3]:

$$\tilde{K} \cdot \Delta u = \tilde{F} \tag{3}$$

with $$\tilde{K} = \frac{2}{\Delta t^2} M + \frac{2\eta}{\Delta t} M + \frac{\rho^c}{\rho^0}[K_e + K_s] \tag{4}$$

$$\tilde{F} = a\left(\frac{2}{\Delta t} M \cdot \dot{u}\right) + \left(\Delta F - \sum \int \sigma dv\right) - M\alpha(t) \tag{5}$$

where, Δu : incremental displacement, K_e : stiffness matrix of linear term, K_s : initial stress matrix caused by rigid rotation, and $\alpha(t)$: time history of earthquake acceleration, ρ^0 is mass density before deformation and ρ^c is mass density after deformation.

Usually $\frac{\rho^c}{\rho^0} \cong 1$ in small deformation of rock blocks and K_s is neglected.

2.2. DISCUSSION ON DAMPING EFFECTS

2.2.1 Parameter for quasi-static and dynamic problems

Here, our discussions focused on Eq. (4) and Eq. (5). The original DDA [2] uses the parameter "a (k01 in other literatures)" in Eq. (5) and it is defined as "a=0" for quasi-static problems and as "a=1.0" for dynamic problems. In the case of earthquake or rock fall dynamic analyses, we empirically have known that the parameter "a" could be set in the range from 0.90 to 0.99 to achieve a stable solution [Tsesarsky, 8].

As an example, here we assume a=0.95, then,

$$\left\{\frac{2}{\Delta t^2} M + \frac{0.05 \times 2}{\Delta t} M + [K_e + K_s]\right\} \cdot \Delta u = 0.95\left(\frac{2}{\Delta t} M \cdot \dot{u}\right) + \left(\Delta F - \sum \int \sigma dv\right) - M\alpha(t) \tag{6}$$

During discussions among us and Prof. Hatzor, he pointed out that the result of Eq. (6) is equivalent to introducing a 5% viscous damping defined as η_e in Eq. (2) . To check this idea, let's make calculation.

$$\{\frac{0.05 \times 2}{\Delta t} M\} \cdot \Delta u = 0.05 \{\frac{2}{\Delta t} M\} \cdot \Delta u = 0.05 (\frac{2}{\Delta t} M \cdot \frac{\Delta t}{2} \dot{u}) = 0.05 (M) \cdot \dot{u} \tag{7}$$

As a result, this equation is equivalent to defining η_e =0.05 in Eq. (2).
However, the above definition can only be used on a homogeneous model. In inhomogeneous or more complex models, our choice is to use Eq. (4) with η_e =0.05.

2.2.2 VISCOUS DAMPING

Eq. (1) include viscous matrix C to represent various damping effects such as damping of the rock and rock mass itself and also air resistance around the rock surface when it flies. Chen et al [11]and Shinji et al [5] proposed to use viscous damping to consider energy losses during rock fall. Energy loss may be caused by rock crushing, rock plastic deformation, drug force of grass and woods on the ground, etc. However, there is no general criterion to determine the viscous coefficient. The selection of the coefficient can be done by trial and error procedure or back-analysis of experiments.

2.2.3 NEWMARK ALGORITHMIC DAMPING

According to the previous studies (Wang et. al. [6] and O`Sullivan & Bray [7]), the time integration method in DDA is one of the Newmark-type approaches, and Newmark-type equations can be expressed as follows:

Let $A = \ddot{x}$ and $V = \dot{x}$

$$\Delta u^{(n)} = V^{(n)} \Delta t^{(n)} + \frac{(\Delta t^{(n)})^2}{2} (1 - 2\beta) A^{(n)} + (\Delta t^{(n)})^2 \beta A^{(n+1)} \tag{8a}$$

$$V^{(n+1)} = V^{(n)} + (1 - \gamma) A^{(n)} \Delta t^{(n)} + \Delta t^{(n)} \gamma A^{(n+1)} \tag{8b}$$

where "$A^{(n+1)}$" is the acceleration vector at time step n+1, the parameters "β" and "γ" define the variation of acceleration over the time step and determine the stability and accuracy characteristics of the method. With the Newmark-type approach, the requirement for unconditional stability is satisfied when $2\beta \geq \gamma \geq 0.5$.

The time integration scheme in DDA introduces β=0.5 and γ=1.0; this is equivalent to take the acceleration at the end of the time step to be constant over the time step. This approach confirms that DDA approach is implicit and unconditionally stable.

Supposed that one rigid particle with mass "M" and weight "w" is located at the height of "h" above the ground level, and the spring with stiffness "k" always connects the particle to the ground shown in Fig. 2. The initial velocity of the problem is 0. No damper is concerned in the system, and the time integration method to calculate the particle behavior is the same as DDA.

With the gravity load, the particle should do SHM (simple harmonic motion) from its equilibrium position without any energy losses. If $-x_0$ is the equilibrium extension at which the force of spring and gravity balance, then

$$w = -Mg = kx_0 \tag{6-4}$$

For any extension x, the net force on the falling particle is

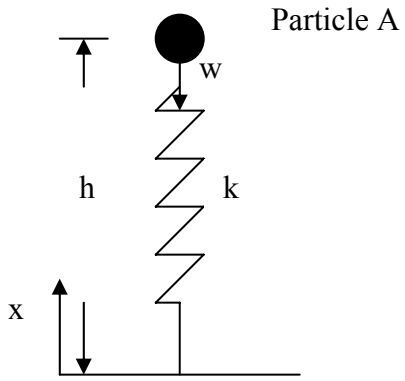

Fig. 2 Simple Particle-Spring Connecting System

$$F = -Mg - kx = -k(x - x_0) = -kx' \tag{6-5}$$

where, $x'=x-x_0$ is the displacement from the equilibrium position.

According to Newton's second law (F=MA) applied to the particle, which means

$$A = -\frac{k}{M}x' \tag{6-6}$$

Since the acceleration $A=d^2x'/dt^2$, equation (6-6) can be rewritten as

$$\frac{d^2x'}{dt^2} + \frac{k}{M}x' = 0 \tag{6-7}$$

Equation (6-7) is the same form as the simple harmonic motion with an angular frequency

$$\omega = \sqrt{\frac{k}{M}} \tag{6-8}$$

Hence, the displacement from equilibrium can be given as

$$x(t) = (Amp)\sin(\omega t + \phi) = (h + x_0)\sin(\omega t + \phi) \tag{6-9}$$

where "Amp" is the amplitude of the oscillation, and "ϕ" is the phase constant.

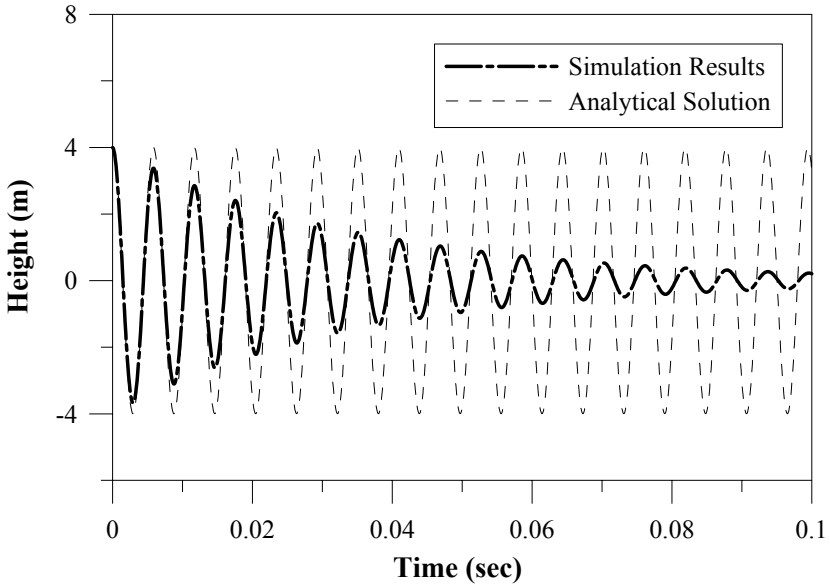

Fig. 3 Simulation Results with Time Delta Equals to 0.0001 sec

By introducing the numerical method analyzing the same problem with weight (w) equals to 26.0 kN, the height (h) is 4 m, the spring stiffness (k) is 3000 MN/m, and the time interval equals to 0.0001 sec, the simulation result in Fig. 3 shows the particle track with "damping", and the total potential energy (including, potential energy, kinetic energy and the spring energy) decreases. In addition, the total energy decreases exponentially with time, and the relation between total energy and the time can be expressed as follow:

$$TotalEnergy = E_0 \cdot e^{-\lambda t} \tag{6-10}$$

where, "E_0" is the initial total energy, "t" is the time, and "λ" is the coefficient of damping.

As shown in Fig. 4, it is clear that the "coefficient of damping" is related to not only the spring stiffness but also the time interval [9]. These results indicate the existence of algorithmic damping in the numerical analysis when the system is "particle-spring connected", which was pointed out by many researchers (ex.[6][7]). In addition, the coefficient of damping increases with the time increment and spring stiffness in the computations.

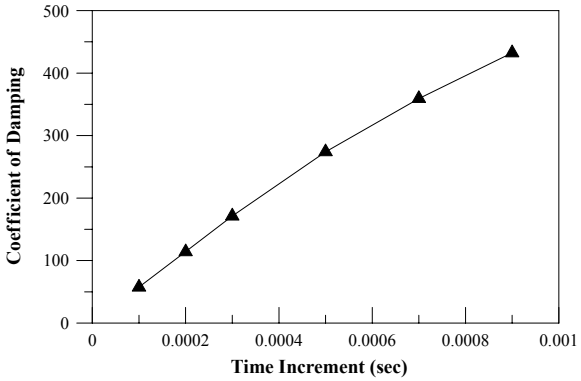

(a) Relation between Coefficient of Damping and Time Increment

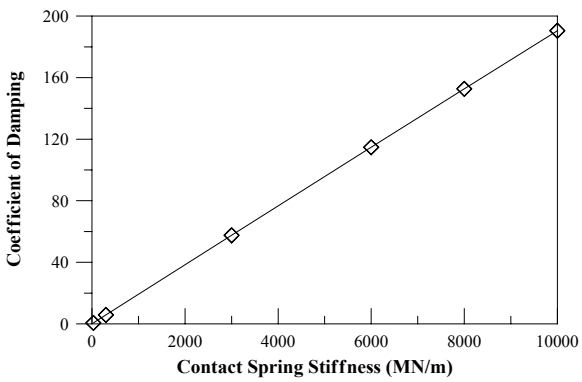

(b) Relation between Coefficient of Damping and Contact Spring Stiffness

Fig. 4 Changes of Energy Damping Coefficient

2.3. CHARACTERICTICS OF THE NUMERICAL STABILITY OF KINEMATIC EQUATION MATRICES (Effect of time increment)

We discuss the characteristics of the numerical stability of the global matrix as Eq. (4).

$$\widetilde{K} = \frac{2}{\Delta t^2} M + \frac{2\eta}{\Delta t} M + \frac{\rho^c}{\rho^0}[K_e + K_s] \tag{8}$$

The characteristics of matrix K are expressed as an Eigen problem:

$$[(\frac{2}{\Delta t^2} M + \frac{2\eta}{\Delta t} M + \frac{\rho^c}{\rho^0}[K_e + K_s]) - \lambda I]\{\phi\} = \lambda\{\phi\} \tag{9}$$

where, λ: Eigen value of the matrix [A], {φ}: Eigen vectors.

The solution condition for the calculation except zero solution is defined by:

$$\det[(\frac{2}{\Delta t^2} M + \frac{2\eta}{\Delta t} M + \frac{\rho^c}{\rho^0}[K_e + K_s]) - \lambda I] = 0 \tag{10}$$

The inverse matrix of K is expressed by Eigen values and Eigen vectors.

$$[\frac{2}{\Delta t^2} M + \frac{2\eta}{\Delta t} M + \frac{\rho^c}{\rho^0}[K_e + K_s]]^{-1} = \sum_{i=1}^{n} (\frac{1}{\lambda_i}) \phi_i \phi_i^T \tag{11}$$

The cancellation of significant digits depends on the spectral radius as the condition number of matrix [A] defined in Eq. (12).

$$Cond[A] = \frac{\lambda_{\max}}{\lambda_{\min}} \tag{12}$$

where, $\lambda_{\max}$: the maximum Eigen value of the matrix [A], $\lambda_{\min}$: the minimum Eigen value of the matrix [A].

In the case of a condition number under 1,000, the numerical solution is stable in experience. Poor conditions of the matrix K depend on the time increment.

$$[\frac{2}{\Delta t^2} M + \frac{2\eta}{\Delta t} M + \frac{\rho^c}{\rho^0}[K_e + K_s]] = [A] \tag{13}$$

The existence condition of a solution to matrix [A] is positive definite and the condition is defined by Eq. (14).

$$\det[A] \neq 0 \tag{14}$$

One factor inducing instability in matrix [A] is selecting a very small time increment Δt for instance. As a result, the first term on the left hand side of Eq. (13) becomes disproportionately large while the third term on the right hand side of Eq. (13) becomes relatively small, and the determinant of the matrix [A] is close to zero. Thereupon, the numerical condition of matrix [A] becomes unstable as shown in Eq. (15).

$$\frac{\rho^c}{\rho^0}[K_e + K_s] \leq \frac{2}{\Delta t^2} M + \frac{2\eta}{\Delta t} M \tag{15}$$

For simplicity, we assume the stiffness matrix as follows:

$$\frac{\rho^c}{\rho^0} = 1.0, \quad [K_e + K_s] \cong [K] \tag{16}$$

Eq. (15) is given by:

$$[K] \leq \frac{2}{\Delta t^2} M \tag{17}$$

As the conditions of matrix [A] become close to Eq. (17), the potential for numerical instability increases. For simplicity, if Eq. (17) is shown one dimensionally as Eq. (18), the time increment of the lower limit can be estimated.

$$\Delta t \le \sqrt{\frac{2M}{K}} \tag{18}$$

If we use a smaller time increment than Eq. (18), the characteristics of the stiffness matrix [K] are loosened and the solutions become unstable. For example, if we assume the rocks elastic modulus is 1 GPa (1,000,000 kN/m^2), the area of the block is 1 m^2, the unit mass is 25 kN/m^3, then the time increment is calculated by Eq. (19).

$$\Delta t \le \sqrt{\frac{2 \times 25}{1{,}000{,}000}} = 0.007 \tag{19}$$

The result of Eq. (19) shows that the chosen time increment might affect the optimal value. Hence, the value of the chosen time increment should not be extremely small.

In the discussion with Dr. Wu [9], he pointed out that the algorithmic damping in DDA diminishes as shown in Fig. 5 if he takes a very small amount of time increment. However, as indicated in the Eqs.(18) and (19), too small time increment will cancel the existence of M in Eq. (13) and consequently the algorithmic damping effect disappear. As a conclusion, we can only choose a time increment in a certain range and can not avoid the algorithmic damping if we use Newmark method with β=0.5 and γ=1.0.

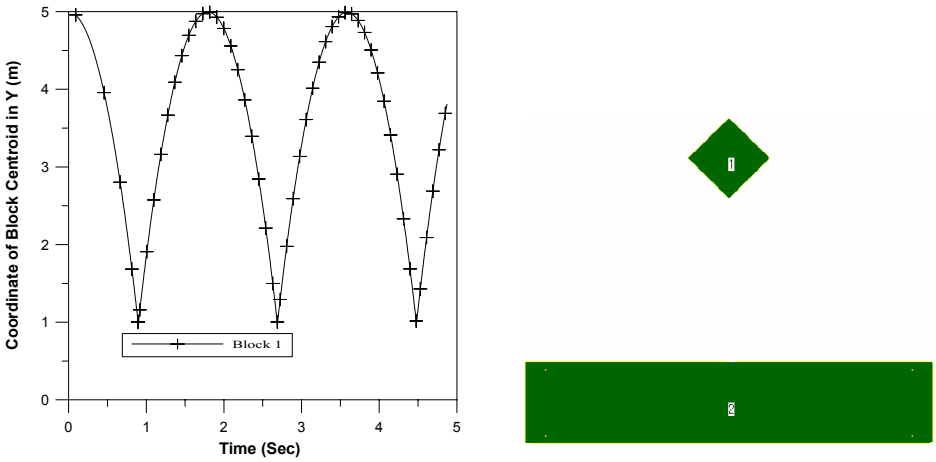

Fig. 5 Block drop and bouncing analysis

2.4. PARAMETERS FOR BLOCK CONTACT (selection of the optimal penalty value)

The potential energy of the contact between discontinuous planes, and is evaluated by the least squares method by using a penalty as follows:

$$\Pi_{PL}^{i,j} = \frac{1}{2} k_N [(u^j - u^i) \cdot n]^2 - \frac{1}{2} k_T [u_T^j - u_T^i]^2 \tag{20}$$

where, k_N: penalty coefficient in the normal direction, k_T: penalty coefficient in the shear direction, $(u^j - u^i) \cdot n$: amount of penetration in the normal direction, u_T: amount of slip in the shear direction, and n: direction cosine of the contact plane.

The global stiffness matrix with Penalty is expressed by:

$$\begin{bmatrix} K_{11} & \cdots & \cdots & \cdots & \cdots & K_{1n} \\ \vdots & \ddots & & & & \vdots \\ \vdots & & (K_{ii}+K_N+K_T) & \cdots & (K_{ij}-K_N-K_T) & \vdots \\ \vdots & & \vdots & \ddots & \vdots & \vdots \\ \vdots & & (K_{ji}-K_N-K_T) & \cdots & (K_{jj}+K_N+K_T) & \vdots \\ K_{n1} & \cdots & \cdots & \cdots & \cdots & K_{nn} \end{bmatrix} \begin{Bmatrix} u_1 \\ \vdots \\ u_i \\ \vdots \\ u_j \\ u_n \end{Bmatrix} = \begin{Bmatrix} f_1 \\ \vdots \\ f_i+(u_i-u_j)(K_N+K_T) \\ \vdots \\ f_j+(u_j-u_i)(K_N+K_T) \\ f_n \end{Bmatrix} \tag{21}$$

In the case of dynamic analysis, especially for rock fall problems, the reaction forces of contact blocks are defined on the right hand side of Eq. (21). If we choose a large value for the penalty coefficient, the reaction force becomes very large, and then the rebound motion of the block is also very large. Accordingly, the penalty coefficient might be chosen as the same value as the elastic modulus of the penetrated block side, which would result in a very large value as defined in Eq. (22).

(Elastic modulus) × (block area) / (penalty coefficient) (22)

In the event that the value of Eq. (22) is less than 1/1000, this condition is equivalent to a small block or a small elastic modulus of the materials. In this state, the cancellation of significant digits results on the left hand side of Eq. (21) between the block stiffness and penalty, hence, the characteristics of the block stiffness are dispersed and the solution diverges. Therefore, we should also select the optimal penalty value.

2.5. RESTITUTION COEFFICIENT (Bouncing phenomenon)

It is important to have the best possible knowledge of rock-fall trajectories and energies in order to determine accurate risk zoning and construct adequate defense structures near the threatened area. The ground's restitution coefficient is evaluated according to the ration between the total energy of the falling block before and after its impact on the ground.

Motion of a rock at bouncing is mainly observed to analyze restitution (repulsive) coefficients and velocity energy ratio. In DDA rock-fall simulation, mass density, elastic modulus and Poisson's ratio are used as input parameters. In addition, viscous damping coefficient and velocity energy ratio to control the bouncing motion and rolling of rock-fall are required in DDA. Energies are assessed by measuring both rotational and translational block velocities, slope inclination and sizes of the block at impact.

When a block drops on a ground, it bounces and settles with energy loss. This energy loss phenomenon can be modeled by Restitution coefficient (Rn: normal direction, Rt: tangential) and velocity energy ratio (γ) as shown in Fig. 5 that are defined on the basis of the repulsion between falling rock and slopes. Since the velocity is a vector, it is direction dependent. As discussed above (Section 2.2.2), this energy loss may be modeled by viscous effects.

Many experiments of rock-fall in-situ have been reported and their parameters have changed on each site [10]. The magnitude of change for this parameter have yet been unknown. We still are under investigation with recorded data for falling rocks in field experiments.

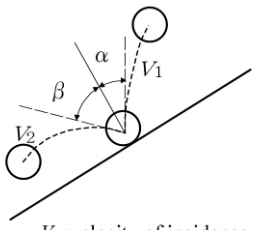

V_1:velocity of incidence
V_2:velocity of reflection
α:angle of incidence
β:angle of reflection

$$\gamma = \frac{1/2\, mV_2^2}{1/2\, mV_1^2} = \frac{V_2^2}{V_1^2}$$

$$Rn = \frac{V_2 \cos\beta}{V_1 \cos\alpha}$$

$$Rt = \frac{V_2 \sin\beta}{V_1 \sin\alpha}$$

Fig. 6 Definitions for velocity energy ratio

2.6. (Additional discussion) VISCOUS DAMPING AT BLOCK CONTACT

It is an important issue to discuss whether DDA can simulate earthquake response of (rock) structures like as FEM. In FEM analysis it is conventional to prevent the reflection of seismic waves from the boundary to the soil mass in the analysis area by using dash-pot damping elements as shown in Figure 1. We therefore introduce Voigt-type viscous damping elements between blocks as shown in Figure 2.

DDA was formulated by defining penalty parameters for the normal direction K_n and the shear direction K_s. we also introduced parameters for the normal damping η_{pn} and the shear damping η_{ps} based on the original DDA theory. In the case of Voigt-type damping, the penetration d and the velocity strain $d/\Delta t$ are expressed by:

$$f_t = f_p + f_\eta = pd + \eta_p \cdot \dot{d} = pd + \eta_p \frac{d}{\Delta t} \tag{23}$$

The total reaction force of the penetration f_t is expressed as the summation of the force by penalty f_p and the force by dash pot f_η as follows:

$$f_t = f_p + f_\eta = pd + \frac{\eta_p}{\Delta t} d = (p + \frac{\eta_p}{\Delta t}) d \tag{24}$$

The potential energy of the penetration between blocks considering contact viscous damping is expressed by:

$$\Pi_{p\eta} = f_t d = \frac{1}{2}(p + \frac{\eta_p}{\Delta t}) d^2 \tag{25}$$

As a result, the penalty value is expressed by the function of the penalty, the viscose dumping coefficient, the penetration displacement and time increment as shown in Eq. (25). This formula automatically introduces the influence of the velocity of penetration, and this scheme can save the surplus penetration.

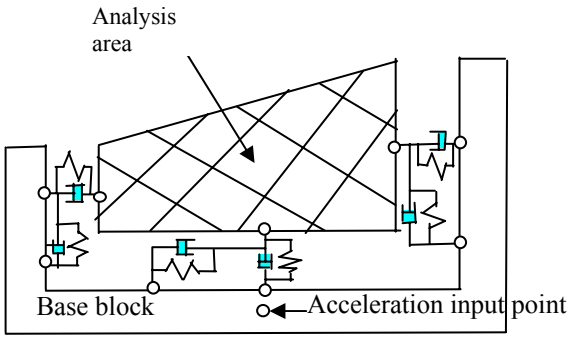

Fig. 7. Boundary conditions for earthquake response analysis

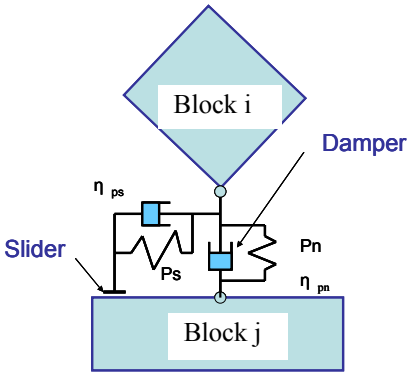

Fig. 7. Voigt-type viscous damping of friction

3. CONCLUSIONS

The Japanese research group has been working on studies of the DDA and Manifold method in terms of its application to actual problems since 1991. Some of the discussion results in our group were shown in this paper. Many problems are still left unsolved when we try to use DDA in practical application.

Here, we introduced a discussion of the parameters for calculation with a focus purely on numerical stability. We will examine the above problems in the future with some example calculation and application.

REFERENCES

1. Monma K., Chida Y., Ma G-C., Shinji M. and Ohnishi Y. (2004): Study on the application of DDA to evaluate the mechanism of rock slope instability, Proc. JSCE, No-III, 2004
2. Shi G.H. 1989: Block system modeling by discontinuous deformation analysis, *Univ. of California*, Berkeley, Dept. of Civil Eng. August.
3. Hatzor Y.H., A.A. Arzi and M. Tsesarsky. 2002. Realistic dynamic analysis of jointed rock slopes using DDA, *Proc. of ICADD-5*, pp. 47–56, BALKEMA.
4. Sasaki T., et al. 2004. Earthquake response analysis of a rock falling model by Discontinuous Deformation Analysis, In *Proceedings of the ISRM Symposium 3rd Asia Rock Mechanics Symposium*, *Kyoto, 1-3 December 2004*, eds. Y. Ohnishi et al., pp. 1267–1272, Millpress.
5. Shinji, M., Ohno, H., Otsuka, Y. and Ma, G. (1997): Viscosity coefficient of the rock fall simulation, ICADD-2, Kyoto, Japan
6. Wang, C-Y., Chuang, C-C. and Sheng, J. (1996): Time integration theories for the DDA method with FE meshes, ICADD-1, Berkeley, Calif., TSI Press.
7. O'Sullivan, C. and Bray, J.D. (2001): A comparative evaluation of two approaches to discrete element modeling to particulate media, ICADD-4, Glasgow, Scotland
8. Tsesarsky, M. (1994): Stability of underground openings in stratified and jointed rock, Ph. D Dissertation, Ben Grion Univ., Israel
9. Wu, J-H (1994): Application of DDA, Ph. D Dissertation, Kyoto Univ., Japan
10. Shimauchi, T., Sakai, N., Ohnishi, Y. and Nishiyama, S.(2004):Safety assessment of rock slope by discontinuous analyses considering impact angle, Third Asian Rock Mech. Symposium, Kyoto, Japan